TECHNISCHE UNIVERSITÄT MÜNCHEN

Physik Department
Lehrstuhl für Funktionelle Materialien E13

Forschungs-Neutronenquelle Heinz Maier-Leibnitz

Coupled Neutronics and Thermal Hydraulics of High Density Cores for FRM II

Harald Breitkreutz

Vollständiger Abdruck der von der Fakultät für Physik der Technischen Universität München zur Erlangung des akademischen Grades eines

Doktors der Naturwissenschaften (Dr. rer. nat)

genehmigten Dissertation.

Vorsitzender: Univ.-Prof. Dr. W. Weise

Prüfer der Dissertation:
1. Univ.-Prof. Dr. Winfried Petry
2. Univ.-Prof. Rafael Macián-Juan, Ph.D.

Die Dissertation wurde am 28. Februar 2011 bei der Technischen Universität München eingereicht und durch die Fakultät für Physik am 4. März 2011 angenommen.

Die Mehrheit bringt der Mathematik Gefühle entgegen, wie sie nach Aristoteles durch die Tragödie geweckt werden sollen, nämlich Mitleid und Furcht. Mitleid mit denen, die sich mit der Mathematik plagen müssen, und Furcht: daß man selbst einmal in diese gefährliche Lage geraten könne.

Paul Epstein (1883 - 1966)

Alles was lediglich wahrscheinlich ist, ist wahrscheinlich falsch.

René Descartes

Abstract

According to the 'Verwaltungsvereinbarung zwischen Bund und Land vom 30.5.2003' and its updating on 13.11.2010, the *Forschungs-Neutronenquelle Heinz Maier-Leibnitz*, FRM II, has to convert its fuel element to an uranium enrichment which is significantly lower than the current 93%, in case this is economically reasonable and doesn't impact the reactor performance immoderate. In the framework of this conversion, new calculations regarding neutronics and thermal hydraulics for the anticipated core configurations have to be made.

The computational power available nowadays allows for detailed 3D calculations, on the neutronic as well as on the thermal hydraulic side. In this context, a new program system, 'X^2', was developed. It couples the Monte Carlo code MCNPX, the computational fluid dynamics code CFX and the burn-up code sequence MONTEBURNS. The codes were modified and extended to meet the requirements of the coupled calculation concept.

To verify the new program system, highly detailed calculations for the current fuel element were made and compared to simulations and measurements that were performed in the past. The results strengthen the works performed so far and show that the original, conservative approach overestimates all critical thermal hydraulic values. Using the CFD software, effects like the impact of the combs that fix the fuel plates and the pressure drop at the edges of the fuel plates were studied in great detail for the first time.

Afterwards, a number of possible new fuel elements with lower enrichment, based on disperse and monolithic UMo (uranium with 8 wt.-% Mo) were analysed. A number of straight-forward conversion scenarios was discussed, showing that a further compaction of the fuel element, an extended cycle length or an increased reactor power is needed to compensate the flux loss, which is caused by the lower enrichment. This flux loss is in excess of 7%. The discussed new fuel elements include a 50% enriched disperse UMo core with different densities at two reactor power levels, and two 40% enriched monolithic UMo cores, one with flat plates and one with plates that have a thickness gradient. Again, two different power levels were regarded.

To estimate the uncertainty of the performed calculations, a sensitivity analysis was conducted. This includes results of neutronics, burn-up and thermal hydraulics. The identified uncertainties are generally quite small.

Zusammenfassung

Die „Verwaltungsvereinbarung zwischen Bund und Land vom 30.5.2003“ und deren Fortschreiben zum 13.11.2010 fordern eine Senkung der Anreicherung des im Brennelement der *Forschungs-Neutronenquelle Heinz Maier-Leibnitz*, FRM II, verwendeten Urans von derzeit 93% auf ein geringeres Level, sofern dies ökonomisch vertretbar ist und die Performance des Reaktors nicht über die Maßen beeinträchtigt. Im Rahmen dieses Konversionsprogrammes müssen neue, gekoppelte Berechnungen für die Neutronik und die Thermohydraulik der möglichen zukünftigen Kerne durchgeführt werden.

Die heute verfügbare Rechenleistung erlaubt es, detaillierte dreidimensionale Berechnungen, sowohl für die Neutronik als auch für die Thermohydraulik, durchzuführen. In diesem Zusammenhang wurde das Programmsystem „X^2 “ entwickelt, das den Monte Carlo-Neutronikcode MCNPX, den numerischen Strömungsmechanikcode CFX und den Abbrandcode MONTEBURNS koppelt. Die genannten Codes wurden modifiziert und erweitert um den Anforderungen des gekoppelten Konzeptes zu genügen.

Zur Verifizierung des neuen Programmsystemes wurden detaillierte Berechnungen für das gegenwärtige Brennelement durchgeführt und mit den aus früheren Rechnungen und Messungen verfügbaren Ergebnissen verglichen. Die Ergebnisse bestätigen die bisher durchgeführten Arbeiten und zeigen, dass die ursprüngliche, konservative Vorgehensweise alle kritischen thermohydraulischen Parameter überschätzt. Zudem wurden erstmals detailliert die Effekte der Kämme, die die Brennstoffplatten fixieren und die Druckverhältnisse an den Kanten der Brennstoffplatten untersucht.

Darauf aufbauend wurde eine Anzahl möglicher neuer Brennelemente mit einer geringeren Anreicherung untersucht. Als Brennstoffe wurde UMo, Uran mit 8 Gew.-% Molybdän, in disperser und in monolithischer Form verwendet. Aus der Diskussion einiger direkte Konversionsszenarien ergab sich, dass eine weitere Kompaktierung des Brennelements, eine Verlängerung der Zyklusdauer oder eine erhöhte Reaktorleistung nötig sind um den durch die geringere Anreicherung bedingten Flußverlust zu kompensieren. Die berechneten Verluste betragen minimal 7%. Die in diesem Rahmen diskutierten Brennelementkonfigurationen beinhalten Kerne mit 50%ig angereichertem dispersen U8Mo, für das zwei unterschiedliche Dichten und zwei verschiedene Reaktorleistungen betrachtet wurden, und Kerne mit 40%ig angereichertem monolithischen U8Mo. Hier wurden ein Platte konstanter und eine Platte variabler Dicke untersucht, letztere ebenfalls für zwei verschiedene Reaktorleistungen.

Eine Sensitivitätsanalyse wurde durchgeführt um die Unsicherheiten der Berechnungen abschätzen zu können. Diese Analyse schließt sowohl die Neutronik, als auch den Abbrand und die Thermohydraulik ein. Die ermittelten Unsicherheiten sind vergleichsweise gering.

Contents

Abstract I

1 General Conditions 1
1.1 Basic Properties of the Current Fuel Element of FRM II . . . 1
1.2 Conversion to Uranium with 50% Enrichment or less . . . 4
1.3 This Work . . . 4
1.3.1 Choice of Codes . . . 4

I Neutronics 7

2 Basics of Monte Carlo Calculations 9
2.1 Fundamental Terms . . . 10
2.2 Interactions . . . 11
2.2.1 Choice of Interaction . . . 11
2.3 Cross Sections . . . 12
2.3.1 Scattering Cross Sections . . . 12
2.3.2 Unresolved Resonances . . . 14
2.3.3 Absorption . . . 15
2.3.4 Temperature Adjustment in MCNP . . . 15
2.4 Variance Reduction . . . 16
2.5 Uncertainties in Monte Carlo Calculations . . . 17
2.5.1 Statistical Tests . . . 17
2.5.2 Uncertainty of k_{eff} . . . 21
2.5.3 Source Entropy . . . 22
2.5.4 Uncertainty of other Quantities . . . 23
2.5.5 Perturbation Theory in Monte Carlo Calculations . . . 23
2.6 Particle Production . . . 27
2.6.1 Production of Prompt Particles . . . 27
2.6.2 Delayed Particle Production . . . 28
2.6.3 Photon Physics . . . 28

3 Cross Sections 29
3.1 Used NJOY Modules . . . 30
3.2 Uncertainties . . . 31

4 Burn-Up 33
4.1 Burn-up Equations . . . 33
4.2 Burn-Up Code System . . . 34
4.2.1 Cinder90 . . . 34
4.2.2 MonteBurns / Origen 2.2 . . . 35

4.2.3 Implementation . . . 35
4.3 Materials . . . 36
4.4 Uncertainty Propagation . . . 37
4.4.1 Equations . . . 37
4.4.2 Algorithm . . . 40
4.4.3 Uncertainty treatment in X^2 . . . 41

II Thermal Hydraulics 43

5 Heat Conduction in Solids 45
5.1 The Diffusion Equation . . . 45
5.2 Implementation in CFX . . . 46

6 Classical Consideration 47
6.1 Calculation of Basic Quantities and Ratios . . . 47
6.2 Heat Transfer . . . 50
6.3 Safety Margins . . . 51
6.3.1 Onset of Nucleate Boiling . . . 52
6.3.2 Departure from Nucleate Boiling . . . 52
6.3.3 Onset of Flow Instability . . . 52
6.3.4 Implementation in CFX . . . 53

7 Fluid Mechanics 55
7.1 Fundamentals . . . 55
7.1.1 Continuity Equation . . . 55
7.1.2 Navier Stokes Equation . . . 56
7.1.3 Energy Equation . . . 57
7.1.4 Unification . . . 60
7.1.5 Initial and Boundary Conditions . . . 60
7.1.6 Dimensionless Form . . . 61
7.2 Turbulence . . . 61
7.2.1 Fundamental Equations . . . 61
7.2.2 Turbulence Models . . . 63
7.2.3 Turbulence Wall Modeling . . . 67
7.3 Implementation in the CFX Solver . . . 71
7.3.1 Calculation of Special Terms . . . 71
7.3.2 General Solution Strategy . . . 73
7.4 Transient simulations . . . 75

8 Multiphase CFD – Subcooled Boiling 77
8.1 Correlations . . . 77
8.1.1 Wall . . . 77
8.1.2 Fluid . . . 79
8.2 Possible Implementation . . . 81

III Coupling of Codes, Application 83

9 Neutronic Modelling 85
9.1 The MCNPX Model . . . 85
9.1.1 Modelling of Involutes . . . 86
9.1.2 Averaging of Built-in Components and Loss Mechanisms . . . 87
9.2 Meshes . . . 90

9.2.1 Tallied Quantities . . . 90
9.2.2 Mesh resolution . . . 90
9.3 Burn-up zones . . . 93
9.3.1 Control rod . . . 93

10 Thermal Hydraulic Modelling 95
10.1 Modelling in Ansys CFX . . . 96
10.1.1 Mesh Generation . . . 97
10.1.2 Estimation of Turbulence Parameters . . . 99
10.1.3 Boundary Conditions . . . 100
10.1.4 Interfaces . . . 100
10.1.5 Heat Sources and Transfer . . . 101
10.1.6 Flow and Material Properties . . . 102
10.1.7 Initial Conditions . . . 105
10.2 Geometry Modifying Operations . . . 107
10.2.1 Growth of the Oxide-Layer . . . 107
10.2.2 Swelling . . . 108
10.2.3 Thermal Expansion . . . 108
10.3 Convergence Criteria for the Solver . . . 109

11 Coupling of Codes: The X^2 Program System 111
11.1 Implementation . . . 111
11.1.1 Itinerary . . . 111
11.1.2 Plausibility Checks . . . 112

12 Error Sources 115
12.1 Monte Carlo Error Sources . . . 115
12.1.1 Numerical Errors . . . 115
12.1.2 Software Errors . . . 116
12.1.3 Modelling Errors . . . 116
12.1.4 User Errors . . . 116
12.2 CFD Error Sources . . . 116
12.2.1 Numerical Errors . . . 116
12.2.2 Modelling Errors . . . 118
12.2.3 User Errors . . . 118
12.2.4 Application Uncertainties . . . 118
12.2.5 Software Errors . . . 118
12.3 Errors Introduced by X^2 . . . 118
12.3.1 Model Construction . . . 118
12.3.2 Data Transfer . . . 119

IV Results 121

13 General Results 123
13.1 Effect of the Sieve . . . 124
13.2 Effect of Combs . . . 127
13.2.1 Development of a Kármán Vortex Street . . . 127
13.2.2 Inlet Above the Fuel Plates . . . 128
13.2.3 Outlet Below the Fuel Plates . . . 130
13.3 3D Heat Conduction . . . 132
13.4 Flow Profile in Corners . . . 136
13.5 Mixing of Stream Filaments . . . 136
13.6 Pressure Profile . . . 137

13.6.1 Influence of Pressure Profile on Boiling . . . 139
13.7 Burnup of the Beryllium Follower of the Control Rod . . . 141
13.8 Mesh Quality Analysis . . . 142
13.8.1 First Node Distance y^+ . . . 142
13.8.2 Aspect Ratio . . . 143
13.8.3 Face Angles . . . 143
13.8.4 Other Quantities . . . 143

14 Results for the Current Fuel Element 145
14.1 Burn-Up . . . 148
14.1.1 Actinide Inventory at EOL . . . 150
14.1.2 Non-Actinide Inventory at EOL . . . 150
14.1.3 Boron Ring . . . 150
14.2 Power Deposition . . . 152
14.2.1 Begin of Life . . . 152
14.2.2 End of Life . . . 152
14.3 Flux . . . 155
14.3.1 Begin of Life . . . 155
14.3.2 End of Life . . . 155
14.4 Pressure Drop . . . 160
14.5 Temperatures . . . 160
14.5.1 Begin of Life . . . 160
14.5.2 End of Life . . . 162
14.6 Heat Flux . . . 166
14.6.1 Begin of Life . . . 166
14.6.2 End of Life . . . 166

15 Results for a Disperse UMo Fuel Element 169
15.1 Design of the Fuel Plates . . . 170
15.2 Control Rod Reactivity Profile . . . 170
15.3 Burn-up . . . 171
15.3.1 Actinide Inventory . . . 173
15.3.2 Non-Actinide Inventory at EOL . . . 175
15.3.3 Boron Ring . . . 175
15.4 Power Deposition . . . 175
15.4.1 Begin of Life . . . 175
15.4.2 End of Life . . . 175
15.5 Flux . . . 176
15.5.1 Begin of Life . . . 176
15.5.2 End of Life . . . 178
15.6 Pressure Drop . . . 180
15.7 Temperatures . . . 180
15.7.1 Begin of Life . . . 180
15.7.2 End of Life . . . 182
15.8 Heat Flux . . . 184
15.8.1 Begin of Life . . . 184
15.8.2 End of Life . . . 184
15.9 Distance to Boiling . . . 185
15.10 Final Assessment . . . 186
15.10.1 Possible Optimisation . . . 187

16 Results for a Monolithic Fuel Element 189
16.1 Fuel plate design . . . 190

16.2 Control Rod Reactivity profile . . . 191
16.3 Burn-up . . . 192
16.3.1 Actinide Inventory at EOL . . . 193
16.3.2 Non-Actinide Inventory at EOL . . . 194
16.3.3 Boron Ring . . . 194
16.4 Power Deposition . . . 194
16.4.1 Begin of Life . . . 194
16.4.2 End of Life . . . 194
16.5 Flux . . . 197
16.5.1 Begin of Life . . . 197
16.5.2 End of Life . . . 197
16.6 Pressure Drop . . . 202
16.7 Temperatures . . . 202
16.7.1 Begin of Life . . . 202
16.7.2 End of Life . . . 202
16.8 Heat Flux . . . 204
16.8.1 Begin of Life . . . 204
16.8.2 End of Life . . . 204
16.9 Flat Plate . . . 205
16.10 Final Assessment . . . 207
16.10.1 Possible Optimisation . . . 207

17 Sensitivity Analysis: Uncertainty Estimation 209
17.1 Thermal Hydraulic Calculations . . . 209
17.1.1 Influence of Wall Roughness . . . 209
17.1.2 Influence of Turbulence Modelling . . . 210
17.1.3 Influence of Meshes . . . 214
17.1.4 Influence of Viscous Dissipation . . . 215
17.1.5 Influence of Buoyancy . . . 215
17.1.6 Influence of Total Reactor Power . . . 215
17.1.7 Influence of Inlet Parameters . . . 217
17.1.8 Influence of Gamma-heating in Structural Materials . . . 218
17.1.9 Influence of SST Turbulence Model Curvature Correction . . . 220
17.1.10 Overview / Sensitivity Matrix . . . 221
17.2 Burn-Up . . . 221
17.2.1 Control Rod Movement . . . 221
17.2.2 Number of Predictor Steps in MonteBurns . . . 222
17.2.3 Fuel Composition . . . 222

18 Verification 227
18.1 Neutronic Model . . . 227
18.2 NBK . . . 227
18.2.1 Assessment . . . 231
18.3 COMSOL Multiphysics . . . 232
18.3.1 Model Set-up . . . 232
18.3.2 Results . . . 234
18.3.3 Assessment . . . 238
18.4 X^2 . . . 240

19 Conclusions and Outlook 241
19.1 Summary . . . 241
19.2 Outlook . . . 245
19.3 Conclusion . . . 245

V Appendix 247

A Geometrical and Mathematical Considerations on Involutes 249
A.1 Basic Considerations . . . 249
A.1.1 Basic Equations . . . 249
A.1.2 Intersection Points . . . 250
A.2 Coordinate System for Involutes . . . 250
A.2.1 Definition . . . 250
A.2.2 Special Quantities and Operators . . . 251
A.2.3 Special Curves . . . 253
A.3 Special Formulas . . . 254
A.3.1 Integral Values . . . 254

B Modifications to existing codes 257
B.1 MCNPX . . . 257
B.2 MonteBurns . . . 257
B.3 Origen2 . . . 258
B.4 CFX . . . 258
B.5 ENDF2ACE . . . 258

C X^2 Program Flow 259
C.1 Initialisation Phase . . . 261
C.1.1 Reactivity Profile . . . 261
C.2 Main Program Modules . . . 264
C.2.1 Burn-up Run . . . 264
C.2.2 Temperature Convergence . . . 264
C.3 Further Information . . . 265

D X^2 User Guide 267
D.1 Model Creation Advise . . . 267
D.1.1 MCNPX . . . 267
D.1.2 CFX . . . 270
D.1.3 CFX-Pre . . . 271
D.1.4 CFX Solver . . . 273
D.1.5 CFX Post . . . 273
D.1.6 X^2 . . . 273
D.1.7 Including an Oxide Layer . . . 273
D.2 Execution . . . 274
D.2.1 Prerequisites . . . 274
D.2.2 Automatic Execution via X^2 . . . 274
D.2.3 Manual Execution . . . 275

E Definitions, Nomenclature 277

F Tables and Figures 279
F.1 Data on Chemical Media . . . 279
F.1.1 Current Fuel Eelement . . . 279
F.2 Burn-up sets . . . 280
F.3 NJOY Module Sequences . . . 281
F.3.1 Normal Cross Section . . . 281
F.3.2 $S(\alpha, \beta)$ . . . 282
F.4 CFX Mesh Sensitivity Analysis . . . 284

Indices 291

Table of Symbols 291
Table of Abbreviations 297
List of Figures 299
List of Tables 303
Own Bibliography 305
Bibliography 307
Acknowledgment 319
Index 321

CHAPTER 1

General Conditions

1.1 Basic Properties of the Current Fuel Element of FRM II

The design of the current fuel element of FRM II is based on considerations and experiences that have been made with the fuel elements of HFR at the *Institut Laue-Langevin* in Grenoble and HFIR at *Oak Ridge National Laboratory*. Its design is the result of a long series of optimization processes [Röh91a] and safety evaluations [Röh84, Död89, Död95]. It is optimized for a high thermal neutron flux outside the fuel element. The reactor is operated at a thermal power of 20 MW, with an operating range of 60 d. With an undisturbed maximum neutron flux of $8.0 \cdot 10^{14}\,{}^{\mathrm{n}}/_{\mathrm{s\,cm^2}}$, the FRM II has the highest flux-to-power ratio in the world. The FRM II is a light water cooled, light- and heavy-water moderated, heavy-water reflected compact core research reactor.

Being a compact core reactor, the FRM II has only one single fuel element. As can be seen from fig. 1.1 and 1.2, the fuel element consists of 113 involute shaped[1] fuel plates with an evolute radius of 64.025 mm that are fixed between two cylindrical ducts with radii 65 mm and 114.5 mm. The fuel plates have a thickness of 1.36 mm, whereof two times 0.38 mm devolve for the cladding and 0.60 mm for the fuel itself. Currently, the fuel is a disperse U_3Si_2 compound in an Al-matrix with an enrichment of 93% and is therefore considered to be highly enriched uranium, HEU. The fuel zone is 70 cm in height, the uranium density $3.0\,{}^{\mathrm{g}}/_{\mathrm{cm^3}}$ in the inner and $1.5\,{}^{\mathrm{g}}/_{\mathrm{cm^3}}$ in the outer region. The complete uranium inventory of the whole core is 8.1 kg.

In-between the fuel plates, 2.2 mm thick cooling channels are embedded. Because of the involute geometry, the width of these channels is constant throughout the whole core. 274.5 kg water per second run through the channels, corresponding to an average flow speed of $15.91\,{}^{\mathrm{m}}/_{\mathrm{s}}$ [Gie96]. On its way through the fuel element, the water heats up by about 16 K.

An overview of the primary circuit is shown in fig. 1.3. It shows the reactor pool and its build-in components. Deep down in the middle of the pool is the heavy water tank with the fuel element in the centre.

[1] Explanations concerning the mathematics of involutes can be found in appendix A, p. 249. Here, a coordinate system specially designed for the involute geometry will be introduced. This coordinate system will be used several times in this work.

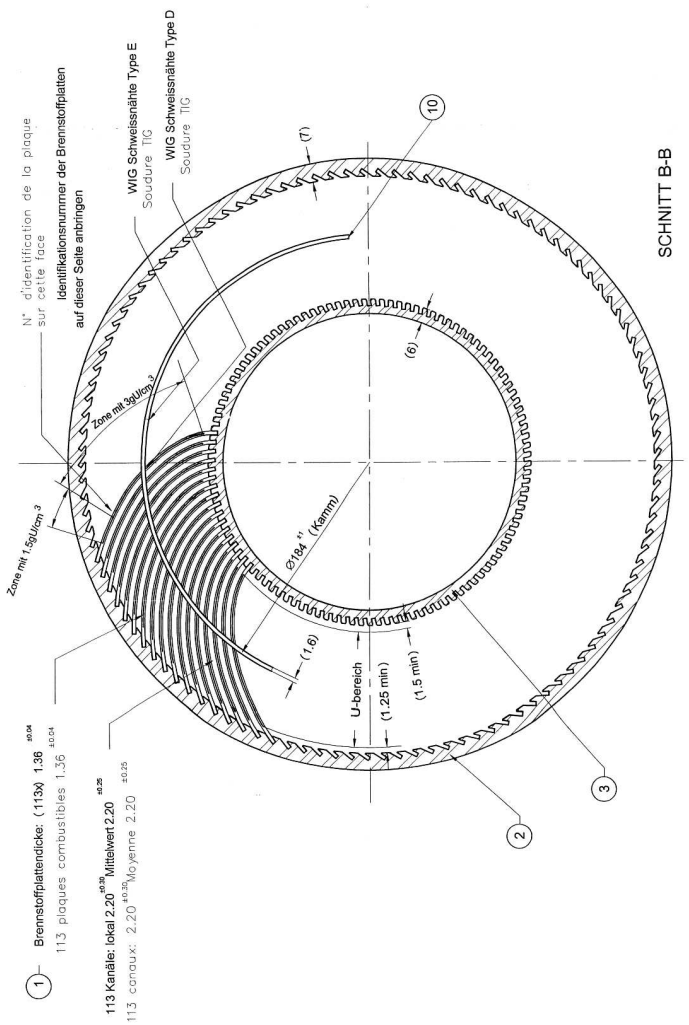

Figure 1.1: *Present fuel element of FRM II, horizontal cut*

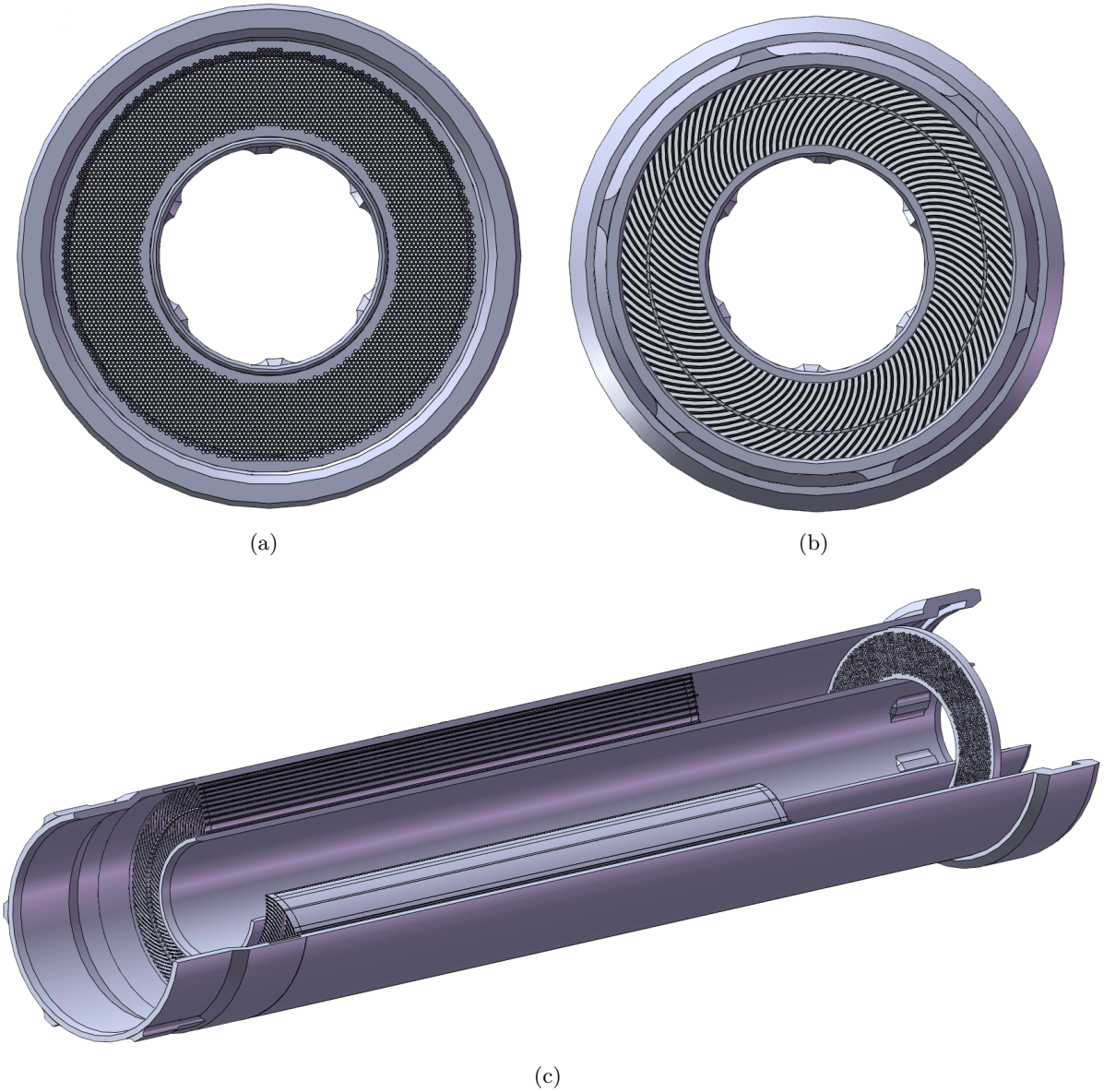

(a) (b)

(c)

Figure 1.2: *Fuel element of FRM II as constructed in SolidWorks for the thermal hydraulic calculations. From above (a), below (b) and a sectional view (c).*

1.2 Conversion to Uranium with 50% Enrichment or less

The nuclear license, 'Dritte Teilerrichtungsgenehmigung', includes a paragraph that requires a substitution of the currently used HEU with a fuel of lower enrichment, as far as this fuel exists. Despite huge worldwide efforts it became clear, that no such fuel will be available until at least 2016. Subsequent licensing of the new fuel element is estimated to need additional two years. The white hope of the scientific community are Uranium-Molybdenum-Alloys (UMo), that can reach uranium densities of up to $15\,\mathrm{g/cm^3}$ in their pure form. Two forms of this fuel are currently under investigation, a disperse form with UMo-grains embedded in an aluminium matrix and a monolithic form. In either case, the outer dimensions of the fuel element must remain unchanged to avoid constructional changes in the surrounding of the reactor core which would require an enormous amount of work, time and money. The general conditions for a conversion are:

- In all aspects, the new core has to be as save as the current one.
- The achievable cycle length must be at least 60 days at 20 MW power (today's value).
- The neutron flux and quality have to be as high as currently (only marginal losses).
- Any conversion to lower enrichment has to be economically reasonable, i. e. operation costs increase only marginally.

Much work has been done by Technische Universität München (TUM) and its partners, on the experimental [Röh08, Lee08, Röh07, Jun07, Pal06, Wie06, Bön04] as well as on the theoretical side [Röh06, Röh05] to allow for the conversion of the fuel element. From the calculations performed so far, an achievable degree of enrichement of 50% for the disperse case and 40% for the monolithic case was derived. An extensive list of all work done by TUM and most experiments world wide in this context is given in [Sch10].

1.3 This Work

In this work, scenarios for conversions to 40%- and 50%-enriched fuel are presented and the arising problems are discussed. To calculate these scenarios, a new program system called 'X^2' was developed. A large part of this work will deal with the theory behind it (chapters 2 to 8), describe the programs that are coupled by X^2 and the way this is done (chapters 9 to 11). The current state of the theory is in some parts documented in greater detail, as by today, the field of computational fluid mechanics, especially turbulence modelling, wall effects and multiphase phenomena, is a fast growing and changing field of research.

The current fuel element is calculated for validation purposes. The results of the calculations (chapters 13 to 14) will deal with general problems like pressure distributions, turbulence and the effects of combs and sieves as well as with fuel-specific details like burn-up, neutron fluxes, power densities, wall heat fluxes, temperatures, boiling and other properties concerning the fuel element and the use of the reactor. Several options for a straight-forward conversion to a lower enrichment are discussed in chapters 15 for disperse and in 16 for monolithic UMo. A sensitivity analysis (chap. 17) is performed to assess the uncertainties of the calculations. The thermal hydraulic calculations are compared to results calculated with another CFD code and an older in-house code, NBK (chapter 18).

1.3.1 Choice of Codes

The first preparational phase of this work consisted of choosing appropriate codes for the calculations. Here, only the selection process is described. Details about the codes and implementations can be found in later chapters.

Neutronics

The choice of the neutronics code was rather straightforward. First, it had to be decided whether a deterministic or a Monte Carlo code should be used. As the goal was a full 3D simulation with high detail, a Monte Carlo code was favoured due to the lower computational requirements. From the numerous available codes, MCNP and MCNPX were chosen as they were readily available, have a large user base and are continuously improved. Both codes are used in this work.

Burn-up

Originally, it was planned to use CINDER90, a burn-up code included in MCNPX for the burn-up calculations. However, it turned out during the course of this work, that the computational requirements to use the in-line code were extremely high and, in an earlier stage, the implementation suffered from a number of bugs. It was therefore chosen to use MONTEBURNS, which is a quite old code, but was readily available for use. A future user of the code system might consider switching to another, newer burn-up code.

CFD

The main focus of this work is drawn towards the thermal hydraulic calculations, as for the time being, they provide most room for improvement and optimisation. At the beginning, three codes were selected for a closer inspection: Star-CD, CFX and COMSOL Multiphysics. The former two are finite-volumes codes, the latter is a finite-elements code, which is for example used at Oak Ridge. All three codes are used in the nuclear industry for different purposes. For this work, the final selection was CFX. COMSOL was abandoned due to the excessive computational requirements of finite-elements and the instable solvers (see discussion in chapter 18.3). The manufacturer of Star-CD failed to reply to a number of questions concerning code-capabilities within a reasonable amount of time, so this code couldn't be considered any further. There were already a number of factors pointing towards CFX, especially the usage of the code at neighbouring institutes (GRS, NTech) working on similar projects. So, finally, CFX was chosen to solve the thermal hydraulics.

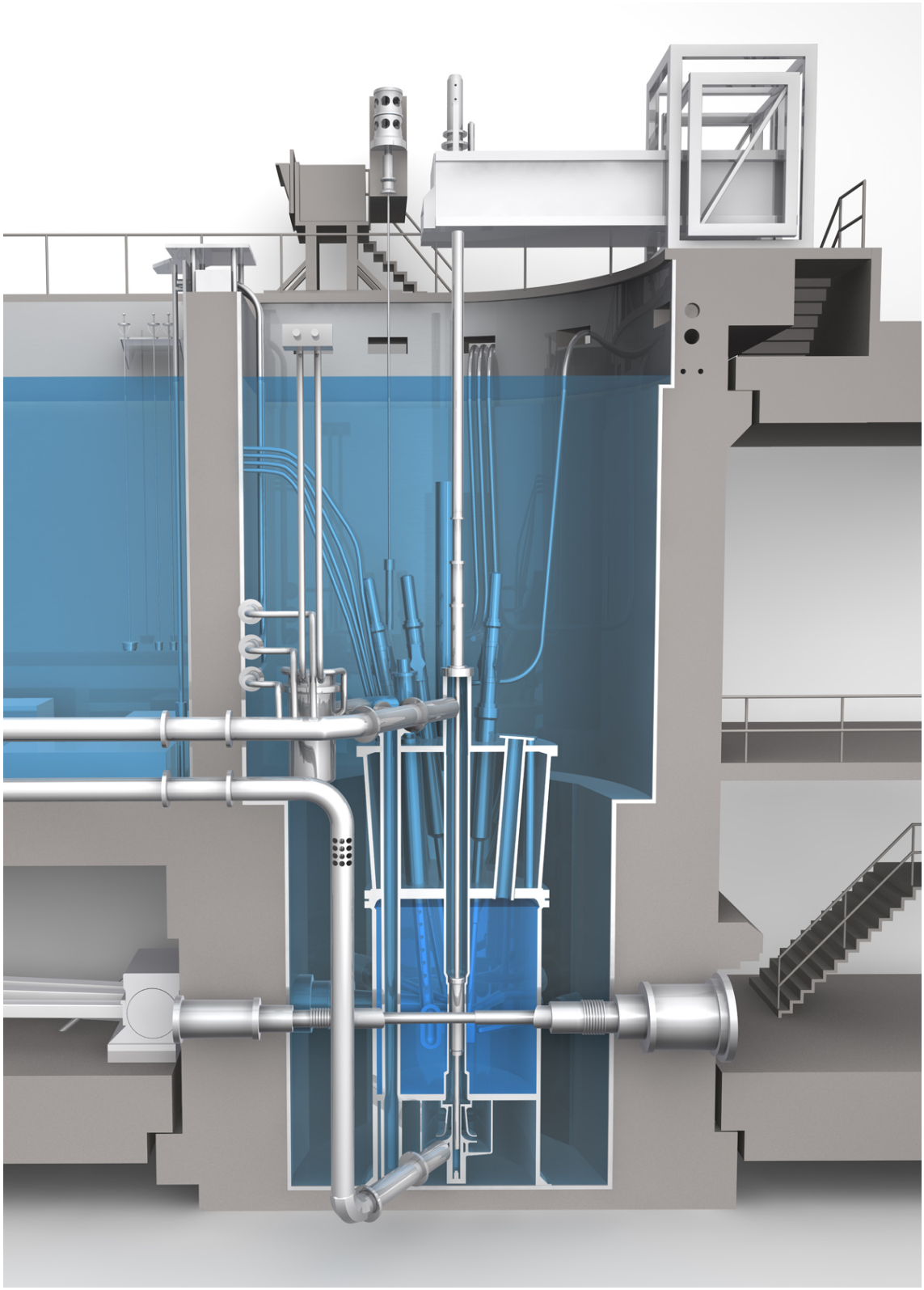

Figure 1.3: *Cut view of FRM II primary circuit. Used with permission of TUM.*

Part I

Neutronics

CHAPTER 2

Basics of Monte Carlo Calculations

Monte Carlo calculations (MCCs) are a possibility to solve the complex steady state transport equations[1] for neutrons

$$\begin{aligned} 0 &= -\Omega\boldsymbol{\nabla}\phi - \Sigma_T\phi + \int_{E'}\int_{\boldsymbol{\Omega}'} \Sigma_S(E', \boldsymbol{\Omega}' \to E, \boldsymbol{\Omega})\phi(\boldsymbol{r},E,\boldsymbol{\Omega}')\,\mathrm{d}E'\,\mathrm{d}\boldsymbol{\Omega}' \\ &\quad + \frac{1}{4\pi}\chi(E)\int_{E'}\int_{\boldsymbol{\Omega}'} \Sigma_f(E')\nu(E')\phi(\boldsymbol{r},E,\boldsymbol{\Omega}')\,\mathrm{d}E'\,\mathrm{d}\boldsymbol{\Omega}', \end{aligned} \tag{2.1}$$

photons and all other particles that do not influence each other[2]. By implementing the relevant physics in the code and modelling the given geometry, specifying the needed material properties and tracking the behaviour of single particles, the solution of the equation is obtained without ever getting in touch with the equation itself and without implementing the equation in the code. If sufficient particles are tracked, the central limit theorem leads to a picture quite close to reality within the limits of statistics. MCCs are therefore not deterministic but stochastic methods. Due to this stochastic behaviour and the computational expense directly connected with this, MCCs are a kind-of 'method of last resort', to be used when deterministic calculations are no more possible or not appreciated.

Quite often the somewhat oblique statement is made that MCCs would solve the integral transport equations

$$\phi(\boldsymbol{r},E,\boldsymbol{\Omega}) = \int_{R'=0}^{\infty} Q(\boldsymbol{r} - R'\boldsymbol{\Omega},E,\boldsymbol{\Omega}) \cdot \mathrm{e}^{-\int_{R''=0}^{R'} \Sigma_T(\boldsymbol{r}-R''\boldsymbol{\Omega},E)\,\mathrm{d}R''}\,\mathrm{d}R' \tag{2.2}$$

$$Q(\boldsymbol{r},E,\boldsymbol{\Omega}) = \int_{E'}\int_{\boldsymbol{\Omega}'} \Sigma_S(E', \boldsymbol{\Omega}' \to E, \boldsymbol{\Omega})\phi(\boldsymbol{r},E,\boldsymbol{\Omega}')\,\mathrm{d}E'\,\mathrm{d}\boldsymbol{\Omega}' \tag{2.3}$$

$$+\frac{1}{4\pi}\chi(E)\int_{E'}\int_{\boldsymbol{\Omega}'} \Sigma_f(E')\nu(E')\phi(\boldsymbol{r},E,\boldsymbol{\Omega}')\,\mathrm{d}E'\,\mathrm{d}\boldsymbol{\Omega}' \tag{2.4}$$

while discrete ordinate methods (DOMs) would solve their integro-differential form as given in eq. 2.1. This statement is based on the fact that MCCs do not use any space- or time-derivatives. But nor are the equations 'solved' in a classical sense, neither are they solved numerically. Anyway, it should be noted that both forms are just different representations of one and the same equation [Eme82, p. 325]. If one is solved, the other is solved, too. But as MCCs in contrast to DOMs do not need to discretise phase space, no weighting and averaging procedures are needed. In particular, this renders possible very detailed representations of geometry and physics which makes it possible for MCCs notwithstanding the mentioned computational effort to solve even the most complicated geometrical problems where classical calculation

[1] There are MCCs that can be used for time-dependent problems, too, but these are not in the scope of this work.

[2] MCCs using MCNP(X) are also carried out for charged particles like electrons and protons under the assumption that the density of these particles is low enough for the particles not to influence each other.

schemes would have surrendered long ago.

In MCCs, single events like scattering and absorptions are modelled with random numbers, whose appearance is correlated with the underlying probability densities. How this is done in detail is discussed in chapter 2.2.[3] An extensive discussion on the general theory of Monte Carlo calculations can be found in [Rub08, Gen03, Lem09].

In this work, the Monte Carlo codes MCNP5 [X-505] by LOS ALAMOS NATIONAL LABORATORY and MCNPX 2.6 [Pel08] are used, as well as a beta-version of MCNPX, v2.7b.

2.1 Fundamental Terms

Before explaining the principle of operation of the Monte Carlo Codes, some basic terms have to be introduced:

Cell: A geometry unit of nearly arbitrary form and complexity, consisting of one single material. The complete geometry of the problem is decomposed into cells and surfaces, where the former is described by the latter.

Cell-Importance ω: A cell can have a weight assigned. This weight is called 'importance' and specifies how important a specific cell is considered to be. In combination with variance reduction techniques, it can be used to turn attention on specific parts of the geometry.

Criticality cycle: In criticality calculations (*KCODE calculations*), MCNP works in so called cycles. Every cycle starts with a certain distribution of source points, a selection of the fission points of the preceding cycle. In every cycle, a given number of histories is calculated. If a particle initiates a fission, no fission is done but the point is saved as a source point for the next cycle.[4] [5] MCNPX distinguishes active and inactive cycles. The former ones are only used to generate a sufficiently good source distribution (see chapter 2.5.3, p. 22), the latter ones are used to calculate the desired results.

History: 'Destiny' of a particle, from the source to its end. Because of variance reduction, one history can include several particle →tracks.

Mesh tally: A mesh tally is a →tally (detector) that is superimposed on and independent of the geometry, while a normal tally is always connected to one or more cells and therefore depends on the geometry.

Particle weight W: Every tracked particle is assigned a weight W. This weight has no bearing on its physical mass but takes the function of a weighting factor when results of any kind are calculated. The weight of a particle is changed by variance reduction techniques (see chap. 2.4, p. 16).

Segment: A segment is a part of a particle →track.

Tally: A tally is a virtual detector. Unlike DOMs, MCCs do not have a grid on which calculations are performed and where information about the phase space is stored for any point. Hence, it has to be specified which information should be stored ('tallied') for which region.

Track: Path of one part of a particle, from its beginning to its end. If particles aren't split, a track is the same as the history.

In the following sections, some of the basic MC principles are discussed. Understanding them is important to be able to judge the reliableness of the results obtained from MCCs.

[3] Based on this analogy on throwing a dice, the name of the method — 'Monte Carlo' - was chosen.
[4] This behaviour is necessary to be able to simulate sub- and supercritical systems.
[5] The number of saved source points is not fixed but moves in a certain interval. If the number of source points grows too large, a pre-selection is done.

2.2 Interactions

The following section is dedicated to introduce the reader into the Monte Carlo principle and some of the techniques used in the codes. It describes how interactions are modelled using random numbers, how cross sections are treated in some special energy ranges and how the code accounts for temperature changes of cross sections. This is surely only a small extract from the theory of Monte Carlo modelling, the documentation of which is not the aim of this thesis. Besides the MCNP documentation [X-505], in-depth information can be found for example in [Rub08, Gen03, Lem09] and many other works.

2.2.1 Choice of Interaction

As an example, regard a particle on its way through a cell. It has then to be decided, whether the particle will interact at all, and if so, with which isotope and which kind of reaction. Therefore, let the particle (neutron or photon) of energy E be at position $\boldsymbol{x}_0$. It should move with the positive velocity $v := |\boldsymbol{v}|$ in direction $\boldsymbol{v}/v$. The next border of the current cell X in this direction can be found at $\boldsymbol{x}_1$.

Interaction Probability

The probability for the particle to interact on its way through the medium with total cross section $\Sigma_T(E)$ to this position is given by [6]

$$p = 1 - \mathrm{e}^{-\Sigma_{T,X}(E)|\boldsymbol{x}_0 - \boldsymbol{x}_1|}. \tag{2.5}$$

A random number $0 \leq r < 1$ decides if an interaction takes place ($r \leq p$) or not ($r > p$). If r is substituted for p and l' for $l = |\boldsymbol{x}_0 - \boldsymbol{x}_1|$, then

$$l' = -\frac{1}{\Sigma_{T,X}(E)} \ln(1 - r). \tag{2.6}$$

As $1 - r$ is distributed in the same manner as r, it can be replaced by r to obtain the well known expression

$$l' = -\frac{1}{\Sigma_{T,X}(E)} \ln(r). \tag{2.7}$$

The decision for an interaction is then made with $l' \leq l$. If this condition is met, l' already contains the distance to the point of interaction.

Choice of Isotope

Normally, every cell is made up of one material which consists of several elements and isotopes.[7] So, as a first step of interaction, an interaction partner has to be chosen from the list of isotopes. This is achieved with a random number $0 \leq r < 1$. Let $\Sigma_{T,\mathrm{all}} := \sum_i \Sigma_{T,i}$ be the sum of all macroscopic total cross sections $\Sigma_{T,i}$ of materials i, then the isotope j is chosen for which holds

$$\frac{1}{\Sigma_{T,\mathrm{all}}} \sum_{i=1}^{j-1} \Sigma_{T,i} < r \leq \frac{1}{\Sigma_{T,\mathrm{all}}} \sum_{i=1}^{j} \Sigma_{T,i}. \tag{2.8}$$

[6] The cell is homogeneous in material and temperature.

[7] The nature of the particle decides if one must differentiate between isotopes or if it is sufficient to distinguish elements. For neutrons, single isotopes have to be regarded, where in contrary for photons in most cases elements are sufficient, except for photonuclear interactions.

Choice of Interaction

The cross sections of all interactions are summed up in the total macroscopic cross section. Examples of its constituents can be found in table 2.1.

Symbol	=	specific cross section
Σ_T	=	total cross section
Σ_n	=	elastic scattering
	=	$\Sigma_\mathrm{n,pot} + \Sigma_\mathrm{n,res} + \Sigma_\mathrm{n,int}$
$\Sigma_\mathrm{n,pot}$	=	potential scattering
$\Sigma_\mathrm{n,res}$	=	resonance scattering
$\Sigma_\mathrm{n,int}$	=	interference scattering (between resonance and potential)
$\Sigma_\mathrm{n'}$	=	inelastic scattering
Σ_S	=	total scattering cross section
	=	$\Sigma_\mathrm{n} + \Sigma_\mathrm{n'}$
Σ_A	=	absorption
	=	$\Sigma_\mathrm{T} - \sigma_\mathrm{S}$
Σ_γ	=	emission of a γ ray: (n,γ) process
Σ_p	=	proton emission: (n,p)
Σ_α	=	emission of an α particle: (n,α)
Σ_2n	=	emission of two neutrons: (n,2n)
Σ_f	=	fission
Σ_X	=	inelastic collision / reaction cross section
	=	$\Sigma_\mathrm{T} - \Sigma_\mathrm{n}$

Table 2.1: *Selection of cross sections for neutrons*

The final choice, which interaction should be performed, is again modelled by a random number. If the individual interactions are consecutively numbered with an index i, the interaction j is chosen for which holds

$$\frac{1}{\Sigma_T}\sum_{i=1}^{j-1}\Sigma_i < r \leq \frac{1}{\Sigma_T}\sum_{i=1}^{j}\Sigma_i. \tag{2.9}$$

2.3 Cross Sections

For the cross sections discussed above, some special cases have to be taken into account. They cannot always be read straight-forward from a library but have to be adjusted to certain conditions.

2.3.1 Scattering Cross Sections

Especially for neutrons with energies below about 4 eV, in the case of scattering on hydrogen for even higher energies, the movement of the atoms of the material the neutrons passes plays a significant role. There are two ways to consider this behaviour:

S(α,β): Thermal Scattering Laws

S(α,β) tables represent the thermal scattering laws to incorporate molecular properties of solid bodies and fluids that go beyond accumulations of single atoms. Use of these libraries is essential especially in problems involving the thermalisation of particles where the neutron is scattered on light particles and incoherent inelastic scattering occurs. In most cases, libraries up to 4 eV are available. Two procedural methods are provided, inelastic scattering (cross section $\sigma_{\mathrm{n}'}$) with correlated energy-angle-distributions on the one hand, elastic scattering (cross section σ_{n}) without influencing the energy of the scattered neutron with an angular treatment derived from lattice parameters on the other hand.

Using the temperature normalized momentum transfer α and the corresponding energy transfer β,

$$\alpha(E,E',\theta) := \frac{E' + E - 2\sqrt{EE'}\cos\theta}{Ak_{\mathrm{B}}T} \tag{2.10}$$

$$\beta(E,E') := \frac{E' - E}{k_{\mathrm{B}}T}, \tag{2.11}$$

the equation for incoherent inelastic scattering is applied:

$$\sigma(E,E',\cos\theta) = \frac{\sigma(T=0)}{2k_{\mathrm{B}}T}\sqrt{\frac{E'}{E}}\exp\left(-\frac{\beta}{2}\right)S(\alpha,\beta)\,. \tag{2.12}$$

E is the energy of the incoming, E' the energy of the outgoing neutrons and θ is the scattering angle. A is the mass number of the scattering nuclide.

Inelastic Scattering: The distribution of secondary energies is represented as a set of equiprobable energy ranges.[8] First, an end energy is selected for a give starting energy $E_i < E < E_{i+1}$:

$$\rho := \frac{E_{i+1} - E}{E_{i+1} - E_i} \tag{2.13}$$

$$p(E'\,|E_i < \xi < E_{i+1}) = \frac{1}{N}\sum_{j=1} N\delta\left[E' - \rho E_{i,j} - (1-\rho)E_{i+1,j}\right], \tag{2.14}$$

where $E_{i,j}$ is the j^{th} discrete end energy for the corresponding starting energy E_i and N the number of equiprobable end energies. For every transition, a set of ν associated scattering angles $\mu = \cos\theta$ exists. With a probability of $1/\nu$ an angle $\mu_{i,j,k}$ is selected and the final scattering angle

$$\mu = \rho\mu_{i,j,k} + (1-\rho)\mu_{i+1,j,k} \tag{2.15}$$

is calculated.

Elastic Scattering: If data is derived from an incoherent approximation, the method described above is applied. For a coherent derivation, a set of parameters D_k is used that is based on Bragg energies E_{Bk} that have been derived from lattice parameters. With $E_{\mathrm{Bk}} < E < E_{\mathrm{Bk}+1}$ and $P_i = D_i/D_k$ (i=1...k) as possibility of scattering from the i^{th} Bragg edge, the scattering angle is

$$\mu = 1 - 2\frac{E_{\mathrm{Bi}}}{E}. \tag{2.16}$$

The elastic scattering treatment is applied with probability $\frac{\sigma_n}{\sigma_n+\sigma_{n'}}$.

[8] Normally, these sets consist of 16 or 32 entries between 10^{-5} eV and 4 eV.

Free Gas Model

If no S(α,β) table for thermal scattering is available, the proper motion of the atoms must be considered elseway. For this, the free gas model is used. The velocity distribution of the atoms $p(v')$ is assumed to be a Maxwellian distribution

$$p(v') = \frac{4}{\sqrt{\pi}}\beta^3 v'^2 \mathrm{e}^{-\beta^2 v'^2} \tag{2.17}$$

with $\beta = \sqrt{AM_n/2k_\mathrm{B}T}$. The relative velocity between the neutron and its interaction partner with scattering angle θ, $v_r := \sqrt{v^2 + v'^2 + 2vv'\cos\theta}$, is used to calculate effective cross sections:

$$\sigma_{\mathrm{S,eff}}(E) = \frac{1}{v}\int\int \sigma_S(v_r) v_r p(v') \mathrm{d}v' \frac{\mathrm{d}\cos\theta}{2}. \tag{2.18}$$

Equation 2.18 corresponds to a probability distribution

$$p(v',\theta) = \frac{1}{2} p(v') \frac{v_r}{v'} \frac{\sigma_S(v_r)}{\sigma_{\mathrm{S,eff}}(E)}. \tag{2.19}$$

However, this calculation is very time or memory consuming and therefore needs to be simplified. For this it is assumed that σ_S varies only weekly with the velocity of the target nucleus.[9] This leads to

$$p(v',\theta) \propto \frac{\sqrt{v^2 + v'^2 + 2vv'\cos\theta}}{v + v'} \left(v'^3 \mathrm{e}^{-\beta^2 v'^2} + v v'^2 \mathrm{e}^{-\beta^2 v'^2} \right). \tag{2.20}$$

The selection of a velocity $\boldsymbol{v}'$ is done as follows:

- A random number $0 \leq r < 1$ is generated.
- With $y := v'^2\beta^2$ and $y' := v'\beta$, a velocity is sampled from

$$p'(v') = \begin{cases} y\mathrm{e}^{-y} & r < \left(1 + \frac{\sqrt{\pi}\beta v'}{2}\right)^{-1} \\ \frac{4}{\sqrt{\pi}} y'^2 \mathrm{e}^{-y'^2} & \text{else.} \end{cases} \tag{2.21}$$

- An angle is chosen from $-1 \leq \cos\theta \leq 1$ with a second random number.
- The result is accepted with a probability

$$p'' = \frac{\sqrt{v^2 + v'^2 + 2vv'\cos\theta}}{v + v'}. \tag{2.22}$$

  If not, the calculation is repeated.

2.3.2 Unresolved Resonances

The region of unresolved resonances (10 keV $< E <$ 149.03 keV for ^{235}U, for other nuclides different intervals) is treated with the help of probability tables. The problem consists of continuous cross sections appearing to be smooth functions of energy in certain regions, where resonances are fine and dense and could not be resolved during measurements. Due to the smooth behaviour, in particular self absorption effects are not accounted for properly.

[9] This assumption is only true for light nuclei. For heavy nuclei it is assumed that moderation effects from collisions are weak and therefore the error of the approximation can be neglected.

The technique used is to generate so called probability tables for the cross sections[10] for a given number of energies. From these tables, a value is chosen and then applied to the reaction of the neutron.

The impact of this technique on results is studied in [Mos99]. In most cases, the impact is negligible. This is also true for FRM II.

2.3.3 Absorption

In MCNP(X), two ways of handling absorption exist: analogue and implicit. In the analogous case, the tracked particle is killed with probability σ_A/σ_T, in the implicit case, its weight is reduced and tracking continues.

$$W_{\mathrm{n}'} = \left(1 - \frac{\sigma_{\mathrm{A}}}{\sigma_{\mathrm{T}}}\right) \cdot W_{\mathrm{n}}. \tag{2.23}$$

Implicit tracking is the default case, as especially in regions of low flux and high absorption, from a statistical point of view, particles are too valuable to be lost due to absorption. With implicit tracking, the (theoretical) loss of the particle is represented within its weight, but it is not needed to calculate a new track to explore what would happen to the particle afterwards.

As a special case, a third technique exists, which is a specific occurrence of the 'Exponential Transform' variance reduction (see chapter 2.4).[11] Equation 2.7 is modified to account only for scattering events while absorption is handled implicitly in the particle weight, i. e.

$$l = -\frac{1}{\Sigma_S} \ln(1 - r) \tag{2.24}$$

$$W' = W \mathrm{e}^{-\Sigma_A l}. \tag{2.25}$$

Analogous treatment is chosen to exclude interactions that would dramatically increase calculation times but contribute little to the result and cannot be totally neglected. A good example is the nuclear photo effect in the heavy water tank of FRM II.

2.3.4 Temperature Adjustment in MCNP

MCNP offers the possibility to specify a temperature for a cell. It is important to know that MCNP currently only Doppler broadens the elastic scattering cross section. It does not adjust resolved and unresolved resonance data, nor thermal scattering kernels $S(\alpha, \beta)$ [Bro08, p. 64]. Furthermore, it does not adjust densities of materials. So it is desirable to generate appropriate cross sections outside of MCNP. This is done using NJOY 99 and is described in chapter 3, p. 29.

As generating cross sections 'on the fly' for all needed temperatures is quite time consuming, an approach with pregenerated libraries and *stochastic interpolation* was used for temperature convergence problems. For this, libraries have been compiled at temperature steps of 50 K. This can be regarded as sufficient for the purposes of this work [Con05].

[10] Typically tables exist for elastic scattering, fission, capture and so called 'Near-Total-Cross section', i. e. cross sections nearly identical to the total cross section but without some rare inelastic reactions.

[11] The path length in flight direction $\mu = 1$ is stretched with $p = \Sigma_A/\Sigma_T$.

Weighted Temperatures

Two sets of cross sections, one for T_0 and one for $T_1 > T_0$ are used. Between those, a $\sqrt{T}$-interpolation[12] is used to determine the atomic weights W_i of both datasets:

$$W_1 = \frac{\sqrt{T} - \sqrt{T_0}}{\sqrt{T_1} - \sqrt{T_0}} \tag{2.26}$$

$$W_0 = 1 - W_1. \tag{2.27}$$

However, this is stochastic interpolation and not linear interpolation: From the point of view of a particle during the random walk, it appears as if there are two different materials, two different kind of atoms, which are represented by the two different cross sections for T_0 and T_1 and the related atomic weights W_0 and W_1. Therefore, for an interaction, one of the two datasets for T_0 or T_1 is chosen randomly (see chapter 2.2.1, p. 11, 'Choice of Isotope'). This will cause differences from the real case, where there would be only one material with temperature T. The accuracy of this approach is discussed in [Con05]. For this work, the accuracy is sufficient.

Scattering Kernels

Scattering Kernels cannot be adjusted by stochastic interpolation, as only one kernel can be used per material (MCNPX limitation). Therefore they have to be generated for every temperature. Here, predefined scattering kernels in 5 K steps are used and the kernel closest to the desired temperature is selected.

Densities

Temperature dependent densities in H_2O and D_2O are taken into account by X^2 in terms of modifying the affected cell parameters. This is because the density coefficient α_ρ has a considerable effect on k_{eff} [Eme93], even for the small temperature ranges of FRM II.

2.4 Variance Reduction

As mentioned before, Monte Carlo methods are in many cases a choice of last resort because of their computational effort. However, this criterion has lost importance regarding nowadays available computational power. Nevertheless, a 'dumb' direct computation of results is in most cases still not affordable. To overcome this, so called *variance reduction techniques* have to be used. The goal of every variance reduction technique is to 'guide' particles in a desired direction, therefore skipping unnecessary calculations in regions of subordinate interest as far as reasonable. For this, particles are split, killed or transported through a medium by adjusting their weight.

Particle Splitting: If a particle coming from a cell with importance ω_A enters a cell with importance ω_B and if $\omega_B > \omega_A$, the particle is split into $\frac{\omega_B}{\omega_A}$ particles[13], the original weight W of the particle is multiplied by $\frac{\omega_A}{\omega_B}$ and transferred to the new particles. By adjusting the weights of the particles, modification of the spectral flux is prevented. As most variance reduction methods, particle splitting reduces the variance by saving calculation time: The same result could be obtained by tracking a larger number of particles, but this way, the time consuming prehistory does not need to be computed again.

[12] The $\sqrt{T}$-law is chosen as this is the known temperature dependence of the Doppler-broadened resonance integral, see [Eme82].

[13] If $\frac{\omega_B}{\omega_A}$ is not an integer, the particle splitting and the reweighting are carried out in a probabilistic way

Russian Roulette: This is the counterpart to particle splitting: If the ratio of the cell importances is smaller than one, $\omega_A > \omega_B$, a particle entering the cell will be killed with probability $p = 1 - \frac{\omega_B}{\omega_A}$. Particles that don't get killed are assigned a weight W' which is the original weight multiplied by $\frac{\omega_A}{\omega_B}$. Russian roulette is used to mask regions of small relevance, e. g. regions dominated by scattered radiation far away from the tallies, whose impact on the result is marginal.

Exponential Transform: Gives a preferred direction to a particle by lowering cross sections in that direction and raising it in other directions. Let θ be the angle between the preferred direction and the flight direction of the particle and p the transformation parameter, then

$$\Sigma_T^* = \Sigma_T \left(1 - p \cos\theta\right) \tag{2.28}$$

represents the virtual cross section. Hereby an unequal treatment of geometric parts is introduced which is balanced by adjusting the particle weight by

$$W' = \frac{\Sigma_T \mathrm{e}^{-\Sigma_T s}}{\Sigma_T^* \mathrm{e}^{-\Sigma_T^* s}} W, \tag{2.29}$$

where s is the distance to the next collision.

A special case is the choice $p = \Sigma_A / \Sigma_T$ with $\cos\theta = 1$. In this case is $\Sigma_T^* = \Sigma_S$ and it is implicit absorption along the flight direction, see chap. 2.3.3.

Weight Windows: Weight windows specify limits for the weight of a particle, so that single particles that by chance keep gaining weight over time do not distort the actual result of the calculation (see chap. 2.5). Three values are specified, W_U as upper limit, W_L as lower limit and W_S as the survival weight. If the weight of a particle surpasses the upper limit, it is split (Particle Splitting). If it drops below the lower limit, Russian Roulette is played and the weight is set to W_S or the particle is killed.

Forced Collisions: Every time collisions play a very important role, it can be convenient to enforce collisions in certain cells. The particle is then split in two parts, an uncollided one with weight $W_u = W_0 \exp\left(-\Sigma_T d\right)$ and a collided part with weight $W_c = W_0 \left(1 - \exp\left(-\Sigma_T d\right)\right)$, where d is the distance from the particles position to the border of the cell in flight direction.

Besides these techniques, a lot of other methods for variance reduction exist, e. g. *Energy Splitting/Roulette* and *Time Splitting/Roulette*, where energy respectively the age of the particles are taken into account and simpler techniques like *Energy Cutoff*, *Time Cutoff* and *Weight Cutoff*.

2.5 Uncertainties in Monte Carlo Calculations

Not only due to their stochastic nature, the results of MCCs suffer from a lot of uncertainties. It is one of the major tasks to reduce these uncertainties as far as possible and to rate the reliableness of the obtained results in any MCC. Besides statistical errors, the unsureness of cross sections and geometries has to be taken into account. In the following section, the procedures used in this thesis to rate the reliability of the results concerning their statistical nature is presented. Later, the reader is given a short glance at Monte Carlo perturbation theory which is used to rate the non-statistical uncertainties. In this work, perturbation theory is mainly used to reveal small differences between calculations and in burn-up calculations. See also chapter 12 for a discussion on uncertainties.

2.5.1 Statistical Tests

A number of statistical tests are performed on any result obtained by a MCC. This is done to ensure the reliableness of the results concerning their statistic nature. A plain overview of these tests is also given in [Shu06].

Uncertainty

After M active cycles or M events in a tally, with x_m being an arbitrary term (e. g. k_{eff}^C in cycle m or the score of the m$^{\text{th}}$ tally event), the expected value is approximated by

$$\bar{x} = \frac{1}{M} \sum_m x_m. \tag{2.30}$$

The strong law of large numbers guarantees that $\bar{x} \to \langle x \rangle$ for $M \to \infty$, provided $\langle x \rangle$ is finite[14]. The variance is estimated by

$$\begin{aligned} \mathrm{Var}\,(\mathrm{x}) &= \frac{1}{M-1} \sum_{i=1}^{M} (x_i - \bar{x})^2 && (2.32)\\ &\approx \overline{x^2} - \bar{x}^2 && (2.33)\\ \mathrm{Var}\,(\bar{\mathrm{x}}) &= \frac{1}{N} \mathrm{Var}\,(\mathrm{x})\,. && (2.34) \end{aligned}$$

Finally, the relative error is given by

$$\begin{aligned} R &= \frac{\sigma(\bar{x})}{\bar{x}} && (2.35)\\ &= \frac{1}{\bar{x}} \sqrt{\frac{\overline{x^2} - \bar{x}^2}{M}}. && (2.36) \end{aligned}$$

$\sigma(x) = \sqrt{\mathrm{Var}\,(\mathrm{x})}$ is the standard deviation of x. Tab. 2.2 shows how this relative error has to be judged by the user. It is this error that has to be minimized with as little computational effort as possible.

Range of R	Quality of result
> 0.5	Meaningless
0.2 to 0.5	Factor of a few
0.1 to 0.2	Questionable
< 0.1	Reliable except for point/ring detectors
< 0.05	Generally reliable

Table 2.2: *Reliableness of Monte Carlo results*

The value of R is determined by two quantities, the history scoring efficiency q, which is the fraction of histories producing non-zero contributions, and the dispersion of non-zero scores. At least for tallies, due to the non-scoring events, the probability density function (PDF) $p(x)$ has a delta peak at $x = 0$. Therefore MCNP breaks up R in two components

$$\begin{aligned} R^2 &= R_{\text{eff}}^2 + R_{\text{int}}^2 && (2.37)\\ R_{\text{eff}}^2 &:= \frac{1-q}{qN} && (2.38)\\ R_{\text{int}}^2 &:= \frac{\sum_{x_i \neq 0} x_i^2}{\left(\sum_{x_i \neq 0} x_i\right)^2} - \frac{1}{qN}, && (2.39) \end{aligned}$$

[14] For a given probability density function $p(x)$,

$$\langle x \rangle = \int_0^\infty x p(x)\, \mathrm{d}x. \tag{2.31}$$

where the former is representing the scoring inefficiency and the latter the intrinsic spread of the non-zero scoring events. As $R_{\text{eff}} = 0$ for $q = 1$ (every source particle contributes), it is desirable to increase the scoring efficiency as much as possible while at the same time making $p(x)$ more concentrated around $\langle x \rangle$ to decrease R_{int}. This is the goal of the usage of the variance reduction techniques discussed in chapter 2.4.

Other Statistical Figures

Figure of Merit: The figure of merit (FOM) is defined as

$$\text{FOM} := \frac{1}{R^2 T}, \tag{2.40}$$

where T is the simulation time, which is normally proportional to the number N of histories run. With $R^2 \propto 1/M$ (eq. 2.36) and $N \propto M$, the FOM should remain relatively constant over the active cycles of a simulation. It is clear that a large FOM is desirable as it goes hand in hand with shorter simulation times to produce a given statistical error:

$$R = \frac{1}{\sqrt{\text{FOM} \cdot T}}. \tag{2.41}$$

Variance of the Variance: The variance of the variance (VOV) is a quantity to judge the accuracy of the estimation of the relative error R. It is defined as

$$\text{VOV} := \frac{\text{Var}\left(\text{Var}\left(\bar{\text{x}}\right)\right)}{\text{Var}\left(\bar{\text{x}}\right)} \tag{2.42}$$

$$= \frac{\sum_{i=1}^{M} \left(x_i - \bar{x}\right)^4}{\left[\sum_{i=1}^{M} \left(x_i - \bar{x}\right)^2\right]^2} - \frac{1}{M}. \tag{2.43}$$

As the VOV involves the third and fourth order moments of the tally PDF $q(x)$, it is much more sensitive to fluctuations in large history scores than R is alone. From eq. 2.43 it is clear that the VOV should decrease $\propto \frac{1}{N}$, which is an important behaviour to judge the proper sampling of infrequent but high scoring events. From the truncated Cauchy formula it can be concluded that VOV < 0.1 is eligible [Shu06].

The Empirical PDF of Tallies

The quality of the confidence interval estimate of the tally mean can be assessed with the PDF $q(x)$, which is reconstructed by MCNP. Especially the high-end tail of this distribution is important as it contains information on infrequent events with high score. The main purpose of a PDF analysis is to detect cases that appear to have properly converged regarding the statistical behaviour of $\bar{x}$, R, FOM and VOV, but in reality $\bar{x}$ is significantly underestimated due to the inadequate sampling of large scoring histories. Normally MCNP relies on the central limit theorem (CLT) to make sure a tally mean will appear to be sampled from a normal distribution with standard deviation $\propto \frac{1}{N}$ if N is sufficiently large. The problem is to determine, how large N has to be in order to be 'sufficient'.

It can be assessed from the existence of the first two moments of the PDF that the CLT holds and therefore N is sufficiently large:

$$E(x) = \int_0^\infty x q(x)\,\mathrm{d}x \tag{2.44}$$

$$E(x^2) = \int_0^\infty x^2 q(x)\,\mathrm{d}x. \tag{2.45}$$

For these two moments to exist, $q(x)$ must either decrease faster than $\frac{1}{x^3}$ or have a finite upper tally cutoff. For the 200 highest scoring histories, the Pareto distribution

$$\Pr_{a,k}(x) := \frac{1}{a \cdot \left(1 + x\frac{k}{a}\right)^{1+\frac{1}{k}}} \tag{2.46}$$

is fitted to the PDF and the slope estimated from

$$\text{SLOPE} = 1 + \frac{1}{k}. \tag{2.47}$$

It can be shown that the SLOPE must be > 3 for the CLT to hold. If the SLOPE cannot be estimated due to insufficient data, MCNP estimates a SLOPE of 0. A decrease faster than $\frac{1}{x^{10}}$ is reported as 10 and considered a 'perfect' value. The approach is discussed in detail in [X-505, p. 2-122].

MCNP Tally Tests

MCNP provides ten statistical tests to assess the reliability of the results. These tests cover the five quantities introduced above:

Tally Mean $\bar{x}$:

1. $\bar{x}$ may only fluctuate randomly in the second half of the MCC. No trend must be exhibited.

Relative Error R:

2. R must be < 0.10, respectively < 0.05.
3. R must decrease monotonically with N in the last half of the problem.
4. R must be $\propto \frac{1}{\sqrt{N}}$ for the last half of the MCC.

Variance of the Variance VOV:

5. VOV must be < 0.1 for all tallies.
6. VOV must decrease monotonically with N in the last half of the problem.
7. VOV must be $\propto \frac{1}{N}$ for the last half of the MCC.

Figure of Merit FOM:

8. FOM must remain statistically constant for the second half of the MCC.
9. FOM must not exhibit a monotonic trend in the second half.

Tally PDF $q(x)$:

10. The SLOPE of the 200 highest scoring events must be > 3.

All these tests have to be passed in order to consider the result reliable from the point of statistics!

2.5.2 Uncertainty of k_{eff}

The *criticality constant* in MCNP with n as atomic density is defined as

$$k_{\text{eff}} = \frac{\text{fission neutrons in generation i}+1}{\text{fission neutrons in generation i}} \tag{2.48}$$

$$= \frac{n\int_V\int_0^\infty\int_E\int_\Omega \nu\sigma_f\phi\,\mathrm{d}V\,\mathrm{d}t\,\mathrm{d}E\,\mathrm{d}\Omega}{\int_V\int_0^\infty\int_E\int_\Omega \boldsymbol{\nabla}\cdot\boldsymbol{j}\,\mathrm{d}V\,\mathrm{d}t\,\mathrm{d}E\,\mathrm{d}\Omega + n\int_V\int_0^\infty\int_E\int_\Omega \sigma_{A'}\phi\,\mathrm{d}V\,\mathrm{d}t\,\mathrm{d}E\,\mathrm{d}\Omega}. \tag{2.49}$$

The numerator of the fraction in equation 2.49 is the number of produced neutrons while the first term of the denominator is the leakage rate from the regarded volume V, and the second term is the loss by absorption. It comprises absorption by (n,γ) processes, fission and other multiplying reactions, such as (n,2n) reactions. As the latter ones are not included in the production term in the numerator, the corresponding terms for neutron production have to be subtracted in the denominator (this is the reason for using $\sigma_{A'}$ instead of σ_A).[15]

For statistical reasons, it is not sufficient just to compare the number of neutrons at the beginning and the end of a KCODE cycle. So MCNP estimates the criticality constant in three different ways:

Collisions

$$k_{\text{eff}}^C = \frac{1}{N}\sum_i W_i \frac{\sum_j f_j\nu_j\sigma_{f_j}}{\sum_k f_k\sigma_{f_k}} \tag{2.50}$$

The sum i runs over all collisions where fission is possible, W_i is the weight of the particle in question. Sums j and k run over all materials in the cell with atomic fraction f_j and fission cross section σ_{f_j}. ν_j is the number of neutrons set free in fission.

Absorptions

Here, only the default case of implicit absorption is discussed:

$$k_{\text{eff}}^A = \frac{1}{N}\sum_i W_i\nu_k\frac{\sigma_{f_k}}{\sigma_{T_k}}. \tag{2.51}$$

The difference to 2.50 is that the sum runs only over the affected nuclides k, not over all nuclides.

Track Length

$$k_{\text{eff}}^{\text{T}} = \frac{1}{N}\sum_i\left(W_i\rho d\sum_k f_k\nu_k\sigma_{f_k}\right) \tag{2.52}$$

d is the distance from the preceding event of the particle. i runs over all particle tracks, ρ is the atomic density of the regarded cell. The estimation arises from $\rho d\sum_k f_k\nu_k\sigma_{f_k}$ being the expected number of fissions on the way d.

Combination of Estimations

The three single estimations are combined with a Maximum-Likelihood-Approach [Hal60], that makes allowance for variances and covariances.[16] Details on how this is done can be found in [Urb95]. The

[15] This is understandable when the equation is multiplied by the denominator and the terms are brought on the corresponding sides by addition, see [X-505, p. 2-168].

[16] In fact, MCNP creates several combinations of two and three factors. Here, only the best one comprising all three factors is regarded.

combination is not ideal as the covariance matrix of the three estimations is unknown and has to be estimated.

With the standard deviation σ_X belonging to estimation k_{eff}^X

$$\Sigma_{11} := \sigma_C^2 \tag{2.53}$$

$$\Sigma_{12} := \begin{pmatrix} \sigma_C^2 - \sigma_{CA}^2 & \sigma_C^2 - \sigma_{CT}^2 \end{pmatrix} \tag{2.54}$$

$$\Sigma_{21} := \begin{pmatrix} \sigma_C^2 - \sigma_{CA}^2 \\ \sigma_C^2 - \sigma_{CT}^2 \end{pmatrix} \tag{2.55}$$

$$\Sigma_{22} := \begin{pmatrix} \sigma_C^2 + \sigma_A^2 - 2\sigma_{CA}^2 & \sigma_C^2 + \sigma_{AT}^2 - \sigma_{CA}^2 - \sigma_{CT}^2 \\ \sigma_C^2 + \sigma_{AT}^2 - \sigma_{CA}^2 - \sigma_{CT}^2 & \sigma_C^2 + \sigma_T^2 - 2\sigma_{CT}^2 \end{pmatrix} \tag{2.56}$$

$$\boldsymbol{d} := \begin{pmatrix} k_{\text{eff}}^A - k_{\text{eff}}^C \\ k_{\text{eff}}^T - k_{\text{eff}}^C \end{pmatrix}, \tag{2.57}$$

after M active cycles one obtains

$$k_{\text{eff}}^{\text{final}} = k_{\text{eff}}^C - \Sigma_{12}\Sigma_{22}^{-1}\boldsymbol{d} \tag{2.58}$$

$$\sigma_{\text{final}}^2 = \left(\Sigma_{11} - \Sigma_{12}\Sigma_{22}^{-1}\Sigma_{21}\right) \cdot \left(\frac{1}{M} + \frac{\boldsymbol{d}\Sigma_{22}^{-1}\boldsymbol{d}}{M-1}\right). \tag{2.59}$$

According to this calculation, $k_{\text{eff}}^{\text{final}}$ is not a point estimation of k but has to be seen in conjunction with σ_{final} as a confidence interval. The estimation that is obtained this way is better than building the arithmetic median of the three single estimations, even when it may happen that $k_{\text{eff}}^{\text{final}}$ lies outside the interval clamped by those [Urb95].[17] [18]

The uncertainty of $k_{\text{eff}}^{\text{final}}$ has already been discussed above. This uncertainty includes solely the statistical error. Errors introduced by imprecise material and geometry definitions as well as uncertainties of measured data included in the calculations (e. g. cross sections) are not considered. To rate these errors, a more sumptuous sensitivity analysis is necessary.

2.5.3 Source Entropy

First, in inactive KCODE cycles, a source distribution as static as possible is generated.[19] This is necessary to obtain realistic results in systems where source point distributions between cycles are closely correlated

[17] This especially happens if the single estimations are strongly positively correlated. Additionally, $k_{\text{eff}}^{\text{final}}$ may show a clear trend over several cycles if source points between cycles are strongly correlated.

[18] Equation 2.59 may be suggestive of that only a large enough number of cycles would have to be calculated to reduce the statistical error to zero. This is not true as the algorithm used in MCNP produces a slightly negative trend in the estimated $k_{\text{eff}}^{\text{final}}$. According to [Gel90], this can be written as

$$\Delta k_{\text{eff}}^{\text{final}} = \frac{M}{2k_{\text{eff}}^{\text{final}}}\left(\sigma_{k_{\text{eff}}}^2 - \sigma_{\text{final}}^2\right), \tag{2.60}$$

where $\sigma_{k_{\text{eff}}}$ is the true deviation with $\sigma_{k_{\text{eff}}}^2 > \sigma_{\text{approx}}^2$. This error rises with an increasing number of cycles. The maximum number of cycles in this work is therefore set to 500, [X-505] indicates 200 – 1000 cycles to be an appropriate choice.

[19] In this context, 'source' means fission points, i. e. the points in the fuel where the particles in the calculation are started. At the very beginning, usually a very limited number of points is specified manually. The evolution of the fission distribution is then followed, until it has reached some kind of equilibrium. This equilibrium is determined by the source entropy. The equilibrium is of course only valid in terms of population density.

[Uek02], which is the case for FRM II. To assess the statistical stability of the source distribution, the *Shannon Entropy* of the source is calculated:

$$H_{\mathrm{src}} = -\sum_{i=1} N_s P_i \cdot \log_2 P_i. \tag{2.61}$$

A grid consisting of N_s cuboidic cells is superimposed on the geometry in question for being a source. P_i is the number of source points in cell i. The source distribution can be considered static if H_{src} approaches a constant value $0 \leq H_{\mathrm{src}} \leq \log_2 N_s$. Every calculation in this work involves an adequate number of inactive cycles to guarantee a static source distribution.

In the present case, starting with a point source, the full source entropy of 6.4 was reached after three cycles. To account also for minor (≤ 0.04) fluctuations, ten cycles were skipped at the beginning of each calculation (compare fig. 2.1).

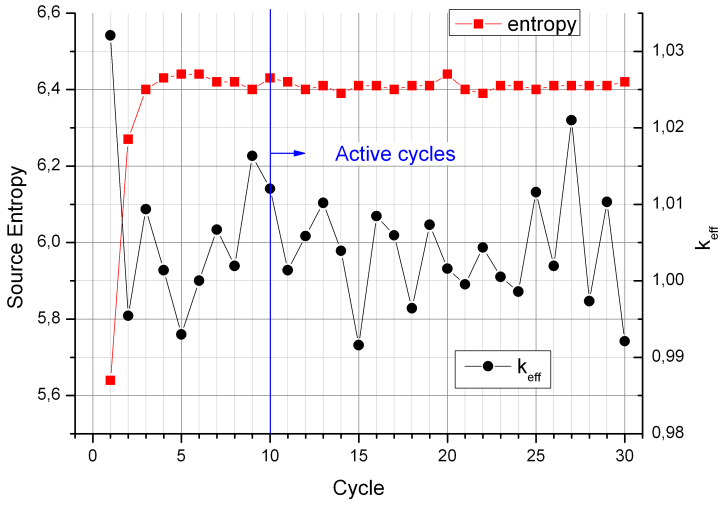

Figure 2.1: *Source entropy and corresponding k_{eff} for FRM II.*

2.5.4 Uncertainty of other Quantities

Beside the discussed statistical effects, other quantities like cross sections, material compositions and small geometrical deviations make a contribution to the total uncertainty of the calculations. However, all these non-statistical contributions are not captured by a normal MCC. While cross sections and material compositions can be taken into account via perturbation theory (see chap. 2.5.5) in MCNP, geometrical uncertainties need to be analysed in a separate sensitivity analysis.

2.5.5 Perturbation Theory in Monte Carlo Calculations

In deterministic calculations, perturbations would be calculated by just inserting the perturbed quantities and comparing results between the two calculations. This approach is useful even for very small perturbations. However, this cannot be done in MCCs as the perturbation response is superimposed on the statistical uncertainty of both calculations. Therefore, small perturbations – if detectable at all - cannot be quantified with adequate precision by comparing the results of two independent calculations. To compensate this deficiency, perturbation theory for Monte Carlo is done via the *Differential Operator Technique*. It was introduced in the early 1960s [Olh62] and later generalised to geometric [Tak70] and

cross section perturbations [Hal80]. It includes effects up to the second order but neglects second order cross terms [X-505].

In the differential operator technique, the change Δc of the Monte Carlo answer c due to changes $\Delta\nu$ in a related data set ν is expressed by a Taylor series:

$$\Delta c = \sum_n \frac{1}{n!}\frac{\mathrm{d}^n c}{\mathrm{d}\nu^n}\cdot\Delta\nu^n \tag{2.62}$$

$$=: \sum_n u_n \Delta\nu^n. \tag{2.63}$$

Let $\sigma \in \Sigma$ be an element from a set of macroscopic cross sections, E an energy from a set of energies and $C_\sigma(E)$ some constant. The Monte Carlo answer c and therewith all u_n are now regarded to be functions of $x_\sigma(E) = C_\sigma(E)\cdot e^\nu$. This choice makes it possible to modify materials, cross sections and geometry when setting $\nu = \Sigma\cdot d$. Then for the data set $x_\sigma(E)$ and a track-based response estimator $c = \sum_j t_j p_j$ with the response estimator t_j and p_j the probability of path segment j, the n^{th} coefficient of the series can be written as[20]

$$u_n = \frac{1}{n!}\sum_j \gamma_{nj} t_j p_j \tag{2.65}$$

$$\gamma_{nj} := \sum_{\sigma\in\Sigma}\sum_E x_\sigma^n(E)\left(\frac{\partial^n}{\partial x_\sigma^n(E)}(t_j p_j)\right)\left(\frac{1}{t_j p_j}\right). \tag{2.66}$$

With some transformations [McK94, Hes98], this can be expressed in terms of histories. So if i runs over all N histories and j' represents only the path segments in history i, the expected value is

$$\langle u_n\rangle = \frac{1}{Nn!}\sum_i\left(\sum_{j'}\gamma_{nj'}t_{j'}\right). \tag{2.67}$$

Departing from here, the first and second order coefficient can be derived. This leads to two perturbation factors that are multiplied to the tally covering the perturbed material. The method including the second order estimator offers acceptable accuracy for response changes up to 20–30%, which is sufficient for this work.

First Order Coefficient

The first order coefficient can be shown to be

$$\langle u_1\rangle = \frac{1}{N}\sum_i\left[\sum_{j'}\left(\sum_{k=0}^{m}\beta_{j'k} + R_{1j'}\right)t_{j'}\right]. \tag{2.68}$$

[20] Path segment j consists of segment $j-1$ plus the current track. Therefore, the probability of path segment j is the product of the track probabilities r_k,

$$p_j = \prod_k r_k. \tag{2.64}$$

r_k takes different forms, depending on what happens with the tracked particle. Examples can be found in [X-505, p. 2-194].

$R_{1j'}$ is the fraction of the reaction rate tally involved in the perturbation. This means $R_{1j'} = 0$ if none of the nuclides is perturbed which is always the case for F1, F2 and F4 tallies without FM cards[21] and $R_{1j'} = 1$ if all nuclide cross sections are perturbed. Generally:

$$R_{1j'} = \frac{\sum_{\sigma\in\Sigma_P}\sum_E x_\sigma(E)}{\sum_{\sigma\in\Sigma_T} x_\sigma(E)}, \tag{2.72}$$

where Σ_T are all cross sections participating on the tally and Σ_P is the subset of perturbed cross sections. $\beta_{j'k}$ is defined as

$$\beta_{j'k} := \sum_{\sigma\in\Sigma_P}\sum_E \frac{x_\sigma(E)}{r_k}\cdot\frac{\partial r_k}{\partial x_\sigma(E)} \tag{2.73}$$

and therefore includes the history of the particle. For example, $r_k = \exp\left[-x_{\sigma_T}(E)\cdot d_k\right]$ for a particle that travels a distance d_k without interaction.

Second Order Coefficient

The approach to derive the second order coefficient is similar to the derivation of the first order coefficient and leads to

$$\langle u_2\rangle = \frac{1}{2N}\sum_i\left[\sum_{j'}\left(\sum_{k=0}^{m}\left(\alpha_{j'k}-\beta_{j'k}^2\right) - R_{1j'}^2 + \left(\sum_{k=0}^{m}\beta_{j'k}+R_{1j'}\right)^2\right)t_j\right]. \tag{2.74}$$

$\alpha_{j'k}$ is similarly to $\beta_{j'k}$ and discussed in detail in [X-505, p. 2-197].

Implementation

For $R_{1j'} = 0$ the first and second order perturbation can be written as

$$P_{1j'} = \sum_{j'}\left(\sum_{k=0}^{m}\beta_{j'k}\right)t_{j'} \tag{2.75}$$

$$P_{2j'} = \sum_{j'}\left(\sum_{k=0}^{m}\left(\alpha_{j'k}-\beta_{j'k}^2\right)\right)t_{j'}, \tag{2.76}$$

so that

$$\langle\Delta c\rangle = \frac{1}{N}\sum_i\sum_{j'}\Delta c_{j'} \tag{2.77}$$

[21] F1 tallies a surface current, F2 a surface flux and F4 is a track length estimate of the cell flux:

$$F1 = \iiiint |\boldsymbol{\Omega}\cdot\boldsymbol{n}|\,\phi(\boldsymbol{r},\boldsymbol{\Omega},E,t)\,\mathrm{d}\Omega\,\mathrm{d}A\,\mathrm{d}t\,\mathrm{d}E \tag{2.69}$$

$$F2 = \frac{1}{A}\iiiint \phi(\boldsymbol{r},\boldsymbol{\Omega},E,t)\,\mathrm{d}\Omega\,\mathrm{d}A\,\mathrm{d}t\,\mathrm{d}E \tag{2.70}$$

$$F4 = \frac{1}{V}\iiiint \phi(\boldsymbol{r},\boldsymbol{\Omega},E,t)\,\mathrm{d}\Omega\,\mathrm{d}V\,\mathrm{d}t\,\mathrm{d}E. \tag{2.71}$$

The assumption $R_{1,j'} = 0$ is also true for F4 tallies with FM card (a tally multiplier) with only positive multiplicative constants.

with

$$\Delta c_{j'} = \left(P_{1j'} \Delta\nu + \frac{1}{2} \left(P_{2j'} + P_{1j'}^2 \right) \Delta\nu^2 \right) t_{j'} \tag{2.78}$$

for $R_{1j'} = 0$ and

$$\Delta c_{j'} = \left(P_{1j'} \Delta\nu + \frac{1}{2} \left(P_{2j'} + P_{1j'}^2 \right) \Delta\nu^2 \right) t_{j'} + \left(R_{1j'} \Delta\nu + P_{1j'} R_{1j'} \Delta\nu^2 \right) t_{j'} \tag{2.79}$$

for $R_{1j'} \neq 0$. That is, the $R_{1j'} \neq 0$ case is just a correction to the $R_{1j'} = 0$ case. So in MCNP, both perturbation factors are accumulated along every track length through a cell and the perturbed tallies are multiplied by the first correction factor and corrected further with the second if necessary.

Details on the implementation in MCNP and the limitations of this technique can be found in [X-505, p. 2-198].

Cross Correlations

Generally it is assumed that if a perturbation changes the relative concentrations of nuclides, the contribution to the perturbation from each nuclide is independent. That means that differential cross terms in the second-order perturbation are neglected by MCNP. A method to calculate these cross correlations is described in [Fav01].

Consider $c(f_1, f_2)$ to be a function of two variables, where the initial unperturbed values are $f_{1,0}$ and $f_{2,0}$. f_1' and f_2' are the perturbed values and $\Delta f_1' := f_1' - f_{1,0}$, $\Delta f_2' := f_2' - f_{2,0}$. Then regard the second order Taylor series

$$\begin{aligned} \Delta c(\Delta f_1', \Delta f_2') &:= c(f_1', f_2') - c(f_{1,0}, f_{2,0}) && (2.80) \\ &= \left. \frac{\partial c(f_1, f_2)}{\partial f_1} \right|_{f_{1,0}, f_{2,0}} \Delta f_1' + \left. \frac{\partial c(f_1, f_2)}{\partial f_2} \right|_{f_{1,0}, f_{2,0}} \Delta f_2' \\ &\quad + \frac{1}{2} \left[\left. \frac{\partial^2 c(f_1, f_2)}{\partial f_1^2} \right|_{f_{1,0}, f_{2,0}} \Delta {f_1'}^2 + 2 \left. \frac{\partial^2 c(f_1, f_2)}{\partial f_1 \partial f_2} \right|_{f_{1,0}, f_{2,0}} \Delta f_1' \Delta f_2' + \right. \\ &\quad \left. + \left. \frac{\partial^2 c(f_1, f_2)}{\partial f_2^2} \right|_{f_{1,0}, f_{2,0}} \Delta {f_2'}^2 \right] && (2.81) \end{aligned}$$

The cross term of the second order term is ignored by MCNP. It can be calculated by the midpoint method using $f_{1,1/2} := \frac{1}{2} (f_{1,0} + f_1')$ and $f_{2,1/2} := \frac{1}{2} (f_{2,0} + f_2')$. With these midpoint values it can be shown that

$$\Delta c(\Delta f_1', \Delta f_2') = 2 \cdot \left[\left. \frac{\partial c(f_1, f_2)}{\partial f_1} \right|_{f_{1,1/2}, f_{2,1/2}} \left(f_1' - f_{1,1/2} \right) + \left. \frac{\partial c(f_1, f_2)}{\partial f_2} \right|_{f_{1,1/2}, f_{2,1/2}} \left(f_2' - f_{2,1/2} \right) \right]. \tag{2.82}$$

This expression is second order accurate. The downside of this method is surely, that it requires a second MCC on top of the one that was used to calculate the unperturbed problem. However, this method cannot be replaced by just doing a MCC for the perturbed values and subtracting their results, as the perturbation may be hidden by statistics (see the discussion above). Even though this method requires a second MC run, the perturbation is calculated directly with its own statistical error and therefore independent from the statistical error of the original MCC. The upside is that this method can be combined with a standard MC endpoint perturbation calculation to calculate the cross term directly[22]. Then it may be shown that the cross term is small and can be neglected, so later MCCs do

[22] For this, calculate $\Delta c_{\text{2nd order}}(\Delta f_1', \Delta f_2') - \Delta c_{\text{MCNP}}(\Delta f_1', \Delta f_2')$.

not require this procedure and the perturbations can be estimated with a conventional endpoint perturbation calculation. A further advantage of the midpoint method is that it can be shown that the third order terms are a factor of 4 smaller than those in the original taylor approximation used by MCNP [Pre07].

The method can easily be generalized to functions of N variables yielding

$$\begin{aligned} \Delta c(\Delta f_1', \ldots, \Delta f_N') &= 2 \cdot \left[\left. \frac{\partial c(f_1, \ldots, f_N)}{\partial f_1} \right|_{f_{1,1/2}, \ldots, f_{N,1/2}} \left(f_1' - f_{1,1/2}\right) + \ldots + \right. \\ &\quad \left. + \left. \frac{\partial c(f_1, \ldots, f_N)}{\partial f_2} \right|_{f_{1,1/2}, \ldots, f_{N,1/2}} \left(f_N' - f_{N,1/2}\right) \right]. \end{aligned} \tag{2.83}$$

Further Limitations

For the track length estimate of k_{eff}, it is assumed that the fission distribution is unchanged in the perturbed configuration.

2.6 Particle Production

2.6.1 Production of Prompt Particles

Photon Production

Photons are generated in every collision if the collision nuclide has a nonzero photon production cross section σ_γ. The number of photons produced depends on neutron weight, neutron source weight, photon weight limits, σ_γ, σ_T and the cell importances. No more than 10 photons are produced per collision. The weight of the produced photon is

$$W_p = \frac{W_n \sigma_\gamma}{\sigma_T}. \tag{2.84}$$

Russian roulette is played on the photons to reduce an overproduction. Both σ_γ and σ_T are evaluated without considering thermal effects as the inelastic cross sections are assumed to be independent of temperature. For further details see [X-505, p. 2-31].

Neutron Production

In KCODE calculations, no fission neutrons are produced but the site of the fission event is stored as a possible source for the next KCODE cycle. The source neutrons then will be produced according to the properties of the neutron initiating the fission event.

Neutrons resulting from photonuclear interactions are produced in an analoguous way. Details can be found in [Whi99] and [X-505, p. 2-64].

No other particles like electrons, positrons or protons are produced by the code, neither in neutron reactions nor decay.[23]

[23] In fact, MCNPX is capable of producing these charged particles. However, in this work, the capability is not used due to extensive computational requirements. The energy deposition by these particles is regarded to be localized on the spot of their suppositional production.

2.6.2 Delayed Particle Production

Delayed Neutrons

The production of delayed neutrons is turned on by default. Delayed neutron data is missing for some rare actinides, but their contribution can be neglected even at a high burnup. For all isotopes of interest (^{233}U, ^{234}U, ^{235}U, ^{236}U, ^{237}U, ^{238}U, ^{237}Np, ^{238}Pu, ^{239}Pu, ^{240}Pu, ^{241}Pu and some more – however, not for ^{239}Np), delayed neutron data is available and used.

Delayed Gammas

Delayed gammas are produced by MCNPX for fission as well as most reactions which include the creation of radioactive isotopes. Produced are all gammas that would be produced in a time frame of up to 10^8 s after the event has occurred [Pel08, McK09, Dur]. MCNPX includes the possibility to create the delayed gammas at discrete energies or in 25 energy groups. In this work, the latter option is chosen as it speeds up the calculation by several orders of magnitude. Details on the creation of delayed gammas by MCNPX, especially on the sampling procedures, can be found in [Dur09a]. Validation calculations have been preformed by [Dur09b] with good results. Some of the underlying transport theory is described in [Dur09c].

2.6.3 Photon Physics

As the role of photons in the calculations of this work is minor, no detailed explanation of the underlying physics, algorithms and their implementation in MCNPX will be given here. The 'detailed physics' mode for photons implemented in MCNPX is used. This means that the following effects are included:

- Photoelectric effect,
- Pair production,
- Compton scattering (incoherent),
- Thomson scattering (coherent) and
- Photonuclear reactions.

An extensive discussion of these features can be found in [X-505, p. 2-57].

CHAPTER 3

Cross Sections

This chapter deals about how cross sections are adjusted from the ENDF-Tapes (*Evaluated Nuclear Data File*) for the Monte Carlo simulations. Actually, most cross sections used in the calculations for this work were pre-compiled and shipped with MCNP or MCNPX. Only in cases were adequate cross sections were not available within the standard cross section set of MCNPX or serious concerns on the reliability of the cross sections existed, new cross sections were compiled from scratch, i. e. generated from newer libraries of raw data. This means that for this work, from the libraries that ship with MCNPX, only cross sections from ENDF/B VI.X were used. In addition, new cross sections were converted from additional libraries outside MCNPX. If new cross section tables had to be generated, most calculations were carried out with a modified version (see app. B.5, p. 258) of ENDF2ACE [Per04], which is based on the NJOY code [Mac94]. Data stems from the ENDF/B VII.0 library [Cha06] and JEFF 3.1.1 [San09].

An example for a case where these cross sections proved to be unreliable is the cross section of molybdenum, which changed drastically from ENDF/B VI.8 to ENDF/B VII.0. This change is visualized in fig. 3.1, where each isotope is plotted in its own colour, two times, one time for ENDF/B VI.8 and one time for ENDF/B VII.0. The changes are clearly visible.

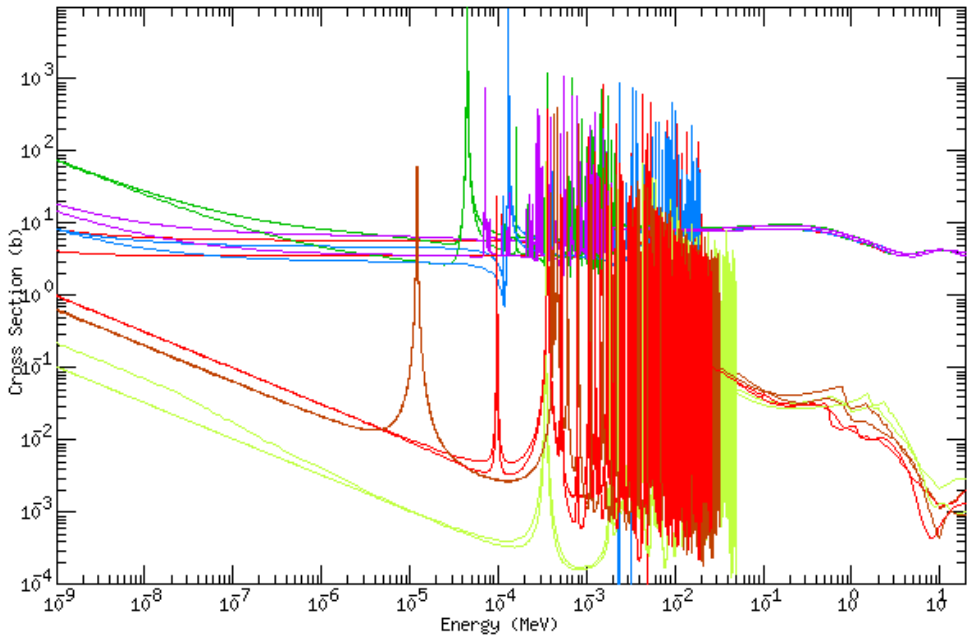

Figure 3.1: *Change in the cross section of Mo from ENDF/B VI.8 to ENDF/B VII.0. Light green:* ^{92}Mo*, red:* ^{94}Mo*, green:* ^{95}Mo*, blue:* ^{96}Mo*, purple:* ^{97}Mo*, soil:* ^{98}Mo *and again in red:* ^{100}Mo.

3.1 Used NJOY Modules

The following modules from NJOY have been used for the cross section adjustments:

RECONR: Reconstructs resonances and sets the energy grid to allow for linear interpolation between discrete energy points with an error up to a given level[1]. Calculates sum reaction from single reactions [Mac94, p. III-1].

BROADR: Generates Doppler-broadened cross sections via kernel broadening starting from piecewise linear cross sections. The input for this is taken from RECONR [Mac94, p. IV-1].

HEATR: This module is used to generate pointwise heat production cross sections and radiation damage energy production for the specified reactions. It takes the input from BROADR [Mac94, p. VI-1].

THERMR: Generates pointwise neutron scattering cross sections in the thermal energy range. Produces inelastic cross sections and energy-to-energy transfer matrices for free atoms or bound scatterers if $S(\alpha, \beta)$ scattering functions are available [Mac94, p. VII-1].

GASPR: Gas production cross section calculation (MT203 - MT207) for particles from protons up to alphas [Sec].

PURR: Must be used instead of UNRESR to generate the probability tables for the unresolved resonance region to treat unresolved resonance self-shielding. Details can be found in [Mac94, p. XXII-1].

MODER: An internal data conversion module [Mac94, p. XII-1].

ACER: A tool to convert data for MCNP [Mac94, p. XVII-1].

[1] MCNP and several NJOY modules require linear-linear-interpolation between discrete cross section points. In ENDF-files, different interpolation schemes are used. More reasons can be found in [njo].

The details on the physics behind the single modules can be found in the given references, including an extensive discussion concerning the nature of these cross sections.

Typical module sequences used in the generation of cross section libraries for McnpX are listed in appendix F.3, p. 281. It should be noted that the cross sections generated this way do not include the production of gamma radiation. Therefore, evaluated cross sections that do include correct photon production terms were used as far as possible.

3.2 Uncertainties

Uncertainties and covariances cannot be calculated for the pointwise cross sections with NJoy but must rather be evaluated for multigroup cross sections. By now, only pointwise cross sections are used in X^2, therefore no cross section uncertainties are taken into account in the calculations. See also the discussion in chapter 4.4 how this affects the correct prediction of the burn-up of the fuel.

CHAPTER 4

Burn-Up

FRM II is a reactor that is driven by a single control rod. Most burn-up programs available today that can be combined with MCNPX cannot account for the changing flux and fission densities when the control rod is moved. Therefore, an average control rod position is often used, e. g. in [Gla05]. For this work, a script system was developed that readjusts the control rod depending on the actual burn-up per time step and therefore increases the precision of the burn-up predictions, especially regarding the spatial distribution of the fission density, which is the primary factor regarding temperatures and heat fluxes. This script system is part of X^2 .

4.1 Burn-up Equations

The general expression for the time dependent evolution of any nuclide i exposed to neutron flux is

$$\begin{aligned}\frac{\mathrm{d}}{\mathrm{d}t}N_i(\boldsymbol{r},t) &= -\left[\int_0^\infty \sigma_a^i(E)\phi(\boldsymbol{r},t,E)\mathrm{d}E + \lambda_i\right] N_i(\boldsymbol{r},t) \\ &\quad + \sum_{j\neq i}\left[\int_0^\infty f_{j\to i}(E)\sigma_a^j(E)\phi(\boldsymbol{r},t,E)\mathrm{d}E + l_{j\to i}\lambda_j\right] N_j(\boldsymbol{r},t). \end{aligned} \tag{4.1}$$

Here, λ_i is the decay constant of nuclide i. $f_{j\to i}$ is the fraction of absorptions in j that lead to a transition to i and $l_{j\to i}$ is the fraction of radioactive decays that lead from j to i. Whilst the first term represents the destruction, it covers all kind of absorption processes like (n,γ), fission, (n,xn), (n,p) etc., the second is the production term and therefore includes all kinds of decays like α- and β-decays – including the de-excitation of meta-stable states that lead to nuclide i.

This set of differential equations needs to be simplified significantly to be able to obtain a solution with reasonable effort in an acceptable amount of time. As a first step, the energy integral is eliminated by introducing spectral averaged cross sections and the total neutron flux:

$$\bar{\sigma}(\boldsymbol{r},t) := \frac{\int_0^\infty \sigma(E)\phi(\boldsymbol{r},t,E)\mathrm{d}E}{\int_0^\infty \phi(\boldsymbol{r},t,E)\mathrm{d}E} \tag{4.2}$$

$$\phi(\boldsymbol{r},t) := \int_0^\infty \phi(\boldsymbol{r},t,E)\mathrm{d}E \tag{4.3}$$

$$\int_0^\infty \sigma(E)\phi(\boldsymbol{r},t,E)\mathrm{d}E = \phi(\boldsymbol{r},t)\cdot\bar{\sigma}(\boldsymbol{r},t). \tag{4.4}$$

The task for McnpX is to calculate the one-group cross sections from eq. 4.2 and the flux from 4.3. The main advantage of this procedure is the inherent provision of self-shielding effects as MCNP averages the flux over a cell. The remaining equation to be solved is

$$\begin{aligned}\frac{\mathrm{d}}{\mathrm{d}t}N_i(\boldsymbol{r},t) &= -\left[\bar{\sigma}_a^i(\boldsymbol{r},t)\phi(\boldsymbol{r},t)+\lambda_i\right]N_i(\boldsymbol{r},t)\\ &\quad+\sum_{j\neq i}\left[f_{j\to i}(\boldsymbol{r},t)\bar{\sigma}_a^i(\boldsymbol{r},t)\phi(\boldsymbol{r},t)+l_{j\to i}\lambda_j\right]N_j(\boldsymbol{r},t).\end{aligned} \tag{4.5}$$

Next, the equations are discretized in space. For this, burn-up zones have to be defined in the fuel, in which the variation of all relevant physical properties is ignored, i. e. they are averaged over the whole cell. Using

$$a_{ij}=\begin{cases}-\sigma_a^i\phi-\lambda_i & \text{for } i=j\\ f_{j\to i}\sigma_a^j\phi+l_{j\to i}\lambda_i & \text{for } i\neq j\end{cases}, \tag{4.6}$$

the equation can be written in matrix form with a matrix $\mathbb{A}$ that is composed of the a_{ij} defined above. The nuclides N_i are combined in a vector $\boldsymbol{N}$. So for every cell / material and burn-up step k, the following equation has to be solved:

$$\frac{\mathrm{d}}{\mathrm{d}t}\boldsymbol{N}(t)=\mathbb{A}(t=t_k)\cdot\boldsymbol{N}(t). \tag{4.7}$$

The solution of this remaining set of differential equations is now the task of the burn-up program. For the solution, it is assumed that the flux ϕ does not change within the regarded time steps. Then the general solution for the equation above is given by

$$\boldsymbol{N}(t_{k+1})=\exp\left[\mathbb{A}(t_k)\cdot\Delta t\right]\boldsymbol{N}(t_k). \tag{4.8}$$

For the time discretisation, the chosen timestep should always satisfy

$$(\lambda_i+\sigma_a^i\phi)\cdot\Delta t\ll 1 \tag{4.9}$$

for any isotope involved [Sta07].

The approach presented above is exemplary for one energy group. The equations can easily be rewritten for a larger number of energy groups by limiting the integrals in equations 4.2 and 4.3 and introducing the correspondent sum beginning with equation 4.4.

4.2 Burn-Up Code System

A large number of burn-up codes was developed over the past decades to solve the equations discussed above. In the following, two of these codes and the implementation of the above equations are shortly presented.

4.2.1 Cinder90

Since version 2.6.0, Cinder90 [Wil97] is integrated into Mcnpx [Fen06]. Using the appropriate input-card (`burn`), the task of calculating the appropriate one-group cross sections and fluxes can be automated. The system performs a predictor-corrector calculation, i. e. calculates the solution for $t+\Delta t$ for the discretised version of eq. 4.8, interpolates to $t+\Delta t/2$ and on the basis of this result calculates a better solution for $t+\Delta t$. For a more detailed explanation of the predictor-corrector scheme see [Pre07, p. 740 ff.].

CINDER90 uses Markov Chains to determine the temporal densities of the nuclides [Wil97]. Each path from each nuclide defined by available nuclear data is followed until all tests of significance fail for a specific path. Most of the decay data and the fission product yields originate from ENDF/B-VI [BNLB, Eng92, Eng89].

This system does not offer the possibility to change the geometry which would be required to account for the moving control rod. Only concentration changes of different materials are allowed. Therefore, the possibility to move the control rod was implemented externally within the framework of X^2.

However, during the development of this work, several problems with CINDER90 arose that due to legal reasons could not be solved[1]. Therefore, another burn-up code, MONTEBURNS was integrated into X^2. The possibility to use CINDER90 is still present in the X^2 code, but not very well tested.

4.2.2 MonteBurns / Origen 2.2

MONTEBURNS [Pos99] is an interface to interchange data between MCNP and ORIGEN 2.2, the latter being another burn-up code [Cro80]. Unlike CINDER90, MONTEBURNS is not integrated into MCNPX but an external program. It uses a large number of tallies and perturbation methods to determine the reaction rate for up to 9999 nuclides in a maximum of 49 burn-up zones[2].

For the purpose of this work, MONTEBURNS was modified to be able to use more materials and to allow for the movement of the control rod. Furthermore, the possibility to use an external, self-calculated cross section library was implemented. A number of other minor changes was made to the code, too. See app. B.2 for further details.

One remaining problem is the burn-up of ^{6}Li which heavily relies on the (n,t) reaction. Although this is covered by MONTEBURNS, the reaction is masked as (n,α) by the program, therefore not producing the right amount of ^{3}H [Pos99, p. 46]. Due to this deficiency, all burn-up calculations regarding the burn-up of ^{9}Be, which produces ^{6}Li, are carried out with CINDER90. For most other calculations, MONTEBURNS is used.

4.2.3 Implementation

To account for the moving control rod, a set of Perl-scripts was developed and included in X^2, that uses one of the before mentioned burn-up codes for the burn-up calculations and automatically readjusts the control rod position to criticality. Normally, over one timestep, Δk is small. Then the new control rod position is calculated based on curves like the one shown in fig. 4.1, which shows the reactivity of a fresh core in current design[3]. The final position for k_{eff} is then obtained via interpolation between the guessed and the old value. The guessed result is tested and new tries are made until

$$k_{\text{eff}} - k_{\text{desired}} \leq \Delta k_{\max}. \tag{4.11}$$

[1] In February 2009, the Department of Energy (DOE) took control over the export of MCNPX, which was formerly controlled by the Department of Commerce (DOC). After that, new rules were formulated which took several months, stalling the development process of the program system. Therefore it was chosen to include another burn-up code in the system as it was not clear at that time how the export rules for MCNPX and therefore CINDER90 were going to change and when access to these codes would be granted again.

[2] The value of 49 materials is quoted in the manual but it was found during this work that the code produces errors in the MCNPX input files if the maximum number of materials was used. Up to about 40 materials proved to work fine [Tre09].

[3] For the current fuel element at begin of live (BOL), the reactivity depending on the control rod position z was calculated to be

$$k_{\text{eff}} = -5.16(15)\,10^{-5} \cdot z^2 + 4.50(5)\,10^{-3} \cdot z + 1.0339(5). \tag{4.10}$$

The quadratic fitting residual is $\chi^2 = 0.999$.

Due to the statistical nature of the MCC, k cannot be adjusted exactly to criticality. Therefore, a maximum tolerance $\Delta k_{\max}$ for the deviation from the desired k is defined. Normally, $\Delta k_{\max} \leq 0.001$ or smaller. For this maximum deviation to be meaningful, the number of active cycles and particles per cycle has to be chosen in a way that the statistical uncertainty of the calculated k_{eff} is approximately $\sigma(k_{\text{eff}}) \lesssim 0.5 \Delta k_{\max}$. Only then the fulfillment of criterion 4.11 is also meaningful in terms of the control rod position. An autosensing feature was implemented to ensure δz of the control rod does not exceed a specified value. More on this in chapter 11.

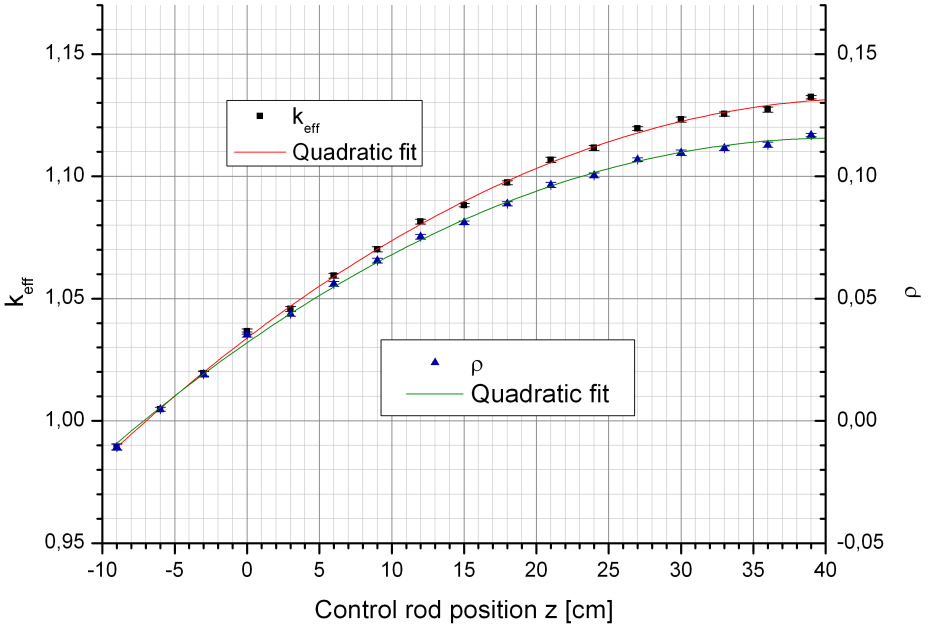

Figure 4.1: *k_{eff} and ρ over control rod position for a fresh core of the current fuel element.*

4.3 Materials

A more or less open question is which isotopes have to be tracked in burn-up calculations. In the script system described above, four options are given:

1. Track all materials where microscopic cross sections are available.
2. Track the subset given in [Gie96].
3. Track the subset given in [Gla05].
4. Track the subset given in [Röh09].

The first set is the only set that from its original composition also tracks activation products in the cladding and structural materials. It was furthermore the only way among these three to consider the burn-up of the boron-ring below the fuel plates and the beryllium follower in the control rod [Röh91a]. To overcome these deficiencies, the other three sets were expanded to be able to include the burn-up for the boron-ring. Therefore, in the implementation in X^2, all four sets can track the burn-up of the boron ring and the beryllium follower.

For the purpose of this thesis, a fifth set was compiled that includes only the most important fission product, but all actinides that appear and some more important activation products for structural materials or fuel additives. This cross section set is largely based on the set from Röhrmoser, [Röh09]. All fission products that were not tracked were lumped up in an average cross section entitled 45117.90c for ^{235}U and 46119.90c for ^{239}Pu[4] [Pos99, p. 28]. These cross sections therefore do not refer to $^{117}_{45}$Rh or $^{119}_{46}$Pd if they appear in the output of X^2 . In some cases, computational problems with these two cross sections arose, therefore they were not used in every calculation that is presented in this work. Due to computational limitations, in most cases it was not possible to use the cross section set 1 that tracks all materials. To account for the loss of mass due to neglectance of some of the fission products, the densities of the corresponding materials were adjusted proportionally.

The burn-up cross section sets available in X^2 are listed in appendix F.2, p. 280. In this work, mostly the specially compiled fifth set discussed above was used.

4.4 Uncertainty Propagation

Because of the uncertainties of MCCs themselves (statistical errors and the mechanisms described in chapter 2.5), burn-up calculations are additionally sensitive to errors in the results as they evolve with further timesteps: MC errors at the beginning of a depletion time step (DTS) lead to errors at the end, which introduces further errors in the next MC step and sums up with the new uncertainties introduced there. This leads to a degradation of data quality with an increasing number of time steps. It is therefore necessary to quantify the error that is introduced by this for all relevant quantities. The most rigorous approach to treat these uncertainties is discussed in [Shi08] and presented here in a strongly shorted version:

$$\sigma^2 [Q] = \sigma_\mathrm{s}^2 [Q] + \sigma_\mathrm{N}^2 [Q] + \sigma_\mathrm{X}^2 [Q] + \sigma_\mathrm{NX}^2 [Q] . \tag{4.12}$$

The single terms represent the uncertainties due to the statistical error[5], nuclide density uncertainties, cross sections and the correlation of the latter two.

4.4.1 Equations

Using the indices

Index	**Meaning**
α	Reaction type
g	Energy group of neutrons
i	Nuclide
j	Nuclide
k	k-th input set
m	Cell
n	Depletion time index

and the following quantities based on them

Quant.	**Equation**	**Meaning**

[4] Only for MonteBurns, both cross sections are used as this code has native support for them. For Cinder90, only 45117 is used and is summed up by X^2.

[5] Please note that in this chapter, σ is used for the statistical error as well as for the cross sections. However, its meaning is easily distinguishable from the context.

$r^{j,n}_{\alpha,m}$	$\int_{V_m}\int_0^\infty\int_{4\pi}\sigma^j_a(E)\phi(\boldsymbol{r},E,\Omega,t_n)\,\mathrm{d}V\,\mathrm{d}E\,\mathrm{d}\Omega$	reaction rate
$n^n_{m,i}$	-	Nuclide number density
$\sigma^i_{\alpha,g}$		cross section
Q	$Q\left(\ldots,n^n_{m,i},\ldots,\sigma^i_{\alpha,g},\ldots\right)$	MC estimate
Q_k	$Q\left(\ldots,(n^n_{m,i})_k,\ldots,(\sigma^i_{\alpha,g})_k,\ldots\right)$	MC estimate from k-th input set
$\gamma^n_{m,ij}$	$\sum_\alpha f_{\alpha,ij}r^{j,n}_{\alpha,m}$	Reaction from j to i
$\gamma^n_{m,i}$	$r^{i,n}_{a,m}$	Absorption in i
$f_{\alpha,ij}$	-	Number of formed i when α takes place in j,

the four summands in eq. 4.12 can be calculated. The first term, $\sigma^2_\mathrm{s}[Q]$, comes from the statistical uncertainty of the MC estimate Q. The second and third are uncertainties of the nuclide number density and the cross sections, while the last one represents the correlation between those two:

$$\sigma^2_\mathrm{N}[Q] = \sum_m\sum_i\sum_{m'}\sum_{i'}\rho\left[n^n_{m,i},n^n_{m',i'}\right]\cdot\delta\left\langle Q\left[n^n_{m,i}\right]\right\rangle\cdot\delta\left\langle Q\left[n^n_{m',i'}\right]\right\rangle \tag{4.13}$$

$$\sigma^2_\mathrm{X}[Q] = \sum_i\sum_\alpha\sum_g\sum_{i'}\sum_{\alpha'}\sum_{g'}\rho\left[\sigma^i_{\alpha,g},\sigma^{i'}_{\alpha',g'}\right]\cdot\delta\left\langle Q\left[\sigma^i_{\alpha,g}\right]\right\rangle\cdot\delta\left\langle Q\left[\sigma^{i'}_{\alpha',g'}\right]\right\rangle \tag{4.14}$$

$$\sigma^2_\mathrm{NX}[Q] = \sum_m\sum_i\sum_{i'}\sum_{\alpha'}\sum_{g'}\rho\left[n^n_{m,i},\sigma^{i'}_{\alpha',g'}\right]\cdot\delta\left\langle Q\left[n^n_{m,i}\right]\right\rangle\cdot\delta\left\langle Q\left[\sigma^{i'}_{\alpha',g'}\right]\right\rangle. \tag{4.15}$$

The triangular brackets $\langle\,\rangle$ designate the expected value of of the parameter that is to be estimated by MCCs. Therefore, the factors $\delta\langle Q(X)\rangle$ are determined by MC perturbation calculations as they are described in chapter 2.5:

$$\frac{\partial\langle Q\rangle}{\partial X}\cong\frac{\left\langle Q\left(\overline{X}+\sigma[X]\right)\right\rangle-\left\langle Q\left(\overline{X}\right)\right\rangle}{\sigma[X]}=\frac{\delta\langle Q(X)\rangle}{\sigma[X]} \tag{4.16}$$

So the remaining task is to calculate the correlation coefficients ρ that are defined by

$$\rho[X,Y]:=\frac{\mathrm{cov}[X,Y]}{\sigma[X]\cdot\sigma[Y]}. \tag{4.17}$$

$\mathrm{cov}[X,Y]$ is the covariance between X and Y.

Cross Section Correlation Coefficients

The cross section correlation coefficients $\rho\left[\sigma^i_{\alpha,g},\sigma^{i'}_{\alpha',g'}\right]$ can be calculated with NJOY for multigroup cross sections as described in chapter 3.2. These coefficients need the variances and covariances of the cross sections as input.

Number Density Correlation Coefficients

It is clear that $\rho\left[n^n_{m,i},n^n_{m',i'}\right]$ stems from uncertainties in the nuclide number densities at $t=t_n$. At the beginning of the first DTS, all nuclide number densities are supposed to be known without uncertainties, i. e. $\rho\left[n^1_{m,i},n^1_{m',i'}\right]=0$. The propagation of the error from the MCCs is then caused by the solution of the burn-up equations given in eq. 4.8. $(\boldsymbol{n}^{n+1}_m)_k$ is therefore a function of $(\boldsymbol{n}^n_m)_k$ and $(\mathbb{A}^n_m)_k$ and can be

expanded into a taylor series around the expected values of these quantities. The correlation coefficients can then be calculated in a recursive manner:

$$\begin{aligned}
\sigma^2\left[n_{m,i}^{n+1}\right] &= \sum_{i'}\sum_{i''}\rho\left[n_{m,i'}^{n},n_{m,i''}^{n}\right]\cdot\delta n_{m,i}^{n+1}\left[n_{m,i'}^{n+1}\right]\cdot\delta n_{m,i}^{n+1}\left[n_{m,i''}^{n+1}\right] \\
&\quad+\sum_{j,\alpha}\sum_{j',\alpha'}\rho\left[r_{\alpha,m}^{j,n},r_{\alpha',m}^{j',n}\right]\cdot\delta n_{m,i}^{n+1}\left[r_{\alpha,m}^{j,n}\right]\cdot\delta n_{m,i}^{n+1}\left[r_{\alpha',m}^{j',n}\right] \\
&\quad+2\sum_{i'}\sum_{j,\alpha}\rho\left[n_{m,i'}^{n},r_{\alpha,m}^{j,n}\right]\cdot\delta n_{m,i}^{n+1}\left[n_{m,i'}^{n+1}\right]\cdot\delta n_{m,i}^{n+1}\left[r_{\alpha,m}^{j,n}\right] \qquad (4.18)\\
\operatorname{cov}\left[n_{m,i}^{n+1},n_{m',i'}^{n+1}\right] &\cong \sum_{i''}\sum_{i'''}\rho\left[n_{m,i''}^{n},n_{m',i'''}^{n}\right]\cdot\delta n_{m,i}^{n+1}\left[n_{m,i''}^{n+1}\right]\cdot\delta n_{m',i'}^{n+1}\left[n_{m,i'''}^{n+1}\right] \\
&\quad+\sum_{j,\alpha}\sum_{j',\alpha'}\rho\left[r_{\alpha,m}^{j,n},r_{\alpha',m}^{j',n}\right]\cdot\delta n_{m,i}^{n+1}\left[r_{\alpha,m}^{j,n}\right]\cdot\delta n_{m',i'}^{n+1}\left[r_{\alpha',m}^{j',n}\right] \\
&\quad+\sum_{i''}\sum_{j',\alpha'}\rho\left[n_{m,i''}^{n},r_{\alpha',m}^{j',n}\right]\cdot\delta n_{m,i}^{n+1}\left[n_{m,i''}^{n+1}\right]\cdot\delta n_{m',i'}^{n+1}\left[r_{\alpha',m}^{j',n}\right] \\
&\quad+\sum_{i'''}\sum_{j,\alpha}\rho\left[r_{\alpha,m}^{j,n},n_{m',i'''}^{n}\right]\cdot\delta n_{m,i}^{n+1}\left[r_{\alpha,m}^{j,n}\right]\cdot\delta n_{m',i'}^{n+1}\left[n_{m,i'''}^{n+1}\right] \qquad (4.19)\\
\sigma^2\left[r_{\alpha,m}^{j,n}\right] &= \sigma_s^2\left[r_{\alpha,m}^{j,n}\right] \\
&\quad+\sum_{m''}\sum_{i''}\sum_{m'''}\sum_{i'''}\rho\left[n_{m'',i''}^{n},n_{m''',i'''}^{n}\right]\cdot\delta r_{\alpha,m}^{j,n}\left[n_{m'',i''}^{n}\right]\cdot\delta r_{\alpha,m}^{j,n}\left[n_{m''',i'''}^{n}\right] \\
&\quad+\sum_{i''}\sum_{\alpha''}\sum_{g''}\sum_{i'''}\sum_{\alpha'''}\sum_{g'''}\rho\left[\sigma_{\alpha'',g''}^{i''},\sigma_{\alpha''',g'''}^{i'''}\right]\delta r_{\alpha,m}^{j,n}\left[\sigma_{\alpha'',g''}^{i''}\right]\delta r_{\alpha,m}^{j,n}\left[\sigma_{\alpha''',g'''}^{i'''}\right] \\
&\quad+2\sum_{m''}\sum_{i''}\sum_{i'''}\sum_{\alpha'''}\sum_{g'''}\rho\left[n_{m'',i''}^{n},\sigma_{\alpha''',g'''}^{i'''}\right]\delta r_{\alpha,m}^{j,n}\left[n_{m'',i''}^{n}\right]\delta r_{\alpha,m}^{j,n}\left[\sigma_{\alpha''',g'''}^{i'''}\right] \qquad (4.20)\\
\operatorname{cov}\left[r_{\alpha,m}^{j,n},r_{\alpha',m'}^{j',n}\right] &= \operatorname{cov}\left[r_{\alpha,m}^{j,n},r_{\alpha',m'}^{j',n}\right]_s \\
&\quad+\sum_{m''}\sum_{i''}\sum_{m'''}\sum_{i'''}\rho\left[n_{m'',i''}^{n},n_{m''',i'''}^{n}\right]\cdot\delta r_{\alpha,m}^{j,n}\left[n_{m'',i''}^{n}\right]\cdot\delta r_{\alpha,m}^{j,n}\left[n_{m''',i'''}^{n}\right] \\
&\quad+\sum_{i''}\sum_{\alpha''}\sum_{g''}\sum_{i'''}\sum_{\alpha'''}\sum_{g'''}\rho\left[\sigma_{\alpha'',g''}^{i''},\sigma_{\alpha''',g'''}^{i'''}\right]\delta r_{\alpha,m}^{j,n}\left[\sigma_{\alpha'',g''}^{i''}\right]\delta r_{\alpha,m}^{j,n}\left[\sigma_{\alpha''',g'''}^{i'''}\right] \\
&\quad+\sum_{m''}\sum_{i''}\sum_{i'''}\sum_{\alpha'''}\sum_{g'''}\rho\left[n_{m'',i''}^{n},\sigma_{\alpha''',g'''}^{i'''}\right]\delta r_{\alpha,m}^{j,n}\left[n_{m'',i''}^{n}\right]\delta r_{\alpha,m}^{j,n}\left[\sigma_{\alpha''',g'''}^{i'''}\right] \\
&\quad+\sum_{m'''}\sum_{i'''}\sum_{i''}\sum_{\alpha''}\sum_{g''}\rho\left[\sigma_{\alpha'',g''}^{i''},n_{m''',i'''}^{n}\right]\delta r_{\alpha,m}^{j,n}\left[\sigma_{\alpha'',g''}^{i''}\right]\delta r_{\alpha',m'}^{j',n}\left[n_{m''',i'''}^{n}\right] \qquad (4.21)\\
\operatorname{cov}\left[r_{\alpha,m}^{j,n},n_{m',i'}^{n}\right] &= \sum_{m''}\sum_{i''}\rho\left[n_{m'',i''}^{n},n_{m',i'}^{n}\right]\cdot\delta r_{\alpha,m}^{j,n}\left[n_{m'',i''}^{n}\right]\cdot\sigma\left[n_{m',i'}^{n}\right] \\
&\quad+\sum_{i''}\sum_{\alpha''}\sum_{g''}\rho\left[\sigma_{\alpha'',g''}^{i''},n_{m',i'}^{n}\right]\delta r_{\alpha,m}^{j,n}\left[\sigma_{\alpha'',g''}^{i''}\right]\cdot\sigma\left[n_{m',i'}^{n}\right] \qquad (4.22)
\end{aligned}$$

Please note that

$$\rho\left[n_{m,i}^{1},n_{m',i'}^{1}\right]=\rho\left[n_{m,i''}^{1},r_{\alpha',m}^{j',1}\right]=\rho\left[r_{\alpha,m}^{j,1},n_{m',i'''}^{1}\right]=0 \qquad (4.23)$$

at $n=1$ because the uncertainties of the nuclear number densities were assumed to be 0 at the beginning of the first DTS. This is of course a rather courageous assumption regarding manufacturing tolerances of the fuel, but it simplifies the calculation greatly.

Equations 4.20 to 4.22 were obtained by treating the reaction rates $r^{j,n}_{\alpha,m}$ as MC estimates Q and regarding their variance. In fact, the reaction rates are obtained from MC tallies.

Mixed Correlation Coefficients

In the above equations, the mixed correlation coefficients are not known. They can be obtained by regarding the taylor series mentioned above.

$$\begin{aligned}\operatorname{cov}\left[n^{n+1}_{m,i},\sigma^{i'}_{\alpha',g'}\right] &\approx \sum_{i''}\rho\left[n^{n}_{m,i''},\sigma^{i'}_{\alpha',g'}\right]\cdot\delta n^{n+1}_{m,i}\left[n^{n}_{m,i''}\right]\cdot\sigma\left[\sigma^{i'}_{\alpha',g'}\right]\\ &\quad+\sum_{j,\alpha}\rho\left[r^{j,n}_{\alpha,m},\sigma^{i'}_{\alpha',g'}\right]\cdot\delta n^{n+1}_{m,i}\left[r^{j,n}_{\alpha,m}\right]\cdot\sigma\left[\sigma^{i'}_{\alpha',g'}\right] \qquad (4.24)\\ \operatorname{cov}\left[r^{j,n}_{\alpha,m},\sigma^{i'}_{\alpha',g'}\right] &\approx \sum_{m''}\sum_{i''}\rho\left[n^{n}_{m'',i''},\sigma^{i'}_{\alpha',g'}\right]\cdot\delta r^{j,n}_{\alpha,m}\left[n^{n}_{m'',i''}\right]\cdot\sigma\left[\sigma^{i'}_{\alpha',g'}\right]\\ &\quad+\sum_{i''}\sum_{\alpha''}\sum_{g''}\rho\left[\sigma^{i''}_{\alpha'',g''},\sigma^{i'}_{\alpha',g'}\right]\cdot\delta r^{j,n}_{\alpha,m}\left[\sigma^{i''}_{\alpha'',g''}\right]\cdot\sigma\left[\sigma^{i'}_{\alpha',g'}\right] \qquad (4.25)\end{aligned}$$

4.4.2 Algorithm

MC calculations are used to compute $\overline{r^{j,n}_{\alpha,m}}$ on the assumption that

$$\overline{r^{j,n}_{\alpha,m}} = \left\langle r^{j,n}_{\alpha,m}\left(\ldots,\overline{n^{n}_{m,i}},\ldots,\overline{\sigma^{i}_{\alpha,g}},\ldots\right)\right\rangle. \qquad (4.26)$$

The unbiased sample variances $\sigma^2_s\left[r^{j,n}_{\alpha,m}\right]$ and $\rho\left[r^{j,n}_{\alpha,m},r^{j',n}_{\alpha',m}\right]$ are then calculated using equations 4.20 to 4.22. The missing correlation coefficients $\rho\left[n^{n}_{m'',i''},n^{n}_{m''',i'''},\right]$ and $\rho\left[n^{n}_{m'',i''},\sigma^{i'''}_{\alpha''',g'''}\right]$ are calculated recursively by equations 4.18 and 4.19 respectively 4.24 and 4.25. As already mentioned, the correlation coefficients $\rho\left[\sigma^{i''}_{\alpha'',g''},\sigma^{i'''}_{\alpha''',g'''}\right]$ are calculated by NJoy.

Then, $\overline{n^{n+1}_{m'',i''}}$ is calculated from the solution of 4.7, 4.8. $\sigma^2\left[n^{n+1}_{m,i}\right]$ is calculated using eq. 4.18.

Optimization

The algorithm described above is accurate but slow. To overcome this problem, Shim et al. have showed that the computation time can be reduced by a factor of ten by only summing over neighbouring cells and regarding only the following nuclides: ^{234}U, ^{235}U, ^{236}U, ^{238}U, ^{239}Pu, ^{240}Pu, ^{241}Pu, ^{242}Pu, ^{135}Xe, ^{135}I, ^{149}Sm and ^{152}Sm [Shi08]. However, it can be shown that in the case of Frm II the burn-up zones in the fuel plate are strongly correlated in radial direction, so that all cells must be taken into account. The nuclides can be reduced to the mentioned set, though. Fig. 4.2 shows this correlation for the example cell r3/z4: the brighter the colour, the more neutrons originate from the corresponding cell and cause fission events in cell r3/z4.

Possible implementation

In this work, only point-wise cross sections are used. However, the algorithm above is for multigroup cross sections. As in the point-wise case the uncertainties of the cross sections cannot be treated the way described above, $\delta X\left[\sigma\right] = 0$ has to be assumed (see also chapter 3.2). Following that constraint, the mixed correlation coefficients in equations 4.24 and 4.25 are always zero. Additionally, equations 4.20 to

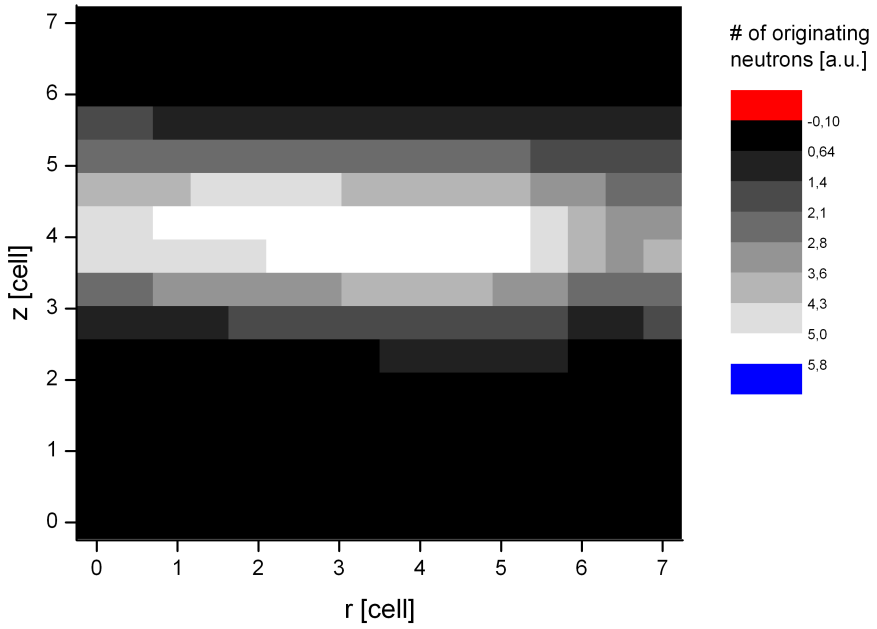

Figure 4.2: *Correlation of cells: cells from where the neutrons originate that cause fission events in cell r3/z4.*

4.22 are greatly simplified, while 4.18 and 4.19 don't change. Finally, in equation 4.12, $\sigma_{\mathrm{X}}^2[Q]$ and $\sigma_{\mathrm{NX}}^2[Q]$ become zero, so this equation is reduced to

$$\sigma^2[Q] = \sigma_{\mathrm{s}}^2[Q] + \sigma_{\mathrm{N}}^2[Q]\,. \tag{4.27}$$

4.4.3 Uncertainty treatment in X^2

In X^2, currently only the statistical uncertainty of k_{eff} from the last time step is regarded. This statistical uncertainty of k_{eff} is transformed into a control rod position uncertainty and included in the plots. As discussed in chapter 2.5.2, the value for k_{eff} has to be seen as a confidence interval, together with its uncertainty. Naturally, the same holds for the exact position of the control rod and its uncertainty. No uncertainties are calculated for the composition of the fuel in a single burn-up run.

However, as the above discussion showed, $\sigma_{\mathrm{s}}^2[Q]$ and $\sigma_{\mathrm{N}}^2[Q]$ depend only on the statistical uncertainty of the MCNP calculations if the uncertainty of the fuel composition at $t = 0$ is assumed to be zero. Therefore, the uncertainty of the fuel composition can be estimated from a series of statistically independent X^2 burn-up runs. The same holds for the statistical uncertainty of the control rod position, which is underestimated by a single X^2 run.

To estimate uncertainties for the fuel composition, the method described above is employed, too. As the burn-up calculation has to be repeated several times, this means of course quite a long calculation time, but it circumvents the large amount of work that would be needed to implement the uncertainty propagation technique described in chapters 4.4.1 and 4.4.2 into existing burn-up codes. Both methods do not take the systematic uncertainties of the cross sections and the covariant uncertainties of fuel composition and cross sections into account if point-wise cross sections are used. Additionally, as MonteBurns uses

perturbation theory to calculate reaction rates, the covariance terms discussed in section 2.5.5 are not taken into account. Some of these terms were calculated manually and turned out to be small for the FRM II burn-up calculations.

The statistical independence of the multiple X^2 runs is achieved by manipulating the MCNP random number generator. It should be noted that the results achieved with this method can not simply be obtained by increasing the particle number in MCNP in a single X^2 run, as this would not provide the uncertainties that are caused by differing fuel compositions.

Part II

Thermal Hydraulics

CHAPTER 5

Heat Conduction in Solids

In this chapter, heat transport in solid bodies is introduced. The interaction with the fluid and its convective mechanisms are treated in a later chapter.

5.1 The Diffusion Equation

The change of temperature T in a volume element of a solid body is described by the heat equation

$$\frac{\partial T}{\partial t} = \boldsymbol{\nabla} \left(a \boldsymbol{\nabla} T \right) + S. \tag{5.1}$$

S is a source term, a the *thermal diffusivity*, that is defined by

$$a := \frac{\kappa}{c_p \rho}. \tag{5.2}$$

Its unit is therefore $^{m^2}/_{\mathrm{s}}$. The other quantities are the thermal conductivity κ, the specific heat capacity at constant pressure c_p and the density ρ.

The source term S is regarded as a temperature source with units $^{\mathrm{K}}/_{\mathrm{s}}$:

$$S := \frac{Q}{c_p \cdot \rho}. \tag{5.3}$$

Q is the energy created per volume element and time. In the stationary case $\partial T / \partial t = 0$ holds and one obtains

$$\boldsymbol{\nabla} \left(a \boldsymbol{\nabla} T \right) = -S. \tag{5.4}$$

In a homogeneous body, the equation can be multiplied by $\rho c_p / \kappa$ to obtain[1]

$$\Delta T = -\frac{Q}{\kappa}. \tag{5.5}$$

This equation has the form of a Poisson equation and is therefore analogous to the corresponding equation in electrostatics. According to Fourier's law, the *heat flux density* is

$$q = -\kappa \cdot \boldsymbol{\nabla} T. \tag{5.6}$$

[1] The temperature dependence of ρ, c_p and κ was neglected here.

For $Q = 0$, i. e. without internal heat source,

$$\Delta T + \frac{\boldsymbol{\nabla} \cdot q}{\kappa} = 0. \tag{5.7}$$

Since the general static case is considered here, i. e. inhomogeneous and with heat sources, the equation that actually has to be solved is 5.4. Applying the divergence theorem to a volume element one obtains from eq. 5.4 that

$$\int \boldsymbol{\nabla} \left(a \boldsymbol{\nabla} T\right) \mathrm{d}V = \oint a \boldsymbol{\nabla} T \mathrm{d}\boldsymbol{A} \tag{5.8}$$

$$= -\int S \mathrm{d}V, \tag{5.9}$$

which together with eq. 5.6 leads to the trivial conclusion that in the static case, all energy set free in the volume element has to flow out through the volume elements borders.

5.2 Implementation in CFX

The equation actually solved by Ansys Cfx is a form of 5.1, which includes an additional term to account for the motion of a solid body. However, as no motion of solid bodies is regarded in this work, the calculation of this term has been disabled.

CHAPTER 6

Classical Consideration

The thermal-hydraulic results of this work, which are obtained by numerical solution of the Navier Stokes Equations, are compared to results for the current fuel element which were obtained by classical calculation schemes for verification purposes (see chapter 18.2). Such a scheme is for instance implemented in the program NBK of Anton Röhrmoser, which is discussed in detail in [Röh84, Död89]. These classical schemes use a set of dimensionless numbers derived from similitude theory and a number of correlations that can only be applied for a certain range of cases. Some of these numbers and correlations find their way back into computational fluid dynamics (CFD) calculations when models have to be used, e. g. for boiling or near-wall phenomenons. Here, only a short overview of these relations and quantities is given. They are discussed in greater detail as needed later on.

6.1 Calculation of Basic Quantities and Ratios

Hydraulic diameter: The hydraulic diameter is an effective length that makes allowance to use the relations developed for circular pipes and turbulent flows on non-circular pipes.[1] It is defined as

$$d_h := 4\frac{A}{u}, \tag{6.1}$$

where A is the passed through area and u the moistured perimeter. Using an arc length for the fuel plate of 69.4 mm, a channel width of 2.2 mm and a passed through area per cooling channel of 131.7 mm^2, for the FRM II the hydraulic diameter is $d_h = 4.26\,\text{mm}$.

Reynolds Number: The Reynolds number is the ratio between inner friction and mass forces or the inertial forces and viscous forces. It is therefore a measure for the dynamic similitude of fluid flows. It follows that the turbulent behaviour of geometrically related bodies is identical for equal Reynolds numbers. Laminar flows with smooth and constant motion occur for low Reynolds numbers, which means that viscous forces are dominant. At high Reynolds numbers, inertial forces dominate, which produce flow instabilities like eddies and vortices. The flow is then turbulent.

$$\text{Re} := \frac{vd}{\nu}. \tag{6.2}$$

v is the velocity of the fluid, d a characteristic dimension of the pipe, here the hydraulic diameter d_h. The Reynolds number depends on the temperature of the fluid through the kinematic viscosity ν.

[1] In principle, the hydraulic diameter cannot be applied to laminar flows, even if this is done in some literature.

With a coolant velocity of 15.91 m/s using the hydraulic diameter calculated above, and 37 ℃ temperature for the coolant, $\mathrm{Re} \approx 1 \cdot 10^5$ between the fuel plates. This is well above the critical value of $\mathrm{Re}_{\mathrm{crit}} \approx 2300$, which defines the transition from a laminar to a turbulent flow.[2]

Prandtl Number: The Prandtl number describes the thermal properties of a flow by the ratio of the momentum diffusivity to the thermal diffusivity a (see eq. 5.2) and is defined as

$$\mathrm{Pr} := \frac{\nu}{a}. \tag{6.3}$$

It is therefore a measure to describe the ratio between convective and conductive heat transfer. In problems involving heat transfer from a wall, the Prandtl number is also a measure for the ratio of the thicknesses of the flow and the temperature boundary layer:

$$\frac{d_S}{d_T} = \sqrt{\mathrm{Pr}}. \tag{6.4}$$

Using a temperature of 37 ℃, for current conditions at FRM II is $\mathrm{Pr} \approx 4.56$.

Nusselt Number: The Nusselt number is the ratio of convective heat transfer and heat conduction at a boundary within a fluid through a layer of thickness d, i. e. the enhancement of heat transfer by convection:

$$\mathrm{Nu} := \frac{\alpha d}{\kappa}. \tag{6.5}$$

α is the *heat transfer coefficient*. The calculation of the heat transfer coefficient depends strongly on the conditions, e. g. on the fluid, the flow regime, the geometry etc.

For turbulent flows in rectangular channels, according to Gnielinski [Gni75], the Nusselt number is connected to the Prandtl and the Reynolds number by:[3]

$$\mathrm{Nu}_0 = \frac{1}{8\left(1.82 \log_{10} \mathrm{Re} - 1.64\right)^2} \frac{(\mathrm{Re} - 1000)\,\mathrm{Pr}}{1 + \frac{12.7}{\sqrt{8}(1.82 \log_{10} \mathrm{Re} - 1.64)} \left(\mathrm{Pr}^{\frac{2}{3}} - 1\right)} K_{\mathrm{Pr}}. \tag{6.7}$$

where

$$K_{\mathrm{Pr}} = \left(\frac{\mathrm{Pr}_F}{\mathrm{Pr}_w}\right)^{0.11} \tag{6.8}$$

is a correction factor for the temperature profile near the wall. Pr_F and Pr_w are the Prandtl numbers of the fluid at the median fluid temperature T_F and the wall temperature T_w. This number has to be corrected for the friction at the pipe walls. Here, empirical relations exist, too [Nor70]:

$$\mathrm{Nu} = \mathrm{Nu}_0 \left(\frac{\zeta_r}{\zeta_g}\right)^{0.68 \cdot \mathrm{Pr}^{0.215}} \cdot f_k. \tag{6.9}$$

[2] Actually, a flow with $\mathrm{Re} > \mathrm{Re}_{\mathrm{crit}}$ is not inevitably turbulent, but for the FRM II Reynolds number, it can be well concluded that the flow is turbulent.

[3] Another empirical relation is given by Colburn [Roh73], that was also used for the design of HFR in Grenoble:

$$\mathrm{Nu} = 0.023 \cdot \mathrm{Re}^{0.8} \cdot \mathrm{Pr}^{0.34}. \tag{6.6}$$

Some more relations and a discussion, where they are applicable, can be found in [Röh84], p. 39

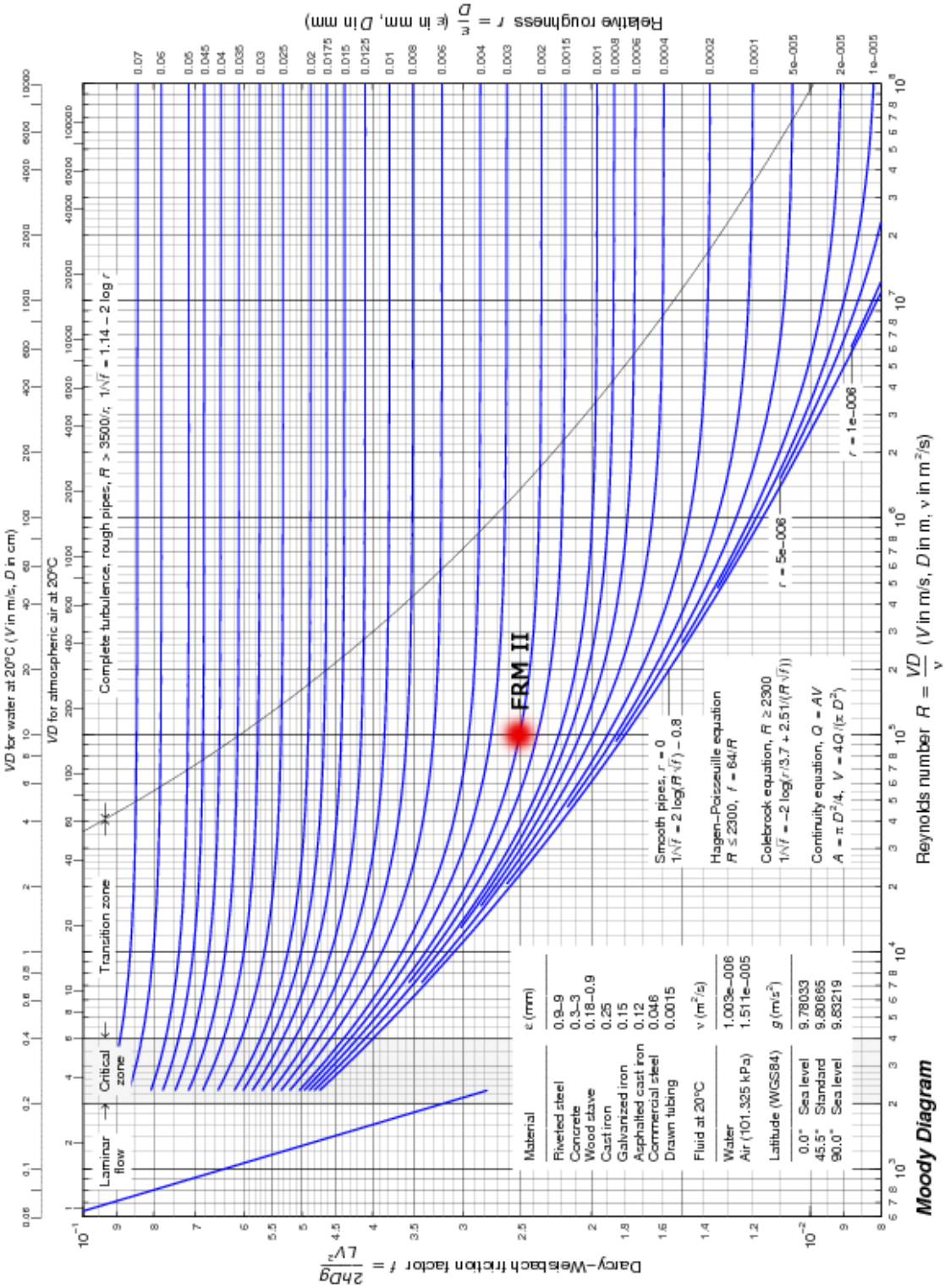

Figure 6.1: *Moody-Diagramm*

f_k is a correction factor for the shape of the tube[4], ζ_r the friction factor for a rough-textured, ζ_g for a sleek tube. This relation is valid as long as the ratio is smaller than 4. The friction factor of a sleek tube is according to Prandtl calculated by

$$\frac{1}{\sqrt{\zeta_g}} = 2\log_{10}\frac{\mathrm{Re}^*\sqrt{\zeta_g}}{2.51}, \tag{6.10}$$

where the modified Reynolds number Re^* has to be plugged in. This relation has a theoretic deduction and is therefore well-founded compared to other, purely empiric relations. According to Jones, d_h is not suitable to calculate Re for this special purpose. In this case, $\mathrm{Re}^* = 0.7\,\mathrm{Re}$, with the prefactor being a function of the channel width. According to Petukhov [Pet79], due to the wall heating and the temperature dependence of the viscosity, this number has to be further corrected by

$$\zeta_g = \frac{1}{6}\zeta_{g,0}\left(7 - \frac{\mu_F}{\mu_W}\right). \tag{6.11}$$

The friction number of the rough-textured tube can be calculated with a formula of Colebrook and White[5] [Wag61]:

$$\frac{1}{\sqrt{\zeta_r}} = -2\log_{10}\left(\frac{\epsilon}{3.71} + \frac{2.51}{\mathrm{Re}\sqrt{\zeta_r}}\right). \tag{6.13}$$

The *relative roughness* ϵ is given by $\epsilon = \frac{k}{d_h}$, where k is the absolute roughness. For new, technically flat, pultruded aluminium tubes, the absolute roughness is about 0.0015 mm, comparable tubes made of steel have 0.01 mm–0.05 mm. This legitimates the assumption of $\epsilon \approx 1/500$ as it is made in [Död89]. If this number is seen together with a Reynolds number of approximately 10^5, one is settled in the transition region between flat and rough-textured tubes in the Moody diagram in Fig. 6.1[6]. Therefore, eq. 6.13 may be used to determine the friction of the tube [Mer00]. Again, the heating of the wall has to be considered [Ihl75]:

$$\zeta_r = \zeta_{r,0}\left(\frac{\mu_F}{\mu_W}\right)^{0.182+\frac{800}{\mathrm{Re}+18000}}. \tag{6.14}$$

6.2 Heat Transfer

The heat flux density q_W at the wall can be calculated by using the heat transfer coefficient α, which can be calculated using eq. 6.5:

$$q_w = \alpha \cdot (T_W - T_F) \tag{6.15}$$

[4] According to Kakaç [Kak87], no correction has to be applied ($f_k = 1$), whereas [Död89] recommends $f_k \approx 0.94$.

[5] In the *Arbeitsbericht zur thermohydraulischen Kernauslegung des FRM II*, [Gie96], the more convenient to calculate formula

$$\zeta_r = 0.0055\left(1 + \sqrt[3]{20000\epsilon + \frac{10^6}{\mathrm{Re}}}\right) \tag{6.12}$$

is used. The values obtained are about 5% too large compared to those of eq. 6.13 in the range of $4 \cdot 10^3 < \mathrm{Re} < 1 \cdot 10^7$. For FRM II working conditions, the deviation is about 1.5%.

[6] Reynolds number on lower x-axis, relative roughness on right-y axis.

6.3 Safety Margins

During normal operation of FRM II, no boiling occurs. The importance of safety margins to the point of boiling can be assessed from fig. 6.2: At the *Onset of Nucleate Boiling* (ONB), boiling starts, vapour is produced within the cooling channel. The pressure drop continues to fall and the void fraction rises as the flow velocity is decreased. This continues past the *Onset of Significant Voiding* (OSV) until a point called *Onset of Flow Instability* (OFI) is reached. The presence of steam in the bulk liquid causes an increasing frictional drag. New acceleration and buoyancy effect also influence the pressure drop. At the OFI, this increase compensates the pressure drop losses due to the decreased velocity. A further velocity reduction causes the pressure drop to rise again. This can cause the fluid to be redistributed into other cooling channels, which destabilises the whole system and results in excursive or Ledinegg instabilities [Led38].

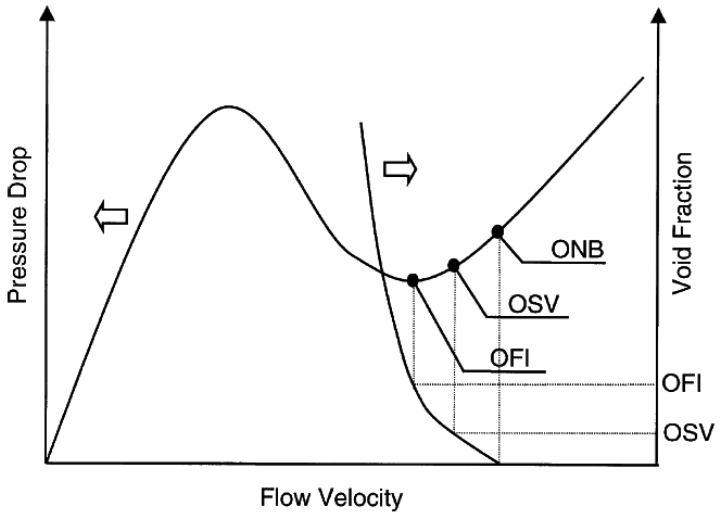

Figure 6.2: *Typical boiling curve: Pressure drop depending on the flow velocity. Taken from [Li,04].*

To be able to calculate the safety margin against different phenomena, two quantities have to be introduced: ΔT_{sub} is the subcooling of the liquid, the difference between boiling temperature T_s and the temperature of the fluid T_f. ΔT_{sat} is the difference between the wall temperature T_w and the boiling temperature:

$$\Delta T_{\text{sub}} := T_s - T_f \tag{6.16}$$

$$\Delta T_{\text{sat}} := T_w - T_s. \tag{6.17}$$

A CFD based approach will be discussed in chapter 8. However, to come to the point, it was not possible to implement that approach into CFX for the time being, therefore the approach discussed in the next subsections was used to calculate safety margins.

6.3.1 Onset of Nucleate Boiling

The distance to the onset of nucleate boiling can be estimated by solving the following two equations iteratively:

$$q_{\mathrm{ONB}} = \alpha(T) \cdot (\Delta T_{\mathrm{sub}} + \Delta T_{\mathrm{sat,ONB}}) \tag{6.18}$$

$$q_{\mathrm{ONB}} = \frac{p^{1.156}}{8.928} \left(1.8 \Delta T_{\mathrm{sat,ONB}}\right)^{2.18 \cdot p^{-0.0234}} \tag{6.19}$$

$$S_{\mathrm{ONB}} := \frac{q_{\mathrm{ONB}}}{q} \tag{6.20}$$

Here, $\Delta T_{\mathrm{sat,ONB}}$ is the wall super heating at the onset of nucleate boiling. α should be calculated for one-phase heat transfer and temperature dependent. However, as this would take very long when a CFD code is used, in this work, α is only calculated once. The safety margin is the minimum value of S_{ONB}, a localized value. It has no direct predication for the power margin of the whole core to ONB.

6.3.2 Departure from Nucleate Boiling

The heat flux to estimate the departure from nucleate boiling can be calculated by [Mir59]:

$$q_{\mathrm{DNB}} = 151 \, (1 + 0.1197 \, v) \, (1 + 0.00914 \, \Delta T_{\mathrm{sub}}) \, (1 + 0.186 \, p) \tag{6.21}$$

$$S_{\mathrm{DNB}} := \frac{q_{\mathrm{DNB}}}{q} \tag{6.22}$$

Sometimes, S_{DNB} is smaller than S_{ONB} or larger than S_{OFI}, which seems unphysical. However, it is not the absolute scale of these factors which really matters but more the fluid velocity v_x where $S_X = 1$. As the slope of each of the $S_X(v)$ is different, they will cross $S_X = 1$ in the correct order. See [Död89, p. 52] and [Röh84, p. 17] for more details.

6.3.3 Onset of Flow Instability

A non-local criterion for the onset of flow instability was developed by Whittle and Forgeen [Whi67], which depends only on the temperatures and pressures at in- and outlet:

$$R = \frac{T_{\mathrm{out}} - T_{\mathrm{in}}}{T_{\mathrm{s,out}} - T_{\mathrm{in}}} \tag{6.23}$$

$$R_c = 0.697 + 0.00063 \frac{L_H}{d_H} \tag{6.24}$$

$$S_{\mathrm{OFI,WF}} = \frac{R_c}{R} \tag{6.25}$$

A localized model was developed by Bowring [Bow62] and later corrected by Moritz [Mor89] and Owen [Owe63]:

$$\eta = \frac{\Delta T_{\mathrm{sub}}}{q} v \tag{6.26}$$

$$\eta_{H'} = (21.2 + 0.77 \, v) \, 10^{-6} \mathrm{Km^3/J} \tag{6.27}$$

$$\eta_H = \eta_{H'} + K\sigma \tag{6.28}$$

$$\eta_H = (36.5 + 0.77 \, v) \, 10^{-6} \mathrm{Km^3/J} \tag{6.29}$$

$$S_{\mathrm{OFI}} = \frac{\eta_H}{\eta} \tag{6.30}$$

6.3.4 Implementation in CFX

The calculation of the safety margins above relies on a quantity T_f, the averaged temperature of the fluid along a straight line through the channel. Thinking in terms of CFD calculations, this quantity is unknown to the code, as the temperature is only known for discrete locations. However, equation 6.15 still holds and CFX also calculates a heat transfer coefficient α. How this is done is described in chapter 7.2.3, after the underlying theory has been explained.

From the known parameters q, α and T_w, the unknown fluid temperature T_f can be calculated. However, this is not the average fluid temperature across the channel, but a so called 'Near-wall fluid temperature', which is considerably higher than the average temperature. As a second option, the average fluid temperature can be calculated for every CFX mesh node on the wall by solving a line integral through the channel, which is quite time consuming. However, it turns out that T_f indeed must be calculated using the line integrals, otherwise the safety margins would be too conservative, as all safety margins decrease with decreasing ΔT_{sub}.

CHAPTER 7

Fluid Mechanics

7.1 Fundamentals

The fundamental equations of fluid mechanics are the *Navier Stokes Equations*, corresponding to conservation of momentum, and the *Continuity Equation*, corresponding to conservation of mass. Additionally, the *Energy Equation* controls the conservation of energy. These equations are derived by regarding an infinitesimal volume element. Many of the following equations make use of *Reynolds transport theorem* in their deduction[1]:

$$\frac{\mathrm{d}}{\mathrm{d}t}\int_{V_t} f\,\mathrm{d}V = \int_{V_c\equiv V_t}\frac{\partial f}{\partial t}\,\mathrm{d}V + \int_{S_c\equiv S_t} f\boldsymbol{v}\cdot\boldsymbol{n}\,\mathrm{d}S \tag{7.1}$$

V_t is a moved volume element, V_c a fixed one, that is identical with V_t at time t. S_c and S_t are the surfaces of these control volumes. $\boldsymbol{v}$ is the velocity of the fluid. The function f is a general field quantity. The Reynolds transport theorem is essentially a three-dimensional generalisation of the Leibniz integral rule and connects the Euler and the Lagrange approach for a control volume. In the Euler approach, the control volume is regarded as fixed in space and the flow passes through it, while it is moved with the flow in the Lagrange approach.

7.1.1 Continuity Equation

The continuity equation is derived by regarding the mass conservation in a volume element, i. e. from the condition

> **T**emporal change of mass in the volume =
> $\sum$ incoming mass flows -
> $\sum$ outgoing mass flows.

The mass flow through an area $\mathrm{d}x_j \cdot \mathrm{d}x_k$ is $\rho v_i \cdot \mathrm{d}x_j \cdot \mathrm{d}x_k$ with i, j, k unequal. The volume is treated as fixed in space.

$$\begin{aligned}
\frac{\mathrm{d}m}{\mathrm{d}t} &= \frac{\mathrm{d}}{\mathrm{d}t}\int_{V_t}\rho\,\mathrm{d}V && (7.2)\\
&= \int_{V_c\equiv V_t}\frac{\partial\rho}{\partial t}\,\mathrm{d}V + \int_{S_c\equiv S_t}\rho\boldsymbol{v}\cdot\boldsymbol{n}\,\mathrm{d}S && (7.3)\\
&= 0. && (7.4)
\end{aligned}$$

[1] For clarity reasons, space- and time-dependencies of the regarded quantities are not explicitly written down. It is self-explaining, which quantities comprise these dependencies.

The change of mass in the volume element is equal to the sum of currents through the surfaces. This

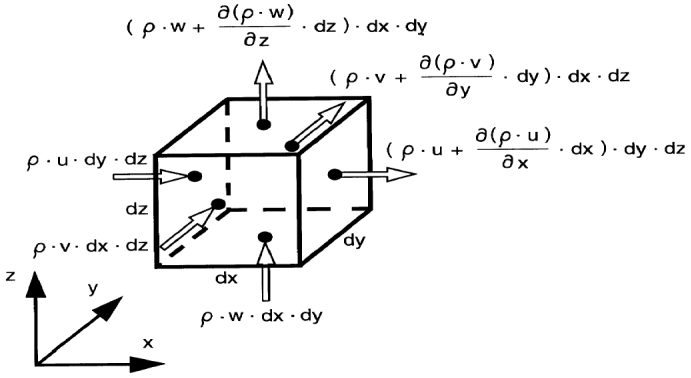

Figure 7.1: *On the deduction of the continuity equation. Taken from [Oer03].*

is just the Reynolds transport theorem, where the density ρ is used as the field quantity. Using Gauß theorem the continuity equation is derived:

$$\boxed{\frac{\partial \rho}{\partial t} + \nabla \cdot (\rho \boldsymbol{v}) = 0.} \tag{7.5}$$

7.1.2 Navier Stokes Equation

The Navier Stokes Equation represents the conservation of momentum in a volume element. The condition is

> **T**emporal change of momentum in the volume element =
> $\sum$ incoming momentum currents -
> $\sum$ outgoing momentum currents +
> $\sum$ forces acting on the volume element.

In the volume element the fluid has the momentum $\rho \boldsymbol{v}\, \mathrm{d}V$. As the volume element is fixed in space, the total time derivation can be replaced by partial time derivations of this quantity plus the momentum, that is transfered by the flow through the surface.

Momentum Current

Let the momentum current through a surface $\mathrm{d}x_j\, \mathrm{d}x_k$ be $\rho v_i v_i\, \mathrm{d}x_j\, \mathrm{d}x_k$. On the opposite site, the current $\left(\rho v_i v_i + \frac{\partial(\rho \cdot v_i \cdot v_i)}{\partial x_i}\, \mathrm{d}x_i\right)\, \mathrm{d}x_j\, \mathrm{d}x_k$ flows through the surface. The incoming current can leak through other surfaces, but then with velocity component v_j or v_k. Equally, the current leaving through the surface element named above could have entered through the other surface elements. All in all, this results in a term[2] $(\rho \boldsymbol{v} \otimes \boldsymbol{v}) \cdot \boldsymbol{n}\, \mathrm{d}S$.

Forces

Surface forces (normal stress, shear stress, pressure) can be included by introducing a *stress tensor* $\boldsymbol{\sigma}$ (Cauchy stress tensor):

$$\boldsymbol{\sigma} = -p\mathbb{1} + \boldsymbol{\tau}. \tag{7.6}$$

[2] $\boldsymbol{v}\boldsymbol{v}^T = \{v_i v_j\}_{ij} = \boldsymbol{v} \otimes \boldsymbol{v}$

$\mathbb{1}$ is the unity matrix. By introducing a negative algebraic sign for the pressure p, it is understood as a negative normal stress. For the stress-strain tensor $\boldsymbol{\tau}$ holds:

$$\tau_{ii} = \lambda \boldsymbol{\nabla} \cdot \boldsymbol{v} + 2\mu \frac{\partial v_i}{\partial x_i} \tag{7.7}$$

$$\tau_{ij} = \mu \left(\frac{\partial v_i}{\partial x_j} + \frac{\partial v_j}{\partial x_i} \right). \tag{7.8}$$

This relationship is derived from an extended version of Newtons friction law $\tau = \mu \frac{\mathrm{d}v_i}{\mathrm{d}x_j}$ $(i \neq j)$, the friction law by Stokes. It is $\lambda \approx -\frac{2}{3}\mu$. μ is the dynamic viscosity, λ is called *bulk viscosity*. From the upper equation follows directly $\tau_{ij} = \tau_{ji}$. Furthermore, for incompressible fluids ($\rho = \text{const.}$) or if $\lambda + \frac{2}{3}\mu = 0$, it follows because of $\operatorname{tr} \tau = 0$:

$$p = \frac{1}{3} \operatorname{tr} \sigma. \tag{7.9}$$

The whole tensor can be subsumed to

$$\boldsymbol{\tau} = (\lambda \boldsymbol{\nabla} \cdot \boldsymbol{v})\, \mathbb{1} + 2\mu \mathbb{D}(\boldsymbol{v}) \tag{7.10}$$

with[3]

$$\mathbb{D}(\boldsymbol{v}) := \frac{1}{2} \left(\mathbb{J}(\boldsymbol{v}) + \mathbb{J}(\boldsymbol{v})^T \right). \tag{7.11}$$

Body forces like gravity and electromagnetic forces appear as an acceleration $\boldsymbol{g}$ on the element. Together with the surface forces, the combined force on the volume can be written as

$$\boldsymbol{f} = \rho \boldsymbol{g} \mathrm{d}V + \boldsymbol{\sigma} \cdot \boldsymbol{n}\, \mathrm{d}S. \tag{7.12}$$

Navier Stokes Equation

Following the contemplations above, besides equation 7.12 also holds

$$\boldsymbol{f} = \frac{\partial (\rho \boldsymbol{v})}{\partial t} \mathrm{d}V + (\rho \boldsymbol{v} \otimes \boldsymbol{v}) \cdot \boldsymbol{n}\, \mathrm{d}S. \tag{7.13}$$

The forces from equations 7.12 and 7.13 must compensate, as the volume element is declared fixed in space. Inserting both equations in each other and applying Reynolds transport theorem togehter with Gauß theorem ($\boldsymbol{\sigma} \cdot \boldsymbol{n}\, \mathrm{d}S = \boldsymbol{\nabla} \cdot \boldsymbol{\sigma}\, \mathrm{d}V$), the *Navier Stokes Equation* is obtained:

$$\boxed{\frac{\partial(\rho \boldsymbol{v})}{\partial t} + \boldsymbol{\nabla} \cdot (\rho \boldsymbol{v} \otimes \boldsymbol{v}) = -\boldsymbol{\nabla} p + \boldsymbol{\nabla} \cdot \boldsymbol{\tau} + \rho \boldsymbol{g}.} \tag{7.14}$$

7.1.3 Energy Equation

For the energy conservation in the volume element holds:

Temporal change of inner and kinetic energy in the volume element =
$\sum$ incoming and outgoing energy flux +
$\sum$ flow of energy by heat conduction +
$\sum$ work done by forces per unit time +
$\sum$ energy addition from outside

[3]The second term in equation 7.11 could also be written as $\boldsymbol{\nabla} \otimes \boldsymbol{v}$.

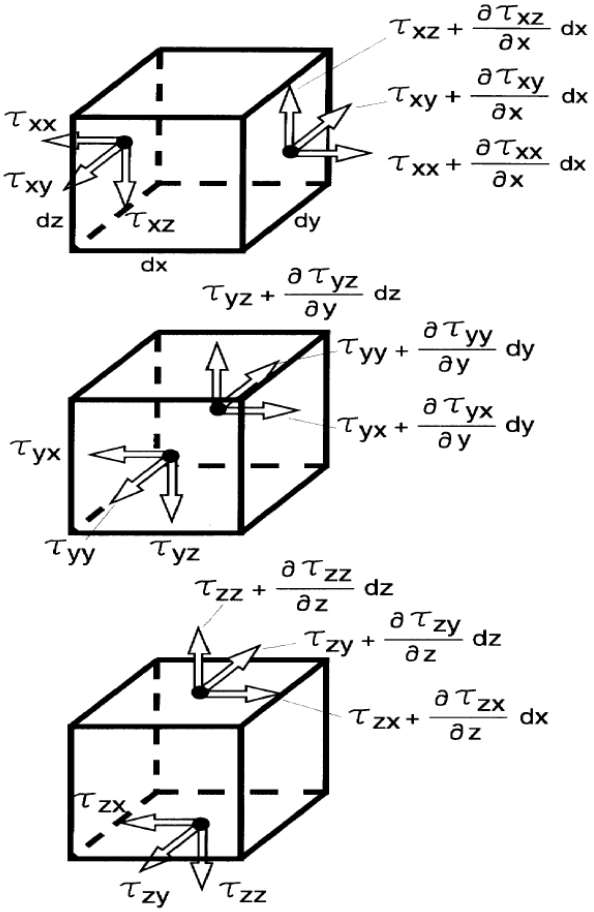

Figure 7.2: *On the deduction of the Navier Stokes Equation. Taken from [Oer03].*

Using the first law of thermodynamics, this means

$$\mathrm{d}U = \delta Q + \delta W. \tag{7.15}$$

The energy inside the volume[4], $\rho E \,\mathrm{d}V$, comprises the inner energy $\rho e \,\mathrm{d}V$ and the kinetic energy of the fluid $\rho|\boldsymbol{v}|^2 \,\mathrm{d}V$:

$$\rho E \,\mathrm{d}V = \rho e \,\mathrm{d}V + \rho|\boldsymbol{v}|^2 \,\mathrm{d}V. \tag{7.16}$$

Transport

The temporal change of energy is made up of the change of inner energy and the transport of energy through the side walls of the volume element:

$$\frac{\mathrm{d}}{\mathrm{d}t}\int (\rho E)\ \mathrm{d}V = \int \frac{\partial\,(\rho E)}{\partial t}\,\mathrm{d}V + \int \rho E \boldsymbol{v}\cdot\boldsymbol{n}\,\mathrm{d}S. \tag{7.17}$$

The last term equals the energy flux through the outwalls.

[4] E and e are specific energies, $U := \rho E V$.

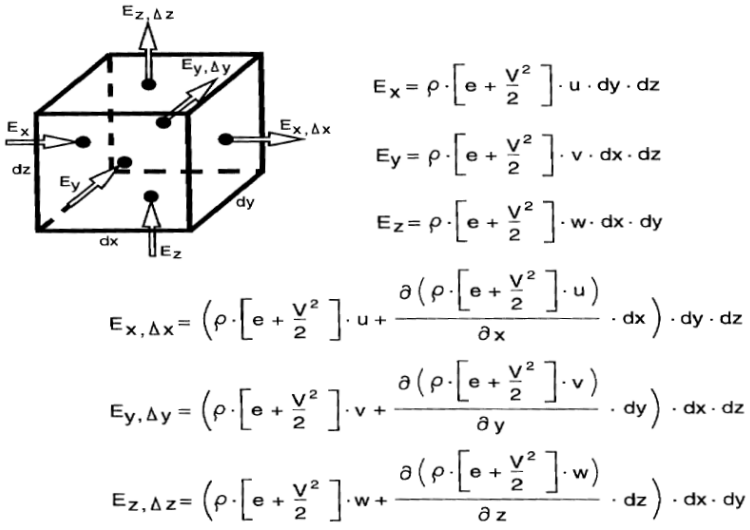

Figure 7.3: *On the deduction of the energy equation. Taken from [Oer03].*

Heating

By thermal conduction and heat sources within the element (e. g. chemical reactions and energy transported by neutrons that is deposited in the element through collisions), energy is changed. The heat sources can be included with $\rho q \, \mathrm{d}V$, where q is the strength of the source (in $^{\mathrm{W}}/_{\mathrm{kg}}$). Heat conduction is included with Fourier's law by a term $-\kappa \boldsymbol{\nabla} T \, \mathrm{d}S$.

$$\mathrm{d}\dot{Q} = \rho q \, \mathrm{d}V - \kappa \boldsymbol{\nabla} T \, \mathrm{d}S \tag{7.18}$$

Work

The work done per unit time is the cross product of the acting force and the velocity. In agreement with the explanations on the Navier Stokes equation given before, the work is

$$\mathrm{d}\dot{W} = \rho \boldsymbol{g} \cdot \boldsymbol{v} \, \mathrm{d}V + \boldsymbol{v} \cdot (\boldsymbol{\sigma} \cdot \boldsymbol{n}) \, \mathrm{d}S. \tag{7.19}$$

Energy Equation

After pasting in the said values and some conversions, the time derivation of equation 7.15[5] after applying Gauß' Theorem yields the *energy equation*:

$$\boxed{\frac{\partial(\rho E)}{\partial t} + \boldsymbol{\nabla} \cdot (\rho E \boldsymbol{v}) = \boldsymbol{\nabla} \cdot (\kappa \boldsymbol{\nabla} T) + \rho q - \boldsymbol{\nabla} \cdot (p \boldsymbol{v}) + \boldsymbol{v} \cdot (\boldsymbol{\nabla} \cdot \boldsymbol{\tau}) + \mathbb{J}(\boldsymbol{v}) : \boldsymbol{\tau} + \rho \boldsymbol{g} \cdot \boldsymbol{v}.} \tag{7.22}$$

[5]

$$\begin{aligned} \boldsymbol{\nabla} \cdot (\boldsymbol{\sigma} \cdot \boldsymbol{v}) &= -\boldsymbol{\nabla} (p \boldsymbol{v}) + \boldsymbol{\nabla} \cdot (\boldsymbol{\tau} \cdot \boldsymbol{v}) && (7.20) \\ &= -\boldsymbol{\nabla} (p \boldsymbol{v}) + \boldsymbol{v} \cdot (\boldsymbol{\nabla} \cdot \boldsymbol{\tau}) + \mathbb{J}(\boldsymbol{v}) : \boldsymbol{\tau} && (7.21) \end{aligned}$$

7.1.4 Unification

Equations 7.5, 7.14 and 7.22 comprise the *compressible Navier Stokes Equations*. They can be combined in a conservation equation:

$$\boxed{\frac{\partial \boldsymbol{U}}{\partial t} + \boldsymbol{\nabla} \cdot \mathbb{F} = \boldsymbol{Q}.} \tag{7.23}$$

Here is ($\boldsymbol{U} \in \mathbb{R}^5$, $\mathbb{F} \in \mathbb{R}^{3\times 5}$, $\boldsymbol{Q} \in \mathbb{R}^5$):

$$\boldsymbol{U} := \begin{pmatrix} \rho \\ \rho \boldsymbol{v} \\ \rho E \end{pmatrix} \tag{7.24}$$

$$\mathbb{F} := \begin{pmatrix} \rho \boldsymbol{v} \\ \rho \boldsymbol{v} \otimes \boldsymbol{v} + p \mathbb{1} - \boldsymbol{\tau} \\ (\rho E + p)\, \boldsymbol{v} - \kappa \boldsymbol{\nabla} T - \boldsymbol{\tau} \cdot \boldsymbol{v} \end{pmatrix} \tag{7.25}$$

$$\boldsymbol{Q} := \begin{pmatrix} 0 \\ \rho \boldsymbol{g} \\ \rho\,(q + \boldsymbol{g} \cdot \boldsymbol{v}) \end{pmatrix} \tag{7.26}$$

$$\tag{7.27}$$

The system of equations 7.23 is strongly under-determined. It can be solved only by introducing additional assumptions, especially 7.10, 7.11, $\lambda \approx -\frac{2}{3}\mu$ and some thermodynamical relations, e. g. $E = c_V T$.

7.1.5 Initial and Boundary Conditions

Many possibilities for initial and boundary conditions exist. The ones most commonly used are presented in the following.

The region Γ in the arrangement to be studied consists of the region Γ_{in} for the incoming flow, Γ_{out} for the outgoing flow and the walls Γ_{w}. The interior zone that is studied is Ω, the whole region $\bar{\Omega} := \Omega \cup \Gamma$.

$$\Gamma := \Gamma_{\text{in}} \cup \Gamma_{\text{out}} \cup \Gamma_{\text{w}} \tag{7.28}$$

$$\Gamma_{\text{in}} := \{\boldsymbol{x} \in \Gamma : \boldsymbol{v} \cdot \boldsymbol{n} < 0\} \tag{7.29}$$

$$\Gamma_{\text{out}} := \{\boldsymbol{x} \in \Gamma : \boldsymbol{v} \cdot \boldsymbol{n} > 0\} \tag{7.30}$$

$$\Gamma_{\text{w}} := \{\boldsymbol{x} \in \Gamma : \boldsymbol{v} \cdot \boldsymbol{n} = 0\} \tag{7.31}$$

Initial Conditions

For transient simulations or as initial guesses for the solver:

$$\rho|_{t=0} = \rho_0(\boldsymbol{x}) \tag{7.32}$$

$$\boldsymbol{v}|_{t=0} = \boldsymbol{v}_0(\boldsymbol{x}) \tag{7.33}$$

$$E|_{t=0} = E_0(\boldsymbol{x}) \tag{7.34}$$

$$\tag{7.35}$$

Boundary Conditions

Inflow: Entry of the flow Γ_{in}

$$\rho = \rho_{\text{in}} \tag{7.36}$$

$$\boldsymbol{v} = \boldsymbol{v}_{\text{in}} \tag{7.37}$$

$$E = E_{\text{in}} \tag{7.38}$$

Outflow: Region of outflow Γ_{out}. Boundary conditions most times include assumptions on the average static pressure.

Wall: Normally, there is no flow perpendicular to a wall Γ_{w}. In addition, the so called *no-slip condition* is formulated. It belongs to the set of hydrodynamic boundary conditions, which signifies that there is no flow at the wall at all:

$$\boldsymbol{v}_{\Gamma_{\text{w}}} = 0. \tag{7.39}$$

Furthermore, thermodynamic boundary conditions of the third kind are useful:

$$T(x \to \Gamma_{\text{w}}) = T(\Gamma_{\text{w}} \leftarrow x) \tag{7.40}$$

$$\kappa_1 \frac{\partial T_1}{\partial x}\bigg|_{x\to\Gamma_{\text{w}}} = \kappa_2 \frac{\partial T_2}{\partial x}\bigg|_{\Gamma_{\text{w}}\leftarrow x}. \tag{7.41}$$

These signify that there is no jump in temperature when going from material 1 to material 2. The same holds for the heat flux density.

7.1.6 Dimensionless Form

For the numeric solution of equation 7.23, dimensionless quantities are introduced, in parts based on the initial conditions:

$$t^* := \frac{t}{t_0} \tag{7.42}$$

$$\boldsymbol{x}^* := \frac{\boldsymbol{x}}{L_0} \tag{7.43}$$

$$\boldsymbol{v}^* := \frac{\boldsymbol{v}}{v_0} \tag{7.44}$$

$$p^* := \frac{p}{\rho\,|\boldsymbol{v}_0|^2} \tag{7.45}$$

$$T^* := \frac{T - T_0}{T_1 - T_0}. \tag{7.46}$$

7.2 Turbulence

7.2.1 Fundamental Equations

The whole physics of turbulence is included in 7.23. The problem arises in the spatial resolution required to account for all turbulences as the extent of turbulent structures spreads over several orders of magnitude. Even today on modern large capacity computers, it is only possible to a limited extend to capture even the smallest eddies on sub-millimetre scales.[6] So the phenomenons of turbulence have to be modeled in a suitable way. For this, quasi-stationary states are regarded, where turbulences can be averaged statistically (*Favre average*):

$$\bar{f} := \frac{1}{t}\int_0^t f\,\mathrm{d}t'. \tag{7.47}$$

Especially the time interval t has to be chosen carefully, so that the fluctuations of interest are not averaged, too (compare fig. 7.4). This is one of the tasks of the turbulence model.

[6] The equations have to be discretized to be solved numerically. The resulting mesh would require a resolution in the order of some ten micrometres, producing a mesh with an unfeasible number of nodes.

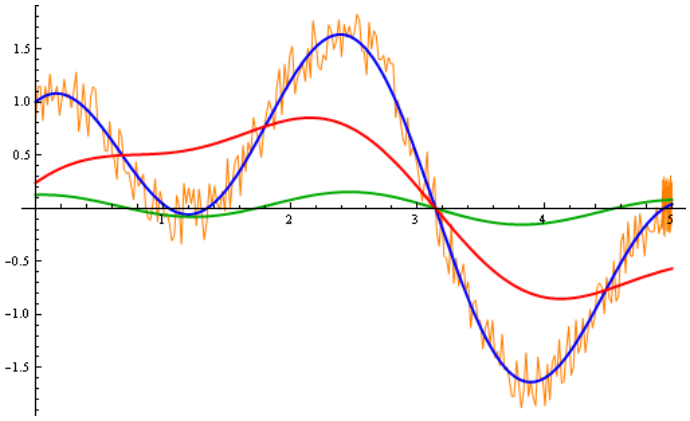

Figure 7.4: *Choosing the proper averaging interval: Real function with fluctuations (orange), ideal average (blue) and wrong averages (red, green).*

Furthermore, mass-averaged quantities are used:

$$\tilde{\boldsymbol{v}} := \frac{\overline{\rho \boldsymbol{v}}}{\bar{\rho}} \tag{7.48}$$

The original quantities can be expressed as a sum of averaged quantities and a *fluctuating quantity*:

$$\rho = \bar{\rho} + \rho' \tag{7.49}$$
$$p = \bar{p} + p' \tag{7.50}$$
$$\boldsymbol{v} = \tilde{\boldsymbol{v}} + \boldsymbol{v}'' \tag{7.51}$$
$$T = \tilde{T} + T'' \tag{7.52}$$
$$E = \tilde{E} + E'' \tag{7.53}$$

p and ρ naturally are not mass-averaged, their fluctuating quantities are therefore represented with only one $'$. For the fluctuating quantities is $\overline{f''} \neq 0$, but $\overline{\rho f''} = 0$. Furthermore is $\bar{\bar{f}} = \bar{f}$ and $\overline{\partial f}/\partial s = \partial \bar{f}/\partial s$.

The time average of the system of equations 7.23 yields:

$$\frac{\partial \bar{\rho}}{\partial t} + \nabla \cdot (\bar{\rho} \tilde{\boldsymbol{v}}) = 0 \tag{7.54}$$
$$\frac{\partial (\bar{\rho} \tilde{\boldsymbol{v}})}{\partial t} + \boldsymbol{\nabla} \cdot (\bar{\rho} \tilde{\boldsymbol{v}} \otimes \tilde{\boldsymbol{v}}) = -\boldsymbol{\nabla} \bar{p} + \boldsymbol{\nabla} \cdot \bar{\boldsymbol{\tau}} + \bar{\rho} \boldsymbol{g} + \boldsymbol{\nabla} \cdot \boldsymbol{\tau}_t. \tag{7.55}$$
$$\frac{\partial (\bar{\rho} h_{\text{tot}})}{\partial t} - \frac{\partial \bar{p}}{\partial t} + \nabla \cdot (\bar{\rho} \tilde{\boldsymbol{v}} h_{\text{tot}}) = \nabla \cdot \left(\kappa \nabla \boldsymbol{\tau} + \rho \overline{\boldsymbol{v}'' h} \right) + \nabla \cdot (\tilde{\boldsymbol{v}} \cdot \bar{\boldsymbol{\tau}}) + Q \tag{7.56}$$

Here, Q is the internal energy source, h the specific enthalpy and $h_{\text{tot}} = h + \frac{1}{2} \boldsymbol{v} \cdot \boldsymbol{v}$ the total enthalpy. The enthalpie depends on temperature and pressure. If additional variables (ϕ) have to be computed, the transport equation for them is [CFX06b, p. 74]

$$\frac{\partial \bar{\rho} \phi}{\partial t} + \nabla \cdot (\bar{\rho} \tilde{\boldsymbol{v}} \phi) = \nabla \cdot \left(a \nabla \phi - \bar{\rho} \overline{\boldsymbol{v}'' \phi} \right) + S_\phi \tag{7.57}$$

with S_ϕ being the source term of the additional variable. Additional variables are later introduced via turbulence models.

$\bar{\boldsymbol{\tau}}$ includes the time average of all components of $\boldsymbol{\tau}$:

$$\bar{\tau}_{ij} := \mu\left(\frac{\partial\tilde{v}_i}{\partial x_j}+\frac{\partial\tilde{v}_j}{\partial x_i}\right)+\mu\left(\frac{\partial\overline{v_i''}}{\partial x_j}+\frac{\partial\overline{v_j''}}{\partial x_i}\right) \tag{7.58}$$

$$\approx \mu\left(\frac{\partial\tilde{v}_i}{\partial x_j}+\frac{\partial\tilde{v}_j}{\partial x_i}\right). \tag{7.59}$$

The second term in 7.58 is very small for 'real' applications and can be neglected in most cases. The same holds for the so called 'Reynolds pressure' that arises from the fluctuating quantity of the pressure, p'. For the term called *Reynolds Stress Tensor*, $\boldsymbol{\tau}_t$, in eq. 7.55 holds

$$\tau_{t,ij} := -\overline{\rho v_i'' v_j''}. \tag{7.60}$$

After the approximations made above, it comprises the fluctuating quantities and therefore is the central element in the turbulence treatment.

7.2.2 Turbulence Models

Turbulence can be divided in three parts: Large, energy-carrying eddies with non-viscous flow, small viscous eddies that tend to isotropy and an intermediate range. It has to be distinguished between global processes like convection and diffusion that transport turbulent properties through space and are therefore differential, and local algebraic properties like the production and dissipation of turbulence. These characteristics have to be taken into account when a turbulence model is chosen. Due to the need of transporting turbulence, no algebraic models are suitable for the calculation of the flow through the fuel element of FRM II.

All turbulence models deal with modelling $\boldsymbol{\tau}_t$ from eq. 7.60. Most models are based on the *Boussinesq Approximation*, that assumes that the fluctuating quantity $\tau_{t,ij}$ can be modeled analogue to the stresses τ_{ij}:

$$\boldsymbol{\tau}_t = 2\mu_t\mathbb{D}(\tilde{\boldsymbol{v}}). \tag{7.61}$$

μ_t is called the *exchange quantity*. It is no material constant but a time- and space-dependent quantity. As the quantity to be modeled, μ_t, is a scalar, the tensor character of $\boldsymbol{\tau}_t$ is not accounted for properly and the direction dependence is lost. μ_t is comparable to the viscosity and therefore also called *turbulent viscosity*. Thereupon, a quantity called *turbulence intensity* can be defined:

$$I := \frac{1}{1000}\frac{\mu_t}{\mu}. \tag{7.62}$$

Another quantity called *turbulent kinetic energy* can be introduced:

$$K := \frac{1}{2}\sum_i \overline{v_i''\cdot v_i''}. \tag{7.63}$$

It determines the energy in the turbulence and allows for the representation

$$\tau_{t,ij} = \mu_t\left(\frac{\partial\bar{v}_i''}{\partial x_j}+\frac{\partial\bar{v}_j''}{\partial x_i}\right)-\frac{2}{3}\rho K\delta_{ij}. \tag{7.64}$$

The second term is a *turbulent pressure* and can be neglected [Oer03, p. 49] as it is done in the CFX-Solver [CFX06b, p. 73]. In addition, a *turbulent thermal diffusivity* and a *turbulent thermal conductivity* can be introduced:

$$-\overline{v_i'' \cdot T'} = a_t \cdot \frac{\partial T}{\partial x_i} \tag{7.65}$$

$$a_t = \frac{\kappa_t}{\rho \cdot c_V}. \tag{7.66}$$

For fluids with low thermal conductivity like water, the turbulent thermal diffusivity and the turbulent viscosity can be correlated by the so-called *Turbulent Prandtl number* $\mathrm{Pr}_t = \nu_t / a_t$ where $\nu_t = \mu_t / \rho$ is the *kinematic turbulent viscosity* with $\mathrm{Pr}_t \approx 0.9$. This reduces the task of turbulence modeling to model the turbulent viscosity. In component notation of eq. 7.55 using sum convention, the turbulent viscosity then is just added to the molecular viscosity:

$$\frac{\partial \bar{v}_i}{\partial t} + \frac{\partial}{\partial x_j}\left(\bar{v}_j \cdot \bar{v}_i\right) = -\frac{\partial \bar{p}}{\partial x_i} + \frac{\partial}{\partial x_j}\left[(\nu + \nu_t) \cdot \left(\frac{\partial \bar{v}_i}{\partial x_j} + \frac{\partial \bar{v}_j}{\partial x_i}\right)\right]. \tag{7.67}$$

It should be noted that the application of these approximations requires turbulence to be isotropic, as all turbulence parameters are modeled via one quantity. Especially near walls, turbulence is anisotropic up to a factor of two between wall-parallel and -orthogonal fluctuations [Oer03, p. 51].

All models presented in the following depend on the validity of the continuum hypothesis and that the Stokes stress-strain relation holds even for the smallest structures [Wol09]. This is characterised by a sort of *Knudsen number*, which gives the ratio of the length scale of molecular motion, $l_{\mathrm{mfp}} = \nu / c$ with c being the speed of sound, and small turbulent fluctuations, $l_k = \nu^{3/4} / \epsilon^{1/4}$:

$$\mathrm{Kn} = \frac{l_{\mathrm{mfp}}}{l_k} \tag{7.68}$$

$$= \frac{\mathrm{Ma}}{\mathrm{Re}^{1/4}} \frac{\sqrt{K}}{v}. \tag{7.69}$$

Kn obviously is only large for small Reynolds numbers Re and large Mach numbers $\mathrm{Ma} = v/c$, which is not the case for FRM II ($\mathrm{Kn} \ll 1$). Therefore, the above assumptions are considered valid.

K-ϵ Model

The K-ϵ model is a two equation model and considered as the industry standard model. It is one of the most frequently used turbulence models. It has proven to be stable and numerically robust and has a well established regime of predictive capability. Therefore, it is a good compromise in terms of accuracy and robustness.

As the name suggests, the K-ϵ model relies on two quantities, the turbulent kinetic energy K defined in eq. 7.63 and the *turbulent dissipation*

$$\epsilon := \nu \cdot \overline{\frac{\partial v_i''}{\partial x_k} \cdot \frac{\partial v_i''}{\partial x_k}}. \tag{7.70}$$

This quantity can be thought of as the variable determining the length scale of the turbulence. Using this quantity, the turbulent viscosity can be modeled as

$$\mu_t = \rho C_\mu \frac{K^2}{\epsilon} \tag{7.71}$$

with the model constant $C_\mu = 0.09$. For both quantities, K and ϵ, the transport equation 7.57 has to be solved. Therefore, initial values for K and ϵ have to be provided at the inlet of the flow.

One of the major drawbacks is its inability to model turbulent low-Reynolds number flows near heated walls [CFX06a, p. 127] correctly or requiring extremely fine meshes ($y^+ < 0.2$, see chap. 7.2.3 on what this means) without wall functions. Even though wall functions are used in this work, this is one of the most important properties to be simulated in this work. The K-ϵ model is not the model of choice for this problem. Furthermore, the eddy viscosity assumption is only valid for equilibrium effects.

K-ω Model

The K-ω model is very similar to the K-ϵ model. It has the same transport equations for turbulence generation and dissipation. The model constants have other values and one of the constants in the ϵ-transport equation is replaced by a function of ϵ, ρ and the shear production of turbulence. This approach is based on the renormalization group analysis of the Navier-Stokes equations [CFX06b, p. 77].

In comparison to K-ϵ, its advantage is the near wall treatment for low-Reynolds number computations, i. e. in principle no complex non-linear damping functions are required, resulting in improved accuracy and robustness. Several flavours of the K-ω model exist. They are based on the approach of linking the turbulent viscosity with the turbulent kinetic energy and a *turbulent frequency*, also called *specific dissipation*:

$$\mu_t = \rho \frac{K}{\omega}. \tag{7.72}$$

Regarding its functionality, ω can be compared to ϵ, this time determining the time-scale of the turbulence.

The first and one of the most common K-ω models is the *Wilcox K-ω model* [Wil98]. It solves two transport equations, one for K and one for ω. Without the use of wall functions, the K-ω model would require $y^+ < 2$ (see eq. 7.90 for definition). Several modifications exist for this model [Wil04]. The Wilcox model is very sensitive to initial freestream conditions [Men93a], making it not an appropriate choice for the mostly unknown turbulence properties in FRM II.

SST Model

First, the BSL model was introduced to overcome the deficiencies of the Wilcox mode. It uses an approach that combines the K-ϵ with the K-ω model. The transition between both models is achieved using blending functions and subsequent addition of the original model equations and was developed by Menter [Men98]. A good overview of the underlying mathematics is given in [CFX06b, p. 80].

Both the K-ϵ and the K-ω model do not account for the transport of turbulent shear stress, resulting in an overprediction of the eddy-viscosity. This naturally also applies for the BSL model. To overcome this, another model combining K-ϵ and K-ω was developed, the SST (Shear Stress Transport) model [Men93b]. It uses the K-ω formulation in the inner parts of the boundary layer, making the model usable all the way down to the wall through the viscous sublayer. In the free stream it switches to the K-ϵ behaviour, thus avoiding the K-ω problem of being to sensitive to the inlet free-stream turbulence properties. In addition, the eddy-viscosity is limited by a limiter factor, thus avoiding the mentioned overprediction.

The model is known to produce slightly too large turbulence levels in regions with large normal strain, but not as bad as this would be done by the K-ϵ model.

The SST model is the model of choice in this work. It is also recommended by ANSYS, the developer of the CFX code. Its formulation is rather complex and therefore only a short overview on the governing

equations is given here. It can be looked up in great detail in [CFX06b] and [Men03]. The transport equation of K and ω are

$$\frac{\partial(\rho K)}{\partial t} + \boldsymbol{\nabla}\cdot(\rho v_i K) = \tilde{P}_k - \beta^*\rho K\omega + \boldsymbol{\nabla}\cdot[(\mu+\sigma_k\mu_t)\boldsymbol{\nabla}K] \tag{7.73}$$

$$\frac{\partial(\rho\omega)}{\partial t} + \boldsymbol{\nabla}\cdot(\rho v_i\omega) = \alpha\rho S^2 - \beta\rho\omega^2 + \boldsymbol{\nabla}\cdot[(\mu+\sigma_\omega\mu_t)\boldsymbol{\nabla}\omega] + 2(1-F_1)\rho\sigma_{\omega 2}\frac{1}{\omega}\boldsymbol{\nabla}K\,\boldsymbol{\nabla}\omega. \tag{7.74}$$

The model uses two blending functions[7],

$$F_1 = \tanh\left(\min\left[\max\left[\frac{\sqrt{K}}{\beta^*\omega y}, \frac{500\nu}{y^2\omega}\right], \frac{4\rho\sigma_{\omega 2}K}{\mathrm{CD}_{K\omega}y^2}\right]^4\right) \tag{7.75}$$

$$F_2 = \tanh\left(\max\left[\frac{2\sqrt{K}}{\beta^*\omega y}, \frac{500\nu}{y^2\omega}\right]\right) \tag{7.76}$$

with y the distance to the nearest wall,

$$\mathrm{CD}_{K\omega} = \max\left[2\rho\sigma_{\omega 2}\frac{1}{\omega}\boldsymbol{\nabla}K\,\boldsymbol{\nabla}\omega, 10^{-10}\right], \tag{7.77}$$

the *turbulent eddy viscosity*

$$\nu_t := \frac{a_1 K}{\max[a_1\omega, SF_2]}, \tag{7.78}$$

the invariant measure of the strain rate S

$$S := \sqrt{2S_{ij}S_{ij}} \tag{7.79}$$

$$S_{ij} = \frac{1}{2}\left(\frac{\partial v_i}{\partial x_j} + \frac{\partial v_j}{\partial x_i}\right) \tag{7.80}$$

$$= \frac{1}{\mu}\tau_{ij} \tag{7.81}$$

and the production limiter

$$P_k = \mu_t S\Omega \tag{7.82}$$

$$\tilde{P}_K = \min[P_k, 10\beta^*\rho K\omega], \tag{7.83}$$

which limits the build-up of turbulence in stagnation regions. Here, Ω is a modification to the original SST-Model proposed by [Kat93] with the magnitude of the *vorticity rate* Ω and the vorticity tensor Ω_{ij}:

$$\Omega := \sqrt{2\Omega_{ij}\Omega_{ij}} \tag{7.84}$$

$$\Omega_{ij} = \frac{1}{2}\left(\frac{\partial v_i}{\partial x_j} - \frac{\partial v_j}{\partial x_i}\right). \tag{7.85}$$

The other constants are computed by blend from the corresponding constants of the K-ϵ- and the K-ω-model via

$$\alpha = \alpha_1 F_1 + \alpha_2(1-F_1). \tag{7.86}$$

The corresponding values are $\beta^* = 0.09$, $\alpha_1 = \frac{5}{9}$, $\beta_1 = \frac{3}{40}$, $\sigma_{k1} = 0.85$, $\sigma_{\omega 1} = 0.5$, $\alpha_2 = 0.44$, $\beta_2 = 0.0828$, $\sigma_{k2} = 1$, $\sigma_{\omega 2} = 0.856$.

[7] $F_1 = 0$ away from the surface (K-ϵ) and $F_1 \approx 1$ inside the boundary layer (K-ω).

The model was extended by Hellsten to handle rough surfaces as required for the computation of the cooling channels of FRM II [Hel97].

Compared to to the K-ϵ-model, the SST Model predicts lower near wall-flow temperatures and slightly lower maximum wall temperatures (and consequently a lower maximum fuel temperature), which is equal to the prediction of a higher heat transfer coefficient. Compared to K-ω, predictions of wall-related properties are naturally very similar due to the underlying K-ω-wall treatment in the SST model.

Still, the SST model is a two equation model based on the Boussinesq Assumption, therefore inheriting all weaknesses that are a direct consequence of neglecting the possibility of the Reynolds stress tensor being not proportional to the strain rate tensor. This assumptions is especially invalid in flows with strong curvature, acceleration or decelleration. Here, Reynolds stress models have to be used to account for the anisotropy of the turbulence. This is especially true at the very beginning and end of the fuel plates, but fortunately the first few mm are not relevant for cooling. Therefore, the SST model is usually sufficient to calculate the cooling of the plates.

As the SST model is also an eddy-viscosity based model, it is insensitive to streamline curvature. CFX offers the possibility to include a production correction term. The effect of this is very small as the curvature of the fuel plates on a mesh-cell basis is very small. The theory on this topic is therefore not discussed here and the reader is referred to [CFX09b, Spa97, Smi08], for further information.

Reynolds Stress Models

In Reynolds Stress Models, every component of the Reynolds Stress tensor is calculated, that means, the Boussinesq Approximation is not used. As the cooling of a fuel element is not an isothermal flow, the energy equation has to be taken into account, too. One of the most robust Reynolds Stress Models is the *SSG Model*. Compared to the K-ϵ model, six additional transport equations have to be solved. In addition, source terms are more complex. This leads to an increased computational effort and may additionally result in slower convergence.

In this work, Reynolds Stress Models are only used when direct effects of the sharp plate borders or the combs are studied. For this reason the Reynolds Stress Models are not explained here. Extensive documentation can be found for example in [CFX09b, p. 65 et sqq.].

7.2.3 Turbulence Wall Modeling

Measurements and mathematical analysis have shown that the near-wall region can effectively be divided in two layers, an almost laminar-like *viscous sublayer* where viscosity plays a dominant role in momentum and heat transfer, and a *logarithmic layer*, where turbulence dominates the mixing process. Sometimes a so called *buffer layer* is quoted inbetween them, a sublayer between those two where turbulent and viscous effects play an equal role. See fig. 7.5 for a plot of the velocity law near the wall.

Wall Functions

To overcome the need for very fine meshes to account for all the different flow properties close to the walls, so called *wall functions* are introduced. These functions use empirical or semi-empirical formulas that impose suitable conditions near to the wall without resolving the boundary layer itself. In this work, so called *scalable wall functions* and *automatic wall functions* are used, i. e. wall functions that allow for arbitrarily fine meshes by relying on logarithmic wall functions if the mesh is not fine enough to resolve the viscous sublayer. If the mesh is fine enough though, the viscous sublayer will be resolved without using the logarithmic approach.

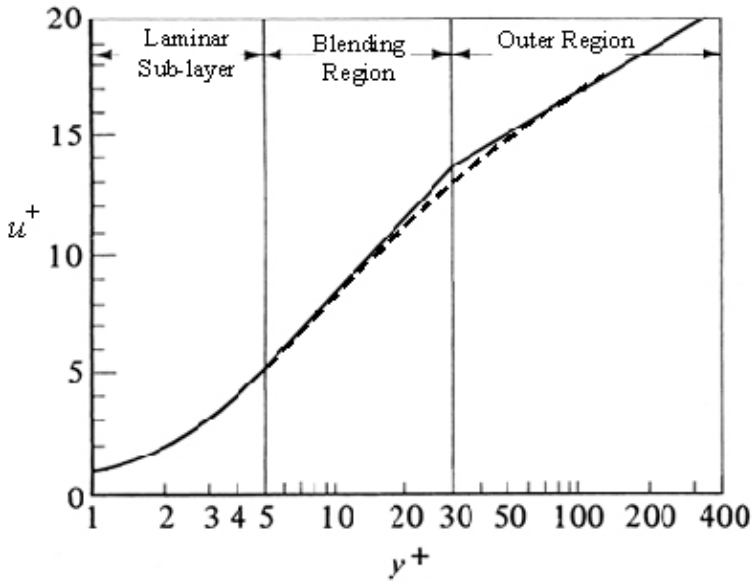

Figure 7.5: *Turbulent flow near the wall. Taken from [law].*

The logarithmic approach is based on analytic solutions of the Navier Stokes equation in simple geometries like a duct:

$$v^+ = \frac{1}{\kappa} \cdot \ln y^+ + C. \tag{7.87}$$

$\kappa = 0.41$ is called the *Kármán constant*, $C = 5.5$. Here, so called dimensionless *wall units* are used:

$$v^+ = \frac{\bar{v}}{v_\tau} \tag{7.88}$$

$$v_\tau = \sqrt{\tau_w \rho} \tag{7.89}$$

$$y^+ = \frac{y \cdot v_\tau}{\nu} \tag{7.90}$$

with τ_w being the average wall shear stress. v_τ has the dimension of a velocity and is called *wall shear stress velocity*, y is the real distance from the wall.

In the viscous sub-layer, the linear approach $v^+ \propto y^+$ is valid while the logarithmic approach can not be applied. The logarithmic region starts at about $y^+ = 26$. For this reason, a minimum distance of the first mesh node from the wall of $y^+ > 26$ must hold if wall functions are used.

Scalable Wall Functions

Scalable wall functions overcome the deficiencies of normal wall functions when the grid resolution near the wall extends in the blending region or even the linear region. Using scalable wall function, arbitrary fine grids can be applied without being forced to figure out if wall functions can be used or not. For this, a

modified velocity law is used where v^+ cannot become zero, for example at separation points with $v_t = 0$. The approach in eq. 7.87 is slightly modified [Esc03] to

$$v_\tau = \frac{v_t}{\frac{1}{\kappa} \cdot \log \tilde{y}^* + C} \tag{7.91}$$

$$\tau_\omega = \rho v^* v_\tau \tag{7.92}$$

$$v^* = C_\mu^{0.25} k^{0.5} \tag{7.93}$$

$$y^* = \frac{\rho v^* \, \Delta y}{\mu} \tag{7.94}$$

$$\tilde{y}^* := \max\left[y^*, y^*_{\mathrm{lim}}\right] \tag{7.95}$$

with $y^*_{\mathrm{lim}} = 11.06$. 11.06 is the intersection between the logarithmic and the linear near wall profile. The introduction of this limiting factor prevents the first grid point from sliding into the linear profile area. This means that all points are assumed to be outside the viscous sublayer and inconsistencies caused by the fine grid are avoided.

For the treatment of the energy equation near the wall, the following algebraic formulation derived by Kader [Kad81] links the temperature (in a dimensionless form Θ^*) and the wall heat flux q_w:

$$\Theta^* = \mathrm{Pr} \cdot y^+ \mathrm{e}^{-\Gamma} + \left[2.12 \, \ln\left(1 + y^+\right) + \left(3.85 \, \mathrm{Pr}^{1/3} - 1.3\right)^2 + 2.2 \, \ln(\mathrm{Pr})\right] \cdot \mathrm{e}^{-1/\Gamma} \tag{7.96}$$

$$\Gamma := \frac{0.01 \, \left(\mathrm{Pr} \cdot y^+\right)^4}{1 + 5 \, \mathrm{Pr}^3 \cdot y^+} \tag{7.97}$$

$$\Theta^* := \frac{T_w - T}{T_\tau} \tag{7.98}$$

$$T_\tau = \frac{q_w}{\rho c_p v_\tau}. \tag{7.99}$$

This formulation is valid through the entire y^+ range of the viscous sublayer and the logarithmic profile for a large range of Prandtl numbers. For scalable wall functions, y^+ has to be replaced by $\tilde{y}^*$ in eq. 7.96 and 7.97.

Automatic Near-Wall Treatment

Instead of using wall functions, a fine-grid analysis extending through the viscous sublayer could be carried out. However, this is not desirable for larger problems due to the required very fine grid spacing. Automatic wall functions allow for the combination of both techniques, fine grids and scalable wall functions. Blending functions are used to blend between the behaviour for the viscous sublayer and the logarithmic region. Although automatic wall treatment is used in this work for ω-based turbulence models like SST, it will not be discussed here in detail as in all cases y^+ is so large that scalable wall functions are applied.[8] This is also to circumnavigate problems that may appear in connection with rough walls, where a manual adjustment of model coefficients would be needed.

Details on the automatic near-wall treatment in CFX can be found in [CFX09b, p. 88] and [Esc03].

Treatment of Rough Walls

At rough walls, the logarithmic profile can still be applied but moves closer to the wall: As rough walls tend to increase the turbulence production near the wall, the wall shear stress and the wall heat transfer coefficients increase significantly. To be able to account for all effects of the roughness (height, shape, distribution), the *sand grain roughness* is plugged into the corresponding equations instead of the absolute

[8] In fact, automatic wall functions are the only option offered by CFX for the SST model.

roughness. The sand grain roughness averages the technical roughness which has peaks and valleys of different sizes and shapes by assuming that the wall is made of a layer of closely packed spheres with an average roughness height h_s (see fig. 7.6.

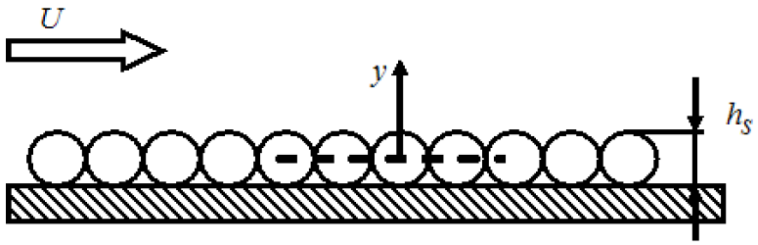

Figure 7.6: *Concept of the sand-grain roughness. Taken from [CFX09b, p. 90].*

To account for the roughness, the approach in eq. 7.91 is modified to

$$v^+ = \frac{1}{\kappa} \cdot \log \tilde{y}^+ + C - \Delta B. \tag{7.100}$$

For the dimensionless sand grain roughness h_s^+,

$$h_s^+ := h_s \frac{v_\tau}{v}, \tag{7.101}$$

the relation

$$\Delta B = \frac{1}{\kappa} \ln\left(1 + 0.3\, h_s^+\right) \tag{7.102}$$

holds. The effect of this shift on the logarithmic boundary layer velocity profile is shown in fig. 7.7. It has to be noted that for large h_s^+, approximately $h_s^+ \gtrsim 70$, the use of the blending function in the SST model becomes increasingly unphysical as the viscous sublayer disappears and the flow at the wall becomes fully turbulent.

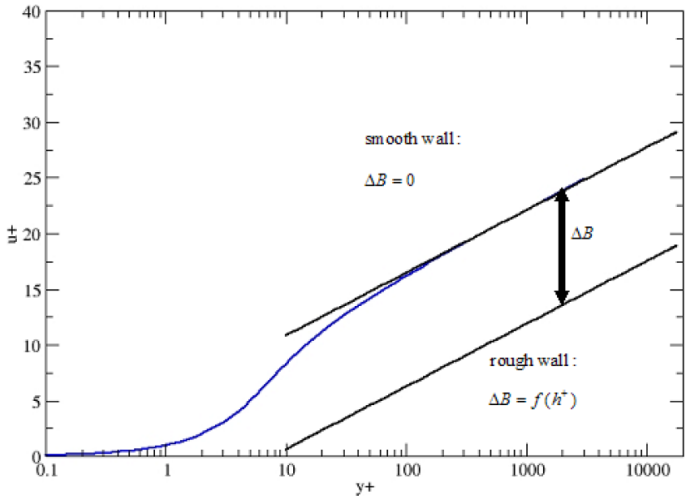

Figure 7.7: *Downward shift of logarithmic wall velocity profile due to rough walls. Taken from [CFX09b, p. 90].*

For the temperature in the logarithmic region, the following law is applied:

$$\Theta^+_{\log} = 2.12 \ln\left(\mathrm{Pr}\cdot\tilde{y}^+\right) + \left(3.85\,\mathrm{Pr}^{1/3} - 1.3\right)^2 - \frac{1}{\kappa}\ln\left(1 + 0.3\,C\cdot\mathrm{Pr}\cdot h_s^+\right). \tag{7.103}$$

The last term includes the correction for the rough wall. The model constant C was calibrated experimentally to $C = 0.2$ [CFX09b, p. 89]. It has to be noted that this calibration was done for air, not for water. However, as no energy coefficient for water was available, $C = 0.2$ was used also for the calculations here.

Wall Functions and the SST Model

As already stated, the SST model was used for the simulations with CFX in this work. The SST model was combined with automatic scalable wall functions to be able to choose larger y^+-values and avoid the use of very fine meshes [Esc03]. The robustness of this approach is shown in [Men03].

Calculation of the Heat Transfer Coefficient α

The heat transfer coefficient is calculated according to

$$q_w = \frac{\rho c_p v^*}{\Theta^*}\left(T_w - T_f\right) \tag{7.104}$$

$$\alpha = \frac{\rho c_p v^*}{\Theta^*}. \tag{7.105}$$

With this definition, the upper equation takes the same form as eq. 6.15. T_f is the 'near-wall fluid temperature'. Unfortunately, the documentation of CFX does not specify the exact definition of this term. However, in the case of the FRM II cooling channels, this temperature is somewhat higher than the average fluid temperature across the cooling channel.

7.3 Implementation in the CFX Solver

The set of equations solved by ANSYS CFX are the unsteady Navier Stokes equations in their conservative form as discussed before [CFX09b, p. 17]. The method used is an element-based finite volume method. The volumes are represented by a mesh that discretizes the bodies in space. These volumes are used to conserve relevant quantities such as energy, mass and momentum. In these volumes, eq. 7.23 or one of the deduced equations that contain turbulence parameters and wall properties are integrated over the volume element and the divergence theorem is applied. It is required that the control elements do not deform with time, otherwise equations more complex than the ones described in the following have to be used. Next, the integrals are discretized. Volume integrals are discretized within each element sector and accumulated to the control volume to which the sector belongs, whereas surface integrals are discretized at the so-called integration points (IP), which are located at the centre of each surface segment within an element and then distributed to the adjacent control volumes (see fig. 7.8). This way, the surface integrals are locally conservative.

7.3.1 Calculation of Special Terms

Shape Functions

Solution fields and other properties are stored at the mesh nodes, but for the evaluation of many terms, the value at the integration points is needed and must therefore be approximated. This is accomplished via finite-element shape functions. The variation of a variable X in an element is described by

$$X = \sum_{i\in\mathrm{Nodes}} N_i X_i \tag{7.106}$$

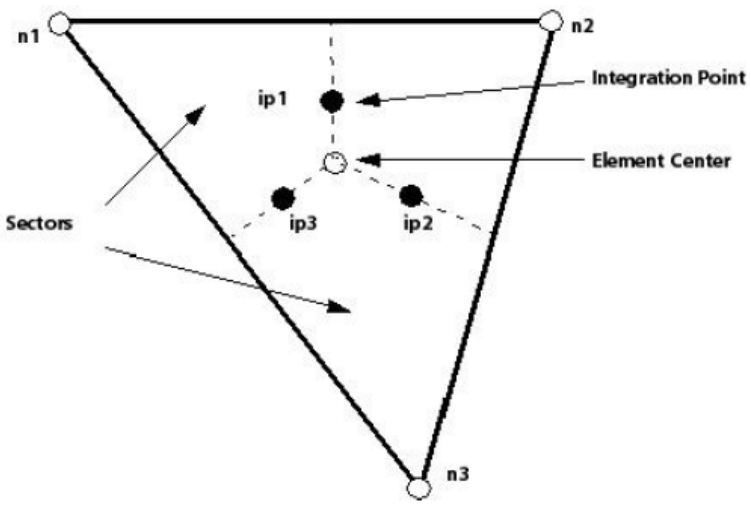

Figure 7.8: *On the concept of finite volumes. Taken from [CFX09b, p. 240].*

where x_i is the value stored at the mesh node i and N_i the shape function of the node. The shape functions are tri-linear and also used for geometric calculations as 7.106 also holds for the coordinates. An overview of these function and their form depending on the shape of the volume element is given in [CFX09b, p. 241]. In this work, hexahedral and tetrahedral elements are used.

Control Volume Gradients

If gradients are required at nodes, they are evaluated using the divergence theorem

$$\boldsymbol{\nabla} X = \frac{1}{V} \sum_{i \in \mathrm{IP}} (X \boldsymbol{n})_{\mathrm{IP}_i} \,. \tag{7.107}$$

X is evaluated at IP_i using shape functions.

Diffusion Terms

Spatial derivatives for all diffusion terms are also calculated using shape functions:

$$\left.\frac{\partial X}{\partial x}\right|_{\mathrm{IP}} = \sum_{i \in \mathrm{Nodes}} \left.\frac{\partial N_i}{\partial x}\right|_{\mathrm{IP}} x_i \tag{7.108}$$

Transient Term

Depending on the desired application, either the First Order Backward Euler scheme or the Second Order Backward Euler scheme can be applied for time discretization.

The Coupled System of Equations

By applying the finite volume method to all elements in the domain, the linear set of equations that arises are discrete conservation equations that for the control volume i can be written in the form

$$\sum_{n_i \in \text{Neighbours of i}} a_{i,n_i} x_{i,n_i} = b_i. \tag{7.109}$$

The sum runs over all neighbours of i. For scalar equations, a_{i,n_i}, x_{i,n_i} and b_i are just numbers, for the coupled 3D mass-momentum equation set, they are matrices and vectors.

7.3.2 General Solution Strategy

The CFX solver is a coupled solver that retains the coupling in question at the equation level described above. This approach has a great number of advantages compared to non-coupled or segregated solvers, e. g. robustness, generality, efficiency and simplicity. The trade-off is the need for a large amount of memory to store all the coefficients.[9] Also for steady-state problems, the time-dependent equations are solved as this behaves as a kind of 'acceleration' to guide the approximate solutions in a physically based manner to a steady-state solution.

General Solution

Fig. 7.9 shows a simplified flowchart of the CFX solver. Unused capabilities of the solver have been excluded from this chart.

Two numerically intensive operations are required for each set of field equations for each time step: The coefficient generation where the non-linear equations are linearised and assembled into the solution matrix, and the equation solution itself. The outer iteration is controlled by the (false) time step. The inner linearisation operations is performed only once per outer iteration in steady state analysis and multiple times per time step in transient analyses.

Linear Equation Solver

The CFX solver uses the *Incomplete Lower Upper* factorization technique (ILU) to solve the discretised system of linearised equations. It is an iterative solver. If the system of equations (e. g. resulting from the discretisation of 7.23) is considered to be

$$\mathbb{A}\boldsymbol{X} = \boldsymbol{b}, \tag{7.110}$$

it starts with an approximate solution $\boldsymbol{X}_n$ that is to be improved by $\boldsymbol{X}'$ yielding

$$\boldsymbol{X}_{n+1} = \boldsymbol{X}_n + \boldsymbol{X}', \tag{7.111}$$

where $\boldsymbol{X}'$ is the solution of

$$\mathbb{A}\boldsymbol{X}' = r_n. \tag{7.112}$$

r_n is the residual obtained from

$$\boldsymbol{r}_n = \boldsymbol{b} - \mathbb{A}\boldsymbol{X}_n. \tag{7.113}$$

It is inherent to ILU-Solvers that their performance decreases rapidly with an increasing number of mesh elements and large element aspect ratios.

The Algebraic Multigrid Method

The CFX solver is a so-called *Multigrid solver*. This means that early iterations are performed on a fine grid that is progressively coarsened in later operations. Finally, the results are transferred back from the coarsest mesh to the original fine mesh. This technique greatly enhances the convergence of many matrix inversion techniques. The advantage of this can be found by looking at the numerical behaviour of

[9] Segregated solvers solve the momentum equations first, based on a guessed pressure, which is later corrected. CFX uses a coupled solver that solves all hydrodynamic equations for u, v, w and p as a single system.

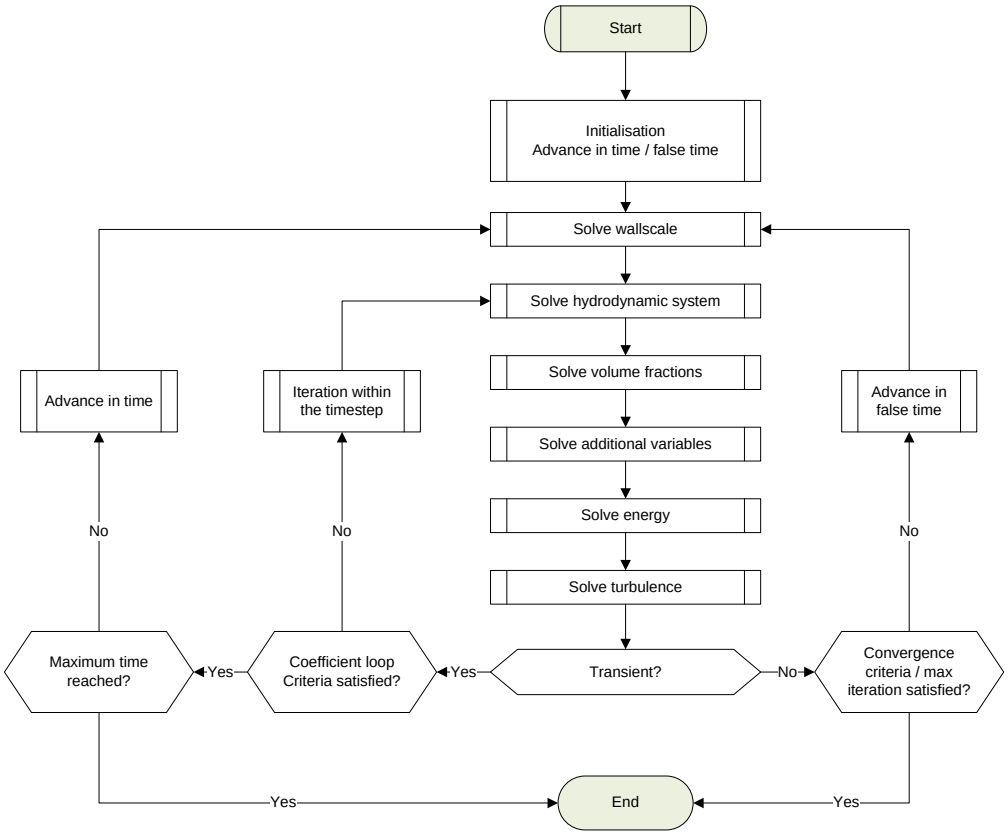

Figure 7.9: *Simplified flowchart for the CFX solver.*

discretization errors: For a given mesh size, iterative solvers are efficient only at reducing errors with a wavelength of the order of the mesh spacing. Errors with larger wavelengths take very long to disappear. This is adressed by the coarser meshes in the multigrid method. CFX calculates the coarser meshes by summing the fine mesh equations and therefore bypasses the need to explicitly model the coarser meshes. This method is called *Algebraic Multigrid*. In addition, this method is less time consuming than other multigrid methods as the discretization of the non-linear equations is performed only once for the finest mesh. The particular implementation used by CFX is called *Additive Correction*. It takes advantage from the discrete equations being representative of the balance of conserved quantities over a control volume. The coarse mesh equations can therefore be created by merging the finer control volumes. By this, the coarse mesh equations impose conservation requirements over a larger volume and therefore reduce the error components at longer wavelenghts.

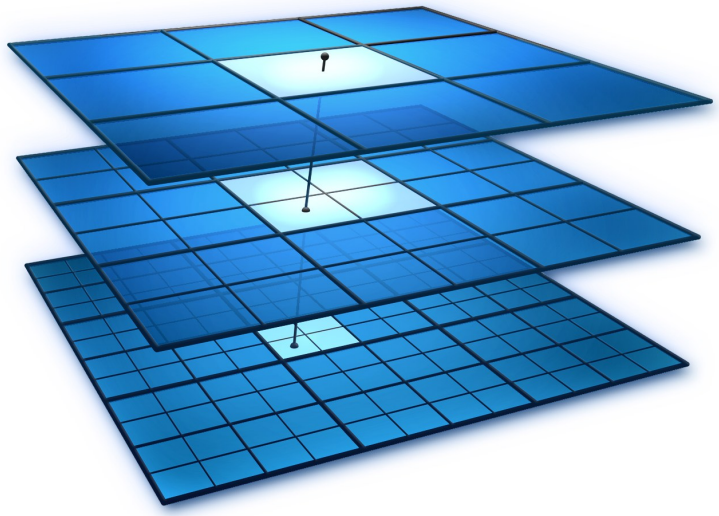

Figure 7.10: *The Algebraic Multigrid method: From fine meshes to coarser ones. Taken from [mul10].*

7.4 Transient simulations

Some transient simulations have been performed in this work to study the time-dependent behaviour of the flow, e. g. the development of a Kármán vortex street behind the combs that fix the fuel plates. When solving the time-dependent Navier Stokes equations, for explicit solvers the Courant-Friedrichs-Lewy condition has to be fulfilled with the Courant number c [Cou28]:

$$\sum \frac{v_i \cdot \Delta t}{\Delta x_i} < \mathrm{c}. \tag{7.114}$$

c depends of the type of partial differential equation to be solved and on the discretization technique. Δx is given by the mesh, v by the velocity of the fluid. Therefore this criterion is used to determine the maximum size of timesteps that can be chosen to capture the relevant transient physics for the grid. For example, for explicit Euler solvers, $\mathrm{c} = 1$ applies.

However, as Cfx is an implicit solver, this criterion does not need to be applied in its full strictness. Nevertheless, it delivers important information on how timesteps have to be chosen to capture all relevant phenomena. Therefore, emphasis was put on fullfilling 7.114 also in this case.

CHAPTER 8

Multiphase CFD – Subcooled Boiling

As already discussed in chapter 6.3, it is important to judge the safety margin that is available until boiling occurs.

In CFX, routines for the treatment of boiling are implemented within the framework of the RPI boiling model [Ego04]. However, this model aims on high pressure scenarios, for example boiling water reactors. In low pressure environments, the implemented correlations are not suited to describe boiling phenomena. The implementation of subcooled boiling in CFD codes is a field of ongoing research, with theory and correlations changing fast [Pod09]. One rather simple but promising approach for cooling channels like the ones at FRM II is described by [Li,04, Dil06, Tu,02, Yeo04]. This model was further extended to overcome some of the deficiencies of the correlations listed in chapter 8.1, namely the approach of one-sized bubbles, as in fact the bubble diameters vary at one location [Yeo06, Che09]. That means, that there is no real 'steady state', but that in the case of boiling phenomena the steady state is a time average. The underlying improved model is called *MUSIG*, multi-size-group model. Here, only the simpler model is discussed.

8.1 Correlations

There are numerous correlations available to describe the different important parameters in subcooled boiling. The most important parameters are: Bubble size distribution, interfacial area concentration, partition of wall heat flux, bubble departure diameter and bubble departure frequency [Li,04]. From this great variety, the most promising for the situation at FRM II are presented in the following.

8.1.1 Wall

The heat flux from the wall to the fluids, q_w, consists of mainly three components: The heat flux due to evaporation, q_e, due to surface quenching, q_q, and due to turbulent convection, q_c.

$$q_w = q_q + q_e + q_c \tag{8.1}$$

If heat transferred from the wall to the fluid in the vicinity of nucleation sites does not contribute to evaporation, it contributes to super heating of the liquid phase as it displaces the bubbles. This process is additionally split up in two sub-processes, the heat flux corresponding to convective heat transfer and the heat flux corresponding to quenching, i. e. it is transported between the bubble departure and the next bubble formation at the same nucleation site. So in this model, no super-heating of the vapour is taken into account, in other words, the vapour is saturated everywhere.

Heat Transfer due to Evaporation

The heat transfer due to evaporation mainly depends on the characteristics of the bubbles on the wall: How many there are, how long they take to grow, how large they grow and how often they depart. Accordingly, q_e is [Bow62]

$$q_e = nf\left(\frac{\pi}{6}d_{\mathrm{bw}}^3\right)\rho_g h_{\mathrm{fg}}. \tag{8.2}$$

In this equation, n is the nucleation site density, f the bubble departure frequency, d_{bw} the bubble departure diameter, ρ_g the density of the vapour and h_{fg} the latent heat of boiling.

Heat Transfer due to Surface Quenching

As described above, the heat transfer due to surface quenching depends on the fluid as well as on the bubbles. It is mainly heat transfer to the place, where bubbles used to be, but are not present at the moment. The heat transfer itself depends on the thermal properties of the fluid and the temperature difference between wall and fluid [Mik69]:

$$q_q = \left(\frac{2}{\sqrt{\pi}}\sqrt{\kappa_l \rho_l C_{p,l}}\sqrt{f}\right) A_q \left(T_w - T_l\right) \tag{8.3}$$

Here, T_w is the temperature of the wall, T_l the temperature of the liquid. A_q is a measure for the surface fraction subjected to surface quenching and therefore naturally depends on the nucleation site density and the the bubble size:

$$A_q = nK\left(\frac{\pi d_{\mathrm{bw}}^2}{4}\right). \tag{8.4}$$

K is the ratio of the area around a nucleation site influenced by heat transported by a nucleate boiling to the projected bubble area at bubble departure. Often, a value $K = 2$ is quoted. A more general correlation suggested by Kenning and Victor [Ken81] is:

$$K = 4.8 \cdot \mathrm{e}^{-\frac{\mathrm{Ja}}{80}}. \tag{8.5}$$

Ja is the Jacobs number, a measure for the subcooling. It is defined by

$$\mathrm{Ja} = \frac{\rho_l}{\rho_g}\frac{C_{p,l}\left(T_{\mathrm{sat}} - T_l\right)}{h_{\mathrm{fg}}} \tag{8.6}$$

Heat Transfer due to Turbulent Convection

Turbulent convection is the heat transfer mechanism in the area, where the wall is not disturbed by the presence of bubbles. It therefore depends only on liquid parameters, the temperature difference between wall and fluid and the remaining wall fraction from eq. 8.4 [Kur91]:

$$q_c = \mathrm{St}\,\rho_l C_{p,l} v_l \left(T_w - T_l\right)\left(1 - A_q\right) \tag{8.7}$$

The Stanton number, St, characterises the ratio of heat transferred into the fluid to the thermal capacity of the fluid:

$$\mathrm{St} = \frac{h_c}{C_{p,l} v_l \rho_l} \tag{8.8}$$

$$= \frac{\mathrm{Nu}}{\mathrm{Re}\,\mathrm{Pr}}. \tag{8.9}$$

In newer approaches, the Stanton number is replaced by a turbulent heat transfer coefficient h_c which depends on the fluid field near the wall and uses wall functions. Here, the Nusselt number is calculated according to equation 6.7, p. 48. According to [Kal], most of the time the simplified calculation scheme after Dittus-Bölter [Dit30] can be used:

$$\mathrm{Nu} = 0.023 \cdot \mathrm{Re}^{\frac{4}{5}} \cdot \mathrm{Pr}^{\frac{1}{3}} \cdot K_{\mathrm{Pr}}. \tag{8.10}$$

Interphase Mass Flux

Due to the boiling at the wall, mass is transferred from the fluid to the vapour. This mass transfer is naturally connected to the heat flux due to evaporation:

$$m_{wg} = \frac{q_e}{h_{\mathrm{fg}} + C_{p,l}\left(T_{\mathrm{sat}} - T_l\right)} \tag{8.11}$$

Wall Bubble Characteristics

It was shown before, that the heat flux on the wall mainly depends on the characteristics of the bubbles. A number of correlations are quoted for these characteristics. A selection of them which can be applied to the temperature and pressure regime of FRM II is quoted in the following.

The number of bubbles per area is given by the nucleation site density [Koc95]:

$$n = \frac{1}{d_{\mathrm{bw}}^2}\left[\frac{2\sigma T_{\mathrm{sat}}}{\left(T_w - T_{\mathrm{sat}}\right)\rho_g h_{\mathrm{fg}}}\frac{2}{d_{\mathrm{bw}}}\right]^{-4.4} \cdot f\left(\rho^*\right). \tag{8.12}$$

Here, ρ^* is the density ratio,

$$\rho^* = \frac{\rho_l - \rho_g}{\rho_g}, \tag{8.13}$$

and

$$f\left(\rho^*\right) = 2.157 \cdot 10^{-7}\left(\rho^*\right)^{-3.2}\left(1 + 0.0049\rho^*\right)^{4.13}. \tag{8.14}$$

The nucleation site density itself depends also on the bubble departure diameter [Koc95]:

$$d_{\mathrm{bw}} = 2.469 \cdot 10^{-5}\left(\frac{\rho_l - \rho_g}{\rho_g}\right)^{0.9}\theta\sqrt{\frac{\sigma}{g\left(\rho_l - \rho_g\right)}} \tag{8.15}$$

with the equilibrium contact angle between wall and bubble [Rog94]:

$$\theta = 80^\circ. \tag{8.16}$$

σ is the surface tension between liquid and vapour, g the gravitational acceleration. The remaining characteristic size is the bubble departure frequency [Col60]:

$$f = \sqrt{\frac{4g\left(\rho_l - \rho_g\right)}{3d_{\mathrm{bw}}\rho_l}}. \tag{8.17}$$

8.1.2 Fluid

When the bubbles have detached from the wall, they are further transported by the fluid. Depending on the temperature of the fluid, which in the case of FRM II is normally lower than the wall temperature, heat and mass are transfered from the vapour to the fluid and the other way round. All these mechanisms

depend again on the characteristics of the bubbles and the interfacial area A_{lg} the bubbles offer to the fluid. This area is estimated by

$$A_{\mathrm{lg}} = \frac{6\alpha}{d}, \tag{8.18}$$

where α is the void fraction and d the bubble diameter.

Interphase Mass Flow

In subcooled liquid, there is bulk condensation from the gas phase to the liquid:

$$m_{gl} = \max\left[\frac{h_{\mathrm{lg}} A_{\mathrm{lg}} \left(T_{\mathrm{sat}} - T_l\right)}{h_{\mathrm{fg}}}, 0\right] \tag{8.19}$$

If the liquid is superheated, it evaporates and mass is transferred to the vapour:

$$m_{lg} = \max\left[\frac{h_{\mathrm{lg}} A_{\mathrm{lg}} \left(T_l - T_{\mathrm{sat}}\right)}{h_{\mathrm{fg}}}, 0\right]. \tag{8.20}$$

Interphase Heat Transfer

Through the phase boundary, heat can be transferred from and to the bubble without a mass transfer. This naturally depends on the temperature difference between both phases, the area the bubbles offer to the liquid, and an interphase heat transfer coefficient:

$$q_{\mathrm{lg}} = h_{\mathrm{lg}} A_{\mathrm{lg}} \left(T_g - T_l\right). \tag{8.21}$$

The interphase heat transfer coefficient is given by

$$h_{\mathrm{lg}} = \mathrm{Nu} \cdot \frac{\kappa_l}{d}. \tag{8.22}$$

In this case, the Nusselt number Nu is determined by the Ranz-Marshall correlation [Ran52],

$$\mathrm{Nu} = 2 + 0.6\,\mathrm{Re}_b^{0.5}\mathrm{Pr}_l^{0.3}, \tag{8.23}$$

with the Bubble Reynolds number

$$\mathrm{Re}_b = \frac{\rho_l \left|v_g - v_l\right| d}{\mu_l} \tag{8.24}$$

and the liquid phase Prandtl number Pr_l

$$\mathrm{Pr} = \frac{\mu_l C_{p,l}}{\kappa_l}. \tag{8.25}$$

$|v_g - v_l|$ is the local slip velocity of the bubbles.

Bubble Drag Force

The drag force per unit volume on liquid or gas is given by

$$F_{\mathrm{lg}}^d = -F_{\mathrm{gl}}^d = \frac{1}{8}\rho_l A_{\mathrm{lg}} C_D \cdot \left|v_g - v_l\right| \cdot \left(v_g - v_l\right) \tag{8.26}$$

with the drag coefficient C_D that has to be determined experimentally. In this work, the correlation by Ishii and Zuber is used.

Bubble parameters

The mean bubble diameter d is estimated by the Sauter bubble diameter [Zei97]:

$$D_s = \sqrt{\frac{\sigma}{g\left(\rho_l - \rho_g\right)}} \cdot \frac{0.0683 \cdot \left(\frac{\rho_L}{\rho_g}\right)^{1.326}}{\mathrm{Re}^{0.324} \cdot \left(\mathrm{Ja} + \frac{149.2 \cdot \left(\frac{\rho_L}{\rho_g}\right)^{1.326}}{\mathrm{Bo}^{0.487}\mathrm{Re}^{1.6}}\right)}. \tag{8.27}$$

Bo is the boiling number, given by

$$\mathrm{Bo} := \frac{q_w}{G h_{\mathrm{fg}}}, \tag{8.28}$$

with G mass flux, and h_{fg} again the latent heat of boiling. It is noteworthy that this parameter again depends on the heat flux from the wall, although the Sauter mean diameter is a number that characterizes the bubbles in the cooling channel and not those on the wall.

8.2 Possible Implementation

In the approach described above, only one bubble size is regarded. This is usually enough to get a correct answer for the axial bubble characteristics, but not for the radial parameters (distance to wall). If the latter is desired, more complex models like the Musig model have to be used.

However, in the given time frame, it was not possible to implement this model for this work due to technical problems with CFX: Up to version 12.1, it is not possible to modify the RPI model according to the requirements for the solution discussed above. More precisely, it is yet not possible to determine the average fluid temperature T_l which is required in many of the formulas, without using a large amount of a-priori information like stream-filament integrated heat fluxes and intermixing conditions that probably loose their validity at the onset of boiling: For the standard operation of FRM II, it can be assumed that the flow between the plates can be regarded by means of non-intermixing stream filaments, see chapter 13.5. The fluid temperature can then be determined by the energy balance of the appropriate stream filament, beginning at the top of the plate. However, this situation is subject to change as the radially inhomogeneous power distribution causes significantly differing densities in the filaments at the onset of boiling. Therefore, using this a-priori information is probably only possible for homogeneously heated channels, as it was done in some of the references quoted in this chapter. The above is therefore regarded as a literature review and collection for further work on this topic. The safety margins quoted in this work were calculated as discussed in chapter 6.3.

Part III

Coupling of Codes, Application

CHAPTER 9

Neutronic Modelling

This chapter describes some of the details how the MCNP model was constructed.

9.1 The MCNPX Model

The MCNPX Model used in this work is in most parts based on a model built by A. Röhrmoser, with averaged built-in components in the D_2O-tank (see section 9.1.2). Fig. 9.1 shows a MCNPX plot of the central part of this model, including the actual core. During the course of this work, only minor modifications have been made to this model, e. g. slight changes in the modelling of the involutes (see section 9.1.1) and a new fragmentation of the plates for burn-up calculations. In later calculations for new cores with UMo fuel, larger changes were made to the fuel plates to be able to model thickness gradients.

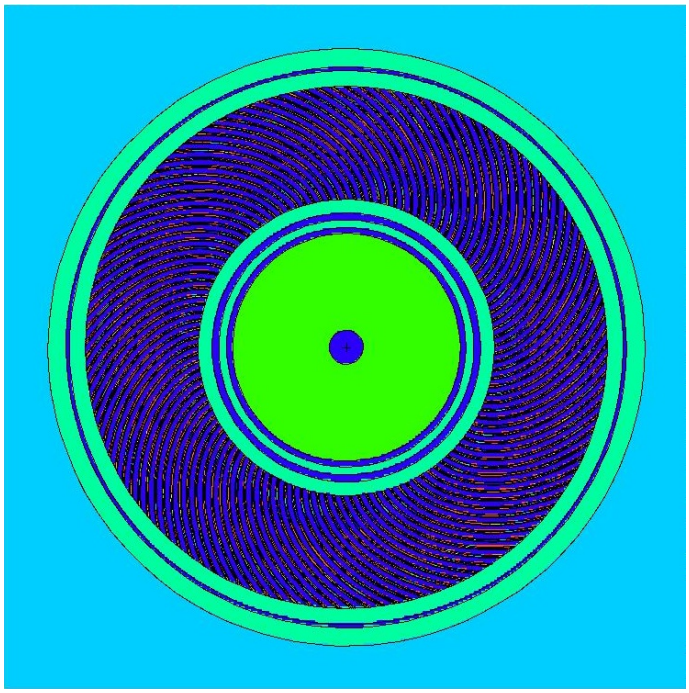

Figure 9.1: *MCNPX model of core. Light blue is the D_2O, dark blue is light water. Light green is aluminium, in the center is the control rode.*

9.1.1 Modelling of Involutes

MCNP provides no possibility to directly model the involutes. Therefore evolutes are combined from two parts, a parabola for the inner part ($r \lesssim 8\,\text{cm}$) and a hyperbolic outer part. The equations for these are as follows:

$$y = \begin{cases} a_2 x^2 + a_1 x + a_0 & x < x_0 \\ b_0 - \sqrt{b_1 \cdot (x - x_1)^2 + b_2} & x \geq x_0. \end{cases} \tag{9.1}$$

The parameters for the current fuel element are (in m)

$$x_0 = 0{,}08 \tag{9.2}$$
$$x_1 = 0{,}0534079 \tag{9.3}$$
$$a_0 = 0{,}08465807 \tag{9.4}$$
$$a_1 = -2{,}83910 \tag{9.5}$$
$$a_2 = 23{,}6529 \tag{9.6}$$
$$b_0 = 0{,}0632933 \tag{9.7}$$
$$b_1 = -1{,}95524 \tag{9.8}$$
$$b_2 = 0{,}004340712. \tag{9.9}$$

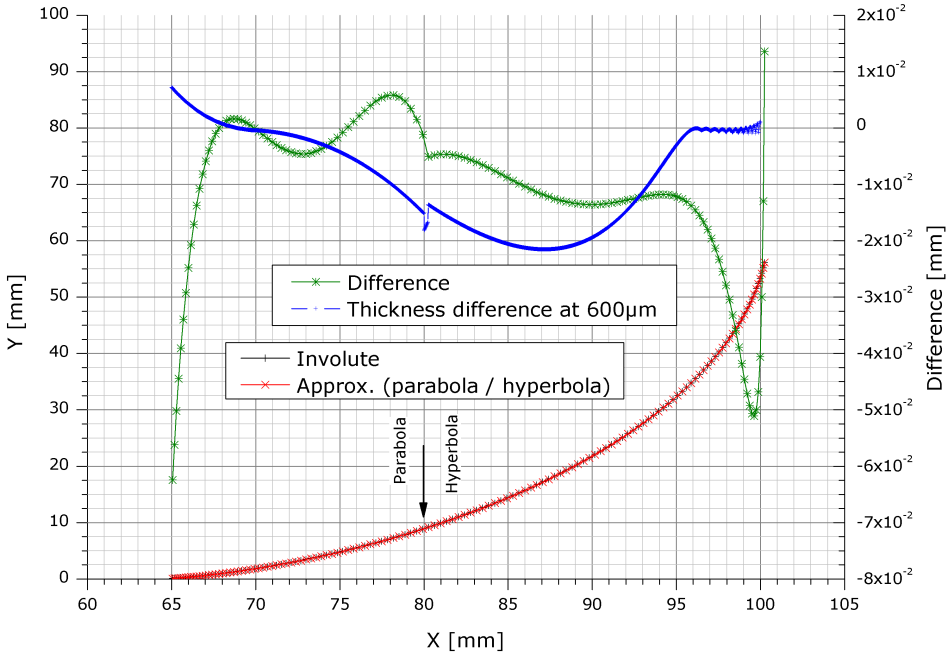

Figure 9.2: *Approximation of involutes by parabolas and hyperbolas. The black curve is a real involute in a x-y-coordinate system. The red curve is an approximation of this involute using a parabola and a hyperbola. The green curve (right axis) shows the deviation between the involute and the appproximation in y-direction. The blue curve shows the difference in the thickness of a* 600 µm *plate normal to the surface that is caused by the approximation.*

Fig. 9.2 shows how accurate these approximations are. Deviations up to 60 µm in total appear. However, this difference in modelling the involutes gets less pronounced when the difference in the thickness of the model plates is regarded. The plates itself are constructed by rotating the parabola-hyperbola-construction around the origin. This leads to an attenuation of the modeling errors resulting in a maximum deviation of about 20 µm, which is 3.3% compared to the total thickness of 600 µm. The parameters were chosen in a way to model the thickness at the borders of the fuel plate close to exactness.

The model used implies a trend to smaller plates. This means, that the model under normal conditions would slightly underestimate the total uranium content of the core. To compensate this, densities in the corresponding cells were adjusted in accordance, so that the density weighted thickness is approximately constant and the total uranium content of the core matches. However, it has to be mentioned that small deviations of this order of magnitude are also present in the real fuel plates due to manufacturing tolerances. A closer view of the fuel plates in the MCNPX model is shown in fig. 9.3.

9.1.2 Averaging of Built-in Components and Loss Mechanisms

For most of the calculations performed in this thesis, built-in components and loss mechanisms like leakage through beam guides and absorption in structural materials where averaged as a symmetric model of the core was regarded. This was achieved by changing the properties of the heavy water moderator. For this, the heavy water tank was split into three zones, one core-near pure D_2O-zone and two zones further away containing the averaged equipment (see fig. 9.4). This was averaged by adjusting the densities and materials according to their average values in the zone. The procedure was conducted analogous to the averaging for the 2D-calculations with DOT, details can be found in [Röh10a].

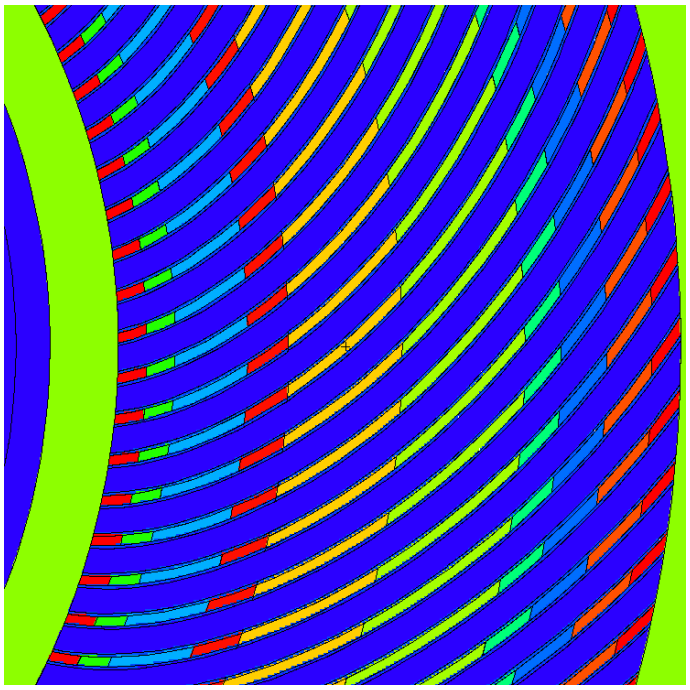

(a) X-Y-View

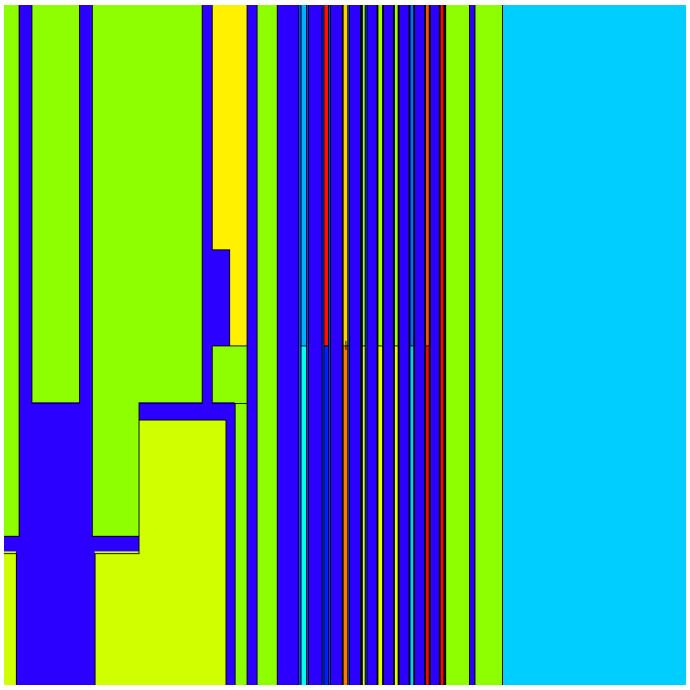

(b) X-Z-View

Figure 9.3: *Involutes in the MCNPX model: Dark blue are the cooling channels, light green the two aluminium tubes. The multicoloured part is the fuel zone, which has been split into several zones for the burn-up calculations. In (b), also the control rod (yellow and green, left) and parts of the D_2O (light blue, right) are visible.*

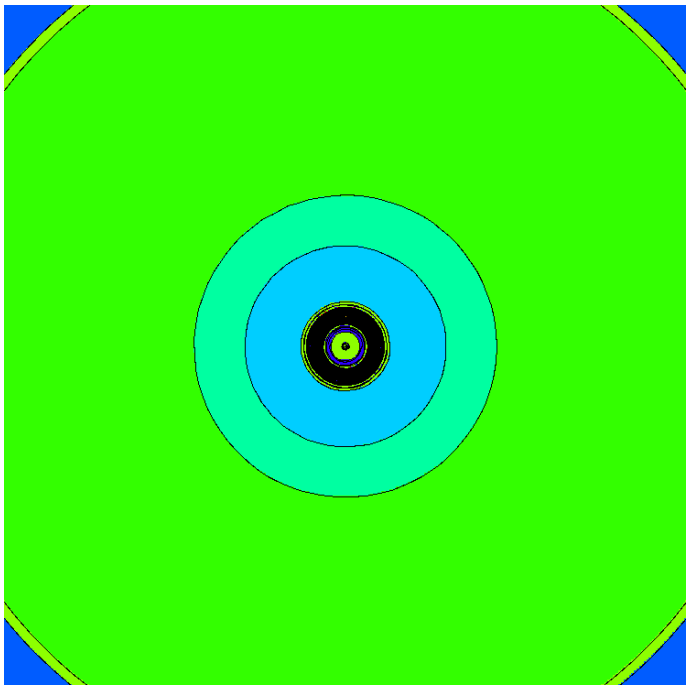

(a) X-Y-View

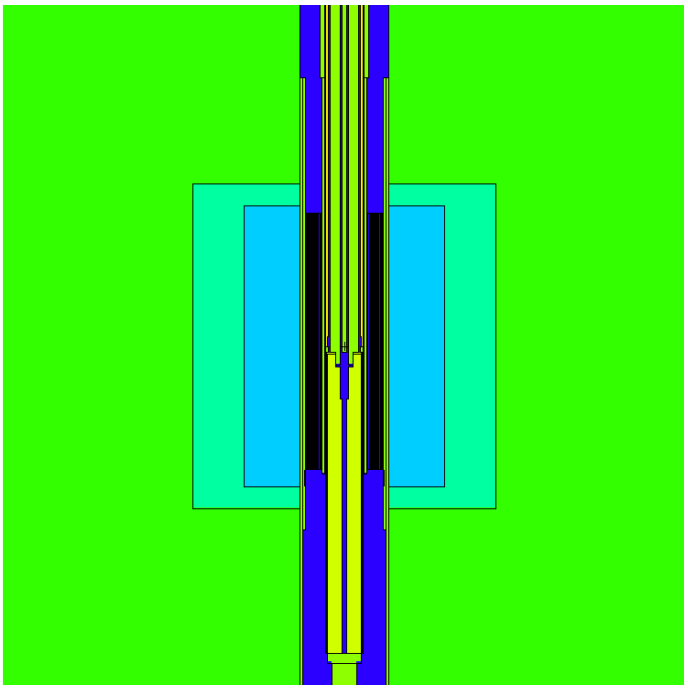

(b) X-Z-View

Figure 9.4: *MCNPX model with averaged built in components: The three large green and blue zones represent the D_2O tank with different additions and densitied to represent the built in components. The dark blue zone is light water, the black zone are the fuel plates. The yellow zone in the middle is the Beryllium reflector of the control rod. In (a), the light water surrounding the heavy water can be seen in the corners of the figure (blue).*

9.2 Meshes

9.2.1 Tallied Quantities

To tally the results of the calculations, a Type3-Mesh was used which is nearly identical to a +F6 tally. This type of tally sums up the deposited energies by using heating numbers. In MC terms, the tallied quantity S is calculated using

$$S = W \cdot d \cdot \sigma_t(E) \cdot H(E) \cdot \frac{n}{m}, \tag{9.10}$$

with W being the particle weight, d the track length in the tallied cell and $H(E)$ the energy dependent heating number. The tallied physical quantity is

$$H_t = \frac{n}{m} \int\int\int\int \mathrm{d}E\,\mathrm{d}t\,\mathrm{d}V\,\mathrm{d}\Omega \cdot \sigma_t(E) \cdot H(E) \cdot \phi(\boldsymbol{r},\Omega,E,t). \tag{9.11}$$

The heating numbers are calculated for neutrons

$$H(E) = E - \sum_i p_i \left[\bar{E}_{i,\mathrm{out}}(E) - Q_i + \bar{E}_{i,\gamma}(E)\right] \tag{9.12}$$

with $p_i = \sigma_i(E)/\sigma_T(E)$ being the probability for reaction i to take place, $\bar{E}_{i,\mathrm{out}}$ the average exciting neutron energy for reaction i at neutron incident energy E, Q_i the Q-value of the reaction and $\bar{E}_{i,\mathrm{out}}$ the average exiting gamma energy; for photons

$$H(E) = E - \sum_{i=1}^{3} p_i(E) \cdot \bar{E}_{i,\mathrm{out}}(E) \tag{9.13}$$

where the sum runs over incoherent scattering with form factors (1), pair production (2) and photoelectric absorption (3, $\bar{E}_{i,\mathrm{out}} = 0$). The main difference between +F6 and MESH3 is that the former gives the result in $^{\mathrm{MeV}}/_{\mathrm{g\,particle}}$ while latter gives $^{\mathrm{MeV}}/_{\mathrm{cm^3\,particle}}$.

9.2.2 Mesh resolution

The mesh resolution is determined by two quantities: In the border zones or more general in zones with rapid change of the tallied quantity, the mesh resolution was chosen to be at maximum about a quarter of the mean free path of thermal neutrons

$$l = \frac{1}{\sum_i \sigma_i n_i}, \tag{9.14}$$

where i runs over all isotopes of the material in the cell. For the worst case, the monolithic uranium molybdenum alloy, which has the highest macroscopic absorption cross section, a mesh resolution of down to $\approx 10\,\mu\mathrm{m}$ was chosen in critical areas like the lower border of the fuel zone. This resolution is already in the regime of the physically meaningful range. For even finer resolutions to make sense, effects like the motion of fission products would have to be taken into account and approximations like the deposited power being equal for the whole thickness of the fuel would have to be given up. In areas with smaller changes, coarser resolutions were chosen to save calculation time. A finer mesh in these areas would not provide any new details.

The need for low statistical errors is in conflict with the need for very fine meshes to capture drastic changes: All mesh cells average the quantities in them. This is especially problematic when the values of narrow peaks have to be determined. In all of the calculations done in this work, the peaks are situated either at outer border of the mesh or at a known location, e. g. near the density jump. If the worst case

scenario of an exponential drop is applied (compare fig. 9.5), then it can be concluded that for a cell thickness d in the direction of interest the relation between the maximum value and the mesh cell averaged value is

$$\frac{\phi}{\phi_0} = \frac{1}{d}\int_0^d \mathrm{e}^{-x/l}\mathrm{d}x \tag{9.15}$$

$$= -\frac{l}{d}\left(\mathrm{e}^{-d/l} - 1\right). \tag{9.16}$$

For $l/d = 0.25$ this yields $I/I_0 = 0.88$. A mesh resolution of 2% of the mean free path is required for $I/I_0 = 0.99$ which means to calculate 25 times more particles compared to the other case. For the worst case described above, $\lambda_t \approx 500\,\mu\mathrm{m}$, therefore the chosen mesh resolution of $\approx 10\,\mu\mathrm{m}$ is sufficient to satisfy $I/I_0 = 0.99$. This ultra-fine resolution was of course only applied at the very end of the fuel zone.

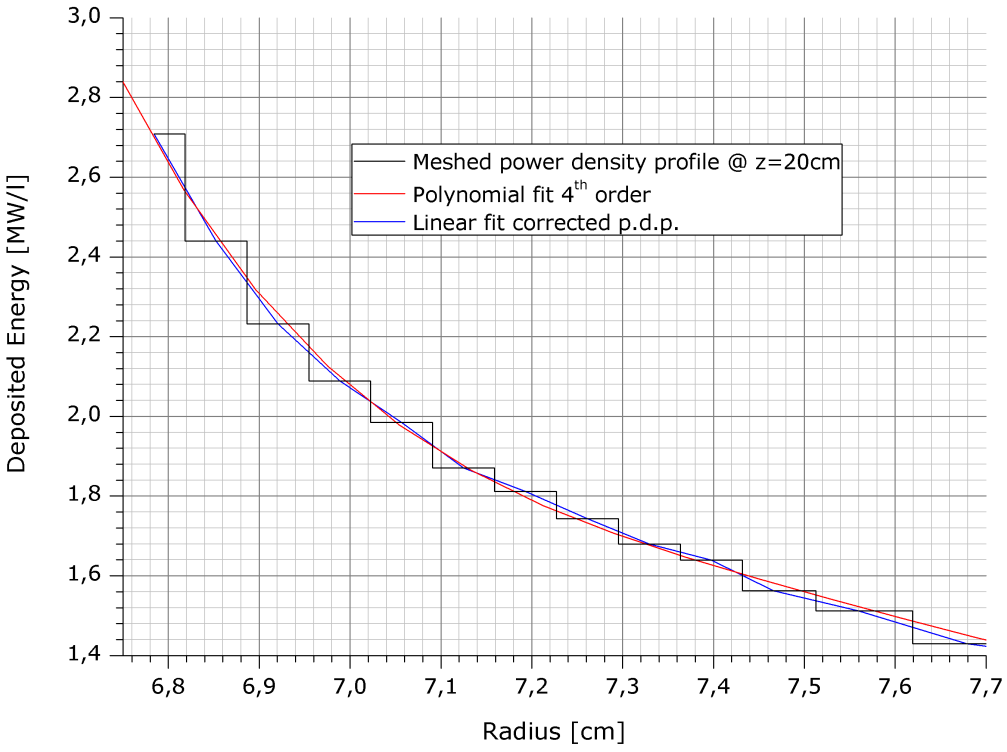

Figure 9.5: *Example for an MCNPX mesh tally and a fit that shows that mesh needs to be refined.*

A correction factor to estimate the upper boundary of ϕ_0 can be derived from the upper equation:

$$C_{I_0} = \frac{d}{l}\frac{1}{1-\mathrm{e}^{-d/l}}. \tag{9.17}$$

It will be seen later, that because of 3D heat conduction the maximum heat flux is not situated exactly over the point of the highest fission density but on top of a comparably hot zone where much heat flux

from surrounding spots accumulates.[1] This relativises the importance of the exact mesh resolution and the statistical error of the specific mesh cell, as a specific point value in the thermal hydraulic calculation turns out to be a weighted average of the point itself and several surrounding points. However, the high resolution is necessary to determine the maximum power deposition. A higher mesh resolution can also be approximated by interpolation as shown in fig. 9.6. So called *histopolation* has to be used to estimate the densities correctly. The general approach for this in a MCNP-context is described in [Pou10], however, in this case, it must be generalized to a 2D-case. Parts of the theory for this are in [Sch91].

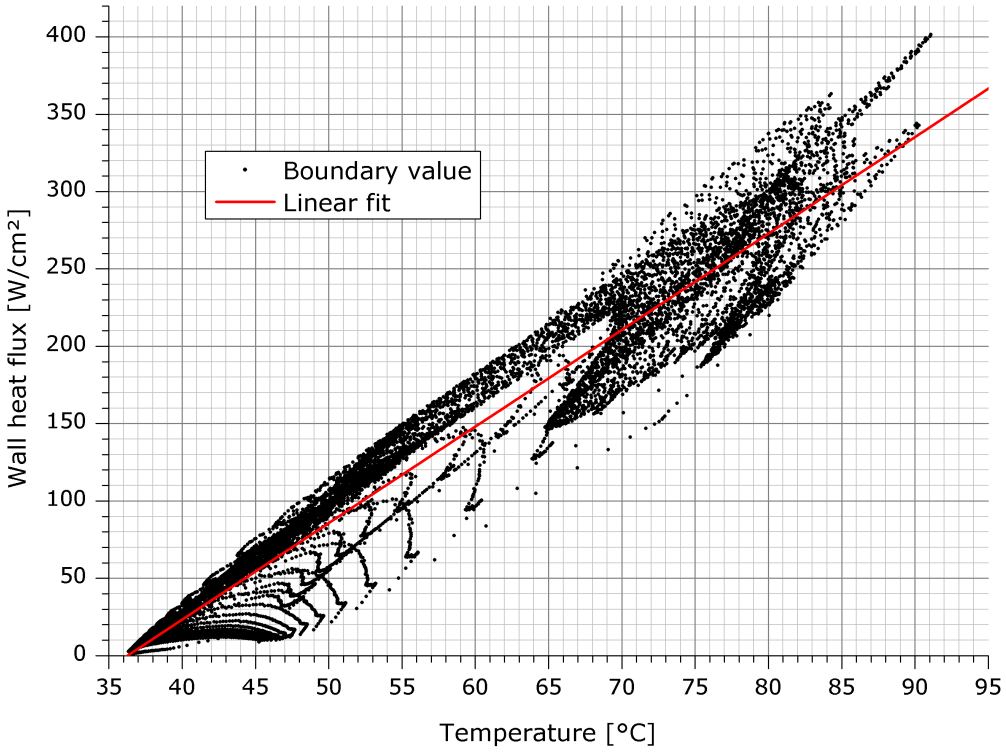

Figure 9.6: *Correlation of heat flux and temperature at the surface of the cladding in the current fuel element. Each dot represents a mesh node.*

It is clear that a mesh resolution of 10 µm is on the very border of a physically meaningful value and well beyond what is reasonable for engineering purposes. The physical validity is limited by two factors: First, in disperse fuels, the approach of homogeneity is not valid any more when the resolution approaches the grain size of the uranium containing particles. These particles usually have sizes of some dozen µm, therefore the fuel cannot be regarded as homogeneous on this scale. Second, the stopping distance of fission products is in the same order of magnitude. McnpX does not track these products but deposits their energy locally. Both factors result in an overestimation of the real energy deposition. It is therefore of advantage to define a second mesh to measure the energy distribution, just for the purpose of calculating values reasonable for engineering purposes. The stopping distance of the fission products is of minor importance in this context, emphasis has to be put on the profile flattening due to 3D heat conduction and the homogeneity approach. A good indicator for the flattening due to heat conduction is the thickness of

[1] Approximately, the heat flux densities at the plate surface can be seen as the result of the power density profile in the plate folded with a blurring function due to the 3D heat conduction.

the cladding, 380 µm. On this scale, the fuel can be started to be seen as homogeneous, too. Therefore, for the determination of the power density for engineering purposes, a mesh resolution of 300 µm was chosen.

9.3 Burn-up zones

To calculate the burn-up accurately, the fuel zone must be split in several parts. While a low number of parts is sufficient to obtain correct results for the residual reactivity at EOL [Gla05], a higher number is required to correctly resolve the maximum burn-up[2] and the isotopic composition of the fuel at EOL. While going to smaller and smaller scales produces higher burn-up numbers, the ultra-fine resolution becomes irrelevant when it comes to swelling, which poses the limit on the maximum burn-up (see e. g. [Bön09]). Therefore in accordance with [Röh10d], a width of 5 mm has been chosen as the finest resolution for burn-up zones.[3]

9.3.1 Control rod

The position of the control rod is defined as the distance between the Hf/Be-boundary and the mid-plane of the current core.

The control rod burn-up that is calculated in this work is more a feasibility study than a detailed calculation. That said, the calculations used an intermediate control rod position and only one burn-up zone. As already pointed out by Röhrmoser [Röh91a, p. 65], two or better even more zones are needed. Additionally, the movement of the control rod has to be considered as the flux shape in the beryllium follower changes drastically during the cycle (see for example fig 14.5 in chapter 14.3, 157).

[2] That is the maximum number of time-integrated fission events per volume.

[3] Given a radius R and a width l of the burn-up zone, the next inner/outer radius can be calculated according to eq. A.27 and A.6 as $R' = \sqrt{R^2 \pm 2\,r\,l}$.

CHAPTER 10

Thermal Hydraulic Modelling

Ansys CFX is the code of choice in this work for calculating the thermal hydraulics. It is basically a finite volume code (FVM) which lends out some elements from finite element methods (FEM). Details on the working concept of the solver have already been given in chapter 7.3, p. 71.

The decision for Cfx in favour of other codes was primarily made because of the robustness of the implementation regarding mesh aspect ratios, turbulence models and wall heat transfer combined with a state-of-the-art solver while maintaining ease of use and flexibility. See also the short discussion in chapter 1.3.1. For the purpose of this work, the code had to be extended via the programming API called 'user fortran' to account for heat deposition and oxide layers as well as some minor details.

This chapter deals with the modelling of the fuel plates for Cfx, the calculation of boundary conditions, material properties and some details on geometry modifying operations. The basis is a relatively complete model of central channel, fuel element and control rod as shown in fig. 10.1. Depending on the desired applications, different parts were taken from this model and used in Cfx.

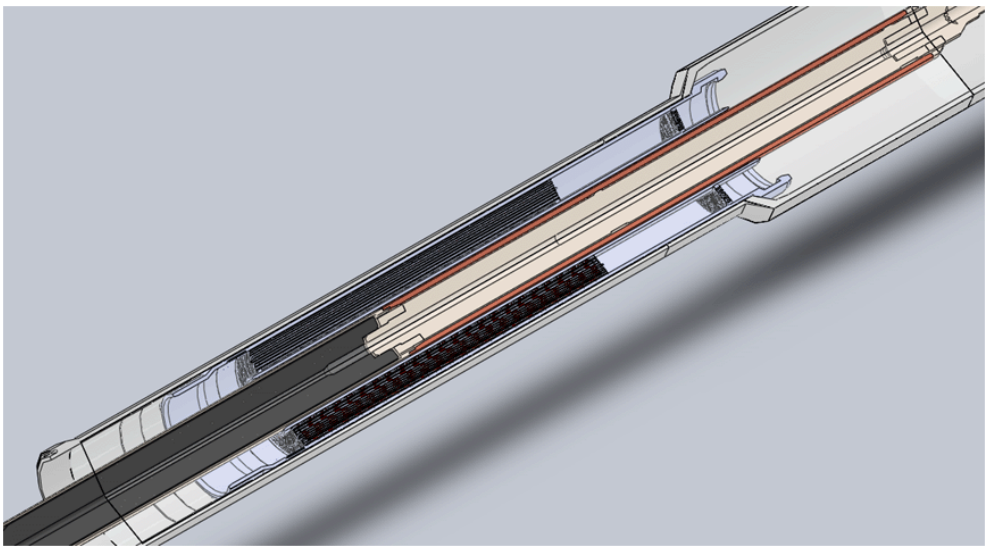

Figure 10.1: *Complete CAD model of central channel, fuel element and control rod.*

10.1 Modelling in Ansys CFX

For performance reasons, only one fuel plate and its attached was modelled for CFX. For simplicity, the fuel plates were not split but the cooling channel was halved on each side of the plate and a periodic boundary was set up there.

The original model of the fuel plate was created in SOLIDWORKS and then imported into CFX. The model was then divided in three parts, each consisting of several bodies. The three parts were a) the inlet of the fluid and the upper part of the fuel plate down to the beginning of the fuel, b) the middle part including the fuel and the third part c) began at the lower fuel border and ranges down to the outlet. Beside the fuel plate, the inner and outer ducts of the fuel element were modelled. Above and below the fuel plate, some additional centimetres of space for water and ducts were left to allow for a study of inlet and outlet effects. For the simulations on the old fuel element, all details were modelled as described in the construction plans. This especially includes the combs above and below the fuel plate.

Fig. 10.2 shows how the model was set up and how the results discussed in chapter 14 have to be interpreted: The inner and outer duct surrounding the fuel plates have been modelled at their full width, here looking like a solid extension to the cooling channel. Some additional centimeters have been modelled above and below the fuel plates to be able to simulate the corresponding effects caused by the combs and the change in cooling channel width. What looks like the surface of water here is in fact the middle of the cooling channel. Circular symmetric boundary conditions have been defined to allow for this. The beginning of the actual fuel in the plate is marked by a black line in all the figures. In addition the fuel zone was inked slightly red.

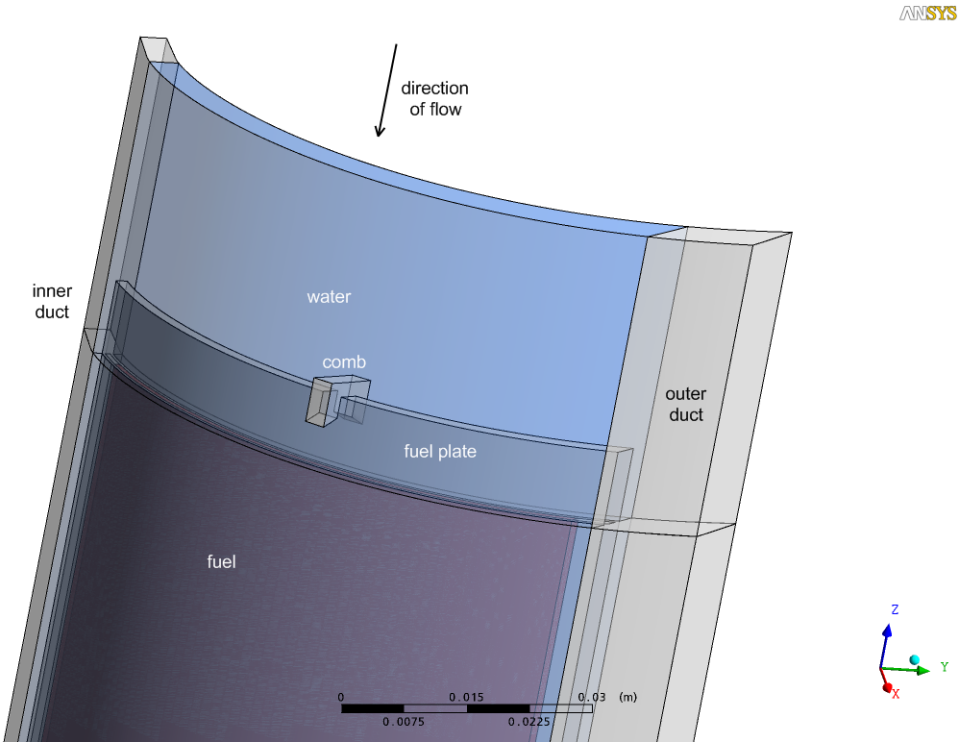

Figure 10.2: *Overview of modelled part of the fuel plates.*

10.1.1 Mesh Generation

As mentioned before, the mesh is glued together from three different pieces: The inlet, the outlet and the main part of the fuel plate. Outlet and inlet are very similar, whereas the meshing on the main fuel part is different. A detail of the mesh can be seen in fig. 10.3.

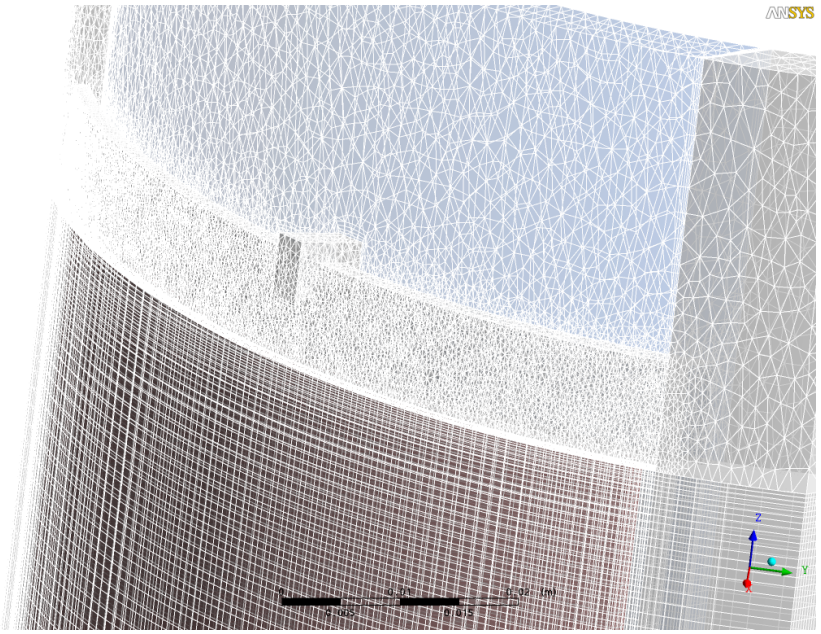

Figure 10.3: *Detail of the CFX mesh used for most thermal hydraulic calculations: Top of the plate and upper main part.*

Inlet and Outlet

Semi-automatic mesh generation was used to make up the mesh at the inlet and at the outlet. This mesh was generated using the *advancing front* algorithm and the *Delaunay triangulation* method. For the default face spacing, a width of 2 mm was chosen to reduce the computational effort at the inlet and the very outlet. Proximity was applied for edges and faces to ensure a fine enough mesh in regions were the uniform flow is disturbed, e. g. near the comb and at the edges of the fuel plates. This was combined with a minimum face spacing of 0.05 mm to prevent over-refinement of the mesh. For practical reasons, a default body spacing of 2 mm was chosen as well. Inflation of five layers was applied at fluid-solid-boundaries to be able to account for border effects like rough walls and the no-slip-condition appropriately. These layers were specified via first layer thickness and first prism height (0.1 mm). As a last measure to reduce the number of vertices and therefore to reduce the computational effort, mesh stretching was applied stretching the mesh by a factor of 5 in flow-direction (z) and approximately 1.5 in pseudo-radial-direction.[1]

Fuel Plate and Cooling Channel

The main part of the fuel plate was meshed manually. This was done to be able to switch from triangular meshes as applied to inlet and outlet to a more structured hexahedral mesh which is more suitable for the special geometry of this part.

[1] More precisely the mesh was stretched in y-direction which is nearly radial direction in the inner part of the plates near the inner fuel element duct.

As already mentioned in chap. 7.2.3, care had to be taken about the distance of the first node in the fluid domain from the wall. A value of Δy^+ of about 50–80 has been chosen for the first node which is suitable for use with automatic wall treatment in CFX [CFX06a, p. 130] ($20 \lesssim y^+ \lesssim 100$, compare fig. 10.4).

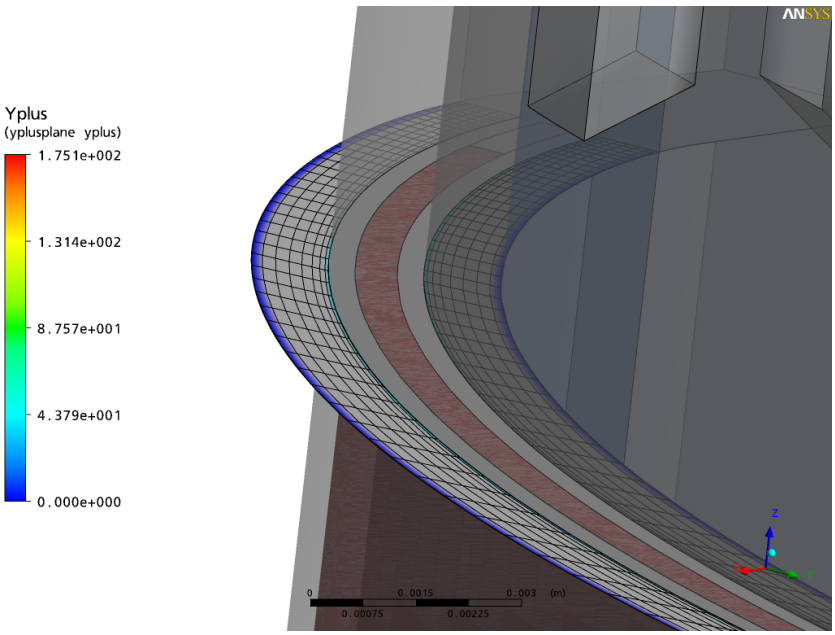

Figure 10.4: *y^+ for the first node of the mesh: The red part is the fuel zone, they grey part the cladding. The surface with the superimposed grid is a horizontal cut through the cooling channel. The light blue colour at the fluid solid interface indicates a y^+ value of about 30.*

The final mesh consists of about a million nodes for the main part. Along the z-axis, 180 nodes are distributed by a bigeometric law that enforces a higher node-density at the top and at the bottom. For the cooling channels, 130 nodes are placed in φ-direction[2] and $2 \cdot 13$ nodes in θ-direction. The cladding has the same number of nodes in φ- but only 5 for each side in θ-direction. The fuel is meshed with 100×7 nodes, the remaining frame with 15×7 nodes on each side. The attached parts of the inner and outer tubes are meshed with 9×39 nodes each.[3]

Mesh Connections

As mentioned above, the mesh was split into three pieces. The pieces were glued together via so called *GGI Connections*, the *General Grid Interface*. This interface had to be used as due to the different nature of the mesh pieces, direct One-to-One connections could not be applied. GGI connections can introduce slight numerical inaccuracies, so special care was taken about these when interpreting the results. Anyhow, for the present case, [CFX06a, p. 147] recommends GGI connections to be used. The underlying theory is described in [CFX06a, p. 119].

Concerning the rotational periodicity boundary condition, a One-to-One connection was applied whenever possible as the grid points on one side correspond to the grid points on the other side.

[2] See app. A for explanations on the coordinate system.

[3] Note that these numbers are for the standard-mesh used for the calculation of the current fuel element. They differ slightly in other calculations and are just here for you to get an impression about the dimensions of the mesh.

10.1.2 Estimation of Turbulence Parameters

The turbulence parameters at the inlet are estimated as follows [Aut08]: The hydraulic diameter for a coaxial circular tube can according to eq. 6.1 be calculated as

$$d_h = 4\frac{\frac{\pi d_o^2}{4} - \frac{\pi d_i^2}{4}}{\pi d_o + \pi d_i} \tag{10.1}$$

$$= d_o - d_i. \tag{10.2}$$

In fully developed pipe flows, the turbulence length scale can be estimated to be 7% of the hydraulic diameter, ergo[4]

$$l = 0.07\, d_h. \tag{10.3}$$

In the $K-\epsilon$ model, the length scale is connected to K and ϵ (compare chap. 7.2.2, p. 63) by the relation

$$l = C_\mu^{\frac{3}{4}} \frac{K^{\frac{3}{2}}}{\epsilon} \tag{10.4}$$

with $C_\mu = 0.09$. From this equation, ϵ can be calculated if K is known. To calculate K at the inlet, the reynolds number has to be calculated (eq. 6.2) using d_h:

$$\mathrm{Re} := \frac{v d_h}{\nu}. \tag{10.5}$$

For a fully developed pipe flow, the turbulence intensity can be estimated by

$$I = 0.16 \cdot \mathrm{Re}^{-\frac{1}{8}}. \tag{10.6}$$

As I also holds

$$I = \frac{|\boldsymbol{v}'|}{|\widetilde{\boldsymbol{v}}|}. \tag{10.7}$$

Using this relation, the turbulence energy can be calculated according to

$$K = \frac{3}{2}\left|\boldsymbol{v}'\right|^2. \tag{10.8}$$

The specific turbulent dissipation rate for the ω-based models can also be calculated from K and l:

$$\omega = C_\mu^{-\frac{1}{4}} \frac{\sqrt{K}}{l}. \tag{10.9}$$

Applied to the circumstances at FRM II, in the fuel element above the fuel plates, the values given in table 10.1 are estimated. A turbulence intensity of 2.7% belongs to the medium-turbulent cases.

[4] This formula is especially valid for pipe flows but can also applied as a rough estimation for the coaxial circular tube.

Quantity	Symbol	Value
Hydraulic diameter	d_h	99.0 mm
Reynolds number	Re	$1.4 \cdot 10^6$
Turbulence intensity	I	2.7%
Turbulence energy	K	$0.11\,\mathrm{m^2/s^2}$
Turbulence length scale	l	6.9 mm
Specific turbulent dissipation rate	ω	$87.8\,1/\mathrm{s}$
Turbulent dissipation	ϵ	$0.83\,\mathrm{m^2/s^3}$

Table 10.1: *Data input for the simulation of the old fuel element. Inlet is above the fuel plates.*

Please note that the values in table 10.1 are calculated for the stream in the annulus above the fuel plates, not between them!

10.1.3 Boundary Conditions

Inlet

An inlet velocity of $9.83\,\mathrm{m/s}$ was specified for the fluid regardless the distances to the walls. This means that a flow profile had to develop first to account for the no-slip wall boundary conditions. Therefore, enough room was left at the top of the model for this to happen. A static temperature was defined at the inlet, 37 °C. The turbulence parameters were chosen as estimated in chapter 10.1.2.

Different values are around for the inlet temperature: 37 °C in [Gie96] and 38 °C in [Röh09]. In this work, 37 °C were chosen. This choice has to be factored in when comparing the results of different works! In addition, different values are around for the flow speed between the fuel plates. These depend on whether the whole $300\,\mathrm{kg/s}$ are assumed to pass between the fuel plates ($17.5\,\mathrm{m/s}$) or the actual $274.5\,\mathrm{kg/s}$ ($15.91\,\mathrm{m/s}$). For obvious reasons, in this work the latter value is chosen.

Outlet

Only one boundary condition was defined for the outlet, an average static pressure of 2.3 bar. This means that the pressure averaged over the whole outlet is set to the system pressure of FRM II. This allows for non-vertical flow direction as required by the macroscopic turbulences introduced by the lower comb.

Walls

For all solid walls at the outer regions of the model that are not part of a symmetry condition, the wall is assumed to be adiabatic, that is $q = 0$. Affected walls are the inner border of the inner duct, the outer border of the outer duct as well as their corresponding ends above and below the fuel plates.

10.1.4 Interfaces

Interfaces are boundaries between different regions of the model, for example between water and cladding, cladding and fuel but also between high density and lower density fuel. Normally, the only boundary condition at these interfaces is a conservative interface flux for the heat transfer.

In case an oxide layer is included, the interface fulfils another function: It shelters a so called thin interface. Every interface consists of a pair of surfaces with zero distance. In the case of thin interfaces, this distance is virtually increased to a finite value. The space in-between can be filled with an arbitrary material. The important point is, that this thin layer doesn't have to be resolved by a mesh. Therefore, thin interfaces

are – as the name suggests – suited for very thin layers of material. How this can be used to model an oxide layer is explained in chapter 10.2.1.

10.1.5 Heat Sources and Transfer

Heat Source

For the heat source, a subdomain covering the whole fuel was created. A FORTRAN program was developed that was plugged into CFX via *User Fortran* routines. That script is called in every time step or false time step. Then the source energy density ($^{J}/_{s \cdot cm^2}$) is determined from a file that was computed by MCNP for every vertex.

A small approximation has been made here: MCNP sums up the deposited energies in water, cladding and fuel in the area of the fuel plates. Therefore, a separate calculation was run to determine the amount of energy that was deposited in water and cladding. They were fixed to about 2% in the water and 0.5% in the cladding, thus making an energy deposition of 97.5% of the whole energy deposition in the fuel.[5] It was assumed that the spatial distribution of the energy deposition itself is the same in liquid, cladding and fuel, which is surely a disputable assumption but not of considerable effect as the amount of energy deposited in liquid and cladding is comparably small.

Similar subdomains were introduced for the cladding. The energy deposition for each domain was taken from the full energy deposition determined by MCNP and then multiplied by the corresponding factors described above. Further heat sources were created for the frame of the fuel and the inner and outer duct using a similar mechanism.

Due to limitations on the side of CFX, no direct heating of the water could be taken into account. Therefore, the before-mentioned 2% were added to the heat deposited in the cladding.

It must be noted that no variation of the deposited heat in θ-direction was assumed for the subdomains. As the thickness of the fuel plates is approximately one mean free path for thermal neutrons, this means that the variation of deposited power over the thickness is approximately -4% in the middle / +8% at the boundary compared to the averaged power distribution.[6] Due to the high amount of work that would be needed to implement this feature while no new relevant results are expected, the variation was neglected.

Heat Transfer

Thermal Radiation

Although CFX provides the possibility to model heat transport by thermal radiation, no radiation transport was modeled as it makes up less than 1% of the total heat transport and is very time consuming to calculate.[7] In addition, no radiation transport parameters are known for the fuel materials.

According to the Stefan-Boltzmann law, the radiation transport can be estimated for a maximum temperature difference of 80 K in the fuel element,

$$\frac{P}{A} = \sigma \, \Delta T^4 \tag{10.10}$$

$$\approx 2 \, ^{W}/_{m^2}. \tag{10.11}$$

[5] Please note that this consideration is made only for the fuel plates and the liquid between them!
[6] Calculated by assuming an exponential slope of the fission density, neutrons from two sides and a thickness of the fuel plate of one mean free path of the regarded neutrons.
[7] Radiation transport is computed with a Monte Carlo model in CFX.

This is negligible.

10.1.6 Flow and Material Properties

Water

Simple formulas to calculate c_p, ρ, κ and the viscosities ν and η (chap 6, p. 47ff.) which are important for the heat transport in fluids can be found in [Död89, Röh84]. More complex and exact formulas that take both temperature- and pressure-dependence into account are given in [Lem05, Wag02, Coo07, Fer98, Wan03]. The pressure dependency is small in most cases.

In this work, the values predefined for water in Ansys Cfx were used. They rely on the IAPWS-IF97 database [Wag00]. This database includes data for subcooled water, supercritical water/steam, superheated steam, saturation data and high temperature steam[8]. No modifications were made.

Aluminium

In [Gie96], a thermal conductivity of 216 $^{\mathrm{W}}/_{\mathrm{m\,K}}$ is used for the aluminium cladding. This is somewhat smaller than the 237 $^{\mathrm{W}}/_{\mathrm{m\,K}}$ of pure aluminium [EFU08] because the cladding is made of AlFeNi and aluminium alloys tend to have a smaller thermal conductivity than the pure substance. So 216 $^{\mathrm{W}}/_{\mathrm{m\,K}}$ although quoted without a source in [Gie96] seems to be a reasonable value in this case.

The frame surrounding the fuel is made of AlMg2 which has a thermal conductivity of only 150 $^{\mathrm{W}}/_{\mathrm{m\,K}}$ [Cop87]. This value is ignored in [Gie96] and the value of AlFeNi is applied here, too. This approximation does not have too much impact since the resulting difference in the thermal conduction in the directions parallel to the plate is small. For comparability and simplicity, 216 $^{\mathrm{W}}/_{\mathrm{m\,K}}$ is applied to all aluminium based components in this work, too.

Due to lack of data, no thermal effects on the thermal conductivity were taken into account for all aluminium based components. As the thermal conductivity of pure aluminium varies just about 1% in the regarded temperature range [EFU08], the effect can probably be neglected anyway.

The specific heat capacity in $^{\mathrm{J}}/_{\mathrm{kg\,K}}$ of pure Aluminium is given by

$$c_P^{\mathrm{Al}}(T) = 892 + 0.46 \cdot T, \tag{10.12}$$

where the temperature T has to be inserted in ℃ [Com88, p. A13].

Fuel: U_3Si_2-Al

U_3Si_2-Al is a dispersion fuel, that is small U_3Si_2-particles in an aluminium matrix. The volume fraction of porosity in the fuel is calculated by [Sne87]

$$V_P = 0.072 \cdot V_F - 0.275 \cdot V_F^2 + 1.32 \cdot V_F^3, \tag{10.13}$$

where V_F is the volume fraction of the fuel. The remaining volume is attributed to the aluminium matrix.

Specific Heat Capacity: The specific heat capacity of pure U_3Si_2 in $^{\mathrm{J}}/_{\mathrm{kg\,K}}$ is

$$c_P^{\mathrm{U_3Si_2}}(T) = 199 + 0.104 \cdot T, \tag{10.14}$$

[8] The data for high temperature steam is not included in the database of Cfx, which is no problem in this case as these properties are for steam with temperatures higher than 1073.15 K.

T in ℃. The specific heat capacity of the dispersion fuel can be calculated by

$$c_P^{U_3Si_2-Al}(T) = 0.0122 \cdot V_F \cdot c_P^{U_3Si_2}(T) + 0.0027 \cdot (1 - V_F - V_P) \cdot c_P^{Al}(T), \tag{10.15}$$

where $c_P^{Al}(T)$ is taken from eq. 10.12 and $c_P^{U_3Si_2}(T)$ from eq. 10.14. Please note that this equation uses the units $^{MJ}/_{m^3\,K}$. See [Com88, p. A-11] for details.

Thermal Conductivity: Models for the calculation of the thermal conductivity are developed in [Res95, Res92] and have been measured at ANL. The results are given in [Com88]. For low Uranium loadings, the thermal conductivity is proportional to the amount of Aluminium in the fuel. For higher loads, the thermal conductivity approaches the one of pure U_3Si_2 ($\approx 15\,^{W}/_{K\,m}$) and even drops below this value because of the poor thermal contact between the single particles. In the intermediate loading range, the thermal conductivity generally drops faster than the amount of Aluminium would suggest.

No temperature dependence of the thermal conductivity is given in [Com88].

No known data exists for the thermal conductivity of irradiated fuel [Com88]. No change is expected for low and high Uranium loadings. For intermediate loadings up to medium burn-up, the thermal conductivity is expected to grow slightly because the swelling fuel particles consume the built-in porosity. For higher burn-up, the thermal conductivity is expected to drop again because of irradiation-enhanced creep of the matrix and the formation of fission gas bubbles.

Used Data: At BOL the data given in [Gie96] is used for the fuel, see table 10.2. This data is calculated according to the formulas given above.

Quantity	Value inner zone	Value outer zone
λ [$^{W}/_{m\,K}$]	109	165
c_p [$^{J}/_{kg\,K}$]	475.0	630.4
ρ [$^{g}/_{cm^3}$]	5.20	3.96

Table 10.2: *Data for fuel of old element at BOL*

The reduction of the thermal conductivity could be estimated as described in [Res95] if the fuel is already irradiated.

Fuel: Monolithic UMo

Monolithic UMo is one of the options for a future fuel in FRM II. Currently, an alloy of Uranium with 8 wt-% Molybdenum, U8Mo, is favored. Properties of unirradiated U8Mo have been measured for various temperatures by [Hen08][9]. The following properties have been measured:

$$a = (4.08 \pm 0.14)^{mm^2}/_{s} + (0.0175 + 9.7 \cdot 10^{-5})^{mm^2}/_{s\,^\circ C} \cdot T \tag{10.16}$$

$$c_P = 0.155^{J}/_{kg\,K} \tag{10.17}$$

$$\rho = (17.282 \pm 0.050)^{g}/_{cm^3} \tag{10.18}$$

$$\kappa = (11.17 \pm 1.18)^{W}/_{m\,K} + (0.0454 \pm 0.0081)^{W}/_{m\,K\,^\circ C} \cdot T \tag{10.19}$$

Data for irradiated fuel has also been measured by [Hen08] but is unusable due to large errors and yet not understood systematic deviations. For this reason, in this work, the data for unirradiated U8Mo is also used for irradiated U8Mo.

[9] The measured data is in agreement with [Lee01].

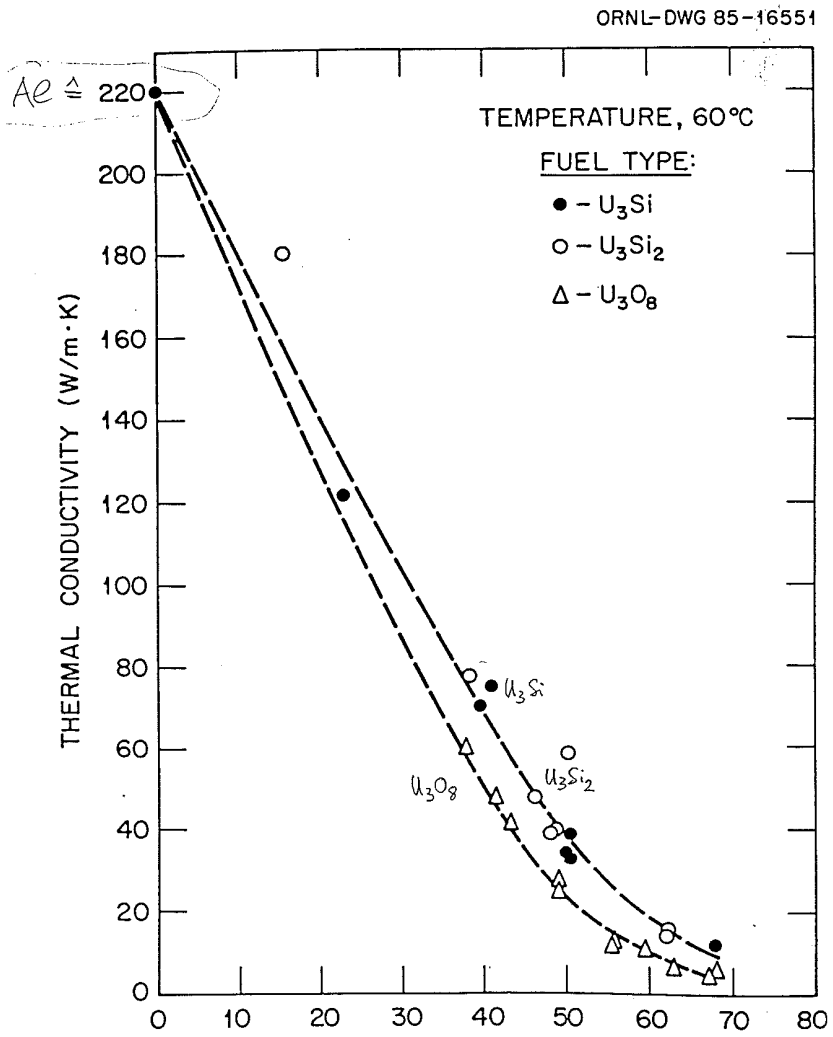

Figure 10.5: *Thermal conductivity of U_3Si_2-Al dispersion fuel depending on the volume fraction of actual fuel (taken from [Com88, p. A-16]).*

Fuel: Disperse UMo

U8Mo can also be used in a dispersive form. Data has been measured by [Jun06] but is unusable due to very large errors, yet not understood systematic deviations and erroneous data evaluation. Reliable laser-flash measurements have been performed by [Lee03, Lee01, Lee07] for unirradiated fuel. The data used is shown table 10.3. It was obtained by inter- and extrapolation of the data of the quoted measurements for U8Mo as shown in fig. 10.6. Calculated results for uranium densities of $8.0\,\mathrm{g/cm^3}$ and $4.0\,\mathrm{g/cm^3}$ are given in table 10.3.

Quantity	**Value** $8.0\,\mathrm{g/cm^3}$ **U**	**Value** $4.0\,\mathrm{g/cm^3}$ **U**
λ [W/m K]	82.1	142.1
c_p [J/kg K]	236	394
ρ [g/cm³]	10.04	6.37

Table 10.3: *Data for UMo disperse fuel at BOL at room temperature*

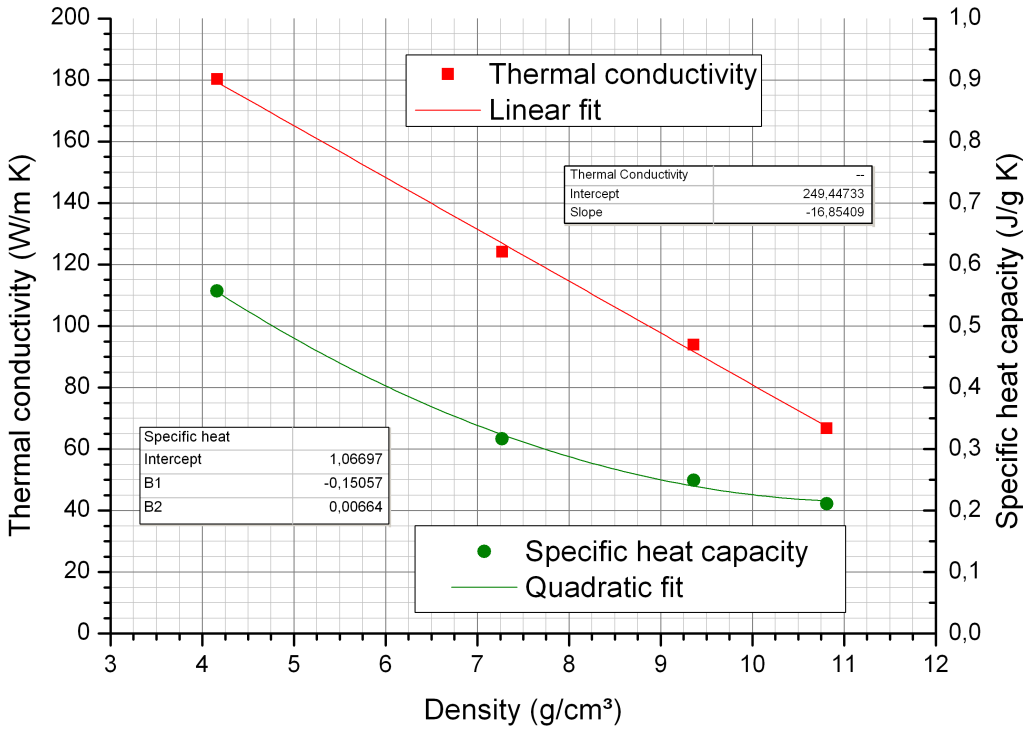

Figure 10.6: *Thermophysical data for disperse U8Mo, based on [Lee07].*

The temperature dependent change of the specific heat capacity is nearly independent of the total density of the alloy (see fig. 10.7). This, however, is not true for the thermal conductivity which reveals large differences (see fig. 10.8). To calculate the temperature dependent change in the thermal conductivity, the data was fitted with polynoms of second and third order and then interpolated to the actual material composition. The change of the thermophysical properties listed in tab. 10.3 is respected in the simulation.

Up to date, no measured data is available for irradiated fuel. A microscopic model of the fuel particles in the matrix could be used to calculate the average macroscopic properties based on the microscopic properties of pure U8Mo measured by [Hen08] and Aluminium by a Lagrangian approach with the program LagMeat. This program was developed in-house by [Här05]. However, no thermal conductivity is known for the interdiffusion layer, which makes the calculation somewhat questionable. Therefore, as in the case of monolithic UMo, it was assumed that there is no change of the thermal conductivity due to irradiation.

10.1.7 Initial Conditions

For steady state calculations, simple assumptions were used as initial conditions: $v = v_z = v_{\text{in}}$, $T_{\text{Wasser}} = T_{\text{in}}$ and somewhat higher temperatures for aluminium and fuel components. The initial pressure was chosen to be a linear decreasing function, approximately representing the final pressure profile. The use of these conditions is mostly limited to speeding up the calculation a bit and less frequently to prevent unphysical or oscillatory behaviour during the iteration of the solution.

For transient simulations, results obtained from steady state calculations were used as initial conditions.

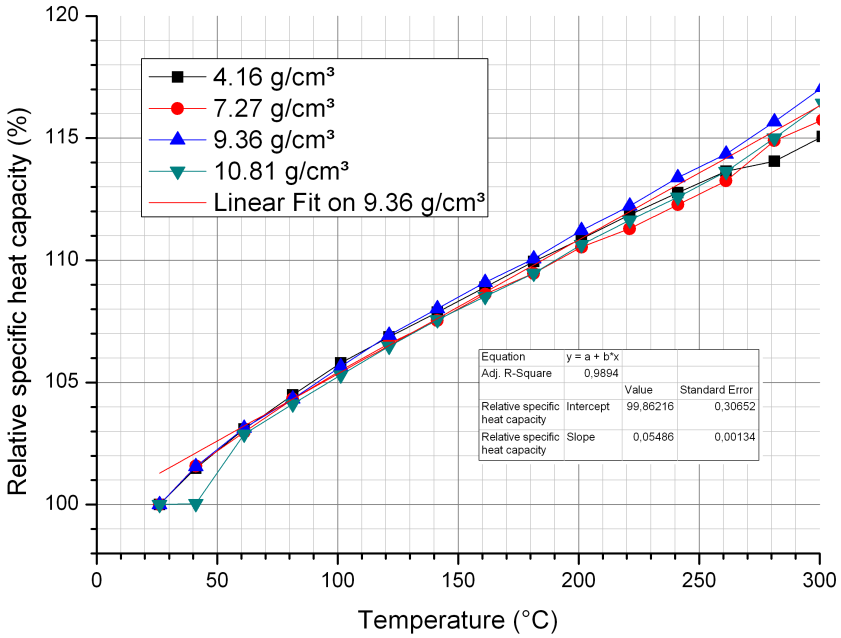

Figure 10.7: *Relative temperature dependence of the specific heat of disperse U8Mo, based on [Lee07].*

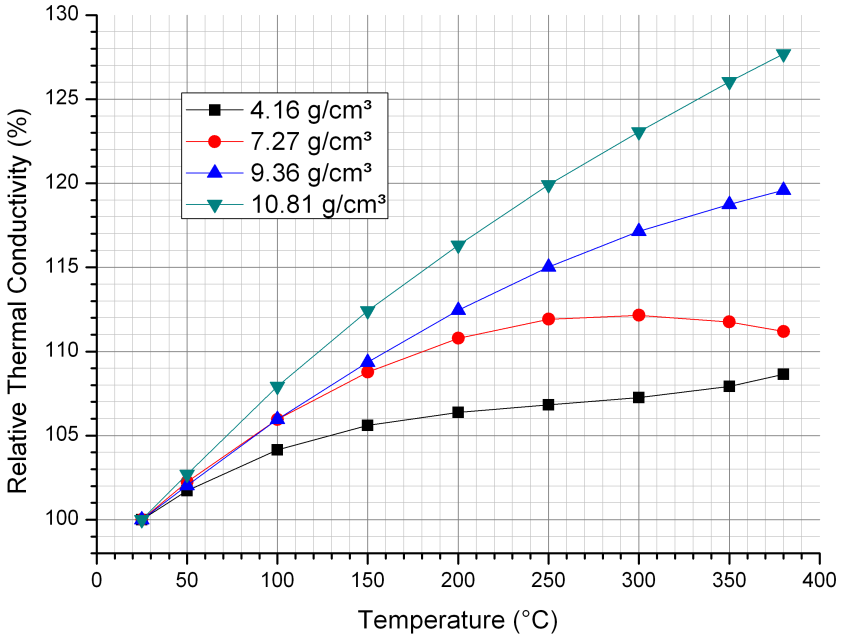

Figure 10.8: *Relative temperature dependence of the thermal conductivity of disperse U8Mo, based on [Lee07].*

10.2 Geometry Modifying Operations

During the operation of the fuel element, several processes modify the geometry of the fuel plates. Among these are the growth of the oxide layer due to the heat flux through the cladding in the cooling fluid, the swelling of the meat due to the production of noble gases in fission and deformation of the plates by thermal expansion.

10.2.1 Growth of the Oxide-Layer

The growth of the oxide layer was computed with a formula given in [Gys96][10] and also mentioned in [Gie96],

$$d_{\mathrm{Ox}} = 7.835 \cdot 10^6 \cdot \left(t \cdot \exp\left[-\frac{-9154}{T_S + 1.056 \cdot q} \right] \right)^{0.74} . \tag{10.22}$$

This gives the thickness of the oxide layer (in µm) depending on the surface temperature T_S (in K), the heat flux q (in $^{\mathrm{MW}}/_{\mathrm{m}^2}$) and the duration t (in days). This correlation is valid for a pH-value of the cooling fluid of 5. According to [IAE92], this formula can be applied to pH-values from 5 to 6.5. In anticipation of the results discussed in chapter 14, p. 14, the maximum thickness of the oxide layer after 60 days of use can be estimated to be less than 10 µm.

However, the above formula does not take the variing surface temperatures and heat fluxes during the cycle into account. A more detailled formula is given in [McL67, p. 21]:

$$X_k = 443 \left(\psi_{k-1} + \theta_k \right)^{0.778} \cdot \exp\left[-\frac{8290}{T_{S,k}} \right] \tag{10.23}$$

$$\psi_k = \left(\psi_{k-2} + \theta_{k-1} \right) \cdot \exp\left[10656 \frac{T_{S,k-1} - T_{S,k}}{T_{S,k-1} T_{S,k}} \right] . \tag{10.24}$$

Here X_k is the thickness of the oxide layer in mils ($2.54 \cdot 10^{-5}$ m), θ the time in h and T_S the surface temperature in Rankine ($T_{\mathrm{Kelvin}} = T_{\mathrm{Rankine}} \cdot \frac{5}{9}$). k is the number of the timestep. $\psi_0 = 0$.

The oxide layer is considered in two complementary ways: The thickness growth of the fuel plate is modelled by mesh deformation, while the effect on heat conduction and the accompanying rise in temperature is modelled by a 'thin surface' in CFX. A thin surface does not modify the mesh. It permits heat conduction through the oxide layer only in 1D, which is a conservative assumption regarding the small thickness. Unfortunately, CFX in version 12.0.1 does not allow to set a variable thickness for the thin surface. This issue was resolved using variable material properties for the oxide layer:

- A default thickness $d_0 = 1$ µm was set for the thin surface
- The default thermal conductivity was set to $\kappa_0 = 2.5\ ^{\mathrm{W}}/_{\mathrm{m\,K}}$.

[10] [Död89] (p. 43) uses the old formula of [Gri61],

$$d_{\mathrm{Ox}} = 0.7 \cdot 1.334 \cdot 10^5 \cdot t^{0.778} \cdot \exp\left[-\frac{4600}{T_S} \right] , \tag{10.20}$$

which does not take the heat flux into account. A more recent formula can be found in [Ond88, p. 29], which was used for the calculations during the Advanced Neutron Source planning:

$$d_{\mathrm{Ox}} = 17.3 \cdot \dot{q} \cdot t^{0.778} \cdot \exp\left[-\frac{1880}{T_S} \right] . \tag{10.21}$$

Please note that in this equation, $\dot{q}$ has to be inserted in units of $^{\mathrm{Btu}}/_{\mathrm{h\,ft}^2}$

- From $\boldsymbol{q} = -\kappa \boldsymbol{\nabla} T$ follows for 1D:

$$\Delta T = -q \left(\frac{\Delta x}{\kappa} \right). \tag{10.25}$$

- As $\Delta x = d_0$ is fixed, the thermal conductivity of the material can be misused to take the thickness variation d_{real} into account by setting

$$\kappa' := \kappa_0 \frac{d_0}{d_{\text{real}}}, \tag{10.26}$$

yielding the final expression

$$\Delta T = -q \left(\frac{d_0}{\kappa'} \right) \tag{10.27}$$

$$= -q \left(\frac{d_{\text{real}}}{\kappa_0} \right). \tag{10.28}$$

For an average cladding temperature of 60 °C and an average heat flux density of 160 $^{\text{W}}/_{\text{cm}^2}$, after 60 days of operation, the oxide layer results in an average fuel temperature increase of about 1.3 °C.

10.2.2 Swelling

Swelling of the fuel is mainly caused by the production of noble gases in fission. This swelling leads to a deformation of the fuel zone and the surrounding cladding. Fig. 10.9 shows the increase in volume of U_3Si_2 as an example. Actual experimental data for the current fuel can be found in [Bön09]. Swelling data for disperse UMo can be found in [Pet08].

Currently, no swelling is taken into account in X^2. It could be implemented in a similar but more complicated way to the growth of the oxide layer. Potentially, swelling will be implemented in X^2 in the framework of the diploma thesis of M. Däubler.

10.2.3 Thermal Expansion

No thermal expansion of solid materials was considered. However, the possibility exists to couple the CFX-Solver to an external finite elements solver that can solve the appropriate equations.

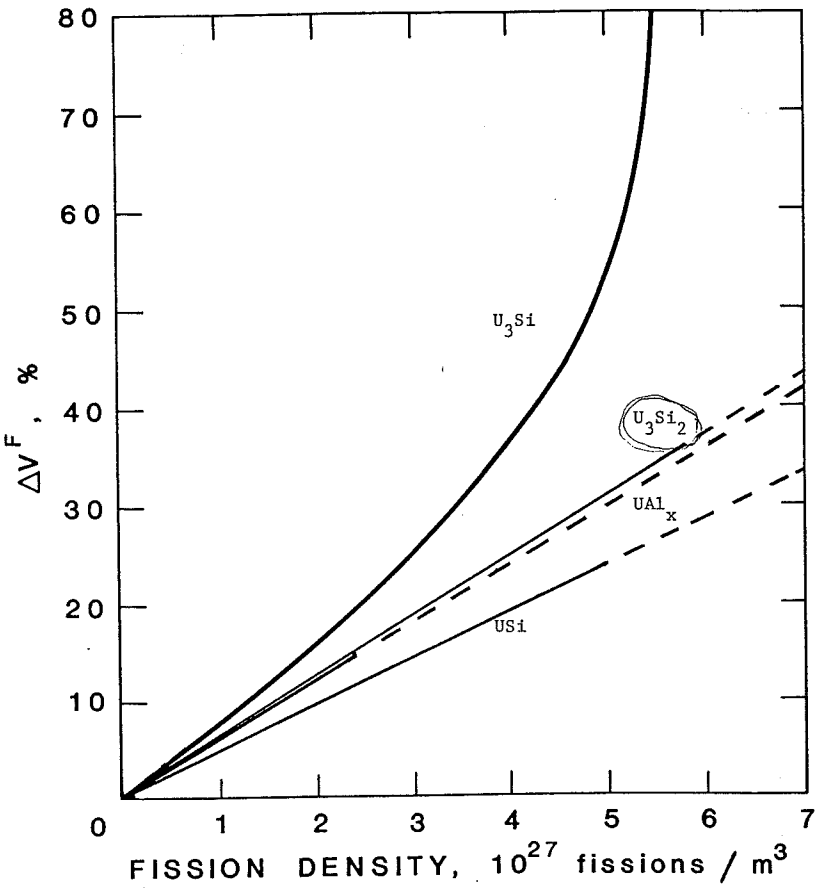

Figure 10.9: *Swelling of U_3Si_2-Al dispersion fuel (taken from cite[p. A-30]nureg1313).*

10.3 Convergence Criteria for the Solver

All results of the thermal hydraulic calculations have an average RMS $< 10^{-5}$. The maximum RMS is $< 10^{-3}$, yielding a maximal calculational residual error of 1 ‰. All important quantities reported in the tables of chap. 17, p. 209, were explicitly monitored to reach their final values at the end of the calculation.

CHAPTER 11

Coupling of Codes: The X^2 Program System

The framework which couples all the before-mentioned codes, McnpX, Cfx, Cinder90 and MonteBurns / Origen2, was named X^2 (*x square*), referring to the trailing X's of the two main components, McnpX and Cfx.

11.1 Implementation

Most parts of X^2 are written in Perl, a portable scripting language. The tasks of these Perl scripts can be subsumed to

- Parametric model construction
- Data conversion for input and output
- Data analysis and error detection
- Execution of external programs with correct parameters and data
- Runtime parameter adjustments
- Plausibility checks of results and
- Primarily result analysis.

The data API for Cfx has been written in Fortran and needs to be compiled against the Cfx-libraries. This data API will be named FSource in the following. Furthermore, the data API for the simulation of the oxide layer is also written in Fortran.

In addition, MonteBurns 2.1 has been modified to include McnpX fission source distributions, multi-processor support and personal cross section libraries. This applies to both the Perl- and Fortran-part of MonteBurns. The code was extended to be able to handle more than 40 different materials and now supports up to 450 materials / burn-up zones. The data-handling of the code was changed to be able to account for the moving control rod. The position finding routine is implemented in X^2 , the runs of MonteBurns are automatically interrupted and restarted by X^2 as needed.

11.1.1 Itinerary

The internal program flow of X^2 is displayed in fig. 11.1. The program flow is explained in detail in appendix C, p. 259. Basically, the system can be divided in two subsystems: The burn-up module and the temperature-convergence module. Both modules can be used alone, but they can also be coupled together. The combination of both modules will be referred to as a 'fully coupled' run. This kind of calculation is very time consuming (about two weeks on 16 E64 Opteron cores), therefore in most cases the modules

were used separately. The burn-up run is then conducted with an average temperature distribution. Due to the rather low temperature variation, the effect on the isotopic composition can be regarded as very small and is neglected. The temperature convergence run is then separately conducted at BOL and EOL. See appendix D.2.3 for a more detailed explanation how this is done.

11.1.2 Plausibility Checks

X^2 currently does not perform plausibility checks itself.[1] Therefore the user must perform these checks himself. The checks cover various features. Naturally, these checks apply more to the thermal hydraulic coupling than to the burn-up calculations.

MCNPX

- Does a +F6 tally for the active zone deliver the same result as the appropriate part of the mesh tally?
- Is the difference between F7 and +F6 reasonable?
- Are the values for F6:N and F6:P reasonable?

Coupling

- Were the McnpX results normalized to $k_{\text{eff}} = 1.0$?
- Do the volumes and shapes of the fuel zones in McnpX and Cfx match?
- Is the deposited energy in Cfx identical to that calculated in McnpX?

CFX

- Do the area integrated heat fluxes through the interfaces match the power deposited within the corresponding bodies?
- Is the overall heating of the fluid reasonable?

Details on some of these checks are given in the user guide for the system, appendix D, p. 267.

[1] This was implemented in a former version during development, but caused numerous problems and errors due to fixed coded tally numbers, varying surface numbers and labels in Cfx etc. Due to this issues, the automatic plausibility checks were removed from X^2 and it is left to the user to perform adequate checks.

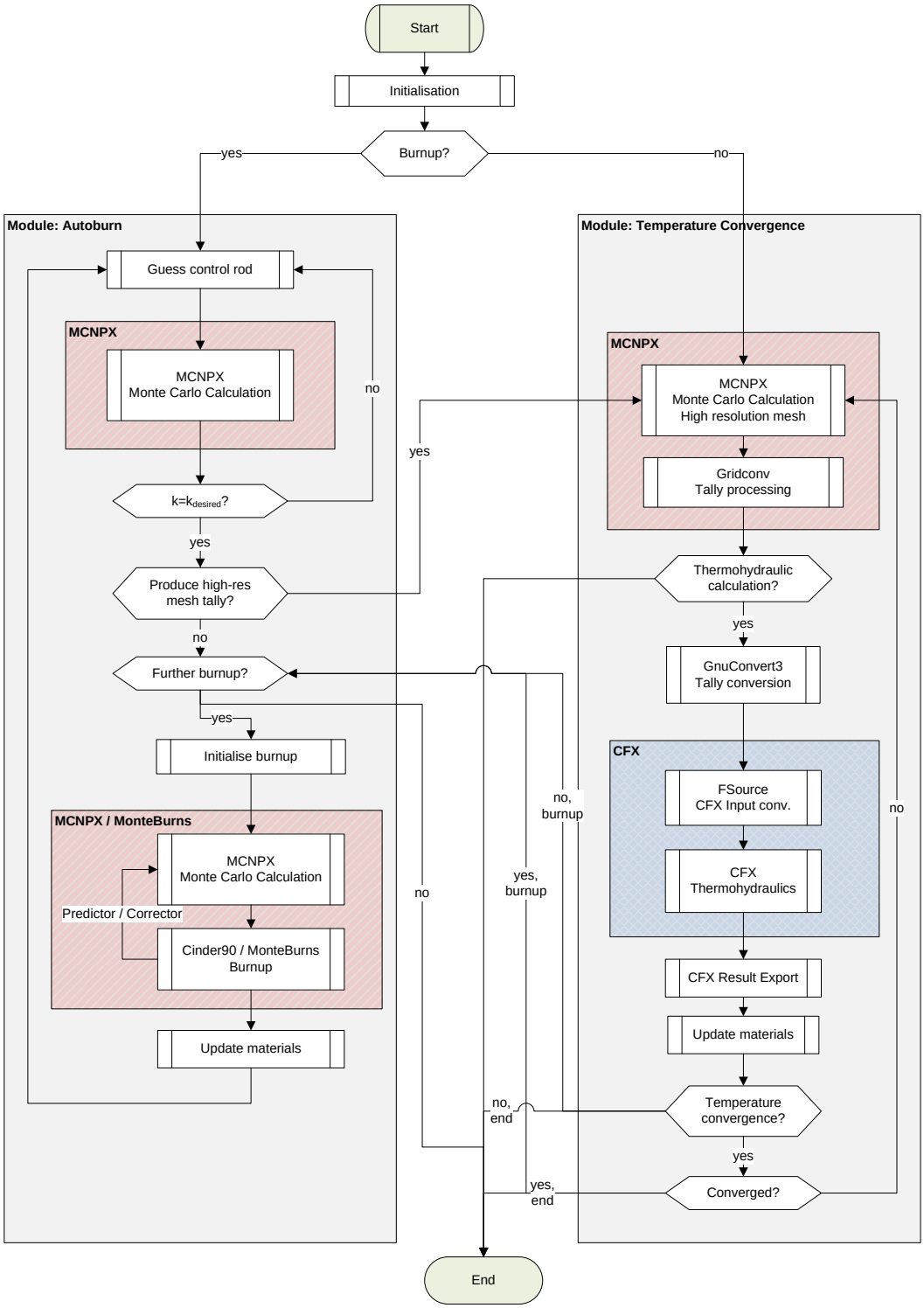

Figure 11.1: *Flowchart for the* X^2 *program system.*

CHAPTER 12

Error Sources

In a complex application like the one presented in this work, numerous error sources contribute to an overall uncertainty of the results. Especially in the field of nuclear reactor science, it is essential to assess these errors as close as possible.

12.1 Monte Carlo Error Sources

The errors sources in Monte Carlo calculations are numerous. Besides the errors that can be caused by the statistical nature of the calculation (see chap. 2.5), errors can be introduced by a number of other sources. They will be discussed in the following.

12.1.1 Numerical Errors

Numerical errors in the results of MCCs arise mainly from the statistical nature. The tracking of these errors was already discussed in chapter 2.5. Other possible numerical error source are

- The random number generator
- Finite precision (round-off errors)
- Lost particles due to complicated geometrical constructions

The concept of the random number generator and its limitations are discussed in [Bro02]. Due to the multi-purpose use of the random numbers in MCCs, the finite number of random numbers is not considered to be of major importance [X-505].

The MCCs in this work were carried out using double precision, this means about 16 significant digits of accuracy. Combined with the continuous approach of the geometry, finite precision itself is not considered to be a source of errors that is worth a debate for this work. However, the finite precision can lead to a loss of particles in combination with geometric effects: Lost particles normally occur due to geometric errors in the MC model. However, they can also appear in special situations, for example when particles fly tangentially to a curved surface. If the particle reaches the surface within a given distance, the code tries to determine the next cell for the particle to travel through. As the surface is curved, there is no direct next cell for a particle travelling tangentially. Therefore the code fails to determine the next cells and neglects the particle. In this work, the curved surfaces of the fuel plates are the main source for lost particles. About one out of 100.000 particles is lost due to this phenomenon. As there is no possibility to 'repair' this, the error introduced by this mechanism is neglected. A similar mechanism which causes lost particles is when the next cell is ambigous, for example if a cylinder touches a cube and a particle travels exactly (within the limited geometric precision) from the cube into the cylinder. The code then fails to determine if the next cell is the cylinder or the cell surrounding the cube and the cylinder and looses the particle [Sev09]. However, no lost particles due to this mechanism were observed in this work.

12.1.2 Software Errors

Software errors are caused by the implementation of the routines in the software. The MC codes chosen for this work enjoy a good reputation and are well tested by a broad user base. Furthermore, the source code of these applications is available. However, it is way beyond the scope of this work to perform a review of the source code of MCNP and MCNPX. It is therefore assumed that both codes work reliable within their specified scope. However, new features are introduced to MCNPX with a comparably high frequency, which makes it necessary to closely follow the mailing list of this code. An example is the erroneous implementation of the delayed gamma ray production which was discovered during this work [Pel10].

Additional errors may be introduced to the model during the automated creation process within the framework of X^2 . This is discussed later in this chapter in section 12.3.

12.1.3 Modelling Errors

Modelling errors arise from the required simplification of the model. The models used in this work are based on production work models of Anton Röhrmoser [Röh10a]. These models have proven robust in the everyday work for FRM II. They are therefore considered to be sufficiently detailed for the purposes of this work. Critical parts like the fuel plates have been reviewed separately by the author of this work.

12.1.4 User Errors

User Errors are introduced by inadequate usage of the code. Even though all users are potentially affected, especially inexperienced users are prone to this error source. This error source can only be avoided by extensive cross checking of models and results with multiple users. In this work, results and models (in parts) were cross checked between three users.

12.2 CFD Error Sources

A good overview on the possible errors on the CFD side is given in [Men]. Many of the error sources are similar to those discussed in section 12.1. The main difference arises from the different computational nature, statistical versus deterministic calculation.

12.2.1 Numerical Errors

Numerical errors arise from the implementation of equations in the CFD software. It is therefore necessary to know the solution strategies of the used solver as described in chapter 7.3, p. 71.

From a practical standpoint, the most relevant errors are *solution* or *discretisation errors*. They emerge from the need to numerically solve equations instead of being able to specify analytic solutions. Most important for the calculations presented in this work are *spatial discretisation errors*. For a p^{th} order discretisation scheme, the error can be estimated by

$$f_{\text{numerical}} - f_{\text{exact}} = \sum_{i=1} pc_i f^{(i)} \Delta^i, \tag{12.1}$$

where $f^{(i)}$ is the i^{th} derivative of the exact solution at a given location and Δ the grid spacing. Problems with the discretisation arise especially concerning the diffusion term in the Navier Stokes equation 7.14, if the mesh grid lines are not aligned to the flow direction. It was therefore ensured that the grid is parallel to the flow in all relevant areas. CFX uses a second order discretisation scheme, which is considered to be sufficiently accurate. Besides the additional computational effort, higher order discretisation schemes suffer from increasing numerical problems. This is why the 2^{nd}order approach is considered to be a good

compromise.

In transient simulations, the *time discretisation* is subject to similar errors as the spatial discretisation. As for the spatial discretisation, a second order accurate scheme was used, a modified version of the Second Order Backward Euler scheme.

Details on the discretisation used by CFX are given in [CFX09b, p. 239].

Another error source is the *iteration error*, which arises from false time steps used in steady-state simulations and is therefore similar to the coefficient loop error described above. When the steady-state solution is computed, the iterative process has to be interrupted at some point, long before the solution has fully converged. The need to do this arises from the computational expense of computing a fully converged solution, while only insignificant improvements of the solution are obtained over a long time range towards the end of the calculation. It is this error which is quantified in terms of a residual in the calculations. To minimize the iteration error, target variables are defined, this means special variables which are monitored during the computation of the solution. Examples for these variables are minimum and maximum heat fluxes, temperatures, pressures, the overall pressure drop etc. The iterative process must not be stopped until these variables have converged. Practically, these variables are chosen in a way that they are identical or similar to the most important goals of the simulation.

Often talked about but less important are round-off errors which arise from the limited precision of floating point variables in the computer. Normally, single precision is used, which means about eight digits of accuracy. This is doubled in double precision runs, paid-off by increased computational effort and memory requirements. Round-off errors express themselves in terms of random behaviour of the solution.

The solution error can normally estimated by systematic grid refinement and/or time step reduction. If the grids are already fine enough to be in the asymptotic range, the difference between the solutions on successively refined grids can be used to estimate the error. This further allows for the application of Richardson extrapolation [Ric11, Ric27, Pre07]: If h_i is a linear measure of the grid spacing in refinement step i, then

$$f_{\text{exact}} = f_i + g_1 h_i + g_2 h_i^2 + \cdots \tag{12.2}$$

For second order accurate schemes, $g_1 = 0$. If two different grids are used, then g_2 can be eliminated from the equations yielding

$$f_{\text{exact}} - f_1 = \frac{f_1 - f_2}{r^p - 1} + \cdots , \tag{12.3}$$

with $r = h_2/h_1$. However, this assumption is only valid for structured meshes. The meshes used in the calculations of this work are unstructured. Therefore, the refinement level has to be redefined as

$$r_{\text{eff}} = \left(\frac{N_1}{N_2} \right)^{\frac{1}{3}} , \tag{12.4}$$

where N_i is the number of grid points in the iþrefinement step. The exponent arises from the three-dimensionality of the problem.

It is important to note that theses considerations do not impose an upper limit on the real error but are only estimators for numerical quality of the results. As mentioned above, for these considerations, the mesh resolution already has to be in the asymptotic range. Especially in three-dimensional calculations, this is not easy to ensure. Therefore, three different grid levels have to be used.

12.2.2 Modelling Errors

Modelling errors arise from the same source as in the MC case, mostly from oversimplification of the model. In the calculations presented in this work, only few simplifications were made:

- The surface roughness of the plates was not explicitly modelled but included in the form of correlations in the wall functions, see chapter 7.2.3, p. 69.
- The sieve which is placed over the fuel plates to filter large particles was drastically simplified. The approach is described in chapter 13.1. However, these simplifications have the nature of a systematic error as the results of this preparational calculation affect all other calculations in the same way and with the same magnitude.

The models were cross checked by calculating volumes and surfaces and comparing them to the real situation.

12.2.3 User Errors

User errors in CFD are of the same origin as in the MC case. They arise from insufficient experience or a sloppy work habit. The first is normally resolved by expert advise, while the latter can only be treated with good documentation and cross checking between multiple persons. In this work, two users were involved in the cross checking procedure. Expert advise was requested whenever a need for this was felt. This work, [Sar11] and the accompanying data serve as documentation.

12.2.4 Application Uncertainties

Application uncertainties show up when specific models are used in situations they were not made for. Concerning this work, the most important models are that of wall functions, turbulence and multi-phase correlations. For this reasons, the models and there applicability were extensively discussed in chapters 7.2.2, 7.2.3and 8.

12.2.5 Software Errors

As before, software errors arise from misprogramming of the application. If these errors are small, they can only be detected by comparison of the calculated results to an experiment. Of course, larger errors which lead to unphysical results can easily be identified. Concerning CFX, it is important to watch the Class-3-Error list of the program that is published on the ANSYS website.

12.3 Errors Introduced by X^2

The program system X^2 is probably the major source of possible errors as it was developed especially for this work by a single developer. That code was cross-read by [Sar11] and results produced by the code were cross-checked to other code systems, such as Mf2dAb [Röh91a].

12.3.1 Model Construction

The model construction in X^2 consists of several parts. It is left to MCNPX and CFX to check for the correct syntax of their models. X^2 does some checking on its own input files but surely cannot detect all errors. Therefore the program has extensive logging capabilities and the user is advised to check the log-files of X^2 after each run.

12.3.2 Data Transfer

One of the most prominent error sources is the data transfer from McnpX to Cfx. This part of X^2 consists of two sub-parts, one written in Perl and one written in FORTRAN. Both parts were extensively cross-read concerning correct index-handling of the arrays. Necessary conversion constants are calculated from user parameters specified in Cfx. Hard-coded constants were double-checked.

However, it must be admitted, that no error checking was implemented regarding damaged files or invalid syntax. It is assumed that misformattings and file damages that were introduced by X^2 itself either lead to unphysical results or crash the program.

Part IV

Results

CHAPTER 13

General Results

In this chapter, general results that are applicable to most configurations that will be discussed in the following chapters are presented. Table 13.1 lists the standard input parameters for all simulations if not stated otherwise. Important normalisation factors are given in table 13.2.

Quantity	Value
Reactor power	20 MW
net core throughput	274.5 $^{kg}/_{s}$
absolute roughness of walls	2.4 µm
flow temperature at inlet	37 °C
average static pressure at outlet	2.3 bar

Table 13.1: *Data input for the simulation of the current fuel element*

Quantity	Value
Neutrons per fission (BOL)	2.44
Energy per fission (BOL)	202.0 MeV

Table 13.2: *Used normalisation factors*

The data given in table 13.1 has been derived from [Gie96] using the dimensions of the fuel element and/or fundamental quantities. The net core throughput given above is partially derived from the net throughput of the primary cooling circuit of 300 $^{kg}/_{s}$ with 91.5 % of the fluid entering between the fuel plates. This number is also given explicitly in [Gie96]. The absolute wall roughness of 2.4 µm is calculated from experimental results from [Gie96, Sie93]. [Död89] lists 1.5 µm, actual working plans specify 1.6 µm (Rugotest N7). For the reproducebility of measurements, most calculations have been performed with an absolute wall roughness of 2.4 µm. The influence of the roughness on thermal hydraulic results is studied in chapter 17.1.1, p. 209 (table 17.1).

Some other important quantities derived from the figures above are presented in table 13.3.

Quantity	Value
Number of neutrons produced per second	$1.51 \cdot 10^{18}\,\mathrm{n/s}$
averaged velocity above sieve	$9.43\,\mathrm{m/s}$
averaged velocity above fuel plates	$9.83\,\mathrm{m/s}$
averaged velocity between fuel plates	$15.91\,\mathrm{m/s}$

Table 13.3: *Derived data for the simulation of the fuel element*

For a short overview on how the pictures presented in the following have to be interpreted see fig. 10.2, p. 96.

Remarks

1. In the CFD calculations, all edges have been assumed to be sharp and not deburred as required by the constructional drawings of the fuel plates.
2. The velocity of the flow at the inlet some centimeters above the sieve has been set to a constant number in disregard of any boundary profiles. However, there is sufficient room to develop the actual boundary profile before the flow enters between the fuel plates.
3. The system pressure at the outlet has been averaged over the whole outlet. It is therefore not constant in the whole area.

13.1 Effect of the Sieve

28.65 cm above the inlet to the plates, a sieve is located in the fuel element (see fig. 1.2). The purpose of this sieve is to filter all particles with sizes $> 1.8\,\mathrm{mm}$, that is all particles that could theoretically block the cooling channels between the plates even if those were assembled with the lowest possible margin, 1.9 mm [Fel96, p. 69] instead of nominal 2.2 mm. The sieve has a porosity of 47% but does not extend over the whole width of the annulus, therefore representing a bottleneck for the flow. This leads to an acceleration of the flow and a detachment as the annulus widens up after the sieve.

Due to its very fine structure, the sieve was not simulated in full detail. Instead, the bottleneck was modelled but the sieve itself was just represented by a superimposed momentum source of $-1.1 \cdot 10^{7}\,\mathrm{kg/m^2\,s^2}$, that was adjusted to produce the measured pressure drop of 1.11 bar [Gie96, p. 40]. The walls in the bottleneck were changed to free-slip walls to prevent the development of an untrue boundary layer in this part.

The main goal of this simulation was to calculate the actual velocity profile and the turbulence parameters of the flow some centimeters above the beginning of the fuel plates. This profile is shown in fig. 13.1(b). It shows a variation between approximately $6\,\mathrm{m/s}$ and $11\,\mathrm{m/s}$ in the relevant part of the flow. However, the influence of this profile on the actual cooling of the plates is negligible as the choking of the fluid above the fuel plates and especially the tightening of the channel lead to a reformation of the boundary profile (fig. 13.2) that flattens the velocity profile in the parts of the channel relevant for cooling.

It has to be admitted that this simulation of the sieve itself is surely a rather unsubtle approximation, but its aim is not to simulate the sieve itself as close as possible but to calculate a reliable boundary profile and to determine the starting conditions for later simulations, that means for the simulation of the cooling channels between the fuel plates. Therefore the profile shown in fig. 13.1(b) is used in later simulations as the starting profile of the flow, together with relevant turbulence properties.

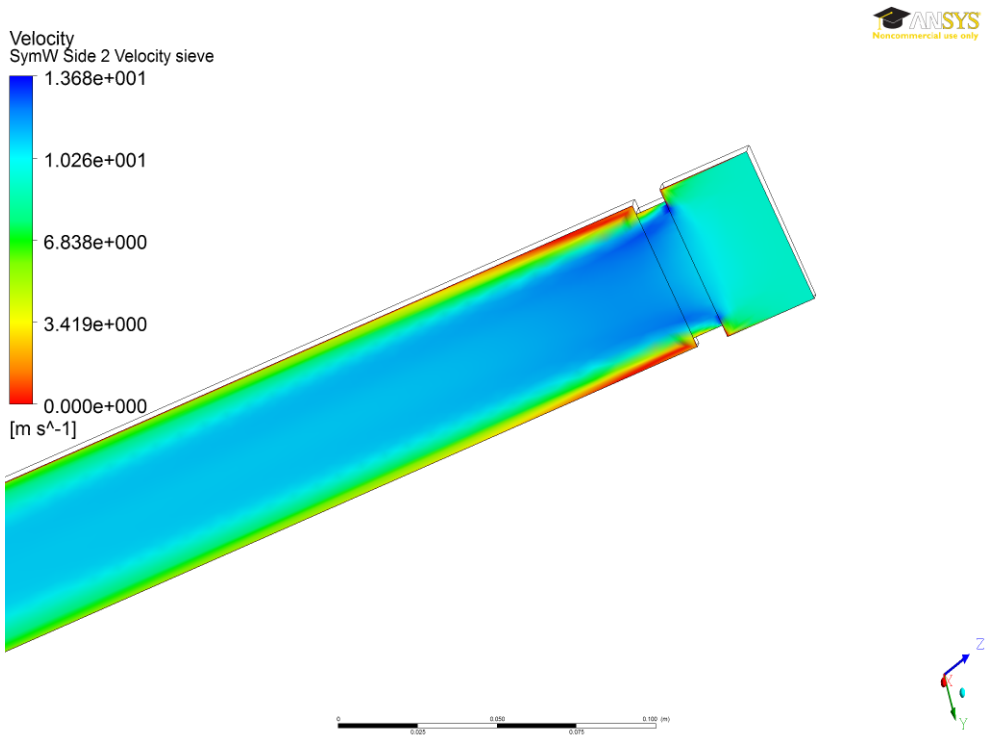

(a)

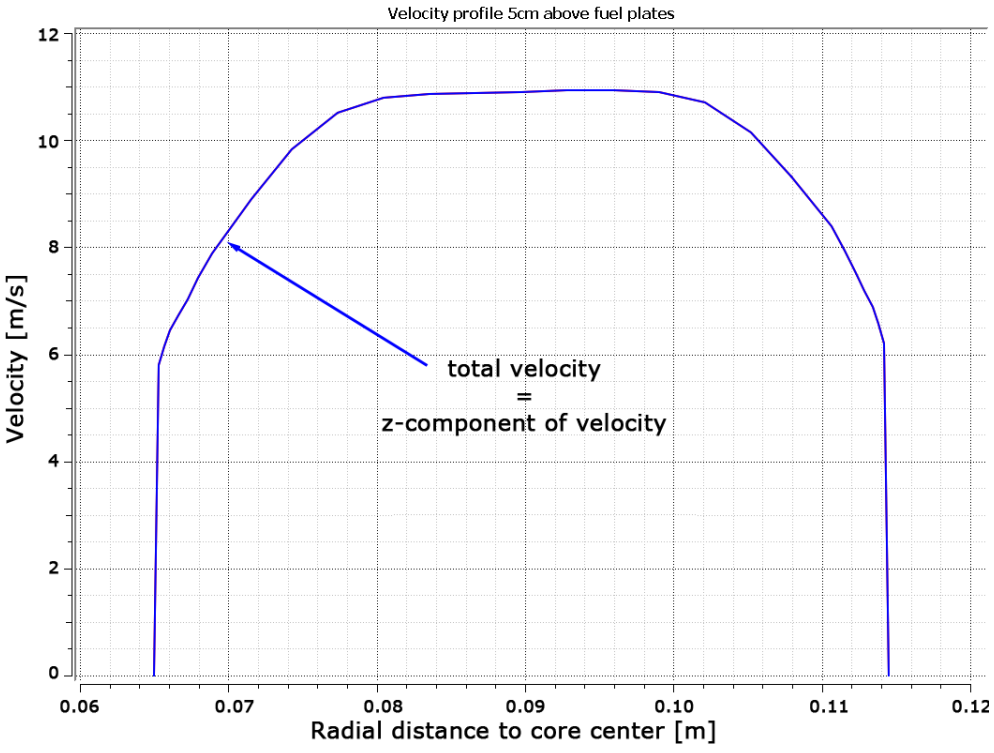

(b)

Figure 13.1: *Development of velocity profile after the sieve: Development of flow (a) and actual velocity profile 5 cm above the inlet to the fuel plates depending on the radial distance to the center of the core (b).*

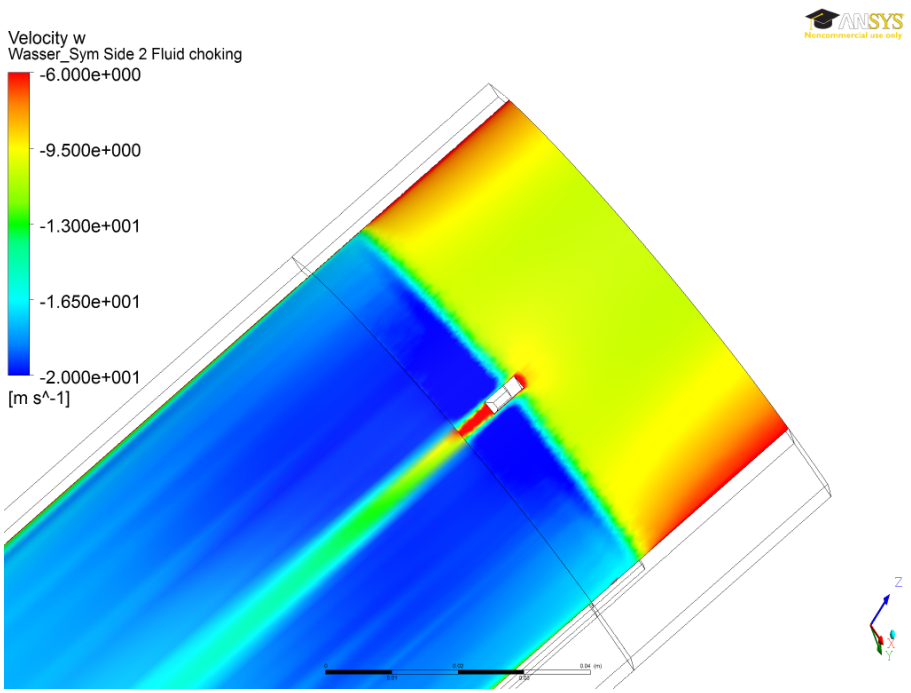

(a)

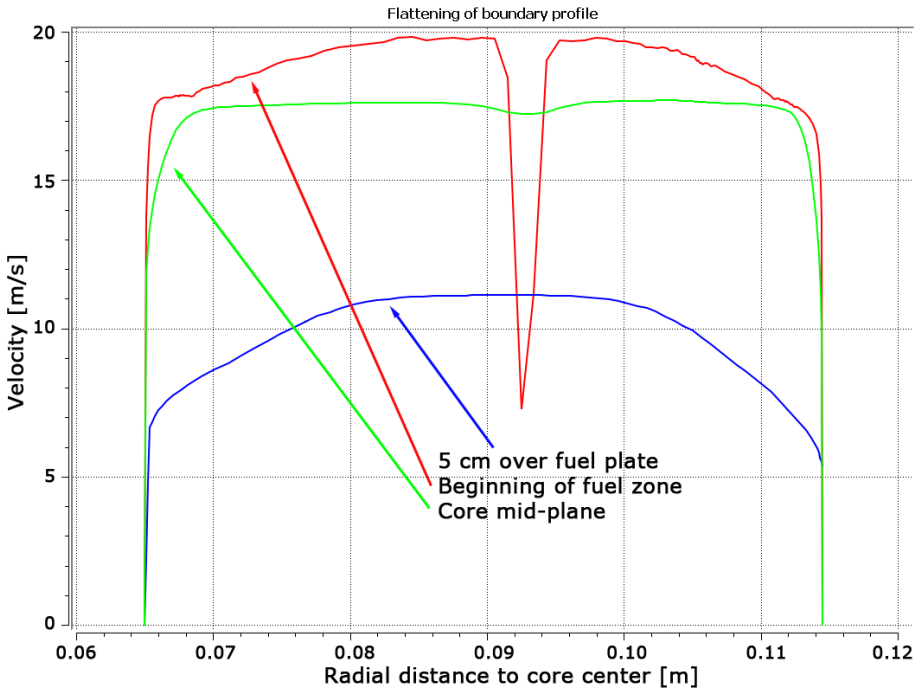

(b)

Figure 13.2: *Distortion of boundary profiles over fuel plates and the development of the profile with increasing depth in the middle of the cooling channel. In (b), the blue curve is the radial velocity profile at the inlet, the red curve the profile at the beginning of the fuel zone below the upper comb and the green curve the profile in the middle of the fuel zone (core mid-plane).*

13.2 Effect of Combs

An interesting property that has not been investigated yet is the effect of the combs stabilising the fuel plates at the inlet and at the outlet.

13.2.1 Development of a Kármán Vortex Street

A Kármán vortex street is expected to develop after the combs. From fig. 13.3, a Strouhal number of $\mathrm{Sr} \approx 0.2$ is derived for a Reynolds number of $\mathrm{Re} = 10^5$. From

$$f = \frac{\mathrm{Sr} \cdot v}{d}, \tag{13.1}$$

a characteristic frequency of vortex shedding $f \approx 450\,\mathrm{Hz}$ can be calculated for a fluid velocity $v = 15.91\,\mathrm{m/s}$ as well as $f \approx 280\,\mathrm{Hz}$ for $v = 9.83\,\mathrm{m/s}$ and a characteristic length of $d = 7\,\mathrm{mm}$ for the combs.[1]

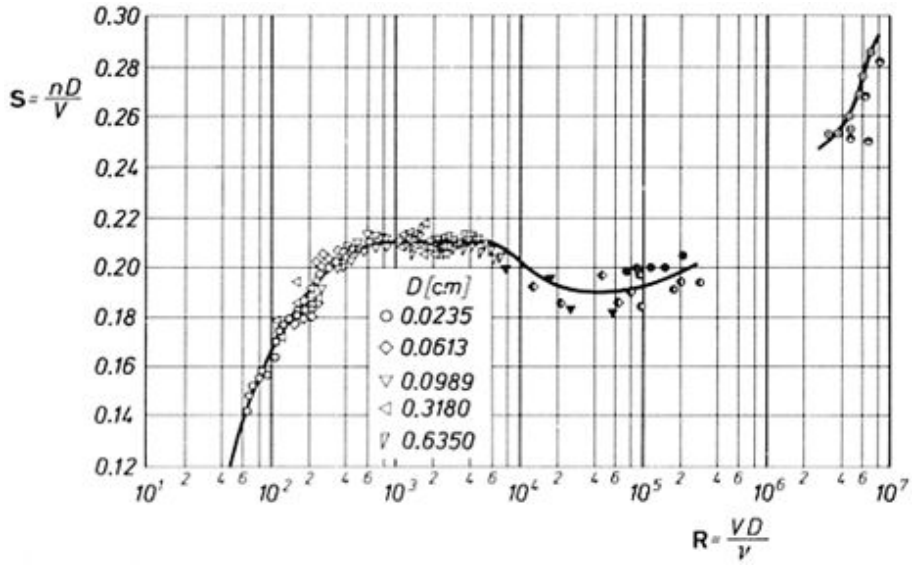

Figure 13.3: *Strouhal number over Reynolds number. Taken from [str].*

Considering the development of a Kármán vortex street after the combs, it must be concluded that the steady-state results produced by the CFX Solver are a time average where the development of the vortices is not explicitly calculated. This averaged vortex street constitutes the 'smear' described in later chapters.

The development of vortices below the lower comb also leads to oscillations in the temperature of up to 0.3 K directly at the end of the calculation approximately 5 cm below the end of the fuel plates. This is due to the alternating sides of vortex detachment, mixing streamlines with different temperatures. This oscillation is an efficient measure for the frequency of vortex detachment which was determined to be $f \approx 349.59(5)\,\mathrm{Hz}$ from the simulation, a value approximately in the middle of the two calculated ones (see fig. 13.4). This could be expected as the fluid is decelerating while flowing around the lower comb and the comb reaches down to the lower-velocity regime, which is where the eddies detach.

No vortex street could be observed in the simulations behind the upper comb, although its development is expected.

[1] This length was calculated as diameter from the outer lengths of the combs.

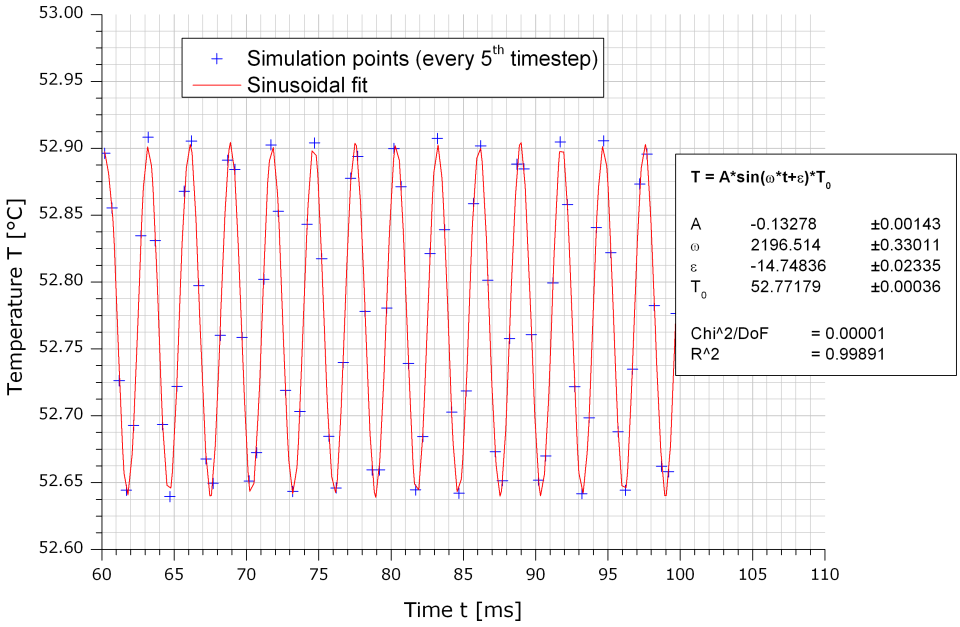

Figure 13.4: *Fluid temperature oscillations below the lower comb. These oscillations suggest the development of a Kármán vortex street after the combs.*

13.2.2 Inlet Above the Fuel Plates

Obviously the comb at the inlet is of much greater interest. It generates a smear in the velocity profile that reaches deep down between the plates.

Fig. 13.5(a) shows the vertical velocity v_z in the middle of the cooling channel. Coming from above, the fuel plate starts at the border between the green and the blue part. As there is less space for the fluid – 2.20 mm instead of 3.56 mm – it is accelerated from 9.83 m/s to 15.91 m/s. The grey window in there is a cut through the comb. This comb proves to be the origin of the smear that can be seen nearly over the half plate[2]. It creates strong turbulences, even inducing backward flow right beneath it.[3] Looking at fig. 13.5(d) reveals that the flow is already accelerated some millimeters above the beginning of the plate as the fluid directly over the plates is choked and therefore pressing the fluid above in smaller, faster flow channels beside it. This can also be observed in the green curve in fig. 13.6(b).

In fig. 13.5(a) and (b), there seems to be a slight jump in the velocities, which is an artifact of the calculation, as two different meshes are glued together here. If the velocity profile is recorded along this black line, the graph in fig. 13.6(a) is the result. It shows a huge dip where the comb is located.[4] The fluid velocity in the middle of the cooling channel drops down to 4 m/s at the beginning of the fuel. However, due to the induced strong turbulences, the cooling is better in this small stream filament than in the filaments besides, running contrary to the expectations of a poorer cooling due to the reduced flow velocity. In anticipation of later results, it should be noted that the smear does not affect the cooling in a significant way, even at the end of the cycle where the temperature distribution is shifted to higher values

[2] As stated before, this smear is probably the time-average of a Kármán vortex street.
[3] Fig. 13.5(b) shows the $v_z = 0$-isosurface, i.e. the flow within the yellow surface is directed upwards.
[4] Please note that this graph is somewhat stretched in x-direction.

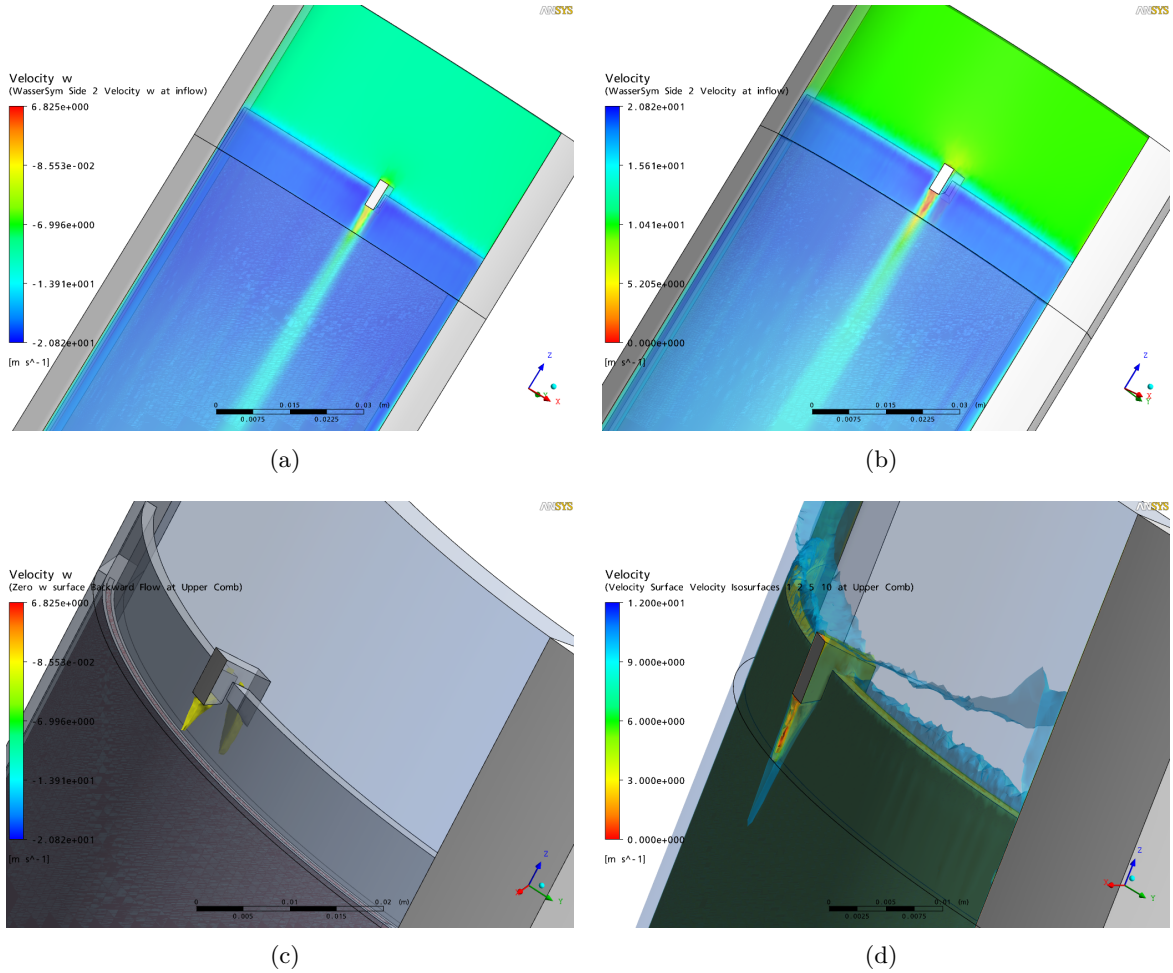

Figure 13.5: *Flow properties above the fuel plates of the current fuel element. (a) shows the vertical velocity of the stream in the middle of the cooling channel. (b) shows the overall velocity. (c) is an isosurface representing zero vertical flow velocity. (d) are a group of isosurfaces for 1, 2, 5, and 10 m/s overall velocity. The control rod is located to the left of the plate, the heavy water to the right.*

in the upper fuel plate where the smear resides.

When looking at fig. 13.5(a) and 13.5(c), it should be emphasised that the velocities shown are only the z-parts, i. e. $v_z = \boldsymbol{v} \cdot \boldsymbol{e}_z$. Except at the surfaces (no-slip condition), there is of course always $v > 0$.

The over-acceleration seen in the green curve in fig. 13.6(b) can be explained by the detachment of the flow from the fuel plates upper corner which leads to an increased speed of the flow in the middle of the cooling channel (see also fig. 13.7). Without regarding the effect of the upper comb, the velocity profile reaches its intended form at about 8 cm after the beginning of the plate. The flow under the comb is not accelerated to its full speed until the very end of the plate.

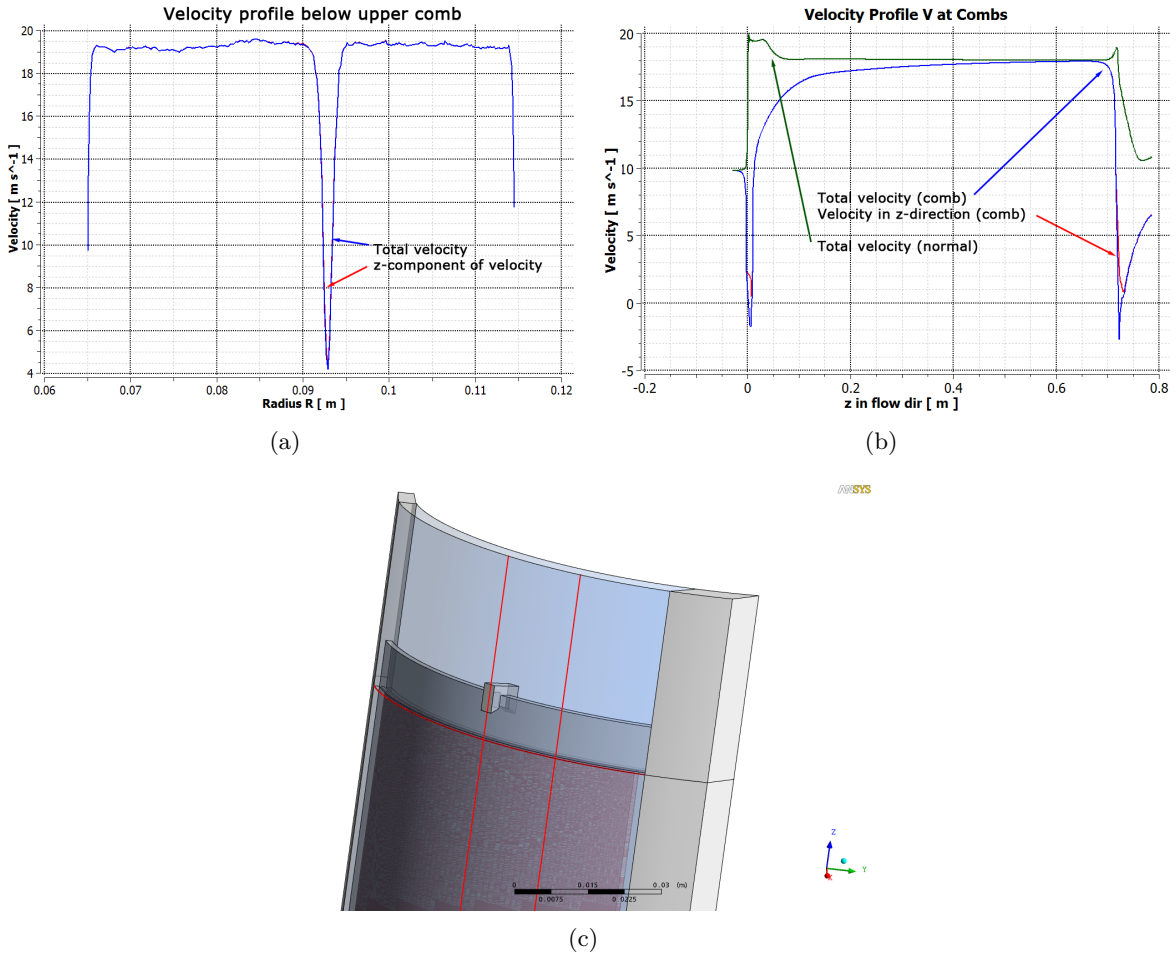

Figure 13.6: *Flow around the upper comb of the current fuel element. (a) shows the vertical velocity (blue) and the overall velocity (red, mostly hidden by the blue curve) of the stream in the middle of the cooling channel at the beginning of the fuel. (b) shows the vertical velocity (blue) and the overall velocity (red, mostly hidden by the blue curve) vertically through the whole channel just where the combs are located and the 'normal' profile (green). (c) shows the corresponding locations (red lines): The horizontal line is where the curve in (a) was recorded, the vertical lines represent the positions for the comb-distroted and the normal profile in (b).*

13.2.3 Outlet Below the Fuel Plates

Fig. 13.8(a) shows the vertical velocity at the outlet of the fuel elements cooling channels. Again, the black line marks the end of the fuel zone, whilst the actual end of the fuel plate is 1 cm below this. The gray box in the middle is the lower comb.

At the end of the plate, a choking effect can be observed again, this time from the lower comb. It is important to mention that at this critical point, no cooling problems occur as the choking in anticipation of the comb takes place about 5 mm below the end of the fuel whereas even in the worst case the fuel does not extend to more than 7.5 mm above the end of the plate. The fluid in the middle of the cooling channel is again accelerated a bit by the detachment of the flow from the lower end corner of the plate and then drops back to slightly more than the expected 9.83 m/s. This can be explained by the fact that the part of the fluid under the plate is not accelerated to its full speed in the regarded distance. The

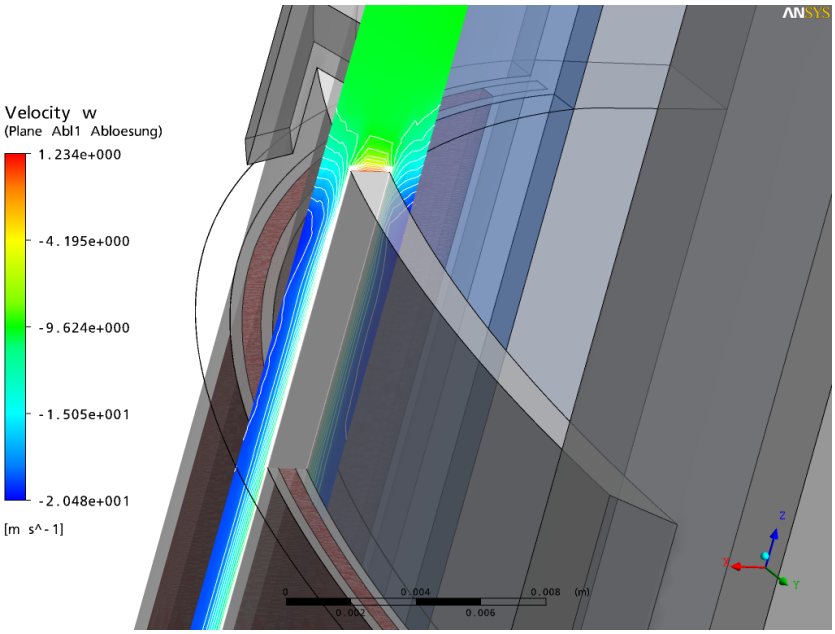

Figure 13.7: *Detachment of flow at the upper fuel plate border: The picture shows a model of the fuel plate between the two outer tubes without water. The grey area is aluminium, the red is fuel. The coloured face is a vertical cut through the cooling channel, where the colours represent the different z-velocities. White lines are iso-velocity lines. From these lines, the detachment of the flow can be seen.*

lower comb produces an even bigger smear – larger vortices – than the upper, but this time without any noteworthy effect on any important quantity of the cooling.

As the cooling channel widens up again after the end of the fuel plate, the velocity drops nearly to the old velocity above the inlet. Differences in the velocity are due to changed fluid densities, caused by the heat up. The lower comb again creates a smear, due to the lower velocity wider than the smear of the upper comb. Again, upwards directed flows can be observed. On top of the comb, a small zone of slower flux is created, a tailback from the soon-coming comb. It has no influence on the cooling of the fuel, though.

Information on temperature distributions at the outlet can be found later in chapter 14.5, especially fig. 14.9. They depend strongly on the geometrical distribution of the fuel that is used. As already stated, the system pressure has been averaged over the whole outlet as due to the effect of the comb the pressure is nearly but not fully constant over the whole area (see also fig. 13.13(c)).

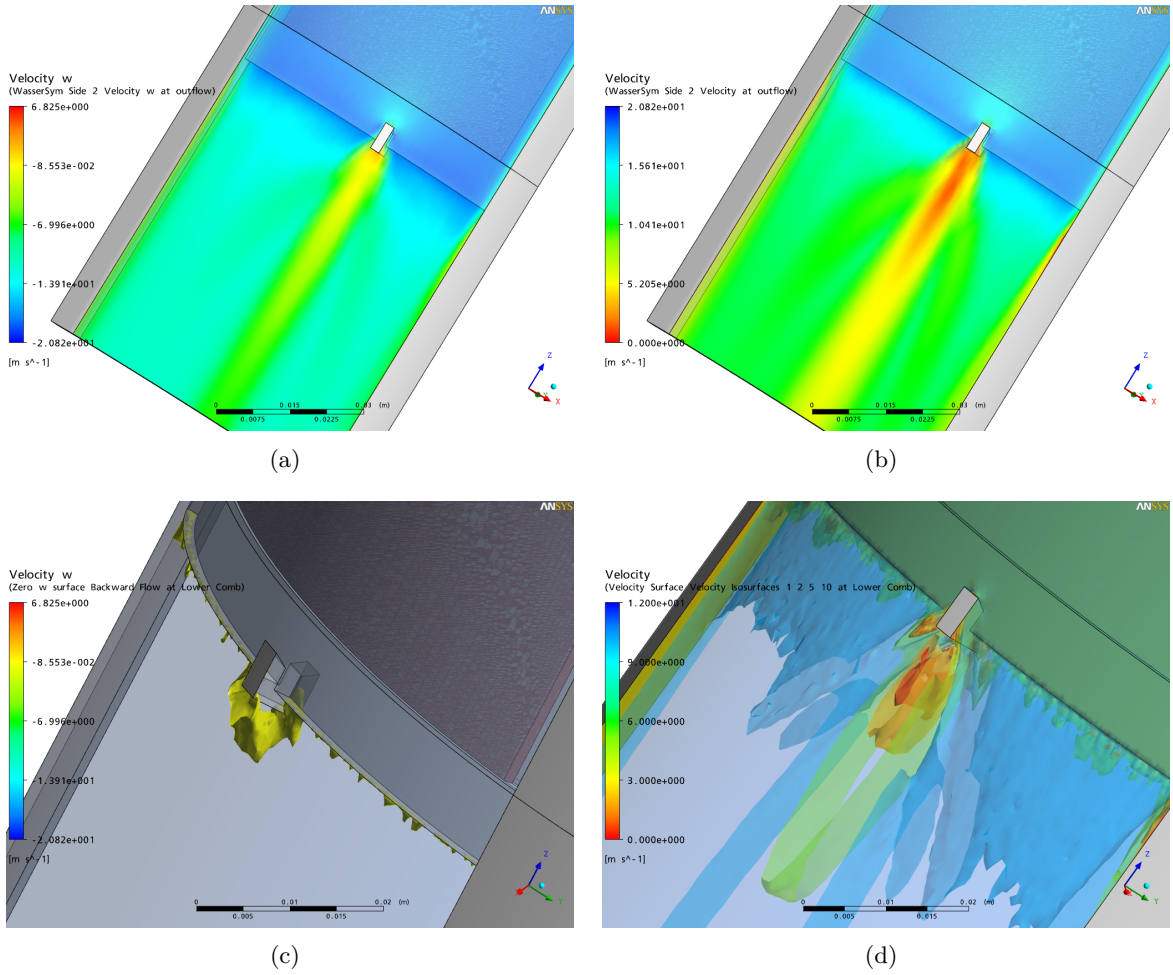

Figure 13.8: *Flow properties at the outlet of the current fuel element. (a) shows the vertical velocity of the stream in the middle of the cooling channel. (b) shows the overall velocity. (c) is an isosurface representing zero vertical flow velocity. (d) are a group of isosurfaces for 1, 2, 5, and 10 $^m/_s$ overall velocity. The control rod is located to the left of the plate, the heavy water to the right.*

13.3 3D Heat Conduction

The effect of 3D heat conduction in the solid and the 'resistance' that is connected to the heat transfer over the wall is best studied by using a homogeneous heat source instead of the inhomogeneous, original power distribution in the fuel plate. The heat flux on the surface is shown in fig. 13.9. Base model is a monolithic, flat fuel plate of UMo with a homogeneous power distribution. The border of the fuel zone is marked by a white rectangle. According to these calculations, the heat flux at the limits of the fuel zone is affected by the 3D heat conduction up to about 3 mm from the borders[5]. It is notable that this zone widens up towards the lower end of the fuel plate. This is probably connected to the development of a boundary profile (compare fig. 13.6(b)), where decreasing velocities near the wall yield lower heat transfer coefficients. As $1/\alpha$ can be interpreted as some kind of resistance, this softens the gradient near

[5]The sawtooth-like structure in fig 13.9(b) is an effect of the GGI interface between the meshes and has no physical meaning.

the border of the heated zone as it hinders the heat transport from the solid to the fluid.[6]. Additionally, the increased turbulences after the upper comb are also clearly visible as they 'tear' the heat flux towards the turbulence.

Approximately the same holds for the temperature as shown in fig. 13.10(a). In addition, the temperature distribution is more affected by the border region, as – thinking in stream filaments – the fluid picks up less heat near the border. Therefore the fluid is cooled, which leads to disproportionately lower wall temperatures. A profile of temperatures and heat fluxes 5 cm below the upper and 5 cm above the lower border of the fuel zone is shown in fig. 13.10.

[6] According to [Kal], the inlet correction factor $K_L = 1 + \left(\frac{d_H}{L}\right)$ for the Nusselt number is about unity for $\frac{L}{d_H} \gtrsim 200$. For $d_H = 4.26\,\text{mm}$, this yields $L \approx 80\,\text{cm}$, which is about the length of the channel in flow direction.

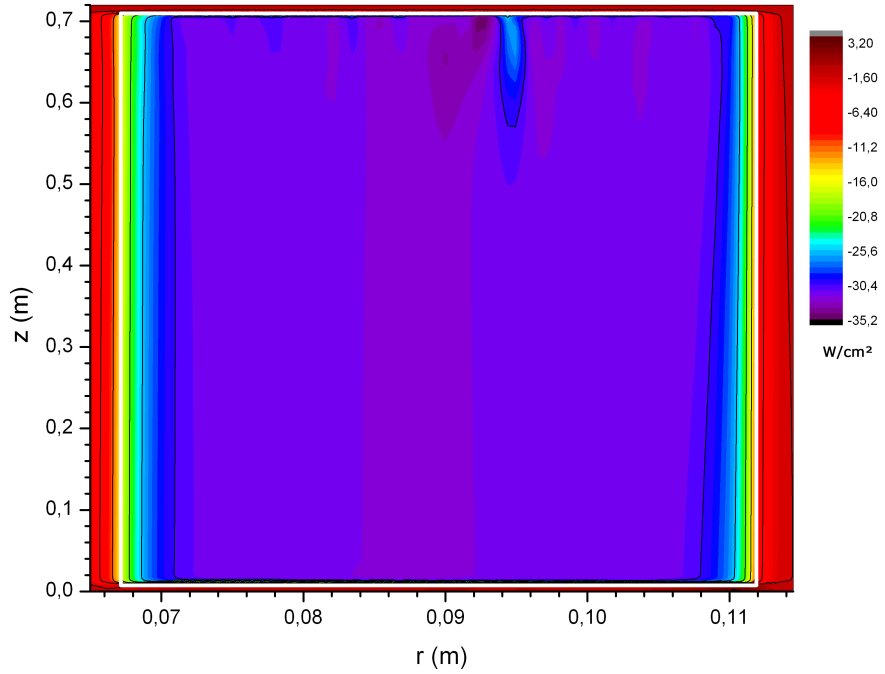

(a) Heat flux

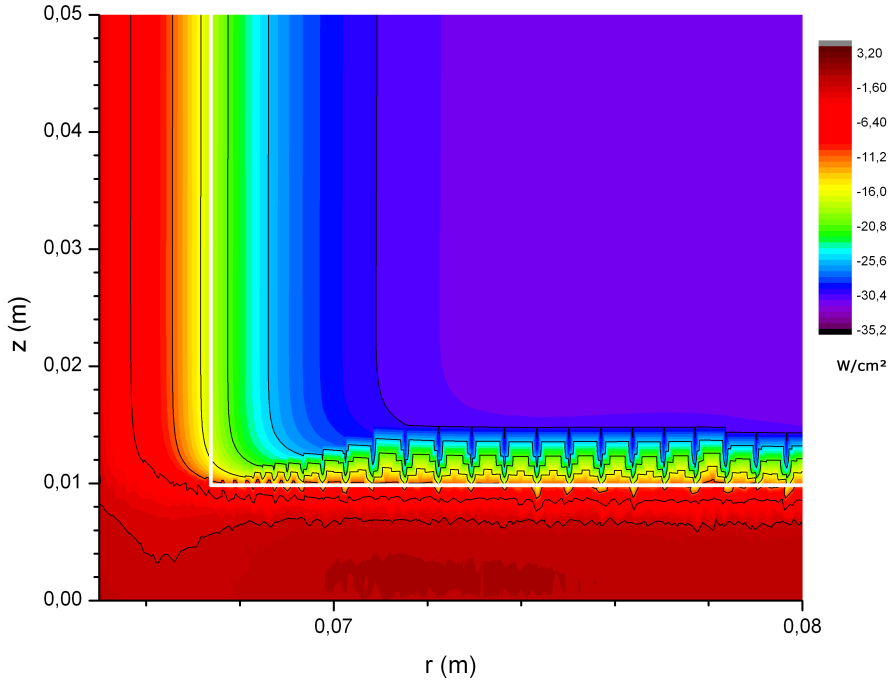

(b) Heat flux (zoom)

Figure 13.9: *Heat flux for homogeneous heating in* $\mathrm{W/cm^2}$*. (b) is a zoom to the lower, inner corner. Negatvie numbers mark a heat flux from the plate into the coolant, positive numbers mark heat flux from the coolant into the cladding. The white line marks the borders of the active zone.*

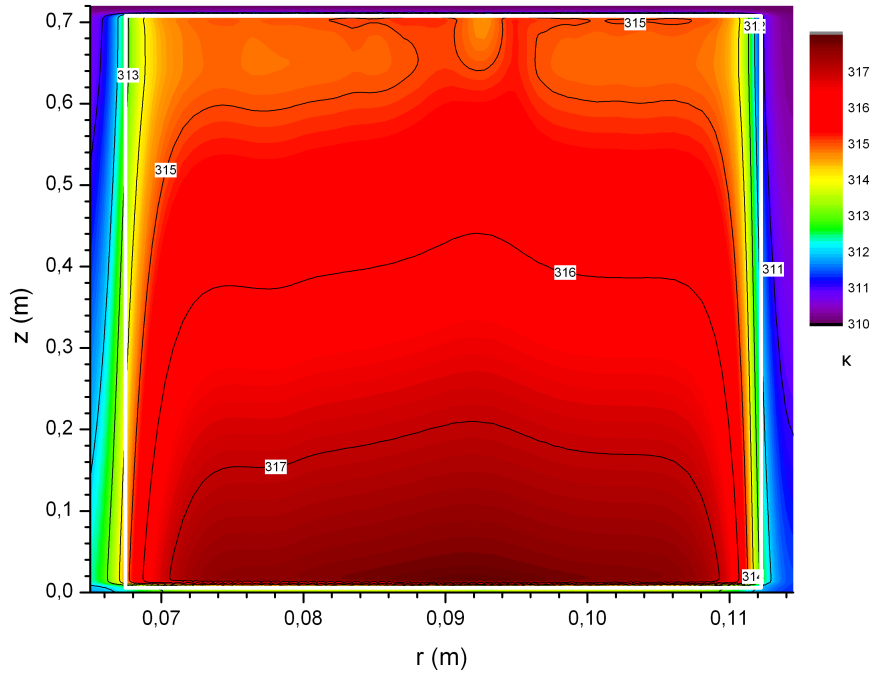

(a) Surface temperature in K

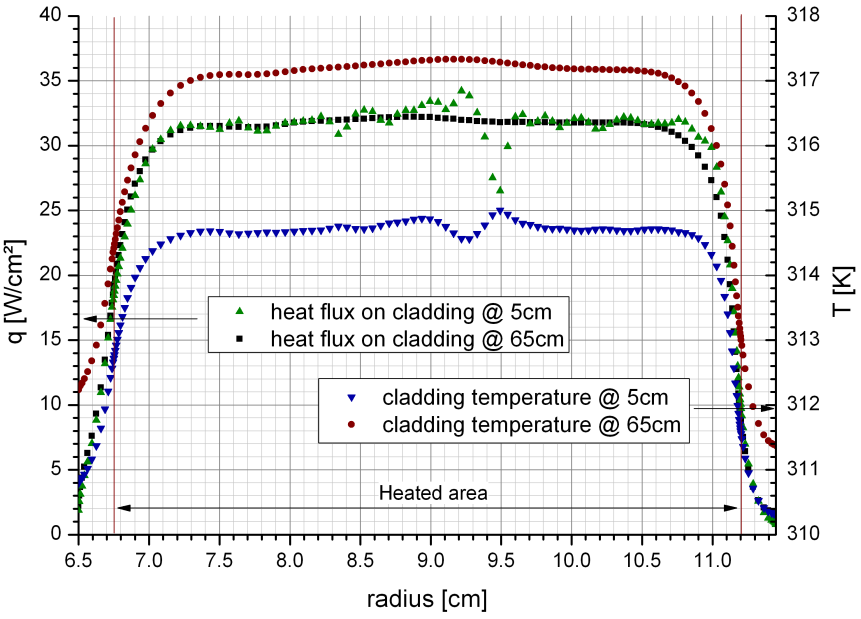

(b) Profiles

Figure 13.10: *Surface temperatures in K for a homogeneously heated fuel plate (a) and a profile 5 cm above and below the lower / upper limit of the fuel zone (b): Green is the radial heat flux profile 5 cm above the lower fuel limit, black the same curve 5 cm below the upper end of the plate. Blue and red are the respective curves for the cladding surface temperature.*

13.4 Flow Profile in Corners

Concerns were expressed in [Död89] about the velocity profile in the outer pointy corners where the fuel plates are attached to the outer pipe. As can be seen from fig. 13.11, the stream is at its full velocity near the fuel zone, so the pointy corner has no considerable effect on the cooling of the fuel.

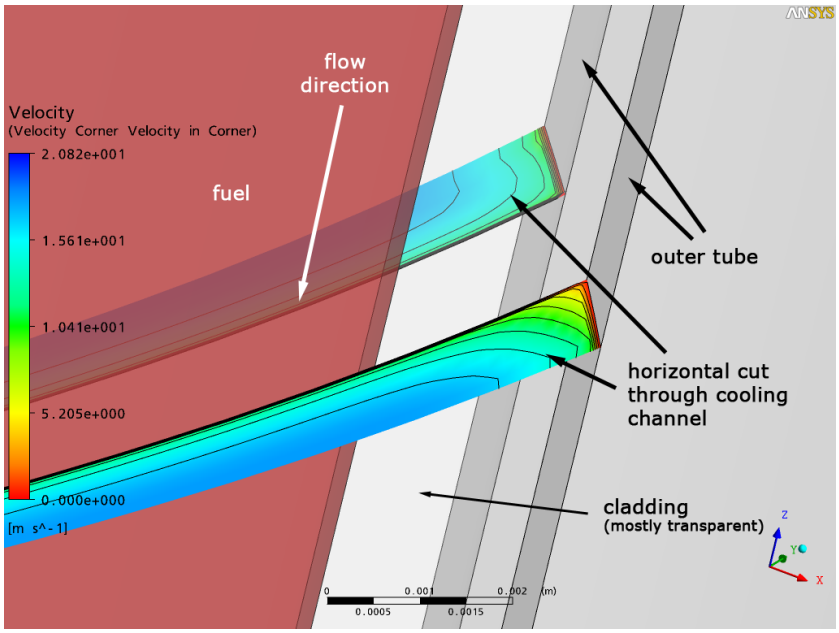

Figure 13.11: *Velocity profile in the outer pointy corner. The red box is the fuel zone, the coloured faces are a horizontal cut through the cooling channels (partly hidden by the fuel zone). For the sake of visibility of the second part of the cooling channel, the cladding is nearly transparent. The grey faces to the right mark the outer radial end of the cooling channels. The colours in the horizontal cut mark the spacially dependent fluid velocities. In the middle of the cooling channel (front end of horizontal cut), the flow is at its full speed above the fuel zone.*

13.5 Mixing of Stream Filaments

Another variable which was more or less unknown is the mixing between subchannels, if the stream filaments approach is chosen (see [Död89] and [Röh84]). To study this effect in CFX, a two-fluid approach was chosen: Using a series of step functions, the fluid at the inlet was alternately ‘water1’ or ‘water2’, always with a volume fraction of either 0 or 1. This can be interpreted as some kind of ‘tagging’ and is very similar to the technique of cell flagging in MCNP. Later on, down the cooling channel, the volume fractions of ‘water1’ and ‘water2’ are analysed. From the resulting profiles, the mixing can be estimated. From fig. 13.12, the following conclusions can be made:

- Most of the mixing occurs at the inlet into the cooling channel itself. The comb forces the stream filaments away from a straight line, therefore causing a shift of the filaments and a rather strong mixing, together with the sudden narrowing of the channel (compare red and green curve).
- Between the fuel plates, not much mixing occurs (compare green and pink line). It seems as if there is a slight deviation from a straight vertical line, but this may be a numeric effect and is not of greater interest.
- Stronger mixing occurs again just below the fuel plate, where the other comb and the sudden widening of the channel cause a lot of turbulence (compare pink and blue line).

The lines were recorded in the centre of the cooling channel. The most important point is indeed that there does not seem to be much mixing between stream filaments in the active zone. This is however mitigated near the inner and outer tube, where the boundary profiles develop (see discussion in preceding section).

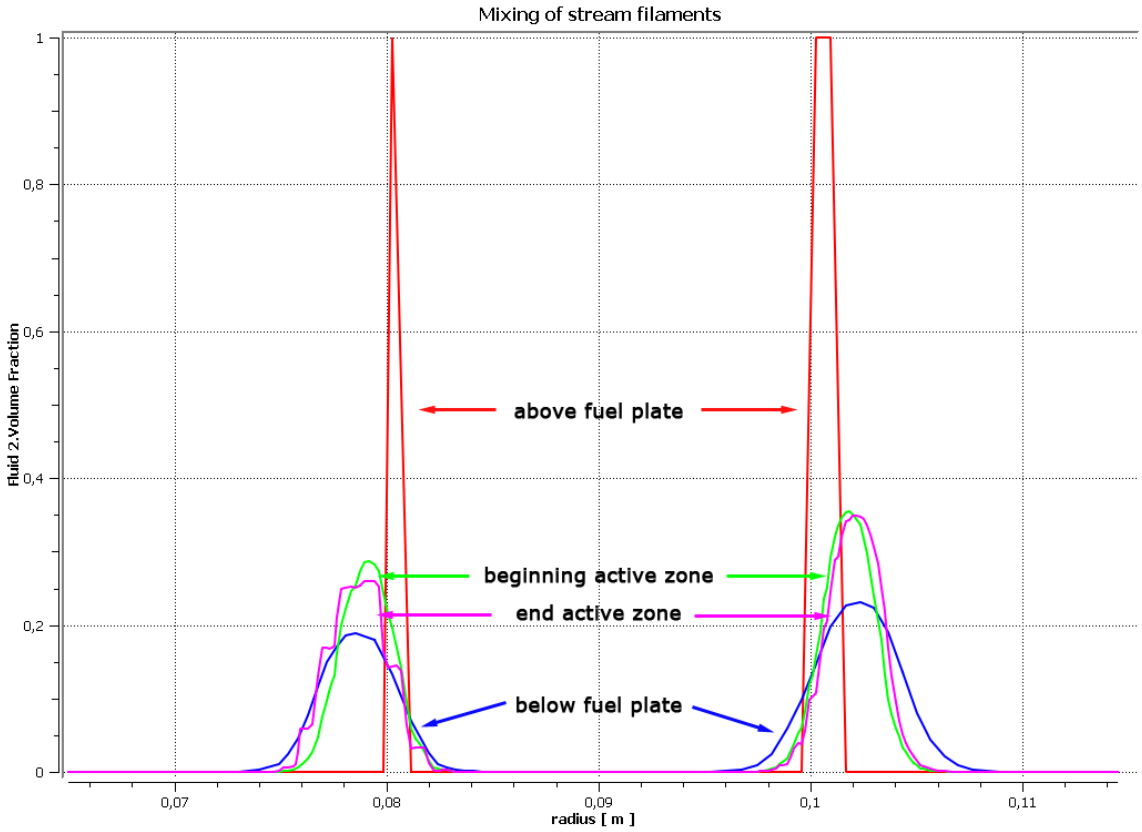

Figure 13.12: *Mixing of stream filaments. The red curve is the distribution of two example filaments at the inlet above the fuel plates. The green curve is their distribution at the beginning of the active zone, the purple curve at the end of the active zone. The blue curve is the distribution at the outlet below the fuel plate. Mixing occurs primarily at the beginning and at the end of the fuel plate.*

13.6 Pressure Profile

Fig. 13.13 shows the pressure in the middle of the cooling channel. The expected pressure drop at the beginning of the fuel plate can be observed very well, though there is a distorted zone around the comb (fig. 13.13(b)). The resulting differences in pressure are outweighted soon. All over the fuel plate, the pressure steadily drops. It increases slightly as the channel widens up at the end of the fuel plate. Again, the pressure distribution is distorted by the comb, this time more notably than by the upper comb, similarly to the vertical velocities discussed above.

The pressure drop over the fuel plates is 5.20(10) bar. This value is in good agreement with [Gie96] that quotes a measured pressure drop of 5.13 bar[7]. At the entry, a pressure drop of 1.4(1) bar was calculated,

[7]The quoted pressure drop is 6.24 bar, with 1.11 bar resulting from the upper sieve that is not regarded at this point. Actually, the roughness of the walls is calculated from these results.

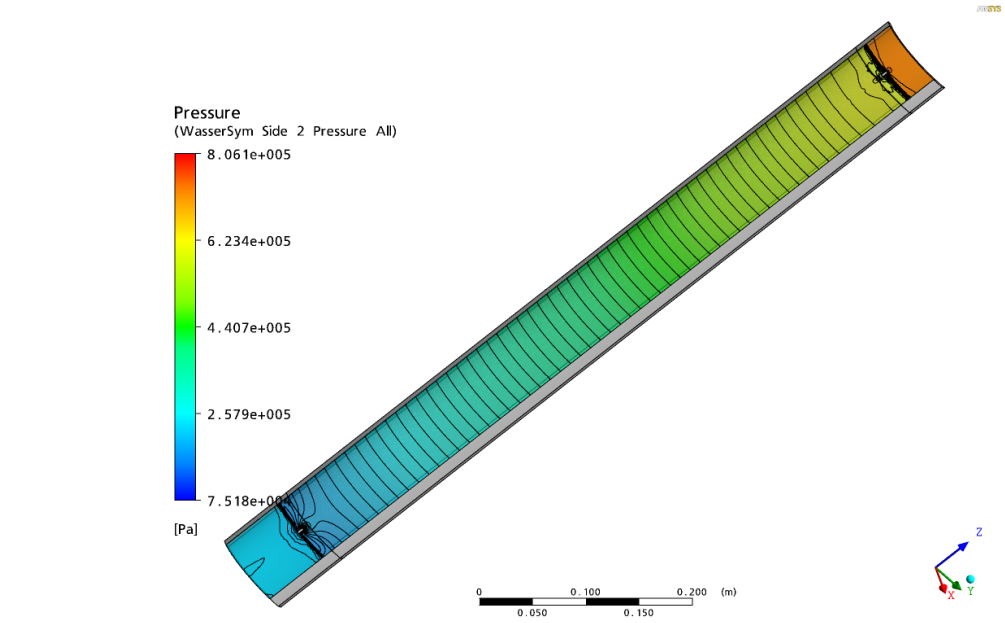

(a)

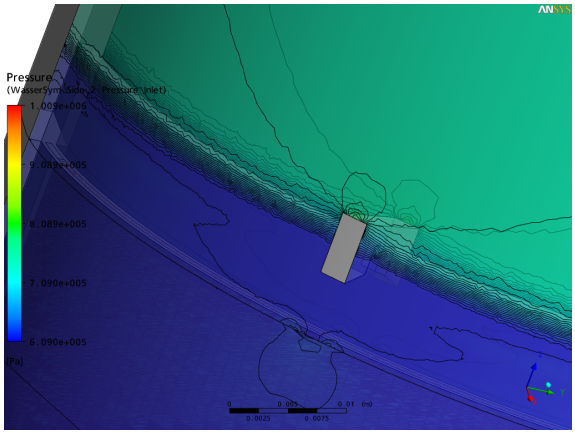

(b)

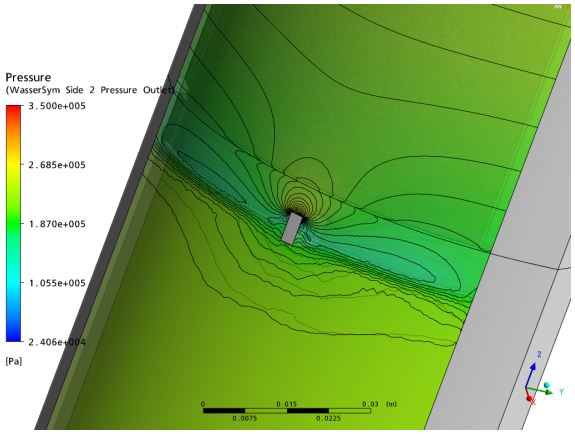

(c)

Figure 13.13: *Flow properties of the current fuel element: Pressure drop. (b) and (c) are detailed views of the inlet and the outlet.*

whereas the pressure gain at the outlet is roughly 0.5(1) bar. The maximum pressure can be found right above the upper comb, 8.44(10) bar, whereas the lowest pressure, 0.75(3) bar, can be found below the lower comb, exactly under the middle of the fuel plate.

The behaviour of the pressure is also modified near the combs. In flow direction In front of the combs, choking can be observed that leads to a pressure gain of 0.3(1) bar (inlet) resp. 1.25(5) bar (outlet) compared to the normal flow channels, whereas a pressure depression can be seen beyond them (0.20(5) bar / 0.5(1) bar). In addition, the flow delamination at the beginning and end of the fuel plate can be observed well (compare fig. 13.14). Some small numeric uncertainties occur where the three grids are connected (0.01 m and 0.71 m).

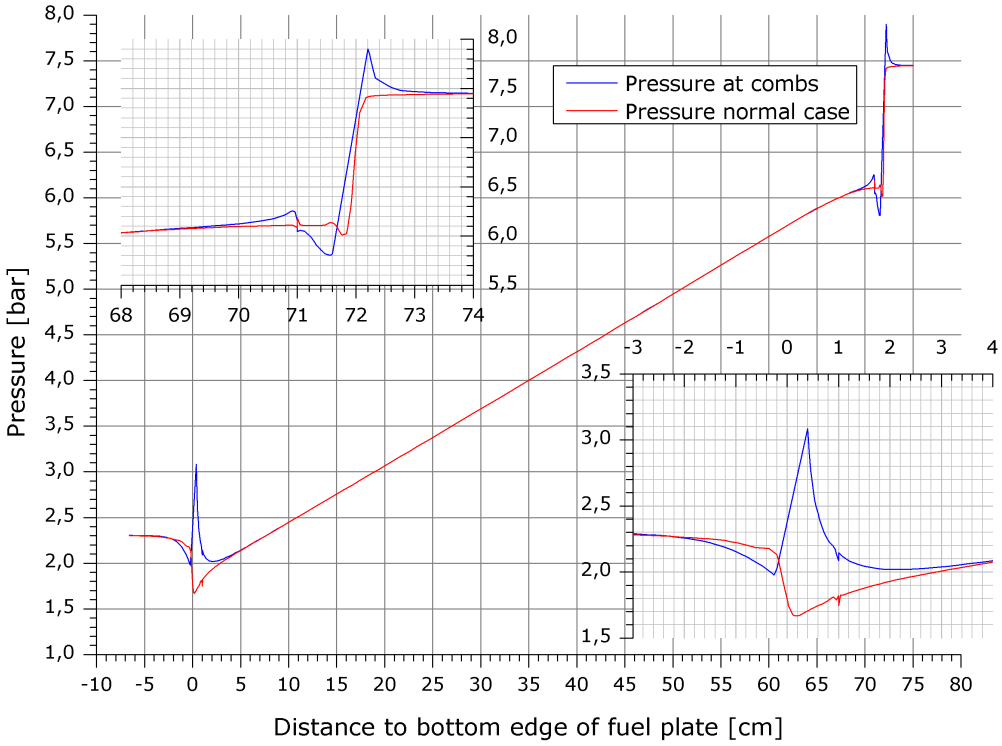

Figure 13.14: *Pressure drop of the flow through the fuel element.*

13.6.1 Influence of Pressure Profile on Boiling

The pressure profile is also connected to the allocation of nucleation sites in case of boiling. More general, it strongly influences the distance to saturation temperature of the coolant at normal operating conditions. Fig. 13.15 shows a cut through the cooling channel. The coloured surface represents the pressure in the channel, so do the isolines. The arrows mark the direction and velocity of the coolant flow while the red semi-transparent iso-surface shows the volume with the smallest distance to boiling, i. e. the volume where boiling is most likely to occur in non-standard operation conditions.

In principle there are two spots with nearly equivalent distances to boiling: The lower end of the active zone near the density jump, i. e. the lower heated end of the hot stream filament, and a spot located below the former, at the end of the fuel plate in the same stream filament. While the former is straight-forward to explain, the second requires a closer look at the pressure distribution below the fuel plate. As stated before, the flow will detach from the plate at the end, creating a cavity with low pressure. This already starts some millimetres above the actual end of the plate as can bee seen in fig. 13.15 within the red isosurface. Therefore, there is already a zone of lower pressure above the end of the plate which is directly attached to the wall. As shown in equation 7.87, p. 68, the flow velocity follows a logarithmic law towards the wall, which means that it heats up much faster at the wall. Due to 3D heat conduction in the plate, the fluid is still heating up somewhat below the end of the active zone, but heat is also transported to the middle of the cooling channel by convection. The mixture of both processes keeps the water that is transported into the zone of low pressure at a comparably high temperature (see arrows in fig. 13.15). Due to the strong pressure dependence of the saturation temperature (see for example [Pol09, p. 377]), the distance to boiling decreases, even though the temperature of the coolant stays constant or also decreases

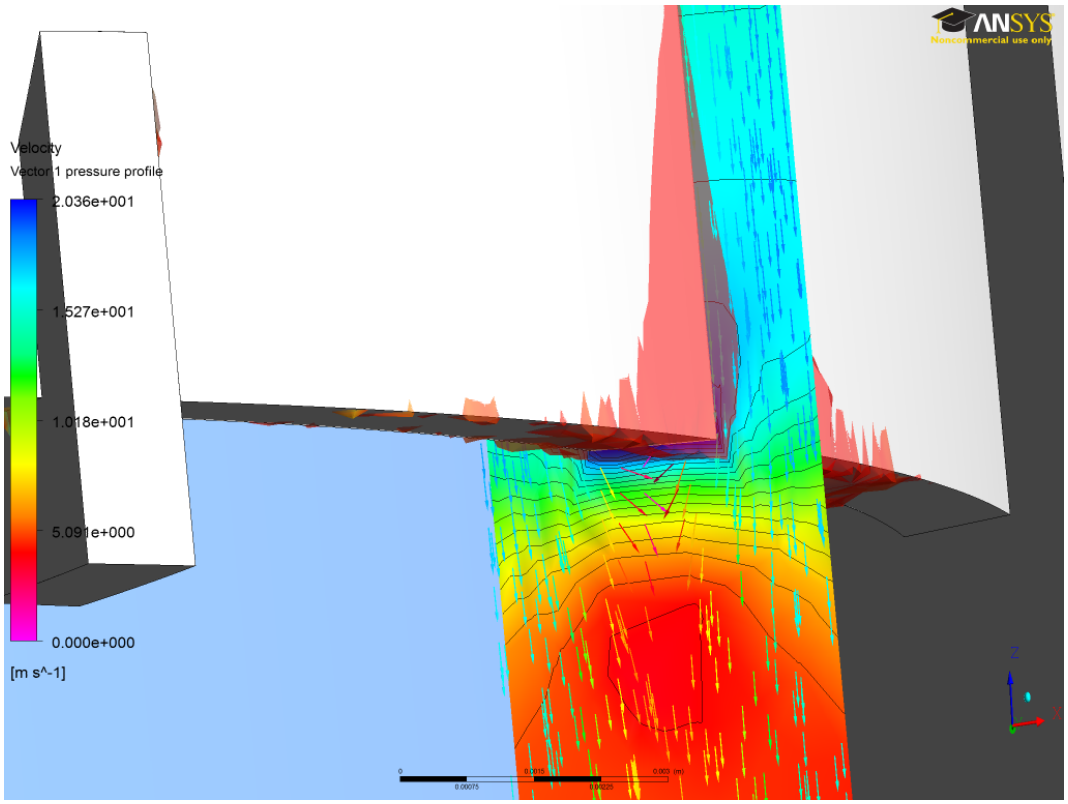

Figure 13.15: *Pressure distribution below the fuel plate and its influence on boiling. The picture shows the lower end of a fuel plate (white) with a comb (left) and the outer tube (right). The coloured face is a vertical cut through cooling channel, where the colours on the face represent the pressure (blue: lower, red: higher, not in the legend). The lines on this face are isobars. The arrows on this face show the velocity of fluid, where blue is a higher and red a lower velocity (see legend). Finally, the red irregular face is a 3d isosurface representing a given distance between the temperature of the fluid and and the saturation temperature. Boiling is most likely to start within the volume surrounded by this isosurface.*

slightly due to convective mixing. This process creates the red zone shown in fig. 13.15. It is therefore of importance not only to analyze the fluid at the end of the active zone but also at the very end of the fuel plates and directly below them. However, two remarks have to be made: First, boiling at the very end of the plate, outside the active zone, is of no major importance regarding the heat transfer from the fuel to the water. Second, as discussed in chapter 7.2.2, p. 65, the SST model is based on the Boussinesq approximation and is therefore of questionable applicability in this region of strong flow deceleration and curvature.

13.7 Burnup of the Beryllium Follower of the Control Rod

As stated in [Röh91a, p. 65], the beryllium follower is exposed to non-negligible burnup, too. The main reaction pathway to produce the two strong absorbers ^{6}Li and ^{3}He is

$$^{9}\mathrm{Be} + \mathrm{n}_f \longrightarrow {}^{4}\mathrm{He} + {}^{6}\mathrm{He} \tag{13.2}$$

$$^{6}\mathrm{He} \xrightarrow{\beta^-,\ 806.7\,\mathrm{ms}} {}^{6}\mathrm{Li} \tag{13.3}$$

$$^{6}\mathrm{Li} + \mathrm{n}_{\mathrm{th}} \longrightarrow {}^{4}\mathrm{He} + {}^{3}\mathrm{H} \tag{13.4}$$

$$^{3}\mathrm{H} \xrightarrow{\beta^-,\ 12.32\,\mathrm{a}} {}^{3}\mathrm{He}. \tag{13.5}$$

It is obvious that the effect of ^{3}He sets in much later than that of ^{6}Li, which is already saturated after three cycles of 60 days each. For results displayed in fig. 13.16, a cycle length of 60 days followed by an average break of 30 days was assumed.

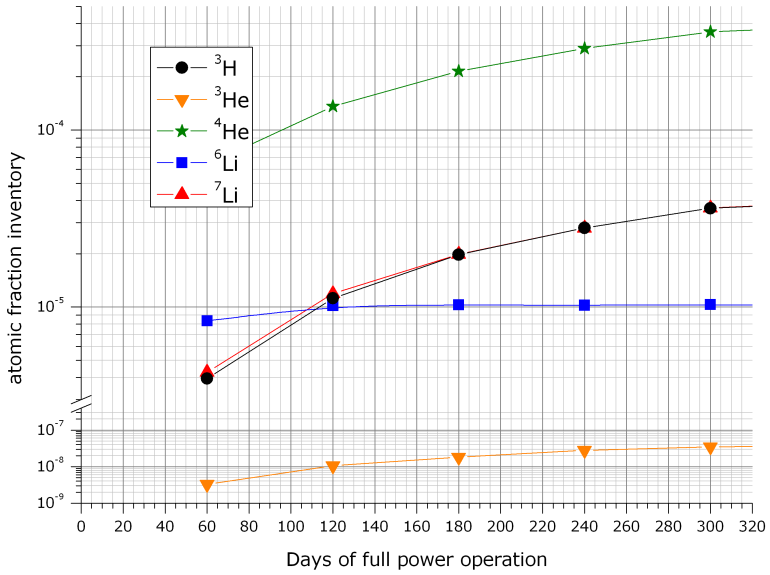

Figure 13.16: *Burnup of Be-follower. A 30 days break was included after each 60 days cycle, which is not shown here.*

The effect of the Be-burnup on k was calculated by means of perturbation calculations (see chap. 2.5.5, p. 23). Please note, that as discussed in chapter 9.3.1, the burn-up calculations for the control rod presented here are more of a feasibility study. More detailed calculations will supersede the rather gross calculations shown here.

As can be seen in fig. 13.17, the reactivity change caused by ^{6}Li can be estimated to be $\Delta k \approx -0.0011$. This is the saturation value. However, the continuing production of ^{3}He increases this value significantly over time. In 11/2009, the effective multiplication factor at the beginning of the cycle will already have decreased by $\Delta k = -0.0023$. In this work, the material composition of the beryllium fololower as calculated for cycle 6 (260 full power days)[8] was chosen, as later control rod movement calculations will compare this burn-up results to measured control rod position data of this cycle.

[8] Up to then, a cycle had only 52 days.

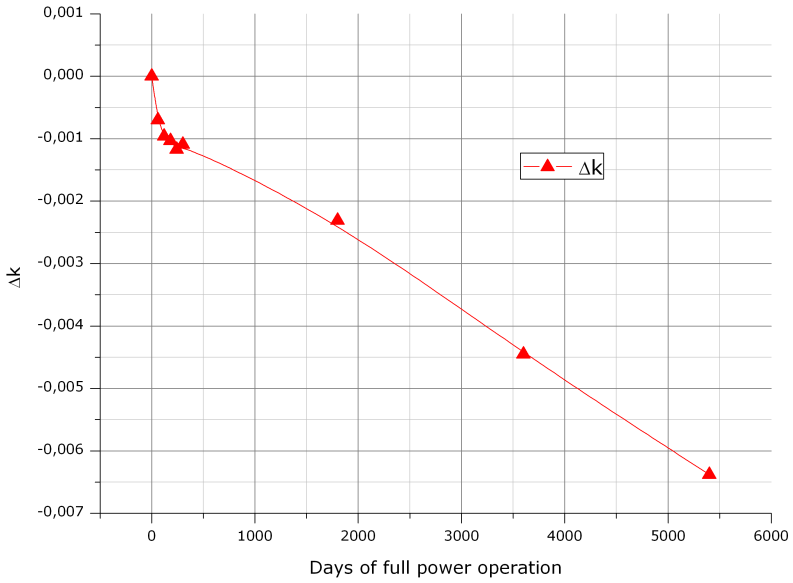

Figure 13.17: *Reactivity change due to burnup of Be-follower.*

13.8 Mesh Quality Analysis

The mesh quality isn't actually a real result of the calculations, but a high quality of the mesh is laying the foundation for trustworthy results. Therefore, the results of the mesh quality analysis are presented at this point. This analysis is carried out only for the 'default mesh', this means the mesh which was used to carry out most calculations. Other meshes, if needed, were generated with similar parameters and expose similar quality. The criterions for the acceptable boundary values were taken from [CFX09a, p. 380]. In addition, a sensitivity analysis is carried out later (chap. 17.1.3) to assess of the uncertainties that were introduced by the mesh.

13.8.1 First Node Distance y^+

As stated earlier in chapter 7.2.3, the dimensionless distance of the first node in the fluid regime to the wall is of importance regarding the applicability of wall functions. It was already stated that a value of $y^+ > 26$ for the use of normal wall functions is needed. The upper boundary for y^+ depends on the Reynolds number and is usually in the range of some hundreds. Fig. 13.18(a) shows the distribution of the number of mesh nodes concerning their value of y^+. The red histogramm is the complete mesh, the blue histogramm only the important middle part of the mesh, which is where the actual active zone is located. It can be seen that most mesh points satisfy the given limit. Mesh points with $y^+ < 26$ lie in the pointy corners of the cooling channel near the outer duct where velocities are low[9] and do not have much influence on the overall cooling of the fuel plate. The largest y^+-values can be found in the corners near the inner duct, where relatively large distances were used.

[9] Low velocities imply a flater velocity gradient near the wall, which means a lower friction velocity u^* due to the lower wall shear stress τ_w and therefore a smaller value for y^+.

However, in most calculations performed in this work, scalable or automatic wall function were used which are less sensitive and constricting regarding the value of y^+ (see chapter 7.2.3 for the theory on this topic). Therefore, the mesh is considered adequate concerning this quantity.

13.8.2 Aspect Ratio

The elongated geometry of the fuel plate and the cooling channel already suggest a mesh with high aspect ratios if the mesh has to be made up from a reasonable number of nodes. The aspect ratio is important regarding discretization errors. For the CFX-Solver, aspect ratios up to about 100 are acceptable. The default mesh satisfies this criterion for most nodes except for a small number of nodes located inside the fuel domain near the center of the fuel plate. Actual values are shown in fig. 13.18(b). However, this is inside a solid body and not in the fluid domain and therefore considered less problematic.

13.8.3 Face Angles

The general acceptable range for angles between mesh faces is $> 10°$ and $< 170°$. The default mesh satisfies this criterion for all important mesh points, as shown in fig. 13.18(c) and 13.18(d).

13.8.4 Other Quantities

The element volume ratio, which is the ratio of largest to smallest element volumes that surround a node, is a measure for the gradient of the size of the element volumes and their corresponding faces. This value plays a role especially in transient simulations and when body forces are regarded. The limit < 20 is easily satisfied by the default mesh, as most element volume ratios are < 2.

Also, the orthogonality angle, an area-weighted average of $\arccos(n \cdot s)$ for all integration point surfaces of a control volume, is distributed between 32° and 90°, which is clearly above the limit of 20° for the important middle part.

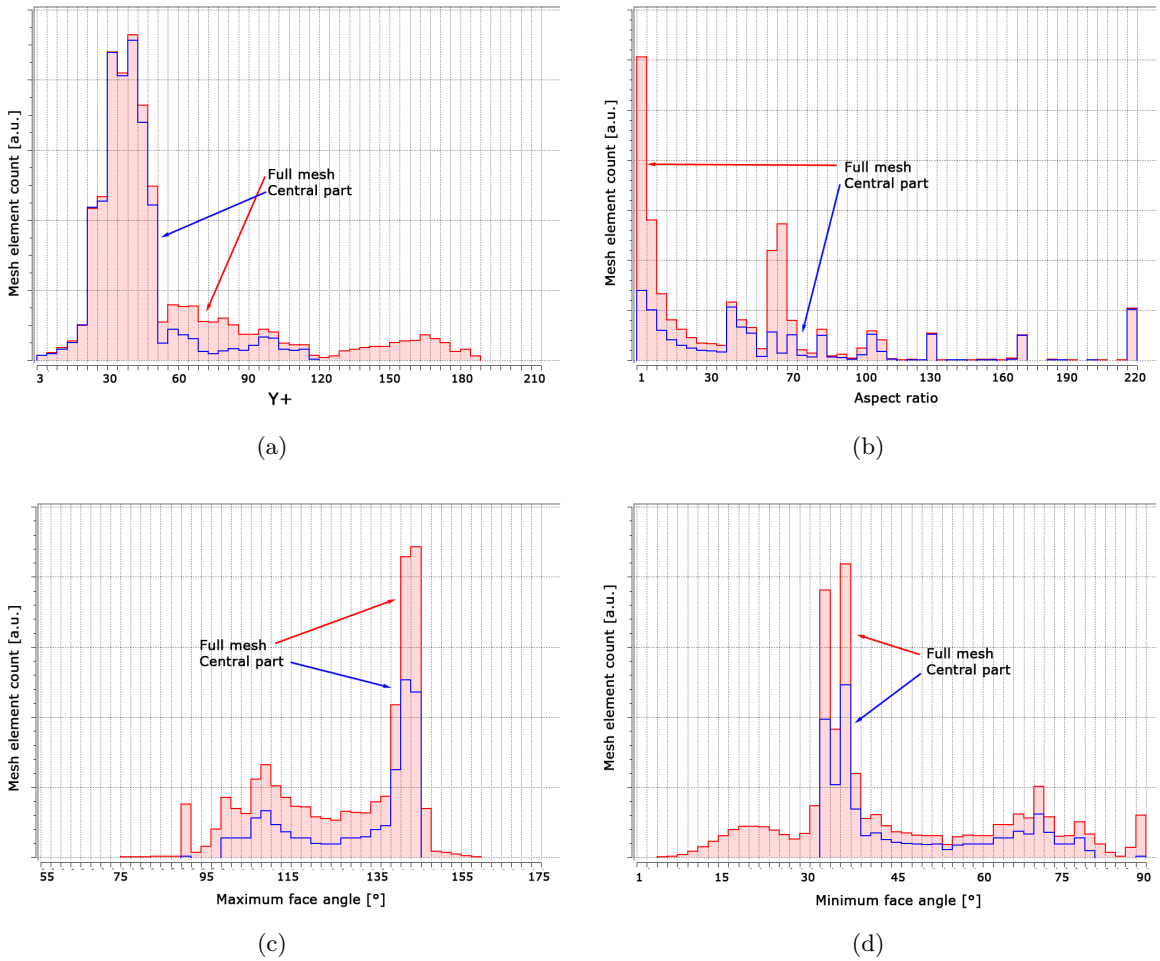

Figure 13.18: *Mesh quality analysis: y^+ (a), aspect ratio (b), maximum (c) and minimum face angle (d).*

CHAPTER 14

Results for the Current Fuel Element

First of all, the properties for the current fuel element are calculated with the new code system. For this, the data provided in tables 13.1 and 13.3 were used. These calculations act as a verification of the developed code system in a code-to-code comparison. Where available, measured data were compared to the simulation results. Detailed comparisons to the results obtained by other codes can be found in chapter 18.

Important results are summarized in tables 14.1 and 14.2. This data is discussed in detail in the subsequent sections. The origin of the used coordinate system is the centre of the core, core mid-plane ($z = 0$) is the half height of the active zone of the fuel plates. If not quoted otherwise, all data in these and similar tables if for BOL.

All fluxes given this work are disturbed fluxes, i. e. including the flux loss due to averaged built-in components in the D_2O-tank (see chap. 9.1.2, p. 87). With a 'clean' D_2O-tank, the thermal neutron flux would be considerably higher ($8.0 \cdot 10^{14}$ $^1/_{s\,cm^2}$). To quantify the overall neutron yield over a reactor cycle of length T_c at given position $\boldsymbol{x}$, the 'cycle neutron yield' (CNY) Φ is introduced, which is defined by

$$\Phi(\boldsymbol{x}) := \int_0^{T_c} \phi(\boldsymbol{x}, t)\,\mathrm{d}t \tag{14.1}$$

$$\approx \sum_i^{\text{steps}} \phi(\boldsymbol{x}, t_i) \cdot \Delta t_i. \tag{14.2}$$

This quantity will be useful in later chapters, when a possible elongation of the cycle length for new fuel elements is discussed.

All deposited power densities are calculated for the core average (fuel + cladding + water), not for the fuel itself. To convert the power densities, the given value has to be multiplied by the total width of a fuel plate plus the cooling channel and then divided by the width of the fuel.[1].

The enrichment of the core is calculated to be the fraction of ^{235}U compared to the total uranium mass, including minor isotopes like ^{234}U and ^{236}U.

The absolute burn-up numbers are fissions per cm^3 meat, which includes the matrix for disperse fuels. This is not the number of fission products, which is two times as large. To obtain the fission density in the disperse fuel particles themselves, the above mentioned number has to be divided by the volume fraction of praticles compared to the total meat volume.

[1] Currently: $3.56/0.6 = 5.93$.

Quantity	*Value active zone / Value*	*Value structural zone / Remarks*
Fuel plate parameters (BOL)		
Max. deposited power	3.70(7) $^{MW}/_{l}$	-
Deposited power	18.02 MW	0.16 MW
by fission and neutrons	17.35 MW	0.04 MW
by primary photons	0.33 MW	0.06 MW
by secondary photons	0.34 MW	0.06 MW
^{235}U inventory BOL	7.5 kg	Total U: 8.1 kg
Burn-up (60 d)		
Max. Burn-up	52.6(2)%	After 52 d: 47.1(3)%
Max. Burn-up absolute	$1.98(1) \cdot 10^{21}$ $^{1}/_{cm^3}$	After 52 d: $1.76(1) \cdot 10^{21}$ $^{1}/_{cm^3}$
Avg. Burn-up	20.4(1)%	After 52 d: 17.4(2)%
Min. Burn-up	5.8(1)%	After 52 d: 4.5(1)%
Avg. residual enrichment	87.4(1)%	After 52 d: 88.3(2)%
Fluxes $[^{1}/_{s\,cm^2}]$		
Max. thermal D_2O	$6.36(1) \cdot 10^{14}$	$r = 21.5\,\mathrm{cm}$, $z = -10.5\,\mathrm{cm}$
Max. thermal overall	$7.47(5) \cdot 10^{14}$	inside BE follower
Max. fast	$9.18(1) \cdot 10^{14}$	$r = 7.5\,\mathrm{cm}$, $z = -16.5\,\mathrm{cm}$
Cycle neutron yield $[^{1}/_{cm^2}]$	$3.21(2) \cdot 10^{21}$	

Table 14.1: *Results for the simulation of the current fuel element (neutronics)*

Quantity	*Value*	*Remarks*
Temperatures [°C]		
Max. Fuel	102.9(5)	-
Avg. Fuel	66.7(5) / 73.7(5) / 68.0(5)	inner / outer zone / total
Max. Wall	89.6(3)	-
Avg. Wall	62.2(3)	active zone
Avg. Outlet	53.0(1)	-
Heat Flux [W/cm^2]		
Max. Wall	382.3(15)	-
Avg. Wall	161.3(5)	active zone
Pressure [bar]		
Avg. pressure drop	5.20(10)	-
Max. pressure	8.44(10)	-
Min. pressure	0.75(3)	-
Safety margins		
S_{ONB}	2.51	at hotspot
S_{DNB}	2.48	at hotspot
S_{OFI}	5.61	at hotspot

Table 14.2: *Results for the simulation of the current fuel element (thermal hydraulics). All values are at BOL if not quoted otherwise.*

14.1 Burn-Up

The measured control rod position of operational cycles 6 and 15 of FRM II was the major verification for the burn-up procedure that was incorporated into X^2 . Details on the implementation are given in chap. 11, p. 111. It was found during the calculations with MONTEBURNS, that one predictor step is not sufficient to predict the burn-up accurately. Instead, three predictor steps are necessary in the first burn-up step and two for the following steps.

As a result of this burn-up calculation it can be stated, that the averaged model (chap. 9.1.2) gives very good predictions of the measured control rod movement. However, slightly better results can be achieved if instead of $k_{\text{eff}} = 1.0000$ a value of $k_{\text{eff}} \approx 1.0012$ is chosen. This reproduces the control rod position correctly and is a little more conservative. This has also been found independently by [Röh10b]. Consequently, this value has been chosen for all averaged models. The simulated results are shown in fig. 14.1. The simulated curve is in good agreement with the measured values from FRM II operation cycle 6 (52 d) and cycle 15 (60 d). An uncertainty analysis for this curve is performed in chapter 17.2.1.

The steep incline of the curves in fig. 14.1 at the beginning stems from the build-up of ^{135}Xe, a strong neutron poisson, and later (up to about 7 d) from additional fission products, especially ^{149}Sm. The further, less steep increase stems from the contious consumption of ^{235}U and the build-up of further fission products, linearly decreasing the available reactivity. The accelerated control rod movement towards the end of the cycle is caused by the lower reactivity worth per unit length of rod movement, compare fig. 4.1, p. 36. The orange curve in fig. 14.1 shows the predicted control rod movement for a very simple model of a linear decrease of the reactivity with time and fixed fission product reactivity worth. The similarity to the measured curves strengthens the above argumentation.

The maximum relative burn-up (=^{235}U consumption) was determined to be 52.6(2)% after 60 d, 47.1(3)% after 52 d ([Fel96]: 51.2%, [Gla05]: 50.2%). This maximum was found in the most outer half centimetre of the fuel plate between core midplane and ten centimetres below. As already stated in chap. 9.3, p. 93, the dimensions of the burn-up zones were chosen on the lower technically reasonable limit of 5 mm. This however makes it hard to compare peak-values or minimum-values of the burn-up with the results from other works where different zone dimensions were chosen. It is clear that a width of 5 mm does not give 'real' peak values for burn-up densities, so smaller zones at the outer borders of the fuel zones would produce higher values. Anyhow, these values would be of no technical relevance as swelling effects are not sensitive to very small scales [Röh10d]. This has to be kept in mind when comparing numbers as done below.

The average burn-up after 60 d is 20.4(1)%, which is identical to the value calculated by Röhrmoser using Mf2dAb and very similar to 20.2% calculated by Röhrmoser using MONTEBURNS [Röh10c]. It has to be mentioned that the MONTEBURNS approach by Rörmoser used a very similar approach, also respecting the moving control rod by manually adjusting its position. The Mf2dAb approach also uses a moving control rod. After 52 d, the average burn-up is 17.4(2)%, which agrees well with the value of 17.5% calculated by [Fel96, p. 67], 17.7% by Mf2dAb [Röh] and 17.6% by [Gla05, p. 165]. Of course, this key-number should be the same for every burn-up calculation, depending only on the chosen normalisation for the energy per fission (200.0 MeV / 202.0 MeV / 202.3 MeV). The minimum burn-up after 60 d is 5.8(1)%, 4.5(1)% after 52 d compared to 4.2% [Fel96] and 8.8% [Gla05]. In addition to the resolution of the burn-up zones, the increasing differences to [Gla05] can in parts be explained by the fact that [Gla05] does not account for the moving control rod. The differences to [Fel96] are probably in parts due to the different slope of the control rod movement (see [Fel96, p. 139]).

Concerning the absolute fission densities (number of fissions per cm^3), the maximum can be found at the same height as the relative maximum burn-up, between core mid-plane and ten centimetres below, but this time at inner border of the 3.0 g/cm^3-fuel zone close to the control rod. The relative burn-up here is only 33.7(1)%, but the absolute value for the meat is $1.98(1) \cdot 10^{21}$ 1/cm^3, compared to $1.58(1) \cdot 10^{21}$ 1/cm^3 in the above mentioned outer zone. A zone of high absolute burn-up can also be found at the outer border

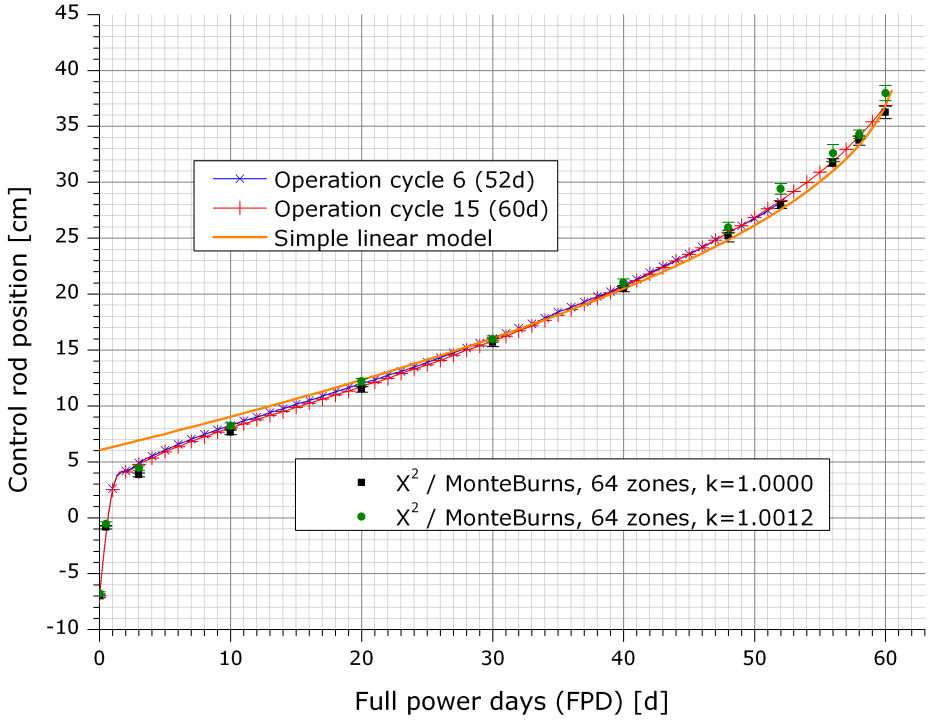

Figure 14.1: *Control rod position depending on the number of full power days (FPDs).*

of the 3.0 g/cm³-fuel zone, with 31.7(5)% / $1.90(1) \cdot 10^{21}$ 1/cm³, and also in the lower inner corner where also the high power density can be found at EOL (32.3(2)% / $1.94(1) \cdot 10^{21}$ 1/cm³). After 52 d, the maximum burn-up in the inner zone is 29.3(4)%, equivalent $1.76(1) \cdot 10^{21}$ 1/cm³ which is 15.0% lower than the value of $2.07 \cdot 10^{21}$ 1/cm³ quoted by [Fel96]. This again can be attributed to the different sizes of the burn-up zones and the required data pre-treatment involved in the calculation procedure of [Fel96]. Better agreement was achieved with [Röh90], where $1.86 \cdot 10^{21}$ fis./cm³ were predicted. [Röh90] used a $2.5 \times 2.5\,\text{mm}^2$ element, which is finer than the resolution chosen in this work. Therefore, a slightly higher absolute fission density had to be expected. In addition, [Röh90] finds this value at the outer border of the 3.0 g/cm³-fuel-zone, not on the inner side as calculated in this work. However, the values for both zones are very similar: While there were $1.76(1) \cdot 10^{21}$ 1/cm³ on the inner side of the 3 g-part, the fission density on the outer side of this zone is $1.72(2) \cdot 10^{21}$ 1/cm³. Furthermore, [Röh90] and other caclulations have to be scaled to match the correct energy per fission. Generally, values calculated in the framework of the FRM II conception prior to 1990 defined 20 MW as the pure fission power, excluding resulting activations and radioactive decays. This was changed then to include the full thermal power. Regarding the value quoted above, the fission density from [Röh90] yields $1.78 \cdot 10^{21}$ fis./cm³, which agrees even better with the value calculated in this work.

Adverting to the fission density in a fuel particle, the maximum can again be found in the outer zone. The absolute burn-up there was $1.57(1) \cdot 10^{21}$ 1/cm³ after 60 d, $1.41(1) \cdot 10^{21}$ 1/cm³ after 52 d. This leads to a local fission density in the fuel particles themselves (without the aluminium matrix) of up to $11.8(1) \cdot 10^{21}$ 1/cm³ after 60 d, $10.6(1) \cdot 10^{21}$ 1/cm³ after 52 d. This is 13% lower than the value of $12.2 \cdot 10^{21}$ 1/cm³ determined by [Fel96] and 9.8% lower than the $11.8 \cdot 10^{21}$ 1/cm³ of [Gla05]. Again, the values are hardly comparable due to the different sizes of the burn-up zones.

14.1.1 Actinide Inventory at EOL

The total plutonium production during a cycle was estimated to be 12.30(2) g at EOL (60 d), of which are 10.62(1) g ^{239}Pu. The latter will increase to 11.51(2) g after a cooling period of one month, while the total Pu-inventory will increase to 13.19(3) g. At EOL, the average enrichment of ^{239}Pu is 86.3(1)%, the maximum 96.6(1)%. Conversion is most efficient in the very inner part of the fuel where up to 2.76(3)% of the initial ^{238}U content are converted to ^{239}Pu. In total, 1532.7(12) g ^{235}U and 15.84(2) g ^{238}U were consumed. These values compare well to the ones calculated by A. Röhrmoser using the Mfd2Ab sequence, 10.90 g ^{239}Pu / 12.60 g Pu / 0.96 g ^{239}Np by a total consumption of 1531.9 g ^{235}U and 16.2 g ^{238}U. Also, the numbers for the inventory of ^{234}U (60.40(2) g / 59.8 g) and ^{236}U (298.6(2) g / 297 g) compare very well. It has to be pointed out, that the calculations based on the MF2DAB procedure performed by Röhrmoser utilise a completely different approach (see [Röh10a]). MONTEBURNS calculations by Röhrmoser yielded an EOL ^{239}Pu content of 10.7 g, which is even closer to the value calculated in this work. This had to be expected as the methodology is very similar.

For comparison, after 52 d, the calculated ^{239}Pu inventory is 9.51(3) g, 10.77(3) g total Pu. This is slightly less than [Röh90] has calculated (10.10 g / 11.35 g)[2], more than [Fel96] 8.58 g / 9.67 g, and more than [Gla05], 8.79 g / 9.94 g, but again compares very well to Mf2dAb values calculated by Röhrmoser, 9.70 g ^{239}Pu and 11.02 g Pu. The same is true for the values calculated earlier [Röh91b], 9.65 g / 10.83 g. As discussed before the difference to [Fel96] can be explained by the required data pre-treatment for their calculations.

The total inventory of all actinides with quantities larger than 0.01 g after 60 FPDs (full power days) is shown in table 14.3.

14.1.2 Non-Actinide Inventory at EOL

The non-actinide inventory is also shown in table 14.3. It comprises the inventory of the fuel zone and the boron ring.

Comparison data of the actinide and the non-actinide inventory can be found in [Död93] for a cycle length of 52 FPDs.

14.1.3 Boron Ring

After 60 FPDs, only 0.100(1) g ^{10}B are left in the boron ring, yielding a consumption of 93.3(1)%. It turns out in the uncertainty analysis that the calculation of the consumption of the boron ring yields differences of the remaining boron of more than 30%, equalling a consumption of only 90%, when X^2 is not configured to use two predictor steps.

[2] See the notes in the precending section regarding the power normalisation!

Isotope	*Quantity* [g]	*Isotope*	*Quantity* [g]	*Isotope*	*Quantity* [g]
Actinides					
^{234}U	60.396 ± 0.022	^{237}Np	4.676 ± 0.006	^{240}Pu	0.996 ± 0.003
^{235}U	5989.176 ± 1.176	^{238}Np	$0.043 \pm 8.634 \cdot 10^{-5}$	^{241}Pu	0.412 ± 0.002
^{236}U	298.582 ± 0.114	^{239}Np	0.892 ± 0.001	^{242}Pu	$0.023 \pm 1.520 \cdot 10^{-4}$
^{237}U	1.617 ± 0.006	^{238}Pu	$0.250 \pm 5.601 \cdot 10^{-4}$		
^{238}U	500.201 ± 0.023	^{239}Pu	10.619 ± 0.015		
Non-Actinides					
^{1}H	$0.002 \pm 1.950 \cdot 10^{-6}$	^{98}Mo	30.537 ± 0.010	^{143}Ce	1.481 ± 0.001
^{2}H	$3.059 \cdot 10^{-7} \pm 3.165 \cdot 10^{-10}$	^{100}Mo	33.495 ± 0.012	^{141}Pr	19.047 ± 0.011
^{3}H	$9.095 \cdot 10^{-4} \pm 8.818 \cdot 10^{-4}$	^{99}Tc	28.580 ± 0.008	^{143}Pr	13.629 ± 0.003
^{3}He	$2.293 \cdot 10^{-13} \pm 8.337 \cdot 10^{-14}$	^{101}Ru	27.564 ± 0.008	^{143}Nd	27.574 ± 0.005
^{4}He	$0.555 \pm 7.569 \cdot 10^{-4}$	^{102}Ru	23.367 ± 0.011	^{145}Nd	29.210 ± 0.011
^{7}Li	$0.968 \pm 8.901 \cdot 10^{-4}$	^{103}Ru	10.201 ± 0.002	^{146}Nd	24.443 ± 0.009
^{9}Be	$7.180 \cdot 10^{-7} \pm 2.951 \cdot 10^{-10}$	^{103}Rh	5.949 ± 0.002	^{147}Nd	4.358 ± 0.001
^{10}B	0.100 ± 0.001	^{105}Rh	$0.175 \pm 8.289 \cdot 10^{-5}$	^{148}Nd	14.152 ± 0.006
^{11}B	$1.980 \cdot 10^{-4} \pm 0$	^{105}Pd	4.693 ± 0.001	^{147}Pm	10.787 ± 0.003
^{12}C	$5.864 \cdot 10^{-10} \pm 3.880 \cdot 10^{-12}$	^{109}Ag	$0.264 \pm 8.146 \cdot 10^{-5}$	^{148m1}Pm	$0.128 \pm 1.836 \cdot 10^{-4}$
^{13}C	$7.248 \cdot 10^{-16} \pm 7.868 \cdot 10^{-18}$	^{113}Cd	$0.009 \pm 7.724 \cdot 10^{-6}$	^{149}Pm	$0.564 \pm 4.068 \cdot 10^{-4}$
^{27}Al	6135.180 ± 0	^{129}I	4.495 ± 0.002	^{149}Sm	$0.412 \pm 3.524 \cdot 10^{-4}$
^{28}Si	592.973 ± 0.009	^{131}I	$3.870 \pm 8.663 \cdot 10^{-4}$	^{150}Sm	8.415 ± 0.003
^{29}Si	$31.213 \pm 1.578 \cdot 10^{-8}$	^{135}I	$0.297 \pm 3.288 \cdot 10^{-4}$	^{151}Sm	$1.008 \pm 2.925 \cdot 10^{-4}$
^{30}Si	$21.287 \pm 5.827 \cdot 10^{-4}$	^{131}Xe	14.949 ± 0.005	^{152}Sm	$3.938 \pm 9.624 \cdot 10^{-4}$
^{83}Kr	$2.259 \pm 7.919 \cdot 10^{-4}$	^{133}Xe	5.931 ± 0.001	^{153}Sm	$0.152 \pm 2.874 \cdot 10^{-4}$
^{93}Zr	31.539 ± 0.010	^{135}Xe	$0.046 \pm 1.026 \cdot 10^{-5}$	^{153}Eu	1.869 ± 0.002
^{95}Zr	23.767 ± 0.008	^{133}Cs	39.001 ± 0.016	^{154}Eu	$0.199 \pm 3.896 \cdot 10^{-4}$
^{95}Nb	5.856 ± 0.002	^{134}Cs	1.141 ± 0.002	^{155}Eu	$0.085 \pm 5.241 \cdot 10^{-5}$
^{95}Mo	2.662 ± 0.001	^{135}Cs	5.737 ± 0.001	^{156}Eu	$0.157 \pm 1.517 \cdot 10^{-4}$
^{96}Mo	$0.043 \pm 8.150 \cdot 10^{-5}$	^{139}La	47.815 ± 0.012	^{157}Eu	$0.002 \pm 8.017 \cdot 10^{-7}$
^{97}Mo	29.834 ± 0.005	^{141}Ce	24.659 ± 0.005	^{157}Gd	$0.003 \pm 2.709 \cdot 10^{-6}$

Table 14.3: *Result of burn-up calculation for current fuel element, EOL after 60 d.*

14.2 Power Deposition

14.2.1 Begin of Life

The maximum power deposition density can be found in the inner lower corner of the fuel plate at BOL. The maximum power deposition density on the very fine length scale discussed in chapter 9.2.2 is 3.70(7) MW/l. This value differs significantly from values quoted in [Fel96, p. 60], 2.9 MW/l. This value does not consider the built in components and has to be corrected by +19(3)% (p. 66), yielding 3.5(1) MW/l. The remaining difference can be attributed to the differing power deposition mesh resolutions, modelling differences and the rather coarse correction factor determination used by [Fel96, p. 168].

The power deposition profile shown in fig. 14.2 clearly reflects the density step in the fuel at $r = 10.56\,\mathrm{cm}$. The structure of this profile is explained as follows (compare fig. 10.1): To the left, the control rod is located. The rod comprises a hafnium absorber in the upper part and a beryllium reflector in the lower part. The neutrons reflected by the beryllium cause the bump in the lower left corner. The valley in the upper left part is caused by the thermal flux depression due to the hafnium absorber and the missing reflectivity. To the right, the D_2O is located. It acts as reflector, too. The neutrons coming back from the D_2O don't 'feel' the presence of the control rod this much and are therefore distributed more homogeneously in z-direction. As the whole fission distribution is drawn towards the lower part of the fuel plates at BOL, the light water from the cooling below acts also as reflector for thermal neutrons and causes high fission densities at the very bottom of the fuel plates. The combination of all these reflectors leads to very high fission densities at the lower corners of the fuel plates. Therefore, in the outer part, a boron ring is build into the fuel element to absorb thermal neutrons. This boron ring eases the situation in the lower right corner. In the inner tube, no boron ring is inserted. This leads to the formation of a hotspot in the lower left corner. This hotspot is observable in the fission densities as well as in the surface temperatures and heat flux densities.

On the larger length scale of 300 µm (see discussion in chapter 9.2.2, p. 90), the maximum power deposition is 3.60(6) MW/l.

14.2.2 End of Life

At EOL, the maximum power deposition has decreased to roughly the half of the BOL value, now only 2.14(9) MW/l. The spot of this maximum power is located at the density jump and can be found equally at the upper and lower edge of the fuel. At the former hot spot in the lower left corner, the power density has decreased to 1.57(5) MW/l.

It should be noted that due to the burn-up, the power deposition at the very outer border of the fuel element is now lower than some millimetres further in. The discontinuities in the power deposition shown in fig. 14.3 are artefacts from the limited number of burn-up zones. A higher number of zones would remove these discontinuities, but no new information could be extracted. In contrary, the computational effort would increase significantly.

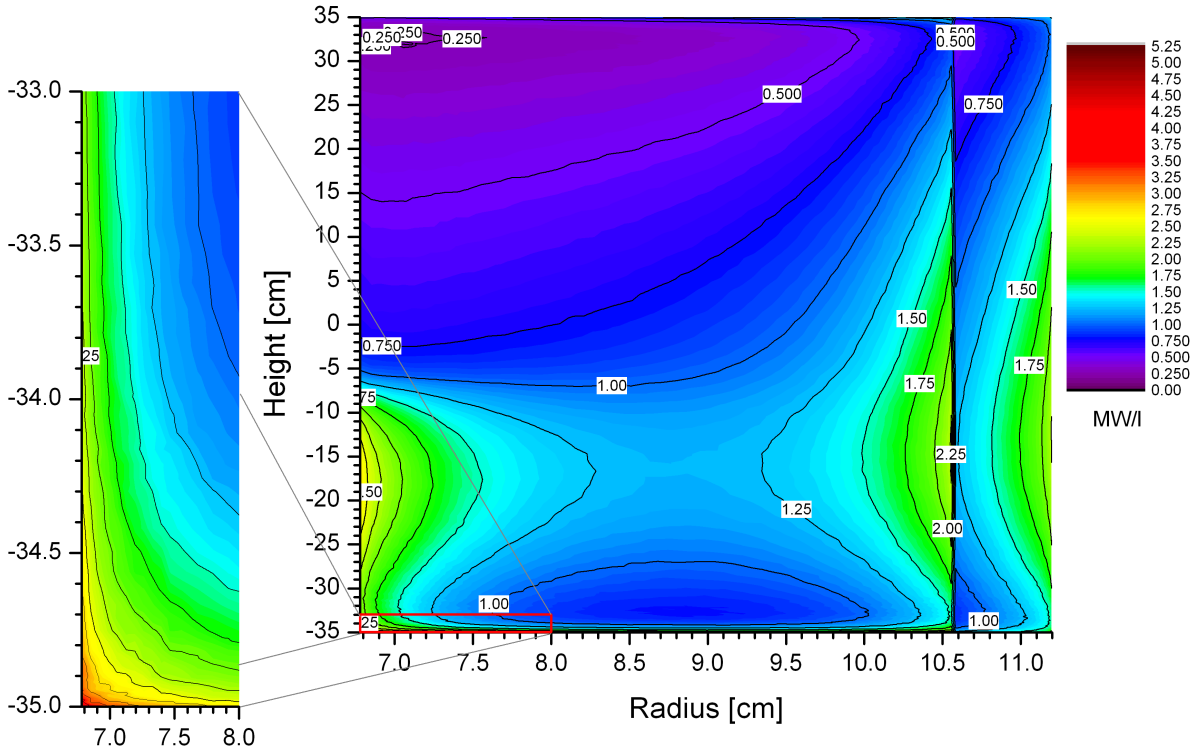

Figure 14.2: *Power deposition for the current fuel element in* $^{MW}/_{l}$ *at BOL.*

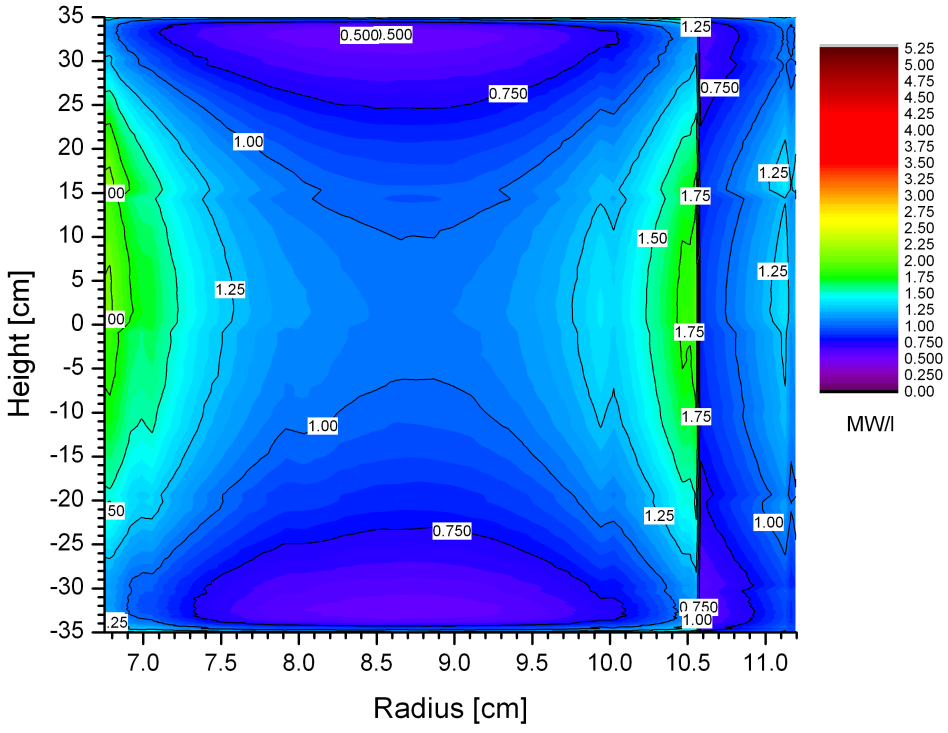

Figure 14.3: *Power deposition for the current fuel element in* $^{MW}/_{l}$ *at EOL.*

14.3 Flux

14.3.1 Begin of Life

The highest thermal neutron flux ($\leq 0.625\,\mathrm{eV}$) at BOL can be found inside the beryllium follower of the control rod, $7.47(5) \cdot 10^{14}\,{}^{1}/_{\mathrm{cm}^2\,\mathrm{s}}$. Inside the D_2O-tank, a maximum thermal neutron flux of $6.36(1) \cdot 10^{14}\,{}^{1}/_{\mathrm{cm}^2\,\mathrm{s}}$ was calculated at a height of 10.5 cm below the core midplane in a distance of 21.5 cm from the middle axis of the core. The position of the fuel plates and the boron ring is obvious in the 2D flux diagram 14.4(a).

As could be expected, the fast flux (100 keV – 20 MeV, fig. 14.4(b)) concentrates in the fuel plates and in their adjancies, exhibiting a clear step at the light-water boundaries. Fluxes up to $9.18(1) \cdot 10^{14}\,{}^{1}/_{\mathrm{cm}^2\,\mathrm{s}}$ were calculated 16.5 cm below the core midplane at a radius of 7.5 cm.

Fig. 14.5 shows the flux profile from fig. 14.4(a) in combination with the CAD model from fig. 10.1 to get a general idea about the geometry–flux interlinkage and the proportions. This picture shows very good the inhomogeneous flux distribution in the beryllium follower of the control rod that was discussed in chapters 9.3.1 and 13.7. In addition, the distribution changes drastically with the withdrawal of the control rod during the cycle.

14.3.2 End of Life

At end of life, the zone of a thermal neutron flux $> 6.0 \cdot 10^{14}\,{}^{1}/_{\mathrm{cm}^2\,\mathrm{s}}$ has notably expanded due to the better distribution of the fission sources in the fuel plates (see fig. 14.6(a), compare fig. 14.3). This can also be seen in the distribution of the fast flux (fig. 14.6(b)) which is distributed much more symmetrically over the fuel plate compared to BOL. The expansion of the high flux zone also leads to a slightly higher maximum thermal flux of $6.48(1) \cdot 10^{14}\,{}^{1}/_{\mathrm{cm}^2\,\mathrm{s}}$, now located 1.0 cm over the core mid plane, 21.0 cm from the middle axis of the core. This movement, induced by the withdrawn control rod, is clearly visible from the BOL-EOL-difference contour plot in fig. 14.7.

The BOL thermal flux peak in the beryllium follower has notably decreased, now a peak flux of $6.10(1) \cdot 10^{14}\,{}^{1}/_{\mathrm{cm}^2\,\mathrm{s}}$ can be found there. Of course, the displacement of the control rod causes strong variations of the flux in the respective geometric areas. Differences rise up over 10'000%. As the neutron capturing ^{10}B in the boron ring is nearly fully consumed at EOL, the variation in this area is also very strong (see chap. 14.1.3).

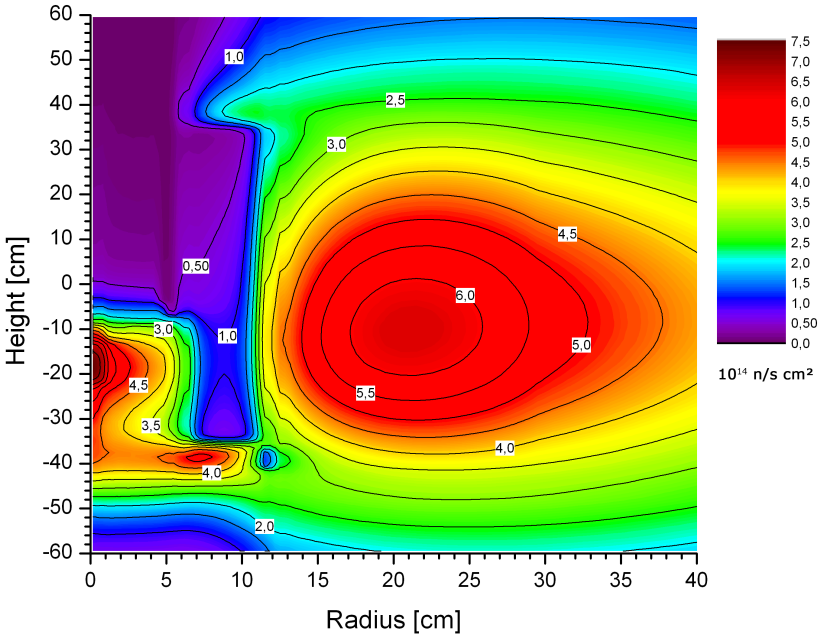

(a) Thermal flux

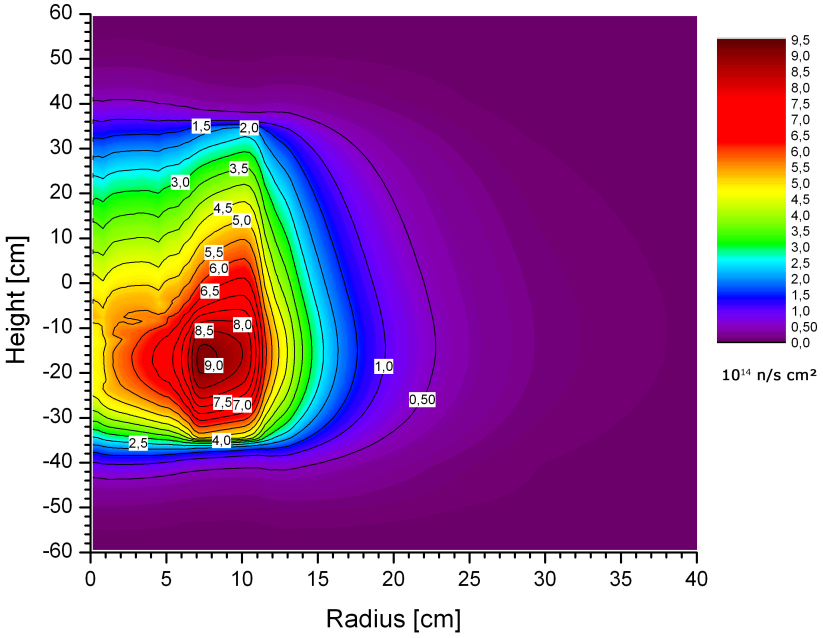

(b) Fast flux

Figure 14.4: *Flux profiles in* $10^{14}\,\mathrm{n/s\,cm^2}$ *for the current fuel element at BOL: (a) is the thermal flux* $\leq 0.625\,eV$*, (b) the fast flux* $\geq 100\,keV$*.*

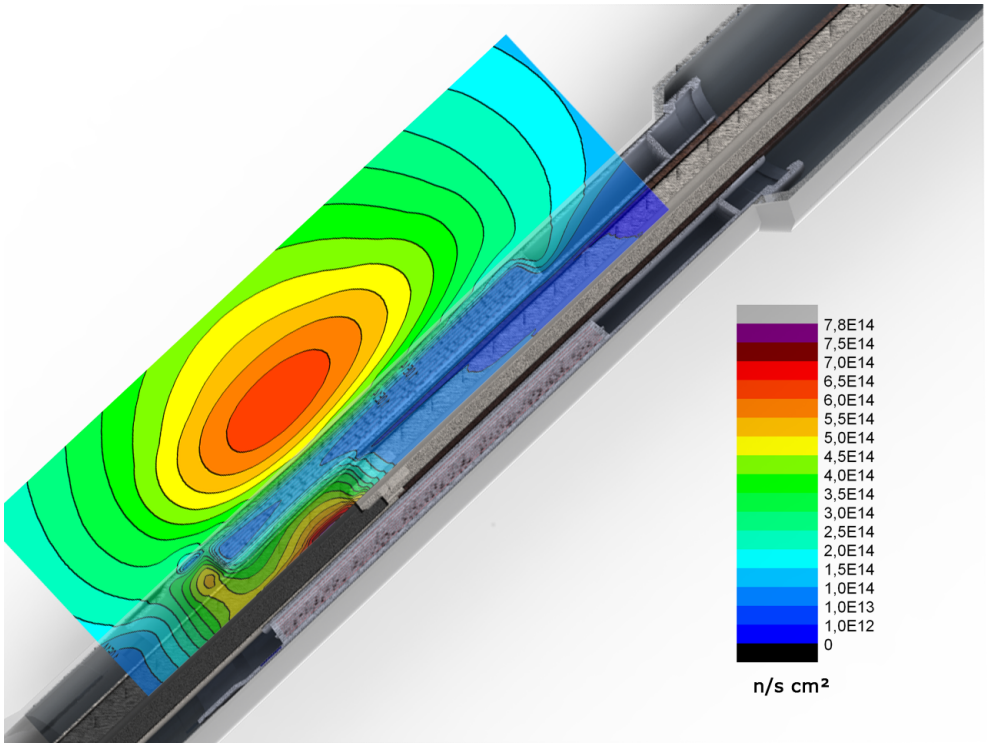

Figure 14.5: *Complete CAD model of central channel, fuel element and control rod with superimposed thermal neutron flux.*

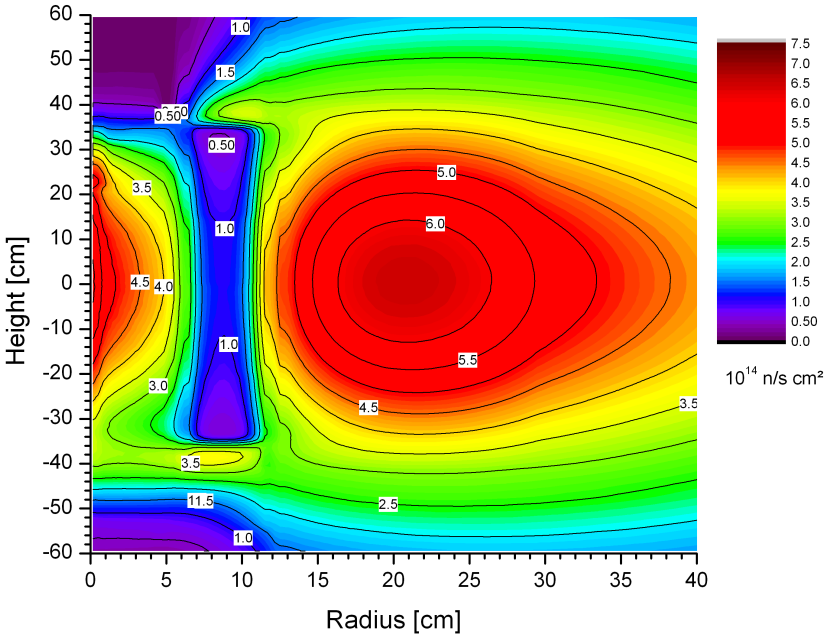

(a) Thermal flux

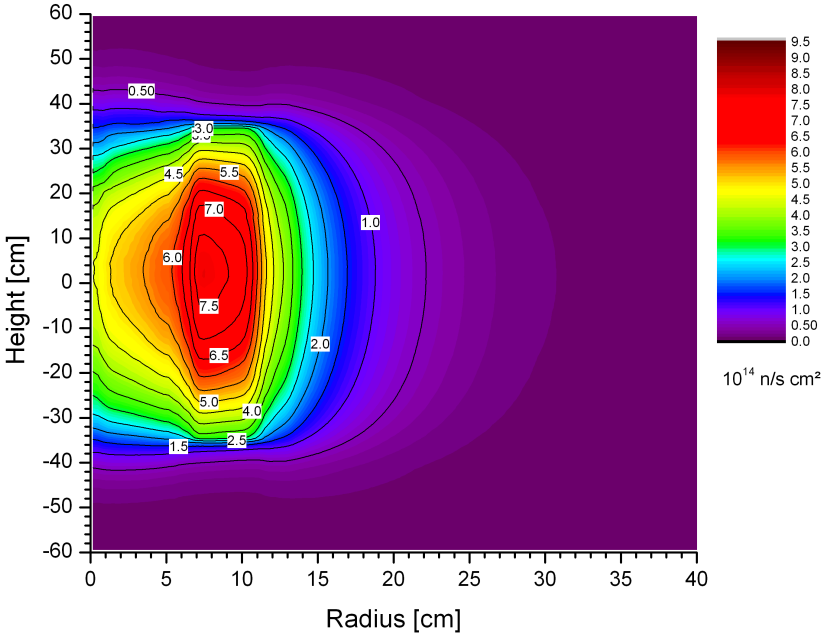

(b) Fast flux

Figure 14.6: *Flux profiles for the current fuel element at EOL: (a) is the thermal flux $\leq 0.625\,eV$, (b) the fast flux $\geq 100\,keV$.*

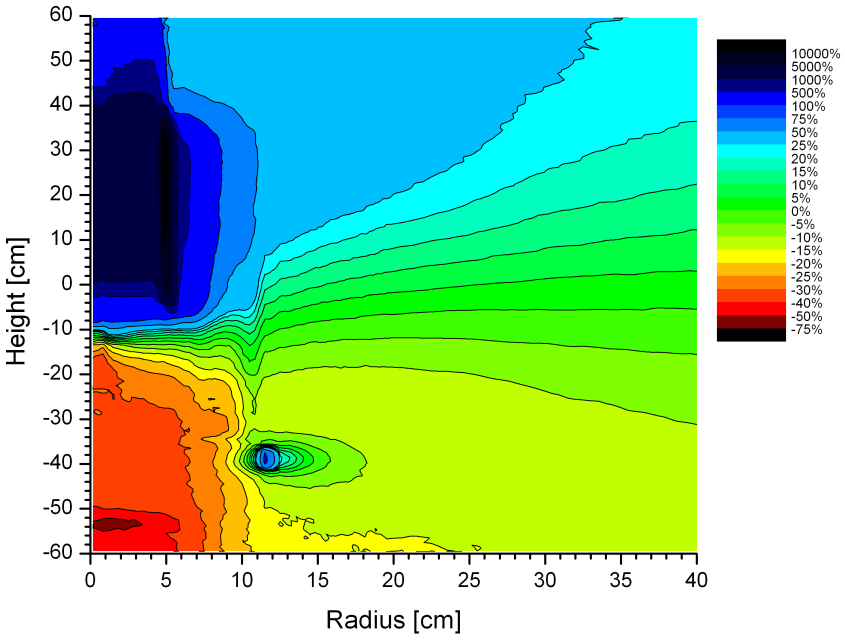

Figure 14.7: *Relative difference in thermal flux between BOL and EOL for the current fuel element. The scale is non-linear. It can be seen how the flux distribution in the D_2O moves upwards when the control rod is withdrawn. The largest changes naturally occur in the area of the control rod and in the boron ring, which is burnt during the cycle.*

14.4 Pressure Drop

No changes were observed compared to the behaviour described in chapter 13.6, p. 137. At EOL, a slight decrease in the pressure drop of about 0.01 bar was calculated, but this can also be due to numerical errors.

14.5 Temperatures

14.5.1 Begin of Life

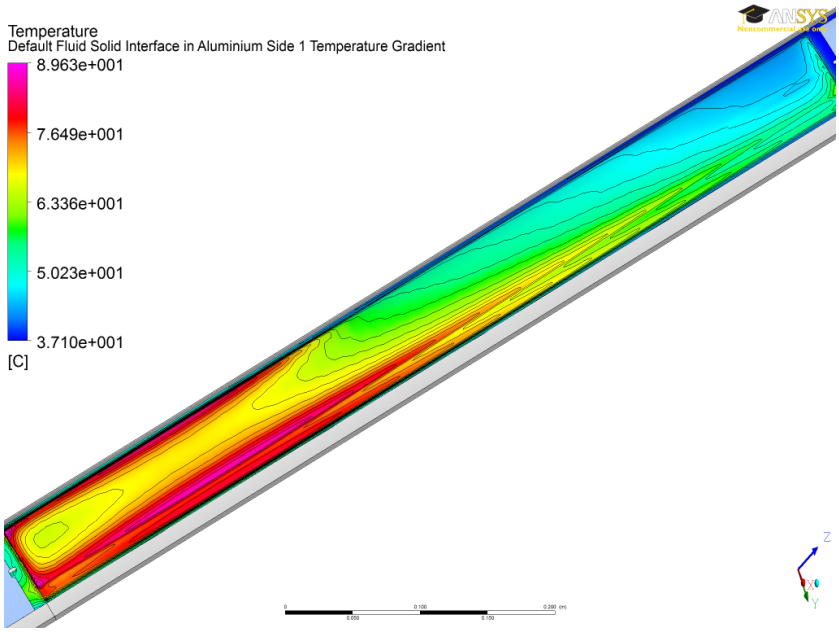

(a)

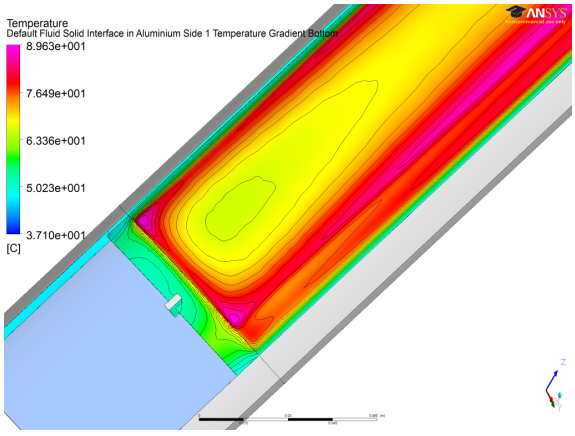

(b)

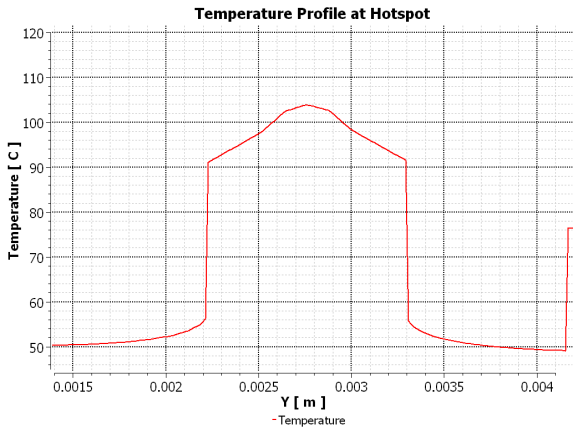

(c)

Figure 14.8: *Temperature distribution of the current fuel element at BOL: (a) shows the temperature distribution at the surface of the fuel plate. (b) is a closer view of the hotspot area. (c) is the temperature profile of the hotspot.*

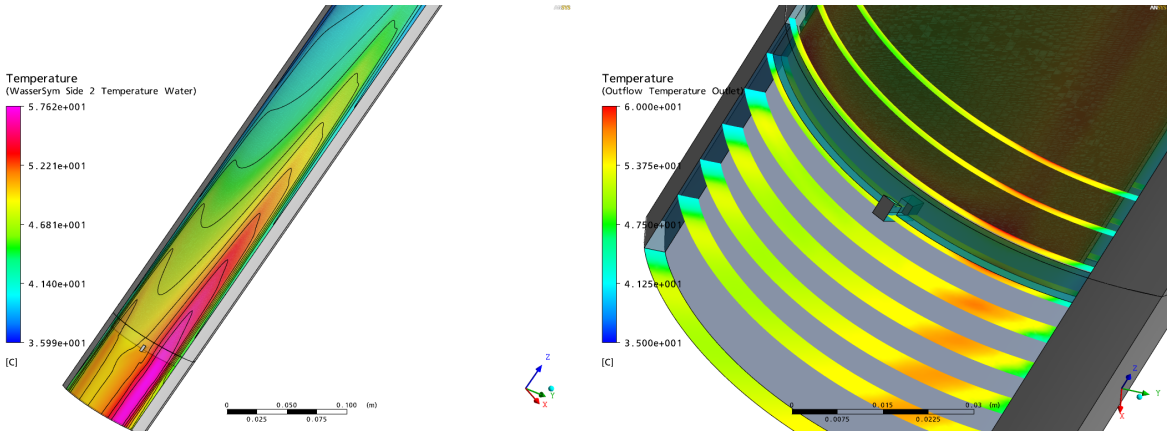

(a) (b)

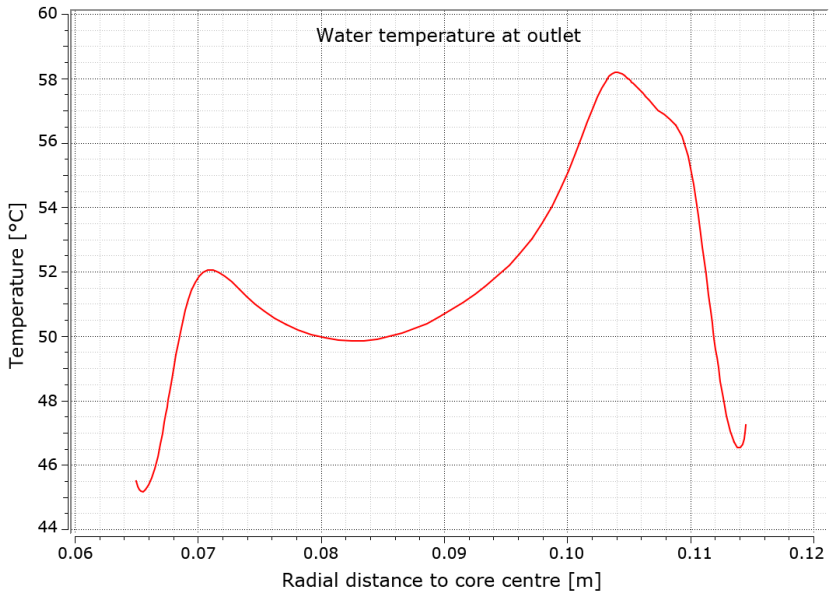

(c)

Figure 14.9: *Temperature distribution of the current fuel element at BOL: (a) is the temperature of the cooling fluid in the middle of the cooling channel. (b) shows the temperature in the fluid near the hotspot. (c) is the temperature profile of the fluid in the middle of the cooling channel at the end of the fuel in the fuel plate.*

The averaged temperature of the fluid at the outlet has been determined to be 53.0(1) ℃, slightly but lightweight higher than the one determined by [Gie96], 52.7 ℃. This is connected with the inclusion of the gamma- and collision-heating of structural components like the inner and outer duct as well as the frame of the fuel. Fig. 14.9(c) shows the temperature of the fluid in the middle of the cooling channel at the end of the fuel. These temperatures would be higher if the channel was divided in subchannels and then averaged, as the hotter fluid can be found near the cladding and not in the middle of the channel. Its structure is somewhat more pronounced than the comparable figure in [Gie96, Abb. 10-2, p. 73]. Five centimetres below the end of the fuel plate the maximum temperature in the water is 58.5(1) ℃.

The hottest spot is located in the meat near the lower inner corner. Its temperature was determined to be 102.9(5) ℃ at BOL. A. Röhrmoser [Röh] predicts a considerably higher fuel peak temperature of 126.7 ℃ using the NBK code. This is due to modelling differences and the missing heat conduction in axial direction in the solid in NBK. A more detailed explanation for this can be found in the detailed comparison in chapter 18.2. Another hot spot can be found at the same height – the lower bound of the fuel – near the density jump which is approximately 3 degrees colder. A quite big hot zone is located near the density jump of the fuel which is just about 5 degrees colder (97.8(5) ℃). With its far larger dimension it makes up the hottest stream filament of the cooling fluid. The last mentionable hot zone is at the same height as the before-mentioned but on the inner side of the plate with a temperature of max. 96.5(5) ℃. The median temperature of the fuel is 68.0(5) ℃, 66.7(5) ℃ in the inner zone and 73.7(5) ℃ in the outer zone. The maximum temperature drop in the fuel is 6.2(1) ℃ which compares well to the value quoted by [Gie96] for BOL, 6.3 ℃.

On the cladding surface, temperatures up to 89.6(3) ℃ can be found. These temperatures occur at both of the hotspots mentioned above. The difference in the inner temperature are due to the different thermal conductivities of the materials in the inner- and in the outer zone. Consistently, [Röh] again predicts a considerably higher wall temperature of 111.0 ℃. According to the current working plans, the end of the actual fuel is located between 7.5 mm and 13.5 mm above the end of the plate[3]. The pressure at this point is approximately 1.8 bar, yielding a water boiling temperature of 118 ℃.

A detailed discussion of the surface temperatures and a comparison with calculations made with NBK by A. Röhrmoser can be found in chapter 18.2, p. 227.

14.5.2 End of Life

Fig. 14.10 shows the results for the fuel plates at the end of a reactor cycle (60 d). According to 14.10(a), the heat is now distributed better over the whole plate. Still two hotspots exist at the bottom of the plate despite the higher burn-up that can be found there. As the control rod position has changed, the hottest spot of the plate moved from the inner end to the location of the density jump. Its temperature has decreased to 89.9(5) ℃.

At the top of the cladding, the maximum temperature has also decreased to 80.6(3) ℃. The mean temperature of the fuel slightly decreased to 71.0(5) ℃. The effect of the oxide layer becomes manifest in an average increase of the fuel temperature of 1.2 ℃. This fits well with the estimate from chap. 10.2.1, which, based on an untender model, predicted 1.3 ℃.

At the outlet, the average temperature of the fluid has slightly increased to 53.1(1) ℃, in accordance with the increased heat deposition. The hottest fluid 5 cm below the end of the fuel plate is now 56.9(1) ℃.

The comb-induced flow disturbances still have no significant impact on the cooling of the fuel plates (see chapter 13.2.2). Fig. 14.11(b) shows only a very weak impact: Black lines indicate velocity levels of the flow in the middle of the cooling channel while white lines indicate temperature levels on top of the plates.

[3] Manufacturing tolerance.

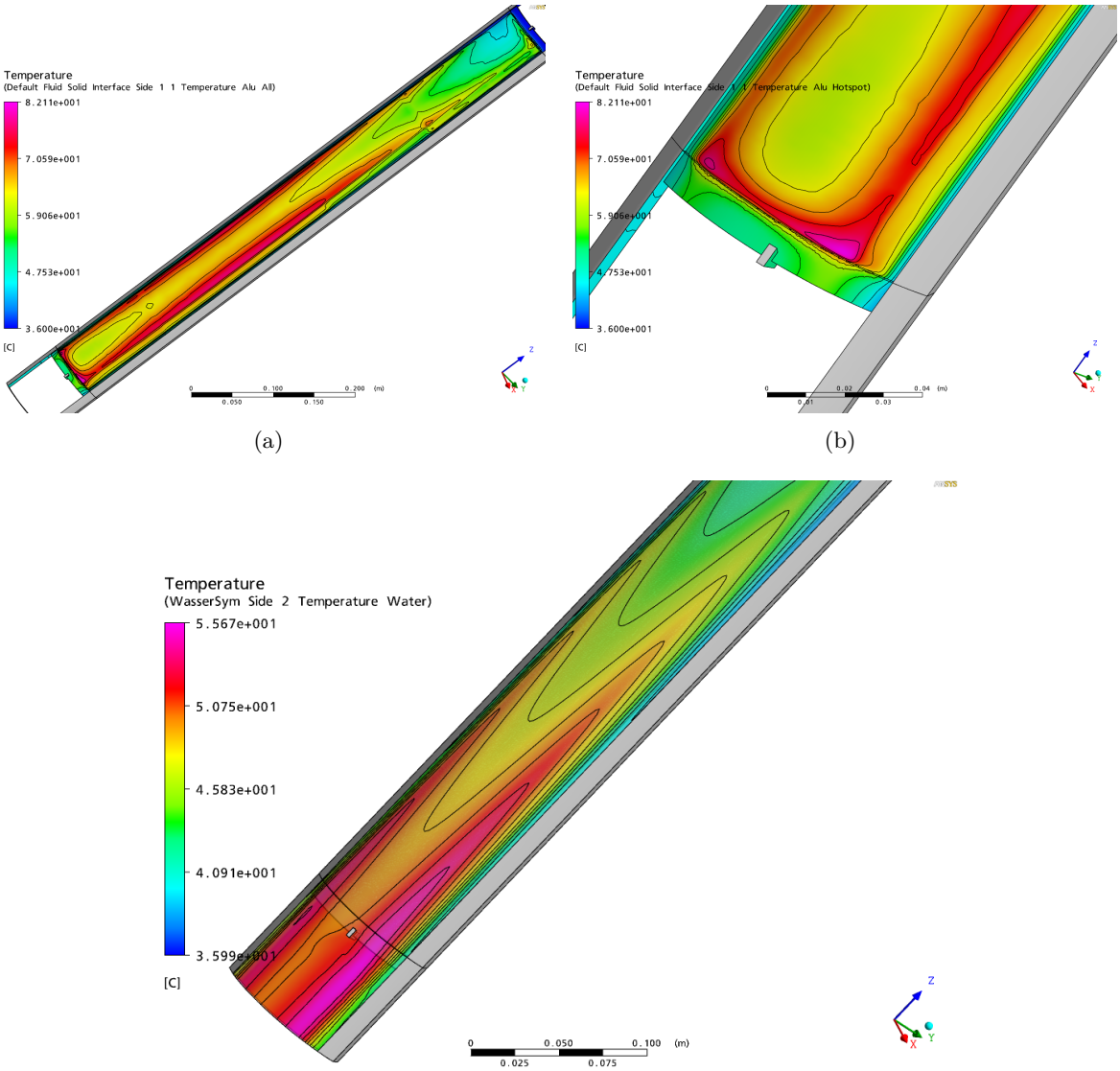

(a) (b)

(c)

Figure 14.10: *Temperature distribution of the current fuel element at EOL: (a) shows the temperature distribution at the surface of the fuel plate. (b) is a closer view of the hotspot area. (c) is the temperature distribution in the flow at the middle of the cooling channel.*

Although the flow below the comb is slower, the induced heavy turbulences enhance the cooling of the surface of the fuel plate. This can be seen in fig. 14.11(a) in the orange curve.

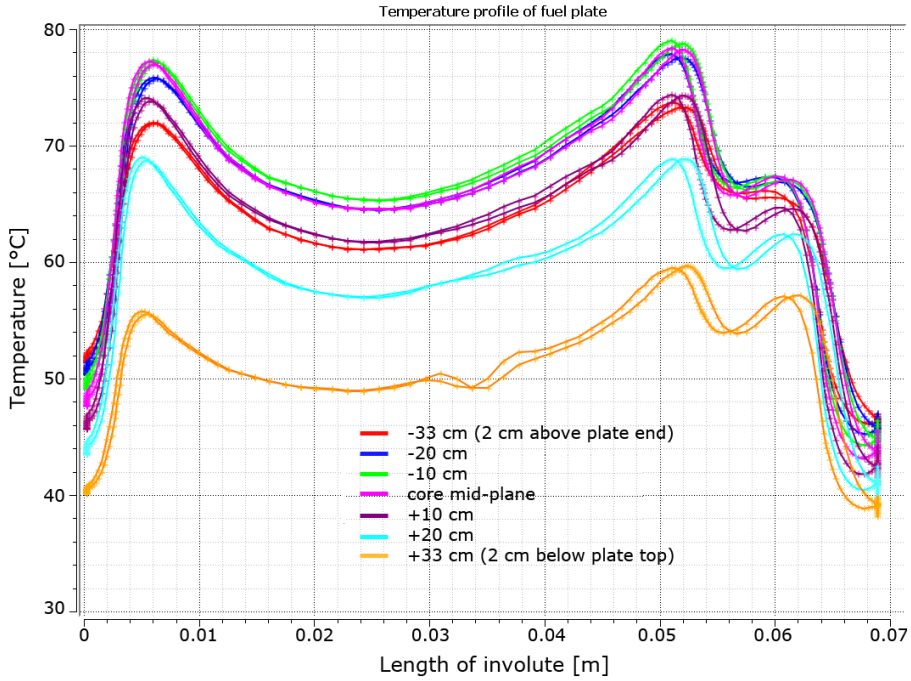

(a)

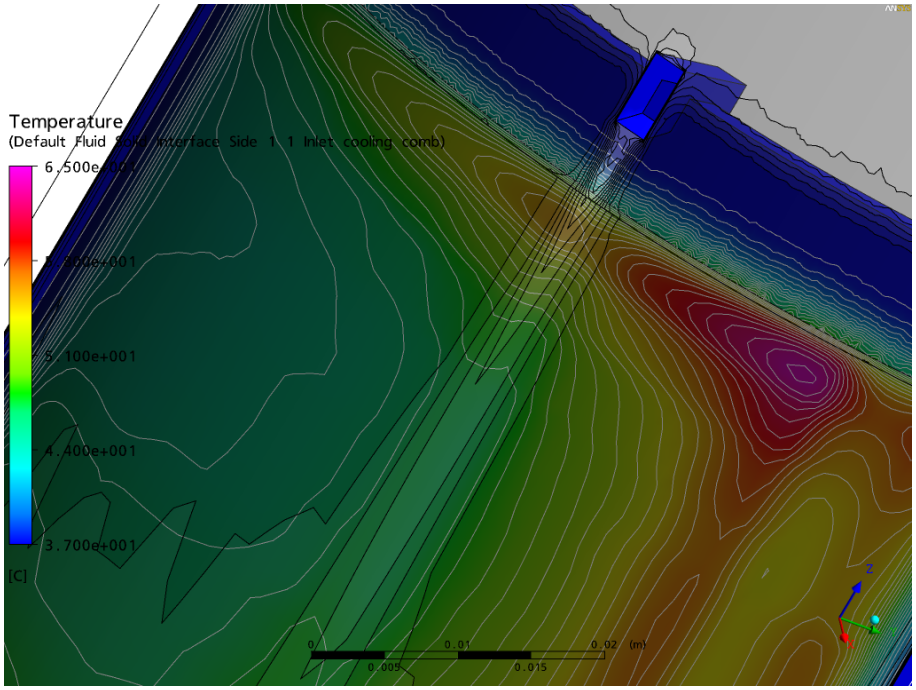

(b)

Figure 14.11: *Transverse temperature profiles of the flow at the surface of the cladding at -33 cm (red), -20 cm (blue), -10 cm (green), core mid-plane (purple), +10 cm (dark purple), +20 cm (light blue) and 33 cm (orange) are shown in (a), the temperatures at the top of the fuel plate at EOL in (b).*

14.6 Heat Flux

14.6.1 Begin of Life

The maximum wall heat flux at BOL was determined to be 382.3(15) $^{W}/_{cm^2}$. This is 8.4(3) % lower than the value given in [Gie96], 417.2 $^{W}/_{cm^2}$. As [Gie96] claims to use 3D-heat propagation, too, a part of this difference is explained by the use of correction factors in [Gie96] to account for the equipment installed in the moderator tank and a control rod position of $z = -10.5$ cm instead of the true $z = -6.9$ cm. A CFX calculation with a control rod position of $z = -10.5$ cm yields a maximum heat flux of 389.7(15) $^{W}/_{cm^2}$, reducing the difference to 6.6%. The value of 382.3(15) $^{W}/_{cm^2}$ is also much lower than what was calculated by Röhrmoser using NBK, 509.7 $^{W}/_{cm^2}$. This however can be explained by the missing axial heat conduction in the solid, as this value is found in the lower inner corner of the plates, where steep power deposition gradients in axial direction are present. This is discussed in greater detail in chapter 18.2.

If heat conduction was only one dimensional, the above mentioned 3.70(7) $^{MW}/_{l}$ would result in a heat flux of 659(10) $^{W}/_{cm^2}$, 70% more than in the three dimensional case. This emphasizes the importance of three dimensional calculations especially at the very border of the fuel. Nevertheless, this is a theoretical case assuming equal fuel densities in the respective fuel zones. In contrary, the actual working plans allow for reduced fuel densities / thicknesses at the very borders, which acts as an additional safety margin: A lower amount of fuel in an area goes hand in hand with lower fission densities, lower power deposition and therefore lower heat fluxes.

The median heat flux through the cladding of the active zone is reported to be 161.2 $^{W}/_{cm^2}$ in [Gie96], which compares very well to the value determined in this work, 161.3(5) $^{W}/_{cm^2}$.

An interesting detail can be found in fig. 14.12(b): The hot water channels below the two hotspots lead to a netto flux of heat from the fluid into the cladding (very blue spots on the lower end of the plate). This reaches dimensions up to 27.5 $^{W}/_{cm^2}$.

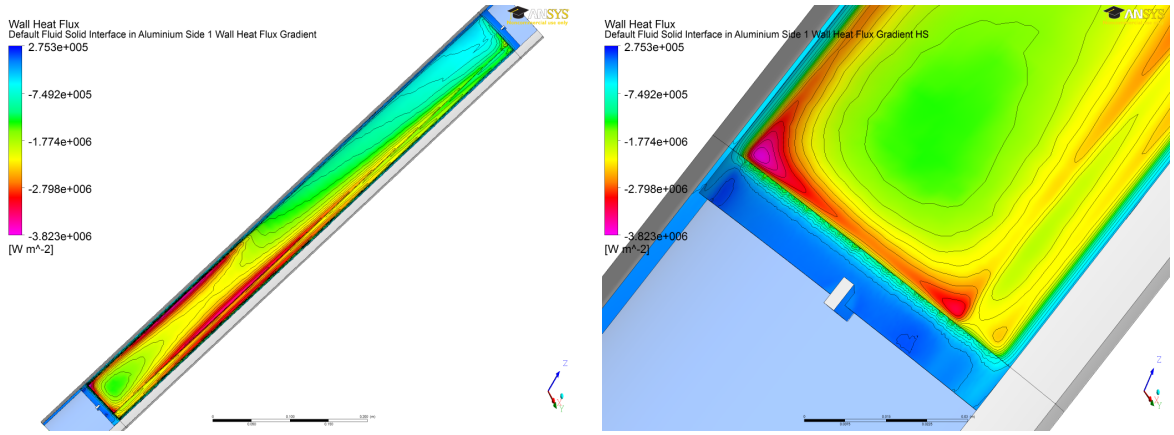

(a) (b)

Figure 14.12: *Wall heat flux of the current fuel element at BOL: Overall (a) and hotspot (b).*

14.6.2 End of Life

Fig. 14.13 shows the situation at the end of the cycle. Similar to the temperature distribution, the heat flux is much more distributed over the whole plate, resulting in a maximum heat flux at the wall of 292.5(15) $^{W}/_{cm^2}$, more than 20% lower than at BOL – another indicator that the behaviour of the fuel

element in critical situations has to be studied more at BOL rather than at EOL. The average heat flux has increased to 161.9(5) $^{W}/_{cm^2}$, according to the increased heat deposition in the fuel element.

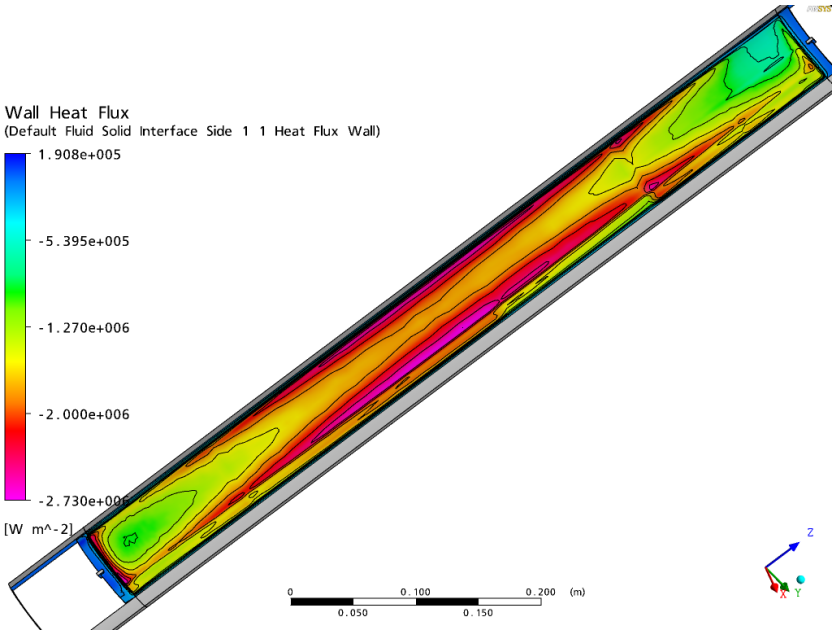

Figure 14.13: *Wall heat flux of the current fuel element at EOL.*

CHAPTER 15

Results for a Disperse UMo Fuel Element

One of the straight-forward conversion options is to keep the current design of the fuel plates and just replace the fuel by disperse UMo with a correspondingly higher density. The fuel was taken to be U8Mo (see chap. 10.1.6), this means an uranium-molybdenum alloy with 8 weight-% of molybdenum. The enrichment of the uranium was chosen to be 50%.

Quantity	*8 g/60 d/20 MW*	*8 g/60 d/22 MW*	*8 g/66 d/20 MW*	*7.5 g/60 d/20 MW*
Fuel plate parameters (BOL)				
Max. deposited power	4.6(1) $^{MW}/_{l}$	5.1(2) $^{MW}/_{l}$	4.6(1) $^{MW}/_{l}$	4.34(9) $^{MW}/_{l}$
Deposited power	18.07+0.23 MW	19.88+0.25 MW	18.07+0.23 MW	17.96+0.24 MW
BOL Content ^{235}U / U	10.7 kg/21.7 kg	10.7 kg/21.7 kg	10.7 kg/21.7 kg	10.0 kg/21.3 kg
Burn-up				
Max. Burn-up	43.0%	46.4%	46.4%	44.4%
Max. Burn-up absolute	$2.13 \cdot 10^{21}$ $^{1}/_{cm^3}$	$2.34 \cdot 10^{21}$ $^{1}/_{cm^3}$	$2.30 \cdot 10^{21}$ $^{1}/_{cm^3}$	$2.04 \cdot 10^{21}$ $^{1}/_{cm^3}$
Avg. Burn-up	14.2%	15.6%	15.6%	15.2%
Min. Burn-up	3.9%	4.6%	4.6%	4.5%
Avg. residual enrichment	45.1%	44.7%	44.7%	44.9%
Fluxes $[^{1}/_{s\,cm^2}]$				
Max. thermal D_2O	$5.91(1) \cdot 10^{14}$	$6.48(2) \cdot 10^{14}$	$5.91(1) \cdot 10^{14}$	$5.97(1) \cdot 10^{14}$
Max. thermal overall	$6.58(5) \cdot 10^{14}$	$7.23(6) \cdot 10^{14}$	$5.91(5) \cdot 10^{14}$	$6.75(4) \cdot 10^{14}$
Max. fast	$8.89(1) \cdot 10^{14}$	$9.78(2) \cdot 10^{14}$	$8.89(1) \cdot 10^{14}$	$8.91(1) \cdot 10^{14}$
Cycle neutron yield $[^{1}/_{cm^2}]$	$3.02(2) \cdot 10^{21}$	$3.33(3) \cdot 10^{21}$	$3.31(3) \cdot 10^{21}$	$3.05(2) \cdot 10^{21}$
Flux compared to current fuel element [%]				
In thermal max. D_2O	-7.7(3)%	+1.3(3)%	-7.7(3)%	-6.7(3)%
In thermal max. overall	-15.3(5)%	-6.9(4)%	-15.3(5)%	-13.1(4)%
In fast max.	-3.6(3)%	+6.1(3)%	-3.6(3)%	-3.4(3)%
Cycle neutron yield	-7.1(4)%	+2.5(4)%	+1.8(4)%	-6.2(4)%

Table 15.1: *Results for the simulation of a disperse UMo fuel element (neutronics). All values are at BOL if not quoted otherwise.*

Quantity	*Value 8 g/20 MW*	*Value 8 g/22 MW*	*Value 7.5 g/20 MW*	*Remarks*
Temperatures [℃]				
Max. Fuel	108.2(5)	114.6(5)	108.2(5)	up 5.3 ℃
Avg. Fuel	66.6(5) / 76.8(5) / 68.4(5)	69.4(5) / 80.5(5) / 71.4(5)	66.9(5) / 76.2(5) / 68.6(5)	inner / outer / total
Max. Wall	91.8(3)	96.7(3)	91.1(3)	up 2.2 ℃
Avg. Wall	62.3(3)	64.6(3)	62.2(3)	active zone
Avg. Outlet	52.9(1)	54.5(1)	52.9(1)	-
Heat Flux [$\mathrm{W/cm^2}$]				
Max. Wall	407.1(15)	449.0(15)	400.9(15)	up 17.7 $\mathrm{W/cm^2}$
Avg. Wall	161.5(5)	177.7(5)	160.6(5)	active zone
Pressure [bar]				
Avg. pressure drop	5.20(10)	5.19(10)	5.20(10)	unchanged
Max. pressure	8.44(10)	8.43(10)	8.44(10)	unchanged
Min. pressure	0.75(3)	0.75(3)	0.75(3)	unchanged
Safety margins				
S_{ONB}	2.35	2.12	2.38	-
S_{DNB}	2.30	2.06	2.34	-
S_{OFI}	5.18	4.58	5.28	-

Table 15.2: *Results for the simulation of a disperse UMo fuel element (thermal hydraulics). All values are at BOL if not quoted otherwise.*

15.1 Design of the Fuel Plates

The principal design of the fuel plates was not changed for the disperse fuel elements. Size and shape of the fuel zones were kept, and so was the ratio of the uranium density in the inner and outer zone of 2:1.

The boundary conditions for the flow are the same as those for the current fuel element, as there should be no change in the cooling system. Hence, the data can be taken from table 13.1. Data for materials has been listed in chapter 10.1.6, p. 102.

In this chapter, all data discussed is for the scenario with a uranium content of $8\,\mathrm{g/cm^3}$, 60 d cycle length and 20 MW power if not quoted otherwise. The reason that this scenario is focused is given in the discussion at the end of this chapter, sec. 15.10, p. 15.10: 8g U/cc-20MW-60d is the most realistic of these straight-forward conversion scenarios for disperse UMo in the case of FRM II.

15.2 Control Rod Reactivity Profile

Due to the larger parasitic absorption in the core (^{238}U), the reactivity profile of a fresh core made from disperse UMo is flatter than that of the current core (see fig. 15.1). This means, that at BOL the excess reactivity is lower than in the current case. This is due to the changed uranium/water ratio as the uranium density is increased.

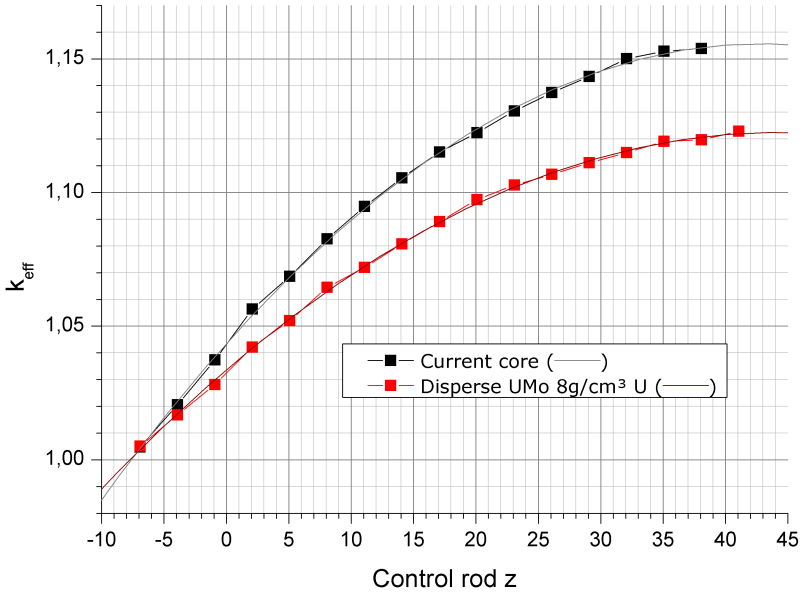

Figure 15.1: *k_{eff} over control rod position for a fresh core of the current fuel element and of a dispers UMo fuel.*

15.3 Burn-up

Due to the problem of unresolved resonances with an increasing fraction of ^{238}U, burn-up calculations have slightly larger uncertainties. These uncertainties are not yet captured by the uncertainty treatment of a single X^2 run but can be estimated by the procedure described in chapter 4.4.3, as long as they are not of a systematic nature. For the following results, uncertainties have not been calculated explicitly but can be estimated to be about 1% (see discussion in chapter 17.2).

Calculations show that an uranium content of 7.5 g/cm³ in the inner zone and 3.75 g/cm³ in the outer zone will be sufficient for 60 d reactor cycle length. This value is slightly lower than the 7.7 g/cm³ reported by [Röh05] for a 52 d cycle. This value refered to the new fuel element having the same reactivity reserve after 52 d as it is currently the case. For 60 d with no reserve ($\Delta\rho = 0$), Röhrmoser has also derived a value of 7.5 g/cm³ for 60 d [Röh] using Mf2dAb, therefore the calculations agree very well. To leave the possibility for further installations in the reactor open and as reactor materials will degrade regarding neutronic properties in the future due to increased absorption caused by the burn-up of the beryllium follower and structural materials, mainly fuel plates with a density of 8.0 g/cm³ will be the subject of the following analysis (see also the discussion on this topic in [Röh05]). This also leaves room for further installations near the reactor core, e. g. the planned ^{99}Mo production facility [Ger10, Tho10].

The movement curve of the control rod is shown in fig. 15.2. For comparison, the measured curve of FRM II reactor cycle 15 is also shown. It can be seen that the driveway is slightly modified due to the exchanged fuel. At the beginning, the flatter reactivity profile caused by the increased absorption due to ^{238}U leads to a steeper control rod curve. During the cycle, depending on the fisisonable uranium inventory, the higher uranium content compared to fission products results in a flattening of the curve, crossing or approaching the current control rod driveway. The general steepening towards EOL is again caused by the lower control rod reactivity worth when the control rod is mostly withdrawn (see flattening

of reactivity profile in fig. 15.1).

For the 8.0 g/cm³-case, the maximum relative burn-up is 43.0% in the outer zone and 25.2% in the inner zone, the average burn-up 14.2%, the minimum 3.9%. This leaves an average enrichment of 45.1% at EOL. Quoting absolute numbers (fission densities per cm^3 meat), this means $1.86 \cdot 10^{21}$ 1/cm³ in the outer and $2.13 \cdot 10^{21}$ 1/cm³ in the inner zone. Especially the latter is 8% higher than the maximum value for the current U_3Si_2-fuel, reflecting the inferior neutronic properties of the UMo dispersion fuel. Again, all these values refer to burn-up zones with a minimum width of 5 mm. The local fission density in the UMo grains themselves is $7.41 \cdot 10^{21}$ 1/cm³ in the outer and $4.24 \cdot 10^{21}$ 1/cm³ in the inner zone. These values are for obvious reasons lower than those for the current HEU-case but barely comparable due to the different nature and isotopic composition of the grains.

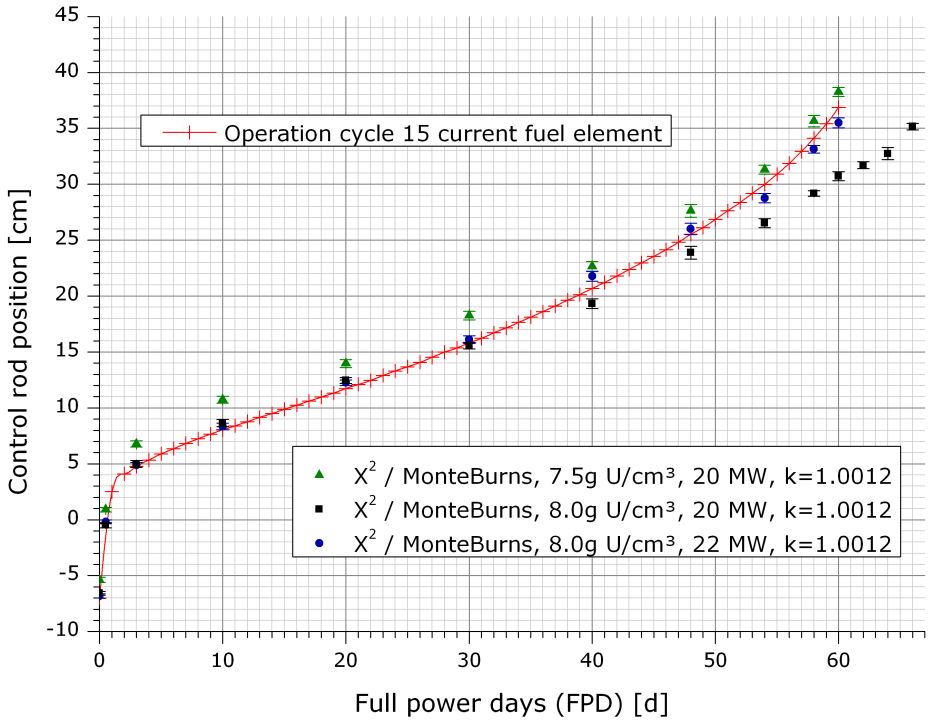

Figure 15.2: *Control rod position depending on the number of full power days (FPDs) for various uranium densities in disperse UMo.*

As will be seen later, the change of the fuel towards lower enrichment goes hand in hand with a lower flux. This may be compensated either by a higher reactor power or a longer cycle length T_c. The change can be quantified with the cycle neutron yield introduced in equation 14.1.

As shown in fig. 15.2, a uranium density of 8.0 g/cm³ would allow for a cycle length of 66 d if the fuel could be qualified for the correspondingly higher burn-up. The increase in the absolute burn-up is about 7% in the maximum, up to $2.30 \cdot 10^{21}$ 1/cm³ at the inner border of the inner zone, 0 cm to 10 cm below core mid-plane. The maximum relative burn-up is 46.4% in the outer zone at the same height. These values are practically the same for 60 d cycle length but 22 MW power. The thermal hydraulic difficulties for the latter are discussed later in this chapter.

15.3.1 Actinide Inventory

The fuel inventory after 60 FPDs for the 8.0 g/cm³-case is listed in tab. 15.3. The plutonium production increased nearly sevenfold compared to the current fuel element, up to 72.61 g. ^{239}Pu makes up 90% of this, slightly more than now – probably an effect of the changed spectrum in the fuel plates. In total, 107.4 g ^{238}U were consumed. The time-dependent concentration of the most important actinides is shown in fig. 15.3.

Isotope	*Quantity* [g]	*Isotope*	*Quantity* [g]	*Isotope*	*Quantity* [g]
Actinides					
^{234}U	88.161	^{237}Np	4.687	^{240}Pu	4.900
^{235}U	9187.370	^{238}Np	0.034	^{241}Pu	1.648
^{236}U	319.078	^{239}Np	5.379	^{242}Pu	0.067
^{237}U	1.553	^{238}Pu	0.206		
^{238}U	10755.080	^{239}Pu	69.537		
Non-Actinides					
^{1}H	0.001	^{98}Mo	489.675	^{143}Ce	1.472
^{2}H	$1.343 \cdot 10^{-7}$	^{100}Mo	220.683	^{141}Pr	19.056
^{3}H	$1.427 \cdot 10^{-6}$	^{99}Tc	28.749	^{143}Pr	13.624
^{3}He	$1.360 \cdot 10^{-13}$	^{101}Ru	27.533	^{143}Nd	28.048
^{4}He	0.539	^{102}Ru	23.445	^{145}Nd	29.258
^{7}Li	0.942	^{103}Ru	10.426	^{146}Nd	24.295
^{9}Be	$7.173 \cdot 10^{-7}$	^{103}Rh	6.133	^{147}Nd	4.419
^{10}B	0.137	^{105}Rh	0.197	^{148}Nd	13.950
^{11}B	$1.930 \cdot 10^{-4}$	^{117}Rh	$1.259 \cdot 10^{-10}$	^{147}Pm	11.202
^{12}C	$4.910 \cdot 10^{-10}$	^{105}Pd	5.128	^{148m1}Pm	0.128
^{13}C	$5.390 \cdot 10^{-16}$	^{119}Pd	$3.458 \cdot 10^{-10}$	^{149}Pm	0.540
^{27}Al	4447.310	^{109}Ag	0.346	^{149}Sm	0.690
^{28}Si	0.344	^{113}Cd	0.017	^{150}Sm	8.025
^{29}Si	$1.285 \cdot 10^{-5}$	^{129}I	4.568	^{151}Sm	1.403
^{30}Si	$3.070 \cdot 10^{-10}$	^{131}I	3.886	^{152}Sm	3.686
^{83}Kr	2.282	^{135}I	0.297	^{153}Sm	0.135
^{93}Zr	31.390	^{131}Xe	15.178	^{153}Eu	1.777
^{95}Zr	23.670	^{133}Xe	5.951	^{154}Eu	0.167
^{95}Nb	5.841	^{135}Xe	0.076	^{155}Eu	0.097
^{92}Mo	262.857	^{133}Cs	39.284	^{156}Eu	0.151
^{94}Mo	167.908	^{134}Cs	0.956	^{157}Eu	0.002
^{95}Mo	291.286	^{135}Cs	8.849	^{157}Gd	0.005
^{96}Mo	313.388	^{139}La	47.714		
^{97}Mo	209.391	^{141}Ce	24.714		

Table 15.3: *Result of burn-up calculation, disperse UMo, 8.0 g/cm³, EOL after 60 d at 20 MW.*

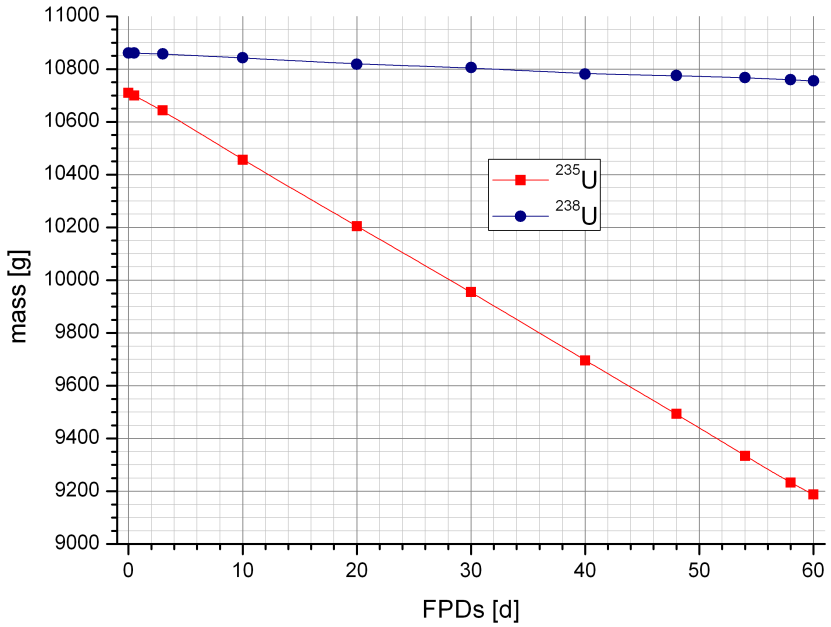

(a)

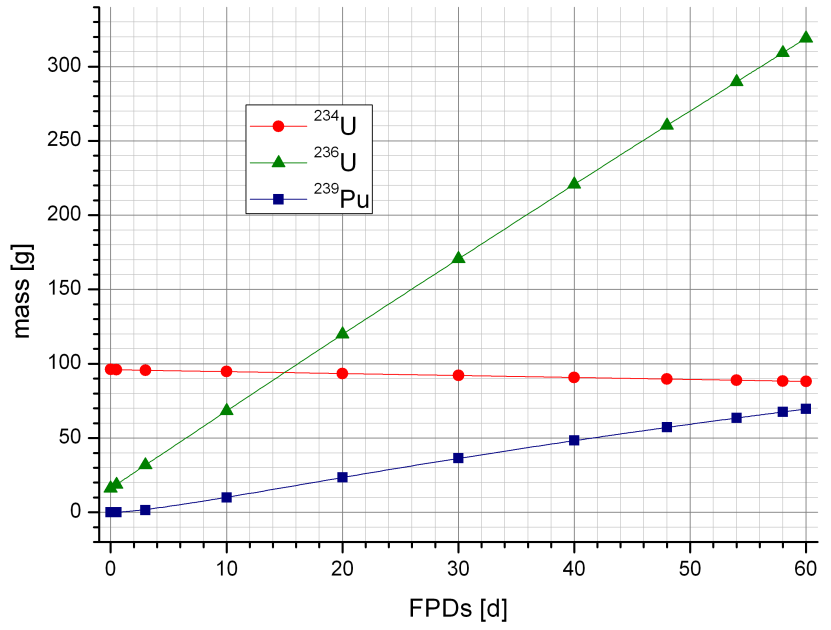

(b)

Figure 15.3: *Actinide inventory for the disperse fuel:* ^{235}U *and* ^{238}U *(a),* ^{234}U, ^{236}U *and* ^{239}Pu *(b).*

15.3.2 Non-Actinide Inventory at EOL

The non-actinide inventory is also shown in table 15.3. It comprises the fuel plates and the boron ring. The inventory of non-actinides of the disperse case is nearly the same as in the case of the current fuel element (tab. 14.3, p. 151).[1]

An interesting side note is that due to the uranium consumption and the molybdenum production through fission, the average composition of the UMo alloy changed from 8.0 to 8.9 weight-% molybdenum at EOL.

15.3.3 Boron Ring

Only 0.137 g ^{10}B are left in the boron ring, a consumption of 92%. However, as discussed in chapters 14.1.3 and 17.2, this value bears rather large uncertainties.

15.4 Power Deposition

From the increased absorption of the new fuel element due to the higher ^{235}U content and other absorbers like ^{238}U and Mo, a more disadvantageous distribution of the fission density can be expected. Assuming equal reactor power and cooling flow boundary conditions, this will decrease the safety margins of reactor operation. However, it will be seen later that this decrease is rather small: Even though the peak power deposition values are higher, the gradients are steeper, too. The bluring of the power profile due to the 3D heat conduction causes a smaller relative increase of the maximum heat flux, see chapter 15.8.

15.4.1 Begin of Life

The maximum power deposition in the active zone has increased to 4.6(1) MW/l, up 20.2% from the current 3.67(6) MW/l. This is of course in large parts due to the comparably higher ^{235}U density of the fuel. The power deposited in the structural materials surrounding the active volume has increased to 0.24 MW/l. The power deposition relevant for cooling is now 18.30 MW, up 0.7%. Fig. 15.4 shows the new distribution of power deposition, which is very much comparable to the current distribution.

15.4.2 End of Life

At EOL, a slight increase in the power deposition in the active zone can be observed. It is now 18.40 MW, up about a half percent from BOL. Again, the maximum power density is drastically lower than at BOL, 2.66(10) MW/l.

[1] Of course, large differences can be found in the Al-, Si- and Mo-inventory as the fuel type has changed.

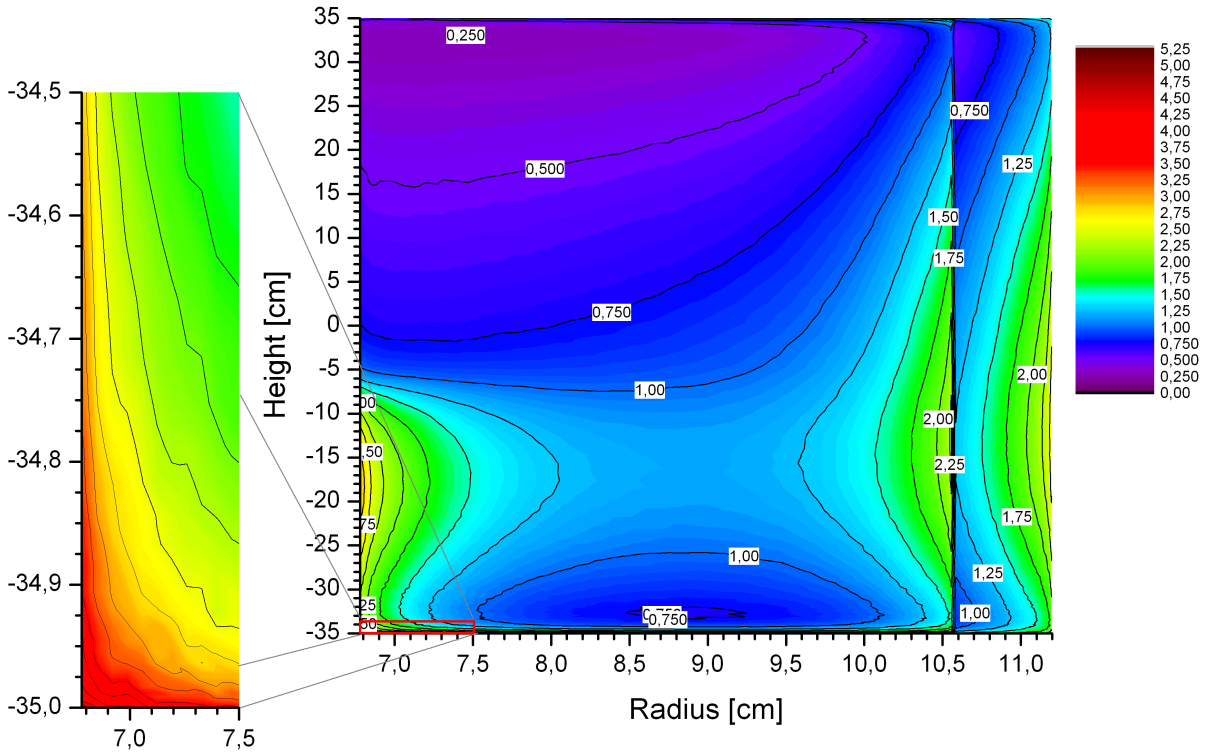

Figure 15.4: *Power deposition for the disperse fuel element with* $8.0\,\mathrm{g\,U/cm^3}$ *in* $\mathit{MW/l}$ *at BOL.*

15.5 Flux

The increased absorption in the fuel element will lead to significantly lower thermal and fast neutron fluxes. While this is not relevant for the fuel plates themselves, a drop of the thermal peak flux in the D_2O will result in comparably lower efficiency at the linked experiments.

15.5.1 Begin of Life

At BOL, the peak thermal flux in the D_2O has decreased by 7.7(3)%, now $5.91(1) \cdot 10^{14}\,\mathrm{n/s\,cm^2}$. The position of this peak remained at 21.5 cm / -10.5 cm. Simultaneously, the overall maximum thermal flux in the beryllium follower has decreased by 15.3(5)% to $6.58(5) \cdot 10^{14}\,\mathrm{n/s\,cm^2}$. Similarly, the maximum fast flux has decreased by 3.6(3)% to $8.89(1) \cdot 10^{14}\,\mathrm{n/s\,cm^2}$ at 7.5 cm / -16.5 cm which is still in the fuel plate, again reflecting the increased absorption. The cycle neutron yield Φ at the BOL thermal flux maximum in the D_2O only decreased 7.1(4)%, slightly less than what would be expected from the BOL loss of 7.7(3)%. Besides statistical uncertainties, this can be attributed to the lower EOL control rod position which keeps the flux higher in the regions below core mid-plane.

Flux densities are shown in fig. 15.5(a) for the thermal and 15.5(b) for the fast flux. The difference of the thermal flux compared to the current fuel element is shown in fig. 15.6. It can be seen that in the relevant zones of the D_2O-tank, the flux decreases averagely between 6% and 8%. The flux loss increases with decreasing distance to the fuel plates. The fine grained structures in the upper left corner of fig. 15.6 are noise resulting from insufficient statistics in the hafnium-part of the control rod.

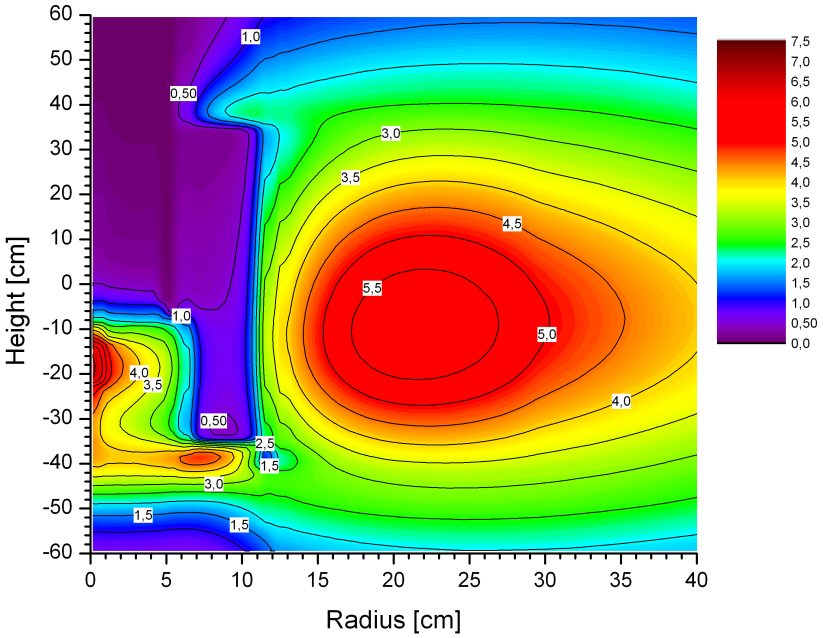

(a) Thermal flux

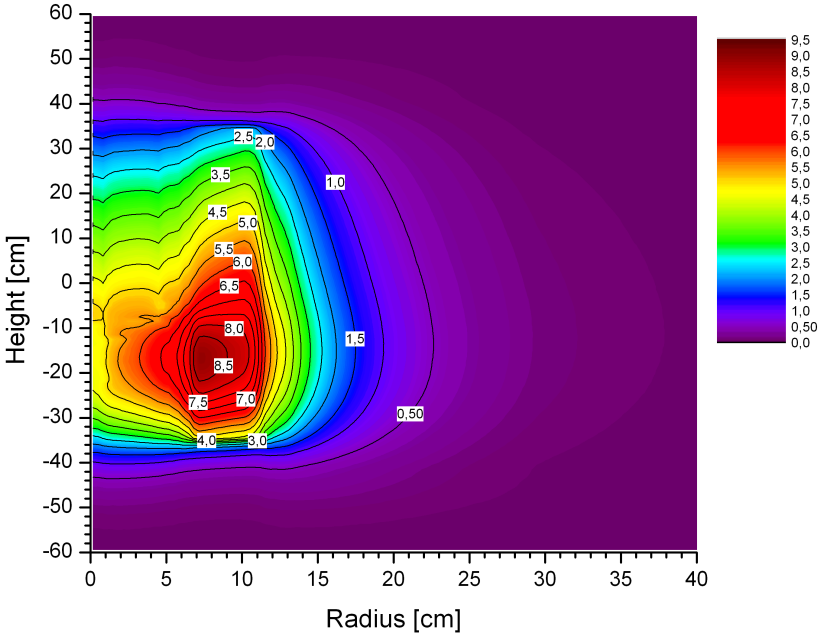

(b) Fast flux

Figure 15.5: *Flux profiles for a disperse UMo fuel element with* $8.0\,\mathrm{g\,U/cm^3}$ *at BOL: (a) is the thermal flux* $\leq 0.625\,eV$*, (b) the fast flux* $\geq 100\,keV$*.*

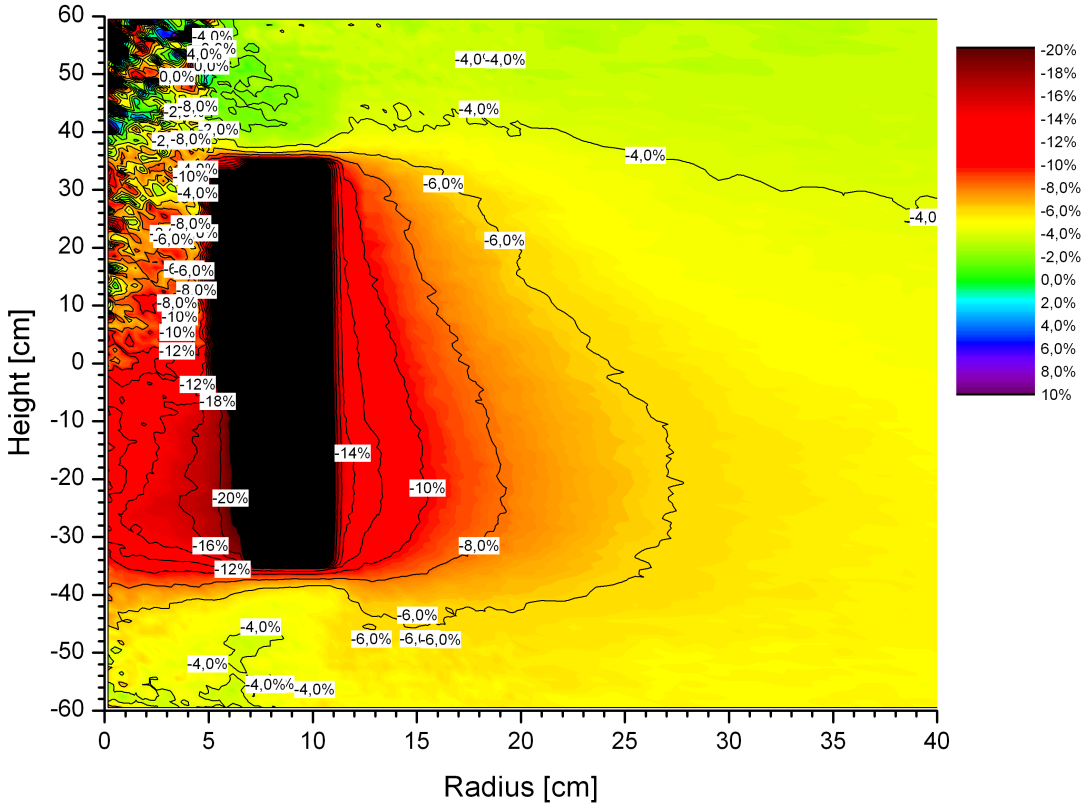

Figure 15.6: *Thermal flux difference between disperse UMo with* $8.0\,\mathrm{g\,U/cm^3}$ *and current fuel element at BOL*

15.5.2 End of Life

Concerning flux, the situation gets worse at EOL. Indeed, the well known expansion of the high flux zone can be observed, but the peak drop is now -8.3(3)%, down to $5.94(1) \cdot 10^{14}\,\mathrm{n/s\,cm^2}$. The location of this maximum remained at 21.0 cm / 1.0 cm. The maximum thermal flux in the beryllium follower is -13.6(5)% down to $5.27(4) \cdot 10^{14}\,\mathrm{n/s\,cm^2}$ compared to the current situation, and 19.9(5)% down from BOL. Flux densities are shown in fig. 15.7(a) for the thermal flux and 15.7(b) for the fast flux.

Thermal flux differences to the current fuel element are shown in fig. 15.8. The scale is unchanged from fig. 15.6 which indicates a much stronger and widespread loss of thermal neutrons in the D_2O approaching the fuel element. The small flux increase at 1.0 cm / 20.0 cm stems from different control rod positions at EOL.

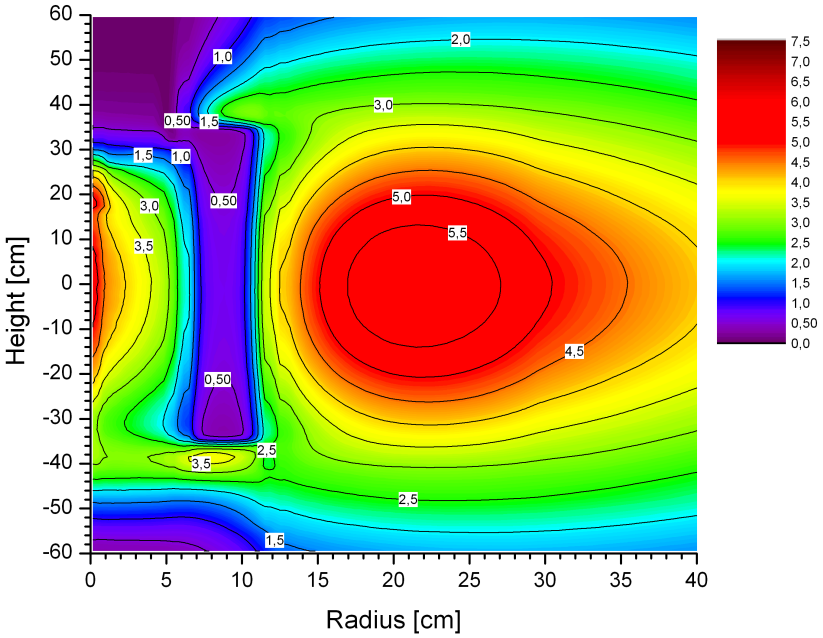

(a) Thermal flux

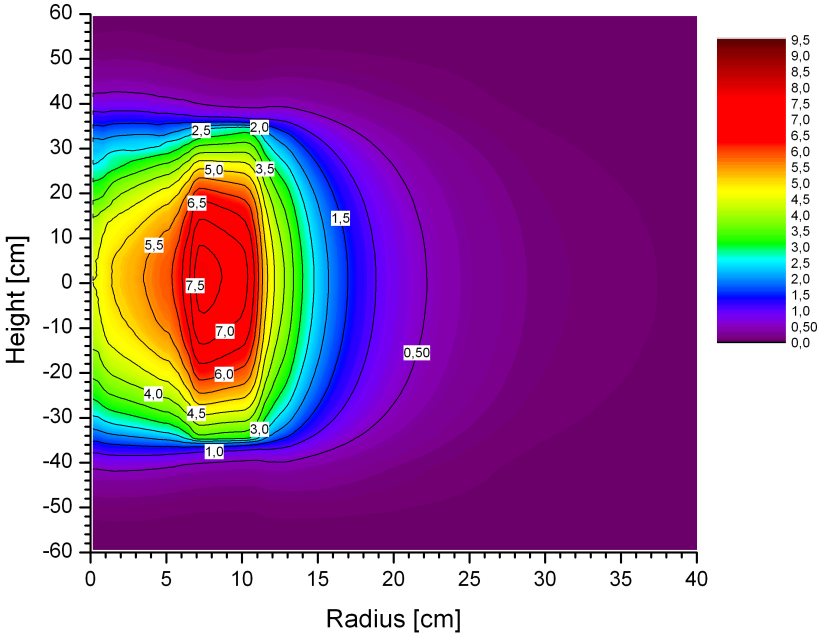

(b) Fast flux

Figure 15.7: *Flux profiles for a disperse UMo fuel element with* $8.0\,\mathrm{g\,U/cm^3}$ *at EOL: (a) is the thermal flux* $\leq 0.625\,eV$*, (b) the fast flux* $\geq 100\,keV$*.*

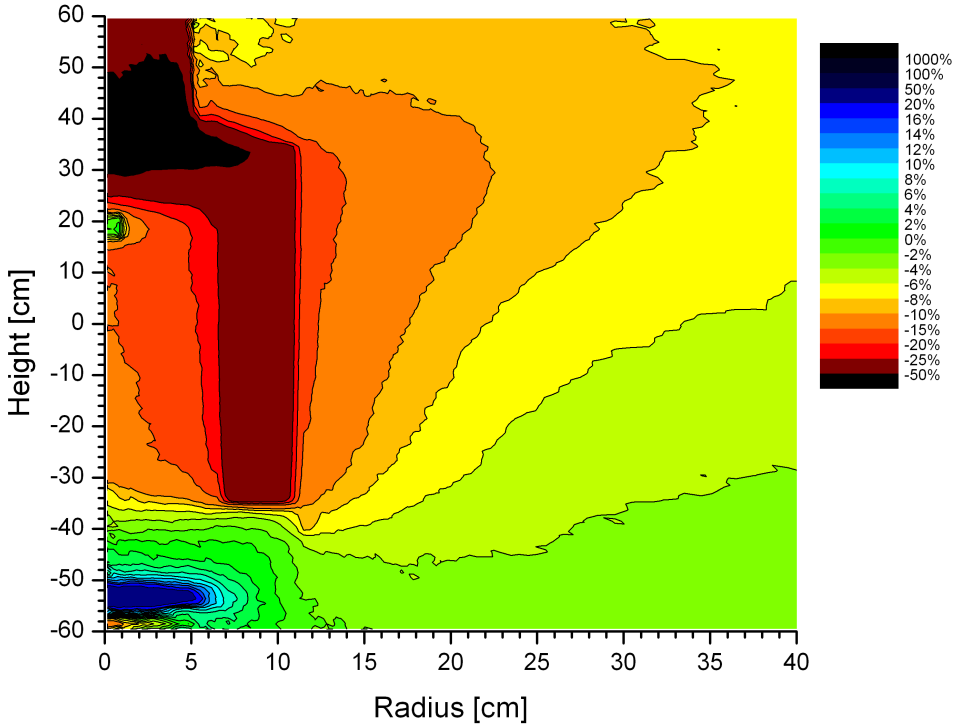

Figure 15.8: *Thermal flux difference between disperse UMo with* $8.0\,\mathrm{g\,U/cm^3}$ *and current fuel element at EOL.*

15.6 Pressure Drop

No changes were observed in the pressure drop of $5.20(10)\,\mathrm{bar}$.

15.7 Temperatures

As the thermal conductivity of disperse UMo with the given densities is only about 10% lower than that of the current fuel, no drastic changes in fuel temperatures are expected. Due to the increased absorption and somewhat inferior neutronic properties, the maximum fuel and wall temperature have slightly increased.

15.7.1 Begin of Life

The maximum temperature of the fuel has risen to $108.2(5)\,^\circ\mathrm{C}$, $5.3\,^\circ\mathrm{C}$ higher than now, reflecting the higher fission density and power deposition in the lower inner corner of the fuel plates. Average temperatures are mainly unchanged, $66.6(5)\,^\circ\mathrm{C}$ in the inner zone, $76.8(5)\,^\circ\mathrm{C}$ in the outer zone and $68.4(5)\,^\circ\mathrm{C}$ overall. Accompanying this, the maximum wall temperature has risen by $2.2\,^\circ\mathrm{C}$ to $91.8(3)\,^\circ\mathrm{C}$. The average wall temperature remains unchanged at $62.3(3)\,^\circ\mathrm{C}$. The temperature distribution is shown in fig. 15.9.

Fig. 15.10 shows the water temperature in the middle of the cooling channel at the lower end of the fuel zone. The more pronounced structure of the temperatures on the fuel zone surface can also be identified in the coolant: In comparison to the current fuel element, the hot stream filament is significantly

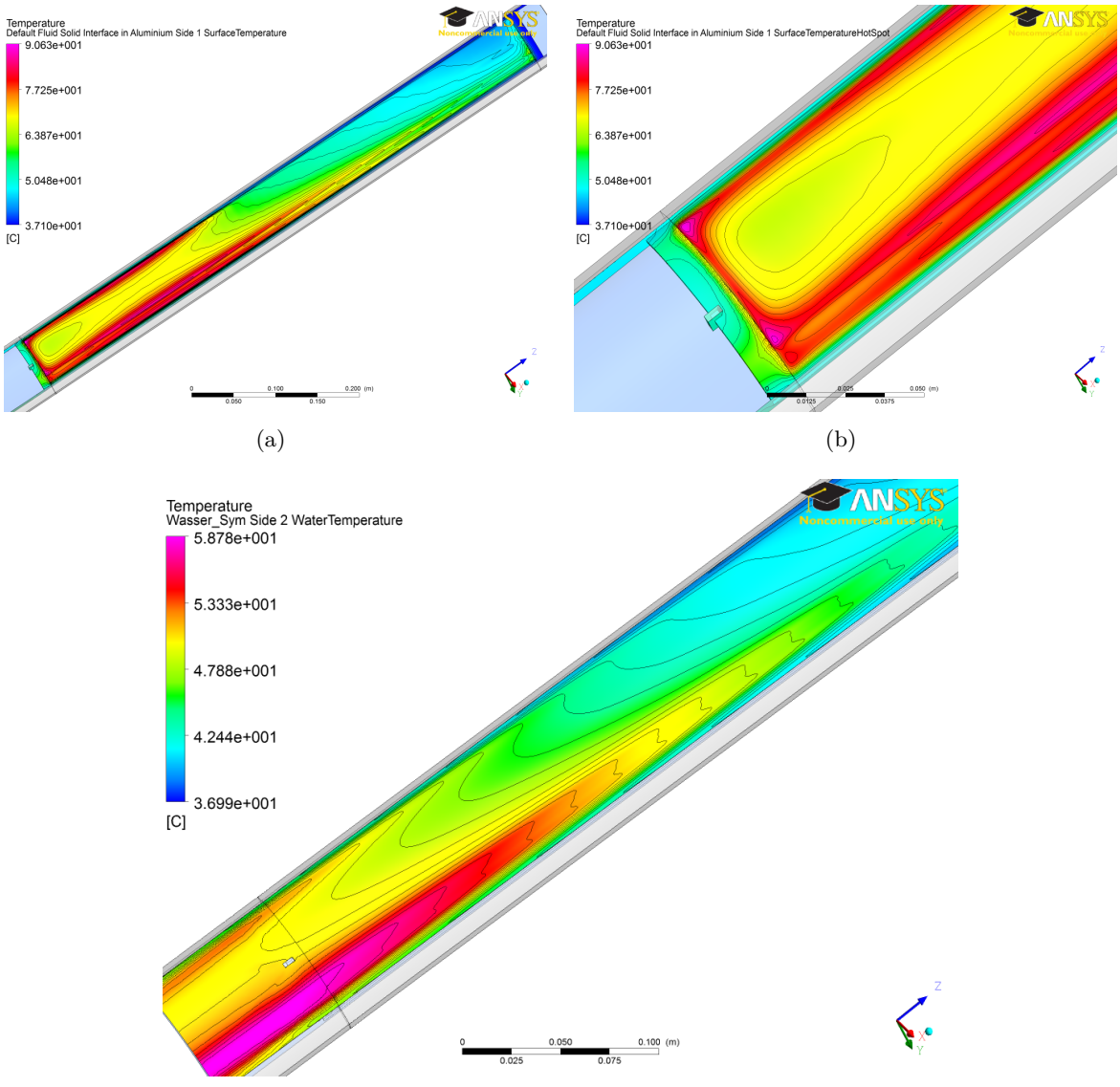

Figure 15.9: *Temperature distribution of a disperse UMo fuel element with* $8.0\,\mathrm{g\,U/cm^3}$ *at BOL: (a) shows the temperature distribution at the surface of the fuel plate. (b) is a closer view of the hotspot area. (c) is the temperature distribution in the flow at the middle of the cooling channel.*

broadened. This is again a sign for the more unfortunate power distribution in the disperse UMo fuel element, compared to the current solution.[2]

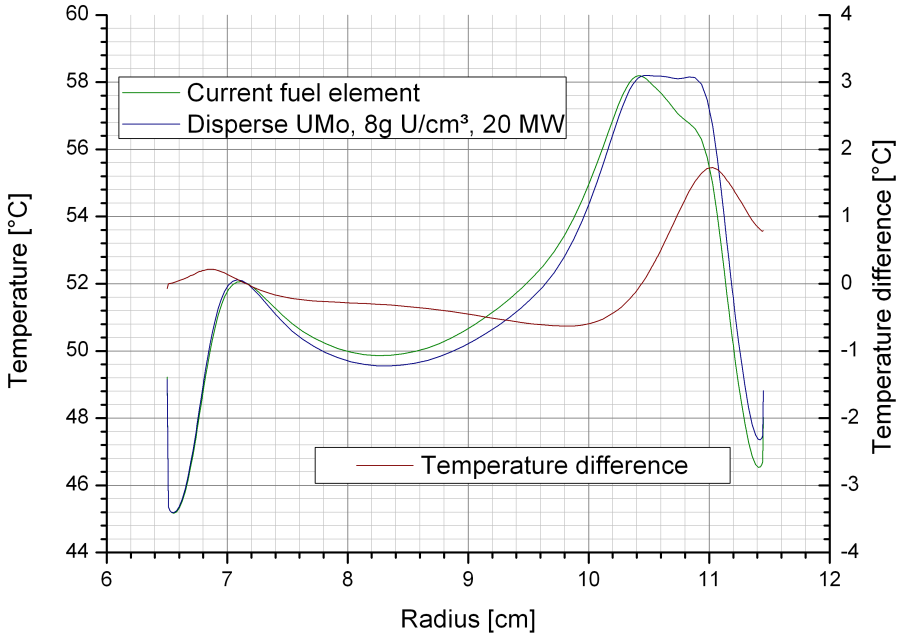

Figure 15.10: *Comparison of the water temperature in the middle of the cooling channel at the fuel zone end at BOL.*

15.7.2 End of Life

As for the current fuel element, the maximum fuel temperature at EOL is significantly lower than at BOL because of the more homogeneously distributed fission density. The maximum temperature is now 92.9(5) °C in the inner and 86.2(5) °C in the outer zone. Averaged fuel temperatures are 70.8(5) °C in the inner, 72.5(5) °C in the outer zone and 71.1(5) °C overall. Also, the maximum wall temperature is considerably lower, now 82.8(3) °C. The average wall temperature has risen 2.4 °C to 64.7(3) °C. The outlet temperature is 53.1(1) °C. Temperatures are shown in fig. 15.11.

[2]It must be noted, that due to the location in the middle of the cooling channel at the end of the fuel zone, the full profile is not yet developed. However, this is the case for the current fuel element as well as for the disperse one. Therefore, the comparison is reasonable.

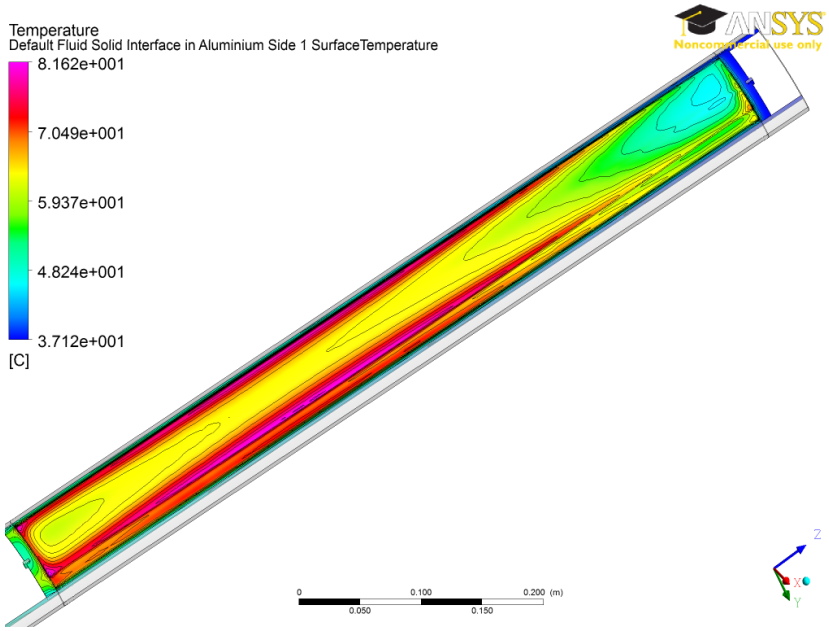

(a)

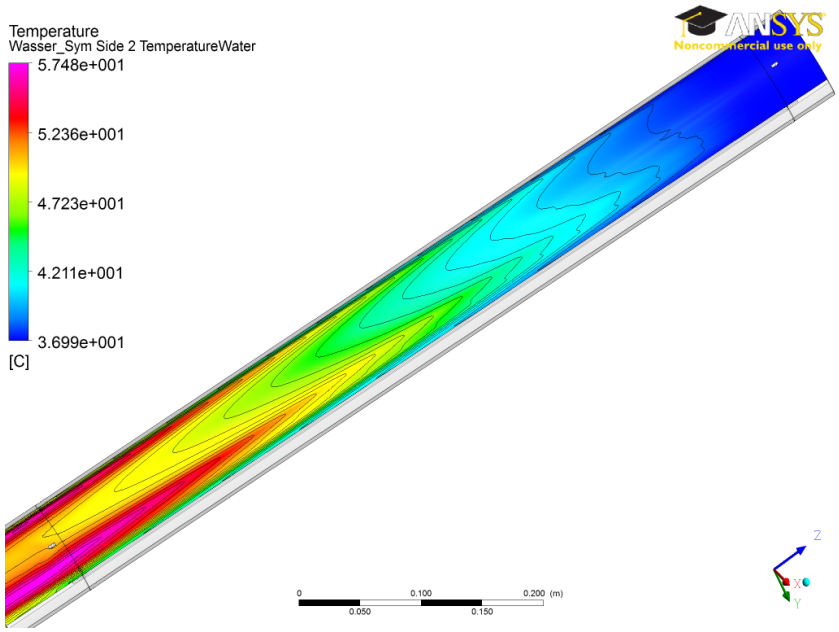

(b)

Figure 15.11: *Temperature distribution of a disperse UMo fuel element with* $8.0\,\mathrm{g\,U/cm^3}$ *at EOL: (a) shows the temperature distribution at the surface of the fuel plate. (b) is the temperature distribution in the flow at the middle of the cooling channel.*

15.8 Heat Flux

The same considerations that were made for the temperatures also hold for the heat fluxes.

15.8.1 Begin of Life

The maximum wall heat flux is now 407.1(15) $\mathrm{W/cm^2}$, 6.5% more than in the current case. This goes hand in hand with the higher maximum power deposition. Together with the higher power deposition in the active zone, the average heat flux density has also increased by 0.1% to 161.5(5) $\mathrm{W/cm^2}$.

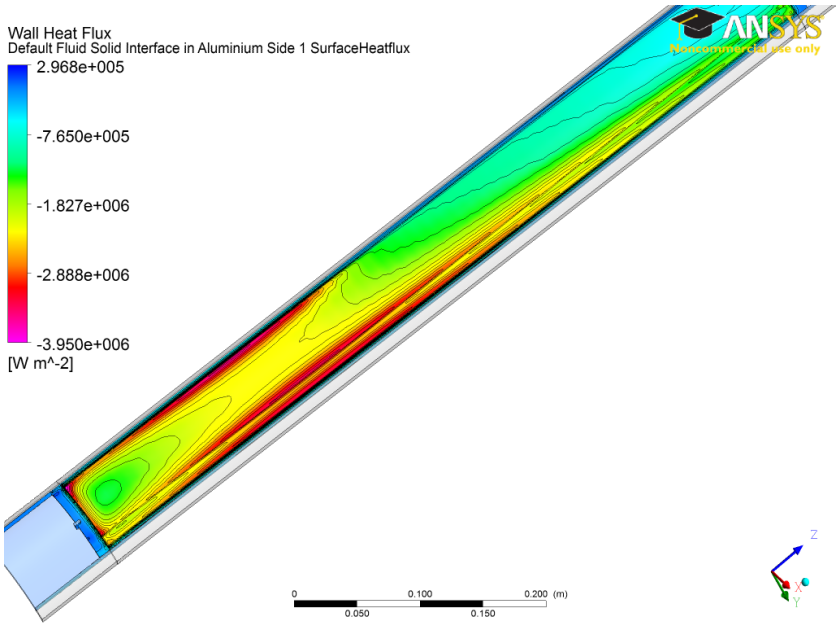

Figure 15.12: *Wall heat flux of a disperse fuel element with* 8.0 $\mathrm{gU/cm^3}$ *at BOL.*

15.8.2 End of Life

Again, the maximum heat flux density at EOL is about 25% lower than at BOL, now 296.4(15) $\mathrm{W/cm^2}$. This is only 3.9 $\mathrm{W/cm^2}$ higher than for the current fuel element. The average heat flux density in the active zone is 161.9(5) $\mathrm{W/cm^2}$ which goes hand in hand with the higher deposited power. Heat flux densities at EOL are shown in fig. 15.13.

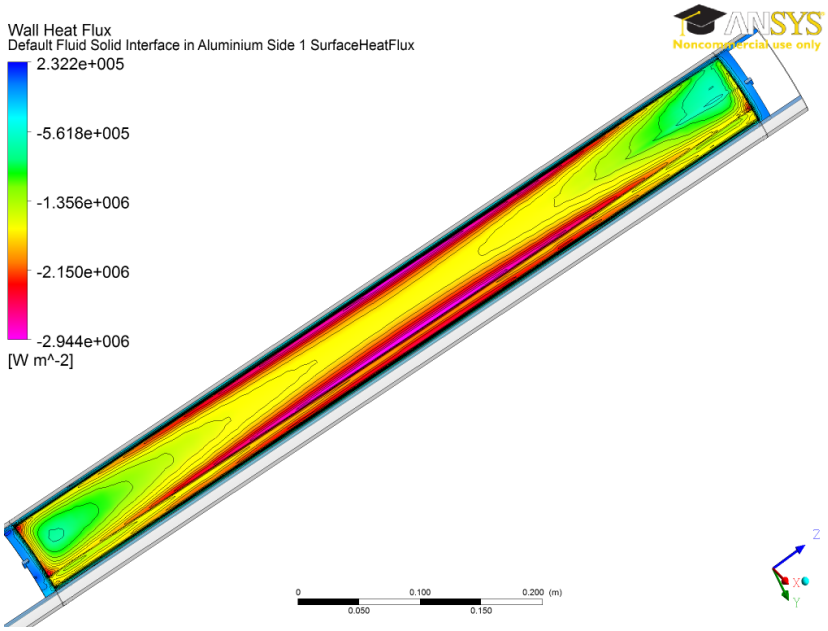

Figure 15.13: *Wall heat flux of a disperse fuel element with* $8.0\,\mathrm{g\,U/cm^3}$ *at EOL.*

15.9 Distance to Boiling

In the framework of disperse UMo, a scenario with a higher reactor power was studied. In this context, it is worthwhile to have a look at the distance to boiling. Concerning the coolant, at 22 MW, the minimum distance is 39 K. This value was calculated in very thin cavities at the edge of the fuel plate adjacent to the lower comb. Due to the multifold effects regarding turbulence in small cavities and the very high resolution required to resolve this region probably, this value is questionable, even more as a hybrid mesh interpolation method was used to determine the value. More credible are the values shown in fig. 15.14. Here, the pressure-effect discussed in chap. 13.6.1, p. 139, can be seen again: Boiling is not likely to occur first over the hotspot or at the end of the fuel zone in the hot fluid element, but at the very bottom of the fuel plate, where the pressure drops rapidly and a cavity is created (red zone figs. 15.14 and 13.15). So, a more realistic value is 50 K.

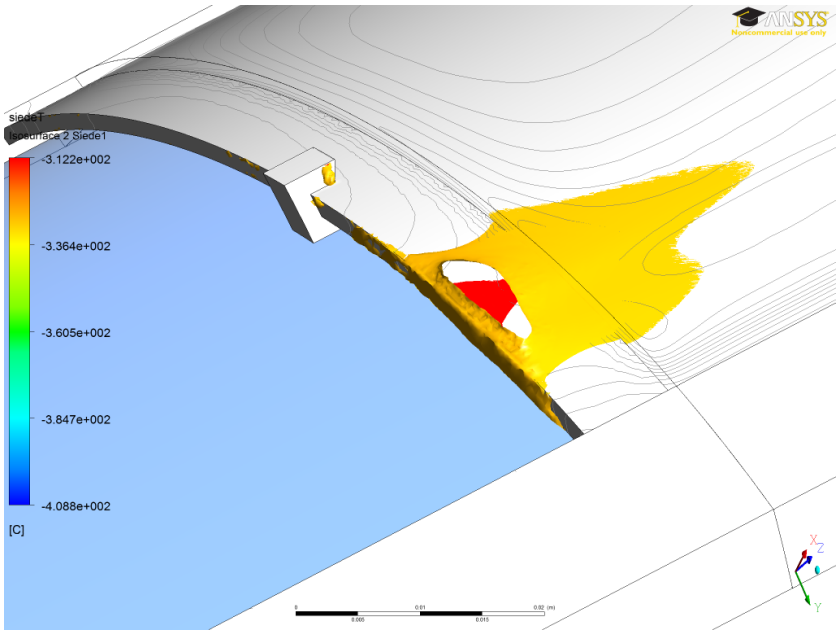

Figure 15.14: *Distance to boiling at 22 MW. Isosurfaces for temperature distance to saturation temperature. Yellow: 55 K, red: 52 K.*

15.10 Final Assessment

The thermal hydraulic properties of the disperse UMo solution are not immoderate inferior to the properties of the current fuel element. For the 8g U/cc-20MW-case, the maximum cladding surface temperature rises only by 2.2 ℃ and the maximum heat flux by 24.8 $^{W}/_{cm^2}$. Both values, maximum temperature and heat flux, are still well below the values that were originally calculated for the present fuel element during the design calculations for FRM II. This means that even if the safety margins for the 8g U/cc-20MW-case calculated in this work are slightly lower than those of the current fuel element, the corresponding values are still higher than what was originally calculated for the present fuel element. Regarding this, even if the current fuel element has physically larger safety margins, the disperse UMo based fuel elements are still very conservative core designs regarding these points when compared just by their numbers to the original calculations for the current fuel element.

The neutronic properties are obviously more unattractive: A flux drop of 6% to 8% in most user areas, 7.7% in the thermal peak and more than 10% for some irradiation positions, up to 8% higher absolute burn-up at EOL, only 7.1% total uranium consumption compared to 15.7% in the current fuel element, about 2.5 times as much radioactive waste[3] and more than six times more plutonium in the spent fuel. This could of course be expected, given the increased uranium content and the increased parasitic absorption due to the severalfold larger ^{238}U content.

It is apparent that 8g U/cc-22MW-60d is the most desirable scenario from the point of view of the scientists using the neutron source as it actually implies no change for users and instrument operators, but it is also the most demanding with respect to fuel qualification and reactor operation and very unlikely to be feasible. A scenario with 8g U/cc-20MW-66d produces the same cycle-neutron-yield without posing the burdens connected to an increase of the reactor power but still suffers from the very high burn-up of the fuel. It is yet unclear, if such a high burn-up can be reached safely. However,

[3] The amount of radioactive waste is calculated under the assumption that the whole remaining uranium inventory including the fission products has to be disposed.

if the current standard of 4 cycles per year should be kept, the shorter reactor down-times (-20%) will imply higher demands on the operational team of the reactor. Accordingly, if feasible at all, only a fractional compensation of the flux loss due to the conversion seems to be a realistic option at the moment.

The two straightforward scenarios, a conversion without increase in cycle length and reactor power, deliver the most disadvantageous performance regarding the cycle neutron yield. Of those two, 8g U/cc-20MW-60d is the most likely scenario and also regarded as the minimum requirement by [Röh05]. 7.5g U/cc-20MW-60d leaves no room for increased reactor usage, neither does it contain any reactivity reserves to compensate reactor degradation due to ageing or other flux depressing effects. Therefore, for a future-proof operation of FRM II using 50% enriched disperse UMo, a minimum uranium density of $8\,\mathrm{g/cm^3}$ is required.

15.10.1 Possible Optimisation

A large variety of parameter scenarios for the current fuel element were already studied in the 1980s [Röh91a]. These studies layed the foundation for the current fuel element. As discussed above, the neutronic and thermal hydraulic properties of the straight-forward disperse UMo solution are inferior to that of the current fuel element. A continuation of theses studies for the new fuel, which changes the parameters, is therefore reasonable. The thermal hydraulic and burn-up properties can be adjusted slightly. An additional density step to lower uranium densities in the inner zone at the side of the control rod will decrease the power deposition per $\mathrm{cm^3}$ active zone and mitigate the hotspot. The latter could also be achieved by means of an additional boron ring, but that would bind reactivity. To ease the situation at the outer border of the fuel element, the density of the outer fuel zone could be reduced slightly. Anyhow, this would aggravate the situation at the original density step, which might make it necessary to include a third density step. It is questionable if this additional effort during fabrication is acceptable.

To compensate the flux loss without a power increase or an increased cycle length, a further compaction of the fuel element will be necessary. The flux gain for a straight-forward decrease, keeping all outer dimensions except the length, is shown in fig. 15.15 (graph is preliminary). However, this is only possible if the thermal hydraulic properties of the straight-forward conversion option that is presented in this work are optimised. There are methods which can more easily be realised than the one depicted above: A skew density step instead of a vertical step would reduce the radial form factor at the step, therefore attenuating the formation of the hot stream filament at the step. Additionally, a slightly skew outer fuel zone margin would also help to attenuate the outer hot stream filament.

Besides the thermal hydraulic and burn-up properties, the compaction is limited by the maximum uranium density that is available, currently about $8.75\,\mathrm{g/cm^3}$ [Jun10]. A compaction of the fuel element would influence the reactivity in a negative way, leading to shorter cycle lengths with the same uranium loading. To compensate this, the width of the cooling channels would have to be varied. As a compaction – if thermal hydraulic properties allow for this – would already utilise the maximum fuel density, the cooling channels can only be widened at the cost of the cladding thickness or by reducing the number of plates.[4] At HFIR, which has comparable thermal hydraulic properties, the cladding thickness is 0.256 mm [IAE], 33% less than what is used at FRM II, giving room for an increase of the cooling channel width of 11%. Obviously, it has to be analysed how the decreased pressure drop due to the higher channel width would affect the overall system in terms of total mass throughput and flow branching. A simple application of the sensitivity matrix (tab. 17.12) is therefore only a rough approximation. Additionally, the mechanical stability of the fuel plate would have to be simulated and probably measured again. In addition, a smaller cladding thickness would reduce the amount of laterally conducted heat and therefore lead to slightly more pronounced peak structures. However, the effect of

[4] Of course it should be discussed if a slight increase of the radial expansion of the fuel is feasible, now that the fluid parameters in the corners between ducts and plates are well known, see chapter 13.4, page 136.

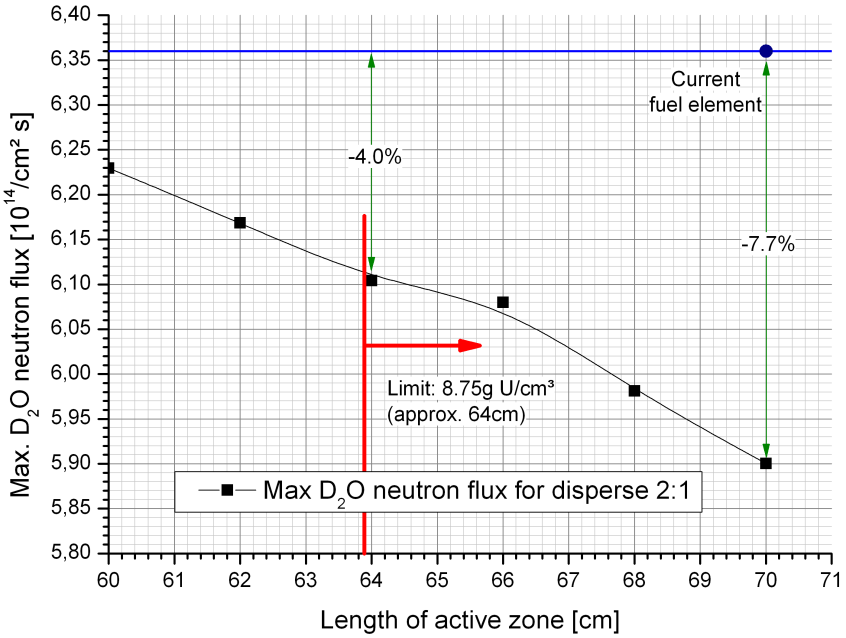

Figure 15.15: *Maximum thermal neutron flux in the D_2O for a disperse UMo fuel element, depending on the length of the active zone [Sar11]. One of the limiting factors is the achievable uranium density, 8.75 g/cm^3. The 7.7% flux loss are for the straight-forward 8 g-conversion. Values are preliminary!*

the latter is only very small if the thermal conductivity of the fuel and the cladding do not deviate too much.

Besides the density, the thickness of the fuel can be varied, too. Steps in the thickness are much more easy to realise in the production process of the fuel plates than density steps. However, this doesn't help much regarding the maximum burn-up of the fuel, which is normally expressed in $^{fissions}/_{cm^3}$.

The optimisation of the disperse element is currently studied by J. Sarvas [Sar11].

CHAPTER 16

Results for a Monolithic Fuel Element

For monolithic UMo, an enrichment of 40% was chosen as the higher density of monolithic UMo allows for a lower enrichment. The fuel zone has a constant density but a variable thickness. The thickness profile was chosen similar to [Röh06], but with a higher maximum thickness, as the study of [Röh06] was conducted with a higher enrichment (50%). The calculations of [Röh06] were conducted for a cycle length of 52 d with a reactivity reserve for one additional week.

Quantity	425 µm	425 µm */22 MW*	425 µm */66 d*	320 µm *flat*
Fuel plate parameters (BOL)				
Max. deposited power	3.63(7) $^{MW}/_{l}$	3.99(8) $^{MW}/_{l}$	3.63(7) $^{MW}/_{l}$	4.00(7) $^{MW}/_{l}$
Deposited power	18.04+0.22 MW	19.84+0.24 MW	18.04+0.22 MW	18.09+0.23 MW
BOL Content ^{235}U / U	11.3 kg/28.6 kg	11.3 kg/28.6 kg	11.3 kg/28.6 kg	9.9 kg/25.1 kg
Burn-up				
Max. Burn-up	40.2%	42.1%	43.3%	34.6%
Max. Burn-up absolute	$5.52 \cdot 10^{21}$ $^{1}/_{cm^3}$	$5.99 \cdot 10^{21}$ $^{1}/_{cm^3}$	$5.96 \cdot 10^{21}$ $^{1}/_{cm^3}$	$4.85 \cdot 10^{21}$ $^{1}/_{cm^3}$
Avg. Burn-up	13.5%	14.8%	14.9%	15.1%
Min. Burn-up	3.9%	4.6%	4.7%	4.4%
Avg. residual enrichment	35.9%	35.6%	35.5%	35.4%
Fluxes $[^{1}/_{s\,cm^2}]$				
Max. thermal D_2O	$5.84(2) \cdot 10^{14}$	$6.42(3) \cdot 10^{14}$	$5.84(2) \cdot 10^{14}$	$5.81(2) \cdot 10^{14}$
Max. thermal overall	$6.74(4) \cdot 10^{14}$	$7.42(6) \cdot 10^{14}$	$6.74(4) \cdot 10^{14}$	$6.77(4) \cdot 10^{14}$
Max. fast	$8.77(1) \cdot 10^{14}$	$9.65(2) \cdot 10^{14}$	$8.77(1) \cdot 10^{14}$	$8.71(2) \cdot 10^{14}$
Cycle neutron yield $[^{1}/_{cm^2}]$	$2.97(2) \cdot 10^{21}$	$3.27(3) \cdot 10^{21}$	$3.29(2) \cdot 10^{21}$	$2.96(3) \cdot 10^{21}$
Flux compared to current fuel element [%]				
In thermal max. D_2O	-8.2(3)%	+0.9(3)%	-8.2(3)%	-8.6(3)%
In thermal max. overall	-9.8(5)%	-0.7(5)%	-9.8(5)%	-9.4(5)%
In fast max.	-4.5(3)%	+5.1(3)%	-4.5(3)%	-5.1(4)%
Cycle neutron yield	-7.5(4)%	+1.9(4)%	+2.5(4)%	-7.8(4)%

Table 16.1: *Results for the simulation of a monolithic UMo fuel element (neutronics). All values are at BOL if not quoted otherwise.*

In [Röh05], a lower limit of 34% enrichment was derived, a purely theoretical neutronic calculation with flat plates without regarding thermal hydraulics. The monolithic plates that were regarded in this work have a radial thickness gradient to flatten the power profile. Additionally, a plate without thickness gradient was regarded. The requirement was again a cycle length of 60 d plus a reactivity reserve.

Quantity	*Value* 425 µm	*Value* 425 µm */22 MW*	*Value* 320 µm *flat*	*Remarks*
Temperatures [°C]				
Max. Fuel	129.9(5)	138.1(5)	136.2(5)	$> +27.0\,\mathrm{K}$
Avg. Fuel	74.8(5)	78.3(5)	74.6(5)	$> +6.6\,\mathrm{K}$
Max. Wall	91.7(3)	96.5(3)	100.0(3)	$> +2.1\,\mathrm{K}$
Avg. Wall	61.9(3)	64.2(3)	62.0(3)	active zone
Avg. Outlet	53.0(1)	54.6(1)	53.0(1)	-
Heat Flux [$\mathrm{W/cm^2}$]				
Max. Wall	401.9(15)	442.9(15)	458.0(15)	$> +5.1\%$
Avg. Wall	161.3(5)	177.5(5)	161.4(5)	active zone
Pressure [bar]				
Avg. pressure drop	5.21(10)	5.20(10)	5.21(10)	unchanged
Max. pressure	8.45(10)	8.44(10)	8.46(10)	unchanged
Min. pressure	0.75(3)	0.75(3)	0.75(3)	unchanged
Safety margins				
S_{ONB}	2.40	2.18	2.29	-
S_{DNB}	2.31	2.08	2.42	-
S_{OFI}	5.15	4.55	4.84	-

Table 16.2: *Results for the simulation of a monolithic UMo fuel element (thermal hydraulics). All values are at BOL if not quoted otherwise.*

16.1 Fuel plate design

It will be shown later in this chapter (sec. 16.9), that a flat plate of monolithic UMo has very unfortunate thermal hydraulic paramters. As an option, a thickness profile was introduced to account for the distribution of fission densities and balance the heat load. It was named 'turkish hat profile', as it somewhat resembles the shape of a turkish fez hat. This thickness profile was originally introduced by [Röh06] for a monolithic FRM II fuel, but as mentioned above with other determining factors in mind, especially a higher degree of enrichment. Therefore, in this work, a significantly larger maximum thickness of at least 400 µm was calculated to be able to use 40%-enriched fuel and guarantee a cycle length of 60 d. However, as in the case of the disperse fuel, for the given shape, this is the absolute minimum possible with the profile shown in fig. 16.1. This means that there is no reactivity reserve at the end of the cycle in this case. It is therefore of advantage to use a slightly higher thickness of 425 µm. This leads to a total uranium content of 28.6 kg at BOL, 11.3 kg ^{235}U (400 µm: 26.9 kg / 10.6 kg). With 50% enriched monolithic UMo, [Röh06] only needed 9.1 kg fissionable uranium. The 400 µm-case is not further regarded for the same reasons as discussed in chapter 15 for the 7.5g U/cc disperse UMo case.

The boundary conditions for the flow are the same as those for the current fuel element, as there should be no change in the cooling system. Hence, the data can be taken from table 13.1.

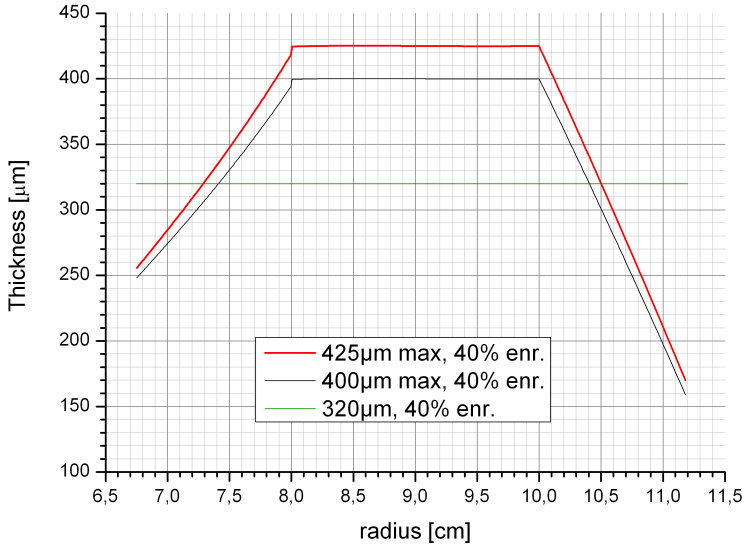

Figure 16.1: *Thickness profile of UMo plate.*

16.2 Control Rod Reactivity profile

As in the case of disperse UMo, due to the larger parasitic absorption in the core (^{238}U), the reactivity profile of a fresh core made from monolithic UMo is flatter than that of the current core (see fig. 16.2).

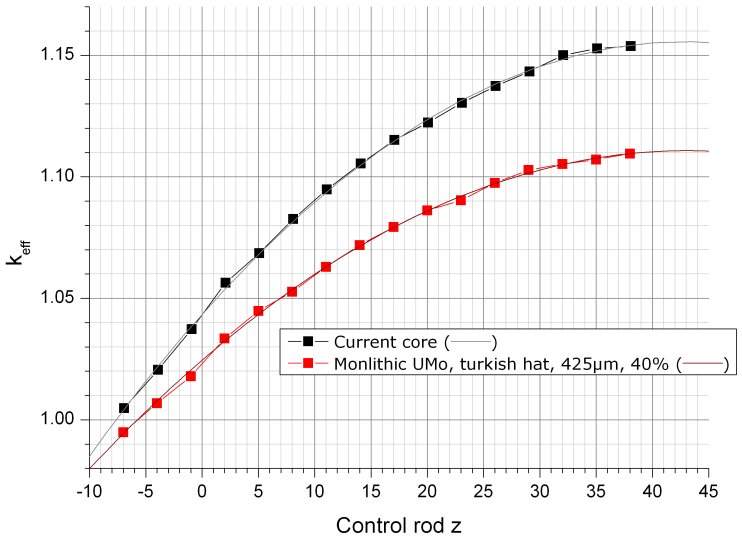

Figure 16.2: *k_{eff} over control rod position for a fresh core of the current fuel element and of a monolithic fuel.*

16.3 Burn-up

With decreasing enrichment of the fuel, the content of fissionable ^{235}U has to be increased further and further to overcompensate the increased absorption due to the multiple times larger ^{238}U content compared to the current HEU design. This will lead to significantly higher absolute burn-ups.

The predicted movement curve of the control rod is shown in fig. 16.3. For comparison, the measured curve of the actual cycle 15 is also shown. Again, it can be seen that the driveway is slightly modified by the overcompensation in the uranium density.

For the 425 µm design, after 60 [d] at 20 MW, the maximum burn-up was determined to be 40.2%, the average burn-up is 13.5%. The residual average enrichment is 35.9%, while in the zone of maximal burn-up the residual enrichment has dropped to 27.6%. In absolute numbers, the maximum burn-up is $5.52 \cdot 10^{21}$ $^1/_{cm^3}$, which is quite high. The spot of this burn-up is located near the core midplane at the outer border of the fuel plates. The burn-up in the controlrod-facing part of the fuel plate is max. $3.65 \cdot 10^{21}$ $^1/_{cm^3}$.

If the cycle length is extended to 66 d or the power increased to 22 MW to compensate the flux loss, the maximum burn-up rises to 43.3% / $5.99 \cdot 10^{21}$ $^1/_{cm^3}$.

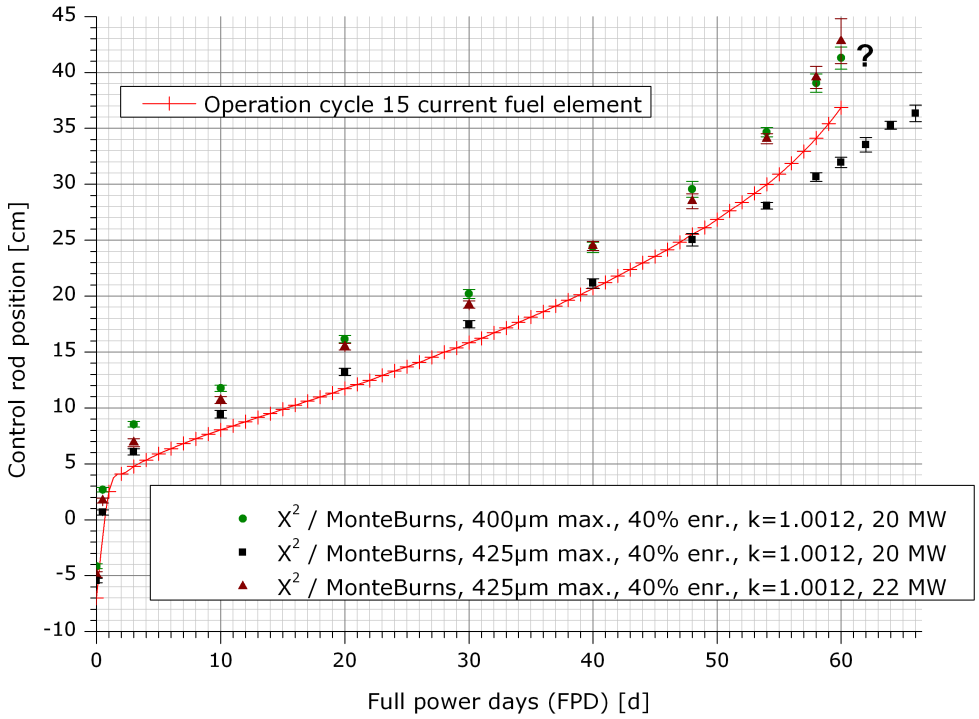

Figure 16.3: *Control rod position depending on the number of full power days (FPDs) for various maximum thicknesses in monolithic UMo.*

16.3.1 Actinide Inventory at EOL

The actinide inventory after 60 d at 20 MW for the 425 µm case is listed in table 16.3. A total of 1.52 kg ^{235}U was consumed. The loss in ^{238}U is 115.6 g, while the Pu-content at EOL is 97.9 g, 89.7 g ^{239}Pu thereof. In addition, 6.8 g ^{239}Np will decay to ^{239}Pu.

Isotope	*Quantity* [g]	*Isotope*	*Quantity* [g]	*Isotope*	*Quantity* [g]
Actinides					
^{234}U	93.360	^{237}Np	4.699	^{240}Pu	5.973
^{235}U	9787.332	^{238}Np	0.032	^{241}Pu	1.909
^{236}U	320.009	^{239}Np	6.806	^{242}Pu	0.072
^{237}U	1.534	^{238}Pu	0.199		
^{238}U	17049.833	^{239}Pu	89.701		
Non-Actinides					
^{1}H	$9.657 \cdot 10^{-5}$	^{98}Mo	642.167	^{143}Ce	1.471
^{2}H	$8.208 \cdot 10^{-9}$	^{100}Mo	282.795	^{141}Pr	19.048
^{3}H	$1.413 \cdot 10^{-6}$	^{99}Tc	28.799	^{143}Pr	13.617
^{3}He	$1.380 \cdot 10^{-13}$	^{101}Ru	27.621	^{143}Nd	28.112
^{4}He	0.533	^{102}Ru	23.493	^{145}Nd	29.280
^{7}Li	0.933	^{103}Ru	10.501	^{146}Nd	24.252
^{9}Be	$7.176 \cdot 10^{-7}$	^{103}Rh	6.187	^{147}Nd	4.434
^{10}B	0.150	^{105}Rh	0.203	^{148}Nd	13.923
^{11}B	$1.910 \cdot 10^{-4}$	^{117}Rh	$1.463 \cdot 10^{-10}$	^{147}Pm	11.297
^{12}C	$4.640 \cdot 10^{-10}$	^{105}Pd	5.257	^{148m1}Pm	0.126
^{13}C	$4.890 \cdot 10^{-16}$	^{119}Pd	$4.527 \cdot 10^{-10}$	^{149}Pm	0.536
^{27}Al	170.000	^{109}Ag	0.375	^{149}Sm	0.752
^{28}Si	0.025	^{113}Cd	0.020	^{150}Sm	7.949
^{29}Si	$1.310 \cdot 10^{-6}$	^{129}I	4.601	^{151}Sm	1.468
^{30}Si	$3.300 \cdot 10^{-11}$	^{131}I	3.896	^{152}Sm	3.666
^{83}Kr	2.287	^{135}I	0.297	^{153}Sm	0.133
^{93}Zr	31.352	^{131}Xe	15.248	^{153}Eu	1.765
^{95}Zr	23.661	^{133}Xe	5.959	^{154}Eu	0.161
^{95}Nb	5.837	^{135}Xe	0.082	^{155}Eu	0.101
^{92}Mo	350.376	^{133}Cs	39.380	^{156}Eu	0.151
^{94}Mo	223.856	^{134}Cs	0.912	^{157}Eu	0.002
^{95}Mo	387.730	^{135}Cs	9.432	^{157}Gd	0.006
^{96}Mo	417.003	^{139}La	47.714		
^{97}Mo	268.847	^{141}Ce	24.702		

Table 16.3: *Result of burn-up calculation for monolithic UMo, EOL after 60 d*

16.3.2 Non-Actinide Inventory at EOL

The non-actinide inventory after 60 d at 20 MW for the 425 µm case is also listed in table 16.3. It comprises the inventory of the fuel zone and the boron ring.

16.3.3 Boron Ring

After 60 FPDs, 0.15 g ^{10}B is left in the boron ring. This is slightly more than in other scenarios.

16.4 Power Deposition

In comparison to the current fuel element and the disperse scenario from the preceding chapter, the monolithic solution has no density step but a continuous thickness profile. This results in a fission density distribution with lower peak values but platier gradients. This leads to a lack of sinks in the power deposition density and therefore to higher heat flux densities, even though the peaks are lower. It is one of the main tasks in the optimisation process to adjust these gradients in a way that delivers an acceptable power density without increasing the burn-up too much.

16.4.1 Begin of Life

The power deposition at BOL is shown in fig. 16.4. The enlarged detail in this figure clearly shows the much less pronounced structure mentioned above in comparison to the disperse solution or the current case. As trade-off, there is a large zone with power densities beyond 1.5 $^{\mathrm{MW}}/_{\mathrm{l}}$ on the outer side of the fuel plate. It will be shown later in this chapter that even though the power density is below 2.25 $^{\mathrm{MW}}/_{\mathrm{l}}$, this zone leads to significant heating of the coolant.

The less pronounced structure is also expressed in the peak power deposition, which is now only 3.63(7) $^{\mathrm{MW}}/_{\mathrm{l}}$, about 10% lower than today. The point of highest fission density is located near the hotspot in the very inner lower corner of the fuel plate. The total power deposition is 18.04 MW in the fuel and 0.22 MW in the surrounding, cooling relevant structural materials. This is about the same as for the current and the disperse solution.

16.4.2 End of Life

Towards EOL, the power deposition is even more homogeneous. The peak power deposition decreases significantly to 2.35 $^{\mathrm{MW}}/_{\mathrm{l}}$. This value can be found at lower border of the fuel, approximately at the place where the outer thickness gradient starts (r =9.8 cm). The total power deposition rises according to the more centred power distribution to 18.24 MW for the active zone, plus 0.23 MW for the structural zone.

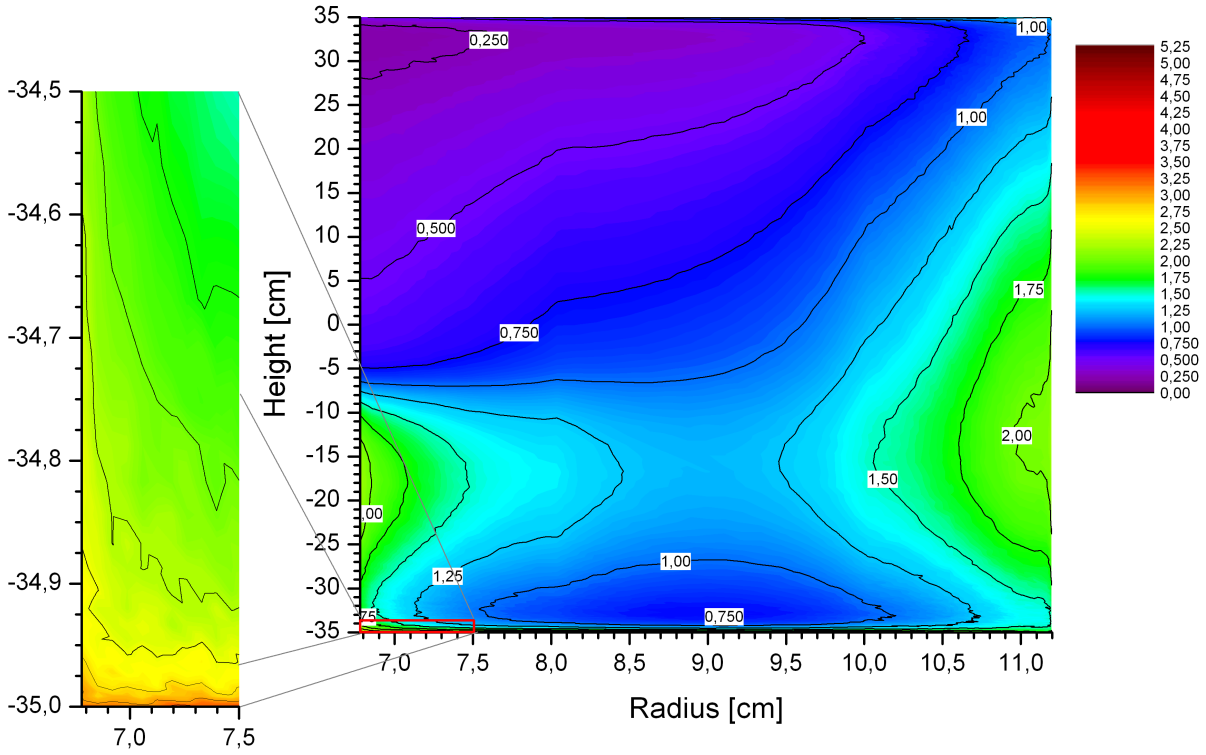

Figure 16.4: *Power deposition for the monolithic UMo fuel element at BOL in* $^{MW}/_{l}$.

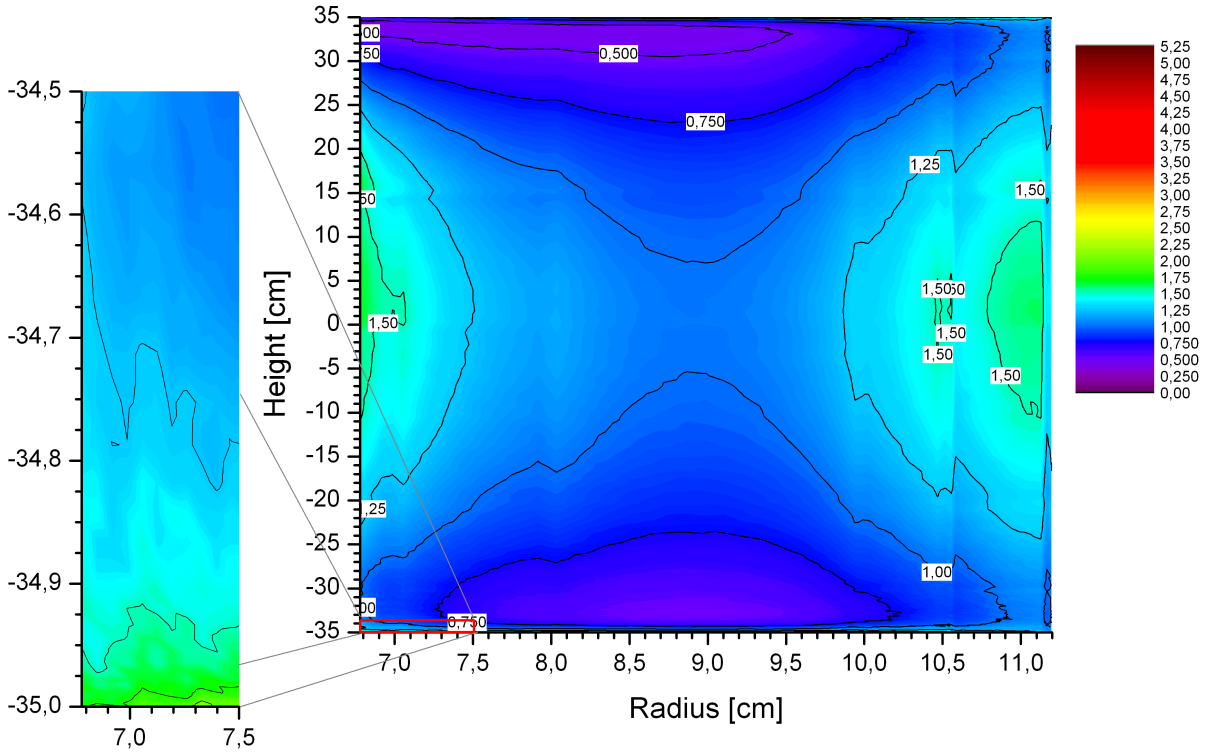

Figure 16.5: *Power deposition for the monolithic UMo fuel element in $^{MW}/_{l}$ after 60 FPDs at EOL.*

16.5 Flux

Again, as in the case of disperse UMo, the increased absorption in the fuel element will lead to significantly lower thermal and fast neutron fluxes. While this is not relevant for the fuel plates themselves, a drop of the thermal peak flux in the D_2O will result in comparably lower efficiency at the linked experiments.

16.5.1 Begin of Life

At BOL, the peak thermal flux in the D_2O has decreased by 8.8%, now $5.84(2) \cdot 10^{14}\,\mathrm{n/s\,cm^2}$. This is even less than in the case of disperse UMo and can be attributed to the even further decreased enrichment. The position of this peak remained at 21.5 cm / -10.5 cm. Also the overall maximum thermal flux in the beryllium follower has decreased stronger, now 13.3%, down to $6.74(4) \cdot 10^{14}\,\mathrm{n/s\,cm^2}$. Similarly, the maximum fast flux has decreased by 4.9% to $8.77(1) \cdot 10^{14}\,\mathrm{n/s\,cm^2}$. The peak fast neutron flux is still located in the fuel plate at 7.8 cm / -17.5 cm.

Flux densities at BOL are shown in fig. 16.6(a) for the thermal and 16.6(b) for the fast flux. The difference of the thermal flux compared to the current fuel element is shown in fig. 16.7. In this case, in the relevant zones of the D_2O-tank, the flux decreases averagely between 7% and 10%. Again, the relative flux loss increases with decreasing distance to the fuel plates. This results in a lower fission density in these regions and could already be observed in fig. 16.4. The fine grained structures in the upper left corner are noise resulting from insufficient statistics.

16.5.2 End of Life

Again, the flux situation gets worse at EOL. The expansion of the high flux zone towards EOL is nearly not present anymore. The peak drop is now -10.2%, down to $5.82(1) \cdot 10^{14}\,\mathrm{n/s\,cm^2}$. The location of this maximum only shifted slightly to 21.0 cm / -0.5 cm. The maximum thermal flux in the beryllium follower is -13.4% down to $5.28(4) \cdot 10^{14}\,\mathrm{n/s\,cm^2}$. Flux densities are shown in fig. 16.8(a) for the thermal flux and 16.8(b) for the fast flux.

At the position of the BOL thermal maximum, the flux has decreased to $5.58(1) \cdot 10^{14}\,\mathrm{n/s\,cm^2}$, 4.5% less than at BOL. All in all, this sums up to a cycle neutron yield for this point of $2.97(2) \cdot 10^{21}\,\mathrm{n/cm^2}$, which is 11.1% less than in the current situation.

Thermal flux differences to the current fuel element are shown in fig. 16.9. The scale is unchanged from fig. 16.7 which indicates a much stronger and widespread loss of thermal neutrons in the D_2O approaching the fuel element. The small flux increase at 1.0 cm / 20.0 cm stems from slightly different control rod positions.

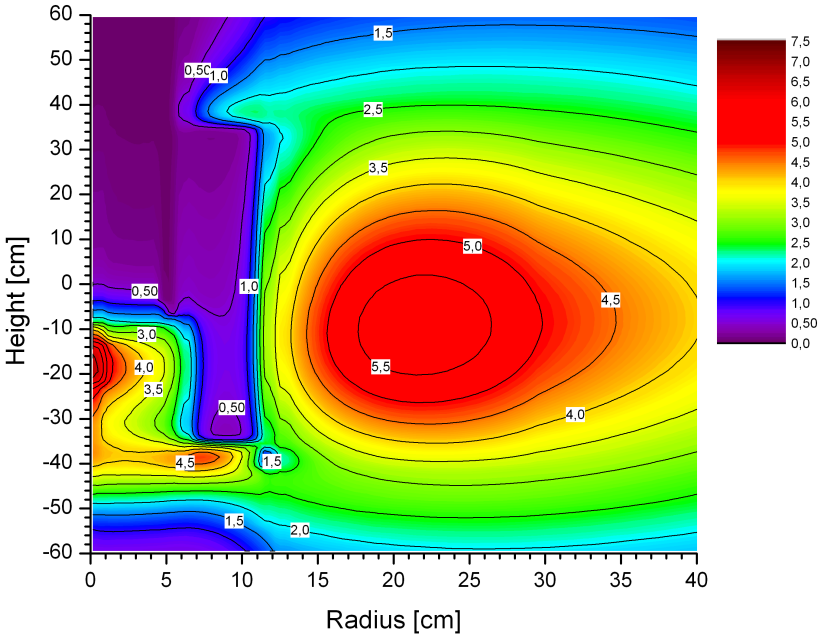

(a) Thermal flux

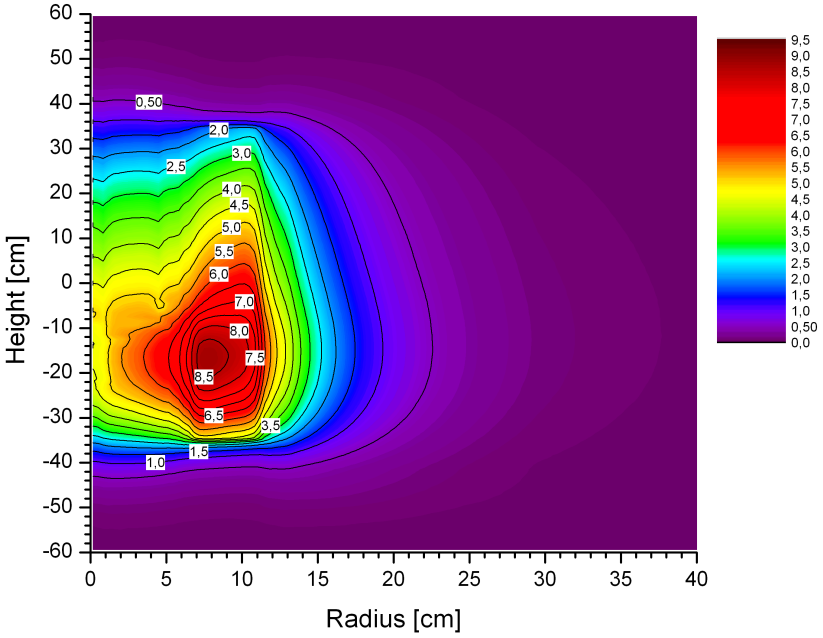

(b) Fast flux

Figure 16.6: *Flux profiles for a monolithic UMo fuel element at BOL: (a) is the thermal flux* $\leq 0.625\,eV$*, (b) the fast flux* $\geq 100\,keV$*.*

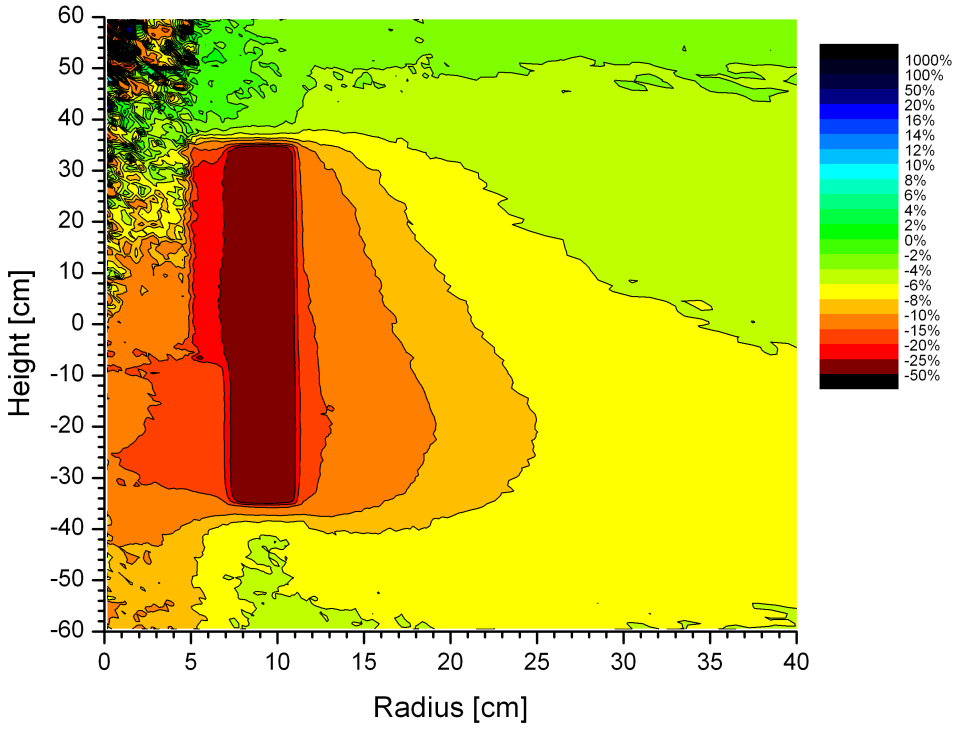

Figure 16.7: *Thermal flux difference between monolithic UMo and current fuel element at BOL.*

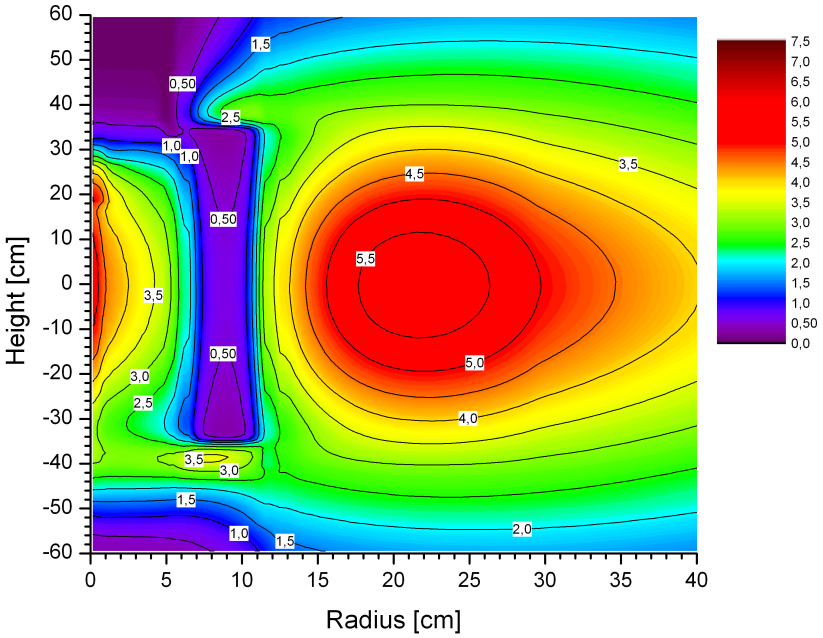

(a) Thermal flux

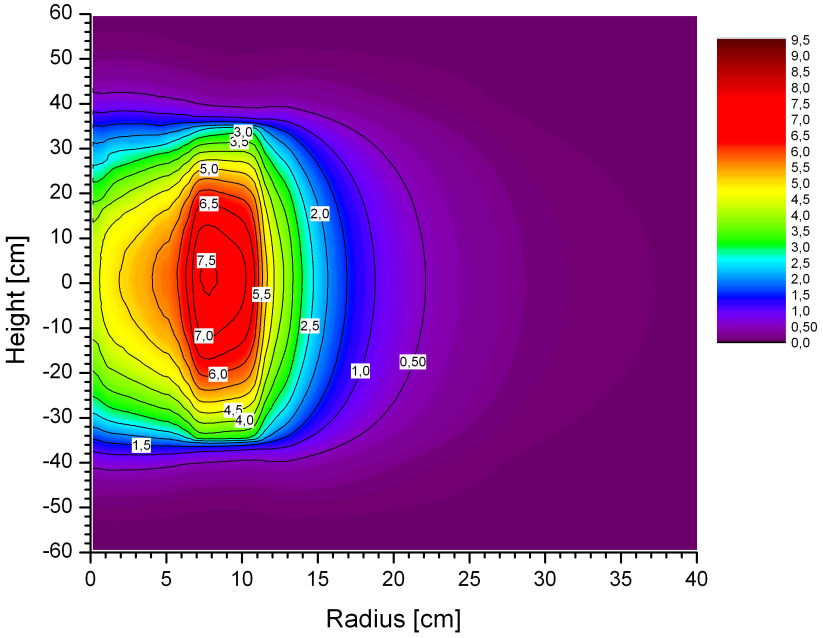

(b) Fast flux

Figure 16.8: *Flux profiles for a monolithic fuel element at EOL: (a) is the thermal flux $\leq 0.625\,eV$, (b) the fast flux $\geq 100\,keV$.*

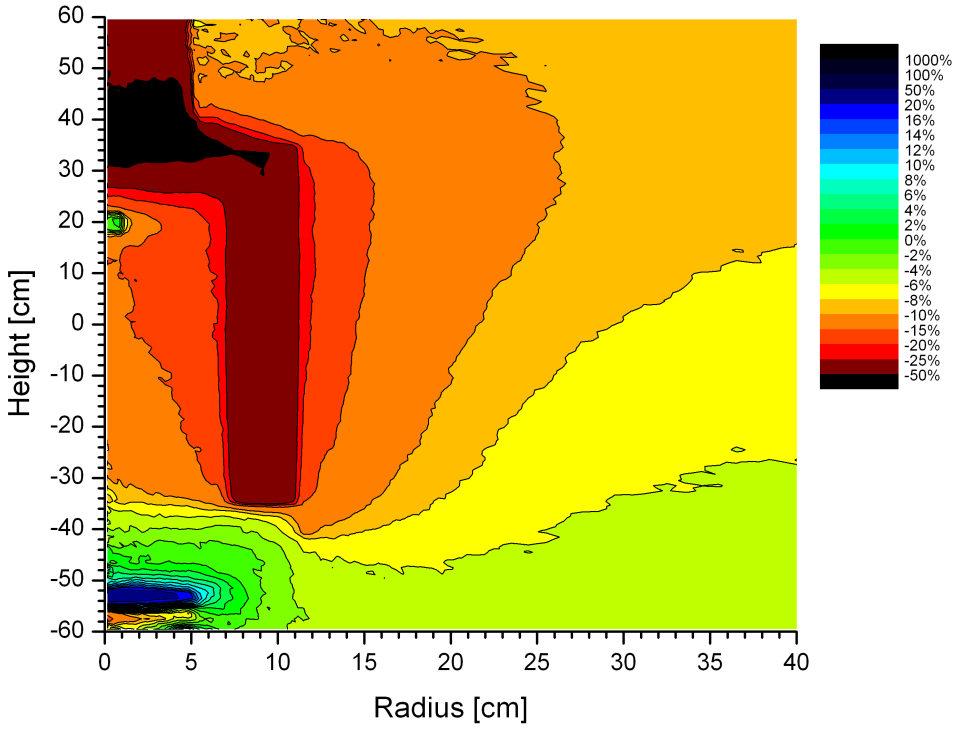

Figure 16.9: *Thermal flux difference between monolithic UMo and current fuel element at EOL.*

16.6 Pressure Drop

No changes were observed in the pressure drop of 5.2(1) bar.

16.7 Temperatures

It is obvious that due to the changed inner plate geometry, the temperature distribution of the monolithic fuel plate will differ significantly from that of the current fuel element and of the disperse scenario. This could already be observed in the power density distribution that was shown in fig. 16.4.

16.7.1 Begin of Life

Due to the low thermal conductivity of monolithic UMo (see chap. 10.1.6, p. 103), the meat temperature rises considerably compared to other solutions. The maximum temperature has risen to 129.9(5) ℃. As before, this hotspot is located in the lower inner corner of the fuel plate, see fig. 16.10(b). It is noteworthy that due to the thickness gradient, the hotspot has notably expanded in radial direction. In fact, the hotspot in the meat is located near the outer border (thicker plate) of the hot spot area. Fuel temperatures above 100 ℃ can also be found near the inner border of the fuel plate, adjacent to the control rod beryllium follower. The outer zones, facing the D_2O, do not heat up to more than 107(5) ℃.

However, regarding surface temperatures, there are two large comparably hot zones at the inner and outer borders of the fuel plate. Fig. 16.10(a) shows the two zones clearly. Again, they do not shelter the hotspot (91.7(3) ℃), but their large extent heats up the fluid in these stream filaments notably. The surface temperature average is 61.9(3) ℃, which seems slightly lower than for the current fuel element and the disperse solution. In this analysis, care must be taken about the influence of the mesh. While the thermal hydraulic calculations for the disperse UMo scenario has been calculated with the same mesh as the current fuel element, a new mesh had to be constructed for the monolithic calculations. This means that all systematic deviations in the disperse-current comparisons cancel, while they do not in the comparison for the monolithic UMo core. In short, for the monolithic UMo core the uncertainties of the calculations must be more considered than for the disperse UMo core.

Fig. 16.11 shows the water temperature in the middle of the cooling channel at the lower end of the fuel zone. The turkish hat profile, compared to the original density step solution, leads to a sharpening of the outer hot stream filament. Also in this case, the power distribution is more unfortunate than today's solution, although it lacks the accentuated peak structure. As mentioned before, the downside is the large zone of relatively high power deposition density with flat gradients.

16.7.2 End of Life

As in all other scenarios, the situation eases up towards EOL. The more fortunate power distribution leads to significantly lower maximum fuel (107.1(5) ℃), maximum surface (82.9(3) ℃) and average wall (56.6(3) ℃) temperatures. The increased power deposition is also reflected by a slightly higher outlet temperature of 53.3(1) ℃.

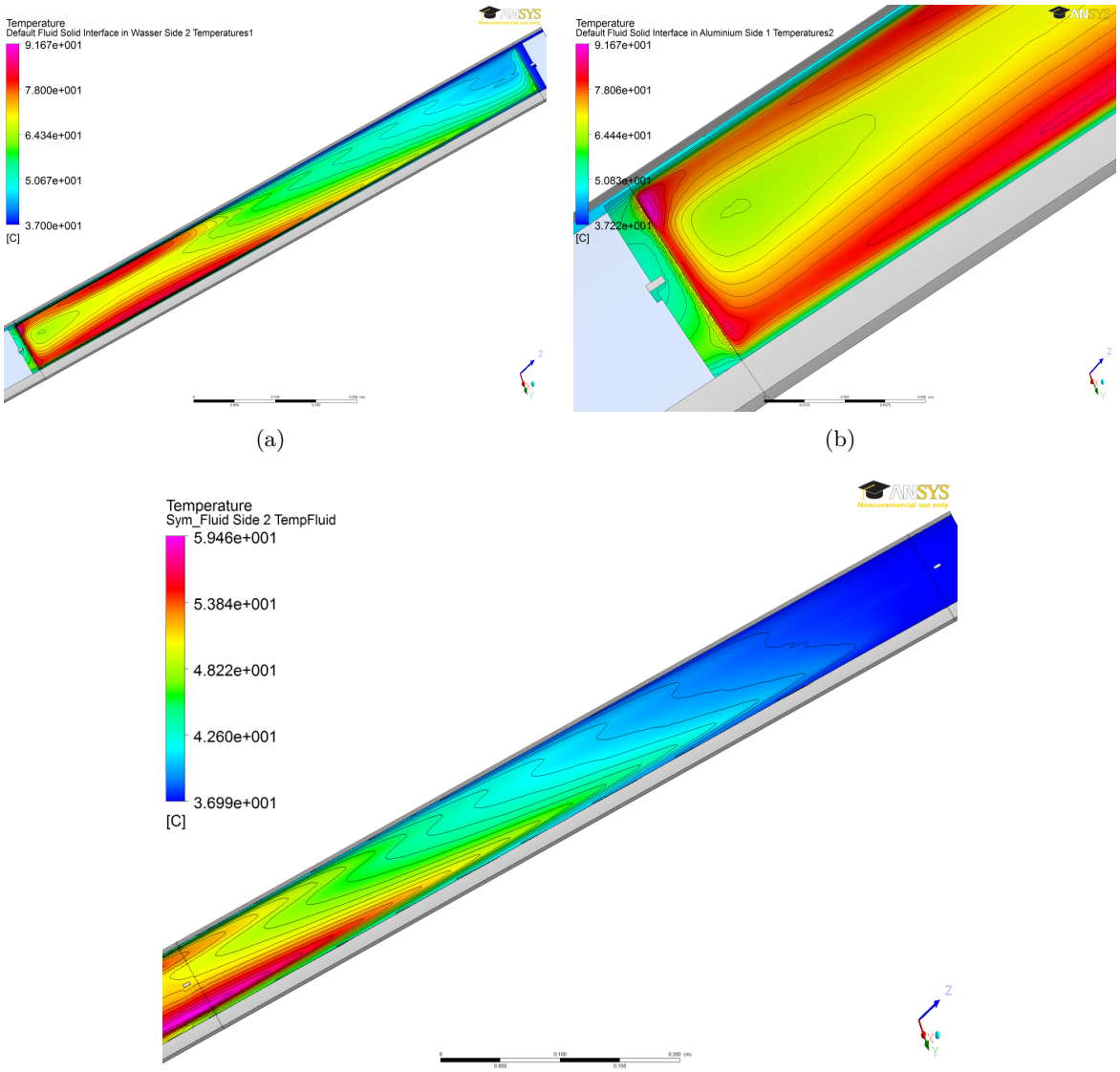

Figure 16.10: *Temperature distribution of a monolithic UMo fuel element at begin of life: (a) shows the temperature distribution at the surface of the fuel plate. (b) is a closer view of the hotspot area. (c) is the temperature distribution in the flow at the middle of the cooling channel.*

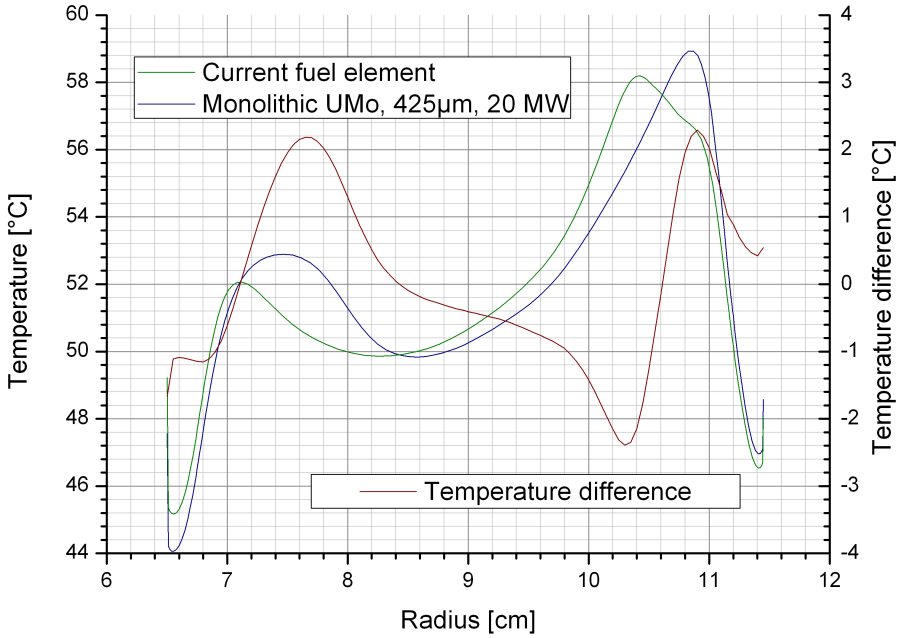

Figure 16.11: *Comparison of water temperature at the lower end of the fuel zone in the middle of the cooling channel at BOL.*

16.8 Heat Flux

As in the disperse case, the same considerations that were made for the temperatures also hold for the heat fluxes.

16.8.1 Begin of Life

The maximum wall heat flux is now 401.9(15) W/cm^2, 5.1(3)% more than in the current case. This goes hand in hand with the higher maximum power deposition. This is slightly lower than what was calculated for the 8g U/cc-20MW-disperse UMo solution, but spread over a much larger area. While this may first look like a contradiction to the lower maximum power distribution, it can be explained by the fact that due to the thickness profile in radial direction the zone of high power distribution is spread over a larger area and not really a point spot in the lower inner corner of the fuel plate. If this is the case, from the point of view of heat flux on the cladding surface, the 3D heat conduction in the solid does not flatten the power distribution as much as it does if there are steep gradients present. Therefore, even though the maximum power distribution value is lower, the maximum heat flux density is higher. The average heat flux density in the active zone is still 161.3(5) W/cm^2, slightly less as the fission density is shifted towards the outer border of the fuel plates and 3D heat conduction guides the heat outside of the active zone.

16.8.2 End of Life

As before, the maximum heat flux density at EOL is about 25% lower than at BOL, now 292.2(15) W/cm^2. This is the same as for the current fuel element. The average heat flux density in the active zone is 161.7(5) W/cm^2 which goes hand in hand with the higher deposited power.

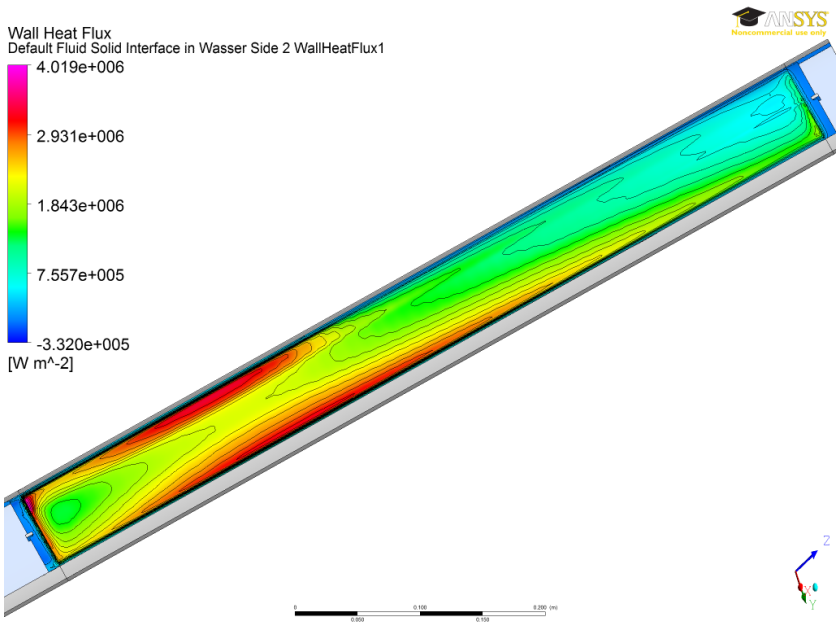

Figure 16.12: *Wall heat flux of a monolithic fuel element at BOL.*

16.9 Flat Plate

Even with the discussed sputtering technique, the fabrication of plates with gradients poses a number of technical hurdles that have to be passed. It therefore suggests itself to discuss the solution of a monolithic plate with constant thickness, i. e. no gradient.

A flat monolithic plate that permits a 60 d cycle with some reserves has a thickness of 320 µm, which makes up 25.1 kg uranium (9.9 kg ^{235}U). This is considerably less than the 28.6 kg discussed above as the core reavitivity generally decreases with convex thickness profiles. The maximum thermal flux of $5.81(2) \cdot 10^{14}$ in the D_2O is comparable to the turkish hat solution, the flux loss compared to the current solution is 8.6%.

The maximum burn-up of the flat plate, $4.85 \cdot 10^{21}$ $^1/_{cm^3}$, is about 12% lower than that of the turkish hat solution. In both cases, the maximum burn-up can be found at the outer border of the plate, some centimetres below core mid-plane. As the turkish hat plate is thinner at the outer end, the average thermal flux in the plate is higher due to less absorption, which yields a higher burn-up.

However, the higher thickness of the flat solution in the outer zones results in a considerably higher heat flux (+19.8% / 75.7 $^W/_{cm^2}$), as the number of fissions per unit volume active zone is higher. In addition, this zone of high heat flux has a much larger dimension than in the case of current fuel element as it is not the small single spot in the inner lower corner but the large zone at the outer limit of the plate. This also results in a notably higher surface temperature of up to 100.0(3) °C over a broad area, significantly decreasing the safety margins. Accordingly, the minimum safety margins also moved to the outer border of the fuel plate. It is interesting to note the $S_{ONB,min}$ is located at approximately $z = -18$ cm, while the other to minimal factors refer to the right lower corner. This is unique for all the safety margins calculated in this work, as normally all three minimums are located directly over the hotspot. The maximum fuel temperature is 136.2(5) °C, which is the same order of magnitude as the turkish hat solution (129.9(5) °C).

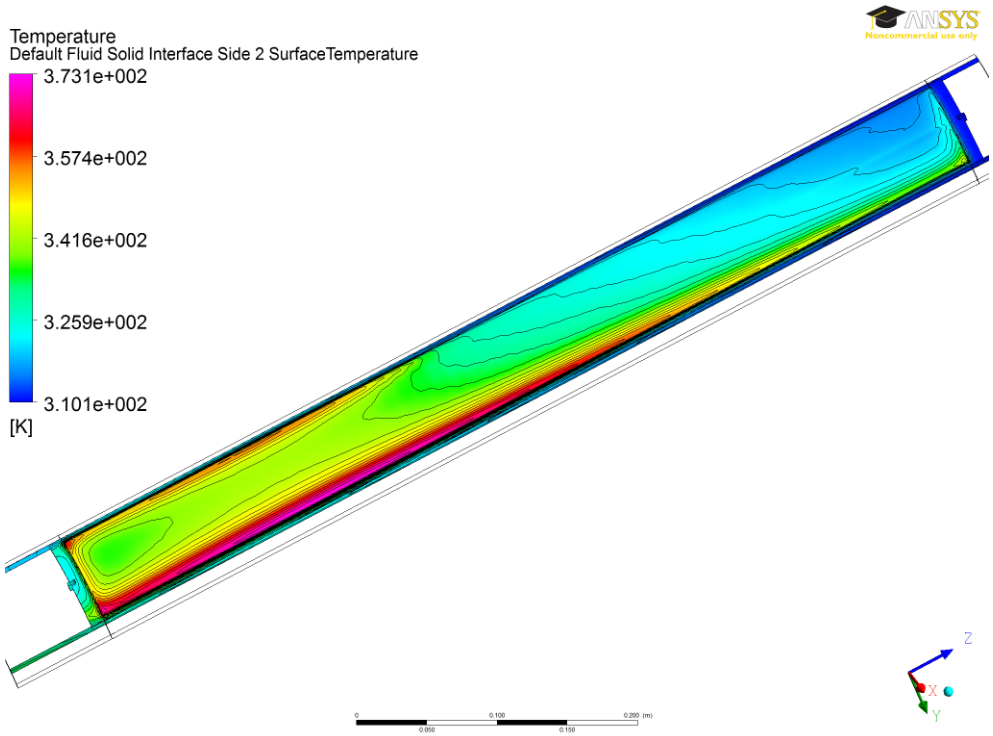

(a) Surface temperatures

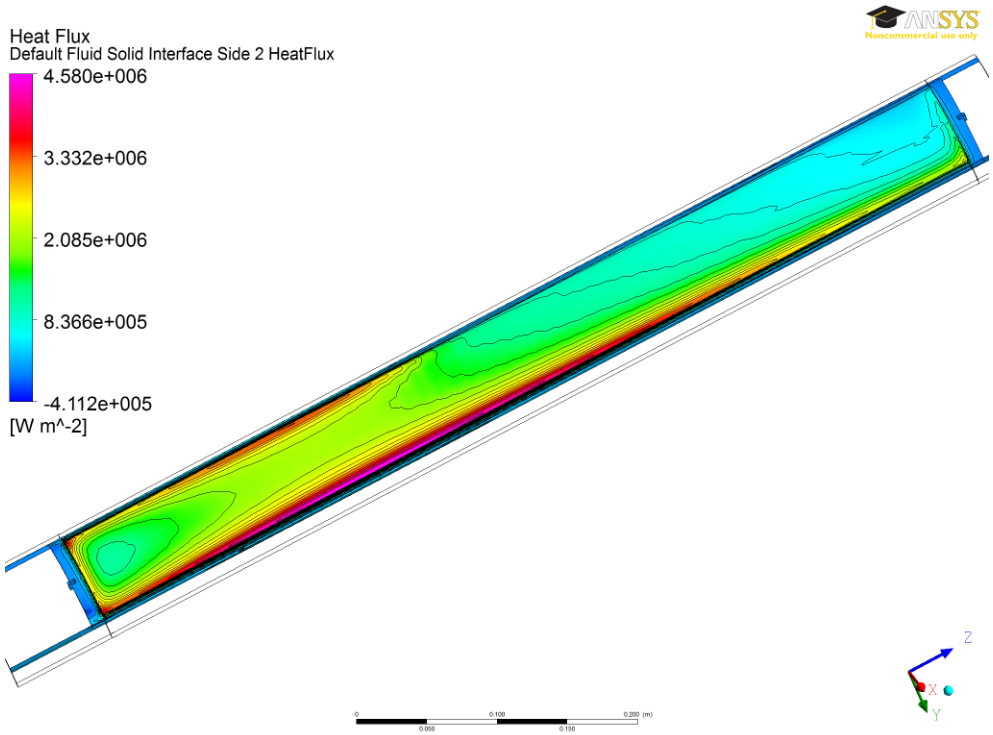

(b) Surface heat flux

Figure 16.13: *Thermal hydraulic properties of a flat monolithic plate at BOL: Temperatures (a) and heat flux (b).*

16.10 Final Assessment

Regarding the thermal hydraulic properties, the situation in the turkish hat solution is comparable to the 8g U/cc-20MW-disperse UMo case. Maximum cladding temperatures and heat fluxes are nearly equal. Even though the zones with high surface temperatures and heat fluxes are comparably larger in the monolithic solution, the calculated safety margins are nearly identical. Therefore, the same considerations regarding these margins that were made in chapter 15.10 for the dispere UMo case also hold for the monolithic turkish hat profile: It is still a conservative core design regarding these points.

The thermal hydraulic properties like maximum surface temperatures and maximum heat fluxes of the flat plate at 20 MW are comparable to those of the turkish hat profile at the increased power of 22 MW. As there is no improvement in the maximum neutron flux for the flat solution compared to the turkish hat profile at 20 MW, this is – form the point of view of neutronics – obviously the worst of all possible conversion options studied so far: If the high heat fluxes and surface temperatures were acceptable from the viewpoint of safety margins, they were better invested in a higher reactor power which would at least partly compensate the flux loss.[1] This is of course only true as long as the fabrication of one of the other solutions, monolithic or disperse, is technically feasible with justifiable effort and if the changes required for an increased reactor power are not immoderately large. From the discussed monolithic solutions, the flat plate is obviously the one which can be manufactured most easily.

On the other hand, the turkish hat profile as discussed above uses considerably more uranium than what is necessary for the flat solution. It is already obvious from this fact that there is much room for optimisation in the monolithic case. Possible optimisations of monolithic plates are discussed in chapter 16.10.1.

The major factor causing the flux loss is again the reduced enrichment. In this case, the enrichment was chosen even lower than in the disperse case, yielding about 1.1% additional overall flux loss (-7.7%...-8.8%). This is again due to the increased ^{238}U content and its parasitic absorption.

Due to the increased uranium loading per core, each cycle will produce more than three times the radioactive waste of the current core, containing more than seven times more Plutonium. This is of course even more than in the disperse UMo case and inevitable when the enrichment is decreased.

16.10.1 Possible Optimisation

Generally, for the optimisation of the monolithic fuel element, the same considerations as for the disperse case made in chapter 15.10.1 hold. Obviously, it is not possible to change the density of the monolithic fuel. Accordingly, only the width of the fuel can be changed. The richness of detail in this variation is again limited by the production technique. Here, the sputtering technique studied by W. Schmid [Sch10] gives room to a great number of possibilities that probably could not be achieved with rolling or pressing that easily.

The turkish hat solution is already a milestone in optimising the thermal hydraulic parameters compared to the flat plate. But there is still room for improvements on the neutronic side. Again, to compensate the flux loss, a further compaction of the fuel element would be needed. The thermal hydraulic parameters of the turkish hat solution are comparable to those of the disperse solution, but the maximum number of fissions per cm^3 meat at the end of the cycle is about 2.5 times larger. This situation will probably get worse with more compact fuel elements. In addition, to maintain reactivity, it is probably necessary to change the width of the cooling channels. As a thickness of 425 µm is already more than the half of one mean free path of thermal neutrons in 40% enriched UMo, it could be considered to increase the number of fuel plates. A reduced cladding thickness and/or other cooling channel thicknesses will allow for this.

[1] The safety margins for the flat profile at 20 MW are comparable to those of the turkish hat profile at 21 MW, even though the before mentioned thermal hydraulic properties are comparable to those at 22 MW.

An increased number of fuel plates also will lower the heat load per plate and therefore decrease heat fluxes. However, an increased number of fuel plates means 'wasting' more space for the cladding, space that is better invested to adjust the uranium/water ratio to increase the reactivity.

The optimisation of the monolithic fuel plates will presumably be studied by M. Däubler, beginning in 2011.

CHAPTER 17

Sensitivity Analysis: Uncertainty Estimation

A sensitivity analysis was performed for the results of the current fuel element discussed in chapter 14. For the thermal hydraulic calculations, the influence of wall roughness, turbulence modelling, meshes, material properties, viscous dissipation, buoyancy, inlet parameters and total reactor power on the critical parameters was emblazed. Also for the current fuel element, the uncertainty of the burn-up calculations was estimated by the method discussed in chapter 4.4.3, p. 41.

17.1 Thermal Hydraulic Calculations

In many of the following tables, the first column represents the results for a simplified calculation of the fuel element as-built.

In this context, 'simplified' means the following:[1]

- The direct heating of the aluminium and water by gammas and neutrons is not taken into account
- The used meshes are the ones used for the final calculation of the current fuel element
- Default parameters are: Roughness 2.4 µm, buoyant, no viscous dissipation, SST turbulence model, no curvature correction for turbulence, automatic wall functions, 18.02 MW deposited power in fuel, model as-built for current fuel element.

The parameters studied in this sensitivity analysis include wall roughness, turbulence models and possible corrections to them, buoyancy, viscous dissipation and inlet parameters. A good overview of the topics where care has to be taken is given in the 'CFD Best Practice Guidelines for CFD Code Validation for Reactor-Safety Applications' [Men].

17.1.1 Influence of Wall Roughness

To study the influence of the wall roughness on all thermal-hydraulic parameters, different calculations have been performed with various absolute roughnesses. All other boundary conditions were kept constant.

All measured temperatures decrease almost linearly with increasing wall roughness, except the averaged outlet temperature which has to stay constant. In contrast, the maximum heat flux density rises with increasing wall roughness, as well as the pressure drop and the maximum pressure. The minimum pressure, which can be found below the lower comb, is not affected by the wall roughness as it is close to the lower boundary of the simulation with the boundary condition of an averaged static pressure of 2.3 bar. The numbers from table 17.1 are plotted in fig. 17.1. All mentioned phenomenons can be explained by the

[1] These calculations were performed in advance to the final calculations to determine the needed parameters, therefore the 'default case' here does not represent the actual results presented in the preceding chapters!

	flat	0.8 µm	1.6 µm	2.4 µm	5.0 µm
Temperatures [℃]					
Max. Fuel	106.6	105.1	103.8	102.5	100.2
Avg. Fuel	68.7 / 76.4	67.9 / 75.7	67.2 / 74.6	66.7 / 73.3	65.3 / 72.2
Max. Wall	93.5	91.9	90.6	89.3	86.8
Avg. Wall	64.1	63.4	62.7	62.1	60.8
Max. Water (first node)	65.0	64.9	64.8	64.7	64.4
Avg. Outlet	52.8	52.8	52.9	52.8	52.9
Heat Flux [W/cm^2]					
Max. Wall	375.8	378.0	380.0	382.0	386.0
Avg. Wall	161.1	161.2	161.2	161.3	161.4
Pressure [bar]					
Avg. pressure drop	4.58	4.80	5.02	5.21	5.75
Max. pressure	7.82	8.04	8.26	8.45	8.99
Min. pressure	0.76	0.75	0.75	0.75	0.75

Table 17.1: *Influence of wall roughness.*

better heat transfer of rough walls from the solid to the fluid. It is obvious that the heat transfer in the solid itself is only marginally affected, which is expressed by the almost parallel slopes of maximum fuel temperature and maximum wall temperature as well as their averaged counterparts.

Data on the slopes of the curves from fig. 17.1 can be found in table 17.12 in chapter 17.1.10, p. 221.

17.1.2 Influence of Turbulence Modelling

To study the influence of the chosen turbulence model, properties for the current fuel element were calculated with three different turbulence models: SST, k-ϵ and SSG-Reynolds-Stress. For this, thermal hydraulic calculations were performed with the same heat distribution in the fuel and equal boundary conditions. The results are shown in tab. 17.2.

The numbers of the SSG-RS result have to be taken with a pinch of salt as the calculation did not converge to $r < 10^{-5}$ but started to diverge at $r \approx 10^{-4}$. The calculation was interrupted at this point and a transient simulation attached.

The SST-model predicts a slightly higher heat transfer than the k-ϵ-model, yielding lower temperatures of fuel and wall. This is in agreement with results from [Esc03]. The latter was validated with measurements and showed better agreement for SST. Although this validation can not directly be transferred to the case of FRM II, it is assumed that the predictions of the SST model are more exact also for this case.

Compared to the k-ω-model, the SST-model predicts nearly the same temperatures. This is due to the fact that both models are ω-based and use the same near-wall treatment. By the combination of k-ω and k-ϵ, the SST model is able to reproduce the measured results for the pressure drop better than the pure k-ω-model, whose deficiencies have already been discussed in chapter 7.2.2, p. 65.

Fig. 17.2 shows the temperature profile in the coolant at the end of the fuel zone in the middle of the cooling channel. The results augment the hitherto argumentation: The results of k-ω and SST are nearly

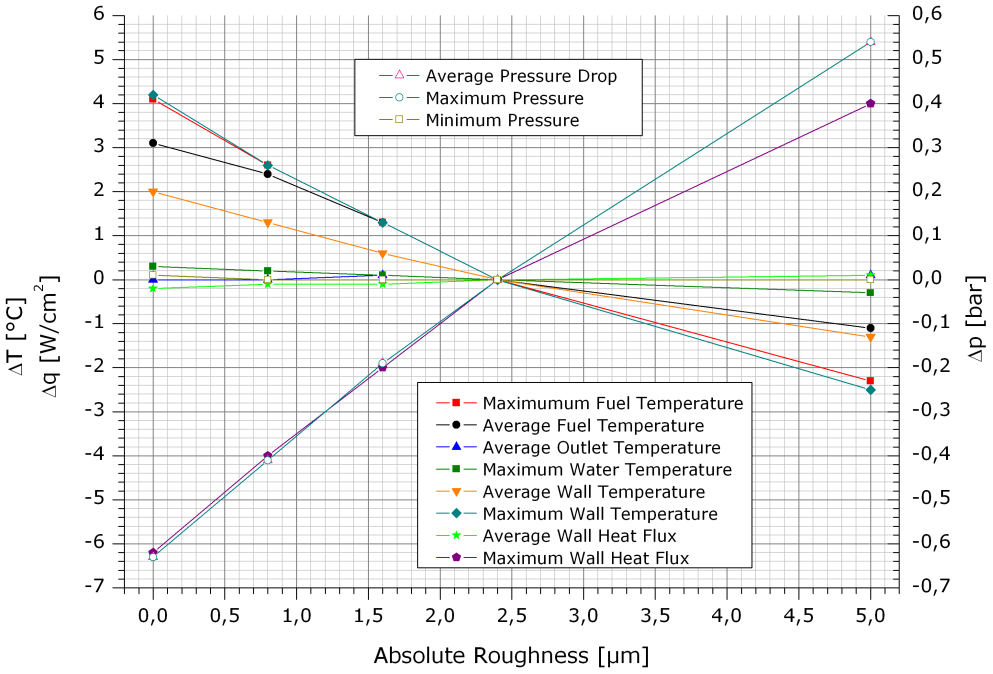

Figure 17.1: *Influence of wall roughness on various results. Normalized to the standard case of* 2.4 µm. *SST model, current BOL, IAPWS IF97, buoyant.*

	SST	*k-ϵ*	*k-ω*	*SSG-RS*
Temperatures [°C]				
Max. Fuel	102.5	103.2	102.7	103.5
Avg. Fuel	66.7 / 73.7	67.1 / 71.4	66.6 / 73.9	66.6 / 73.9
Max. Wall	89.3	89.9	89.4	90.3
Avg. Wall	62.1	62.5	62.1	62.1
Max. Water (first node)	64.7	68.1	64.8	64.7
Avg. Outlet	52.8	52.8	52.9	52.8
Heat Flux [W/cm²]				
Max. Wall	382.0	382.7	381.8	378.9
Avg. Wall	161.3	161.2	161.3	161.3
Pressure [bar]				
Avg. pressure drop	5.21	5.03	5.29	5.29
Max. pressure	8.45	8.27	8.54	8.53
Min. pressure	0.75	0.75	0.80	0.84

Table 17.2: *Influence of turbulence model. Current BOL, absolute roughness* 2.4 µm, *IAPWS IF97, buoyant.*

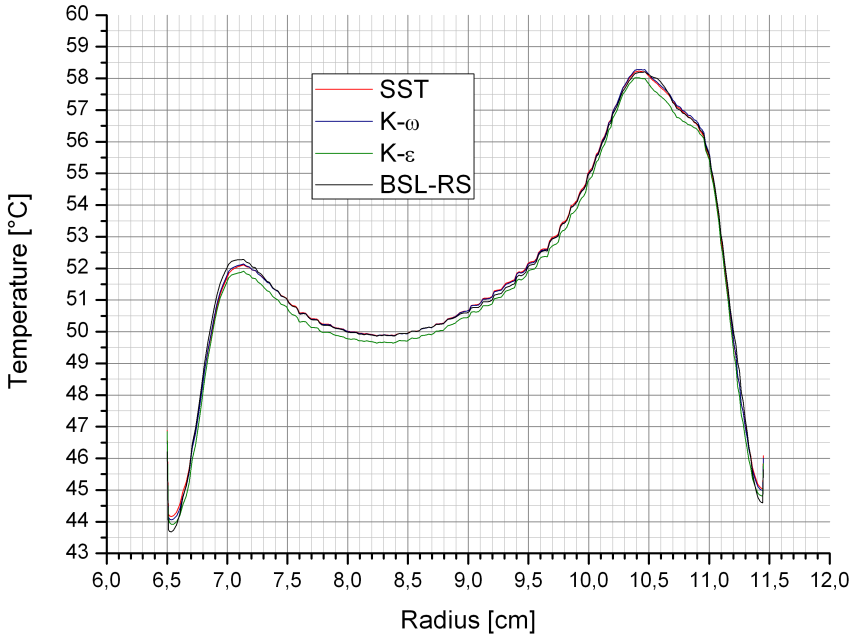

(a) Absolute values

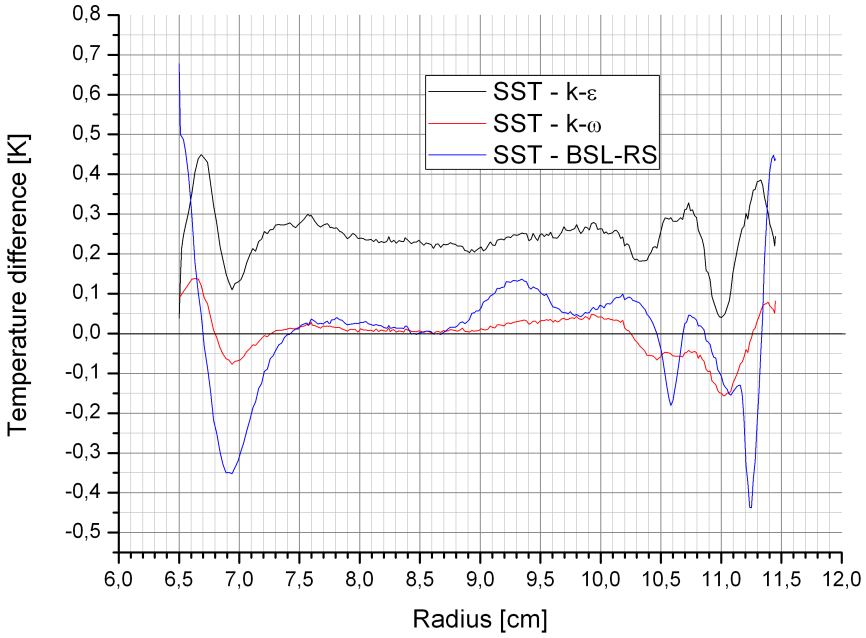

(b) Relative values

Figure 17.2: *Coolant temperature distribution in the middle of the cooling channel at the end of the fuel zone, depending on the turbulence model: Absolute values (a) and relative values (b).*

identical, where k-ω predicts a slightly worse mixing of the stream filaments. k-ϵ clearly predicts a lower commingling, the turbulent heat transfer from the wall to the fluid is worse. A comparison with the BSL-RS model shows significant differences only at the outer borders of the channel near the ducts. SST predicts higher temperatures directly at the walls, but lower temperatures some millimetres off this low speed zone. This zone is not that important for the cooling as shown in fig. 13.11. However, it must be mentioned that SST predicts lower coolant temperatures in the vicinity of the hot stream filaments at the fuel plate borders and the density step. These lower temperatures go hand in hand with higher temperatures at the wall. Therefore, the choice of SST can be regarded as a conservative approach concerning this matter.

Fig. 17.3 shows an actual plot of the surface temperature differences (a) and the temperature difference in the middle of the cooling channel between SST und k-ϵ. It quarries again the fact, that the k-ϵ model predicts a lower heat transfer off the wall, yielding higher surface temperatures. This difference grows as the hotter fluid proceeds down the wall. Accordingly, the fluid temperatures in the middle of the cooling channel are lower the more the fluid passes of its way through the cooling channel. The most obvious differences can be observed in those regions that are naturally most sensitive to turbulence modeling: Detachement and reattachement of the fluid to the wall and strongly changing turbulence parameters near stagnation points and cavities.

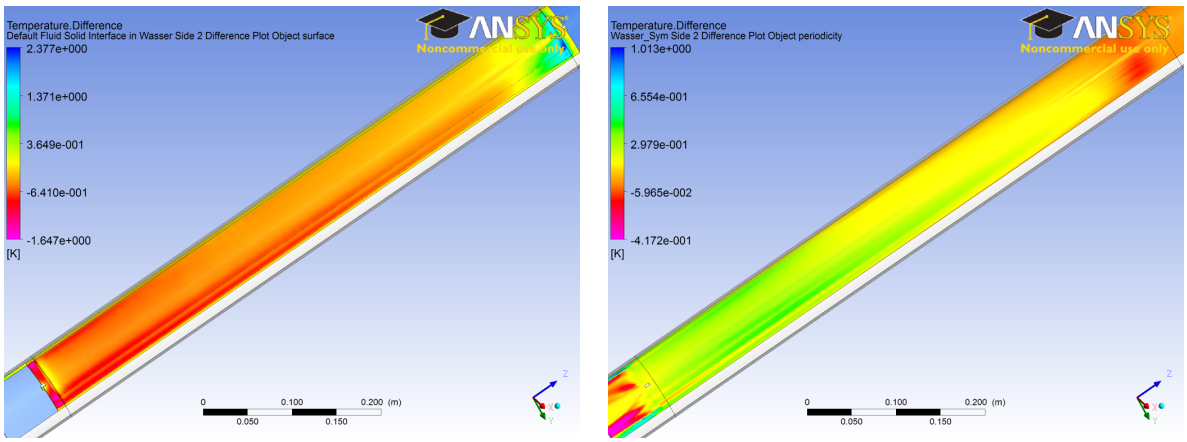

(a) Surface (b) Channel middle

Figure 17.3: *Temperature difference between SST und k-ϵ on the surface of the fuel plate (a) and in the middle of the cooling channel(b).*

All in all, the SST-model seems to be a reasonable choice for the calculations in this work.

Error Introduced by Turbulence Modelling

Though emphasis has been put on choosing an appropriate turbulence model, it has to be pointed out that a hundred per cent validation of the thermal hydraulic calculations can only be conducted experimentally. The addition of the turbulence model to the Navier Stokes equation causes first a loss of information in the averaging process, then adds additional conditions and equations to close the model.

As the exact fluctuating solution of the Navier Stokes equation is not known, it is impossible to set bounds for the error caused by the introduction of the turbulence model! Therefore, in addition to the numerical studies presented in this work, experimental studies may be required to validate the thermal hydraulic calculations made here. A more detailed explanation on this can be found in [Wol09].

17.1.3 Influence of Meshes

CFX

As discussed in chapter 12, the sensitivity of the results to the chosen mesh is one of the major points that has to be regarded in an analysis like it is presented here. For the current case, the mesh sensitivity analysis was split in several parts:[2]

- Influence of mesh density in the head part
- Influence of mesh density in the foot part
- Influence of number of mesh nodes in ϕ-direction in central part
- Influence of number of mesh nodes in θ-direction in central part
- Influence of number of mesh nodes in z-direction in central part
- Influence of y^+ in θ-direction in central part

In summary, it turns out that the effect of the mesh density in the head and foot part is rather small on all important quantities. By far the largest changes can be observed for the θ-dependence in the central part of the pressure drop. Here, the ϕ- and z-dependence has only a rather small influence too. There are always small fluctuations in the solution, even for very high node numbers.

ϕ-dependence

The standard mesh case has 148 nodes in ϕ-direction, 6 (inner duct) + 15 (inner picture frame) + 75 ($3\,\mathrm{g/cm^3}$ fuel) + 25 ($1.5\,\mathrm{g/cm^3}$ fuel) + 15 (outer picture frame) + 9 (outer duct). Increasing this number to 193 (9 + 20 + 100 + 35 + 20 + 9) and halving y^+ yields the following changes: All temperatures change less than 0.1 K, heat flux densities change less than $0.5\,\mathrm{W/cm^2}$. Pressure changes are less than 0.02 bar.

z-dependence

The standard mesh has 180 nodes in z-direction in the active zone. For the sensitivity analysis this number was lowered to 120 and the height of the first cells at the bottom and at the top was doubled. Again, temperature changes were smaller than 0.1 K, heat fluxes changed less than $1.0\,\mathrm{W/cm^2}$. No changes were observed in the pressure drop.

θ-dependence

The θ-dependence of the mesh proved to be the most critical point in the analysis. The originally estimated number of 39 points ($2 \cdot 13$ in the water channel, $2 \cdot 5$ in the cladding and 7 in the fuel) turned out to be the lower border to achieve stable results. Especially the pressure drop showed a high sensitivity, to y^+ even more than to the number of mesh nodes. The following criteria have to be met for stable results:

- Currently, the SST turbulence model can only be used with automatic wall functions in CFX. According to the discussion in chapter 7.2.3, p. 7.2.3, a minimum first node distance of $y^* = 11.06$ must be used to prevent CFX from trying to resolve the viscous sublayer. It could be observed in the sensitivity analysis that a violation of this rule resulted in noticeable shifts in the results, not only in the pressure drop but also in the temperatures. This is because CFX tries to resolve the sublayer by means of mesh points, however the number of mesh points in this area is only one or two, not the recommended number of about 20. Therefore, care has to be taken that y^+ is chosen in a range that is acceptable for the use of scalable wall functions, i. e. somewhere between 20 and some hundreds. A first node distance of $\Delta y \approx 40\,\mu\mathrm{m}$ is reasonable for FRM II standard conditions.

[2] See app. A for the coordinate system.

- About 20 nodes have to be placed in θ-direction for stable results in one half of the cooling channel.
- The number of nodes in the cladding should be at least 5 in each half, in the fuel zone at least 7 nodes.

If these requirements are met, the mesh-induce uncertainties are no larger than 0.5 K in the temperatures and 1.0 $\mathrm{W/cm^2}$ in the maximum heat flux density. The pressure drop and the maximum pressure vary by about 0.1 bar, while the uncertainty in the minimum pressure is only 0.02 bar.

Combined uncertainty

The combined uncertainty Δy is regarded as a function of the number of mesh points, n. As an approximation, the uncertainties of each direction discussed above are regarded as independent. With $n = n_x \cdot n_y \cdot n_z$, it is assumed that

$$\Delta y = \sqrt{\Delta y_x^2 + \Delta y_y^2 + \Delta y_z^2}. \tag{17.1}$$

Altogether, the mesh uncertainties listed in table 17.3 are derived. Again, it must be stressed that these uncertainties are only valid as long as the first node distance is large enough to allow for the use of wall functions. As soon as $y^+ \lesssim 25$, the uncertainties, especially of the pressure drop and the maximum pressure, become significantly larger. The detailed report on the mesh sensitivity analysis, which provides numbers for the statements made above, can be found in appendix F.4.

Quantity	Value
ΔT	0.5 K
Δq_{avg}	0.5 $\mathrm{W/cm^2}$
Δq_{max}	1.5 $\mathrm{W/cm^2}$
$\Delta(\Delta p)$, Δp_{max}	0.10 bar
Δp_{min}	0.03 bar

Table 17.3: *Uncertainties due to mesh sensitivity*

MCNPX

Hints on the effect of the McnpX Mesh resolution were already given in chapter 9.2. As the McnpX mesh depends directly on the Cfx mesh, it is not analysed separately.

17.1.4 Influence of Viscous Dissipation

No significant difference could be observed by enabling the viscous dissipation solver option, see tab. 17.4. Viscous dissipation is the transformation of kinetic energy to internal energy by heating up the fluid in turbulent flows.

17.1.5 Influence of Buoyancy

No changes were observed by disabling buoyancy in the calculations, see tab. 17.5.

17.1.6 Influence of Total Reactor Power

Table 17.6 shows how temperatures and heat fluxes scale with the reactor power. This table may be usefull to analyse the influence of uncertainties in the power measurement.

	Off	*On*
Temperatures [℃]		
Max. Fuel	102.5	102.7
Avg. Fuel	66.7 / 73.7	66.7 / 73.9
Max. Wall	89.3	89.5
Avg. Wall	62.1	62.1
Avg. Outlet	52.8	52.8
Heat Flux [$\mathrm{W/cm^2}$]		
Max. Wall	382.0	381.7
Avg. Wall	161.3	161.3
Pressure [bar]		
Avg. pressure drop	5.21	5.21
Max. pressure	8.45	8.45
Min. pressure	0.75	0.75

Table 17.4: *Influence of viscous dissipation. No changes observed. SST model, current BOL, absolute roughness* $2.4\,\mu\mathrm{m}$*, buoyant.*

	On	*Off*
Temperatures [℃]		
Max. Fuel	102.9	102.9
Avg. Fuel	66.7 / 74.0	66.7 / 74.0
Max. Wall	89.6	89.6
Avg. Wall	62.2	62.2
Avg. Outlet	53.0	53.0
Heat Flux [$\mathrm{W/cm^2}$]		
Max. Wall	382.3	382.3
Avg. Wall	161.3	161.3
Pressure [bar]		
Avg. pressure drop	5.20	5.20
Max. pressure	8.44	8.44
Min. pressure	0.75	0.75

Table 17.5: *Influence of buoyancy. No changes observed. SST model, current BOL, absolute roughness* $2.4\,\mu\mathrm{m}$*.*

	19 MW	*20 MW*	*21 MW*
Temperatures [℃]			
Max. Fuel	99.8	102.9	105.9
Avg. Fuel	65.3 / 72.3	66.7 / 74.1	68.1 / 75.7
Max. Wall	87.2	89.6	92.0
Avg. Wall	61.1	62.3	63.4
Avg. Outlet	52.2	53.0	53.8
Heat Flux [$\mathrm{W/cm^2}$]			
Max. Wall	362.7	382.3	401.9
Avg. Wall	153.2	161.3	169.4
Pressure [bar]			
Avg. pressure drop	5.21	5.21	5.20
Max. pressure	8.45	8.45	8.44
Min. pressure	0.75	0.75	0.75

Table 17.6: *Influence of reactor power.*

17.1.7 Influence of Inlet Parameters

Influence of Turbulence Intensity I

The turbulence intensity I is among those parameters that are only estimated as no measured values are available for them. As can be seen from table 17.7, the inlet turbulence intensity virtually has no influence on the most important parameters. A comparison of the fluid temperatures near the outlet is shown in fig. 17.4. Again, no significant differences can be observed.

	$I = 0.02$	$I = 0.027$	$I = 0.04$
Temperatures [℃]			
Max. Fuel	102.9	102.9	102.9
Avg. Fuel	66.7 / 74.1	66.7 / 74.1	66.7 / 74.1
Max. Wall	89.6	89.6	89.7
Avg. Wall	62.3	62.3	62.3
Avg. Outlet	53.0	53.0	53.0
Heat Flux [$\mathrm{W/cm^2}$]			
Max. Wall	382.3	382.3	382.3
Avg. Wall	161.3	161.3	161.3
Pressure [bar]			
Avg. pressure drop	5.20	5.21	5.21
Max. pressure	8.44	8.45	8.45
Min. pressure	0.75	0.75	0.75

Table 17.7: *Influence of inlet turbulence intensity.*

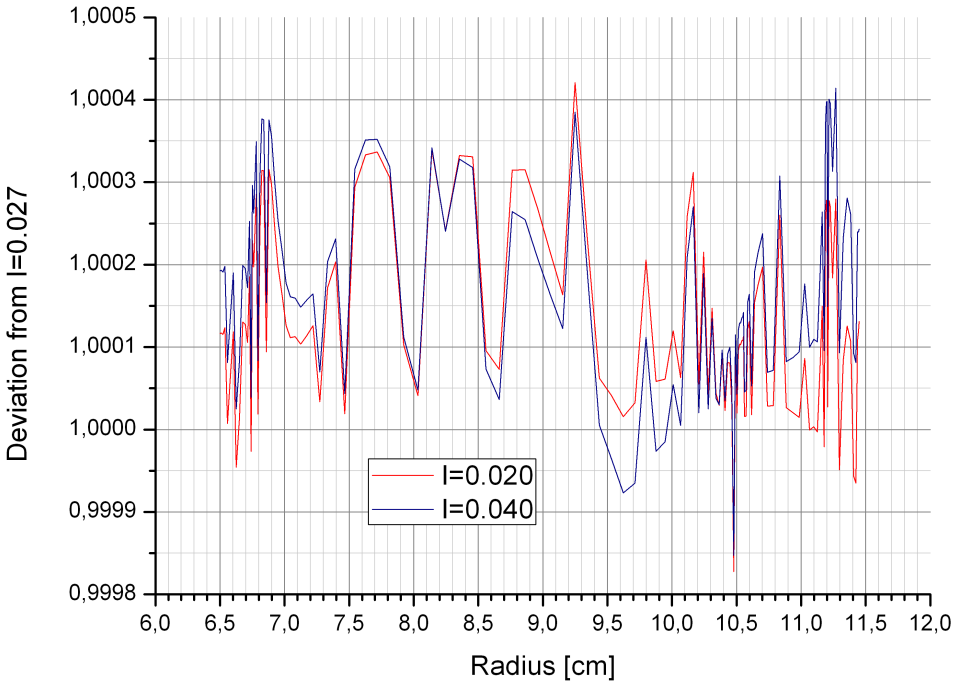

Figure 17.4: *Influence of inlet turbulence intensity on the outlet temperature distribution.*

Influence of Temperature T_{in}

One would expected that small uncertainties in the coolant temperature at the inlet lead to exactly the same deviations in most temperature values, as the non-linearity of the material answer is negligible for small variations. However, the density effect of the water leads to changes in the transport of heat from the wall into the fluid, adding up to 20% of non-linearity in a step of 5 °C. The results for three different inlet temperatures are shown in tab. 17.8. Higher steps than 1 °C were chosen to be able to properly identify any non-linearity.

Influence of Inlet Velocity v_{in}

The average inlet velocity v_{in} above the fuel plates was calculated to be 9.83 m/s. Table 17.9 shows the response of the system to inlet velocity variations that lead to fluid-channel averaged velocity changes of 1 m/s. It is obvious that the most significant change occurs regarding the pressure drop. Heat flux densities are only slightly affected, in the way that lower coolant flow rates lead to a worse transport of heat from the wall, therefore forcing the heat to spread more over the surface, yielding lower heat flux densities but higher wall temperatures.

17.1.8 Influence of Gamma-heating in Structural Materials

If gamma heating in the structural materials, namely the parts of the fuel plate that don't belong to the active zone (the 'picture frame') and the inner and outer duct was not taken into account, a small part of the total heating would be missed. Gamma heating was therefore included in all 'real' calculations. The only purpose of table 17.10 is therefore to be able to assess the effect.

	$T_{\text{in}} = 32\,℃$	$T_{\text{in}} = 37\,℃$	$T_{\text{in}} = 42\,℃$
Temperatures [℃]			
Max. Fuel	99.0	102.9	106.9
Avg. Fuel	62.5 / 70.0	66.7 / 74.1	71.0 / 78.2
Max. Wall	85.8	89.6	93.6
Avg. Wall	58.1	62.3	66.6
Avg. Outlet	48.0	53.0	58.0
Heat Flux [$\mathrm{W/cm^2}$]			
Max. Wall	380.5	382.3	383.9
Avg. Wall	161.3	161.3	161.3
Pressure [bar]			
Avg. pressure drop	5.27	5.21	5.14
Max. pressure	8.51	8.45	8.37
Min. pressure	0.75	0.75	0.75

Table 17.8: *Influence of inlet temperature.*

	$v_{\text{in}} = 9.21\,\mathrm{m/s}$ / $\bar{v}_{\text{plate}} = 14.91\,\mathrm{m/s}$	$v_{\text{in}} = 9.83\,\mathrm{m/s}$ / $\bar{v}_{\text{plate}} = 15.91\,\mathrm{m/s}$	$v_{\text{in}} = 10.45\,\mathrm{m/s}$ / $\bar{v}_{\text{plate}} = 16.91\,\mathrm{m/s}$
Temperatures [℃]			
Max. Fuel	105.4	102.9	100.5
Avg. Fuel	68.1 / 75.8	66.7 / 74.1	65.4 / 72.4
Max. Wall	92.2	89.6	87.2
Avg. Wall	63.7	62.3	60.9
Avg. Outlet	54.0	53.0	52.1
Heat Flux [$\mathrm{W/cm^2}$]			
Max. Wall	379.7	382.3	384.6
Avg. Wall	161.2	161.3	161.4
Pressure [bar]			
Avg. pressure drop	4.60	5.21	5.83
Max. pressure	7.73	8.45	9.19
Min. pressure	0.94	0.75	0.55

Table 17.9: *Influence of inlet velocity.*

	Without	*With*
Temperatures [℃]		
Max. Fuel	102.5	102.9
Avg. Fuel	66.7 / 73.7	66.7 / 74.0
Max. Wall	89.3	89.6
Avg. Wall	62.1	62.2
Avg. Outlet	52.8	53.0
Heat Flux [W/cm^2]		
Max. Wall	382.0	382.2
Avg. Wall	161.3	161.6
Pressure [bar]		
Avg. pressure drop	5.21	5.21
Max. pressure	8.45	8.45
Min. pressure	0.75	0.75

Table 17.10: *Influence of gamma heating in structural material.*

17.1.9 Influence of SST Turbulence Model Curvature Correction

As already discussed in chapter 7.2.2, the SST model is insensitive to streamline curvature. CFX offers the possibility to include a production correction term. However, as the curvature of the fuel plate is rather small, the influence of the curvature correction is also small, as can be seen in table 17.11.

	Without	*With*
Temperatures [℃]		
Max. Fuel	102.5	102.7
Avg. Fuel	66.7 / 73.7	66.9 / 73.9
Max. Wall	89.3	89.5
Avg. Wall	62.1	62.1
Avg. Outlet	52.8	52.8
Heat Flux [W/cm^2]		
Max. Wall	382.0	381.8
Avg. Wall	161.3	161.3
Pressure [bar]		
Avg. pressure drop	5.21	5.19
Max. pressure	8.45	8.43
Min. pressure	0.75	0.74

Table 17.11: *Influence of curvature correction for the SST turbulence model.*

17.1.10 Overview / Sensitivity Matrix

Table 17.12 shows some kind of sensitivity matrix, which tells the dependencies of the most important results on a number of thermal hydraulic parameters. This matrix is the result of a part of the sensitivity analysis performed so far. It does not include the sensitivity of the results to some parameters that are not yet specified, namely manufacturing tolerances of the new fuel plates and the fuel element which result in shifted power distributions or smaller / wider cooling channels. In this matrix, only small deviations are regarded, that means only the linear term of the Taylor series is given. In all calculations that form the basis for this matrix, the parameters are assumed to behave independently from each other; no covariance elements were calculated, as if the deviations that are analysed are small enough to fit within the linear order of the Taylor series, covariance elements are neglected anyway.[3].

	$\partial x/\partial k_{\text{rough}}$ [Y/µm]	$\partial x/\partial T_{\text{in}}$ [Y/K]	$\partial x/\partial v_{\text{in}}$ [Y/(m/s)]	$\partial x/\partial I$ [Y/1]	Δx (mesh)
Temperatures [°C/X]					
Max. Fuel	-1.25	0.80	-4.03	0	±0.5
Avg. Fuel	-0.86	0.83	-1.68 / -2.75	0	±0.5
Max. Wall	-1.31	0.78	-2.42	0	±0.3
Avg. Wall	-0.65	0.85	-2.26	0	±0.3
Avg. Outlet	0	1.00	-1.53	0	±0.1
Heat Flux [W/cm²/X]					
Max. Wall	2.01	0.34	3.95	0	±1.5
Avg. Wall	0.06	0	0.1	0	±0.5
Pressure [bar/X]					
Avg. pressure drop	0.23	0.01	1.00	< 0.01	±0.10
Max. pressure	0.23	0.02	1.18	0	±0.10
Min. pressure	0	0	-0.31	0	±0.03

Table 17.12: *Sensitivity matrix*

17.2 Burn-Up

The uncertainty of the burn-up calculations is estimated by the method discussed in chapter 4.4.3, p. 41. For this analysis, five statistically independent burn-up calculations for the current fuel element were carried out.

17.2.1 Control Rod Movement

As discussed in chapter 4.4.3, a single X^2 run will most probably underestimate the uncertainty of the control rod position as it just converts the statistical uncertainty of k_{eff} of the last timestep to a control rod position uncertainty. To capture the full uncertainty, which is a combined uncertainty of Δk_{eff} of the last timestep and the cumulated uncertainty of the material composition due to the uncertainties of the previous timesteps, it is necessary to either solve the burn-up uncertainty equations as discussed in chapter 4.4.2 or to use the easier solution of multiple statistically independent X^2 runs. In this work, the

[3]The 2D Taylor series up to the linear order includes no covariance terms, $f(x,y) = f(x_0, y_0) + f_x(x_0, y_0)\,\Delta x + f_y(x_0, y_0)\,\Delta y + \mathcal{O}(2)$.

latter option is used.

The cumulated uncertainty of the control rod position is calculated by a weighted average from N statistically independent runs [Blü02, p. 17]. The weighting factor is calculated from the single uncertainties Δz_i:

$$\bar{z} = \frac{\sum_{i=1}^{N} \frac{z_i}{\Delta z_i^2}}{\sum_{i=1}^{N} \frac{1}{\Delta z_i^2}} \tag{17.2}$$

$$\Delta\bar{z} = \sqrt{\frac{1}{\sum_{i=1}^{N} \frac{1}{\Delta z_i^2}}}. \tag{17.3}$$

The result for five independent X^2 runs is shown in fig. 17.5. Note that no measured value was available for 0.5 d, therefore this value was estimated. It must be stressed again that the uncertainty of the control rod position has to be regarded more as a confidence interval rather than as a point estimation, compare chap. 2.5.2 and 4.4.3.

17.2.2 Number of Predictor Steps in MonteBurns

MonteBurns and X^2 offer the possibility to use the predictor-corrector scheme in burn-up calculations. While using only one predictor step yields lower calculation times, it underpredicts the uranium consumption and therefore predicts a slower control rod movement (compare fig. 17.6 for 1 step and 17.5 for two steps). In contrary, especially the amount of highly absorbing fission products, e. g. ^{135}Xe, ^{148m1}Pm, ^{149}Sm and ^{157}Gd is overpredicted. In the end, the calculated reactivity reserve at EOL differs only slightly, while there are notable differences in the plate inventory. As this behaviour could not be observed in comparison calculations by Röhrmoser [Röh] which used a fixed control rod position, it is supposed that the flux density change due to control rod movement, especially in the first two timesteps, is responsible for this behaviour. As the control rod is moved by more the 10 cm during this time, the flux distribution changes drastically in some parts of the plate, causing the same discretization problems that generally appear at the very first timestep. This is why MonteBurns generally uses one additional predictor step for the first timestep. By using two predictor steps in general, this weakness, which is in inherent for the time discretization used in MonteBurns, is overcome.

The fission product inventory at EOL for two predictor steps was already shown in table 14.3, p. 151. An overview of the most important results for one and two predictor steps, as well as the differences are given in tables 17.13, 17.14 and 17.15.

Therefore, in this work, two predictor steps were used in the burn-up calculations if more than a general overview was expected. Especially the error of the nuclide inventory at EOL and the uncertainty of the remaining boron in the boron ring is reduced drastically when two predictor steps are used. The computational expenses are not that dramatic as X^2 spends about two thirds of the time with predicting the correct control rod positions.

17.2.3 Fuel Composition

Of course, the uncertainty of the fuel composition greatly depends on the number of particles per kcode cycle and the number of kcode cycles per burn-up step. If 40 000 particles are used and the number of active cycles per burn-up step is set to 30, most isotopes as listed in chapter F.2 are calculated with an uncertainty $\lesssim 0.5\%$ at EOL. However, as shown in tab. 14.3, this is not true for light elements that are produced in very low quantities and especially not for the boron ring. The burn-up for the single burn-up zones is also calculated with an uncertainty $\lesssim 0.5\%$ at EOL with these settings.

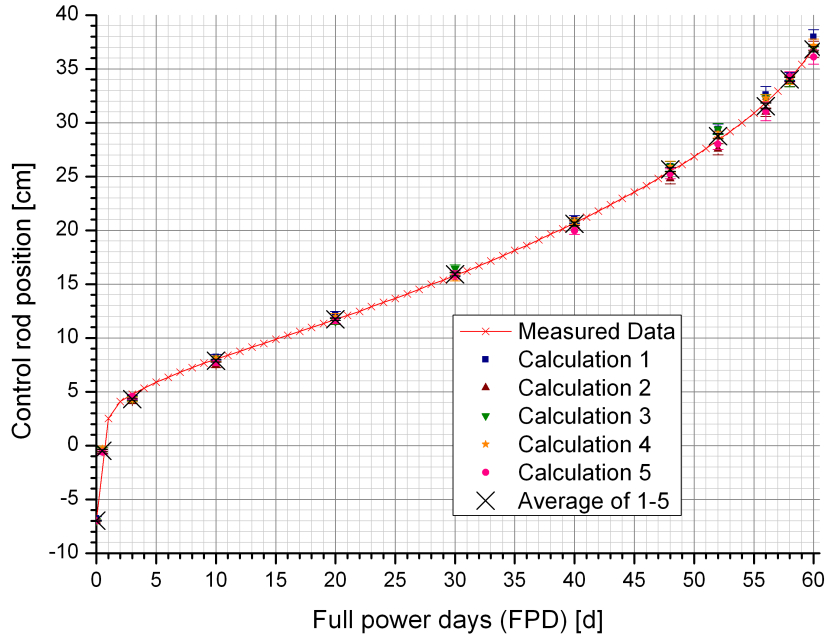

(a) Results of calculations

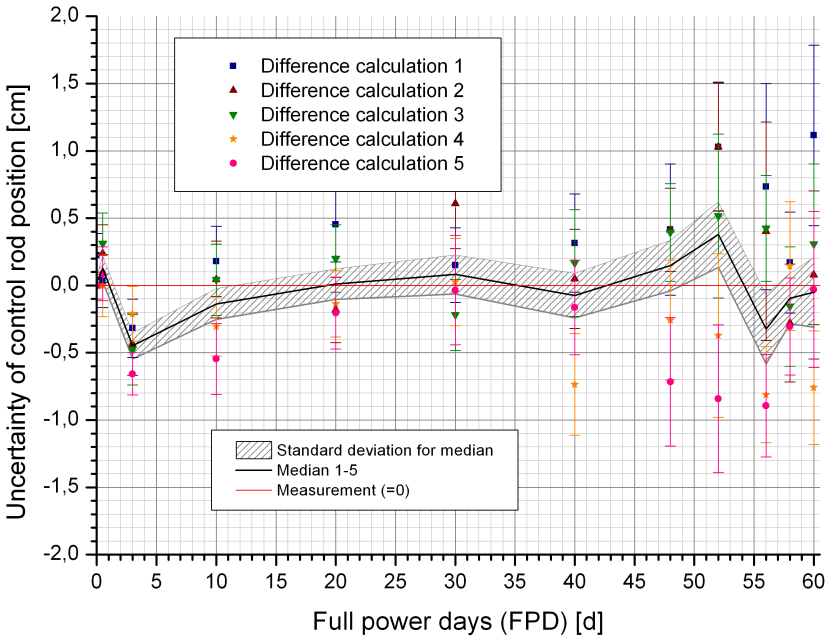

(b) Deviations from measured driveway

Figure 17.5: *Uncertainty of burn-up calculations: Results of calculations (a) and differences to the measured values for 2 predictor steps (b).*

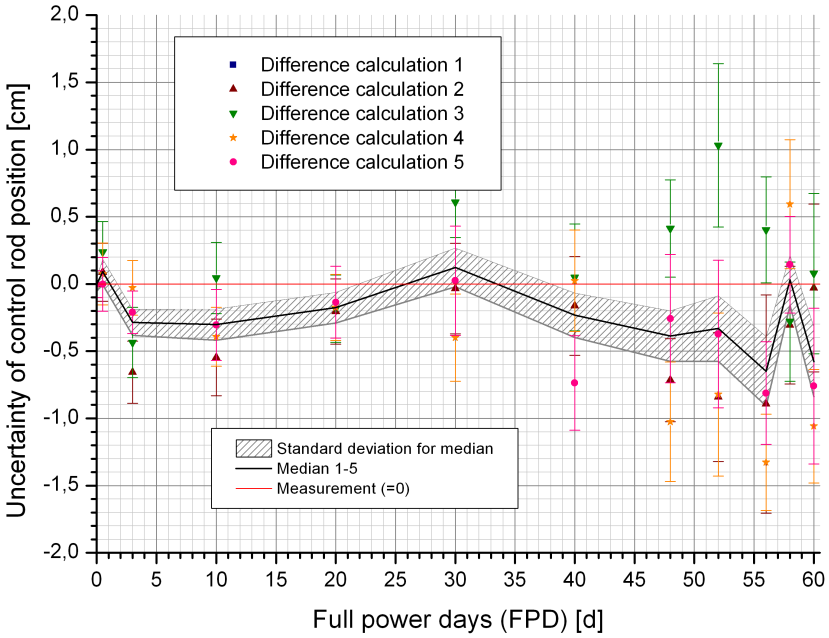

Figure 17.6: *Uncertainty of burn-up calculations: Differences to the measured values for 1 predictor step.*

Isotope	*Quantity 1 step*[g]	*Quantity 2 steps* [g]	*Quantity difference* [g]	*Relative difference*
Actinides				
^{234}U	60.557g±0.012g	60.396g±0.022g	0.161g±0.025g	0.27%± 0.04%
^{235}U	6019.092g±1.403g	5989.176g±1.176g	29.916g±1.831g	0.50%± 0.03%
^{236}U	292.670g±0.161g	298.582g±0.114g	$-5.912 \cdot 10^{+0}$±0.197g	-2.02%± 0.07%
^{237}U	1.608g±0.004g	1.617g±0.006g	$-9.000 \cdot 10^{-3}$±0.007g	-0.56%± 0.45%
^{238}U	500.547g±0.035g	500.201g±0.023g	0.346g±0.042g	0.07%± 0.01%
^{237}Np	4.526g±0.009g	4.676g±0.006g	$-1.500 \cdot 10^{-1}$±0.011g	-3.31%± 0.24%
^{238}Np	0.042g	0.043g	$-1.000 \cdot 10^{-3}$	-2.38%
^{239}Np	0.923g±0.003g	0.892g±$1.000 \cdot 10^{-3}$	0.031g±0.003g	3.36%± 0.33%
^{238}Pu	0.237g±$1.000 \cdot 10^{-3}$	0.250g±$1.000 \cdot 10^{-3}$	$-1.300 \cdot 10^{-2}$±0.001g	-5.49%± 0.61%
^{239}Pu	10.330g±0.017g	10.619g±0.015g	$-2.890 \cdot 10^{-1}$±0.023g	-2.80%± 0.22%
^{240}Pu	0.949g±$1.000 \cdot 10^{-3}$	0.996g±0.003g	$-4.700 \cdot 10^{-2}$±0.003g	-4.95%± 0.33%
^{241}Pu	0.386g±$1.000 \cdot 10^{-3}$	0.412g±0.002g	$-2.600 \cdot 10^{-2}$±0.002g	-6.74%± 0.59%
^{242}Pu	0.021g	0.023g	$-2.000 \cdot 10^{-3}$	-9.52%

Table 17.13: *Difference between one and two burn-up predictor steps for current fuel element, EOL after 60 d, actinides.*

Isotope	*Quantity 1 step*[g]	*Quantity 2 steps* [g]	*Quantity difference* [g]	*Relative difference*
Non-Actinides (1)				
^{10}B	0.147g±$6.267 \cdot 10^{-4}$	0.100g±0.001g	0.046g±0.001g	31.47%± 0.92%
^{11}B	$1.910 \cdot 10^{-4}$	$1.980 \cdot 10^{-4}$	$-7.000 \cdot 10^{-6}$	-3.66%
^{83}Kr	2.223g±$6.620 \cdot 10^{-4}$	2.259g±$7.919 \cdot 10^{-4}$	$-3.600 \cdot 10^{-2}$±0.001g	-1.62%± 0.05%
^{93}Zr	30.980g±0.016g	31.540g±0.010g	$-5.600 \cdot 10^{-1}$±0.019g	-1.81%± 0.06%
^{95}Zr	23.350g±0.011g	23.770g±0.008g	$-4.200 \cdot 10^{-1}$±0.014g	-1.80%± 0.06%
^{95}Nb	5.745g±0.004g	5.856g±0.002g	$-1.110 \cdot 10^{-1}$±0.004g	-1.93%± 0.07%
^{95}Mo	2.613g±0.002g	2.662g±0.001g	$-4.900 \cdot 10^{-2}$±0.002g	-1.88%± 0.08%
^{96}Mo	0.042g±$6.147 \cdot 10^{-5}$	0.043g±$8.150 \cdot 10^{-5}$	$-1.480 \cdot 10^{-3}$±$1.021 \cdot 10^{-4}$	-3.54%± 0.25%
^{97}Mo	29.300g±0.011g	29.830g±0.005g	$-5.300 \cdot 10^{-1}$±0.012g	-1.81%± 0.04%
^{98}Mo	29.990g±0.013g	30.540g±0.010g	$-5.500 \cdot 10^{-1}$±0.016g	-1.83%± 0.05%
^{100}Mo	32.910g±0.016g	33.490g±0.012g	$-5.800 \cdot 10^{-1}$±0.020g	-1.76%± 0.06%
^{99}Tc	28.070g±0.007g	28.580g±0.008g	$-5.100 \cdot 10^{-1}$±0.011g	-1.82%± 0.04%
^{101}Ru	27.080g±0.010g	27.560g±0.008g	$-4.800 \cdot 10^{-1}$±0.012g	-1.77%± 0.05%
^{102}Ru	22.940g±0.010g	23.370g±0.011g	$-4.300 \cdot 10^{-1}$±0.015g	-1.87%± 0.07%
^{103}Ru	10.040g±0.002g	10.200g±0.002g	$-1.600 \cdot 10^{-1}$±0.003g	-1.59%± 0.03%
^{103}Rh	5.850g±0.004g	5.949g±0.002g	$-9.900 \cdot 10^{-2}$±0.005g	-1.69%± 0.08%
^{105}Rh	0.174g±$7.656 \cdot 10^{-5}$	0.175g±$8.289 \cdot 10^{-5}$	$-7.000 \cdot 10^{-4}$±$1.128 \cdot 10^{-4}$	-0.40%± 0.06%
^{105}Pd	4.628g±0.002g	4.693g±0.001g	$-6.500 \cdot 10^{-2}$±0.002g	-1.40%± 0.05%
^{109}Ag	0.259g±$1.018 \cdot 10^{-4}$	0.264g±$8.146 \cdot 10^{-5}$	$-5.000 \cdot 10^{-3}$±$1.304 \cdot 10^{-4}$	-1.93%± 0.05%
^{113}Cd	0.009g±$5.591 \cdot 10^{-6}$	0.009g±$7.724 \cdot 10^{-6}$	$3.400 \cdot 10^{-5}$±$9.535 \cdot 10^{-6}$	0.38%± 0.11%
^{129}I	4.416g±0.002g	4.495g±0.002g	$-7.900 \cdot 10^{-2}$±0.003g	-1.79%± 0.06%
^{131}I	3.821g±0.002g	3.870g±$8.663 \cdot 10^{-4}$	$-4.900 \cdot 10^{-2}$±0.003g	-1.28%± 0.07%
^{135}I	0.296g±$8.084 \cdot 10^{-5}$	0.297g±$3.288 \cdot 10^{-4}$	$-1.300 \cdot 10^{-3}$±$3.386 \cdot 10^{-4}$	-0.44%± 0.11%
^{131}Xe	14.690g±0.012g	14.950g±0.005g	$-2.600 \cdot 10^{-1}$±0.013g	-1.77%± 0.09%
^{133}Xe	5.869g±0.004g	5.931g±0.001g	$-6.200 \cdot 10^{-2}$±0.004g	-1.06%± 0.07%
^{135}Xe	0.048g±$2.686 \cdot 10^{-5}$	0.046g±$1.026 \cdot 10^{-5}$	0.001g±$2.875 \cdot 10^{-5}$	2.88%± 0.06%
^{133}Cs	38.300g±0.018g	39.000g±0.016g	$-7.000 \cdot 10^{-1}$±0.025g	-1.83%± 0.06%
^{134}Cs	1.100g±0.004g	1.141g±0.002g	$-4.100 \cdot 10^{-2}$±0.005g	-3.73%± 0.42%
^{135}Cs	5.687g±$8.070 \cdot 10^{-4}$	5.737g±0.001g	$-5.000 \cdot 10^{-2}$±0.002g	-0.88%± 0.03%
^{139}La	46.970g±0.025g	47.820g±0.012g	$-8.500 \cdot 10^{-1}$±0.027g	-1.81%± 0.06%

Table 17.14: *Difference between one and two burn-up predictor steps for current fuel element, EOL after 60 d, non-actinides, part 1*

Isotope	*Quantity 1 step*[g]	*Quantity 2 steps* [g]	*Quantity difference* [g]	*Relative difference*
Non-Actinides (2)				
^{141}Ce	24.260g±0.016g	24.660g±0.005g	$-4.000 \cdot 10^{-1}$±0.017g	-1.65%± 0.07%
^{143}Ce	1.474g±$6.914 \cdot 10^{-4}$	1.481g±0.001g	$-7.000 \cdot 10^{-3}$±0.001g	-0.47%± 0.09%
^{141}Pr	18.690g±0.015g	19.050g±0.011g	$-3.600 \cdot 10^{-1}$±0.019g	-1.93%± 0.10%
^{143}Pr	13.420g±0.005g	13.630g±0.003g	$-2.100 \cdot 10^{-1}$±0.006g	-1.56%± 0.05%
^{143}Nd	27.090g±0.016g	27.570g±0.005g	$-4.800 \cdot 10^{-1}$±0.017g	-1.77%± 0.06%
^{145}Nd	28.710g±0.009g	29.210g±0.011g	$-5.000 \cdot 10^{-1}$±0.014g	-1.74%± 0.05%
^{146}Nd	24.010g±0.011g	24.440g±0.009g	$-4.300 \cdot 10^{-1}$±0.014g	-1.79%± 0.06%
^{147}Nd	4.305g±0.001g	4.358g±0.001g	$-5.300 \cdot 10^{-2}$±0.002g	-1.23%± 0.04%
^{148}Nd	13.870g±0.007g	14.150g±0.006g	$-2.800 \cdot 10^{-1}$±0.010g	-2.02%± 0.07%
^{147}Pm	10.620g±0.005g	10.790g±0.003g	$-1.700 \cdot 10^{-1}$±0.006g	-1.60%± 0.05%
^{148m1}Pm	0.130g±$6.274 \cdot 10^{-5}$	0.128g±$1.836 \cdot 10^{-4}$	0.002g±$1.940 \cdot 10^{-4}$	1.39%± 0.15%
^{149}Pm	0.562g±$1.583 \cdot 10^{-4}$	0.564g±$4.068 \cdot 10^{-4}$	$-2.800 \cdot 10^{-3}$±$4.365 \cdot 10^{-4}$	-0.50%± 0.08%
^{149}Sm	0.419g±$1.352 \cdot 10^{-4}$	0.412g±$3.524 \cdot 10^{-4}$	0.007g±$3.774 \cdot 10^{-4}$	1.58%± 0.09%
^{150}Sm	8.231g±0.004g	8.415g±0.003g	$-1.840 \cdot 10^{-1}$±0.005g	-2.24%± 0.06%
^{151}Sm	1.008g±$2.114 \cdot 10^{-4}$	1.008g±$2.925 \cdot 10^{-4}$	$0.000 \cdot 10^{+0}$±$3.609 \cdot 10^{-4}$	0.00%± 0.04%
^{152}Sm	3.858g±0.002g	3.938g±$9.624 \cdot 10^{-4}$	$-8.000 \cdot 10^{-2}$±0.002g	-2.07%± 0.05%
^{153}Sm	0.152g±$2.465 \cdot 10^{-4}$	0.152g±$2.874 \cdot 10^{-4}$	$4.000 \cdot 10^{-4}$±$3.786 \cdot 10^{-4}$	0.26%± 0.25%
^{153}Eu	1.824g±0.003g	1.869g±0.002g	$-4.500 \cdot 10^{-2}$±0.003g	-2.47%± 0.18%
^{154}Eu	0.192g±$2.915 \cdot 10^{-4}$	0.199g±$3.896 \cdot 10^{-4}$	$-7.400 \cdot 10^{-3}$±$4.866 \cdot 10^{-4}$	-3.86%± 0.26%
^{155}Eu	0.083g±$3.383 \cdot 10^{-5}$	0.085g±$5.241 \cdot 10^{-5}$	$-2.000 \cdot 10^{-3}$±$6.238 \cdot 10^{-5}$	-2.42%± 0.08%
^{156}Eu	0.153g±$1.133 \cdot 10^{-4}$	0.157g±$1.517 \cdot 10^{-4}$	$-3.200 \cdot 10^{-3}$±$1.893 \cdot 10^{-4}$	-2.09%± 0.12%
^{157}Eu	0.002g±$1.655 \cdot 10^{-6}$	0.002g±$8.017 \cdot 10^{-7}$	$-2.200 \cdot 10^{-5}$±$1.839 \cdot 10^{-6}$	-1.09%± 0.09%
^{157}Gd	0.003g±$1.855 \cdot 10^{-6}$	0.003g±$2.709 \cdot 10^{-6}$	$9.700 \cdot 10^{-5}$±$3.283 \cdot 10^{-6}$	3.55%± 0.12%

Table 17.15: *Difference between one and two burn-up predictor steps for current fuel element, EOL after 60 d, non-actinides, part 2*

CHAPTER 18

Verification

As discussed in chapter 12, the calculations carried out in this work are subject to numerous possible error sources. To address this, the results produced by the code system have to be verified. In this chapter, it is discussed what parts of the validation are required, were already done and which parts remain to be validated.

18.1 Neutronic Model

The MCNPX model used in this work is derived from a model that was validated earlier. This was done with measurements and Code-To-Code comparisons. Details on this process can be found in [Röh10a, Röh04, Röh91b]. The changes made to the model mentioned above during the course of this work are only minor. A short description of these has already been given in chapter 9.1. In addition, the neutronic results for the current fuel element from chapter 14 agree very well with the value calculated in the given references. Actually, chapter 14 can be regarded as the verification.

Concerning the code itself, MCNP was validated successfully for a similar core geometry at ORNL [Cha08]. MCNPX is based on the standard MCNP code. Excluding the delayed photons which cannot easily be calculated using MCNP, the results for MCNP 5 (rev. 1.40) and MCNPX 2.7B agree for the FRM II core regarding flux, power deposition and k_{eff}.

18.2 NBK

As a first verification for the thermal hydraulics which goes beyond the rather simple comparisons made in chapter 14, a comparison with calculations conducted by A. Röhrmoser using the NBK code was made. BOth codes use a completely different approach: NBK is a stream-filament based code which relies on the formulas given in chapter 6, CFX is a CFD code that is based on the models described in chapter 7. To compare both results, a lot of interpolation between the two different calculation grids is necessary, which introduces a number of difficulties in interpreting the results. Especially near steep gradients, unphysical behaviour can occur. Therefore, this results has to be interpreted with care. The general approach was to average the values in the CFX grid in radial direction to match the subchannel (stream filament) width of NBK. In axial direction, the CFX values near the closest NBK grid node were picked for comparison.

The result for the wall temperature of the inner plate side is shown in fig. 18.1. The outer plate side behaves accordingly.

The predicted wall temperatures are very similar in regions with lower heat fluxes. With rising heat fluxes, the temperatures predicted by NBK start to grow higher than those predicted by CFX. A part

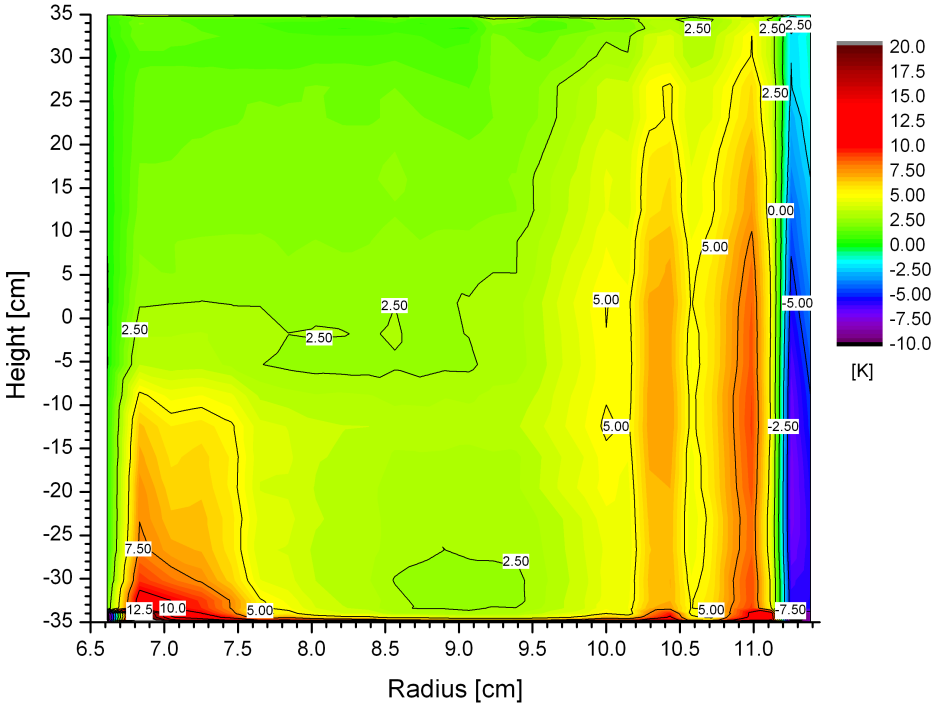

Figure 18.1: *Comparison of wall temperatures at the inner plate side, NBK - CFX.*

of the uncertainty can be explained with the various possibilities to calculate the Nusselt number as discussed in [Röh84, p. 39]. According to [Röh84, Bild 7] and [Röh], the cladding surface temperatures predicted by the chosen correlation for the Nusselt number ('Grenoble') is approximately in the middle of the presented correlations. A more 'aggressive' correlation, e. g. Sieder-Tate, would predict up to 10 °C lower temperatures that would probably be in better agreement with the CFX calculations.

Regarding the heat fluxes at the cladding surface (fig. 18.3), again most parts agree very well. However, some differences can be observed. The largest differences can be observed at the outer border of the fuel plate. A part of this difference can be attributed to a differing input data for the energy deposition in the meat. It can be seen in fig. 18.2 for $z = -16\,\text{cm}$ that the energy deposition input for NBK (green curve) in the outer vicinity of the plate is somewhat larger than that of CFX (blue curve), while near the inner plate border, the energy deposition by CFX is slightly higher. Care has to be taken when this figure is interpreted, as not all lines are recorded exactly at $z = -16\,\text{cm}$: The CFX energy deposition is averaged over a z-length of about 1 cm. Accordingly, the plate surface heat flux in CFX is larger at the inside and lower at the outside. The difference in the input data comes directly from the modelling of the involutes as discussed in chapter 9.1.1. This is not in contradiction with [Röh10c], where a very good agreement regarding the power profiles between diffusion calculations which were used to calculate the NBK source and MCNP calculations was shown: The corresponding MCNP model used concentric fuel plates and not evolutes, therefore this model does not suffer from the difficulties that are introduced when the involutes are modelled.

Another part of the difference can be explained by the difference in the modelling of the outer fuel plate border: As shown in fig. 18.4, in NBK the border of the fuel zone is modelled perpendicular to the involutes, while in CFX, the border is modelled as described by a circle around the centre of the evolute, i. e. strictly as it is the case in the radially symmetric neutronic model with a defined, sudden end of the fuel zone. The truth probably lies somewhere in between both modelling approaches. Regarding fig. 18.3, the modelling differences result in a somewhat higher or lower heat flux at the boundary of the fuel zone,

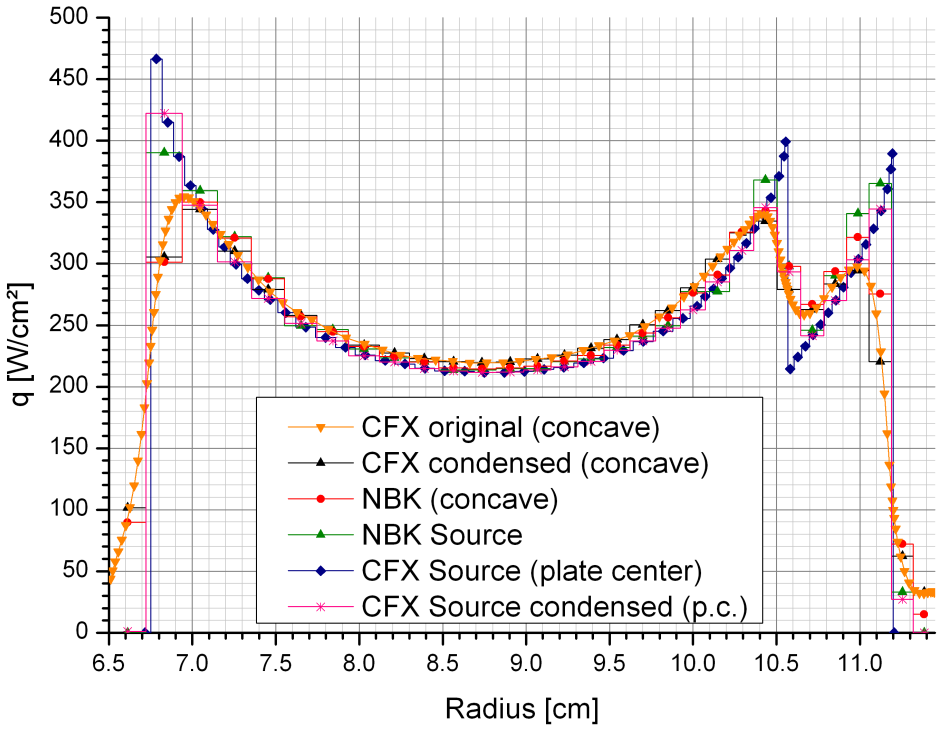

(a) Complete comparison

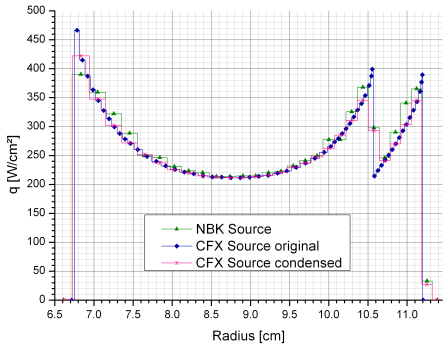

(b) Sources only

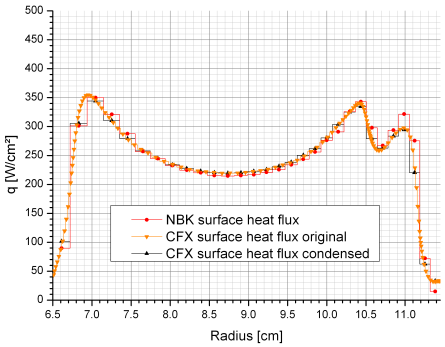

(c) Heat fluxes only

Figure 18.2: *Heat flux difference at z=-16 cm on plate surface and energy deposition. The blue curve is the projected heat source distribution for CFX which is condensed to the NBK grid in the pink curve, the green curve is the projected source for NBK. The orange curve is the original output of the surface heat flux from CFX, which is condensed on the grid structure of NBK in the black curve. The red curve shows the NBK surface heat flux. For a better visibility, (a) is split up into sources in (b) and surface heat fluxes in (c).*

depending on which sides of the plate are compared.

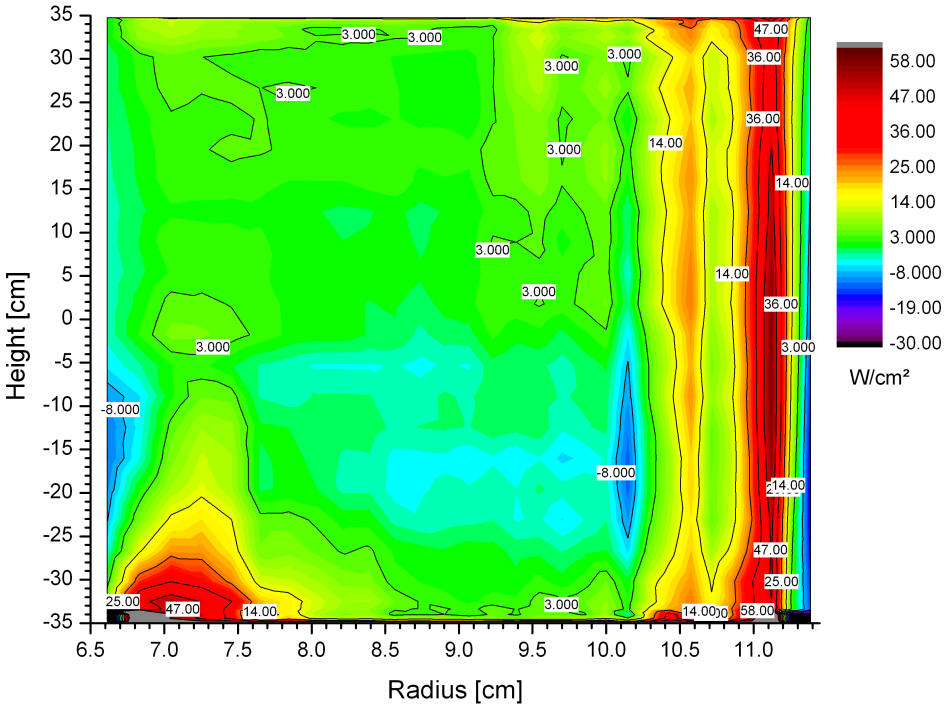

Figure 18.3: *Comparison of heat flux densities (NBK minus CFX).*

However, the modelling difference explains only a part of the occurring differences. A CFX model that was created to represent the plate shape as modelled in NBK showed smaller differences to the original model than it was the case for NBK (see fig. 18.5 where the difference between both CFX modeling approaches is shown). In this special CFX model, in addition, the thermal conductivity of the outer fuel zone was set to the same value as the inner zone, to resemble the NBK model as close as possible. Furthermore, heat transfer from the lower and upper border of the fuel plate in z-direction through these borders was blocked. Unfortunately, unlike COMSOL, CFX does not allow to specify the thermal conductivity as a tensor, only as a scalar. It is therefore not possible to completely block heat transfer in z-direction, which would be equivalent to the implementation in NBK.

The other differences, especially in steep gradients, are mostly due to the interpolation and condensation that was required to compare both calculations and to the interpolation that is done by NBK when weighting the source, as a direct comparison of the energy deposition yielded a good agreement.

As a further difference, a stripe of higher heat fluxes can be observed a little outside the density step. This deviation probably results again from slightly differen power depositions and in parts from the different thermal conductivities for the zone with lower uranium density: NBK assumes the same (lower) thermal conductivity as for the higher uranium density, while this work uses the about 50% higher thermal conductivity of the real material. Therefore, the peak of power deposition at the density step can spread better towards the outer zone.

Larger deviations are also visible at the bottom of the plate. These were expected as NBK has no solid heat conduction parallel to the flow direction of the cooling fluid implemented.

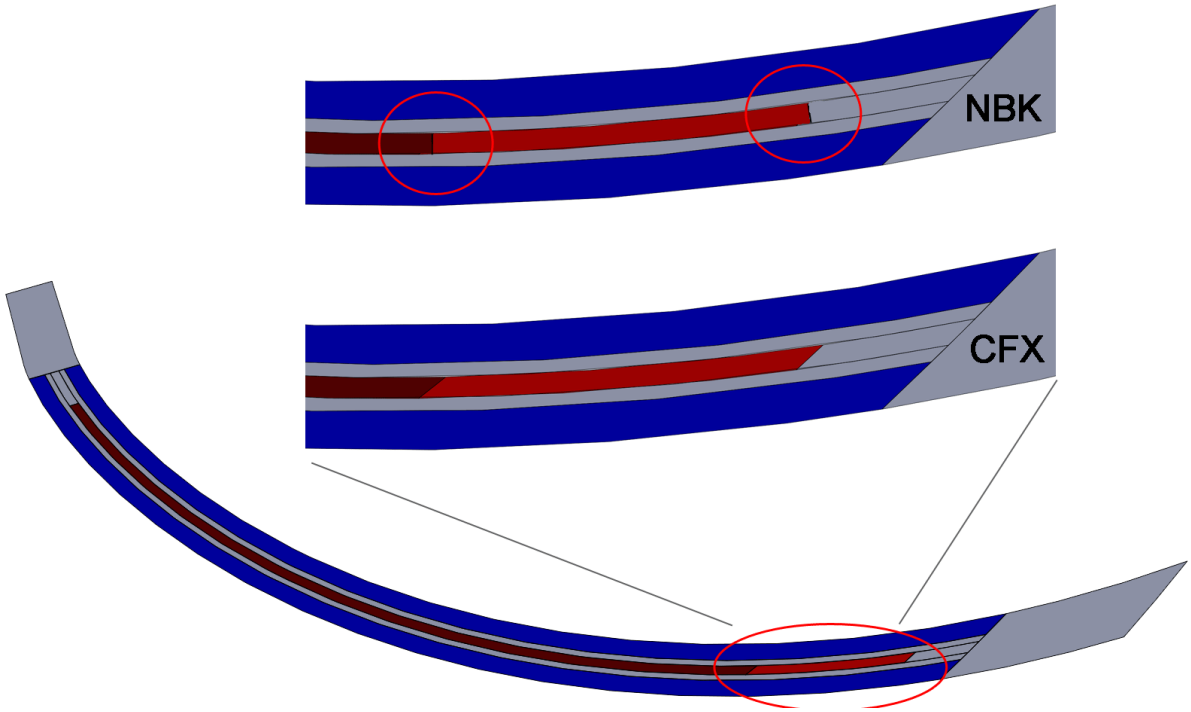

Figure 18.4: *Difference in fuel plate modelling between NBK and CFX*

18.2.1 Assessment

Although there are some differences between CFX and NBK, most of them can be explained and the overall agreement between both codes is good. This probably can be further improved by choosing finer resolutions in NBK and adjusting the CFX model according to the discussion above. The 2D-plots shown above pronounce small differences quite strong, but most of these differences can be explained.

The very different nature of both codes and the required data treatment to be able to compare the results brings a number of difficulties, which have already been discussed and make the results look inferior to the actual situation. It seems therefore worthwhile to compare CFX to a code which uses a more similar approach, e. g. a finite elements fluid dynamic code. This will be done in the next section.

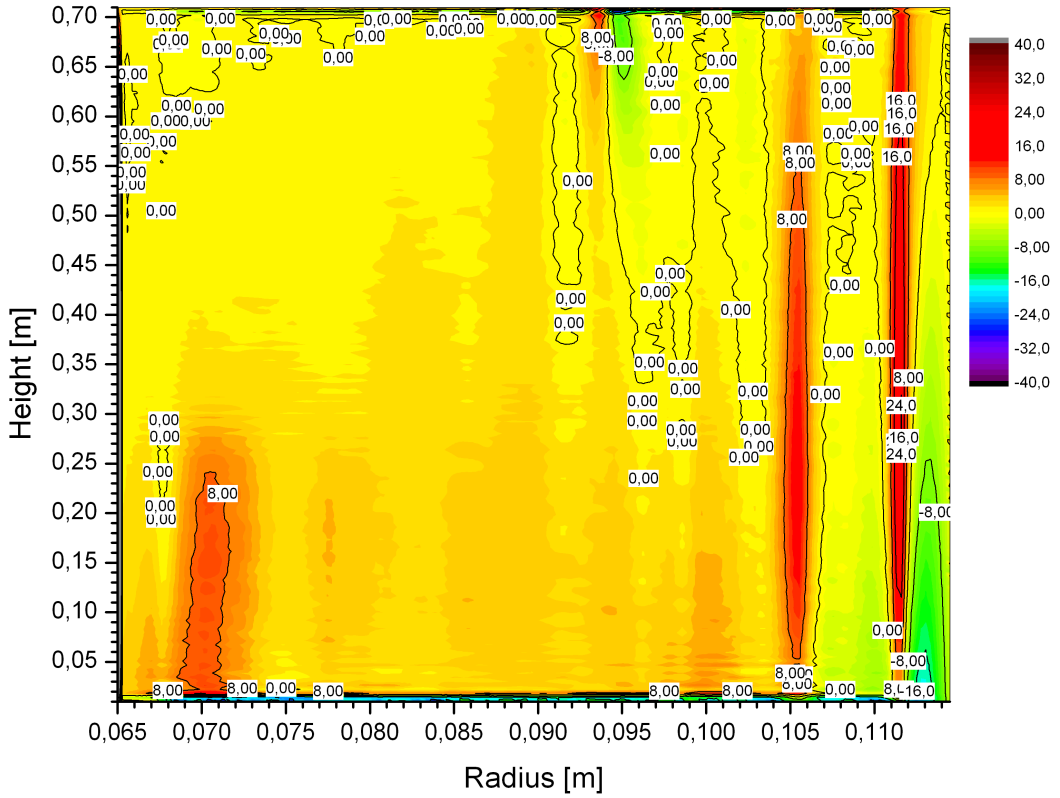

Figure 18.5: *Heat flux difference on plate surface due to different modelling of fuel plates in CFX: Both calculations were carried out using CFX, one with the original model and one which was modified to resemble NBK as close as possible.*

18.3 COMSOL Multiphysics

With the intention to exclude errors in the modelling process in CFX and to ensure that the CFX solver is working properly, a comparison with COMSOL Multiphysics (version 3.5a) which is used at the HFIR at ORNL [Pri09a, Pri09b, Pri10, Fre09] was carried out.[1] For this, the model was created again in COMSOL Multiphysics. Due to computational limitations, not the complete model as used in most of the calculations in this work was set up, but only the important middle part of the fuel plate without the inner and outer tube. For this reason, the results obtained yield different numbers at the borders of the fuel plate, as at the top and the bottom of the active zone, no heat conduction in z-direction was possible as the model ended there. However, this model was derived from the original CFX model, and a similar model was created for the comparison calculation in CFX.

18.3.1 Model Set-up

As the SST turbulence model was not available in COMSOL, the k-ϵ-model was used in the calculations. Accordingly, the CFX model was set to use this turbulence model, too. The sensitivity analysis in chapter

[1] Version 3.5a was the production version of COMSOL during the stay of the author at HFIR. By the time of writing of this work, version 4.0a is the production version, which significantly improves some of the deficiencies discussed in the following.

17.1.2 showed that this model predicts slightly higher wall temperatures and higher wall heat flux densities.

Two different models were created: A slab model, which has equal dimensions as an 'uncoiled' version of the involute model; and an involute shaped model (fig. 18.6). The former includes symmetry conditions in the middle of the cooling channel and in the middle of the solid. The latter includes a complete fuel plate, a complete cooling channel and periodic boundary conditions.

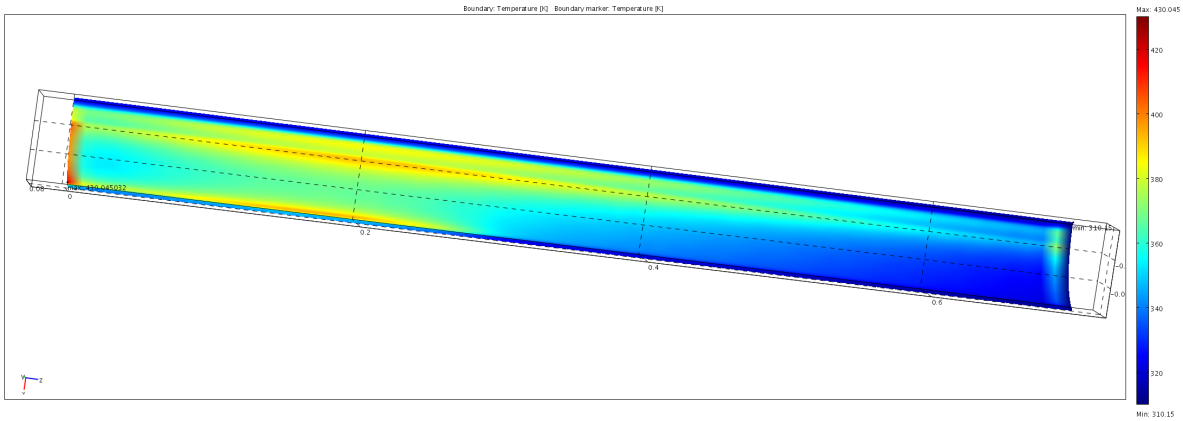

Figure 18.6: *The model of the fuel plate as it was created in COMSOL. Colours indicate the surface temperatures of the solved model.*

For the slab model, a mesh with 140 nodes in z-direction was chosen. Due to computational limitations, for the involute model, only 70 uniformly distributed mesh vertices could be used in z-direction. The memory requirements of COMSOL are much larger than those of CFX. In the present case, the involute model required 64 Gb of RAM. Additionally, the meshing capabilities within COMSOL are limited and the import of a mesh from an external meshing applications always failed or led to erroneous mesh structures which produced unphysical results like stalling flow regions without a physical reason. As CFX is not capable of importing meshes from COMSOL, it was not possible to use one and the same mesh in both applications. Instead, the meshes for both applications were created with two different tools, internal meshing tools for COMSOL and ICEM for CFX. Even though they share most of the parameters, both meshes are different, due to the differing algorithms used for their creation. In this special case, both the CFX and the COMSOL mesh were generated using a semi-automatic algorithm for extruded 2D meshes. The 2D meshes are triangular with rectangular boundary layers (see fig. 18.7).

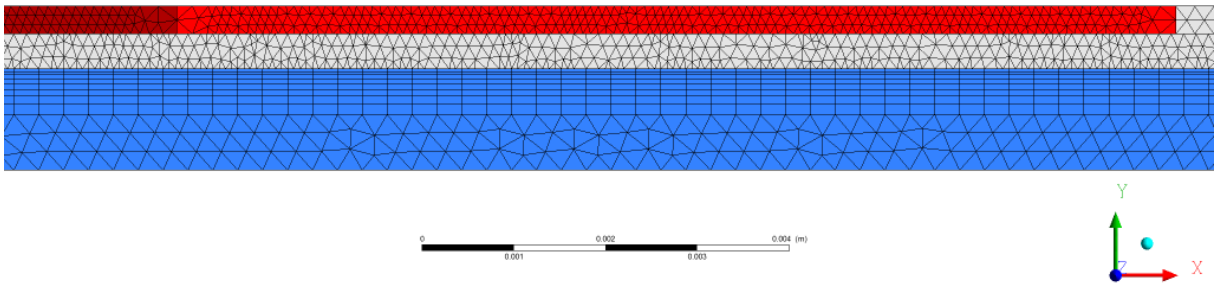

Figure 18.7: *2D mesh for the slab model in CFX. Dark red: high density fuel zone; light red: low density fuel zone; grey: aluminium; blue: water.*

18.3.2 Results

Involute model

Concerning the involute model, the results are presented in figures 18.8 for the heat fluxes and 18.9 for the surface temperatures of the plate. The heat fluxes in CFX and COMSOL compare quite good as soon as the power that is deposited in the plate in total is renormalized accordingly. Differences arise mainly at the outer borders of the fuel zone, where gradients are steep. To understand these differences, the mesh structure has to be taken into account.

Inlet: The boundary condition at the inlet was unphysical, as a homogeneous flow speed of 15.91 $^{m}/_{s}$ was specified, regardless of any wall profile that should exist. In addition, the implementation differences between finite volumes (CFX) and finite elements (COMSOL) cause differences in the evaluation of the results which must be resolved by means of inter- and extrapolation. Also, the differences in the wall functions (see later discussion) will cause differing results in this region.

Outlet: At the outlet, only the implementation differences between finite volumes and finite elements are responsible for the observed differences in the heat flux. In this case, the differences stay smaller than about 20%. At the inlet, they are much larger.

Outer borders of fuel: In radial direction, larger relative differences can be observed at the inner and outer border of the fuel. However, speaking in absolute terms, these differences are rather small ($\approx 10\,{}^{W}/_{cm^2}$) and can be attributed to the differing mesh resolutions near the steep gradients and to the strongly differing surface temperatures.

Density step: The differences near the density step are rather small and probably an effect of mesh resolution and surface temperatures.

$r = 0.068\,m,\ z = 0.30\,m$*:* A combined effect of the very coarse z-resolution of the meshes and the differing implementation of finite elements and finite volumes. The steep gradient in z-direction can not be resolved by the coarse mesh.

While the heat fluxes compare rather well, a completely different picture is drawn by the wall surface temperatures. As expected, large differences can be observed near the unphysical inlet. But, differences up to 36 K are present in the main fuel regions. These differences are strongly positively correlated with the heat flux densities. The temperatures predicted by COMSOL are much higher than those predicted by CFX. COMSOL uses two variables to for the temperatures in the model, T_s for the solid and T_f for the fluid. If T_f is compared at the wall to the wall temperatures of CFX, results agree quite well. However, due to the implementation of the finite elements, this value is read in the middle of the first mesh cell in the fluid near the wall, not exactly at the wall. The value is then extrapolated to the boundary. In contrast, T_s is read in the middle of the first mesh cell in the solid and extrapolated [COM10]. As the temperature gradient is much smaller and more uniform in the solid, it is of advantage to compare T_s to the wall temperatures predicted by CFX (see also the discussion on the slab model later on).

Freels [Fre10] has showed in 2D calculations for the HFIR fuel element, that the results in COMSOL 3.5a strongly depend on the y^+ value,[2] which is not the case for CFX as long as certain conditions are met (see chapter 17.1.3). In this case, for the COMSOL calculation, $y^+ \approx 50$. As can be seen in fig. 18.10(a), a much smaller y^+ value would have been appropriate. It is also shown in this picture that the wall temperature differences can be even higher than what was reported here. Unfortunately, this study was only released several months after the COMSOL calculations were performed for this work. Version 4 of COMSOL significantly improves the results due to the *Low Re-model* [Fre].

The results presented above indicate that is of no use to further discuss the results obtained by COMSOL. The calculations performed so far should be repeated with the new version of COMSOL, which has advanced CFD features in the new CFD module and is said to improve the results drastically. In this

[2] In COMSOL, this value is called δ_w^+.

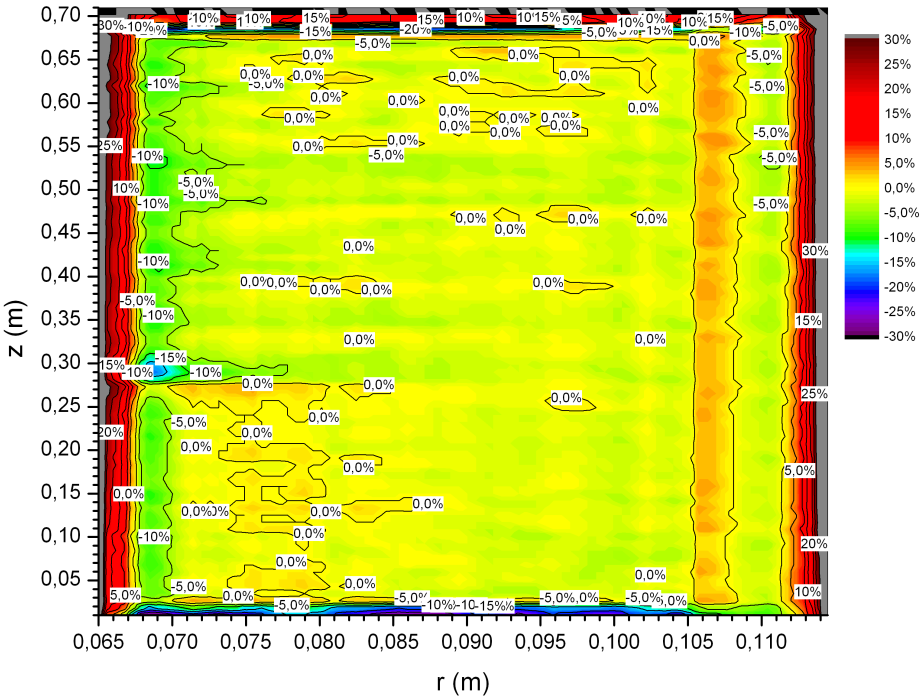

(a) Relative heat flux difference

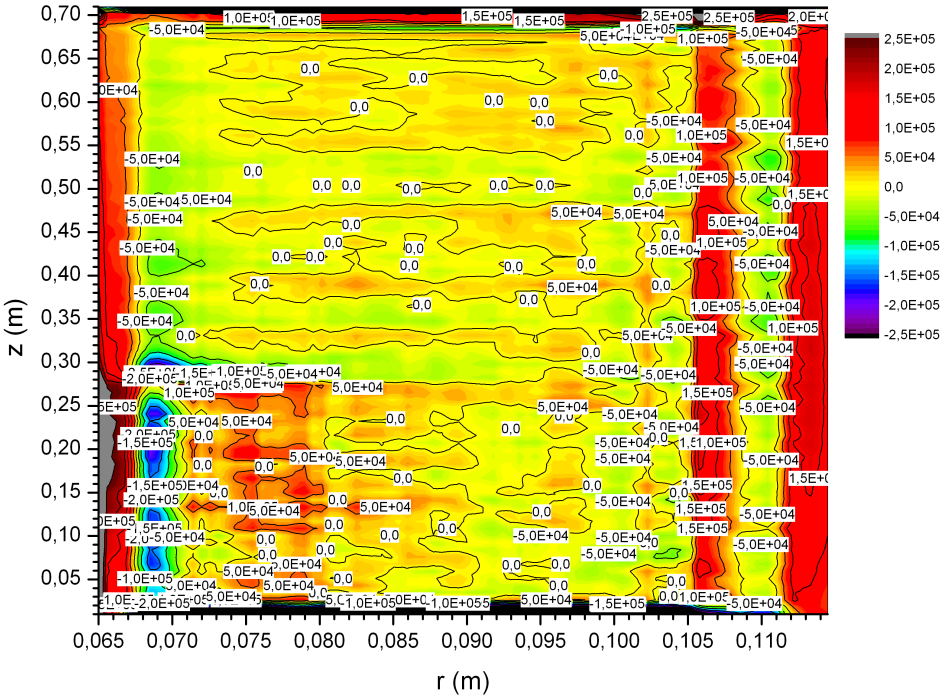

(b) Absolute heat flux difference

Figure 18.8: *Comparison of CFX and COMSOL results for involute model: Heat fluxes. Relative differences (a) and absolute differences (b).*

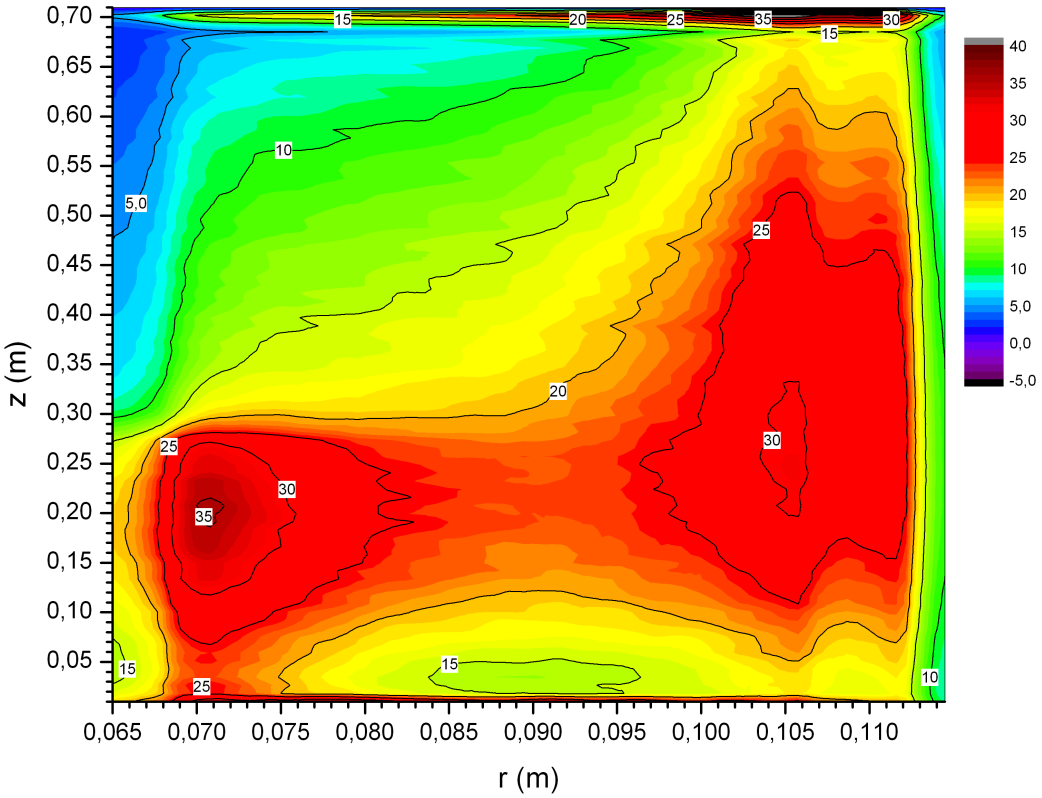

Figure 18.9: *Comparison of CFX and COMSOL results for involute model: Surface temperature differences (COMSOL - CFX).*

context, an extension of the model in z-direction is proposed to get rid of the unphysical inlet condition and the unreal outlet.[3]

Slab Model

The slab model failed to converge in COMSOL to the desired RMS of 10^{-3}. Instead, the calculation stopped slightly above this level. Nevertheless, it was possible to compare the obtained results to a similar CFX calculation. The findings for the fluid-solid-interface were similar to those in the involute case. If T_f near the wall is compared to CFX wall temperatures (fig. 18.11(c)), the results agree quite well. However, if the same comparison is made at the symmetry plane in the middle of the fuel zone (fig. 18.11(d)), high temperature differences appear again. Reason for this behaviour is again the high sensitivity of COMSOL to y^+, and, as discussed above, the finite element implementation.

Again, heat fluxes compare quite good, except at the outer borders near the tubes. The mesh of the slab model has twice as many nodes in z-direction, which gives much better results for in- and outlet than in the involute case. The heat flux differences are shown in figures 18.11(a) and 18.11(b). Analogue reasons as discussed above can explain the differences.

[3] COMSOL 4 offers the possibility to connect several computer nodes via MPI, therefore the old 64 Gb RAM limitation can be circumvented.

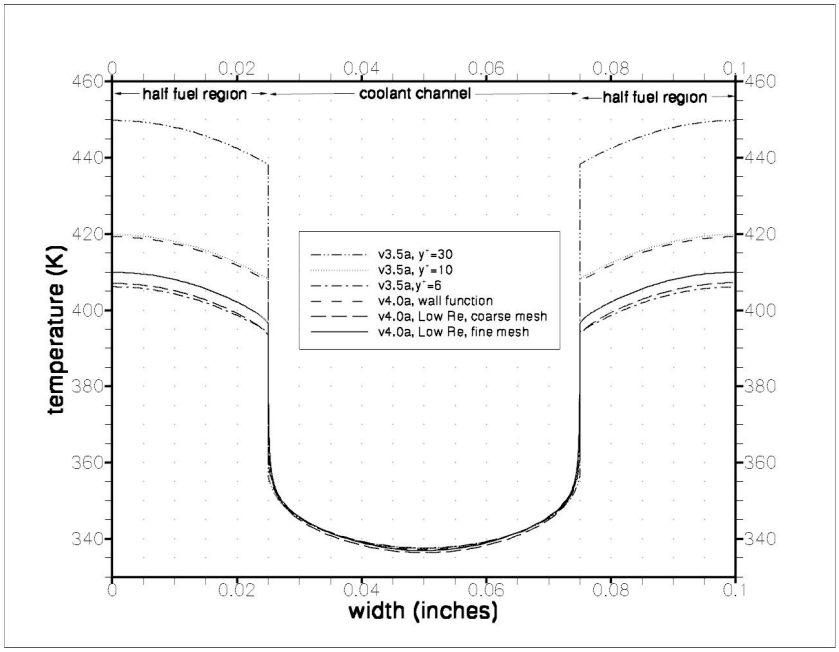

(a) Wall temperatures

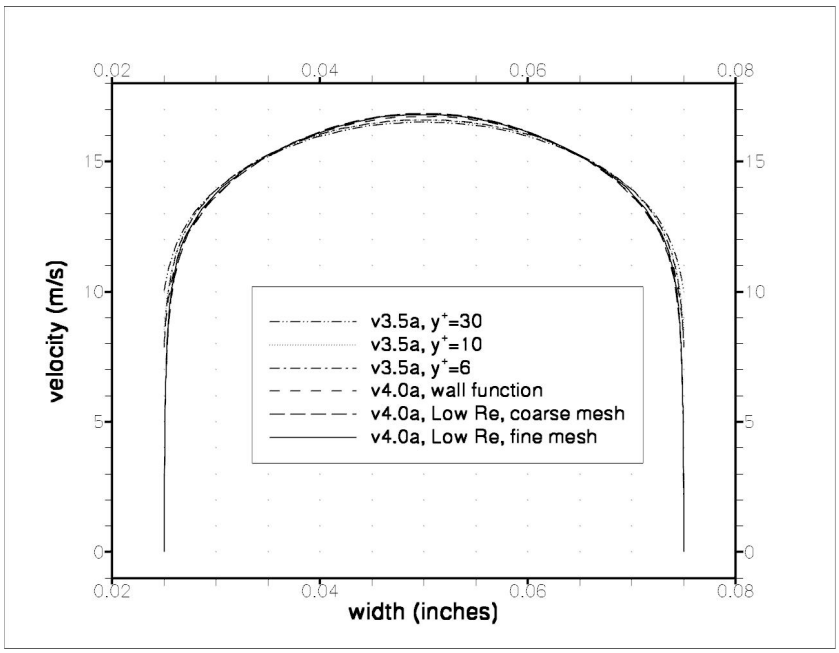

(b) Velocities

Figure 18.10: *Dependency of the wall temperature (a) and velocity (b) on y^+ in COMSOL. Taken from [Fre10].*

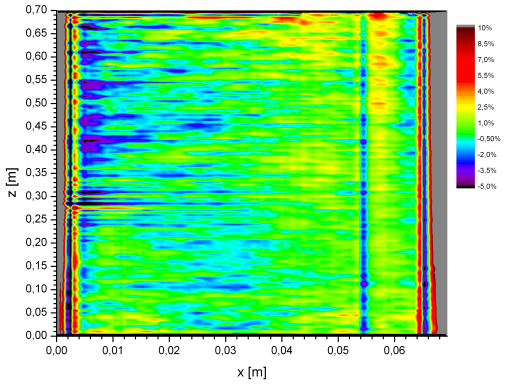

(a) Relative heat flux difference at the fsi

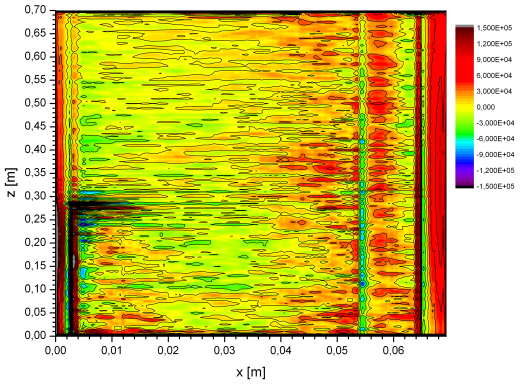

(b) Absolute heat flux difference at the fsi

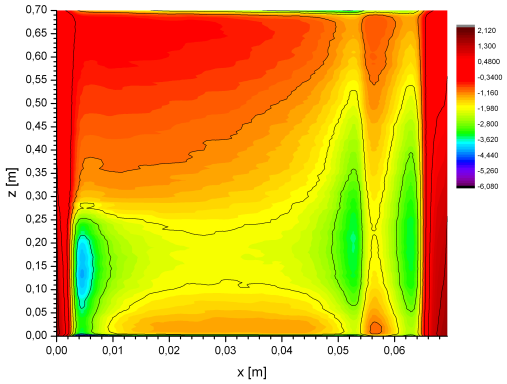

(c) T_f at the fluid-solid interface

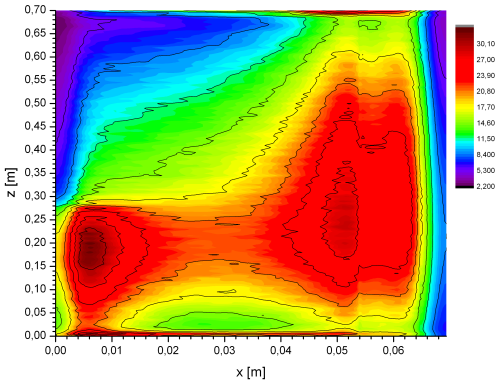

(d) T_s at the solid symmetry plane

Figure 18.11: *Comparison of CFX and COMSOL results for slab model: Heat fluxes (a), (b); Temperatures T_f vs. CFX wall temperature (c) and T_s at the symmetry plane in the middle of the fuel zone (d).*

Looking at velocities in the fluid symmetry plane offers some insight (fig. 18.12) into the near-wall behaviour: The velocities near the wall are up to $2\,^{\mathrm{m}}/_{\mathrm{s}}$ higher in COMSOL than in CFX.[4] This is also an effect of the wall function implementation / y^+ and consistent with what [Fre10] has found (compare fig. 18.10(b)): Larger y^+ values lead to higher velocities near the wall. This, of course, is physically inconsistent with the higher wall temperatures and an implementation issue of COMSOL.

18.3.3 Assessment

It must be concluded that the comparison to COMSOL Multiphysics has failed completely. By now, this comparison can not be used to verify the CFD calculations. Even though the heat fluxes through the cladding surface compare well for the involute as well as for the slab models, the significance of this result can only be judged after the y^+-problem that was discussed above is resolved. It is obvious from the calculated surface temperatures that this problem is present in the calculations presented here. By the time of writing this work, COMSOL has released a new version of its software (4.0 instead of 3.5a), which resolves this problems. Still, the comparison with COMSOL seems to be a promising way to verify the

[4] Higher differences can only be found near the unphysical inlet.

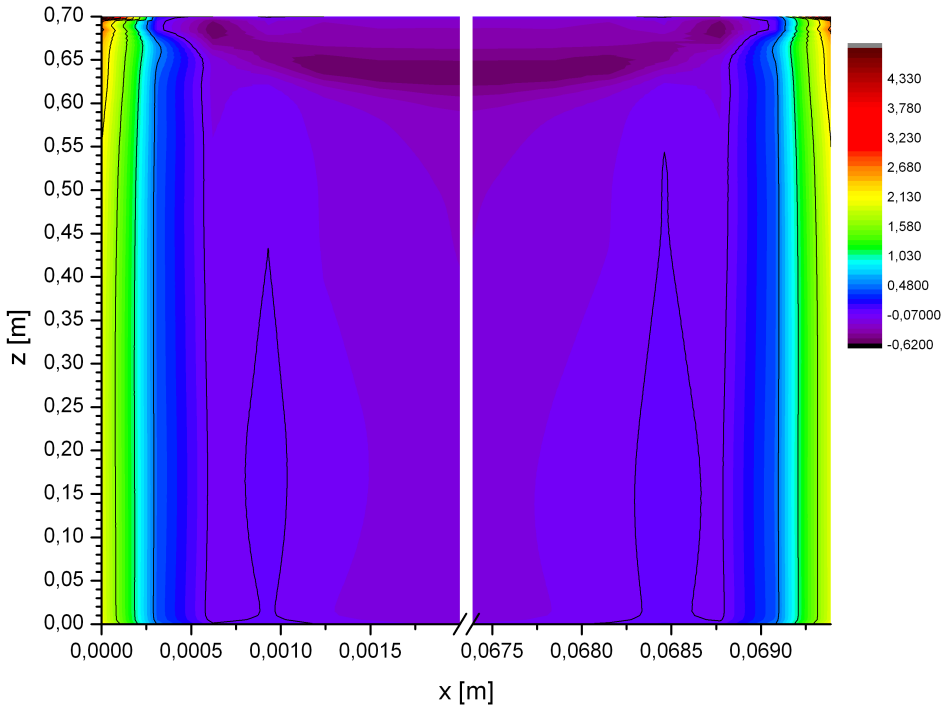

Figure 18.12: *Differences in velocities at the the fluid symmetry boundary (COMSOL - CFX).*

thermal-hydraulic calculations. It therefore seems worthwhile and promising to repeat these calculations at a later time.

18.4 X^2

As stated before, X^2 is a complex system of Perl scripts and Fortran programs that couple other programs and therefore hard to validate. The approach that was followed in this work was to compare for two different scenarios[5] the results from an automated X^2 run to a manual run, where every step was manually executed. Data transfer between the single programs and X^2 was also checked manually. In both scenarios, no differences between the automated and the manual execution were found.

[5]The two different scenarios were the current fuel element and one case of the disperse UMo fuel elements.

CHAPTER 19

Conclusions and Outlook

19.1 Summary

By coupling a Monte Carlo code and a CFD code, a state of the art reactor-physics calculation scheme was established. The system consists mainly of a set of Perl scripts and FORTRAN programs, that couple MCNPX for the neutronics, MonteBurns/Origen2 for the burn-up and CFX for the thermal hydraulics. The theory of the Monte Carlo calculations and especially for the thermal hydraulic calculations has been explained in great detail to keep record of the mathematical and theoretical basis of the calculations performed in this work. The system in which the above mentioned codes were coupled was named X^2. This system was developed especially for this work. An overview of its structure and a user guide can be found in appendix C, D respectively.

To verify the developed code systems, the properties of the current fuel element of FRM II were calculated and compared to results obtained by other codes and authors. These results were presented in chapter 14. The results agree well in most cases and measured values – as far as available – are well in the range of the estimated uncertainty of the calculations. If values calculated by other authors did not match the ones calculated in this work, the differences can be explained. A more detailed comparison was made for the thermal-hydraulic calculations, as they represent the main advantage over former calculations. This comparison was presented in chapter 18. The comparison to the stream filament code NBK which was used in the design calculations of FRM II showed the expected differences plus some differences, that cannot be completely explained by now. However, the overall agreement is very good and the remaining differences are rather small. The more obvious comparison of CFX to the finite element code COMSOL has to be declared a failure as the COMSOL results at that time exposed a strong y^+-dependence of the cladding surface temperatures, which must not be the case for a correct implementation of the wall functions. However, the author still considers a comparison with COMSOL to be the right approach to verify the thermal hydraulic capabilities of CFX, especially since the deficiencies of COMSOL that were addressed in chapter 18.3.3 have been fixed in the mean-time.

To assess the uncertainties of the X^2 calculations, a sensitivity analysis was performed for various parameters. This analysis mostly covers the burn-up sequence and the thermal hydraulic calculation. Referring to the COMSOL comparison described above, the mesh sensitivity analysis for CFX (17.1.3) showed only an insignificant y^+-dependence of the results as long as the first node distance is chosen in the correct regime, which is in agreement with what the CFX manual states. This can be considered the major result of this part of the analysis, as it strongly supports the reliability of the numbers given in this work for temperatures and heat fluxes. As already discussed in chapter 17.1.2, the error introduced by the turbulence modelling cannot be quantified completely by simulations alone[1], only measured, though it

[1] Actually, the error could be quantified if direct numerical simulations without the turbulence models could be performed. This, however, is not possible with reasonable effort at the moment.

seems from the sensitivity analysis (17.1.2) where different turbulence models were compared that – for the case of FRM II – this error is rather small. Furthermore, the inlet parameters for the cooling flow which were required for the calculations were not known from measurements in full detail. Some of the parameters therefore had to be estimated (10.1.2). However, the sensitivity analysis showed that the results depend only insignificantly on these parameters (17.1.7), which again strengthens the results.

The uncertainty analysis of the burn-up calculations (17.2) showed that the influence of the statistical error due to the Monte Carlo calculations is much smaller than systematic errors that can be introduced by the chosen methodology for discretising the burn-up equations. While this work was finished, Röhrmoser discovered another systematic error in MonteBurns [Röh10c]. This error is connected to the treatment of ^{148}Pm and its isomer, which cannot easily be calculated in MCNP(X) at the same time. However, the choice of another burn-up code will not fully solve this problem until a capability is added to the Monte Carlo Codes to include both isomers at the same time. If this has happened, the author suggests to include a new burn-up code into X^2 which is able to use these capabilities.

In principle, there are two ways to completely validate X^2 and the underlying programs: To compare the results to measurements, and to compare the results to those of other codes that are already validated. An example for the validation of a burn-up code is given in [Cha10], where the code ALEPH [Hea05] is validated for the very similar fuel plates and geometry of the HFIR in Oak Ridge by comparison to measurements. Due to the young age and therefore the high activity of the FRM II fuel plates, comparable measurements won't be possible with reasonable effort in the near future. However, MonteBurns was already validated for TRIGA reactors [Dal02], MOX fuel [Mos4] and other cases. The above mentioned systematic mistake is only notable in high flux reactors where ^{148}Pm and ^{148m1}Pm play a significant role. However, it seems from subsequent calculations that the full impact of this bug is rather small.

Also at ORNL, endeavours are made to validate COMSOL by means of a code-to-code comparison and measurements wherever they are available. Should this comparison succeed, the same technique could be used to validate CFX by repeating the calculations discussed in chapter 18.3. This is one of the main reasons that these calculations were performed. Due to the differences that showed up in the comparison calculations so far, additional calculations will have to be performed with the new version of COMSOL to validate CFX.

Based on the assumption that CFX is working well, a series of thermal hydraulic calculations was performed to study some of the details of the fuel element that could not be quantified so far:

- The influence of the sieve was calculated to obtain a physically valid velocity profile of the fluid velocity and turbulence throughout the annular geometry above the fuel plates (13.1). These profiles were later used as starting values in thermal hydraulic calculations, so that the parameters at the inlet of the simulated geometry can be considered physically valid.
- Evidence was found that a Kármán Vortex Street develops after the lower comb which fixes the fuel plate. However, no Vortex Street could be observed below the upper comb. Nonetheless, the influence of the upper comb on the cladding temperatures could be quantified. It turned out that even though the average speed of the fluid below the comb is reduced, the increased turbulences enhance the cooling slightly (13.2.1).
- The 3D solid heat conduction plays a significant role especially at the bottom of the fuel plate where steep power density gradients in axial direction exist (13.3). This capability is the main reason for the lower maximum heat fluxes and temperatures that were calculated by CFX in comparison to other programs which do not have this capability.
- Some problems wregarding the cooling channel that were more than twenty years old and unresolved up to now were adressed, namely the mixing of the stream filaments and the fluid velocities in the pointy corners outside. As assumed before, the pointy corners do not influence the cooling of the fuel zone (13.4). The mixing of the stream filament was simulated using a two fluid-approach which in some sense 'marks' parts of the fluid. It was found, that filament mixing occurs mainly at

the plate top and bottom, but not in the area over the actual fuel (13.5). This again justifies the approach used in NBK.

- The pressure profile (13.6) looks as expected and reproduces the measured pressure drop. As the pressure drop turned out to be the quantity that depends most on the mesh (17.1.10), this is regarded as a strong support for the mesh quality that was analysed last in this chapter (13.8). An interesting result of the pressure analysis is that the temperature distance between the actual fluid and the saturation temperature, where boiling would start, is lowest at the very bottom of the fuel plate and not located over the active zone (13.6.1). The relevance of this was shown again in chapter 15.9, where the change of the safety margins in conjunction with a possible increase of the reactor power was discussed.

As a feasibility study, it was shown in chapter 13.7, that the system is in principle able to calculate the burn-up of the beryllium follower in the control rod. However, unlike in Mf2dAb, no out-of-the-box integral burn-up capability exists in X^2 yet to quantify the change over more than one reactor cycle. In addition, the feasibility study presented here uses only one burn-up zone, which is surely not enough to quantitatively assess the changes [Röh91a].

As all of this work was performed in the framework of the conversion of FRM II to a lower enriched fuel, it was self-evident to use the new code system to discuss a number of possible solutions. Two options were discussed, for disperse (chapter 15) and for monolithic UMo (16). It was shown that FRM II can be converted to a lower enrichment with both options without significantly worsening the thermal hydraulic properties and without overly decreasing the safety margins, so that the new cores can well be considered safe. Regarding the thermal neutron flux, with straight-forward solutions, the flux loss will be considerable, between 7.5% and 8.5%. Naturally, the flux loss rises with decreasing enrichment. As for the disperse UMo case, an enrichment of 50% was chosen, and 40% for the monolithic case, the flux loss is slightly higher for the monolithic fuel plate. In addition, the burn-up will be considerably higher, posing higher burdens for the qualification of the fuel. Table 19.1 compares the current core, the 8g U/cc-20MW-60d disperse UMo and the turkish hat monolithic UMo solution. Both new options have already been assessed in more detail in chapters 15.10 and 16.10, respectively.

It is obvious that the amount of fissionable uranium has to be increased significantly in both cases to over-compensate the increased parasitic absorption due to the higher amount of ^{238}U. Accordingly, the amount of nuclear waste grows in the same order of magnitude, producing nearly ten times the amount of Plutonium.

However, the flux loss in the presented solutions is more than marginally, therefore they will have to be optimised. This is currently done by J. Sarvas for the disperse case and will probably be continued by M. Däubler for the monolithic fuel. Some ideas and entry points for this, especially regarding a further compaction of the fuel element, were discussed in chapters 15.10.1 and 16.10.1, respectively. With the new possibilities offered by X^2, a more detailed analysis of the thermal hydraulic parameters is possible, principally allowing for this further compaction and the compensation of the flux loss this way. However, preliminary calculations showed that at least for the disperse UMo core, the flux loss cannot be compensated fully by a further compaction of the core. It is therefore worthwhile thinking about a combination with the scenarios that included a longer reactor cycle and an increased power. A combination of two or three of these options may in future well be able to yield a fuel element which does not show a significant loss in the cycle neutron yield.

Quantity	*Current core*	*8 g / 60 d / 20 MW disperse U8Mo*	*turkish hat* $425\,\mu m$ */ 60 d / 20 MW monolithic*
Fuel plate parameters (BOL)			
Fuel	U_3Si_2 disperse	U8Mo disperse	U8Mo monolithic
Enrichment	93%	50%	40%
BOL Content ^{235}U / U	7.5 kg / 8.1 kg	10.7 kg / 21.7 kg	11.3 kg / 28.6 kg
Max. deposited power	3.7(1) $^{MW}/_{l}$	4.6(1) $^{MW}/_{l}$	3.6(1) $^{MW}/_{l}$
Deposited power	18.02 + 0.16 MW	18.07 + 0.23 MW	18.04 + 0.22 MW
Burn-up			
Max. Burn-up	52.6%	43.0%	40.2%
Max. Burn-up absolute	$1.98 \cdot 10^{21}\ ^{1}/_{cm^3}$	$2.13 \cdot 10^{21}\ ^{1}/_{cm^3}$	$5.52 \cdot 10^{21}\ ^{1}/_{cm^3}$
Avg. Burn-up	20.4%	14.2%	13.5%
Min. Burn-up	5.8%	3.9%	3.9%
Avg. residual enrichment	87.4%	45.1%	35.9%
Fluxes $[^{1}/_{s\,cm^2}]$			
Max. thermal D_2O	$6.36(1) \cdot 10^{14}$	$5.91(1) \cdot 10^{14}$	$5.84(2) \cdot 10^{14}$
Max. thermal overall	$7.47(5) \cdot 10^{14}$	$6.58(5) \cdot 10^{14}$	$6.74(4) \cdot 10^{14}$
Max. fast	$9.18(1) \cdot 10^{14}$	$8.89(1) \cdot 10^{14}$	$8.77(1) \cdot 10^{14}$
Cycle neutron yield $[^{1}/_{cm^2}]$	$3.21(2) \cdot 10^{21}$	$3.02(2) \cdot 10^{21}$	$2.97(2) \cdot 10^{21}$
Flux compared to current fuel element [%]			
In thermal max. D_2O	-	-7.7(3)%	-8.2(3)%
In thermal max. overall	-	-15.3(5)%	-9.8(5)%
In fast max.	-	-3.6(3)%	-4.5(3)%
Cycle neutron yield	-	-7.1(4)%	-7.5(4)%
Temperatures [°C]			
Max. Fuel	102.9(5)	108.2(5)	129.9(5)
Avg. Fuel	66.7(5) / 73.7(5) / 68.0(5)	66.6(5) / 76.8(5) / 68.4(5)	74.8(5)
Max. Wall	89.6(3)	91.8(3)	91.7(3)
Avg. Wall	62.2(3)	62.3(3)	61.9(3)
Avg. Outlet	53.0(1)	52.9(1)	53.0(1)
Heat Flux $[^{W}/_{cm^2}]$			
Max. Wall	382.3(15)	407.1(15)	401.9(15)
Avg. Wall	161.3(5)	161.5(5)	161.3(5)
Safety margins			
S_{ONB}	2.51	2.35	2.40
S_{DNB}	2.48	2.30	2.31
S_{OFI}	5.61	5.18	5.15

Table 19.1: *Comparison of current, a disperse and a monolithic UMo core*

19.2 Outlook

In the field of computational fluid dynamics, further improvements will surely be related to multiphase calculations and turbulence, and especially the combination of both. It can be expected that appropriate models will be implemented in the common CFD codes within the next few years, allowing for a detailed simulation of boiling phenomena and therefore a reliable, non-conservative prediction of the onset of flow instability and other boiling-related phenomena. Using these capabilities, it will be possible to judge the safety margins of the FRM II fuel elements from a more physical point of view. A possible implementation of this was already discussed in chapter 8. However, as it was not possible to implement that approach into CFX due to technical problems in the given time-frame, safety margins were still calculated by the old and much more conservative approach that was discussed in 6.3. The author considers this to be a field that allows for significant improvements.

Further improvements – apart from possible bug fixes – in MCNPX will not affect the results of this work significantly. Power distributions might become a little more precise when enough computational power is available to include delayed gammas as line spectra and beta-radiation energy transport. However, this won't affect the results in a noticeable way. Improvements that are useful for X^2 can especially be found in the vicinity of the burn-up capabilities and the possibility to include several isomers of the same isotope. This has already been discussed in detail above. Of course, there might be other improvements, e. g. concerning the user-interface, for example a (working) CAD import, but these will not affect the results.

Possible improvements in X^2 itself could include an advanced error treatment and a more flexible inclusion of CFX. Also, some kind of 'full service' calculation routine is imaginable, which includes flux and power distributions at BOL, EOL and a burn-up calculation, but not a fully coupled run, which would take about twice as long. As mentioned before, it is desirable to include a more recent burn-up code and to fully include the uncertainty treatment discussed in chapter 4.4.

19.3 Conclusion

The combination of a Monte Carlo Code and a CFD code is a solution that can be considered state of the art for the next years. Such a system is X^2 . It includes codes that are industry-standards, have a broad user base and a long development history. These codes can be considered to be among the leading codes in their fields. Hopefully, the more detailed calculation possibilities that are possible with X^2 compared to former solutions, especially on the thermal-hydraulic side, will ease the conversion of FRM II while reducing the expected flux loss as far as possible and keeping the high safety standards of the reactor.

Part V

Appendix

APPENDIX A

Geometrical and Mathematical Considerations on Involutes

A.1 Basic Considerations

A.1.1 Basic Equations

Parametric Involute Equation

Involutes are described by a pair of equations:

$$\begin{pmatrix} x(r,\varphi) \\ y(r,\varphi) \end{pmatrix} = r \begin{pmatrix} \varphi\cos\varphi - \sin\varphi \\ \cos\varphi + \varphi\sin\varphi \end{pmatrix}. \tag{A.1}$$

r is the radius of the circle (the evolute) that is used to construct the involute, φ is the angle (see fig. A.1). The equation of an involute whose origin of unwind is turned by θ is obtained by multiplying the vector with a rotary matrix:

$$\begin{pmatrix} x(r,\varphi,\theta) \\ y(r,\varphi,\theta) \end{pmatrix} = r \begin{pmatrix} \cos\theta & -\sin\theta \\ \sin\theta & \cos\theta \end{pmatrix} \begin{pmatrix} \varphi\cos\varphi - \sin\varphi \\ \cos\varphi + \varphi\sin\varphi \end{pmatrix}. \tag{A.2}$$

Using the addition theorem:

$$\begin{pmatrix} x(r,\varphi,\theta) \\ y(r,\varphi,\theta) \end{pmatrix} = r \begin{pmatrix} \varphi\cos(\varphi+\theta) - \sin(\varphi+\theta) \\ \cos(\varphi+\theta) + \varphi\sin(\varphi+\theta) \end{pmatrix}. \tag{A.3}$$

The space between two such involutes is given by $d = r \cdot \theta$ respecitvely $\theta = d/r$. As the length of a tangent on the circle until its intersection with the involute is given by the wind up distance on the circle, the intersection of a tangent being wind up by φ with an involute that is turned by θ can be obtained by the replacement $\varphi \longrightarrow \varphi - \theta$ in eq. A.3.

Distances and Angles

The direct distance between an involute at angle φ and the center of the circle is given by

$$R(r,\varphi) = r\sqrt{1+\varphi^2}. \tag{A.4}$$

The angle between the connecting line of this point with the center of the circle and the connecting line between the beginning of the involute and the center is for $\varphi \in [0 \ldots \pi]$ given by

$$\alpha_\varphi = \arctan\left| r \cdot \frac{\varphi\cos\varphi - \sin\varphi}{\cos\varphi + \varphi\sin\varphi} \right| \tag{A.5}$$

A.1.2 Intersection Points

Circle

From eq. A.4 the point of intersection of an involute and a circle with radius R can be calculated:

$$\varphi = \sqrt{\left(\frac{R}{r}\right)^2 - 1}. \tag{A.6}$$

The coordinates can be obtained by inserting this result in eq. A.1.

Straight line

The point of intersection of a straight line $(x_0 + t\delta x, y_0 + t\delta y)$ and an involute can be calculated with the following equation:

$$f(\varphi) := y_0 + \left(r\left(\varphi\cos\varphi - \sin\varphi\right) - x_0\right)\frac{\delta y}{\delta x} - r\left(\cos\varphi + \varphi\sin\varphi\right) = 0. \tag{A.7}$$

In this equation, the roots depending on φ have to be found numerically and the result has to be inserted into A.1 [1].

A.2 Coordinate System for Involutes

A.2.1 Definition

With equation A.3, using variables $\varphi \in [0, \infty[$ (wind-off from the circle) and $\theta \in [-\pi, \pi[$ (starting angle) with parameter $r \in]0, \infty[$ (radius of circle) and introducing a third coordinate $h = z/r$ (height, comparable to cylindrical coordinates), a coordinate system E with coordinates (φ, θ, h) can be defined[2][3]

$$\begin{pmatrix} x \\ y \\ z \end{pmatrix} = r \begin{pmatrix} \varphi\cos(\varphi+\theta) - \sin(\varphi+\theta) \\ \cos(\varphi+\theta) + \varphi\sin(\varphi+\theta) \\ h \end{pmatrix}. \tag{A.9}$$

The inverse transformation from A.9 is given by

$$\begin{pmatrix} \varphi \\ \theta \\ h \end{pmatrix} = \frac{1}{r} \begin{pmatrix} r \cdot \arccos\left(\frac{\sqrt{x^2+y^2-r^2}}{x\sqrt{x^2+y^2-r^2}+ry}{x^2+y^2}\right) - \sqrt{x^2+y^2-r^2} \\ z \end{pmatrix}. \tag{A.10}$$

[1] To avoid numeric problems with very steep lines ($\delta x \to 0$), the equation is multiplied by δx. The numeric solution can for instance be obtained by the Newton-Raphson-Method of second order:

$$\varphi^{(r+1)} = \varphi^{(r)} - \frac{f'\left(\varphi^{(r)}\right)}{f''\left(\varphi^{(r)}\right)} \pm \frac{\sqrt{f'\left(\varphi^{(r)}\right)^2 - 2f\left(\varphi^{(r)}\right)f''\left(\varphi^{(r)}\right)}}{f''\left(\varphi^{(r)}\right)}, \tag{A.8}$$

where f' is the derivative of f from eq. A.7 after φ.

[2] The system defined here does not cover the whole space, the area in the circle can't be described by these coordinates. A.3 is therefore only a chart of $\mathbb{R}^2$ for $R > r$. A second chart for $R < r$ completes the system to an atlas and therefore a complete coordinate system. Considering geometry and continuity, cylindrical coordinates are suitable. The mapping defined by curve A.3 is homeomorphic and continuous, an inverse function exists, see eq. A.10.

[3] For simplicity in calculations, the z-coordinate is also stretched by a factor r.

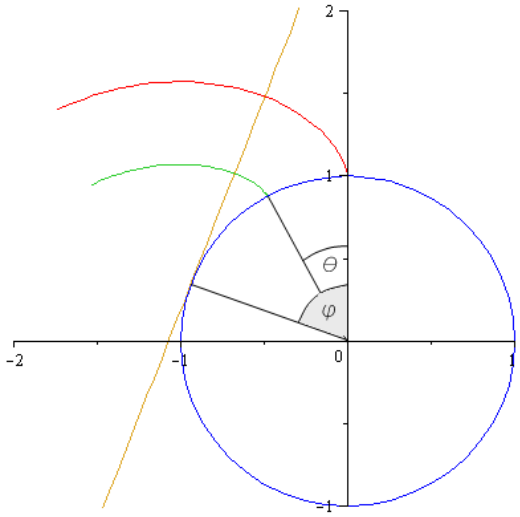

Figure A.1: *Involute coordinate system. φ is always calculated from the beginning of the involute. In the picture above, φ is related to the red curve. A φ, referencing the green curve, has to follow θ in the same rotational direction.*

A.2.2 Special Quantities and Operators

Jacobian Matrix

The Jacobian Matrix of the system is given by

$$\mathbb{J}_{\mathrm{E}}(\varphi,\theta) = r \cdot \begin{pmatrix} -\varphi\sin(\varphi+\theta) & -\varphi\sin(\varphi+\theta) - \cos(\varphi+\theta) & 0 \\ \varphi\cos(\varphi+\theta) & -\sin(\varphi+\theta) + \varphi\cos(\varphi+\theta) & 0 \\ 0 & 0 & 1 \end{pmatrix}, \tag{A.11}$$

its inverse by

$$\mathbb{J}_{\mathrm{E}}^{-1}(\varphi,\theta) = \frac{1}{r} \cdot \begin{pmatrix} -\frac{1}{\varphi}\sin(\varphi+\theta) + \cos(\varphi+\theta) & \sin(\varphi+\theta) + \frac{1}{\varphi}\cos(\varphi+\theta) & 0 \\ -\cos(\varphi+\theta) & -\sin(\varphi+\theta) & 0 \\ 0 & 0 & 1 \end{pmatrix}. \tag{A.12}$$

Metric Tensor

Using $g_{ij} = \sum_k \frac{\partial x_k}{\partial q_i} \cdot \frac{\partial x_k}{\partial q_j}$, the metric tensor is given by

$$g = r^2 \cdot \begin{pmatrix} \varphi^2 & \varphi^2 & 0 \\ \varphi^2 & 1+\varphi^2 & 0 \\ 0 & 0 & 1 \end{pmatrix}. \tag{A.13}$$

The scale factors are $h_1 = \varphi$, $h_2 = \sqrt{1+\varphi^2}$ and $h_3 = 1$.

Jacobian Determinant

Using the considerations made above, the Jacobian[4] is

$$|\mathbb{J}_{\mathrm{E}}(\varphi, \theta)| = r^3 \cdot \varphi. \tag{A.14}$$

The volume element can be derived immediately:

$$\mathrm{d}V = r^3 \varphi \cdot \mathrm{d}\varphi \cdot \mathrm{d}\theta \cdot \mathrm{d}h. \tag{A.15}$$

Unit Vectors

The unit vectors are:

$$\boldsymbol{e}_\varphi := \begin{pmatrix} -\sin(\varphi+\theta) \\ \cos(\varphi+\theta) \\ 0 \end{pmatrix} \qquad \boldsymbol{e}_\theta := \begin{pmatrix} \cos(\varphi+\theta) \\ \sin(\varphi+\theta) \\ 0 \end{pmatrix} \qquad \boldsymbol{e}_h := \begin{pmatrix} 0 \\ 0 \\ 1 \end{pmatrix}. \tag{A.16}$$

The dual basis is identical to the one mentioned above.

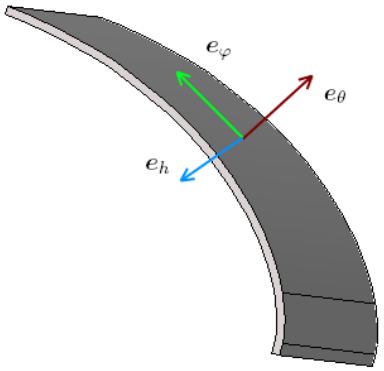

Figure A.2: *Unit vectors in involute coordinates. The direction of the vectors depends on φ and ϑ.*

[4]The Jacobian is for the system-immanent parameter for $r = 0$ also 0. For $r \neq 0$, not the whole space is covered by a coordinate system, even if the system has its origin at $(\varphi = 0, \theta = 0)$. This one is not identical to the cartesian origin though. Concerning this issue, see the remarks made before.

Differentials and Differential Operators

Differentials are obtained by multiplication with the Jacobian, i. e. $\mathrm{d}\boldsymbol{r}_\mathrm{K} = \mathbb{J}_\mathrm{E}(\varphi,\theta)\cdot\mathrm{d}\boldsymbol{r}_\mathrm{E}$:[5]

$$\mathrm{d}\boldsymbol{r}_\mathrm{K} = r\cdot\varphi\,(\mathrm{d}\varphi+\mathrm{d}\theta)\cdot\boldsymbol{e}_\varphi - r\cdot\mathrm{d}\theta\cdot\boldsymbol{e}_\theta + r\cdot\mathrm{d}h\cdot\boldsymbol{e}_h. \tag{A.19}$$

The mixed terms arise from the missing orthogonality of the coordinate system. The gradient is given by

$$\boldsymbol{\nabla}_\mathrm{E} f = \frac{1}{r}\left(\frac{1}{\varphi}\frac{\partial f}{\partial\varphi}\boldsymbol{e}_\varphi + \left(\frac{\partial f}{\partial\varphi}-\frac{\partial f}{\partial\theta}\right)\boldsymbol{e}_\theta + \frac{\partial f}{\partial h}\boldsymbol{e}_h\right), \tag{A.20}$$

the divergence is

$$\boldsymbol{\nabla}_\mathrm{E}\cdot\boldsymbol{A} = \frac{1}{r}\left(\frac{1}{\varphi}\frac{\partial A_\varphi}{\partial\varphi} + \left(\frac{1}{\varphi}+\frac{\partial}{\partial\varphi}-\frac{\partial}{\partial\theta}\right)A_\theta + \frac{\partial A_h}{\partial h}\right) \tag{A.21}$$

with $A_\varphi = -\sin(\varphi+\theta)\,A_x + \cos(\varphi+\theta)\,A_y$, $A_\theta = \cos(\varphi+\theta)\,A_x + \sin(\varphi+\theta)\,A_y$ and $A_h = A_z$. Consequently the Laplacian is given by

$$\Delta_\mathrm{E} = \frac{1}{r^2}\left(\frac{1}{\varphi}\frac{\partial}{\partial\varphi}\left(\frac{1}{\varphi}\frac{\partial}{\partial\varphi}\right) + \frac{1}{\varphi}\left(\frac{\partial}{\partial\varphi}-\frac{\partial}{\partial\theta}\right) + \left(\frac{\partial}{\partial\varphi}-\frac{\partial}{\partial\theta}\right)^2 + \frac{\partial^2}{\partial h^2}\right). \tag{A.22}$$

A.2.3 Special Curves

Involutes

In the coordinate system E, the curve of an involute of the evolute who generated the system and that begins at (0,θ_0,h_0), is given by

$$\boldsymbol{x}_E(\varphi,\theta,h) = \begin{pmatrix}\varphi\\ \theta_0\\ h_0\end{pmatrix}. \tag{A.23}$$

Circle

A circle with radius $r\sqrt{1+\varphi_0^2}$ is given by

$$\boldsymbol{x}_E(\varphi,\theta,h) = \begin{pmatrix}\varphi_0\\ \theta\\ h_0\end{pmatrix}. \tag{A.24}$$

[5] Concerning the differential, it might appear advantageous not to use A.16 but the non-orthogonal basis

$$\boldsymbol{e}_{\varphi_2} := \begin{pmatrix}-\sin(\varphi+\theta)\\ \cos(\varphi+\theta)\\ 0\end{pmatrix} \qquad \boldsymbol{e}_{\theta_2} := \frac{1}{\sqrt{1+\varphi^2}}\begin{pmatrix}-\varphi\sin(\varphi+\theta)-\cos(\varphi+\theta)\\ \varphi\cos(\varphi+\theta)-\sin(\varphi+\theta)\\ 0\end{pmatrix} \qquad \boldsymbol{e}_{h_2} := \begin{pmatrix}0\\0\\1\end{pmatrix}. \tag{A.17}$$

In this basis is $\mathrm{d}\boldsymbol{r} = (\varphi\,\mathrm{d}\varphi, \sqrt{1+\varphi^2}\mathrm{d}\theta, \mathrm{d}h)$. Admittedly, the Nabla-Operator is much more complicated in this basis. The dual basis would be

$$\boldsymbol{e}^{\varphi_2} := \begin{pmatrix}\varphi\cos(\varphi+\theta)-\sin(\varphi+\theta)\\ \varphi\sin(\varphi+\theta)+\cos(\varphi+\theta)\\ 0\end{pmatrix} \qquad \boldsymbol{e}^{\theta_2} := -\sqrt{1+\varphi^2}\begin{pmatrix}\cos(\varphi+\theta)\\ \sin(\varphi+\theta)\\ 0\end{pmatrix} \qquad \boldsymbol{e}^{h_2} := \begin{pmatrix}0\\0\\1\end{pmatrix}. \tag{A.18}$$

The normal on the circle at the cross section with an involute is

$$\begin{aligned} \boldsymbol{n} &= (\sin(\alpha_\varphi + \theta)\sin(\varphi + \theta) + \cos(\alpha_\varphi + \theta)\cos(\varphi + \theta))\, \boldsymbol{e}_\varphi \\ &\quad + (\cos(\alpha_\varphi + \theta)\sin(\varphi + \theta) - \cos(\varphi + \theta)\sin(\alpha_\varphi + \theta))\, \boldsymbol{e}_\theta. \end{aligned} \tag{A.25}$$

Tangent

The tangent on a circle at $(0,\theta_0, h_0)$ is described by

$$\boldsymbol{x}_E(\varphi, \theta, h) = \begin{pmatrix} \varphi \\ \theta_0 - \varphi \\ h_0 \end{pmatrix}, \tag{A.26}$$

it crosses the involute that was begun at $(0,0,h_0)$ at $(\theta_0,0,h_0)$.

A.3 Special Formulas

A.3.1 Integral Values

Lengths

The length of the segment of an involute between φ_0 and $\varphi_0 + \delta\varphi$ is calculated by a line integral[6] or with the help of the coordinate system defined in eq. A.14

$$l = \frac{1}{2} r \left((\varphi_0 + \delta\varphi)^2 - \varphi_0^2 \right). \tag{A.28}$$

For a segment between radii R_2 and R_1, using eq. A.6, a length of

$$l = \frac{1}{2r} \left(R_2^2 - R_1^2 \right) \tag{A.29}$$

can be derived.

Areas

The area that two tangents with intermediate angle $\delta\varphi$ and two involutes with intermediate angle $\delta\theta$ span can be calculated with eq. A.28 by replacing $\varphi_0 \to \varphi_0 - (\theta - \theta_0)$ and integrating over θ:

$$A = r^2 \left(\left(2\varphi_0 \cdot \delta\varphi + \delta\varphi^2 \right) \delta\theta - \delta\varphi \cdot \delta\theta^2 \right). \tag{A.30}$$

If the areas are regarded with $(\pm\delta\varphi, \pm\delta\theta)$ around the point (φ_0, θ), the area is given by

$$A = 4r^2 \cdot \varphi_0 \cdot \delta\varphi \cdot \delta\theta. \tag{A.31}$$

[6] Line integral:

$$l = \int_{\varphi_0}^{\varphi_0 + \delta\varphi} \left| \frac{\mathrm{d}}{\mathrm{d}\varphi} \begin{pmatrix} x(r,\varphi) \\ y(r,\varphi) \end{pmatrix} \right| \mathrm{d}\varphi. \tag{A.27}$$

The area between two circles whose radii are characterized by φ_0 and $\varphi_0 + \delta\varphi$ (eq. A.4 respectively A.6), and two involutes with starting angles θ_0 and $\theta_0 + \delta\theta$ is given by[7]

$$A = \frac{r^2}{2}\left((\varphi_0 + \delta\varphi)^2 - \varphi_0^2\right)\delta\theta. \tag{A.32}$$

Volumes

The volume between two involutes with distance $\delta\theta$ and two tangents on the circle at distance $\delta\varphi$, where the inner one has the rotation angle φ_0 to the involute with the lower θ and two planes $\parallel h$ with distance δh can be obtained by integrating over A.30:

$$V = r^3\left(\left(2\varphi_0 \cdot \delta\varphi + \delta\varphi^2\right)\delta\theta - \delta\varphi \cdot \delta\theta^2\right) \cdot \delta h. \tag{A.33}$$

The volume with $(\pm\delta\varphi, \pm\delta\theta, \pm\delta h)$ around (φ_0, θ, h) is

$$V = 8r^3 \cdot \varphi_0 \cdot \delta\varphi \cdot \delta\theta \cdot \delta h. \tag{A.34}$$

[7] From eq. A.14 the needed surface element $\mathrm{d}A = r^2\varphi \cdot \mathrm{d}\varphi \cdot \mathrm{d}\theta$ can be obtained.

APPENDIX B

Modifications to existing codes

A short overview on the modifications that were made to existing codes.

B.1 MCNPX

Although not desired, some minor changes have to be made to MCNPX to be able to do burn-up calculations with MONTEBURNS with more than 44 materials and do calculations with a large number of materials (several thousands, used during burn-up).

```
Replace in IMCN_jc.F
-      integer(kindi), parameter :: ntalmx=100                    !/*mid5e       2*/
+      integer(kindi), parameter :: ntalmx=200                    !/*mid5e       2*/

Replace in GLOBAL4_mb.F
-      integer(ki4), private, parameter :: MPI_Buffmax = 10       !/*mmp5e       3*/
+      integer(ki4), private, parameter :: MPI_Buffmax = 20       !/*mmp5e       3*/
```

The number behind `ntalmx` sets the maximum number of tallies in a problem. For a burn-up calculation with MONTEBURNS, take the number of materials you want to burn, multiply it by 2 and add the number of extra tallies you use in the problem. Of course, this number can be set larger in advance to avoid the need to recompile the code every time. Bear in mind that a larger number of tallies increases the run time and the memory needed.

B.2 MonteBurns

The changes made to MONTEBURNS were extensive and too many to be listed here. It must be concluded, that if a new version of MONTEBURNS appears, it can not easily replace the version currently used in X^2. For that reason it is recommended to stick with the version in the `3rdparty/montebx495` directory of X^2.

The changes made to MONTEBURNS had the following effects:

- Removed the limit of 44 burnable materials, increased the number to 400[1]
- Removed the limitations that material numbers and tally numbers in the input file had to be < 100. Now < 1000.
- Added the possibility to include an own cross section library at the first step
- Added the possibility to use fission source files

[1] However, the limit of max. 9000 isotopes persists.

- Added support for multiple processors in McnpX runs of MonteBurns
- Some minor improvements in data- and file-handling

There is another version included with X^2, `3rdparty/montebx.f`, this is a only slightly modified code where the first two listed modifications do not apply. To emphasize these changes, the modified codes both are entitled *montebx*, meaning MonteBurns eXtended. To avoid problems with compiler optimization, MontebX should be compiled using the switch `-O0`. This will not affect the performance of X^2 significantly.

B.3 Origen2

No changes made. It is noteworthy that Origen2 did not work properly on the test system when compiled with Intel Fortran 11 with standard options. Instead, the switch `-O0` has to be specified, turning off the optimization, to make Origen2 work correctly.

B.4 CFX

Cfx is closed source, so no changes were made to the program itself. Instead, an extension for the User Fortran-API was developed.

B.5 ENDF2ACE

Endf2Ace was modified to correctly handle some special isotopes and to run on Microsoft Windows XP.

APPENDIX C

X^2 Program Flow

The main program flow was already shown in fig. 11.1. For completeness, this figure is repeated here (C.1).

Directly after start-up, the system is initialised. This is explained in detail in section C.1 below. It is then decided whether a burn-up run or a temperature convergence run should be executed.

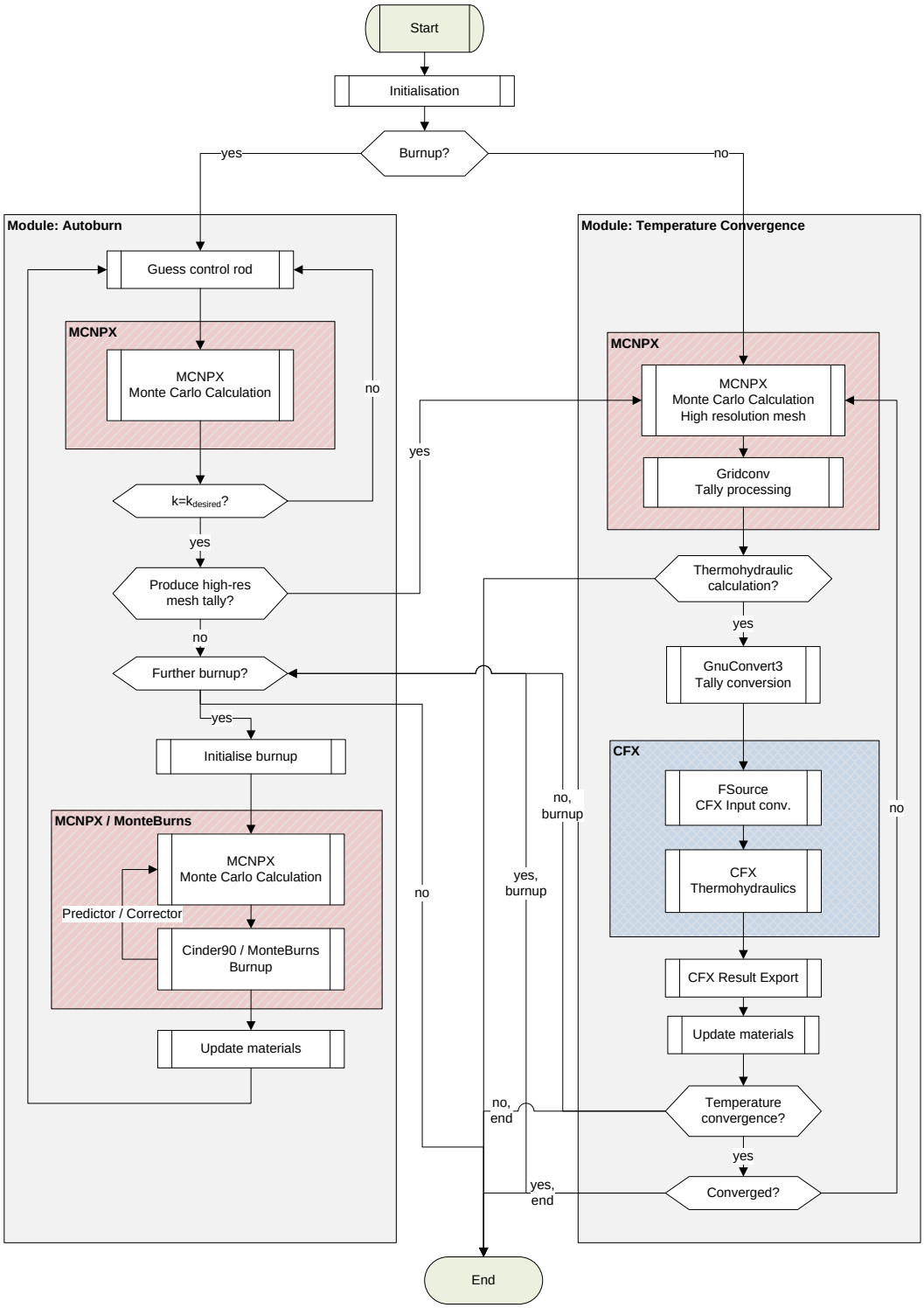

Figure C.1: *Flowchart for the* X^2 *program system.*

C.1 Initialisation Phase

In the general initialisation phase, a number of tasks related to building the model and sanity checks are performed. The detailed sequence is shown in fig. C.2.

- At the very beginning, the configuration files are read, this means the global configuration, the default project values and the project specific values (in this order).
- After this, the result directories are created. Log-files that were created during the configuration loading phase are copied there and appended for the rest of the run.
- The configuration is checked for obvious contradictions.
- The completeness and sanity of the McnpX model is checked as far as possible.[1]
- Material — cell associations are extracted from the model. These associations are the basis for all later materials related processes.
- Check if the model has to be initialised (user option). If so, initialise the material composition, set the cell properties (densities, temperatures), set KCODE to 'low' accuracy and create a model that carries not information on burn-up.
- Check if a temperature profile has to be loaded (command line parameter –load-temperature-profile). If so, load the profile. The exact actions performed are depending on the format of the temperature profile (.res or .csv).
- Check if a reactivity profile should be calculated. If so, see sec. C.1.1.
- Again, if the model has to be initialised, the control rod is set to a position where $k = k_{\text{desired}}$.
- Check if the command line parameter –build-model-only has been specified. If so, about a dozen models in different flavours are created (different accuracies, mesh / no mesh, burn-up etc.) and the program exits. If not, the initialisation phase is complete.

C.1.1 Reactivity Profile

The term *reactivity profile* designates the function $k(z)$ where z is the control rod position and $\mathrm{d}k/\mathrm{d}z$. This function is calculated to guess control rod positions more efficiently later. However, if calculated once, the values can be specified in the run-specific configuration file to save CPU time in later runs. The flow chart for this part of the initialisation phase is shown in fig. C.3.

- The burn-card is removed from the model. KCODE is set to 'low' accuracy, neutrons only. The mesh tallies are removed.
- The inner loop is executed. In this loop, McnpX calculations are performed as long as the control rod position satisfies $z < z_{\max}$. After every step, $z \to z + \Delta z$.
- The calculated values for $k(z)$ are output
- A least squares fit, currently a parabola, is performed for the calculated values.
- The control rod position for $k = k_{\text{desired}}$ is calculated
- The resulting function is plotted.

[1] This will not capture semantic McnpX errors. These will only be identified in the first McnpX run.

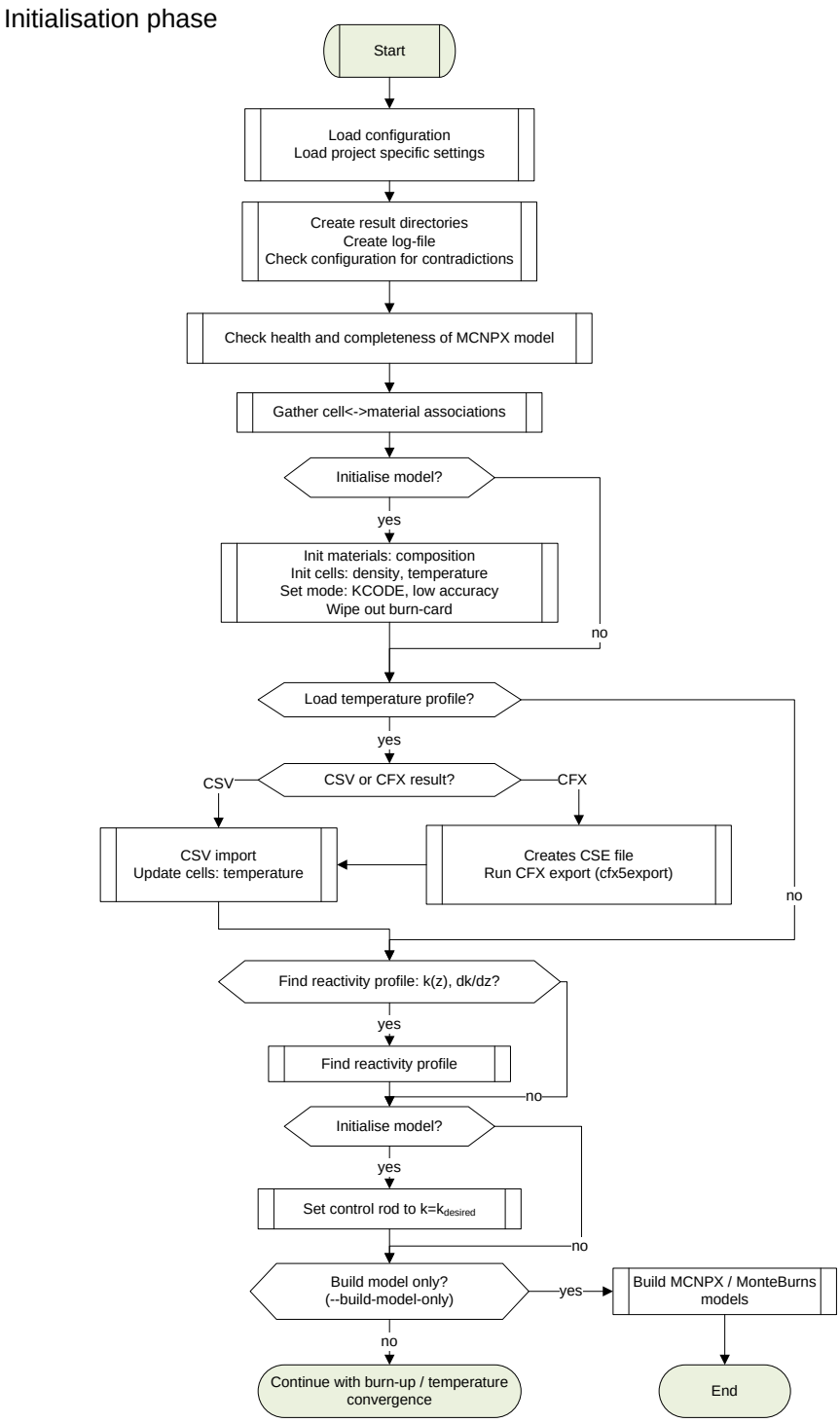

Figure C.2: *Flowchart for the* X^2 *initialisation.*

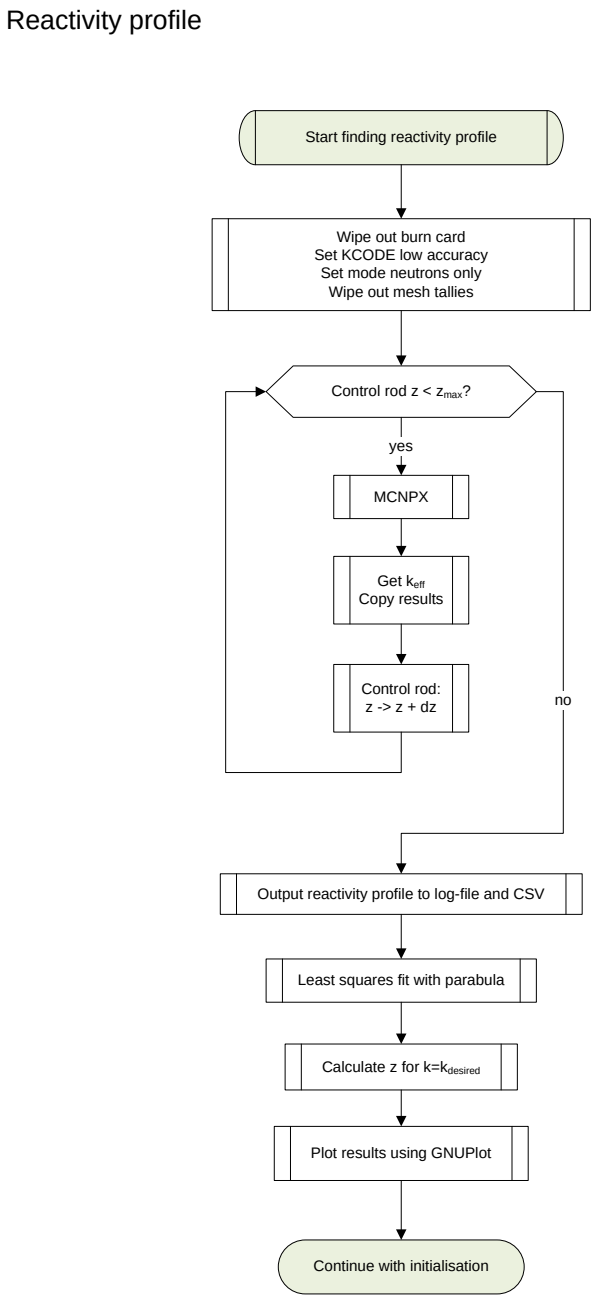

Figure C.3: *Flowchart for the* X^2 *initialisation: Determination of reactivity profile*

C.2 Main Program Modules

C.2.1 Burn-up Run

Burn-up Initialisation

- If MonteBurns (which is recommended) is used as burn-up code, a real separate burn-up initialisation phase is required. In this stage, the additional MonteBurns input files are created.
- If a fully coupled run is requested, some necessary scripts for CFX are created (*.cse files).
- The mesh is removed from the MCNPX model

Burn-up Cycle

The burn-up cycle is run for every time step.

- First, it is checked if a fully coupled run is desired. If so, a high resolution McnpX run with meshes and photons is carried out. The result is plugged into Cfx, the results are exported from CFX and then imported in X[2] . Materials are updated according to the temperatures calculated before.
- Noteworthy that the calculation is exited at this point after the very last cycle, this means that at the very end one additional temperature run is done.
- Before the actual burn-up calculation, the system is set to 'medium' accuracy. Then, the depending on the selected burn-up code, either the burn-card is inserted into the model (McnpX / Cinder90 or the according actions are performed for MonteBurns.
- Run McnpX / MonteBurns
- After the run, the main results (i. e. new material compositions) are exported from the output of MonteBurns and included in the general model.
- The control rod is adjusted to meet $k = k_{\text{desired}}$. This is done with 'low' accuracy.[2] As soon as $|k - k_{\text{desired}}| < \Delta k_{\max}$, the inner control rod adjustment cycle is exited.
- At the end of a burn-up cycle, depending on the chosen burn-up code, models in the run-directories of McnpX and MonteBurns are updated according to the new control rod position and temperature distribution.

End

At the very end, the control rod position over time is exported to a CSV file and plotted with GnuPlot as far as this program is available on the system. Some clean-up work is done.

C.2.2 Temperature Convergence

Initialisation

The temperature convergence mode has a special initialisation phase, too.

[2] It has to be emphasized that this 'low' accuracy is automatically adjusted within the burn-up run so that after some steps this mode can become more precise and time consuming than the 'medium' accuracy that is used in the actual burn-up calculation. The term 'accuracy' does not refer to the quality of the results, but to the number of particles needed to calculate a specific quantity that may already have sufficient statistics while other quantities still have large uncertainties.

- The mesh is inserted into the model and it is assured that no burn-up related information is left in the model.
- Photons are included in the calculation, the run mode is set to 'high' accuracy
- Some basic CFX scripts are created.

Convergence Loop

- Run McnpX
- Collect results and convert input for CFX (GnuConvert).
- Run CFX
- Export results to CSV
- Check if given convergence level is reached, $\left|T_i^j - T_i^{j-1}\right| < \Delta T$ for every cell i in step j. If so, exit loop.
- Update McnpX models (temperatures, densities, materials)

C.3 Further Information

For further information, the author refers the reader to the well documented source code of X^2 and all other scripts that were written for this work. The information that was left out here is of very technical nature and long-winded to explain without the source code, therefore the source code seems to be the right place to store the relevant information.

APPENDIX D

X^2 User Guide

This chapter is meant to be a short user guide for people who intend to use the X^2 program system. It does not describe everything necessary to build a complete model, so a sound knowledge in MCNP and CFX is required. A large amount of information regarding X^2 can be found in the numerous comments in the source code of the system.

D.1 Model Creation Advise

In general, two models have to be created, one for McnpX and one for Cfx. It is easier to start with the McnpX model.

D.1.1 MCNPX

Normally the involutes are approximated by parabolas and hyperbolas. If the involutes have to be modified to include some kind of thickness profile, this is best done by splitting up the original curves at the desired point and then turn them by applying a transformation. This has been done for the monolithic models.

When the McnpX model has been finished, the volumes of the different parts of the fuel plate have to be calculated accurately. If this is not possible analytically, it can be done in a stochastic manner. [X-505, p. 2-187] describes in detail how to do this. There is a script `stoc_vol_calc.pl` in the directory `scripts/mcnpx/stochastic volumes/` of X^2 which helps reading out all the tallies and converting them into the right format.

The McnpX model that is used in X^2 is not a standard McnpX model. It has to be split up in several parts and a special syntax has to be used in some places. This is necessary to be able to account for changing material composition, densities and other properties as long as no powerful MCNP parser has been included in X^2 . Before the model is split up, one normal Mcnp 5 calculation should be made to create a particle source file for KCODE and the Shannon Entropy should be calculated as described in chapter 2.5.3 to ensure a converged source particle distribution. The obtained source distribution has to be kept and copied to the model path.

It will not be explained in detail here, how the model has to be split up. Have a look at one of the numerous examples in the `models/` and `examples` path of X^2 . Generally, the main file normally is only a list of comments in includes. The comments are standard McnpX comments. The includes are realised via [and]. In the simplest case, only the file name is given there. Than this file is only included without special meaning. The filename can be preceeded by a keyword in uppercase. The following keywords are available:

CELLSEGMENTATION: For the segmentation of the cells of the fuel zone.

SURFACESEGMENTATION: For the surfaces that segment the fuel zone.

CONTROLROD: For the control rod position transformation.

MODE: For the particle mode (n, np).

TMESH: For the geometry independent meshes.

There is a third possibility, with the syntax `KEYWORD filename1 FROM filename2`. This reads in `filename2` and creates a file `filename1` during processing. The FROM syntax is to avoid file collisions with other instances of X^2 . Available keywords are:

KCODE: For the KCODE options

MAT: For the burnable materials

PHYSICS: For the physics options

CELDAT: For the cell data like importances, volumes, temperatures etc.

CELLS: For a general list of cells that contain modifiable data (densities ...)

BURN: For the BURN-card if CINDER90 is used. Otherwise, some other items have to be included here!

Note that all content has to be in the right part, elsewise the corresponding properties won't be parsed / adjusted and a McnpX error is likely to occur. X^2 performs some checks if all necessary keywords are available. However, these checks are not very thorough.

When the model is finished and split up, it is a good idea to run X^2 with the command line option `-build-model-only` to create only the models. The models should be checked if they are complete and all options are set as desired.

In the following, the files associated with the keywords are briefly described. In the example projects, you will find some additional files. However, these file were only created for convenience reasons and have no special meaning.

BURN

In the BURN file, the BURN card has to be included for CINDER90. From the possible parameters of the BURN card, at least TIME and POWER have to be used. They should be followed by [TIME] and [POWER] respectively. X^2 looks for these keywords in the file and replaces them as needed.

At the end of the file, include a list of the burnable zones and materials. Please not that presently there should be a bijection, i. e. the cell-material association should be unique. It has been proven a good idea to set material and cell number equally. This list has the following syntax (one line per item, no comments):

MAT:VOLUME Expects a material number and a numeric volume.

MAT:FROM CELL A material, the volume for cell CELL is read from the CELDAT file.

MAT:FROM CELL TIMES X As above, but the volume read is multiplied by X

MAT:FROM CELL TIMES PLATES As above, but X is the number of plates in the model.

Only materials that are listed in this list are burned!

CELDAT

Contains all the cell parameter cards in vertical input format. In the file, the keyword [T] can be used. The temperature for the material is inserted at that point.

CELLS

Contains the usual cell descriptions as normally applied in the first part of a McnpX input file. Instead of the density of a material, the keyword [DF:X] can be used. Then the density is calculated temperature dependent. These functions normally are specified in a file called `densityfunc.pl` in the model directory. X is the material number that is passed to the perl script. See the examples on how the density function file is build.

CELLSEGMENTATION

Contains all the cells for the burnup-zones of the fuel plates. Instead of a density, the keyword [UPD:CELL:DENSITY] is specified, with CELL being the cell number (ok ... this is redundant) and DENSITY being the density of the fuel at BOL.

CONTROLROD

Contains the transformation for the control rod position. Nothing more.

KCODE

Normally includes only the KCODE card. The following keywords (in []) can be used:

NP Instead of the number of particles per cycle (parameter 1).

NS Instead of the number of cycles to be skipped (parameter 3).

NC Instead of the number of cycles to be calculated (parameter 4).

MAT

Contains all burnable materials and only them. No special keywords. This file gets completely rewritten every burn-up time step. So anything in there, that has nothing to do with burnable materials, gets lost.

MODE

Contains only the mode card. Is automatically adjusted depending on the needs of X^2 .

PHYSICS

Contains all information about the physics used in McnpX, especially the PHYS and CUT cards. Only one keyword exists, [DG:X] in the 6th entry of PHYS:P. Here is the information about delayed gammas. Normally, set $X = -101$.

SURFACESEGMENTATION

Includes the surfaces that are used to segment the burn-up zones of the fuel.

TMESH

Includes the TMESH and all other things that may slow down the McnpX execution if not very high details are needed.

Creation of the Geometry Independent Power Deposition Mesh

It is of high importance that the McnpX power deposition mesh matches the Cfx calculation mesh as close as possible to ensure, that the peak heat fluxes are calculated correctly. As it is very hard to match the Cfx mesh to an existing TMESH, the other way is taken. First, create the Cfx mesh as described below, then create the TMESH using the script `create_tmesh_from_cfx5.pl` in the directory `scripts/mesh/`. Note that this script takes care only of the axial component, not of the radial component of the mesh. The radial components are distributed very fine in the Cfx mesh, so a direct generation of the r-component would lead to an extremely fine TMESH. The r-components can be manually adjusted in the script file.

D.1.2 CFX

The model for Cfx should only be created when the McnpX model has reached its final design as it is a good amount of work to create the model. Normally you would start creating the model from scratch (and actual working plans) in SolidWorks or a similar CAD program. Construct only one fuel plate, including its cooling channel, with enough room above and below the actual end of the fuel plate. In principle it is sufficient to create one solid body per material. However, this is unfortunate when it comes to meshing the model. Therefore, divide the model in a number of parts as simple as possible.

SolidWorks offers no possibility to create evolvents directly. You can circumvent this by adding points at the appropriate positions and connect them by lines. It is easier to let a script calculate these points and then import a point cloud.

When you're done creating the model, one very important task remains before creating the meshes: Check the volumes of the involute shaped bodies. They normally match the volumes of the McnpX model to about 1-2%. It is important to note the difference for the fuel zone, as this will be directly reflected in the power. This can be balanced later with the power correction factor in the CFX extension.

Inlet and Outlet

In a first step, it has proven to be a good idea to split the model in three main parts in z-direction: The top of the fuel plate (and the cooling channel) until the beginning of the actual fuel zone ('head'), the middle part including the fuel until the lower end of the fuel zone ('main') and the bottom part of the plate ('foot'). Afterwards, divide the model according to this three pieces. Export head and foot to a STEP file and import them in the ANSYS geometry modeler (direct SolidWorks import does not work due to the involutes). Save the geometry in ANSYS format, and start the CFX mesher. Mesh the model according to the parameters given in chapter 10.1.1, p. 97 and define the required interfaces and boundaries (head: inlet, solid-solid-interface to main, fluid-fluid-interface to main, fluid-solid-interface; foot: outlet, solid-solid-interface to main, fluid-fluid-interface to main, fluid-solid interface).

Main Fuel Plate

The main part is somewhat more complicated. For a typical Frm II fuel plate, there are three areas in the main part: The inner duct, the fuel plate including cooling channel, and the outer duct. The middle part is subdivided in four parts in ϕ direction (fuel frame, fuel 1, fuel 2, fuel frame) and five parts in θ-direction (first half of cooling channel, cladding, fuel / frame, cladding, second half of cooling channel), a total of twenty parts.[1] To apply the rotational periodicity for the model, it is desirable to split the cooling channel. In Cfx, the rotational periodicity cannot be applied at interfaces (water / aluminium, aluminium / fuel etc.) and it is unattractive to split the fuel zone. Therefore split the cooling channel. At the end, in this example, the cooling channel consists of eight parts. Keep them separate, you will join

[1] See chap. A for an explanation of the directions.

them in the mesher.

It is easier to use one of the existing models of the FRM II fuel plates that have been created for this thesis if the outer shape of the fuel plate is not modified but only the fuel zone itself has to be deformed. In `scripts/solidworks/macro`, a perl script (`rotator_2.pl`) can be found that generates a SOLIDWORKS macro. Edit the file to adjust it to the MCNPX model. Then run the script and capture its output. The output is a SOLIDWORKS macro that moves the points of the original evolvents of the fuel plate to new locations according to the MCNPX model.

When everything is alright with the SOLIDWORKS model of the main part, start ICEM CFD. Import the model with the Workbench Readers and do the appropriate blocking. Then, the geometry has probably to be healed. Delete all unnecessary points and lines, group together curves that were split by the points you just deleted. Afterwards, associate the vertices of the blocks to the points of the geometry. Then associate curves and edges. That's a good point to check if the curve healing was o. k.

As soon as all associations are o. k., check them by showing them. Then proceed by creating the three domains 'WATER', 'ALUMINIUM' and 'FUEL' as parts by selecting the appropriate blocking material. Create further parts as interfaces: fluid–solid (water – aluminium), solid–solid (aluminium – fuel), the four surfaces for the rotational symmetry (two in water, two in aluminium) and the four connections to head and foot (water in, water out, aluminium in, aluminium out). Beware of the right z-direction.

After you have named all parts, start the actual meshing process by setting the edge parameters in the pre-mesh setup. You will have to use geometric or bi-geometric laws in ϕ-direction everywhere and in θ-direction in the water. In the aluminium and the fuel, equidistant points are better suited. Set up the parameters for the z-direction only after you have verified the pre-mesh in the other directions. This saves a lot of time.

When you are done with setting the mesh parameters, show the pre-mesh and convert it to an unstructured mesh. Finally, export the mesh with the CFX5 export.

D.1.3 CFX-Pre

In CFX-Pre, import all three meshes (head, foot, main). Define three domains[2], for water, aluminium and fuel. Associate the corresponding parts of head, main and foot.

When the domains are created, set the appropriate material parameters. Make sure you set the options for non-isothermal behaviour (with heat transfer). For water, modify the material to IAPWS 97. Enable table generation for the material properties in an adequate range.

After that, set up the two default interfaces, fluid–solid between aluminium and water and solid–solid between fuel and aluminium if this wasn't done automatically by CFX. After that, create two other domain interfaces for the rotational symmetry conditions. Having done so, set up another four interfaces to connect the meshes head–main and main–foot for the solid as well as for the fluid.

In the fluid domain, enable buoyancy. For the turbulence model, choose SST. Enable heat transfer and include viscous dissipation if desired. Set proper initialisation parameters. These are needed for the other two domains, too.

[2]Depending on the fuel, it might be necessary to define more domains. Although, if it should be considered that the fuel frame is an other material than the cladding and the ducts, separate domains have to be created here. If you do so, this already has to be considered when doing the blocking and defining the interfaces in ICEM CFD.

Go to the water-side of the fluid-solid interface. Set it to a no-slip wall and set the wall-roughness for the rough wall to a sand grain roughness of 2.4 µm.

Create the inlet boundary condition. Set the inlet velocity to the expression inletv(r). Then, create a user function 'inletv'. It is a one-dimensional interpolation. Import the results for the velocity profile from the sieve-simulation. Do the same for the required turbulence parameters.[3] The inlet temperature can be set to 37.0 °C uniformly.

Create the outlet boundary condition with an average static pressure of 2.3 bar.

What remains is to set up the data interface to the MCNPX calculation. Create a new variable 'QDep', scalar, units $^{W}/_{cm^3}$. Go to the fuel domain and enable the calculation of the variable using the algebraic equation QData(1,r,z). Create a subdomain covering the whole fuel domain. Enable it as a source for energy, referring the variable 'QDep'. Do the same for the whole aluminium domain with QData(2,r,z). Now create a junction box routine 'Load Q Data'. The calling name is 'user_input'. Set the library path appropriately and the name to 'fissionsource2.1'. The junction box location is 'User Input'. Now create another User CEL Routine called 'QDataRoutine'. This is a User CEL Function with calling name 'user_qsource'. Same library as before. Now create a User CEL Routine named 'QData'. This is a user function that calls 'QDataRoutine'. Specify the argument list [], [cm], [cm]. The result units are $^{W}/_{cm^3}$. In this function call, the first argument specifies the source number, the second the radial position, the third the z-position. Go to the solver control, enable junction box routines and choose 'Load Q Data'. After that, open the command editor an paste in the user options for the script:

```
&replace USER:
  Input File1 = /home/cluster/hbreitkr/cfx/data/mono_that/425_40/BOL/m_3.in
  Input File2 = /home/cluster/hbreitkr/cfx/data/mono_that/425_40/BOL/m_13.ind
  Reactor Power = 20.0
  Fuel Fraction1 = 0.1685393
Source Power CorFac1 = 1.0
  Thickness File2 = /home/cluster/hbreitkr/cfx/data/mono_that/425_40/BOL/alu_thickness.dat
Thickness Is Radial2 = 0
  User Printing = Yes
Power CorFac = 1.0
END
```

Please refer to the documentation in the FORTRAN source of fissionsource2.1.F how to adjust and set these parameters properly. There, the format of the input files is also explained in detail, too.

Due to some memory management issues, the following expert parameter needs to be set via the command editor, too:

```
FLOW: Flow Analysis 1
  &replace EXPERT PARAMETERS:
    topology estimate factor zif = 1.15
  END
END
```

Finally, go again to the solver control and set the residual convergence target to 10^{-5} (10^{-6} if double precision is used). Then create some CEL expression for important monitor points (pressure drop, minimum pressure, maximum pressure, average and maximum heat flux density, maximum wall and fuel temperature, outlet water temperature). Include them as monitor points in the output control.

[3] In first approximation, you can set the turbulence option to 'Intensity and Auto Compute Length' with an intensity of 0.027.

D.1.4 CFX Solver

Start the solver and create a workspace to monitor all the monitor points. If the solver run finishes before these values have converged, adjust the maximum number of cycles and/or the residual convergence target. Also, control not only the mean RMS but also the maximum RMS. Should be smaller than 10^{-3}.

D.1.5 CFX Post

In CFX Post, first do some checks on your models. Calculate the volumes of all significant parts, especially the fuel. They should match the volumes from SolidWorks by about 0.5%, and that of McnpX by 1%. This way you can ensure that you have chosen the proper power correction factor.

Then calculate some plausibility values:

```
volInt(QDep)@Brennstoff * 113 = Deposited power in fuel?
(volInt(QDep)@Brennstoff + volInt(QDep)@Aluminium) * 113 = Deposited power total?
areaInt(Wall heat flux)@Fluid_Solid_Interface * 113 = Deposited power total?
areaInt(Wall heat flux)@Solid_Solid_Interface * 113 = Deposited power in fuel?
areaAve(Temperature)@Outlet - areaAve(Temperature)@Inlet = Deposited power total / ...
        ... (113 * coolant mass flow * c_p)?
```

They will normally be fulfilled with deviations below 0.5%. If all these checks are passed, you can continue to evaluate the calculation.

D.1.6 X²

To set-up your model in X², copy the files to a new subdirectory in the models-subdirectory of X². The input files of X² closely follow the Windows-Ini file format. Just have a look at one of the example files. They are self explaining and full of helpful comments.

If you set-up X² on a new computer, you have to adjust the file system.ini in the cfg-subdirectory. It includes all information about the system, including paths and execution commands. McnpX, Cfx, MonteBurns, Origen2, Perl and the Intel Fortran compiler have to be set up independently. See chapter B for some remarks on needed modifications and compiler options.

D.1.7 Including an Oxide Layer

Currently, there is no option in X² for the automatic generation of an oxide layer. This has to be included manually. The inclusion of the oxide layer consists of two steps: The modification of the mesh and the modification of CFX model.

Modification of the Mesh

The mesh can be modified with the tools located in the directory `scripts/mesh/` of X². The following parameters are needed: Name of the mesh file (%1), name of the surface to modify (%2), name of the CFX-Export file (%3) containing the information on temperatures and heat fluxes (format: csv; node number, x, y, z, temperature in °C, wall heat flux in W/cm^2, and the duration of oxidation in days (%4),. Call:

```
meshparser.pl %1 %2
prepare_hf.pl %3 %4
oxidelayer.pl %1 %1.parsed %3.conv
```

The files %1.parsed an %3.conv are generated by the first two scripts. These scripts can take a while to execute. They generate two new files, %3.thickness and %1.oxide. The first file contains the thickness profile of the oxide layer, the second is the modified mesh file.

Modification of the Model

The first step is to load the modified mesh into the model. To avoid having to reconstruct the whole model, rename the original main mesh file. Then, copy the new mesh to this place, naming it like the original mesh file. In CFX-Pre, reload the mesh. Now the modified mesh is included in the model.

The oxide layer in CFX cannot be resolved by means of a domain. It is way to small to be meshable with a reasonable amount of nodes. Therefore it is realised via a thin interface. In CFX-Pre, set-up a thin interface on the Fluid-Solid-Interface with a thickness of 1 µm. As the thickness of this interface cannot be varied, the solver must be tricked by specifying varying material properties for the thin interface material (see chap. 10.2.1).

Last, include the oxide layer extension.

D.2 Execution

This section describes in short how to install and execute X^2.

D.2.1 Prerequisites

There are a number of things that are needed to run X^2:

- A working Perl installation currently with some additional packages installed: `Config::IniFiles`, `Config::IniFiles::Import`, `Getopt::Long`, `Pod::Usage`, `File::Spec`, `File::Copy`, `Cwd`, `FileHandle`, `IPC::Open3`, `File::Monitor`, `Algorithm::CurveFit`, `Math::Trig`, `POSIX`, `DateTime`, `Switch` and `Data::Dumper`.
- A CFX installation.
- A MCNPX installation, including data files. Please note that the MCNPX installation will be cluttered with files by X^2, so it's a good idea to have a separate installation for X^2. Also, MCNPX will have to be modified as discussed in chapter B.
- In the same directory as MCNPX, Origen2 and MonteBurnsX must be present. The Origen2 data files can reside somewhere else.
- A FORTRAN compiler will probably be needed to link some programs and the CFX extension.
- A MPICH2 installation for parallel computing.

When all these things are present and working, copy the X^2 files where you like to have them. Then, go to the subdirectory `cfg/` and edit the file `system.ini`. Adjust all the pathes and parameters as needed. On some systems when using parallel computing, you might have to compile one non-parallel and one MPICH2 version of the MCNPX executable. This is due to a bug that appears with MonteBurns and MonteBurnsX.

D.2.2 Automatic Execution via X^2

Normally, on any Linux/Unix system, X^2 can simply be called by changing into the X^2 folder and calling

```
./x2.pl [option] %1
```

where %1 is the relative path to the model file. Several additional options can be passed to X^2. A list of these can be obtained by entering

```
./x2.pl --help
```

Most notably is probably `-build-model-only`, which builds only the MCNP and MonteBurns models.

When X^2 is run normally, it will produce a large number of files in the results-directory. Using these files, it is possible to trace back the complete history of a run.

Automatic execution is always recommended when you do a burn-up calculation or a fully coupled run.

D.2.3 Manual Execution

The manual execution of the components of X^2 is recommended when the main focus is on thermal hydraulics. Though X^2 is able to handle this within the framework of its temperature convergence capabilities, a much higher degree of influence can be achieved with manual execution. To manually execute a BOL calculation with thermal hydraulics, do the following:

1. Build the model %1 with `./x2.pl -build-model-only %1`.
2. Go to the appropriate result folder and copy the file `model_npp_mesh_high.mcnpx` to the MCNPX directory. Depending on your input, you have to edit the file and adjust the control rod position to achieve $k_{\text{eff}} = 1$.
3. If you don't know the control rod position for $k_{\text{eff}} = 1$, do an automatic parametric calculation with X^2 for that: In the input file, set `bFindReactivityProfile=1`, `bEnableBurnup=0`, `bEnableCFX=0` and `bBurnupFullCoupling=0`. When the calculation is finished, go to the log-file and look for the line 'Found reactivity profile'. Look up the parameters for the quadratic fit and calculate z from $az^2 + bz + c = 1$.
4. If available, copy the kcode-source file, too. If not, modify the model to include a ksrc-card.
5. Run the MCNPX calculation.
6. Run `gridconv`, create a text file.
7. Copy the three scripts in `scripts/converters/` and the resulting text file %2 from `gridconv` to a new location.
8. Run `originconvert4.pl %2`. Check the results for plausibility in Origin or a similar calculation.
9. Run `gnuconvert4.pl %2` to create the input data for the FSource extension for CFX.
10. If you have a second power deposition mesh besides the power deposition mesh for the active zone, e. g. for the picture frame and the tubes, run `fissions_discriminator.pl %2.%3.gnudata4`, where %3 is the number of the second mesh. This will set all energy deposition values above a certain threshold (default: 0.0005) to zero. A new file with the extension `discriminated` is created.
11. Update your CFX model to account for $k_{\text{eff}} \neq 1$ (statistics!) and update the paths to the input files in the user section. Set `User Printing = 1`.
12. Run CFX.
13. If you see any messages on the console that the FSource extension tried to locate a energy deposition value which was outside the given mesh, you may be have to adjust the coordinates in the `gnudata4` files slightly. The problem arises from numerical roundoff errors at the border of the fuel plates. In most cases it is sufficient to stretch the very outer borders of the mesh by a tenth of a micron to include the complete fuel plate. Do not let these errors just happen, they will significantly affect the results!
14. Do your analysis with CFX-Post and do the checks discussed in the preceding section.

If you want to do this calculation for an EOL case and include an oxide layer, you will have to do the adjustments to the CFX model discussed in the preceding section. Getting the power distribution for EOL is a little more complicated if you do not want to perform a fully coupled run:

1. Do a normal burn-up calculation.
2. Go to the results folder, subdirectory `input`. Take the very last `mcnpx` file and its associated source distribution and copy it to the MCNPX directory.
3. Create a new MCNPX BOL model as described above.
4. Open the BOL file and copy all meshes and tallies to the EOL file.
5. Adjust the KCODE parameters in the EOL file, set the MODE card to N P and include delayed gammas on the PHYS:P card. Just copy the corresponding lines from the BOL file to the EOL file.
6. If you have performed the burn-up calculation with $k_{\text{eff}} \neq 1$, adjust the control rod position to $k_{\text{eff}} = 1$.
7. Run MCNPX and continue as described above.

APPENDIX E

Definitions, Nomenclature

- CFX:
  CFX is a commercial 3D computational fluid dynamics code which solves the Navier Stokes equation numerically. It features several turbulence models, wall functions, conjugate heat transfer and more.
- Cross Section σ, Σ, $\bar{\sigma}$:
  The microscopic cross section σ is a measure for the interaction probability between two particles. Dumbed down it can figuratively be seen as a kind of surface proposed to other particles for an interaction. For quantum particles this area in contrast to the classical case has nothing in common with an actual geometrical surface. Normally, the cross section is expressed in units of *barn*:

  $$1\,\text{barn} = 10^{-24}\,\text{cm}^2 = 10^{-28}\,\text{m}^2. \tag{E.1}$$

  Cross sections are energy dependent and differ for every possible interaction. A selection of more important cross sections is shown in table 2.1.

  Macroscopic cross section are obtained by multiplying microscopic cross sections with the particle density:

  $$\Sigma = n \cdot \sigma. \tag{E.2}$$

  They have the dimension of an inverse length and can be interpreted as inverse of the mean free path. For absorption processes, the macroscopic cross section is equal to the absorption coefficient.
- Cycle Neutron Yield:

  The time-integrated neutron flux at a specific point. Integration is done over a complete reactor cycle of duration T.

  $$\Phi(\boldsymbol{r}) = \int_0^T \phi(\boldsymbol{r},t) \cdot \mathrm{d}t \tag{E.3}$$

  If no location is specified, the CNY is always calculated at the point of the highest flux in the D_2O tank at BOL.
- ENDF:
  Abbreviation for 'Evaluated Nuclear Data File'. Includes a huge number of nuclear data, e. g. cross sections and half-lifes.
- Enrichment:
  Amount of ^{235}U compared to the total uranium mass, including minor isotopes like ^{234}U and ^{236}U.

- Flux Density ϕ:
  The *flux density* ϕ, laxly *flux*, gives the number of particles N that travel through a surface element $\mathrm{d}A$ per time interval $\mathrm{d}t$:

$$\phi = \frac{\mathrm{d}^2 N}{\mathrm{d}A \cdot \mathrm{d}t}. \tag{E.4}$$

  The unity commonly used is $\left[\frac{1}{\mathrm{cm}^2 \cdot \mathrm{s}}\right]$.

- MCNP:
  MCNP is the abbreviation for **M**onte **C**arlo **N**-**P**article Transport Code. It is a program developed at Los Alamos National Laboratory to simulate the trajectories of neutrons, photons and electrons.

- MCNPX:
  MCNPX is the abbreviation for **M**onte **C**arlo **N**-**P**article Transport Code extended. It is an extended version of MCNP, also developed at Los Alamos National Laboratory.

- **Neutron Temperature**:
  Measure for the energy of neutrons. Die terminology authoritative for this work can be found in table E.1.

Type	kin. energy	wave length
cold	$< 2\mathrm{meV}$	< 6.4 Å
thermal	$2\mathrm{meV} \ldots 625\mathrm{meV}$	$6.4 \ldots 0.36$ Å
intermediate	$625\mathrm{meV} \ldots 100\mathrm{keV}$	-
fast	$100\mathrm{keV} \ldots 20\mathrm{MeV}$	-
relativistic	$> 20\mathrm{MeV}$	-
fission	$100\mathrm{keV} \ldots 10\mathrm{MeV}$	-

Table E.1: *Neutron temperature: Classification of neutrons by their speed. Energies above 1 eV usually are not expressed in terms of wave lengthes.*

- Spectral flux density $\phi(E)$:
  The *spectral flux density* $\phi(E)$, laxly *spectral flux*, relates the flux density ϕ additionally on an energy interval $\mathrm{d}E$. It therefore gives the number of particles N with energy between E and $E + \mathrm{d}E$ traveling through the surface element $\mathrm{d}A$ per time interval $\mathrm{d}t$:

$$\phi(E) = \frac{\mathrm{d}^3 N}{\mathrm{d}A \cdot \mathrm{d}t \cdot \mathrm{d}E}. \tag{E.5}$$

  The unit usually used is $\left[\frac{1}{\mathrm{cm}^2 \cdot \mathrm{s} \cdot \mathrm{MeV}}\right]$.

APPENDIX F

Tables and Figures

F.1 Data on Chemical Media

F.1.1 Current Fuel Eelement

Place	*Value*	*Uncertainty*	*Source*
Uranium load			
Meat inside	3,0 g/cm^3	-	[Gie96]
Meat outside	1,5 g/cm^3	-	[Gie96]
Density			
Meat inside	5,20 g/cm^3	-	[Gie96]
Meat outside	3,96 g/cm^3	-	[Gie96]
Volume fraction fuel			
Meat inside	26,5%	-	[Gie96]
Meat outside	13,3%	-	[Gie96]
Volume fraction pores			
Meat inside	2,50%	-	[Gie96]
Meat outside	0,81%	-	[Gie96]
Thermal conductivity			
Meat inside	109 W/(K·m)	-	[Gie96]
Meat outside	165 W/(K·m)	-	[Gie96]
AlMg3	216 W/(K·m)	-	[Gie96]
	150 W/(K·m)	-	-
Water	-	-	[Fer98]
Specific heat capacity			
Meat inside	475,0 J/(kg·K)	-	[Gie96]
Meat outside	630,4 J/(kg·K)	-	[Gie96]
Aluminium	900 J/(kg·K)	-	Wikipedia
Water	-	-	[Coo07]

F.2 Burn-up sets

The following sets are available in X^2. They were named after similar lists of cross section sets. The original sets were extended by some structural materials and their burn-up products (Li, Be, B, C, Al, Si, Mo) and the ternary fission products (H, He). Unfortunately, it turned out while finishing this work that due to a programming mistake, ^{99}Mo which was present in all of the original lists is missing in the lists that were implemented into X^2. This isotope is therefore not shown here, too. The isotopes ^{117}Rh and ^{119}Pd are not real isotopes but 'lumped up fission product absorption cross sections'. This has already been discussed in chapter 4.2.2.

'Röhrmoser'

Based on [Röh91a, p. 62] with the modifications described above. Additionally, ^{148}Pm was removed from the original list, as MCNP is not able to handle two isomers of the same isotope in the same input file. The same holds for MonteBurns and Cinder90. The impact of this is discussed in [Röh10c]. This cross section set is the only one with a specific choice of isotopes for FRM II to achieve the highest accuracy when memory is limited.

^{1}H, ^{2}H, ^{3}H, ^{3}He, ^{4}He, ^{7}Li, ^{9}Be, ^{10}B, ^{11}B, ^{12}C, ^{13}C, ^{27}Al, ^{28}Si, ^{29}Si, ^{30}Si, ^{83}Kr, ^{93}Zr, ^{95}Zr, ^{95}Nb, ^{92}Mo, ^{94}Mo, ^{95}Mo, ^{96}Mo, ^{97}Mo, ^{98}Mo, ^{100}Mo, ^{99}Tc, ^{101}Ru, ^{102}Ru, ^{103}Ru, ^{103}Rh, ^{105}Rh, ^{117}Rh, ^{105}Pd, ^{119}Pd, ^{109}Ag, ^{113}Cd, ^{129}I, ^{131}I, ^{135}I, ^{131}Xe, ^{133}Xe, ^{135}Xe, ^{133}Cs, ^{134}Cs, ^{135}Cs, ^{139}La, ^{141}Ce, ^{143}Ce, ^{141}Pr, ^{143}Pr, ^{143}Nd, ^{145}Nd, ^{146}Nd, ^{147}Nd, ^{148}Nd, ^{147}Pm, ^{148m1}Pm, ^{149}Pm, ^{149}Sm, ^{150}Sm, ^{151}Sm, ^{152}Sm, ^{153}Sm, ^{153}Eu, ^{154}Eu, ^{155}Eu, ^{156}Eu, ^{157}Eu, ^{157}Gd, ^{234}U, ^{235}U, ^{236}U, ^{237}U, ^{238}U, ^{237}Np, ^{238}Np, ^{239}Np, ^{238}Pu, ^{239}Pu, ^{240}Pu, ^{241}Pu, ^{242}Pu

'Glaser'

Based on [Gla05]. Present only for comparison.

^{1}H, ^{2}H, ^{3}H, ^{3}He, ^{4}He, ^{7}Li, ^{9}Be, ^{10}B, ^{11}B, ^{12}C, ^{13}C, ^{27}Al, ^{28}Si, ^{29}Si, ^{30}Si, ^{83}Kr, ^{93}Zr, ^{92}Mo, ^{94}Mo, ^{95}Mo, ^{96}Mo, ^{97}Mo, ^{98}Mo, ^{100}Mo, ^{99}Tc, ^{101}Ru, ^{103}Ru, ^{105}Rh, ^{117}Rh, ^{105}Pd, ^{119}Pd, ^{109}Ag, ^{113}Cd, ^{129}I, ^{131}Xe, ^{133}Xe, ^{135}Xe, ^{133}Cs, ^{134}Cs, ^{135}Cs, ^{139}La, ^{141}Ce, ^{141}Pr, ^{143}Pr, ^{143}Nd, ^{145}Nd, ^{147}Nd, ^{148}Nd, ^{147}Pm, ^{148m1}Pm, ^{149}Pm, ^{151}Pm, ^{149}Sm, ^{150}Sm, ^{151}Sm, ^{152}Sm, ^{153}Sm, ^{153}Eu, ^{154}Eu, ^{155}Eu, ^{156}Eu, ^{157}Gd, ^{234}U, ^{235}U, ^{236}U, ^{237}U, ^{238}U, ^{237}Np, ^{239}Np, ^{238}Pu, ^{239}Pu, ^{240}Pu, ^{241}Pu, ^{242}Pu, ^{241}Am, ^{243}Am, ^{244}Cu, ^{245}Cu

'Siemens'

Based on [Fel96]. Probably a standard PWR list.

^{1}H, ^{2}H, ^{3}H, ^{3}He, ^{4}He, ^{7}Li, ^{9}Be, ^{10}B, ^{11}B, ^{12}C, ^{13}C, ^{27}Al, ^{28}Si, ^{29}Si, ^{30}Si, ^{95}Zr, ^{95}Nb, ^{92}Mo, ^{94}Mo, ^{95}Mo, ^{96}Mo, ^{97}Mo, ^{98}Mo, ^{100}Mo, ^{99}Tc, ^{101}Ru, ^{102}Ru, ^{103}Ru, ^{104}Ru, ^{103}Rh, ^{105}Rh, ^{117}Rh, ^{104}Pd, ^{105}Pd, ^{108}Pd, ^{119}Pd, ^{109}Ag, ^{110}Cd, ^{132}Te, ^{131}I, ^{135}I, ^{131}Xe, ^{132}Xe, ^{133}Xe, ^{134}Xe, ^{135}Xe, ^{133}Cs, ^{134}Cs, ^{135}Cs, ^{141}Ce, ^{142}Ce, ^{143}Ce, ^{144}Ce, ^{141}Pr, ^{143}Pr, ^{142}Nd, ^{143}Nd, ^{144}Nd, ^{145}Nd, ^{146}Nd, ^{147}Nd, ^{148}Nd, ^{150}Nd, ^{147}Pm, ^{148m1}Pm, ^{149}Pm, ^{147}Sm, ^{148}Sm, ^{149}Sm, ^{150}Sm, ^{151}Sm, ^{152}Sm, ^{153}Sm, ^{154}Sm, ^{153}Eu, ^{154}Eu, ^{155}Eu, ^{156}Eu, ^{157}Eu, ^{152}Gd, ^{153}Gd, ^{154}Gd, ^{155}Gd, ^{156}Gd, ^{157}Gd, ^{158}Gd, ^{160}Gd, ^{159}Tb, ^{160}Tb, ^{160}Dy, ^{161}Dy, ^{162}Dy, ^{163}Dy, ^{164}Dy, ^{165}Ho, ^{234}U, ^{235}U, ^{236}U, ^{237}U, ^{238}U, ^{237}Np, ^{238}Np, ^{239}Np, ^{238}Pu, ^{239}Pu, ^{240}Pu, ^{241}Pu, ^{242}Pu, ^{241}Am, ^{242}Am, ^{243}Am, ^{242}Cu, ^{243}Cu, ^{244}Cu, ^{245}Cu

'Full'

Full list of available isotopes for burn-up calculations. Yet unusable due to excessive memory requirements. Implemented in X^2 for later use.

^{1}H, ^{2}H, ^{3}H, ^{3}He, ^{4}He, ^{6}Li, ^{7}Li, ^{9}Be, ^{10}B, ^{11}B, ^{12}C, ^{13}C, ^{14}N, ^{15}N, ^{16}O, ^{17}O, ^{19}F, ^{23}Na, ^{24}Mg, ^{25}Mg, ^{26}Mg, ^{27}Al, ^{28}Si, ^{29}Si, ^{30}Si, ^{31}P, ^{32}S, ^{33}S, ^{35}Cl, ^{37}Cl, ^{36}Ar, ^{38}Ar, ^{40}Ar, ^{39}K, ^{40}K, ^{41}K, ^{40}Ca, ^{42}Ca, ^{43}Ca, ^{44}Ca, ^{46}Ca, ^{48}Ca, ^{45}Sc, ^{46}Ti, ^{47}Ti, ^{48}Ti, ^{49}Ti, ^{50}Ti, ^{50}Cr, ^{52}Cr, ^{53}Cr, ^{54}Cr, ^{55}Mn, ^{54}Fe, ^{56}Fe, ^{57}Fe, ^{58}Fe, ^{58}Co, ^{59}Co, ^{58}Ni, ^{60}Ni, ^{61}Ni, ^{62}Ni, ^{64}Ni, ^{63}Cu, ^{65}Cu, ^{69}Ga, ^{71}Ga, ^{70}Ge, ^{72}Ge, ^{73}Ge, ^{74}Ge, ^{76}Ge, ^{74}As, ^{75}As, ^{74}Se, ^{76}Se, ^{77}Se, ^{78}Se, ^{79}Se, ^{80}Se, ^{82}Se, ^{79}Br, ^{81}Br, ^{78}Kr, ^{80}Kr, ^{82}Kr, ^{83}Kr, ^{84}Kr, ^{85}Kr, ^{86}Kr, ^{85}Rb, ^{86}Rb, ^{87}Rb, ^{84}Sr, ^{86}Sr, ^{87}Sr, ^{88}Sr, ^{89}Sr, ^{90}Sr, ^{89}Y, ^{90}Y, ^{91}Y, ^{90}Zr, ^{91}Zr, ^{92}Zr, ^{93}Zr, ^{94}Zr, ^{95}Zr, ^{96}Zr, ^{93}Nb, ^{94}Nb, ^{95}Nb, ^{92}Mo, ^{94}Mo, ^{95}Mo, ^{96}Mo, ^{97}Mo, ^{98}Mo, ^{99}Mo, ^{100}Mo, ^{99}Tc, ^{96}Ru, ^{98}Ru, ^{99}Ru, ^{100}Ru, ^{101}Ru, ^{102}Ru, ^{103}Ru, ^{104}Ru, ^{105}Ru, ^{106}Ru, ^{103}Rh, ^{105}Rh, ^{117}Rh, ^{102}Pd, ^{104}Pd, ^{105}Pd, ^{106}Pd, ^{107}Pd, ^{108}Pd, ^{110}Pd, ^{119}Pd, ^{107}Ag, ^{109}Ag, ^{110}Ag, ^{111}Ag, ^{106}Cd, ^{108}Cd, ^{110}Cd, ^{111}Cd, ^{112}Cd, ^{113}Cd, ^{114}Cd, ^{115}Cd, ^{116}Cd, ^{113}In, ^{115}In, ^{112}Sn, ^{113}Sn, ^{114}Sn, ^{115}Sn, ^{116}Sn, ^{117}Sn, ^{118}Sn, ^{119}Sn, ^{120}Sn, ^{122}Sn, ^{123}Sn, ^{124}Sn, ^{125}Sn, ^{126}Sn, ^{121}Sb, ^{123}Sb, ^{124}Sb, ^{125}Sb, ^{126}Sb, ^{120}Te, ^{122}Te, ^{123}Te, ^{124}Te, ^{125}Te, ^{126}Te, ^{127}Te, ^{128}Te, ^{129}Te, ^{130}Te, ^{132}Te, ^{127}I, ^{129}I, ^{130}I, ^{131}I, ^{135}I, ^{123}Xe, ^{124}Xe, ^{126}Xe, ^{128}Xe, ^{129}Xe, ^{130}Xe, ^{131}Xe, ^{132}Xe, ^{133}Xe, ^{134}Xe, ^{135}Xe, ^{136}Xe, ^{133}Cs, ^{134}Cs, ^{135}Cs, ^{136}Cs, ^{137}Cs, ^{130}Ba, ^{132}Ba, ^{133}Ba, ^{134}Ba, ^{135}Ba, ^{136}Ba, ^{137}Ba, ^{138}Ba, ^{140}Ba, ^{138}La, ^{139}La, ^{140}La, ^{136}Ce, ^{138}Ce, ^{139}Ce, ^{140}Ce, ^{141}Ce, ^{142}Ce, ^{143}Ce, ^{144}Ce, ^{141}Pr, ^{142}Pr, ^{143}Pr, ^{142}Nd, ^{143}Nd, ^{144}Nd, ^{145}Nd, ^{146}Nd, ^{147}Nd, ^{148}Nd, ^{150}Nd, ^{147}Pm, ^{148m1}Pm, ^{149}Pm, ^{151}Pm, ^{144}Sm, ^{147}Sm, ^{148}Sm, ^{149}Sm, ^{150}Sm, ^{151}Sm, ^{152}Sm, ^{153}Sm, ^{154}Sm, ^{151}Eu, ^{152}Eu, ^{153}Eu, ^{154}Eu, ^{155}Eu, ^{156}Eu, ^{157}Eu, ^{152}Gd, ^{153}Gd, ^{154}Gd, ^{155}Gd, ^{156}Gd, ^{157}Gd, ^{158}Gd, ^{160}Gd, ^{159}Tb, ^{160}Tb, ^{156}Dy, ^{158}Dy, ^{160}Dy, ^{161}Dy, ^{162}Dy, ^{163}Dy, ^{164}Dy, ^{165}Ho, ^{162}Er, ^{164}Er, ^{166}Er, ^{167}Er, ^{168}Er, ^{170}Er, ^{175}Lu, ^{176}Lu, ^{174}Hf, ^{176}Hf, ^{177}Hf, ^{178}Hf, ^{179}Hf, ^{180}Hf, ^{181}Ta, ^{182}Ta, ^{182}W, ^{183}W, ^{184}W, ^{186}W, ^{185}Re, ^{187}Re, ^{191}Ir, ^{193}Ir, ^{197}Au, ^{196}Hg, ^{198}Hg, ^{199}Hg, ^{200}Hg, ^{201}Hg, ^{202}Hg, ^{204}Hg, ^{204}Pb, ^{206}Pb, ^{207}Pb, ^{208}Pb, ^{209}Bi, ^{223}Ra, ^{224}Ra, ^{225}Ra, ^{226}Ra, ^{225}Ac, ^{226}Ac, ^{227}Ac, ^{227}Th, ^{228}Th, ^{229}Th, ^{230}Th, ^{232}Th, ^{233}Th, ^{234}Th, ^{231}Pa, ^{232}Pa, ^{233}Pa, ^{232}U, ^{233}U, ^{234}U, ^{235}U, ^{236}U, ^{237}U, ^{238}U, ^{239}U, ^{240}U, ^{241}U, ^{235}Np, ^{236}Np, ^{237}Np, ^{238}Np, ^{239}Np, ^{236}Pu, ^{237}Pu, ^{238}Pu, ^{239}Pu, ^{240}Pu, ^{241}Pu, ^{242}Pu, ^{243}Pu, ^{244}Pu, ^{246}Pu, ^{241}Am, ^{242}Am, ^{243}Am, ^{244}Am, ^{241}Cu, ^{242}Cu, ^{243}Cu, ^{244}Cu, ^{245}Cu, ^{246}Cu, ^{247}Cu, ^{248}Cu, ^{247}Bk, ^{249}Bk, ^{250}Bk, ^{249}Cf, ^{250}Cf, ^{251}Cf, ^{252}Cf

F.3 NJOY Module Sequences

In the following, two example module sequences for the generation of cross sections are given.

F.3.1 Normal Cross Section

Below, a typical script for the creation of a normal cross section set is given, here for a natural Zn (30000) composition. The desired temperature is 300 K, the data is extracted from the JEFF 3.11 library.

```
moder
1 -21
*pendf tape for jeff-3.1 30000(0)*/
20 3000
0/
reconr
-21 -22
'pendf tape for jeff-3.1 30000(0)'
3000  1 0 /
.001/
'30000(0) from jeff-3.1'/
0/
broadr
-21 -22 -23
3000 1/
.001/
300/
0/
```

```
heatr
-21 -23 -24/
3000 6 0 1 0 2/
302 303 304 402 443 444
gaspr
-21 -24 -25
thermr
0 -25 -42
0 3000 8 1 1 0 1 221 2
300
0.001 1.0
purr
-21 -42 -41
3000 1 7 20 16/
300
1.e10 1.e5 1.e4 1000. 100. 10. 1
0/
acer
-21 -41 0 26 27
1 0 1 .99/
'30000(0) from jeff-3.1 njoy99'/
3000 300/
/
/
stop
```

F.3.2 $S(\alpha, \beta)$

Example NJOY script for the creation of $S(\alpha, \beta)$ scattering matrix for ^{1}H in H_2O (1001) for 370 K from the ENDFB VI.0 library:

```
moder
1 -21
*pendf tape for ENDFB-6.0 1001(0)*/
20 125
0/
reconr
-21 -22
'pendf tape for ENDFB-6.0 1001(0)'
125  1 0 /
.001/
'1001(0) from ENDFB-6.0'/
0/
broadr
-21 -22 -23
125 1/
.001/
370/
0/
leapr
43
'H IN H2O, ENDF MODEL'/
1 1/
```

```
1 1001./
0.99917 20.478 2 0 0/
1 1. 15.85316 3.8883 1/
97 95 1/
.01008 .015 .0252 .033 0.050406
.0756 0.100812 0.151218 0.201624 0.252030 0.302436 0.352842
0.403248 0.453654 0.504060 0.554466 0.609711 0.670259 0.736623
0.809349 0.889061 0.976435 1.072130 1.177080 1.292110 1.418220
1.556330 1.707750 1.873790 2.055660 2.255060 2.473520 2.712950
2.975460 3.263080 3.578320 3.923900 4.302660 4.717700 5.172560
5.671180 6.217580 6.816500 7.472890 8.192280 8.980730 9.844890
10.79190 11.83030 12.96740 14.21450 15.58150 17.07960 18.72080
20.52030 22.49220 24.65260 27.02160 29.61750 32.46250 35.58160
38.99910 42.74530 46.85030 51.34960 56.28130 61.68680 64.6 67.61050
70.8 74.10280 77.6 81.21920 85.1 89.01800 93.3 97.56480 102.2
106.9310 112. 117.2040 122.8 128.4550 134.6
140.7840 147.4 154.3030 161.7 169.1220 177.2
185.3530 203.1560 222.6530 244.0360
267.4640 293.1410 321.2880 /
0.000000 0.006375 0.012750 0.025500 0.038250 0.051000 0.065750
.0806495 0.120974 0.161299 0.241949 0.322598 0.403248 0.483897
0.564547 0.645197 0.725846 0.806496 0.887145 0.967795 1.048440
1.129090 1.209740 1.290390 1.371040 1.451690 1.532340 1.612990
1.693640 1.774290 1.854940 1.935590 2.016240 2.096890 2.177540
2.258190 2.338840 2.419490 2.500140 2.580790 2.669500 2.767090
2.874450 2.992500 3.122350 3.265300 3.422470 3.595360 3.785490
3.994670 4.224730 4.477870 4.756310 5.062580 5.399390 5.769970
6.177660 6.626070 7.119240 7.661810 8.258620 8.915110 9.637220
10.43200 11.30510 12.26680 13.32430 14.48670 15.76600 17.17330
18.72180 20.42450 22.29760 24.35720 26.62340 29.11650 31.85860
34.87590 38.19360 41.84400 45.85830 50.27490 55.13310 60.47710
66.35540 72.82150 79.93380 90.00000 100.0000 110.0000 120.0000
130.0000 140.0000 150.0000 160.0000/
370/
.00255 67/
0 .0005 .001 .002 .0035 .005 .0075 .01 .013 .0165 .02 .0245
.029 .034 .0395 .045 .0506 .0562 .0622 .0686 .075 .083 .091
.099 .107 .115 .1197 .1214 .1218 .1195 .1125 .1065 .1005 .09542
.09126 .0871 .0839 .0807 .07798 .07574 .0735 .07162 .06974
.06804 .06652 .065 .0634 .0618 .06022 .05866 .0571 .05586
.05462 .0535 .0525 .0515 .05042 .04934 .04822 .04706 .0459
.04478 .04366 .04288 .04244 .042 0./
0.055556 0. 0.444444
2/
.205 .48/
.166667 .333333/
/
moder
43 -42
thermr
-42 -23 -41
1 125 16 1 4 0 2 222 1
370
```

```
.001 2
acer
-21 -41 0 26 27
2 0 1 .24 0/
'THERMAL 1001(0) from ENDFB-6.0 njoy99'/
125 370 hh2o/
1001 0 0/
222 16 0 0 1 2./
stop
```

F.4 CFX Mesh Sensitivity Analysis

The following tables contain the data for the mesh sensitivity analysis discussed in chapter 17.1.3. Table F.1 contains an overview over all cases, tables F.2 to F.13 contain the data for every single case.

Overview

Overview of all mesh cases for the senstivity analysis. If the node number is given as a sum, the summands represent the number of nodes in a single zone. For ϕ, this is: inner duct, inner frame, $3.0\,\mathrm{g/cm^3}$, $1.5\,\mathrm{g/cm^3}$, outer frame, outer duct. For θ: Water, cladding, fuel, cladding, water.

Case	ϕ	ϕ-y^+	θ	θ-Δy	z
ref	9+15+75+25+15+9=148	y+	13+5+7+5+13=43	5,00E-05	180
ϕ_1	9+20+100+35+20+9=193	1/2 y+	ref	ref	ref
z_1	ref	ref	ref	ref	120
$\theta_{1,1}$	ref	ref	20+5+7+5+20=57	5,00E-05	ref
$\theta_{1,2}$	ref	ref	20+5+7+5+20=57	4,00E-05	ref
$\theta_{1,3}$	ref	ref	20+5+7+5+20=57	6,00E-05	ref
θ_2	ref	ref	17+7+9+7+17=57	2,50E-05	ref
$\theta_{3,1}$	ref	ref	30+9+11+9+30=89	1,25E-05	ref
$\theta_{3,2}$	ref	ref	30+9+11+9+30=89	2,50E-05	ref
$\theta_{4,1}$	ref	ref	40+9+11+9+40=109	2,00E-05	ref
$\theta_{4,2}$	ref	ref	40+9+11+9+40=109	1,00E-05	ref
θ_5	ref	ref	50+9+11+9+50=129	2,00E-05	ref

Table F.1: *Mesh sensitivity analysis: Mesh cases.*

Case Data

Quantity	*Overall*	*Fuel 3.0*	*Fuel 1.5*
Temperatures [℃]			
Max. Fuel	102.9	102.9	92.8
Avg. Fuel	68.0	66.7	74.0
Max. Wall	89.6		
Avg. Wall	62.2		
Max. Outlet	58.5		
Avg. Outlet	53.0		
Heat Flux [$\mathrm{W/cm^2}$]			
Max. Wall	382.3		
Avg. Wall	161.3		
Pressure [bar]			
Avg. pressure drop	5.20		
Max. pressure	8.44		
Min. pressure	0.75		

Table F.2: *Mesh sensitivity: Case Reference.*

Quantity	*Overall*	*Fuel 3.0*	*Fuel 1.5*
Temperatures [℃]			
Max. Fuel	102.9	102.9	92.7
Avg. Fuel	67.9	66.6	74.0
Max. Wall	89.6		
Avg. Wall	62.2		
Max. Outlet	58.4		
Avg. Outlet	53.0		
Heat Flux [$\mathrm{W/cm^2}$]			
Max. Wall	382.4		
Avg. Wall	161.0		
Pressure [bar]			
Avg. pressure drop	5.22		
Max. pressure	8.46		
Min. pressure	0.75		

Table F.3: *Mesh sensitivity: Case ϕ_1.*

Quantity	*Overall*	*Fuel 3.0*	*Fuel 1.5*
Temperatures [℃]			
Max. Fuel	102.9	102.9	92.7
Avg. Fuel	68.0	66.7	74.0
Max. Wall	89.7		
Avg. Wall	62.4		
Max. Outlet	58.5		
Avg. Outlet	53.0		
Heat Flux [$\mathrm{W/cm^2}$]			
Max. Wall	382.7		
Avg. Wall	162.6		
Pressure [bar]			
Avg. pressure drop	5.20		
Max. pressure	8.44		
Min. pressure	0.75		

Table F.4: *Mesh sensitivity: Case* z_1.

Quantity	*Overall*	*Fuel 3.0*	*Fuel 1.5*
Temperatures [℃]			
Max. Fuel	102.8	102.8	92.7
Avg. Fuel	67.9	66.7	74.0
Max. Wall	89.5		
Avg. Wall	62.2		
Max. Outlet	58.5		
Avg. Outlet	53.0		
Heat Flux [$\mathrm{W/cm^2}$]			
Max. Wall	382.5		
Avg. Wall	161.3		
Pressure [bar]			
Avg. pressure drop	5.20		
Max. pressure	8.44		
Min. pressure	0.75		

Table F.5: *Mesh sensitivity: Case* $\theta_{1,1}$.

Quantity	*Overall*	*Fuel 3.0*	*Fuel 1.5*
Temperatures [℃]			
Max. Fuel	102.6	102.6	92.6
Avg. Fuel	67.8	66.6	73.8
Max. Wall	89.3		
Avg. Wall	62.1		
Max. Outlet	58.5		
Avg. Outlet	53.0		
Heat Flux [$\mathrm{W/cm^2}$]			
Max. Wall	383.2		
Avg. Wall	161.4		
Pressure [bar]			
Avg. pressure drop	5.27		
Max. pressure	8.51		
Min. pressure	0.75		

Table F.6: *Mesh sensitivity: Case* $\theta_{1,2}$.

Quantity	*Overall*	*Fuel 3.0*	*Fuel 1.5*
Temperatures [℃]			
Max. Fuel	103.0	103.0	92.9
Avg. Fuel	68.0	66.7	74.1
Max. Wall	89.7		
Avg. Wall	62.3		
Max. Outlet	58.5		
Avg. Outlet	53.0		
Heat Flux [$\mathrm{W/cm^2}$]			
Max. Wall	381.9		
Avg. Wall	161.3		
Pressure [bar]			
Avg. pressure drop	5.15		
Max. pressure	8.39		
Min. pressure	0.75		

Table F.7: *Mesh sensitivity: Case* $\theta_{1,3}$.

Quantity	*Overall*	*Fuel 3.0*	*Fuel 1.5*
Temperatures [°C]			
Max. Fuel	106.7	106.7	95.8
Avg. Fuel	70.0	68.7	76.5
Max. Wall	93.6		
Avg. Wall	64.3		
Max. Outlet	58.4		
Avg. Outlet	53.0		
Heat Flux [W/cm^2]			
Max. Wall	376.3		
Avg. Wall	161.1		
Pressure [bar]			
Avg. pressure drop	4.56		
Max. pressure	7.80		
Min. pressure	0.76		

Table F.8: *Mesh sensitivity: Case θ_2.*

Quantity	*Overall*	*Fuel 3.0*	*Fuel 1.5*
Temperatures [°C]			
Max. Fuel	101.4	101.4	91.8
Avg. Fuel	67.1	65.8	73.0
Max. Wall	88.4		
Avg. Wall	61.5		
Max. Outlet	58.5		
Avg. Outlet	53.0		
Heat Flux [W/cm^2]			
Max. Wall	386.8		
Avg. Wall	161.4		
Pressure [bar]			
Avg. pressure drop	5.47		
Max. pressure	8.71		
Min. pressure	0.74		

Table F.9: *Mesh sensitivity: Case $\theta_{3,1}$.*

Quantity	*Overall*	*Fuel 3.0*	*Fuel 1.5*
Temperatures [℃]			
Max. Fuel	101.8	101.8	92.1
Avg. Fuel	67.5	66.2	73.5
Max. Wall	88.8		
Avg. Wall	61.9		
Max. Outlet	58.5		
Avg. Outlet	53.0		
Heat Flux [$\mathrm{W/cm^2}$]			
Max. Wall	385.0		
Avg. Wall	161.4		
Pressure [bar]			
Avg. pressure drop	5.35		
Max. pressure	8.59		
Min. pressure	0.75		

Table F.10: *Mesh sensitivity: Case* $\theta_{3,2}$.

Quantity	*Overall*	*Fuel 3.0*	*Fuel 1.5*
Temperatures [℃]			
Max. Fuel	101.6	101.6	92.0
Avg. Fuel	67.4	66.1	73.4
Max. Wall	88.7		
Avg. Wall	61.8		
Max. Outlet	58.6		
Avg. Outlet	53.1		
Heat Flux [$\mathrm{W/cm^2}$]			
Max. Wall	385.7		
Avg. Wall	161.4		
Pressure [bar]			
Avg. pressure drop	5.39		
Max. pressure	8.63		
Min. pressure	0.75		

Table F.11: *Mesh sensitivity: Case* $\theta_{4,1}$.

Quantity	*Overall*	*Fuel 3.0*	*Fuel 1.5*
Temperatures [℃]			
Max. Fuel	99.3	99.3	90.6
Avg. Fuel	65.2	64.0	70.9
Max. Wall	86.3		
Avg. Wall	59.7		
Max. Outlet	58.5		
Avg. Outlet	53.0		
Heat Flux [$\mathrm{W/cm^2}$]			
Max. Wall	389.4		
Avg. Wall	161.5		
Pressure [bar]			
Avg. pressure drop	5.68		
Max. pressure	8.92		
Min. pressure	0.75		

Table F.12: *Mesh sensitivity: Case* $\theta_{4,2}$.

Quantity	*Overall*	*Fuel 3.0*	*Fuel 1.5*
Temperatures [℃]			
Max. Fuel	101.6	101.6	92.0
Avg. Fuel	67.4	66.1	73.4
Max. Wall	88.6		
Avg. Wall	61.8		
Max. Outlet	58.6		
Avg. Outlet	53.1		
Heat Flux [$\mathrm{W/cm^2}$]			
Max. Wall	385.7		
Avg. Wall	161.3		
Pressure [bar]			
Avg. pressure drop	5.38		
Max. pressure	8.62		
Min. pressure	0.75		

Table F.13: *Mesh sensitivity: Case* θ_5.

Table of Symbols

Formula Symbols

Symbol	Unit	Meaning
A	cm^2	area
A	-	mass number
a	m^2/s	thermal diffusivity
a_i	-	model constant for SST model
a_t	m^2/s	turbulent thermal diffusivity
ΔB	-	modification of the wall functions for rough walls
c	-	Courant number / CFL number
c	m/s	speed of sound
c_V	$\mathrm{J}/\mathrm{kg\,K}$	Specific heat capacity at constant volume V
c_p	$\mathrm{J}/\mathrm{kg\,K}$	Specific heat capacity at constant pressure p
C	div.	in general used for constants
CD_K	-	limiting function for SST turbulence model
d	-	differential
d	cm	thickness
d_h	cm	hydraulic diameter
e	A s	elemental charge $1.6022 \cdot 10^{-19}$C
e	J/kg	specific inner energy
e	-	Euler number ($\mathrm{e} \approx 2.718$)
$\boldsymbol{e}_i$	-	unit vector in direction i
E	MeV	energy (for neutrons)
E	J/kg	specific energy (for elements of the fluid)
$\langle E \rangle$	MeV	median energy
F_i	-	blending function i for SST turbulence model
h_s	mm	sand grain roughness
H	-	source entropy
i	-	index used for counting
I	-	turbulence intensity
IP	-	set of integration points
j	-	index used for counting
j	$1/\mathrm{cm}^2\,\mathrm{s}$	current
$\mathbb{J}$	-	Jacobi matrix
k	-	index used for counting
k	cm	absolute roughness
k	-	criticality factor
K	$\mathrm{m}^2/\mathrm{s}^2$	turbulent kinetic energy
K_{Pr}	-	correction factor for Prandtl number
Kn	-	Knudsen number

l	cm	length (e. g. of a side of a cube)
l	cm	turbulence length scale
l_k	cm	length scale of small turbulent fluctuations
l_{mfp}	cm	length scale of molecular motion
m	kg	mass
M	$^{\mathrm{g}}/_{\mathrm{mol}}$	atomic weight
M	-	Number of active cycles in a KCODE calculation
M_N	MeV	rest mass of the neutron, 939.565 330(38) MeV
Ma	-	Mach number
n	$^{1}/_{\mathrm{cm}^3}$	particle number density
n	-	neutron
$\boldsymbol{n}$	-	surface normal
N	-	number of particles
N_A	$^{1}/_{\mathrm{mol}}$	Avogadros constant (Loschmidt number) $6.0221 \cdot 10^{23} \frac{1}{\mathrm{mol}}$
Nu	-	Nusselt number
p	bar	pressure
p	-	probability
p	-	transformation parameter for Exponential Transform
P_K	$^{\mathrm{kg}}/_{\mathrm{m\,s}^3}$	turbulence production limiter for SST model
$\tilde{P}_K$	-	turbulence production limiter for SST model
Pr	-	Prandtl number
q	$^{\mathrm{J}}/_{\mathrm{s}}$	Source strength (for heat sources)
Q	$^{1}/_{\mathrm{s}}$	Source strength (for neutrons)
Q	J	heat
Q	-	MC estimate
r	-	residual
r	-	random number
r	$^{1}/_{\mathrm{s\,cm}^3}$	reaction rate
R	div.	Uncertainty in MCNP (relative)
Re	-	Reynold number
s	cm	distance
S	-	used in area integrals $\mathrm{d}S$
S	-	scattering matrix $S(\alpha, \beta)$
S	$^{1}/_{\mathrm{s}}$	invariant strain rate tensor
Sr	-	Strouhal number
t	s	time
$t_{\frac{1}{2}}$	s	half life
T	K	temperature
T	s	simulation time
T_c	d	reactor cycle length
T_f	K	temperature of the fluid in COMSOL
T_s	K	temperature of the solid in COMSOL
u	-	lethargy
u	cm	coated perimeter
U	J	inner energy
v	$^{\mathrm{m}}/_{\mathrm{s}}$	velocity
v_τ	$^{\mathrm{m}}/_{\mathrm{s}}$	wall shear stress velocity
v^+	-	dimensionless wall velocity
V	cm^3	volume
W	J	work
W	-	particle weight in Monte Carlo calculations
$\mathrm{Var}\,(\mathrm{X})$	-	variance of X, $\mathrm{Var}\,(\mathrm{X}) = \text{œ}^2$
x	div.	arbitrary quantity

$\boldsymbol{x}$	(cm, cm, cm)	position
X	-	unknown / arbitrary nucleus
y	-	no fixed meaning, used for substitutions
y^+	-	first node wall distance
$\tilde{y}^+$	-	limited first node wall distance
z	cm	control rod position
Z	-	atomic number
α	$^{\mathrm{J}}/_{\mathrm{m^2\,s\,K}}$	heat transfer coefficient
α	-	normalized momentum transfer
α_i	-	model constants for SST model
α_D	$^{1}/_{\mathrm{K}}$	Doppler coefficient
α_T	$^{1}/_{\mathrm{K}}$	Total temperature reactivity coefficient
α_v	$^{1}/_{\mathrm{K}}$	Void coefficient
α_ρ	$^{1}/_{\mathrm{K}}$	Density coefficient
β	$^{\mathrm{s}}/_{\mathrm{m}}$	inverse velocity, $\beta = \sqrt{AM_n/2k_{\mathrm{B}}T}$
β	-	normalized energy transfer
β_i	-	model constants for SST model
β^*	-	model constant for SST model
Γ	MeV	half width of a resonance
Γ	-	Set of borders of the region to be investigated
Γ	-	abbreviation in wall functions for the energy equation
δ_w^+	-	y^+ in COMSOL
Δ	div.	uncertainty of the quantity named thereafter
Δ	-	LaPlace operator
ε	-	Levi-Civita-Symbol
ϵ	-	relative roughness
ϵ	$^{\mathrm{m^2}}/_{\mathrm{s^3}}$	turbulent dissipation
θ	rad	scattering angle
Θ^*	-	Another form of a dimensionless temperature T^*
κ	$^{\mathrm{J}}/_{\mathrm{m\,s\,K}}$	thermal conductivity
κ	-	Kármán constant ($\kappa = 0.41$)
κ_t	$^{\mathrm{J}}/_{\mathrm{m\,s\,K}}$	turbulent thermal conductivity
λ	cm	mean free path length
λ	$^{1}/_{\mathrm{s}}$	decay constant
λ	-	Lamè-Parameter
λ	$^{\mathrm{kg}}/_{\mathrm{m\,s}}$	bulk viscosity / volume viscosity
Λ	$^{1}/_{\mathrm{s}}$	effective decay constant
μ	$^{1}/_{\mathrm{cm}}$	Shielding constant for neutrons
μ	-	friction coefficient
μ	-	cosine ($\mu = \cos\theta$)
μ	$^{\mathrm{kg}}/_{\mathrm{m\,s}}$	dynamic viscosity
μ_t	$^{\mathrm{kg}}/_{\mathrm{m\,s}}$	turbulent viscosity
ν	$^{\mathrm{m^2}}/_{\mathrm{s}}$	kinematic viscosity
ν_t	$^{\mathrm{m^2}}/_{\mathrm{s}}$	kinematic turbulent viscosity
ν	-	neutron fission multiplicity
ρ	$^{\mathrm{g}}/_{\mathrm{cm^3}}$	density
ρ	-	fraction factor in linear interpolation
ρ	-	correlation coefficient, eq. 4.17
σ_{ki}	-	model constants for SST model
$\sigma_{\omega i}$	-	model constants for SST model
σ	barn	cross section, see appendix E, p. 277
σ	-	standard deviation

σ	$^{\mathrm{kg}}/_{\mathrm{m\,s^2}}$	Cauchy stress tensor
Σ	$^{1}/_{\mathrm{cm}}$	macroscopic cross section, $\Sigma := n \cdot \sigma$
τ	s	life time
τ	$^{\mathrm{kg}}/_{\mathrm{m\,s^2}}$	stress strain tensor
τ_ω	$^{\mathrm{kg}}/_{\mathrm{m\,s^2}}$	average wall shear stress
ϕ	$^{1}/_{\mathrm{cm^2\,s}}$	flux density, see appendix E, p. 277
$\phi(E)$	$^{1}/_{\mathrm{cm^2\,s\,MeV}}$	spectral flux density, see appendix E, p. 278
$\boldsymbol{\Phi}(\boldsymbol{x})$	$^{1}/_{\mathrm{cm^2}}$	cycle neutron yield, CNY, see E
ζ	-	pipe friction factor
ω	-	cell weight in Monte Carlo calculations
ω	$^{1}/_{\mathrm{s}}$	specific turbulent dissipation rate
Ω	-	internal space of the region to be investigated
Ω	sr	solid angle
Ω	$^{1}/_{\mathrm{s}}$	vorticity tensor
$\mathbb{1}$	-	unity matrix

Symbols in **bold** represent vectors and matrices.

Generally used indices

Subscript

Index	**Meaning**
$_\gamma$	refers to γ radiation
$_\mathrm{f}$	fast
$_\mathrm{f}$	fluid
$_\mathrm{n}$	refers to neutron radiation
$_\mathrm{s}$	solid
$_\mathrm{t}$	turbulent
$_\mathrm{th}$	thermal ($E_0 \approx 25\,\mathrm{meV}$)
$_\mathrm{Therm}$	thermal ($E_0 \approx 25\,\mathrm{meV}$)
$_\mathrm{K}$	refers to cartesian coordinates
$_\mathrm{E}$	refers to involute coordinates, see chapter A.2, p. 250f.

Supscript

Index	**Meaning**
^{T}	transposed
*	dimensionless

Operators

Symbol	**Definition**	**Name**
$\cdot$	$\boldsymbol{a} \cdot \boldsymbol{b} := \boldsymbol{a}^T \boldsymbol{b}$	scalar product
$\times$	$\boldsymbol{a} \times \boldsymbol{b} := \sum_{ijk} \varepsilon_{ijk} a_i b_j \boldsymbol{e}_k$	cross product

$\otimes$	$\boldsymbol{a} \otimes \boldsymbol{b} := \boldsymbol{a}\boldsymbol{b}^T$	dyadic product
:	$T^1 : T^2 := \mathrm{tr}\left(T^1 \cdot \left(T^2\right)^T\right)$	trace of the tensoric product

Using these definitions, $\boldsymbol{\nabla f}$ is not the divergence but the Jacobian matrix of the vector $\boldsymbol{f}$, $\mathbb{J}(\boldsymbol{f})$.

Table of Abbreviations

Abbr.	**Meaning**
Abbr.	Abbreviation
API	Application programming interface
BSL	Baseline
CDF	Cumulative distribution function
CFD	Computational fluid dynamics
CLT	Central limit theorem
CNY	Cycle neutron yield
DOC	Department of Commerce
DOE	Department of Energy
DOM	Discrete ordinate method
DTS	Depletion time step
DU	Depleted uranium ($< 0.72\%$ ^{235}U)
FOM	Figure of merit
FPD	Full power days
fsi	Fluid-solid interface
HEU	Highly enriched uranium ($>50\%$ ^{235}U)
LEU	Lightly enriched uranium ($>0.72\%$ and $<20\%$ ^{235}U)
MC	Monte Carlo
MCC	Monte Carlo calculation
MEU	Medium enriched uranium ($>20\%$ and $<50\%$ ^{235}U)
NatU	Natural uranium (0.72% ^{235}U)
OFI	Onset of flow instability
ONB	Onset of nucleate boiling
OSV	Onset of significant voiding
PDF	Probability density function
p.d.p.	Power density profile
PDF	Portable document format
RS	Reynolds stress
SST	Shear stress transport
UMo	Uranium Molybdenum alloy
VOV	Variance of the variance

List of Figures

1.1 Fuel element, horizontal cut . . . 2
1.2 Fuel element of FRM II . . . 3
1.3 Cut view through FRM II . . . 6

2.1 Source entropy . . . 23

3.1 Errors in Mo cross section . . . 30

4.1 k and control rod position . . . 36
4.2 Correlation of cells . . . 41

6.1 Moody-Diagramm . . . 49
6.2 Boiling curve . . . 51

7.1 On the deduction of the continuity equation. . . . 56
7.2 On the deduction of the Navier Stokes Equation. . . . 58
7.3 On the deduction of the energy equation. . . . 59
7.4 Choosing the proper averaging interval . . . 62
7.5 Flow near the wall . . . 68
7.6 Concept of the sand-grain roughness . . . 70
7.7 Downward shift of logarithmic wall velocity profile . . . 70
7.8 On the concept of finite volumes . . . 72
7.9 Flowchart for CFX . . . 74
7.10 Algebraic Multigrid . . . 75

9.1 MCNPX model of the core . . . 85
9.2 Approximation of involutes . . . 86
9.3 MCNPX model: Involutes . . . 88
9.4 MCNPX model with averaged built in components . . . 89
9.5 MCNPX Mesh and fit . . . 91
9.6 Correlation of heat flux and temperature . . . 92

10.1 Complete CAD model . . . 95
10.2 Overview of fuel plate . . . 96
10.3 Mesh . . . 97
10.4 First node distance . . . 98
10.5 Thermal conductivity of U_3Si_2-Al dispersion fuel . . . 104
10.6 Thermophysical data for disperse U8Mo . . . 105
10.7 Relative temperature dependence of the specific heat of disperse U8Mo . . . 106
10.8 Relative temperature dependence of the thermal conductivity of disperse U8Mo . . . 106
10.9 Swelling of U_3Si_2-Al dispersion fuel . . . 109

11.1 Flowchart for X^2 . . . 113

13.1 Development of velocity profile after the sieve . . . 125
13.2 Distortion of boundary profiles over plates . . . 126
13.3 Strouhal number over Reynolds number . . . 127
13.4 Outlet temperature oscillations . . . 128
13.5 Flow properties of the current fuel element at inlet . . . 129
13.6 Flow properties of the current fuel element at inlet . . . 130
13.7 Flow detachment . . . 131
13.8 Flow properties of the current fuel element at outlet . . . 132
13.9 Heat flux for homogeneous heating . . . 134
13.10Surface temperatures for homogeneous heating . . . 135
13.11Flow in the corner . . . 136
13.12Mixing of stream filaments . . . 137
13.13Flow properties of the current fuel element: Pressure drop . . . 138
13.14Pressure drop . . . 139
13.15Pressure distribution below the fuel plate . . . 140
13.16Burnup of Be-follower . . . 141
13.17Reactivity change due to burnup of Be-follower . . . 142
13.18Mesh quality analysis . . . 144

14.1 Burn-up for current fuel element . . . 149
14.2 Power deposition at BOL . . . 153
14.3 Power deposition at EOL . . . 154
14.4 Flux profiles for the current fuel element at BOL . . . 156
14.5 Complete CAD model with thermal neutron flux . . . 157
14.6 Flux profiles for the current fuel element at EOL . . . 158
14.7 Flux difference between BOL and EOL . . . 159
14.8 Temperature properties of the current fuel element . . . 160
14.9 Temperature properties of the current fuel element (2) . . . 161
14.10Temperature properties of the current fuel element at EOL . . . 163
14.11Temperatures at the top of the fuel plate at EOL . . . 165
14.12Wall heat flux of the current fuel element at BOL . . . 166
14.13Wall heat flux of the current fuel element at EOL . . . 167

15.1 k and control rod position . . . 171
15.2 Burn-up for disperse fuel element . . . 172
15.3 Actinide inventory of the disperse fuel . . . 174
15.4 Power deposition . . . 176
15.5 Flux profiles for a disperse fuel element at BOL . . . 177
15.6 Thermal flux difference between disperse UMo and current fuel element . . . 178
15.7 Flux profiles for a disperse fuel element at EOL . . . 179
15.8 Thermal flux difference between disperse UMo and current fuel element at EOL . . . 180
15.9 Temperature properties of a disperse UMo fuel element at BOL . . . 181
15.10Comparison of water temperature at fuel zone end . . . 182
15.11Temperature properties of a disperse UMo fuel element at EOL . . . 183
15.12Wall heat flux of a disperse fuel element at BOL . . . 184
15.13Wall heat flux of a disperse fuel element at EOL . . . 185
15.14Distance to boiling at 22 MW . . . 186
15.15Maximum D2O flux depending on length of active zone . . . 188

16.1 Thickness profile of UMo plate. . . . 191
16.2 k and control rod position . . . 191
16.3 Burn-up for monolithic fuel element . . . 192

16.4 Power deposition . . . 195
16.5 Power deposition . . . 196
16.6 Flux profiles for a monolithic fuel element at BOL . . . 198
16.7 Thermal flux difference between monolithic UMo and current fuel element . . . 199
16.8 Flux profiles for a monlithic UMo fuel element at EOL . . . 200
16.9 Thermal flux difference between monolithic UMo and current fuel element at EOL . . . 201
16.10Temperature properties of a monolithic UMo fuel element at BOL . . . 203
16.11Comparison of water temperature at fuel zone end . . . 204
16.12Wall heat flux of a monolithic fuel element at BOL . . . 205
16.13Thermal hydraulic properties of a flat monolithic plate at BOL . . . 206

17.1 Influence of wall roughness . . . 211
17.2 Sensitivity of results to turbulence model . . . 212
17.3 Sensitivity of results to turbulence model (2) . . . 213
17.4 Influence of inlet turbulence intensity . . . 218
17.5 Uncertainty of burn-up calculations. . . . 223
17.6 Uncertainty of burn-up calculations. . . . 224

18.1 Comparison of wall temperatures in NBK and CFX . . . 228
18.2 Difference heat flux densities . . . 229
18.3 Comparison of heat flux densities in NBK and CFX . . . 230
18.4 Difference in fuel plate modelling . . . 231
18.5 Difference in CFX models . . . 232
18.6 Solved COMSOL involute model . . . 233
18.7 2D mesh for the slab model . . . 233
18.8 Comparison of CFX and COMSOL results for involute model: Heat fluxes. . . . 235
18.9 Comparison of CFX and COMSOL results for involute model: Surface temperatures. . . . 236
18.10Wall properties dependence of COMSOL . . . 237
18.11Comparison of CFX and COMSOL results for slab model: Heat fluxes and temperatures. 238
18.12Differences in velocities at the the fluid symmetry face . . . 239

A.1 Involute coordinate system . . . 251
A.2 Involute coordinates: Unit vectors . . . 252

C.1 Flowchart for X^2 . . . 260
C.2 Flowchart for X^2 initialisation . . . 262
C.3 Flowchart for X^2 initialisation: Determination of reactivity profile . . . 263

List of Tables

2.1 Selection of cross sections for neutrons . . . 12
2.2 Reliableness of Monte Carlo results . . . 18

10.1 Data input for the simulation of the old fuel element . . . 100
10.2 Data for fuel of old element at BOL . . . 103
10.3 Data for UMo disperse fuel at BOL at room temperature . . . 104

13.1 Data input for the simulation of the current fuel element . . . 123
13.2 Used normalisation factors . . . 123
13.3 Derived data for the simulation of the fuel element . . . 124

14.1 Results for the simulation of the current fuel element (neutronics) . . . 146
14.2 Results for the simulation of the current fuel element (thermal hydraulics) . . . 147
14.3 Result of burn-up calculation for current fuel element, EOL . . . 151

15.1 Results for the simulation of a disperse UMo fuel element (neutronics) . . . 169
15.2 Results for the simulation of a disperse UMo fuel element (thermal hydraulics) . . . 170
15.3 Result of burn-up calculation, disperse UMo, EOL . . . 173

16.1 Results for the simulation of a monolithic UMo fuel element (neutronics) . . . 189
16.2 Results for the simulation of a monolithic UMo fuel element (thermal hydraulics) . . . 190
16.3 Result of burn-up calculation for monolithic UMo, EOL after 60 d . . . 193

17.1 Influence of wall roughness . . . 210
17.2 Influence of turbulence model . . . 211
17.3 Uncertainties due to mesh sensitivity . . . 215
17.4 Influence of viscous dissipation . . . 216
17.5 Influence of buoyancy . . . 216
17.6 Influence of reactor power . . . 217
17.7 Influence of inlet turbulence intensity . . . 217
17.8 Influence of inlet temperature . . . 219
17.9 Influence of inlet velocity . . . 219
17.10 Influence of gamma heating in structural material . . . 220
17.11 Influence of curvature correction . . . 220
17.12 Sensitivity matrix . . . 221
17.13 Difference between one and two burn-up predictor steps (actinides) . . . 224
17.14 Difference between one and two burn-up predictor steps, non-actinides (1) . . . 225
17.15 Difference between one and two burn-up predictor steps, non-actinides (2) . . . 226

19.1 Comparison of current, a disperse and a monolithic UMo core . . . 244

E.1 Neutron temperature: Classification of neutrons by their speed . . . 278

F.1 Mesh sensitivity analysis: Mesh cases. 284
F.2 Mesh sensitivity: Case Reference 285
F.3 Mesh sensitivity: Case ϕ_1 285
F.4 Mesh sensitivity: Case z_1 286
F.5 Mesh sensitivity: Case $\theta_{1,1}$ 286
F.6 Mesh sensitivity: Case $\theta_{1,2}$ 287
F.7 Mesh sensitivity: Case $\theta_{1,3}$ 287
F.8 Mesh sensitivity: Case θ_2 288
F.9 Mesh sensitivity: Case $\theta_{3,1}$ 288
F.10 Mesh sensitivity: Case $\theta_{3,2}$ 289
F.11 Mesh sensitivity: Case $\theta_{4,1}$ 289
F.12 Mesh sensitivity: Case $\theta_{4,2}$ 290
F.13 Mesh sensitivity: Case θ_5 290

Own Publications

The following own publications are related to this work:

3-Dimensional Coupled Neutronic and Thermohydraulic Calculations for a Compact Core Combining MCNPX and CFX
Harald Breitkreutz, Anton Röhrmoser, Winfried Petry
Proceedings of ANIMMA 2009, Marseille

Coupled 3D neutronic and thermohydraulic calculations for a compact fuel element with disperse UMo fuel at FRM II
Harald Breitkreutz, Anton Röhrmoser, Winfried Petry
Transactions of the RRFM 2010, Marakesh

X^2: A coupled neutronic - thermohydraulic code system for compact research reactor cores
Harald Breitkreutz, Anton Röhrmoser, Winfried Petry
Transactions of the Physor 2010, Pittsburgh

Bibliography

[Aut08] Authors, Several: *CFD-Wiki: Turbulence free-stream boundary conditions*. Internet. `http://www.cfd-online.com/Wiki/Turbulence_free-stream_boundary_conditions`. Version: 11 2008. – Date viewed: 2008-11-19, 15:46

[Blü02] Blüm, P.: Einführung zur Fehlerrechnung im Praktikum / Universität Karlsruhe. 2002. – Forschungsbericht

[Bön04] Böning, L., Röhrmoser, A. Petry, W.: Conversion of the FRM-II. In: *European Nuclear Society Transactions*, 2004, S. 91–95

[Bön09] Böning, K., Petry, W.: Test irradiations of full-sized U2Si3-A fuel plates up to very high fission densities. In: *Journal of Nuclear Materials* 383 (2009), S. 254–263. `http://dx.doi.org/10.1016/j.jnucmat.2008.09.016`. – DOI 10.1016/j.jnucmat.2008.09.016

[BNLB] Brookhaven National Laboratory (BNL), National Nuclear Data Center (. t.: *Evaluated Nuclear Data Files, ENDF/B Version VI*

[Bow62] Bowring, R.W.: Physical model based on bubble detachment and calculation of steam voidage in the subcooled region of a heated channel / Institute for Atomenergi, Halden, Norway. 1962. – Forschungsbericht

[Bro02] Brown, F.B., Nagaya, Y.: The MCNP5 Random Number Generator. In: *Trans. Am. Nucl. Soc.* 87 (2002), S. 230

[Bro08] Brown, F.B., Mosteller, R.D. Martin, W.R.: Monte Carlo - Advances and Challenges (LA-UR-08-05891) / Los Alamos National Laboratory. 2008 (LA-UR-08-05891). – Forschungsbericht

[CFX06a] CFX, ANSYS: ANSYS CFX-Solver Modeling Guide. ANSYS CFX Release 11.0. / ANSYS. 2006. – Forschungsbericht

[CFX06b] CFX, ANSYS: ANSYS CFX-Solver Theory Guide. ANSYS CFX Release 11.0. / ANSYS. 2006. – Forschungsbericht

[CFX09a] CFX: ANSYS CFX-Solver Modeling Guide. ANSYS CFX Release 12.0 / ANSYS. 2009. – Forschungsbericht

[CFX09b] CFX, ANSYS: ANSYS CFX-Solver Theory Guide. ANSYS CFX Release 12.0. / ANSYS. 2009. – Forschungsbericht

[Cha06] Chadwick, M.B.: ENDF/B-VII.0: Next Generation Evaluated Nuclear Data Library for Nuclear Science and Technology. In: *Nuclear Data Sheets* 107 (2006), Nr. 12, S. 2931–3060

[Cha08] Chandler, D., Maldonado, G.I. Primm, R.T.: Validating MCNP for LEU Fuel Design via Power Distribution Comparisons (ORNL/TM-2008/126) / Oak Ridge National Laboratory. 2008. – Forschungsbericht

[Cha10] Chandler, D., Ivan Maldonado, G. Primm III, R.T.: Validation of a Monte Carlo based depletion methodology via High Flux Isotope Reactor HEU post-irradiation examination measurements. In: *Nuclear Engineering and Design* 240 (2010), Nr. 5, S. 1033–1042

[Che09] Chen, E., Wang, L. Li, Y.: Modeling of low-pressurce subcooled boiling flow water via the homogeneous MUSIG approach. In: *Nuclear Engineering and Design* 239 (2009), S. 1733–1743

[Col60] Cole, R.: A photographic study of pool boiling in the region of CHF. In: *American Institue of Chemical Engineers Journal* 6 (1960), S. 533–542

[Com88] Commission, U.S: Nuclear R.: NUREG-1313: Safety Evaluation Report realted to the Evalutaion of Low-Enriched Uranium Silicide-Aluminium Dispersion Fuel for Use in Non-Power Reactors / Office of Nuclear Reactor Regulation. 1988 (1313). – Forschungsbericht

[COM10] COMSOL Tech Support: *COMSOL Knowledge Base, Article 973: My flux calculation seems wrong*. `http://www.comsol.com/support/knowledgebase/973/`. Version: 4 2010

[Con05] Conlin J.L., Martin W.R. Ji W.: Pseudo-Material Construct for Coupled Neutronic-Thermal-Hydraulic Analysis of VHTGR. In: *Trans. ANS.* 91 (2005), S. 225

[Coo07] Cooper, J.R.: Revised Release on the IAPWS Industrial Formulation 1997 for the Thermodynamic Properties of Water and Steam / The International Association for the Properties of Water and Steam. 2007. – Forschungsbericht

[Cop87] Copeland G.L., Hofman G.L. Hobbs R.W.: Performance of Low-enriched U3Si2-Aluminium Dispersion Fuel Elements in the Oak Ridge Research Reactor / Argonne National Laboratory. 1987. – Forschungsbericht

[Cou28] Courant, R:, Lewy, H. Friedrichs, K.: Über die partiellen Differenzengleichungen der mathematischen Physik. In: *Mathematische Annalen* 100 (1928), Nr. 1, 32-74. `http://www.stanford.edu/class/cme324/classics/courant-friedrichs-lewy.pdf`. – Republished as english translation in IBM Journal, "On the partial difference equations of mathematical physics", 3/1967, pp. 215-234.

[Cro80] Croff, A.G. ; Oak Ridge National Laboratory (Hrsg.): *A User's Manual for the Origen2 Computer Code*. USA: Oak Ridge National Laboratory, 7 1980

[Dal02] Dalle,H.M., Postal, C. Jeraj, R.: Validation of the Monteburns Code for Criticality Calculations of TRIGA Reactors. In: *XIII ENFIR, INAC*, 2002

[Död89] Döderlein, C.: *Untersuchungen zur Kühlbarkeit eines kompakten Reaktorkerns mit evolventenförmigen Brennstoffplatten*, Technische Universität München, Diplomarbeit, 12 1989

[Död93] Döderlein, C., Nuding, M.: OPA-139: Uran-Inventar des FRM-II und andere Nuklidmassen bei Zyklusbeginn und Zyklusende / Fakultät für Physik E21, Technische Universität München. 1993. – Forschungsbericht

[Död95] Döderlein, C.: *Kinetik und Dynamik eines Forschungsreaktors mit einem reflektierten Kompaktkern*, Technische Universität München, Diss., 1995

[Dil06] Dilla, E.M., Tu, J.Y. Yeoh, G..: Flow instability prediction in low-pressure subcooled boiling flows using computational fluid dynamic codes. In: *Australia and New Zealand Industrial and Applied Mathematics Journal* 46 (2006), S. C1336–C1352

[Dit30] Dittus, F.W., Boelter L.M.K.: 443 / University of California Publications on Engineering. 1930 (2). – Forschungsbericht

[Dur] Durkee, J.: *Private communication*

[Dur09a] Durkee, J.W. Jr., McKinney, G.W. James, M.R.: Delayed-gamma signature calculation for neutron-induced fission and activation using MCNPX, Part I: Theory. In: *Progress in Nuclear Energy* 51 (2009), 11, Nr. 8, S. 813–827

[Dur09b] Durkee, J.W. Jr., McKinney, G.W. James, M.R.: Delayed-gamma signature calculation for neutron-induced fission and activation using MCNPX. Part II: Simulations. In: *Progress in Nuclear Energy* 51 (2009), 11, Nr. 8, S. 828–836

[Dur09c] Durkee, J.W. Jr., McKinney, G.W. James, M.R.: Delayed-gamma signature calculation for neutron-induced fission and activation using MCNPX, Part III: Transport theory. In: *Progress in Nuclear Energy* 51 (2009), 11, Nr. 8, S. 837–844

[EFU08] EFUNDA Engineering fundamentals: *Aluminium*. Internet. `http://www.efunda.com/materials/elements/TC_Table.cfm?Element_ID=Al`. Version: 11 2008. – Thermal conductivity of Aluminium

[Ego04] Egorov, Y., Menter, E.: Experimental implementation of the RPI wall boiling model in CFX-5.6, Technical Report ANSYS/TR-04-10 / ANSYS GmbH. 2004. – Forschungsbericht

[Eme82] Emendörfer, D., Höcker, K.H.: *Theorie der Kernreaktoren: Band 1: Der stationäre Reaktor*. Bibliographisches Institut AG, 1982

[Eme93] Emendörfer, D., Höcker, K.H.: *Theorie der Kernreaktoren: Band 2: Der instationäre Reaktor*. Bibliographisches Institut AG, 1993

[Eng89] Englang, T.R., Reich, C.W. Mann,F.M.: ENDF/B-VI Radioactive Decay Data and Yield Libraries. In: *Trans. ANS.* 60 (1989), S. 614

[Eng92] England, T.R., Mann, F.M. Katakura, J.: Devay Data Evaluation For ENDF/B-VI. In: *Proceedings of the International Symposium on Nuclear Data Evaluation Methodology* Brookhave National Laboratory (BNL), World Scientific Publishing Co., Singapore, October 12-16 1992, S. pp. 611–622

[Esc03] Esch, T., Menter, F.R.: Heat transfer prediction based on two-equation turbulence models with advanced wall treatment. In: Hanjalic, Tummers Nagano (Hrsg.): *Turbulence Heat and Mass Transfer*. Antalya, 2003

[Fav01] Favorite, J.A., Kent Parsons, D.: Second-Order Cross Terms in Monte Carlo Differential Operator Perturbation Estimates. In: *Proceedings of Internation Conference, Mathematical Methods for Nuclear Applications*. Salt Lake City, Utah, September 9-13 2001

[Fel96] Feltes: Nukleare Kernauslegung / Siemens. 1996 (A1C-1300070-2). – Arbeitsbericht. – FRM II

[Fen06] Fensin, M.L., Trellue, H. Hendricks, J.S.: Incorporation of a predictor-corrector methodology and 1-group reaction rate reporting scheme for the MCNPX depletion capability. In: *Transactions of the American Nuclear Society* 95 (2006), S. pp. 317–319

[Fer98] Fernandez-Prini, R.: Revised Release on the IAPS Formulation 1985 for the Thermal Conductivity of Ordinatry Water Substance / The International Association for the Properties of Water and Steam. 1998. – Forschungsbericht

[Fre] Freels, J.D.: *Private Communication*

[Fre09] Freels, J.D., Lowe, K.T. Arimilli, R.V.: The Role of COMSOL Towards a Low-Enriched Uranium Fuel Design for the High Flux Isotope Reactor. In: *COMSOL Conference Boston 2009, Boston, MA, USA*, 2009

[Fre10] Freels, J.D., Cutone, M. Bodey, I.T.: Exploiting New Features of COMSOL 4 on Conjugate Heat Transfer Problems. In: *COMSOL Conference 2010 USA*, 2010

[Gel90] Gelbard, E.M., Prael, R.: Computations of Standard Deviations in Eigenvalue Calculations. In: *Progress in Nuclear Energy* 24 (1990), S. 237

[Gen03] Gentle, J.E. ; Chamber, J., (Hrsg.): *Random Number Generation and Monte Carlo Methods*. Springer, 2003

[Ger10] Gerstenberg, H., Neuhaus, I. Müller, C.: U-Target Irradiation at FRM II Aiming the Production of Mo-99 - A Feasibility Study. In: *Proccedings of RRFM 2010*, 2010

[Gie96] Giesler, Ehrich Sperber: Thermohydraulische Kernauslegung / Siemens. 1996 (A1C-1301735-0). – Arbeitsbericht. – FRM II

[Gla05] Glaser, A.: *Neutronics Calculations Relevant to the Conversion of Research Reactors to Low-Enriched Fuel*, Technische Universität Darmstadt, Diss., 02 2005

[Gni75] Gnielinski, V.: Neue Gleichungen für den Wärme- und Stoffübergang in turbulent durchströmten Rohren und Kanälen. In: *Forsch. im Ing.-Wis.* 41 (1975), Nr. 1, S. 8–16

[Gri61] Griess, J.C., Rainwater, J.G. Savage, H.C.: Effect of Heat Flux on the Corrosion of Aluminium by Water, Part III, ORNL-3230 / ORNL. 1961. – Forschungsbericht

[Gys96] Gyseler, S., Vanvor: Brennelement / Siemens. 1996 (A1C-1300802). – Arbeitsbericht. – FRM II

[Hal60] Halperin, M.: Almost Linearly Optimum Combination of Unbiased Estimates / Knolls Atomic Power Lab., Schenectady, N.Y. 1960. – Forschungsbericht

[Hal80] Hall, M.C.: *Monte Carlo Perturbation Theory in Neutron Transport Calculations*, University of London, Diss., 1980

[Hea05] Heack, W., Verboomeb, B.: ALEPH 1.1.2 - A Monte Carlo Burn-Up Code (SCK - CEN-BLG-1003) / SCK-CEN Belgien Nuclear Research Centre. 2005. – Forschungsbericht

[Hel97] Hellsten, A., Laine, S.: Extension of the k-omega-SST turbulence models for flows over rough surfaces, AIAA-Paper 97-3577 / AIAA. 1997. – Forschungsbericht

[Hen08] Hengstler, R.: *Thermal and Electric Conductivity of a Monolithic Uranium-Molybdenum Alloy for Research Reactor Fuels*, Technische Universität München, Diplomarbeit, 12 2008

[Hes98] Hess, A.K., Hendricks, S.J. Carter, L.L.: Verification of the MCNP Perturbation Correction Feature for Cross-Section Dependendt Tallies / Los Alamos National Laboratory. 1998 (LA-13520). – Forschungsbericht

[Här05] Härtle, R. ; Technische Universität München (Hrsg.): *LagMeat: Numerische Simulation dreidimensionaler Wärmeleitung in inhomogenen Materialien*. Garching: Technische Universität München, 10 2005

[IAE] IAEA: *Research Reactor Details - HFIR*. Internet. `http://www-naweb.iaea.org/napc/physics/research_reactors/database/RR%20Data%20Base/datasets/report/United%20States%20of%20America%20%20Research%20Reactor%20Details%20-%20HFIR.htm`

[IAE92] IAEA: Water Corrosion of Aluminium Alloy Cladding, Research Reactor Core Conversion Guidebook, Vol. 4: Fuels; IAEA-TECDOC-643 / International Atomic Energy Agency. Wien, 1992. – Forschungsbericht

[Ihl75] Ihle, P., Politzky, H. M. Mahlang, S.: Experimentelle und rechnerische Untersuchungen zum Betriebsverhalten des Brennelementes des HFR Grenoble / Kernforschungszentrum Karlsruhe. 1975 (KFK-Ext. 7/14-1). – Forschungsbericht

[Jun06] Jungwirth, R.: *Thermische und elektrische Leitfähigkeit von hochdichten Uran-Molybdän-Kernbrennstoffen*, Technische Universität München, Diplomarbeit, 2006

[Jun07] Jungwirth, R., Schmid, W. Wieschalla, N.: Thermal conductivity of heavy-ion-bombarded U-Mo/AL dispersion fuel. In: *Proceedings on the 11th International Topical Meeting in Research Fuel Management (RRFM) 2007, Lyon*, 2007

[Jun10] Jungwirth, R.: *Private Communication.* 8 2010

[Kad81] Kader, B.A.: Temperature and concentration profiles in fully turbulent boundary layers. In: *International Journal of Heat and Mass Transfer* 24 (1981), S. 1541–1544

[Kak87] Kakaç, S., Aung, W. Shah, R. K.: *Handbook of single phase convective heat transfer.* J. Wiley and Sons, 1987

[Kal] Kalb, J., Steinhilber, T.: *Arbeitsunterlagen zu den Vorlesungen Wärmetransportphänomene und Wärme- und Stoffübertragung*

[Kat93] Kato, M., KLaunder, B.E.: The Modeling of Turbulent Flow Around Stationary and Vibrating Square Cylinders. In: *Proc. 9th Symposium on Turbulent Shear Flows, Kyoto*, 1993, S. 10.4.1–10.4.6

[Ken81] Kenning, D.B.R., DelValle, M. Victor, H.: Full developed nucleate boiling: Overlap of areas of incluence and interference between bubble sites. In: *International Journal of Heat and Mass Transfer* 24 (1981), S. 1025–1032

[Koc95] Kocamustafaogullari, G., Ishii, M.: Foundation of the interfacial area trasport equation and its closure relations. In: *International Journal of Heat and Mass Transfer* 38 (1995), S. 481–493

[Kur91] Kurul, N., Podowski, M.Z.: On the modeling of multidimensional effects in boiling channels. In: *ANS Proc. 27th National Heat Transfer Conference, Minneapolis, MN*, 1991

[law] `http://www.esru.strath.ac.uk/EandE/Web_sites/05-06/marine_renewables/resource/assets/BL.jpg`

[Led38] Ledinegg, M.: Instability of flow during natural and forced circulation. In: *Die Wärme (translated in USAEC-tr-1861)* 61-4 (1938), S. 819–898

[Lee01] Lee, S.H., Park, J.M. Kim, J.C.: An Investigation of the Thermophysical Properties of U-Mo Dispersion Fuel Meats. In: *Proceedings of the 2000 International Meeting on Reduced Enrichment for Research and Test Reactors (Las Vegas, NV)*, 2001

[Lee03] Lee, S.H., Park, J.M. Kim, J.C.: Effect of Heat Treatment on Thermal Conductivity of U-Mo/Al Alloy Dispersion Fuel. In: *International Journal of Thermophysics* 24 (2003), September, Nr. 5, S. 1355–1371

[Lee07] Lee, S.H., Kim, C.K. Park, J.M.: Thermophysical Properties of U-Mo/Al Alloy Dispersion Fuel Meats. In: *International Journal of Thermophysics* 28 (2007), Oct., Nr. 5, S. 1578–1594. `http://dx.doi.org/10.1007/s10765-007-0212-0`. – DOI 10.1007/s10765–007–0212–0

[Lee08] Leenaers, A., Anselmet, M. VanDenBerghe, S.: Irradiation behavior of atomized and ground U(Mo) dispersion fuel. In: *Transactions of RERTR 2008 - 30th International Meeting on Reduced Enrichment for Research and Test Reactors, 5 - 9 October, 2008*, 2008

[Lem05] Lemmon, E. W., Friend, D.G. McLinden, M. O.: Thermophysical Properties of Fluid Systems. In: *NIST Chemistry WebBook, NIST Standard Reference Database Number 69* (2005)

[Lem09] Lemieux, C.: *Monte Carlo and Quasi-Monte Carlo Sampling.* Springer, 2009

[Li,04] Li, Y., Tu, J.Y. Yeoh, G.H.: Numerical investigation of static flow instability in a low-pressure subcooled boiling channel. In: *Heat and Mass Transfer* 40 (2004), March, Nr. 5, S. 355–364

[Mac94] MacFarlane, R.E., Muir, D.W. ; Los Alamos National Laboratory (Hrsg.): *The NJOY Nuclear Data Processing System.* USA: Los Alamos National Laboratory, 10 1994

[McK94] McKinney, G.W.: Theory Related to the Differential Operator Perturbation Technique / Los Alamos National Laboratory. 1994 (X-6:GWM-94-124). – Forschungsbericht

[McK09] McKinney, G.W.: *Private communication.* 3 2009

[McL67] McLain, H.A.: HFIR Fuel Element Steady State Heat Transfer Analysis Revised Version (ORN-TM-1904) / Oak Ridge National Laboratory. 1967. – Forschungsbericht

[Men] Menter, F.: *CFD Best Practice Guidelines for CFD Code Validation for Reactor-Safety Applications (Contract No. FIKS-CT-2001-00154)*

[Men93a] Menter, F.R.: Multiscale model for turbulent flows. In: *24th Fluid Dynamics Conference. American Institute of Aeronautics and Astronautics*, 1993

[Men93b] Menter, F.R.: Zonal two-equation k-omega turbulence model for aerodynamic flows, AIAA Paper 1993-2906 / AIAA. 1993. – Forschungsbericht

[Men98] Menter, F.R.: Two equation eddy viscosity turbulence models for engineering applications. In: *AIAA Journal* 32 (1998), Nr. 8, S. 1598–1605

[Men03] Menter, F.R., Langtry, R. Kuntz, M.: Ten Years of Industrial Experience with the SST Turbulence Model. In: *Turbulence, Heat and Mass Transfer 4* (2003)

[Mer00] Merker, G. P., Baumgarten, C.: *Fluid- und Wärmetransport, Strömungslehre.* B. G. Teubner, 2000. – ISBN 3–519–06385–9

[Mik69] Mikic, B.B., Rohsenow, W.M.: A new correlation of pool walking data including the fact of heating surface characteristics. In: *ASME Journal of Heat Transfer* 91 (1969), S. 245–250

[Mir59] Mirshak, S., Towell, R.H. Durant, W.S.: DP-355: Heat flux at Burn-Out / Savannah River Laboratory, USA. 1959. – Forschungsbericht

[Mor89] Moritz, U.: Absicherung des Tea-Stabilitätskriteriums für hohe Wassergeschwindigkeiten (Notiz 54.07747.5) / Interatom. 1989. – Forschungsbericht

[Mos99] Mosteller, R., Little, R. C.: Impact of MCNP Unresolved Resonance Probability Table-Treatment on Uranium and Plutonium Benchmarks. In: *Sixth International Conference on Nuclear Criticality Safety*, 1999, S. 552–531

[Mos4] Mosteller: *Validation of Monteburns for MOX fuel using ariane experimental results.* M&C 2003 Technical Program, 2003 4

[mul10] multigrid.org: *Fast poisson solvers.* `http://ccma.math.psu.edu/ccma-wp/?page_id=237`. Version: 11 2010

[njo] *Understanding NJOY99: RECONR: Linearization and Unionization.* `http://t2.lanl.gov/njoy/reco02.html`. – Download on 2009-03-09

[Nor70] Norris, R. H.: *Augmentation on convective heat and mass transfer.* ASME, 1970

[Oer03] Oertel, H.jr., Laurien, E.: *Numerische Strömungsmechanik.* Vieweg, 2003

[Olh62] Olhoeft, J.E.: The Doppler Effect for a Non-Uniform Temperature Distribution in Reactor Fuel Elements, WCAP-2048 / Westinghous Electric Corporation, Atomic Power Division. 1962. – Forschungsbericht

[Ond88] Ondrejcin R.S.: Corrosion of Aluminum at the Savannah River Plant. In: *Report of the ANS Aluminum Cladding Corrosion Workshop*, 1988

[Owe63] Owen, D.B.: Factors for one-sided tolerance limits and for vaiables sampling plans (SCR 607) / SCR. 1963. – Forschungsbericht

[Pal06] Palancher, H., Sabathier, C. Martin, P.: Heavy Ion Irradiation as a Method to Discriminate Research Reactor Fuels. In: *Proceedings on the 'International Conference on Research Reactor Fuel Management RRFM 2006', May 04, 2006, Sofia*, 2006, S. 99–103

[Pel08] Pelowitz, D.B. ; Los Alamos National Laboratory (Hrsg.): *MCNPX Users Manual: Version 2.6.0.* Los Alamos National Laboratory: Los Alamos National Laboratory, 4 2008

[Pel10] Pelowitz, D.B.: MCNPX 2.7.C Extensions, LA-UR-10-00481 / Los Alamos National Laboratory. 2010. – Forschungsbericht

[Per04] Perrot, L., Méplan, O.: *ENDF2ACE User Guide*, 9 2004

[Pet79] Petukhov, B. S.: Heat tranfer and friction in turbulent pipe flows with variable physical properties. In: *Advances in heat transfer* 6 (1979), S. 503–564

[Pet08] Petry, W., Röhrmoser, A.: UMo full size plate irradiation experiment IRIS-TUM - a progress report. In: *RRFM 2008*, 2008

[Pod09] Podowski, M.Z.: Recent Developments in the Modeling of Boiling Heat Transfer Mechanisms. In: *The 13th International Topical Meeting on Nuclear Reactor Thermal Hydraulics (NURETH-13)*, 2009

[Pol09] Polifke, W., Kopitz, J.: *Wärmeübertragung: Grundlagen, analytische und numerische Methoden.* Pearson Studium, 2009

[Pos99] Poston, D.L., Trellue, H.R.: *User's Manual, Version 2.0 for MONTEBURNS Version 1.0, LA-UR-99-4999*, 9 1999

[Pou10] Pounders, J.M., Farzad, R.: Moment-Conserving Histopolating B-Splines for Continous Tally Estimation. In: *PHYSOR 2010 - Advances in Reactor Physics to Power the Nuclear Renaissance*, 2010

[Pre07] Press W. H., Teukolsky S. A.: *Numerical Recipes in FORTRAN, Third Edition.* Cambridge University Press, 2007. – ISBN 978–0–511–33555–6

[Pri09a] Primm, T., Freels, J.D. Chandler, D.: Design Study for a Low-Enriched Uranium Core for the High Flux Isotope Reactor, Annual Report for FY 2008 / Oak Ridge National Laboratory (ORNL); High Flux Isotope Reactor. 2009 (ORNL/TM-2009/87). – Forschungsbericht

[Pri09b] Primm, T., Freels, J.D. Ruggles, A.: Evaluation of HFIR LEU Fuel Using the COMSOL Multiphysics Platform / Oak Ridge National Laboratory (ORNL); High Flux Isotope Reactor. 2009 (ORNL/TM-2008/188). – Forschungsbericht

[Pri10] Primm, T., Freels, J.D. Chandler, D.: Design Study for a Low-Enriched Uranium Core for the High Flux Isotope Reactor, Annual Report for FY 2009 / Oak Ridge National Laboratory (ORNL); High Flux Isotope Reactor. 2010 (ORNL/TM-2009/313). – Forschungsbericht

[Ran52] Ranz, W.E., Marshall, W.R.: Evaporation from drops. In: *Chemical Engineering Progress* 48 (1952), S. 141–148

[Res92] Rest J.: Mechanistic Model for the Irradiation Performance of Intermetallic Dispersion Fuel for the ANS / Argonne National Laboratory. 1992. – Forschungsbericht

[Res95] Rest J., Hofman G.L. Snelgrove J.L.: DART Model for Thermal Conductivity of U3Si2 Aluminum Dispersion Fuel / Argonne National Laboratory. 1995. – Forschungsbericht

[Röh] Röhrmoser, A.: *Private communication*

[Röh84] Röhrmoser, A.: *Untersuchungen zur Kühlbarkeit eines neuartigen Kompaktkerns für Forschungsreaktoren*, Technische Universität München, Diplomarbeit, 6 1984

[Röh90] Röhrmoser, A.: OPA-112: Reaktivitätsbilanz, regelstabcharakteristik und Abbrandzyklus des Kompaktkerns KKE7 bei 20MW / Fakultät für Physik E21, Technische Universität München. 1990. – Forschungsbericht

[Röh91a] Röhrmoser, A.: *Neutronenphysikalische Optimierung und Auslegung eines Forschungsreaktors mittlerer Leistung mit Zielrichtung auf einen hohen Fluß für Strahlrohrexperimente*, Technische Universität München, Diss., 1991

[Röh91b] Röhrmoser, A.: Verifizierung der Rechenergebnisse für die 2d-Darstellung der Kompaktkernanordnung des FRM-II / ZWE-FRM-II. 1991. – Forschungsbericht

[Röh04] Röhrmoser, A.: OPA-306: Leistungsdichteverteilung FRM-II unter Einbezug experimenteller Tankeinbauten / Gamma-Signal der Messeinrichtung die inbetriebsetzung / Forschungsneutronenquelle Heinz Maier-Leibnitz, Technische Universität München. 2004. – Forschungsbericht

[Röh05] Röhrmoser A., Wieschalla, N. Petry W.: Reduced Enrichement Program for the FRM-II, Status 2004/05. In: *Transaction of the 9th International Topical Meeting on Research Reactor Fuel Management (RRFM)*, 2005

[Röh06] Röhrmoser A., Petry W.: Reduced enrichment program for FRM II, actual status and a principal study of monolithic fuel for FRM II. In: *Transaction of the 10th International Topical Meeting on Research Reactor Fuel Management*, 2006

[Röh07] Röhrmoser, A., Boulcourt, P. Petry, W.: Status of UMo full size plates irradiation program IRIS-TUM. In: *Proceedings of the RRFM - IGORR 2007, March 11 - 15, 2007, Lyon*, 2007

[Röh08] Röhrmoser, A., Boulcourt, P. Petry, W.: UMo full plate size irradiation experiment IRIS - TUM - a progress report. In: *Transactions of the RRFM 2008, Hamburg, Germany, March 2008*, 2008

[Röh09] Röhrmoser, A., Petry, W.: Fuel plate temperatures during operation of FRM II. In: *RRFM 2009*, 2009

[Röh10a] Röhrmoser, A.: Core Model of new German Neutron Source FRM II. In: *Nuclear Engineering and Design* 240 (2010), 6, Nr. 6, S. 1417–1432. `http://dx.doi.org/10.1016/j.nucengdes.2010.02.011`. – DOI 10.1016/j.nucengdes.2010.02.011

[Röh10b] Röhrmoser, A.: FRM II, New Burnup Calculations. In: *Proceeding of RERTR 2010*, 2010

[Röh10c] Röhrmoser, A.: FRM II, new Burnup Calculations. In: *RERTR 2010*, 2010

[Röh10d] Röhrmoser, A., Petry, W.: Swelling at the fuel edges of irratiated research reactor plates and derivation of a minimum fuel burn up area for qualification. In: *RRFM 2010*, 2010

[Ric11] Richardson, L.F.: The approximate arithmetical solution by finite differences of physical problems including differential equations, with an application to the stresses in a masonry dam. In: *Philosophical Transactions of the Royal Society of London* A210 (1911), S. 307–357. http://dx.doi.org/10.1098/rsta.1911.0009. – DOI 10.1098/rsta.1911.0009

[Ric27] Richardson, L.F., Gaunt, J.A.: The deferred approach to the limit. In: *Philosophical Transactions of the Royal Society of London* A226 (1927), S. 299–349. http://dx.doi.org/10.1098/rsta.1927.0008. – DOI 10.1098/rsta.1927.0008

[Rog94] Rogers, J.T., Li, J-H.: Prediction of the onset of significant void in flow boiling of water. In: *ASME Journal of Heat Transfer* 116 (1994), S. 1049–1053

[Roh73] Rohsenow, W. M., Hartnett, J. P.: *Handbook of Heat Transfer*. McGraw-Hill, 1973

[Rub08] Rubinstein, R.Y., Kroese, D.P.: *Simulation and the Monte Carlo Method*. Wiley-VCH, 2008

[San09] Santamarina, A., Blaise, P. Bernard, D.: The JEFF-3.1.1 Nuclear Data Library: JEFF Report 22, Validation Results from JEF-2.2 to JEFF-3.1.1 / NEA Data Bank. 2009. – Forschungsbericht

[Sar11] Sarvas, J.: *Optimisation of High Density Fuel Elements for FRM II*, Technische Universität München, Diplomarbeit, 2011

[Sch91] Schmidt, J.W.: Positive, monotone, and S-convex C1-histopolation on rectangular grids. In: *Computing* 47 (1991), S. 87–96

[Sch10] Schmid, W.: *Construction of a sputtering reactor for U-Mo fuel coating and tailored sample production*, Technische Universität München, Diss., 2010

[Sec] http://t2.lanl.gov/njoy/gasp01.html

[Sev09] Several: *Discussion concerning lost particles on MCNP mailing list*. 2009

[Shi08] Shim, H.J., Joo, H.G. Park, H.J.: Uncertainty Propagation in Monte Carlo Depletion Analysis. In: *International Conference on the Physics of Reactors "Nuclear Power: A Sustainable Resource"*. Casion-Kursaal Conference Center, Interlaken, Switzerland, September 14-19 2008

[Shu06] Shultis, J.K., Faw, R.E. ; Dep. of Mechanical and Nuclear Engineering, Kansas State University (Hrsg.): *An MCNP Primer*. Manhattan, KS 66506: Dep. of Mechanical and Nuclear Engineering, Kansas State University, 2006

[Sie93] Siemens/TUM: *Sicherheitsbericht der Neutronenquelle München FRM-II*, 10 1993

[Smi08] Smirnov, P.E., Menter, F.R.: Sensitization of the SST turbulence model to rotation and curvature by applying the Spalart-Shur correction term / ANSYS Germany. 2008. – Forschungsbericht

[Sne87] Snelgrove, J.L., Hofman, G. L. Domagala, R.F.: The Use of U3Si2 Dispersed in Aluminium in Plate-Type Fuel Elements for Research and Test Reactors / Argonne National Laboratory. 9700 South Cass Avenue, Argonne, Illinois 60439, 10 1987 (ANL/RERTR/TM–11 DE 88 003714). – Forschungsbericht

[Spa97] Spalart, P.R., Shur, M.: On the sensitization of turbulence models to rotation and curvature. In: *Aerospace Sci. Tech.* 1 (1997), Nr. 5, S. 297–302

[Sta07] Stacey, W.M.: *Nuclear Reactor Physics*. Second Edition. Wiley-VCH, 2007

[str] http://hmf.enseeiht.fr/travaux/CD0102/travaux/optmfn/gpfmho/01-02/grp6/pages/strouhal.htm

[Tak70] Takahashi H.: Monte Carlo Method for Geometrical Perturbation and its Application to the Pulsed Fast Reactor. In: *Nucl. Sci. Eng.* 41 (1970), S. 259

[Tho10] Thomas, G.S., Maddahi, J.: The technetium shortage. In: *Journal of Nuclear Cardiology* 17 (2010), 8, Nr. 4, 1-6. http://dx.doi.org/10.1007/s12350-010-9281-8. – DOI 10.1007/s12350–010–9281–8

[Tre09] Trellue, H.: *Private communication*. 8 2009

[Tu,02] Tu, J.Y., Yeoh, G.H.: On numerical modelling of low-pressurce subcooled boiling flows. In: *International Journal of Heat and Mass Transfer* 45 (2002), S. 1197–1209

[Uek02] Ueki, T., Brown, F.B.: Stationarity Diagnostics using Shannon Entropy in Monte Carlo Criticality Calculations I: F Test. In: *Trans. Am. Nuc.* 87 (2002), S. 156

[Urb95] Urbatsch, T.J., Prael, R.E. Forster, R.A.: Estimation and Interpretation of k eff Confidence Intervals in MCNP / Los Alamos Laboratory. 1995. – Forschungsbericht

[Wag61] Waggener, J. P.: Friction Factors for Pressure-Drop Calculations. In: *Nucleonics* 19 (1961), Nr. 11

[Wag00] Wagner, W., Dittmann, A. Cooper, J.R.: The IAPWS Formulation 1997 for the Thermodynamic Properties of and Steam. In: *J. Eng. Gas Turbines Power* 122 (2000), Nr. 1

[Wag02] Wagner, W., Pruß, A.: The IAPWS Formulation 1995 for the Thermodynamic Properties of Ordinary Water Substance for General and Scientific Use. In: *J. Phys. Chem. Ref. Data* 31 (2002), Nr. 2

[Wan03] Wantanabe, K.: Revised Release on the IAPS Formulation 1985 for the Viscosity of Ordinatry Water Substance / The International Association for the Properties of Water and Steam. 2003. – Forschungsbericht

[Whi67] Whittle, R., Forgeen, R.: A Correlation for the Minimum in the Pressure Drop Versus Flow-Rate for Subcooled Water Flowing in Narrow Heated Channels. In: *Nuclear Engineering and Design* 6 (1967), S. 89–99

[Whi99] White, M.C., Chadwick, M.B. Littler, R.C.: Photonuclear Physics in MCNP(X). In: *ANS Conference on Nuclear Applications of Accelerator Technology, Long Beach, California*, 1999

[Wie06] Wieshalla, N., Böni, P. Bergmaier, A.: Heavy ion irradiation of U-Mo/Al dispersion fuel. In: *Journal of Nuclear Materials* 357 (2006), Nr. 1-3, S. 191–197. http://dx.doi.org/10.1016/j.jnucmat.2006.06.006. – DOI 10.1016/j.jnucmat.2006.06.006

[Wil97] Wilson, W.B., Herman, M. England, T.R.: Cinder'90 Code for Transmutation Calculations. In: *Conference Proceedings Italian Physical Society*, 1997

[Wil98] Wilcox, D.C.: Re-assessment of the scale determining equation for advanced turbulence models. In: *AIAA Journal* 26 (1998), S. 1414–1421

[Wil04] Wilcox, D.C.: *Turbulence Modeling for CFD*. DCW Industires, Inc., 2004

[Wol09] Wolfshtein, M.: Some comments on turbulence modelling. In: *International Journal of Heat and Mass Transfer* 52 (2009), 8, Nr. 17-18, S. 4103–4107

[X-505] X-5 Monte Carlo Team ; Los Alamos National Laboratory (Hrsg.): *MCNP — A General Monte Carlo N-Particle Transport Code, Version 5*. Los Alamos National Laboratory: Los Alamos National Laboratory, 8 2005

[Yeo04] Yeoh, G.H., Li, Y. Tu, J.Y.: On void fraction distribution during two-phase boiling flow instability. In: *International Journal of Heat and Mass Transfer* 47 (2004), S. 413–417

[Yeo06] Yeoh, G.H., Tu, J.Y.: Numerical modelling of bubbly flows with and without heat and mass transfer. In: *Applied Mathematical Modelling* 30 (2006), S. 1067–1095

[Zei97] Zeitoun, O., Shoukri, M.: Axial void fraction profile in low pressure subcooled flow boiling. In: *International Journal of Heat and Mass Transfer* 40 (1997), S. 867–879

Acknowledgement

The number of people I'd like to thank is large. They all contributed to this work, everybody in his own way.

Prof. Petry for giving me the possibility to do this work, especially for giving me the necessary freedom and confidence to set-up and develop the system all on my own.

Prof. Macián-Juan for many good advices and the possibility to use the NTech equipment for my first experiments.

Dr. Anton Röhrmoser for the supervision, all the lengthy discussion and for pointing out all the subtle mistakes that happened during the course of this work.

The people at Oak Ridge National Laboratory for their help, for making it possible for me to go there and for their warm welcome, namely Kelly Beierschmid, Ronald Croane, Trent Primm and James Freels.

My colleagues, Christian Bogenberger, Lea Canella, Rosmarie Hengstler-Eger, Rainer Jungwirth, Jürgen Sarvas, Robert Schenk, Wolfgang Schmid and Tobias Zweifel for the enjoyable time in the office.

Franz Wagner, for all the things he has done for me and for the productive teamwork at MedApp. Also from MedApp, Michael Jungwirth and Marta Gonzalez.

A number of other people, Prof. Klaus Böning, Dr. Anton Kastenmüller, Elisabeth Jörg-Müller, Silvia Valentin-Hantschel, Jörg Pulz, Fillipo Pellacani and many others for stories, computers, help and 'all the other stuff'.

My Family for their support, no matter when and where. Without them, it would have been much, much harder to complete this work.

And last but not least, but most important, Nathalie Munnikes ♡.

Index

X^2 , 109

Additive Correction, 74
Automatic Near-Wall Treatment, 69
automatic wall functions, 67

Beryllium Follower, 139
Boussinesq Approximation, 63
BSL, 297
BSL model, 65
buffer layer, 67
bulk viscosity, 57
Burn-Up, 33

CDF, 297
Cell, 10
Cell-Importance, 10
central limit theorem, 9, 19
CFD, 297
CFX, 277
Cinder90, 34
cladding, 1
CLT, 297
CNY, 277, 297
conservation equation, 60
Continuity Equation, 55
coordinate system
    involutes, 250
Courant number, 75
Courant-Friedrichs-Lewy condition, 75
covariance matrix, 22
criticality constant, 21
Criticality cycle, 10
Cross Section, 12, 277
Cycle Neutron Yield, 277
cycle neutron yield, 143

Delaunay triangulation, 97
Departure from Nucleate Boiling, 52
Differential Operator Technique, 23
discrete ordinate method, 9
DOC, 297
DOE, 297
DOM, 9, 297
DTS, 297
DU, 297

ENDF, 277
Energy Cutoff, 17
Energy Equation, 55, 57
energy equation, 59
Energy Splitting, 17
Enrichment, 277
error
    relative, 18
errors
    discretisation, 114
        spatial, 114
        time, 115
    iteration, 115
    solution, 114
evolute, 249
exchange quantity, 63
expected value, 18
Explanation of Symbols, 291
Exponential Transform, 17

Favre average, 61
Figure of Merit, 19
fluctuating quantity, 62
Flux Density, 278
Flux density
    spectral, 278
FOM, 297
Forced Collisions, 17
Fourier's law, 59
FPD, 297
Free Gas Model, 14
friction factor, 50
fsi, 297
FSource, 109
Fuel Element, 1

General Grid Interface, 98
GGI Connection, 98

heat equation, 45
heat flux density, 45
heat transfer coefficient, 48
heating number, 90
HEU, 297
HFIR, 1
HFR, 1
History, 10
Hydraulic diameter, 47
hydraulic diameter, 99

Incomplete Lower Upper, 73
Interactions, 11
Involute, 249

Jacobian, 252
Jacobian matrix, 295

K-ϵ Model, 64
K-ω Model, 65
Kármán constant, 68
Kármán Vortex Street, 125
KCODE, 10
kinematic turbulent viscosity, 64
Knudsen number, 64

LEU, 297
List of Abbreviations, 297
logarithmic layer, 67
Low Re-model, 234

Maximum-Likelihood-Approach, 21
MC, 297
MCC, 9, 297
MCNP, 278
MCNPX, 278
    Modifications, 257
Mesh tally, 10
MEU, 297
MonteBurns, 35
MonteBurns eXtended, 258
Multigrid solver, 73
MUSIG, 77

NatU, 297
Navier Stokes Equation, 55–57
Near-Total-Cross section, 15
Neutron Temperature, 278
NJOY 99, 15
no-slip condition, 61
Nusselt Number, 48

OFI, 297
ONB, 51, 297
Onset of Flow Instability, 51, 52
Onset of Nucleate Boiling, 51, 52
Onset of Significant Voiding, 51
Origen, 35
ORNL, 1
orthogonality angle, 141
OSV, 297

Particle Splitting, 16, 17
particle weight, 10
PDF, 297
Perturbation Theory, 23
Prandtl Number, 48

reaction cross section, 12
relative roughness, 50
residual, 73
Reynolds Number, 47
reynolds number, 99
Reynolds pressure, 63
Reynolds Stress Model, 67
Reynolds Stress Tensor, 63
Reynolds transport theorem, 55
Rough Wall, 69
RS, 297
Russian Roulette, 17

S(α,β), 13
sand grain roughness, 69
Scalable Wall Functions, 68
scalable wall functions, 67
Segment, 10
sensitivity analysis, 22
Shannon Entropy, 23
similitude theory, 47
smear, 125
Source Entropy, 22
specific dissipation, 65
specific enthalpy, 62
specific turbulent dissipation rate, 99
SSG Model, 67
SST, 297
SST Model, 65
stochastic interpolation, 15
Stokes law, 57
stress tensor, 56
strong law of large numbers, 18
Strouhal number, 125

Tally, 10
thermal conductivity, 45
thermal diffusivity, 45
thin surface, 107
Time Cutoff, 17

Time Splitting, 17
total enthalpy, 62
Track, 10
Turbulence, 61
turbulence energy, 99
turbulence intensity, 63, 99
turbulence length scale, 99
Turbulence Model, 63
turbulent dissipation, 64
turbulent frequency, 65
turbulent kinetic energy, 63
Turbulent Prandtl number, 64
turbulent pressure, 64
turbulent thermal conductivity, 64
turbulent thermal diffusivity, 64
turbulent viscosity, 63

UMo, 297
Unresolved Resonances, 14

variance, 18
Variance of the Variance, 19
Variance Reduction, 16
viscous sublayer, 67
vortex shedding, 125
VOV, 297

Wall Functions, 67
wall shear stress velocity, 68
wall unit, 68
weight, 10
Weight Cutoff, 17
Weight Window, 17
Weighted Temperatures, 16
Wilcox K-ω model, 65